Boron-Based Conjugated Materials: Structural Analysis, Photophysical Properties, and Redox Chemistry

Kelsie E. Wentz

B.S. Chemistry, West Virginia Wesleyan College, 2017

A Dissertation presented to the Graduate Faculty
of the University of Virginia in Candidacy for the degree of

Doctor of Philosophy

Department of Chemistry

University of Virginia

April 2022

Abstract

Artificial lighting serves as a fundamental necessity to the daily lives of the global population, and consumes around 20% of universal energy production. Although significant progress has been made to the design, fabrication, and synthesis of blue light emitting diodes (LEDs) since their first discovery in the 1990s, the efficiency and quality of these light sources has yet to reach a limit. As an advancement to inorganic LEDs, organic light emitting diodes (OLEDs) produce thinner and more flexible display technologies. Therefore, increasing attention in both the synthetic and materials chemistry communities has been dedicated towards the synthesis of new molecular scaffolds for application in OLED technologies. Boron-based molecules are some of the most promising and highlight the importance of heteroatom-doping in new OLED structures. Due to its inherent electrophilicity, the inclusion of neutral boron moieties into carbon-based materials entirely perturbs the overall electronics of the system and transforms the molecules into much better electron acceptors. In chapter one, an overview of strategies for developing novel main-group materials is highlighted, and relevant seminal discoveries are detailed.

The work highlighted in this dissertation spans a five-year effort to further understand and expand the known chemistry of *p*-block element-based polycyclic aromatic hydrocarbons. Chapter two of this dissertation focuses on the synthesis and characterization of pyrene-fused N-heterocyclic germylenes (NHGe). These extremely twisted and bent NHGes laid the preliminary synthetic foundation for our subsequent studies on luminescent N-heterocyclic boranes featured in chapter three. The tunability of their fluorescence color designates these fused NHBs as promising candidates for functional main-group materials.

While electron deficient boron-based compounds are quite common, nucleophilic species are exceedingly rare, and the majority are highly reactive. However, with the optimum conditions,

anionic species can be stabilized and their reactivity can be harnessed as powerful nucleophiles in synthetic chemistry. Chapter four of this dissertation details the challenging synthesis and structural characterization of 9-carbene-9-borafluorene monoanions. Notably, we prepared six novel carbene-coordinated borafluorene monoanions via two electron chemical reduction of their corresponding neutral tetracoordinate starting materials. Furthermore, the 9-carbene-9-borafluorenes were demonstrated to react as nucleophiles with metal halide substituents. Alternatively, when the borafluorene anions are introduced to diketones, the carbene ligands are displaced and new boron-based spirocycles are accessed. In chapter five, the redox chemistry of the borafluorene monoanions was probed with elemental selenium which resulted in the formation of new boryl-substituted selenides and diselenides, many of which resulted from 2,6-diisopropylphenyl migration.

Chapter six of this dissertation focuses on expanding the structural and electronic tuning of the 9-carbene-9-borafluorene monoanions by modulation of the cation-boron distances. When encapsulating the potassium cations with chelating ligands, the electron rich-ness of the boron center is increased. Therefore, unique optical properties of novel spirocycles can be accessed by introducing the charge-separated 9-carbene-9-borafluorene monoanions to diketones. Reaction modelling via density functional theory supports the formation of the spirocycles to proceed via a single-electron transformation from the boron atom to the diketone, thus demonstrating the ambiphilic nature of the 9-carbene-9-borafluorene monoanions. Furthermore, chapter seven details the activation of carbon dioxide by a 9-carbene-9-borafluorene monoanion which produces the novel trioxaborinanone. Remarkably, photolysis or thermolysis of the trioxaborinanone releases carbon monoxide and a fluorescence response is turned on.

Copyright Information

Chapters Two–Seven contain modified versions of published work which have been reproduced in accordance with the American Chemical Society Journal Publishing Agreement, John Wiley and Sons Publication Agreement, and Royal Society of Chemistry Publication Agreement. Proper citation for each chapter is given below and on the first page of each of the chapters within this thesis.

Chapter Two.

Krantz, K. E.; Weisflog, S. L.; Yang, W.; Dickie, D. A.; Frey, N. C.; Webster, C. E.; Gilliard, R. J., Extremely twisted and bent pyrene-fused N-heterocyclic germylenes. *Chem. Commun.* **2019,** *55*, 14954-14957.

https://doi.org/10.1039/C9CC08703F

Chapter Three.

Krantz, K. E.; Weisflog, S. L.; Frey, N. C.; Yang, W.; Dickie, D. A.; Webster, C. E.; Gilliard Jr., R. J., Planar, Stair-Stepped, and Twisted: Modulating Structure and Photophysics in Pyrene- and Benzene-Fused N-Heterocyclic Boranes. *Chem. Eur. J.* **2020,** *26*, 10072-10082.

https://doi.org/10.1002/chem.202002118

Chapter Four.

Wentz, K. E.; Molino, A.; Weisflog, S. L.; Kaur, A.; Dickie, D. A.; Wilson, D. J. D.; Gilliard Jr., R. J., Stabilization of the Elusive 9-Carbene-9-Borafluorene Monoanion. *Angew. Chem. Int. Ed.* **2021,** *60*, 13065-13072.

https://doi.org/10.1002/anie.202103628

Chapter Five.

Wentz, K. E.; Molino, A.; Freeman, L. A.; Dickie, D. A.; Wilson, D. J. D.; Gilliard, R. J., Reactions of 9-Carbene-9-Borafluorene Monoanion and Selenium: Synthesis of Boryl-Substituted Selenides and Diselenides. *Inorg. Chem.* **2021,** *60*, 13941-13949.

https://doi.org/10.1021/acs.inorgchem.1c02124

Chapter Six.

Wentz, K. E.; Molino, A.; Freeman, L. A.; Dickie, D. A.; Wilson, D. J. D.; Gilliard, R. J., Systematic Electronic and Structural Studies of 9-Carbene-9-Borafluorene Monoanions and Transformations into Luminescent Boron Spirocycles. *Submitted.*

Chapter Seven.

Wentz, K. E.; Molino, A.; Freeman, L. A.; Dickie, D. A.; Wilson, D. J. D.; Gilliard, R. J., Activation of Carbon Dioxide by 9-Carbene-9-Borafluorene Monoanion: Carbon Monoxide-Releasing Transformation of Trioxaborinanone to Luminescent Dioxaborinanone. *Manuscript in Preparation.*

Acknowledgements

Throughout my undergraduate and graduate career, I have been incredibly fortunate to receive support, assistance, and guidance from many people.

First, I acknowledge those who helped me get to a position where I could pursue a degree in chemistry. Thank you to Mr. Gear, my first high school chemistry teacher who taught me the basics and encouraged me to continue in science. I also thank all the many other memorable science and math teachers, Mr. Ramsey, Mrs. Grose, Mrs. Sinsel, Mrs. Mergenthaler, and Mrs. Ludlow who all helped me prepare and apply to West Virginia Wesleyan College.

While at Wesleyan, I was surrounded by extremely talented professors and mentors who I will forever appreciate. To Prof. Ed Wovchko, thank you for your constant support and encouragement of me to seek a graduate degree. I will never forget your witty sense of humor that showed all throughout analytical and physical chemistry lectures, and how many of your early mornings you sacrificed for office hours when I was the only one to show up. Your basket of Reese's cups always motivated me to work on physical chemistry problem sets at 8:00 am in the dead of WV winters. To Prof. Katy Lambson, thank you for teaching me the foundations of organic chemistry, giving me an amazing first summer research experience, for being a wonderful mentor, and a special Highland dancer friend. To Prof. Joanna Webb, I cannot thank you enough for everything you have done for me over the years. You were the first chemistry professor I had at Wesleyan and are the reason I went on to study inorganic chemistry. Thank you for being an all-around amazing professor, research advisor, mentor, and friend to me. I am especially grateful that I have been able to receive supportive emails, text messages, and zoom calls from you even after I have moved on to graduate school. Although you are a mom of three, wife, professor, department chair, and flower business owner, you still made time for me whenever I needed anything. It is because of you I chose UVA and saw potential in myself to pursue a Ph.D.

After nervously moving to a new location, Charlottesville quickly became a welcoming place to call home during my graduate career because of the special people I have been blessed to meet. To my Covenant Church family, thank you for welcoming me from day one with open arms and giving me the love that I needed to get through some of the tougher parts of graduate school. To Pastor Bare, we immediately connected because you too had gone to UVA for your Ph.D., and you and Laila were the new family I needed when I moved here. I will always cherish your birthday phone calls, warm hugs on Sundays, dinners at the Bare Den, and timely messages to strengthen my walk with Christ. To Lori-Ann Strait and the Ladies Life group, thank you for our special Wednesday Bible studies, fellowship nights, endless prayers, and encouraging texts. You all made my time here in Charlottesville amazing and really hard to move on from.

During my time in the UVA Chemistry department there were numerous people who helped me on a day-to-day basis with various tasks that made it easier for me to focus on research. To Susie Marshall, Seth Matula, Eddie Byers, Ed DeBary, Jerry Shifflet, Mike Birckhead, and Danny Via, thank you for your constant support to me as a graduate student. Without the help of many of you, the Gilliard lab would never have been set up as fast as it was. I appreciate all the encouraging

emails shared, smiles when passing in the hall (before COVID of course), and supportive conversations while picking up a bottle of acetone from the stockroom.

The Gilliard lab was very fortunate early on, to have helpful lab neighbors in the Gunnoe lab who sacrificed time helping us learn how to run departmental equipment, and allowing us to borrow essential lab glassware and tools when necessary. I am especially thankful for Drs. Nichole Leibov and Xiaofan Xia for all they did as senior mentors to me. The tenacity to drop everything they were doing to come next door to assist with something, and the time they invested in helping me prepare for my candidacy exam was unmatched and I am extremely grateful for them. Nichole and Xiaofan were two of the first friendly faces I became acquainted with in the department, and even moved around their offices so the first members of the Gilliard lab could have desk space.

To Kaeleigh Olsen, the best friend I never knew I needed, but God knew a special person like you was essential in order for me to survive graduate school. From the first time I met you at the visitation weekend for perspective students in March of 2017, I knew you were someone friendly who was anxious about starting a graduate program – just like me! Little did I know that simple thing would be just one of the many traits we had in common. Fortunately, the first day of TA training, I saw you sitting at a desk and was immediately relieved to see a familiar face in the room. From that day forward, an incredible friendship developed. We pressed on through classes, teaching, starting research projects, and candidacy together. You were always someone I could count on for a quick hall chat, coffee walk, study session, presentation practice, exercise, laughter, or whatever I needed at the time. From planning the Chemistry Department retreat together, being inseparable at all department events, getting called by each other's names, and you being there for me when I married my best friend, we have so many special memories together that I will forever cherish. My graduate school experience certainly would not have been what it was without you. I am so thankful to have met you and know that I have made a lifelong friend.

Thank you to all the ladies within the department (Abigail, Annika, Haleigh, Hannah, Zoë, Kim, Emma, Anna, and Amelia) for your ongoing support and fun nights we shared together to destress. To all those in our prayer group (Josh, Perrin, AC, Kim, Caleb, and Emma), I am so grateful for our Wednesday morning fellowship and time together in Christ. Those mornings were a vital part in making sure my weeks were centered and focused on God so I could do my best work in lab.

I owe so much gratitude to Dr. Wenlong Yang and Dr. Wilson Wang, the first postdocs I worked closely with in the Gilliard lab. You two sacrificed so much of your personal time to teach me every lab technique I needed to know to be able to work independently on my research project. I am especially grateful for Wenlong, your support of me was so evident and you helped me gain confidence in myself that I lacked when first starting graduate school. Thank you Wenlong for being the encouraging postdoc while I was going through candidacy. I could always rely on you to help me with a reaction, EndNote, or just to chat in the office about science. You were a very special mentor to me and helped me publish my first paper!

Sarah Weisflog, the first undergraduate student I was given the privilege of mentoring in lab, I am so proud of how far you have come and what you are doing now. Without you working with me, it would have taken me so much longer to get my pyrene chemistry off the ground. Thank you for

diligently making me grams upon grams of the starting materials we needed for my first project. You helped me become more confident in myself through teaching you how to run reactions, and explaining to you what drives certain compounds to the desired products. I know you will do exciting things in your career if you just keep working hard!

I was very fortunate to have amazing collaborators during my time in the Gilliard group. Thank you, Profs. Edwin Webster and David Wilson for your insightful discussions and guidance on my research projects. I cannot thank Dr. Diane Dickie enough for her constant help running crystals and solving their disordered structures. To Andrew Molino, you are an excellent theoretical chemist and it was a pleasure getting to work with you. Nathan Frey, thank you for all of your contributions to the pyrene chemistry we worked on together. I am so proud of all of your accomplishments and know you will do excellent work in the Gilliard group.

Thank you to my committee members Profs. Charles Machan, Dean Harman, Sen Zhang and Guarav Giri for being supportive to my success as a graduate student. I am grateful for your time invested in me during your courses I was enrolled in, and willingness to give helpful suggestions towards my research project.

To all the previous and current members of the Gilliard gang, each and every one of you made coming to lab every day for 5 years a fun and productive environment to do awesome science. Jacob and Luke - we did it!! From day one we went through everything together and I would not have made it to the end if it was not for your constant encouragement and friendship. We have so many funny memories (some no one else will understand) and good times spent together that I will treasure for a lifetime. Luke, I especially thank you…? for starting my severe coffee addiction, and Jacob, you always knew what to say or do to make me laugh without even trying. Working with you both was so much fun and I could not have asked for better colleagues in you two! To AC I will really miss coming into lab to hear you belting out your favorite song, or see you dancing when doing the base bath. Thank you for being an exceptional friend and supportive lab mate to me since you joined. Kim, I was thrilled when you joined the Gilliard lab, because I could see so much potential in you and wanted you as a lab mate. Thankfully you were not just a lab mate to me, but you quickly became an office mate, glovebox buddy, hood neighbor, and close friend. Our silly conversations, weekly coffee walks, Slack memes (that often got us in trouble in meetings), and chemistry discussions were such an important part to my last 3 years of graduate school. I am so proud of how well you are doing in your research and know you will discover so many new molecules! Caleb, thank you for your random facts to break up the monotonous days of graduate school, and for your super friendly "HELLOs" every morning. Eric, thank you for your unwavering support, encouragement, and compliments every day in the office. You are a very kind lab mate and always know what to say to make someone feel good. Haleigh and Levi, I always enjoyed your baked goods, and office chats when a short break was warranted. Drs. Josh Barker, Chunlin Deng, and Samir Sarkar, you three have brought a tremendous amount of talent to our group and I am so glad our time overlapped. Thank you for stepping up as postdocs and always helping when needed. I know you all will be successful chemists and I look forward to following your projects through upcoming publications.

To my Ph.D. advisor Prof. Robert Gilliard (I guess I can start calling you Robert now?) – thank you for taking me on as one of your very first graduate students. It was truly an incredible journey from day one of opening ChemGlass boxes to where we are now – thriving! For a while, I thought my Ph.D. would be in box cutting. My graduate school experience could not have been any better and I have you to thank for that. When I first met you at visitation weekend, I had no clue what Main-Group chemistry was, and to be honest I still did not quite understand after talking to you at your poster why you would not just use transition metals. I remember anxiously emailing you after the weekend was over about potentially joining your lab, and it was your response that made me decide to come to UVA. Everything in that email that you promised me I would gain from being in your lab came true over the course of 5 years. Thank you for ALWAYS making time for a quick reaction discussion, responding to an urgent message at any hour of the day, having patience with me as I learned new things, and never ceasing to provide me another letter of recommendation. I am especially grateful that you saw potential in me from day one and encouraged me through tough projects so that I could enjoy the rewards of seeing my name on a paper to finally prove that I did it! My time in your lab was so much fun and all that we accomplished together was so fulfilling. Thank you for not only being a research mentor, but for providing career guidance and life lessons that will carry me for many years.

Outside of the lab and UVA chemistry department, I was blessed with an entire family support system cheering me on along the way. To my parents, thank you for your consistent guidance, advice, financial support, and encouragement during my childhood that has carried me far in my young adult life. I am so grateful for all that you two have provided for me and sacrificed over the years so that I was always given more than what I needed to excel. Thank you for always answering my distressed phone calls at any time of day to reassure me that even in the midst of my crises, that everything will be ok and it was not going to be the end of the world. Dad, I am especially thankful for your glowing support of me that is so evident to anyone that meets you. Given that your office door is plastered with my research publications/pictures, and that you proudly wear your Gilliard lab t-shirt I gifted you, I never had to wonder if you were proud of my accomplishments. Mom, thank you for at least pretending to understand my research when I explained it to you. I would not have made it through graduate school without calling you to tell you everything and get your input. Thank you for keeping all my secrets safe that Prof. Gilliard told me not to tell anyone. To my sisters (Mary and Tessa), I am so appreciative that our friendship has not wavered at all even though I have moved farther away. You two have always been just a text message away, and regularly made time when I needed a sister weekend getaway. To my Grandma, I will forever cherish our biweekly phone calls, and all the fun stories you have shared with me. Your support of my education and future career has been so obvious to me. To my In-Laws (Rosemary and Gene), thank you for your ongoing support of my graduate studies and for always sending me home with chocolate.

Finally, I thank my loving husband (Scott) for his endless support and encouragement of my life's aspirations. It has been an incredible journey starting graduate school with you by my side, and getting married in the midst of a global pandemic. Thank you for never ceasing to make me laugh, and showing me that it is essential to take time to relax every now and then. You have been the constant to my life over the past five years when graduate school was a wave of ups and downs. I especially appreciate that you have always been genuinely interested in my research and made sure you were able to tell others what I am working on. You have helped me through the hardest days, and celebrated with me during the best ones! I am so proud of your recent acceptance to medical school and am more than ready to reciprocate to you the support you gave me during my graduate school experience.

Dedication

This thesis is dedicated to my grandfather.

In loving memory,

Keith L. Krantz, Ph.D.

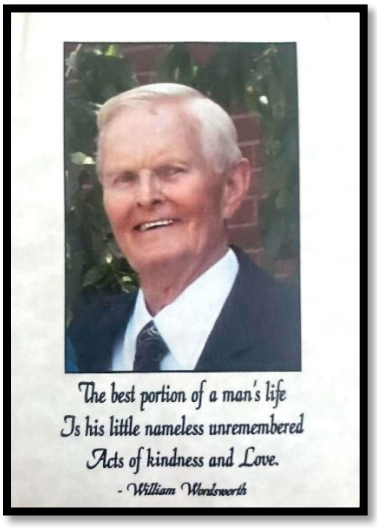

Thank you, Grandpa, for instilling in me an appreciation and love for education from a very young age. I am especially grateful for your persistent encouragement of me to go out of my comfort zone and do the "harder" things in life, to go the extra mile for others, and to pursue what I love. It is because of you; I was inspired to diligently work towards a Ph.D.

Table of Contents **Page**

List of Abbreviations

Au	gold
B	boron
BFA	borafluorene monoanion
BF	borafluorene
Br	bromine
Cl	chlorine
Ge	germanium
H	hydrogen
K	potassium
Li	lithium
Na	sodium
O	oxygen
P	phosphorus
Se	selenium
Å	angstrom
°C	degrees celsius
C_6D_6	deuterated benzene
CAAC	cyclic(alkyl)(amino) carbene
Cp	cyclopentadienyl
DFT	density functional theory
EDA	energy decomposition analysis
HOMO	highest occupied molecular orbital
LUMO	lowest unoccupied molecular orbital
TD-DFT	time dependent-density functional theory
IPr	1,3-bis(2,6-diisopropylphenyl)imidazolin-2-ylidene
K	Kelvin
KC_8	potassium graphite
kcal	kilocalorie

kJ	kilojoule
LiNp	lithium naphthalenide
MeCN	acetonitrile
MeCN-d_3	deuterated acetonitrile
mol	mole
M	molarity
NBO	natural bond orbital
nBuLi	*n*-butyllithium
NHB	N-heterocyclic borane
NHC	N-heterocyclic carbene
NHGe	N-heterocyclic germylene
nm	nanometer
OLED	organic light emitting diode
OFET	organic field effect transistor
OPV	organic photovoltaic
PAH	polycyclic aromatic hydrocarbon
PPh_3	triphenyl phosphine
ppm	parts per million
sIPr	1,3-diisopropylimidazolin-2-ylidene
SET	single-electron transfer
THF	tetrahydrofuran
THF-d_8	deuterated tetrahydrofuran
UV-vis	ultraviolet-visible

List of Figures

Figure 1.10. Molecular structures of neutral tetracoordinate and radical tricoordinate borafluorenes (top). Reaction solutions depicting the tunable colors of the radical species that are dependent on the carbene ligand (bottom).

Figure 2.1. a) Twisted pyrene by incorporation of bulky silyl substituents; b) Tethered substituents to produce a bent pyrene; c) Planar, pyrene-fused bis-carbene; d) This work: Extremely twisted pyrene-fused germylene.

Figure 2.2. a) Pyrene-fused NHGe, b) view showing non-planarity of both the pyrene linker and N-heterocycle, and c) view down N atoms depicting twist angles. Thermal ellipsoids shown at 50% probability and H atoms were omitted for clarity. Selected bond lengths (Å) and angles (°): Ge1–N1: 1.871(3); Ge1–N2: 1.868(3); C1-C2-C8-C9: 49; N1-N2-N3-N4: 64.

Figure 2.3. Molecular structure of **2.3**: a) cis-sIPr coordinated NHGe, b) top view with C_6D_6 molecule, c) sIPr side view, and d) crystal packing view with Me—sIPr centroid interaction. Thermal ellipsoids shown at 50% probability and H atoms were omitted for clarity. Selected bond lengths (Å) and angles (°): Ge1–N1: 1.9430(14); Ge1–N2: 1.9489(14); Ge1–C21: 2.1321(18); N4–C21: 1.359(2); N3–C21: 1.356(2); C2-C1-C2'-C1': 5; N2-N1-N2'-N1': 7; C21-Ge1-Ge1'-C21': 15.

Figure 2.4. UV-vis absorption spectra of **2.1**-**2.3** in toluene at room temperature.

Figure 2.5. LUMO (top) and HOMO (bottom) orbital representations of **2.2** and **2.3** depicting the delocalization on pyrene.

Figure 3.1. a) Pyracene-fused *N*-heterocyclic borane with redox properties; b) boryl-linked tetraazaolefin that oxidizes to the radical cation; c) methylated benzene-fused bis(diazaborole) d) This work: neutral pyrene- and benzene-fused *N*-heterocyclic boranes featuring structural distortions and luminescent properties.

Figure 3.2. Molecular structure of **3.2**: a) front view, b) side view. Thermal ellipsoids shown at 50% probability and H atoms (except B-H) were omitted for clarity. Selected bond lengths (Å) and angles (°): B1–H1: 1.15(3); B1–N1: 1.421(7); B1–N2: 1.433(7); C2–C1–C2′–C1′: 40; N2–N1–N2′–N1′: 52.

Figure 3.3. Molecular structure of **3.3**: a) front view, b) side view. Thermal ellipsoids shown at 50% probability and H atoms were omitted for clarity. Selected bond lengths (Å) and angles (°): B1–F1: 1.335(4); B1–N1: 1.419(5); B1–N2: 1.423(5); C1–C2–C1′–C2′: 0; N1-N2-N1′-N2′: 0, C3–C2–C1–C7: 20.

Figure 3.4. Molecular structure of **3.4**: a) front view, b) side view. Thermal ellipsoids shown at 50% probability. H atoms and co-crystallized solvent were omitted for clarity. Selected bond lengths (Å) and angles (°): B1–C21: 1.573(4); B1–N1: 1.453(4); B1–N2: 1.448(5); C1–C2–C1′–C2′: 0; N1–N2–N1′–N2′: 0, C3–C2–C1–C7: 28; C22–C21–B1–N2: 60.

Figure 3.5. Molecular structure of **3.6**: a) front view, b) view showing planarity of benzene. Thermal ellipsoids shown at 50% probability and H atoms except for boron bound H were omitted for clarity. Selected bond lengths (Å): B1–H1: 1.140(17); B1–N1: 1.426(2); B1–N2: 1.426(2); N1–C2: 1.4166(18); C1–C2: 1.395(2); C1–C3′: 1.398(2).

Figure 3.6. Molecular structure of **3.7**: a) front view, b) view showing planarity of benzene. Thermal ellipsoids shown at 50% probability and H atoms were omitted for clarity. Selected bond lengths (Å): B1–F1: 1.3906(12); B1–F2: 1.3853(12); B1–N1: 1.5690(13), B1–N2: 1.5678(13), C1–N1: 1.3266(11); C1–C2: 1.3968(12); C1–C3′: 1.5062(12).

Figure 3.7. Molecular structure of **3.8**: a) front view, b) view showing planarity of benzene. Thermal ellipsoids shown at 50% probability and H atoms were omitted for clarity. Selected bond lengths (Å) and angles (°): B1–N1: 1.4436(19), B1–N2: 1.440(2), B1–C12: 1.609(6); C13–C12–B1–N1: 93.

Figure 3.8. Molecular structure of **3.9**: a) front view, b) view showing planarity of benzene. Thermal ellipsoids shown at 50% probability and H atoms were omitted for clarity. Selected bond lengths (Å): B1–N1: 1.439(7), B1–N2: 1.460(7), B1–C12: 1.589(8).

Figure 3.9. a) UV-vis absorption of **2.1, 3.2-3.4**; b) emission of **2.1, 3.2-3.4**; c) UV-vis absorption of **5-9**; d) emission of **6-9**. All samples were dissolved in toluene and ran at room temperature. Compounds **2.1, 3.2-3.4** were excited at 380 nm and **3.5-3.9** were excited at 310 nm.

Figure 3.10. Molecular structure of **3.11**: a) front view, b) side view. Thermal ellipsoids shown at 50% probability and H atoms were omitted for clarity. Selected bond lengths (Å) and angles (°): B1–C15: 1.5669(19); B1–N1: 1.4291(18); B1–N2: 1.4272(18); C1–C2–C1′–C2′: 0; N1–N2–N1'–N2': 0, C3–C2–C1–C7: 11; C22–C21–B1–N2: 49.

Figure 3.11. a) UV-vis absorption of **3.10** and **3.11**; b) emission of **3.10** and **3.11**. Samples were dissolved in toluene and run at room temperature. Compound **3.10** was excited at 365 nm and **3.11** was excited at 380 nm.

Figure 4.1. a) Reported boryl anions with cation contacts; b) hydrogen atom abstraction under reducing conditions; c) borafluorene dianion; and d) Lewis base-stabilized borafluorene monoanions (this work).

Figure 4.2. Molecular structures of CAAC-BF-anions [**4.3** (a), **4.4** (b), **4.5** (c)] and NHC-BF-anions [**4.6** (d), **4.7** (e), **4.8** (f)]. Thermal ellipsoids shown at 50% probability and H atoms were omitted for clarity.

Figure 4.3. Solid state structures of **4.5** (a) and **4.8** (b) depicting polymeric and cyclohexameric structures.

Figure 4.4. Plot of HOMO of (a) $[NHC\text{-}BF]^-$ and (b) $[CAAC\text{-}BF]^-$. EDA-NOCV deformation densities (c) $\Delta\rho(1)$ and (d) $\Delta\rho(2)$ associated with orbital interactions $\Delta E_{orb}(1)$ and $\Delta E_{orb}(2)$ for $[NHC\text{-}BF]^-$. Charge flow red→blue (isosurface = 0.003).

Figure 4.5. Bonding models considered for EDA, a) Singlet fragment donor-acceptor model, b) Triplet fragment electron-sharing model.

Figure 4.6. Calculated isotropic out-of-plane $NICS(1)_{ZZ}$ values (ppm) at the B3LYP-D3(BJ)/def2-TZVP level of theory.

Figure 4.7. ACID plots of (a) $[NHC\text{-}BF]^-$ and (b) $[NHC\text{-}Borole]^-$ (isosurface = 0.03).

Figure 4.8. Molecular structures of reactivity products of **9-12** (a-d respectively). Thermal ellipsoids shown at 50% probability and H atoms were omitted for clarity. Selected bond lengths [Å] and angles [°]: **4.9**: B1–Au1 2.223(6), P1–Au1 2.2969(13), B1–Au1– P1 164.85(16); **4.10**: B1–Ge1 2.2079(10); **4.11**: B1–Se1 2.103(6), Se1–C35 1.926(5); **4.12**: B1–Au1 2.184(3), P1–Au1 2.3361(7), B1–Au1– P1 175.04(8).

Figure 4.9. Molecular structures of **4.13** (a) and **4.14** (b). Thermal ellipsoids shown at 50% probability and H atoms were omitted for clarity. Selected bond lengths [Å]: 13: B1–O1 1.5103(15); B1–O2 1.5156(15); O1–C13 1.3796(14); O2–C20 1.3801(14); C13–C20 1.3565(16); 14: B1–O1 1.52(3); B1–O2 1.57(3); O1–C13 1.42(2); O2–C14 1.35(2); C13–C14 1.30(3).

Figure 4.10. Normalized absorption (solid) and emission (dashed) spectra of **4.13** (red) and **4.14** (blue). Solutions were dissolved in THF and ran at room temperature. Compound **4.13** was excited at 410 nm and compound **4.14** was excited at 370 nm.

Figure 5.1. a) PhSe–SePh cleavage by N-heterocyclic gallyl anion; b) reaction of diboraanthracene dianion with Se_2Ph_2; c) activation of elemental selenium by diazaborinine; d) synthesis of a group 13 metal analogue of CO containing an Al=Se multiple bond.

Figure 5.2. Digital images of the samples of single-crystals: a (**5.2**); b (mixture of **5.2** (orange) and **5.3** (colorless)); c (**5.4**); d (**5.5**); e (**5.6**); f (mixture of **5.2** (orange) and **5.5** (red)). Crystals of **a-e** are magnified by 40x on an optical microscope while **f** is not magnified.

Figure 5.3. Molecular structures of **5.2-5.6** (**a-e**, respectively). Thermal ellipsoids set at 50% probability with H atoms and non-coordinated solvent omitted for clarity.

Figure 5.4. Molecular structures of **5.7** (a) and **5.8** (b). Thermal ellipsoids set at 50% probability with H atoms omitted for clarity.

Figure 5.5. Calculated relative free energies (ΔG, kJ mol^{-1}) for the reaction of **4.5** and elemental selenium at the RI-SCS-MP2/def2-TZVP//B3LYP-D3(BJ)/def2-SVP (SMD, Toluene) level of theory.

Figure 5.6. Plots of the HOMO (a) and HOMO-1 (b) of **5.5**. Deformation densities $\Delta\rho$ (c) and (d) of the pairwise orbital interactions for the electron-sharing model of **5.5**. The direction of charge flow for the deformation densities is red → blue. Associated interaction energies given in kcal mol^{-1}. Only the α-pair is shown, see ESI for β-pair. Hydrogen atoms omitted for clarity.

Figure 6.1. a) Examples of structurally unique cyclic boryl anions; b) Borafluorene-based spirocycles obtained from 9-carbene-9-borafluorene monoanion and diketones; c) Frustrated Lewis pair-stabilized boracyclic radicals.

Figure 6.2. Plots of the electrostatic potential (ESP) of **6.1** (a) and **6.3** (b), B3LYP-D3(BJ)/TZ2P (COSMO, THF), isosurface from -2.5e-2 (red) to +8.0e-2 (blue). Plot of the calculated isotropic ^{11}B nuclear shielding of **6.1** with respect to BF--$K(THF)_3$ distance (TPSSh/pcSseg-2 (CPCM, THF)) (c).

Figure 6.3. Molecular structures of **6.1** (a), **6.2** (b), **6.3** (c), and **6.4** (d). Hydrogen atoms omitted for clarity and thermal ellipsoids shown at 50% probability. Selected bond lengths [Å]: **6.1**: B1–C1 1.505(3), B1–C23 1.609(2), B1–C34 1.598(3), B1–K1 3.2363(19); **6.2**: B1–C1 1.519(7), B1–C23 1.586(8), B1–C34 1.617(8), B1---K1 5.911(6); **6.3**: B1–C1 1.495(2), B1–C23 1.601(2), B1–C34 1.616(2) B1---K1 6.891(2); **6.4**: B1–C1 1.504(3), B1–C23 1.607(3), B1–C34 1.600(3), B1---K1 8.095(2).

Figure 7.1. a) Boron nucleophiles react with CO_2 to form borylcarboxylic acid; b) CO_2 capture by Frustrated Lewis Pairs; c) activation of CO_2 by nonpolar double multiple bonds; d) *This Work*: synthesis of trioxaborinanone by borafluorene monoanion activation of CO_2, and elimination of CO to form the fluorescent dioxaborinanone.

Figure 7.2. Molecular structures of **7.2** (a) and **7.3** (b). Hydrogen atoms omitted for clarity and thermal ellipsoids shown at 50% probability. Selected bond lengths [Å]: 2: B1–O1 1.478(4), B1–O3 1.535(3), C1–O1 1.350(3), C1–O2 1.410(3), C2–O2 1.351(3), C2–O3 1.298(3), C2–O4 1.210(3), C1–C3 1.340(4); 3: B1–O2 1.5429(18), B1–O3 1.4746(17), C1–O1 1.2223(17), C1–O2 1.3113(16), C1–C2 1.5517(18), C2–O3 1.3945(16).

Figure 7.3. Calculated relative free energies (ΔG, kJ mol^{-1}) for the reaction of **6.1** with CO_2 to form **7.2** at the B3LYP-D3(BJ)/def2-TZVP//B3LYP-D3(BJ)/def2-SVP (SMD, Toluene) level of theory. All thermochemical values computed at 298.15 K and 3.4 atm.

Figure 7.4. Plots of the reactant fragment orbitals for **TS1** (a) and (b). Plot of the deformation density $\Delta\rho_{(1)}$ (c) indicating charge flow between NOCVs for TS1 and the associated contribution to the total orbital interaction ($\Delta E_{(1)}$, kJ mol^{-1}). Eigenvalue $v_{(1)}$ quantifies the amount of transferred electron density (red: charge depletion, blue: charge accumulation), isosurface = 0.001.

Figure 7.5. Normalized absorption (solid line) and emission (dashed line) spectra of **3**. Solutions were dissolved in THF and ran at room temperature, and excited at 300 nm.

List of Schemes

Scheme 5.4. Proposed mechanism for the direct synthesis of **5** (top). Calculated free energies (ΔG, kJ mol^{-1}) relative to reactants (RI-SCS-MP2/def2-TZVP//B3LYP-D3(BJ)/def2-SVP, (SMD, THF)). Reaction of CAAC-borafluorene radical with Se_2Cl_2 in THF also produces **5.5**.

Scheme 6.1. Synthesis of [K][9-carbene-9-borafluorene] complexes (**6.1**-**6.4**).

Scheme 6.2. Displacement of CAAC ligand by 9,10 phenanthrenequinone and 1,10-phenanthroline-5,6-dione to form spirocyclic borafluorenes **6.5** and **6.6**.

Scheme 7.1. Reaction of 1 with CO_2 yields new 6-membered trioxaborinanone (**7.2**). Heating a solution of **7.2** releases CO and produces 5-membered dioxaborinanone (**7.3**).

List of Tables

Chapter One: Introduction and Overview

1.1 Overview of Main-Group Materials Chemistry

Situated on the outer edges of the periodic table, main-group elements have predominantly been the focus of fundamental research for the past 150 years.[1] However, in the past two decades, there has been a tremendous shift towards expanding main-group chemistry into the horizon of advanced materials chemistry. The main-group elements comprise the *s*- and *p*-blocks of the periodic table (Figure 1.1). Due to their inherently different electronic properties, main-group molecules have been shown to adopt unique structures that have given rise to new or unusual bonding modes that are not commonly observed in carbon-based compounds. Many of the early studies on main-group chemistry were exclusively aimed at investigating and further understanding the structure and bonding of such elements.[1] For example, elements below the third row of the periodic table were once believed to not be able to exhibit multiple bonding. However, numerous studies have since shown that heavier main-group elements can demonstrate double and triple bonding.[2-4] Multiple bonding between *p*-block elements is vital for materials applications in order to achieve the extended π-conjugated networks that are necessary for electron transfer. Now that more is known about the main-group elements, researchers in the field are aware that the different structural and bonding environments represent promising targets as functional materials that possess unique electronic features thus leading to significantly enhanced properties.

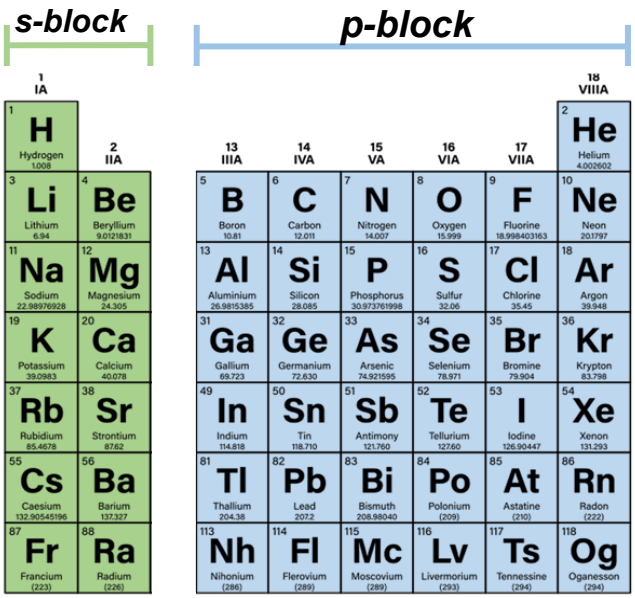

Figure 1.1. Main-group elements that comprise the *s*- and *p*-blocks of the periodic table.

Furthermore, one foundational goal of main-group chemistry research has been the development and discovery of new trends within the groups of the periodic table. Specifically, studies which explore the differences in reactivity, structural geometries, and electronic environments of elements within a certain group are of high interest to synthetic main-group chemists. As an example of this, carbon can be considered an outlier to group 14 since its valence orbitals are very close in size, and therefore hybridize very easily. However, silicon, germanium, tin, and lead all have differently sized valence orbitals thus mixing is more difficult (Figure 1.2).[5-6] Because of this, the lone pair of divalent Si, Ge, Sn, and Pb has high *s*-character and is essentially inert while the lone pair of carbon(II) is highly reactive. Therefore, the empty *p*-orbital on the heavy tetrylenes is more reactive, and can be filled with a donor ligand. Chapter two of this

dissertation focuses on a more detailed discussion of the differences between N-heterocyclic carbenes and germylenes.

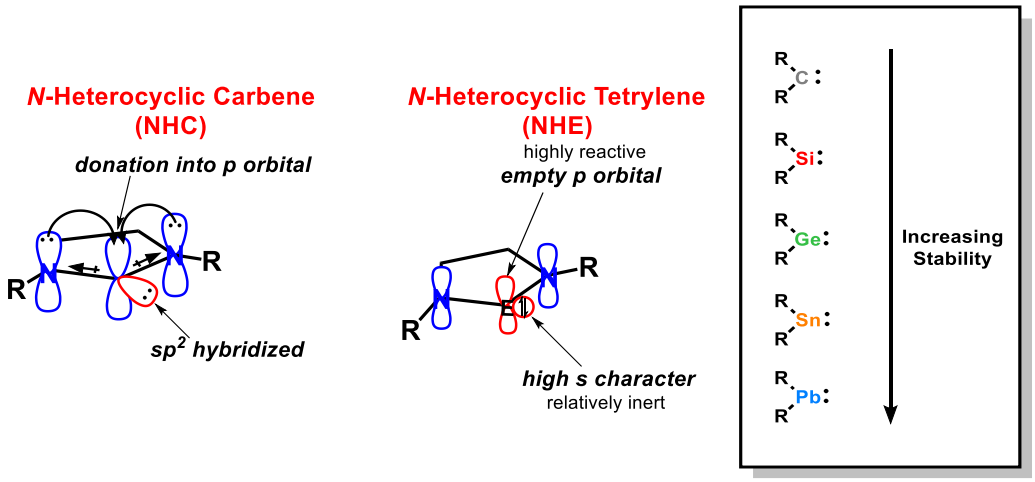

Figure 1.2. Differences in the orbitals and stability of divalent carbon vs heavier group 14 elements.

1.2 Motivation and Strategies for Incorporating Main-Group Elements into Aromatic Systems

Due to the aforementioned drastic differences in electronics and structural properties that can be observed with main-group elements, researchers have been interested in incorporating them into carbon-based aromatic systems.[7-8] The replacement or "doping" of one carbon atom for a different *p*-block element has been shown to dramatically alter the electronic properties of aromatic systems and result in unusual photophysical properties (e.g. phosphorescence, thermally activated delayed fluorescence, aggregation induced emission). Therefore, this strategy of *p*-block element "doping" has been heavily used in synthetic chemistry as a means to access novel molecules for materials applications.[1] For example, Rivard *et. al*. have shown that incorporation of bismuth into a carbon-based heterocycle results in dual emission via fluorescence and phosphorescence promoted by the enhanced spin-orbit coupling available within the excited states of bismuth.[9] While this just represents one example of the photophysical properties that can be achieved with

main-group elements, many other studies exist which feature *p*-block elements within polycyclic aromatic hydrocarbon (PAH) systems.[10] Due to the distinctly different commercially available reagents, "doping" PAH systems with *p*-block elements can be extremely challenging and creative synthetic routes are necessary.

There are three common routes to synthesize main-group element "doped" heterocycles: A) Fagan-Nugent reaction (metallacycle transfer), B) Sn/Si-B exchange, and C) salt elimination via lithiation (Figure 1.3). While other strategies exist for isolating such main-group species, these are the most common within the field. Route A consists of the formation of a zirconium heterocycle bearing cyclopentadienyl (Cp) substituents, and subsequent addition of a main-group halide electrophile (EX_n; E = *p*-block element, X = halide) to yield the new heterocycle.[11-12] Route B is commonly used in boron chemistry for the formation of new boron-based heterocycles, and involves the synthesis of a tin or silicon inorganic ring. The addition of a boron trihalide to the Sn/Si heterocycle then generates the desired boron-based system via elimination of R_2YX_n (Y = Si or Sn).[13-15] In Route C, an initial lithiation takes place at the desired positions for the main-group element placement, and sequential addition of an EX_n reagent eliminates LiX and yields the new heterocycle. Although there are specific benefits to using certain *p*-block elements for particular materials-based applications, this thesis only focuses on the chemistries of germanium and boron.

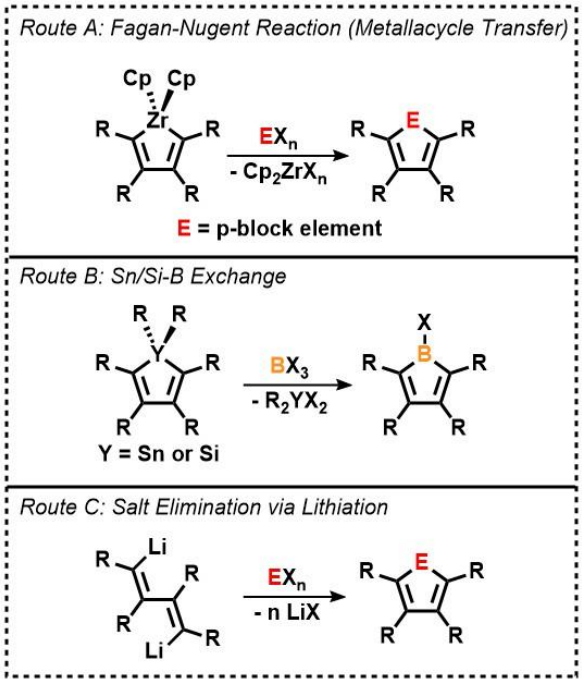

Figure 1.3. Three different routes to synthesizing new *p*-block element containing heterocycles.

1.3 Common Ligands used in Main-Group Chemistry

In main-group chemistry, there are two different carbon-based ligands that are commonly used for stabilizing new molecules. N-heterocyclic carbenes (NHC)[16-20] and cyclic(alkyl)(amino) carbenes (CAAC)[21-23] are both popular strong σ-donor ligands that have been shown to stabilize a plethora of both main-group and transition metal complexes (Figure 1.4). Due to the presence of a quaternary carbon in CAAC ligands instead of the second nitrogen atom, the lowest unoccupied molecular orbitals (LUMOs) of these carbenes are lower, and thus are better π-accepting ligands. The absence of one nitrogen atom decreases the electron donation into the empty *p*-orbital of the carbene carbon and therefore destabilizes the LUMO. In some instances, CAACs have been capable of stabilizing low oxidation state main-group species that NHCs have been unable to.[24-25] These ligands are also highly tunable, and the R-groups can be optimized based on the steric bulk necessary to stabilize the desired low valent species. Although these carbene ligands are less

common in main-group materials chemistry, they were essential for isolating reduced borafluorene species and will be further discussed in chapters four and five of this dissertation.

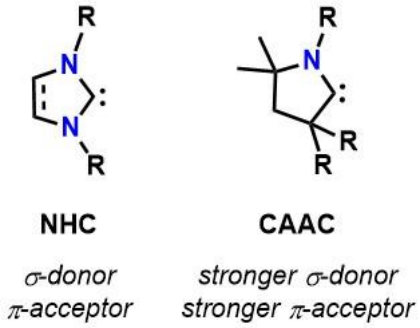

Figure 1.4. Structures of electron donating carbon-based ligands. N-heterocyclic carbene (left) and cyclic(alkyl)(amino) carbene (right).

1.4 Germanium-Based Materials

This subsection describes the importance and motivation for designing novel germanium materials and serves as a brief introduction to chapter two of this dissertation. Due to its semiconducting properties, elemental germanium has been used in a variety of electronic applications including fiber-optic systems, photovoltaics, and light emitting diodes.[26] Germanium has also been widely used as a main-group catalyst for the formation of organic polymers.[27-29] Given the minimal difference in electronegativity between germanium (2.01) and silicon (1.90), in comparison to carbon (2.55) studies on germanium have been limited.[30] Therefore, the high natural abundance and low cost have allowed silicon to be used more extensively for commercial applications. However, there has been an ongoing demand for regulating the electronic properties of organic materials for their specific applications, thus it is important to consider a wide range of elements for tuning the electronic states of functional materials. Given the lower ionization energy of germanium (7.900 eV) than silicon (8.15168 eV) and higher bond dissociation energy of a Ge–

C bond (298 kJ mol^{-1}) than a Si–C bond (290 kJ mol^{-1}), germanium-containing organic heterocycles should be sufficiently stable for materials applications.[1]

Within the last two decades, numerous novel germanium-based heterocycles have been prepared and have had drastically different photophysical properties than their carbon or silicon analogues.[31-33] Rivard *et al.* reported a tetrathienylgermole that displayed enhanced emission via the formation of aggregates in mixed solvents.[34] Moreover, dithienogermoles have proven to be promising targets for photoluminescent materials due to their higher stability. In 2016, Oshita and coworkers synthesized a trimethylsilyl-substituted cyclogermoxane which was highly photoluminescent in solution and as a solid with quantum yields up to 80%. Additionally, it also acts as a nitroaromatic sensor due to its decreased luminescence intensity upon exposure to the aromatic vapors.[35]

While NHCs have been used for a wide range of applications, their heavier analogues, N-heterocyclic germylenes (NHGes) have gained attention in catalysis and supramolecular chemistry due to their stronger π-accepting abilities.[6, 36-39] In order to access different degrees of electron accepting abilities, several types of NHGes have been prepared (Figure 1.5). NHGes of type **A**[40] and **B**[41-42] have one germanium atom available for binding and most closely resemble Arduengo's NHC ligand.[16-17] Bidentate NHGes of type **C**[43] have been shown to be able to bind transition metal chelate complexes. As a means to build extended π-conjugated networks, Hahn *et al*. prepared a rigid ditopic NHGe (**D**).[44] Most recently, Yang and coworkers prepared a triphenylene-based tritopic germylene with three divalent germanium atoms (**E**).[45] Notably, this system could be used to prepare supramolecular materials. While all the aforementioned NHGes with the exception of

type **C** are planar, structurally flexible NHGes are rare. Our work on highly twisted pyrene-fused N-heterocyclic germylenes is described in chapter two of this dissertation.

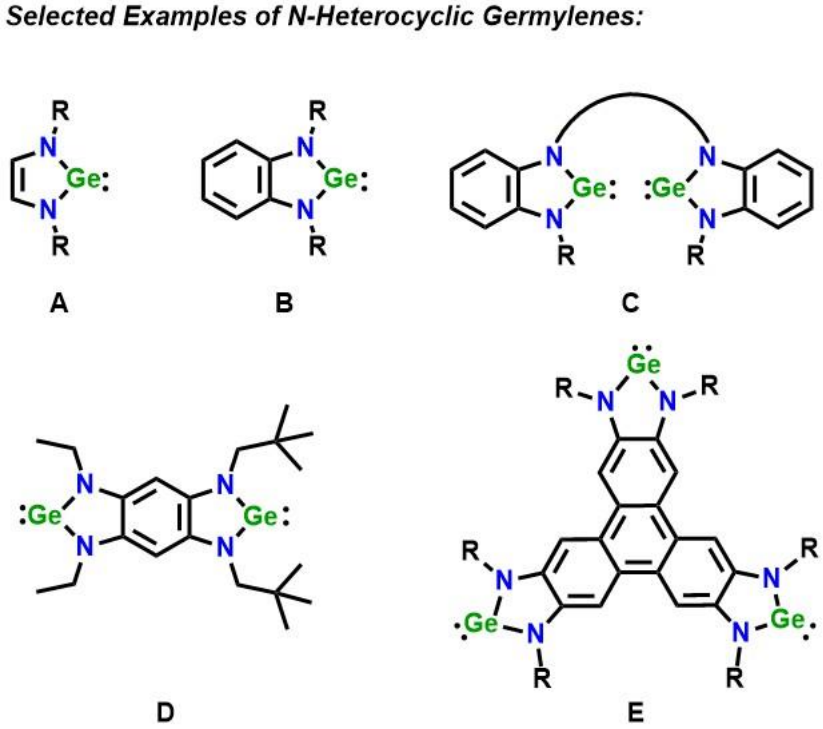

Figure 1.5. Reported examples of mono-, di-, and tri-nuclear N-heterocyclic germylenes.

1.5 Pyrene-Based Materials

This subsection highlights the PAH pyrene, its use in organic electronics, and lays the foundation for our interest in novel pyrene-based main-group materials. In photochemistry, pyrene is the epitome of chromophores for photochemical research due to its unique luminescent properties. Under ambient light, pyrene exists has a yellow crystalline solid, however when irradiated with UV light, pyrene fluoresces blue (Figure 1.6 – right). The modernization of the distillation process of coal tar and the hydrogenation of hard coal has produced large amounts of pyrene, making it readily accessible and inexpensive for commercial use.[46] In addition, the functionalization of pyrene at 1-10 positions has been the focus of many studies and has facilitated

the development of an entire library of pyrene-based organic electronics for uses such as organic light emitting diodes,[47-49] organic field effect transistors,[50] and photovoltaics.[51-52] Positions 1-3 and 6-8 are designated as the "non-K-region" and are easier to modify via electrophilic substitution with the exception of the 2 and 7 positions (Figure 1.6 – left). 1,3,6,8-tetrabromopyrene can be isolated in high yields and used as a precursor to an array of new carbon-functionalized pyrenes by Suzuki or Sonogashira coupling reactions.[53]

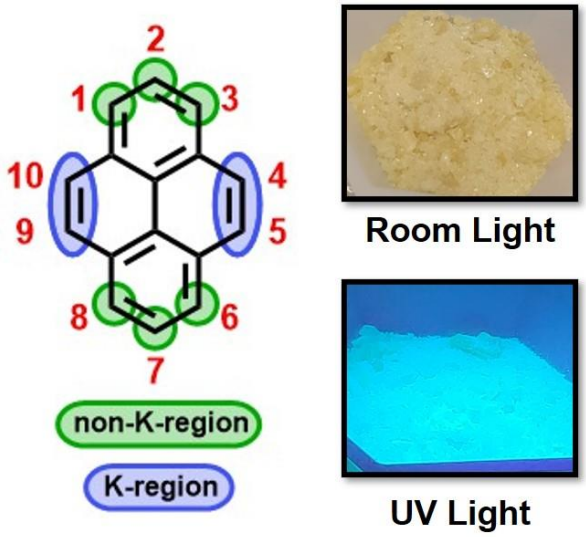

Figure 1.6. Numbering system of pyrene shown in red. The non-K-region and K-region are highlighted in green and blue respectively (left). The color of pyrene under room light and UV light (right).

However, due to the 2- and 7-positions lying within a node, substitution at these positions is more difficult. In an effort to bypass these challenges, pyrene can be reduced to 4,5,9,10-tetrahydropyrene followed by electrophilic substitution and subsequent rearomatization, but these are multistep and low-yielding processes. The 4-, 5-, 9-, and 10-positions of pyrene are considered the "K-region" and are substantially more challenging to functionalize, but are interesting as a means to prepare extended π-conjugated systems. One key route for reaching pyrenes with "K-

region" functionalization involves the oxidation of pyrene by ruthenium(III) chloride and sodium periodate to access pyrene-4,5-dione and pyrene-4,5,9,10-tetraone.[54] An alternative approach to generate 4,5,9,10-functionalized pyrenes is by the protection of the 2- and 7-postitions by *tert*-butyl groups to force bromination at the "K-region".[55-56] This method of substitution was essential for the isolation of the pyrene-fused N-heterocyclic germylenes and boranes discussed in chapters two and three.

1.6 Boron-Based Materials

In this subsection, boron-based materials are introduced, and our motivation for designing the new molecules that are described within chapters three-five of this dissertation are highlighted here. Recently, boron has garnered significant attention from both the synthetic and materials chemistry fields due to its promising properties desirable for electronic applications.[57-61] When boron exists in a tricoordinate state, an empty p_z-orbital is available for accepting electrons and it can then participate in π-conjugation (Figure 1.7).[62-64] Because of this, the replacement of carbon with boron in PAH materials results in lower LUMO levels and renders the system to be better electron acceptors. This is exceptionally useful when designing organic systems which require an electron acceptor moiety for accessing thermally activated delayed fluorescence in organic light emitting diodes.[65-71] In congruence with their electron accepting abilities, boron-based units have been combined with nitrogen-containing electron donor groups to access donor-acceptor materials. BN-doped molecules have been targeted by synthetic chemists due to their B–N bonds being isoelectronic to a C–C bond.[72] Therefore, the replacement of a C–C bond in an organic system with a B–N bond results in the same overall electron valency, however imparts novel photophysical properties on the material.[73-80] Furthermore, boron-based materials have been used

for a variety of other electronic applications including organic field effect transistors,[81-84] sensors,[85-87] and photovoltaics.[88-91]

Figure 1.7. Schematic depicting the empty p_z-orbital of boron accepting electrons.

1.7 Introduction to Borafluorene Chemistry

Herein, the chemistry of borafluorene will be introduced which is the focus of chapters four and five of this dissertation. One key example of an instance when the replacement of a tetracoordinate carbon atom with a tricoordinate boron that results in drastically different photophysics is that of borafluorene. The all-carbon analogue, fluorene, exists as a white solid that emits violet under UV light while borafluorene is a yellow solid that emits a yellow-green color under UV light. Because of its unique photophysical properties, borafluorene has become a popular building block in materials chemistry.[60, 92-97] Borafluorene is an antiaromatic 5-membered ring that is flanked by two phenyl rings (Figure 1.8).[98] From a fundamental standpoint, the chemistry of borafluorene has gained interest due to its existence as an antiaromatic species, and studies which encompass changing its electronics to be more aromatic have been high impact.[99]

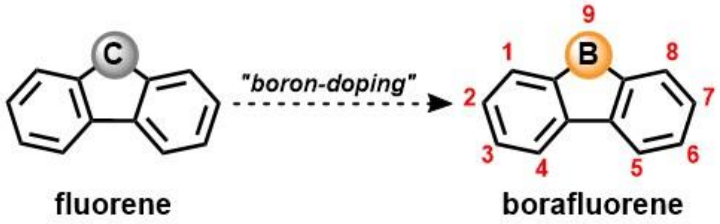

Figure 1.8. Structures of fluorene (left) and borafluorene (right). The numbering of borafluorene is shown in red.

The presence of the empty p_z-orbital on tricoordinate boron species renders them to be exceptionally reactive, and strategies to stabilize these materials are imperative for further understanding the chemistry of borafluorene. One key way to stabilize borafluorene moieties and render them air-stable for photophysical studies is by using a bulky carbon-based group (e.g. 1,3,5-tri-isopropylphenyl or 1,3,5-tri-tert-butylphenyl) to sterically prohibit undesired reactivity from occurring at boron.[96, 100-101] Although these borafluorene species are isolable, they limit other electronic tuning that can be explored because of their sterically crowded boron center. Unlike the tetracoordinate fluorene, borafluorene can accept two electrons from a Lewis base into its empty p_z-orbital and form adducts which display distinctly different luminescent properties than the tricoordinate borafluorenes.[102] This also allows for the stabilization of electron deficient or electron rich borafluorene species due to the kinetic stabilization achieved from filling the *p*-orbital with a donor ligand. The 9-bromo-9-borafluorene is the most commonly used starting material for borafluorene chemistry since it can easily be isolated in high yields via lithiation of 2,2'-dibromo-1,1'-biphenyl and subsequent salt elimination with boron tribromide. In addition, having a halide at the 9-position of borafluorene opens up the potential for many possible reactions to occur at boron.[103] Several studies have also been reported for methods to attach other functional groups (fluorine, methoxy, amine, and thiophene) to the 1-8 positions on the flanking phenyl rings for imparting different degrees of Lewis acidity on the boron center.[101, 104-108]

Borenium ions represent a class of positively charged tricoordinate boron species with the general formula of $[LBR_2]^+$ (L = ligand; R = generic functional group).[63, 109-113] Due to their strong Lewis acidity, borenium ions have been used in chemical synthesis and catalysis.[113-118] Although their electronic properties have been studied in terms of synthesis, the optical properties of borenium ions have only gained attention in recent years.[119-122] The use of neutral two-electron

Lewis bases instead of one-electron covalent carbon-based groups (e.g. 1,3,5-trimethylphenyl or 1,3,5-triisopropylphenyl) as ligands allows for the accessible synthesis of borenium ions. By this strategy, the boron center is both electronically and sterically satisfied, rendering electron-poor boron-based cations isolable. In 2019, Gilliard *et al.* isolated a new class of carbene stabilized borafluorenium ions by halide abstraction from the tetracoordinate borafluorene adducts.[107] The presence of a bulky NHC or CAAC on the 9-bromo-9-borafluorene is essential for stabilizing borafluorene cations (Figure 1.9 – left).[107] Notably, the methoxy substituted 9-carbene-9-borafluorene cation displays thermochromic properties. At room temperature in solution, the cation is red, however at -37 °C the cation turns colorless. This color change is a result of the oxygen atom from the methoxy substituent interacting with the empty p_z-orbital of the boron atom of the borafluorene cation (Figure 1.9 – right). In the case of the borafluorenium heterocycles, they exist as colorful solids that have red-shifted absorption properties from the neutral tetracoordinate carbene-coordinated borafluorene starting materials (Figure 1.9 – left).

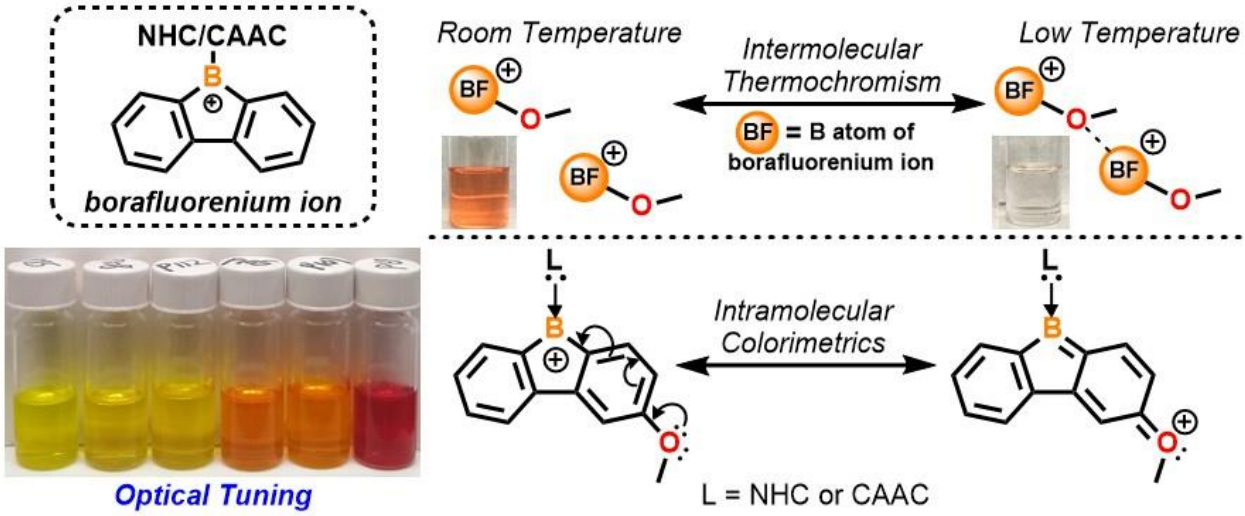

Figure 1.9. Molecular structure and optical tuning of the borafluorenium ions (left); mechanism of thermochromism and colorimetrics observed in the boraluorenium ions (right). The hexafluoroantimonate counteranions are omitted from structures for clarity.

Alternatively, one electron chemical reduction of the neutral tetracoordinate carbene-coordinated borafluorenes with potassium graphite results in stable borafluorene radicals.[123] Notably in this study, the presence of an NHC or a CAAC yields tunable colors of the radical species. The NHC-borafluorene radical is a deep blue color while the CAAC-borafluorene radical is a deep purple color (Figure 1.10). A more detailed discussion on the two-electron reduction chemistry of borafluorene and its reactivity with several substrates can be found in chapters four and five.

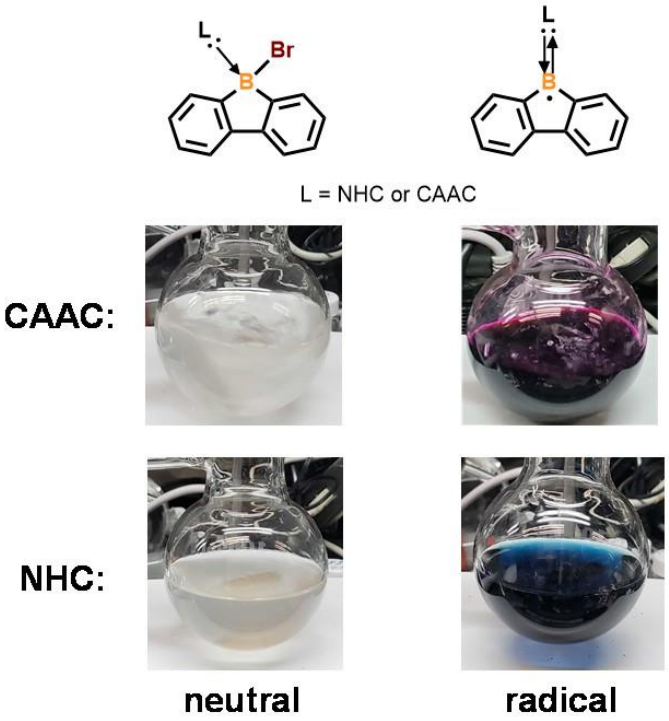

Figure 1.10. Molecular structures of neutral tetracoordinate and radical tricoordinate borafluorenes (top). Reaction solutions depicting the tunable colors of the radical species that are dependent on the carbene ligand (bottom).

Chapter Two: Pyrene-Fused N-Heterocyclic Germylenes

Containing work that was originally published in:

Krantz, K. E.; Weisflog, S. L.; Yang, W.; Dickie, D. A.; Frey, N. C.; Webster, C. E.; Gilliard, R. J., Extremely twisted and bent pyrene-fused N-heterocyclic germylenes. *Chem. Commun.* **2019,** *55*, 14954-14957.

2.1 Introduction to Pyrene-Based Materials

Polycyclic aromatic hydrocarbons (PAHs) have gained significant attention in materials chemistry for their unique photophysical properties useful for organic light emitting diodes (OLEDs),[124] photovoltaics,[124-126] field-effect transistors,[127-128] organic electronics,[129-131] and sensors.[132-133] Pyrene,[46] a highly aromatic molecule comprised of four fused benzene rings, is a ubiquitous building block for synthesizing exceptionally conjugated compounds,[134-137] or polymeric materials.[138-142] While many of these fused-ring systems are planar, nonplanar or twisted conjugated molecules are rapidly emerging due to new applications in nonlinear optics,[143-144] semiconductors,[145] OLEDs,[146] and electronic devices.[147] Notably, twisted molecules have displayed improved stability, enhanced solubility, and provide chiroptical properties[148-149] deeming them versatile in new materials. A new category of distorted ribbon-like PAHs termed pyrene-fused twistacenes have recently been developed and show imminent promise towards incorporation in OLED devices.[150] Twisted pyrene-fused molecules are often characterized by the degree of their torsion angle at the carbon atoms in the K-region of pyrene.[150-151]

Until recent years, the investigation of the electronic properties, utility, and applications of nonplanar aromatic compounds have been limited due to challenging synthetic routes. Several approaches exist for twisting aromatic systems with multiple linearly fused-rings,[151-156] while methods for synthesizing nonplanar pyrene-based molecules of 2-rings or less remains sparse. Although synthetic strategies to yield twisted or bent pyrene-based molecules have been reported, all of the examples are exclusively organic.[153, 157] By incorporating bulky phenyl rings to the silyl substituents on pyrene-fused azaacenes, Mateo-Alonso has established overall twist angles up to 24° (Figure 2.1a).[150, 158] Conversely, Bodwell has developed a strategy of tethering substituents at the 2- and 7-postions on pyrene to produce a negative curve in the structure with bend angles[159] up to 109° (Figure 2.1b).[157, 160] As the number of fused-rings increase, molecules become more

flexible and acenes of 4 or more fused-rings display large twist angles up to 170°.[151-152, 161-162] However, promoting high degrees of structural twisting in PAHs with 3 or fewer linearly fused-rings is rare and highly challenging from a synthetic perspective.

Within the last decade, multinuclear germylenes[40, 44-45, 163] have been isolated, and all conform to a planar molecular geometry. Unlike the strongly σ-donating N-heterocyclic carbenes (NHC), N-heterocyclic germylenes (NHGe) display less nucleophilic character and perform better as electrophiles.[6, 164-165] Owing to the less effective valence orbital overlap between germanium's *s* and *p* orbitals, hybridization is minimal,[5-6] and therefore the electronics at the germanium atom are vastly different from the lighter carbene analogues. Inspired by the pyrene-linked bis-carbene chemistry by Peris,[166] we initially targeted this ligand for coordination to main-group elements (Figure 2.1c). Unfortunately, the free bis-carbene linked by pyrene is not stable and *in situ* deprotonation was necessary for coordination to Rh and Ir. We found this method to be unsuccessful for bis-carbene coordination to a significant number of main-group Lewis acids. We then desired to isolate a stable free "heavy" bis-carbene analogue with germanium instead of carbon (Figure 2.1d).

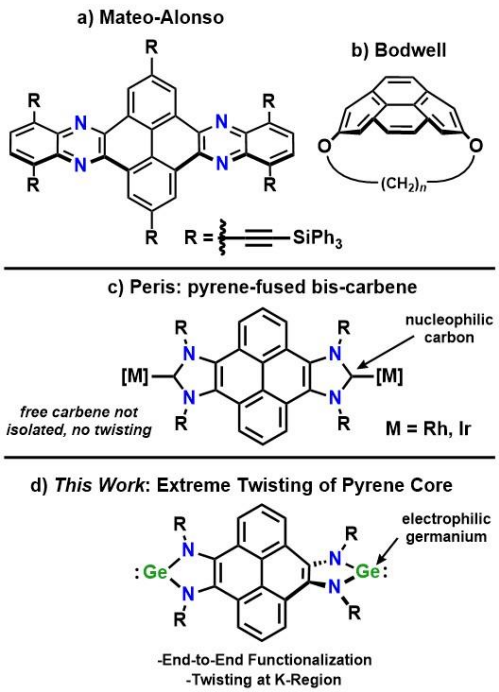

Figure 2.1. a) Twisted pyrene by incorporation of bulky silyl substituents; b) Tethered substituents to produce a bent pyrene; c) Planar, pyrene-fused bis-carbene; d) This work: Extremely twisted pyrene-fused germylene.

Herein we report a new synthetic strategy, molecular structures, and computations of a dual-faced pyrene-fused NHGe. Remarkably, these molecules represent the first examples of highly twisted pyrene-fused germylenes, and they demonstrate the largest reported twist angles spanning only two linearly connected aromatic rings of pyrene.

2.2 Synthesis of Pyrene-Fused N-Heterocyclic Germylene

The starting tetramine (**2.1**) was synthesized using a Buchwald-Hartwig amination.[166] Lithiation of **2.1** with *n*-butyllithium and subsequent salt elimination with germanium dichloride dioxane adduct gave the pyrene-fused germylene (**2.2**) in 75% yield (Scheme 2.1). The ^{1}H NMR spectrum of **2.2** revealed a downfield shift in resonance from 1.26 to 1.85 ppm for the protons on the *N*-(*tert*-butyl) substituents. This can be attributed to a decrease in electronic shielding by the nitrogen-based electrons that are now involved in a π-symmetric interaction with the germanium atoms.

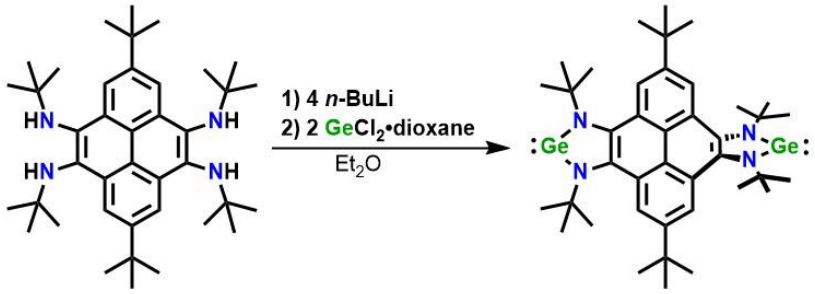

2.1 2.2

Scheme 2.1. Synthesis of highly twisted pyrene-fused N-heterocyclic germylene.

To elucidate the structural properties of compound **2.2** single crystal X-ray diffraction studies were performed. Yellow rod-shaped air- and moisture-sensitive crystals of **2.2** were obtained from a concentrated toluene solution at −37 °C (Figure 2.2a). Surprisingly, both the NHGe rings and the pyrene linker display a severe distortion from planarity (Figure 2.2b). Significantly, twist angles of 49° and 64° were observed for C1−C2−C8−C9 and N1−N2−N3−N4, respectively (Figure 2.2c). The twisting of **2.2** at the pyrene core is completely different than that of **2.1**, which show 0° twist angles. Unfavorable steric interactions between the *N*-(*tert*-butyl) substituents and the hydrogen atoms on pyrene influence the twisting. Notably, the degree of

twisting at the aromatic core with only two linearly fused benzene rings is substantially larger than the longer pyrene-fused azaacenes (twist angles up to 24°).[153, 158, 167]

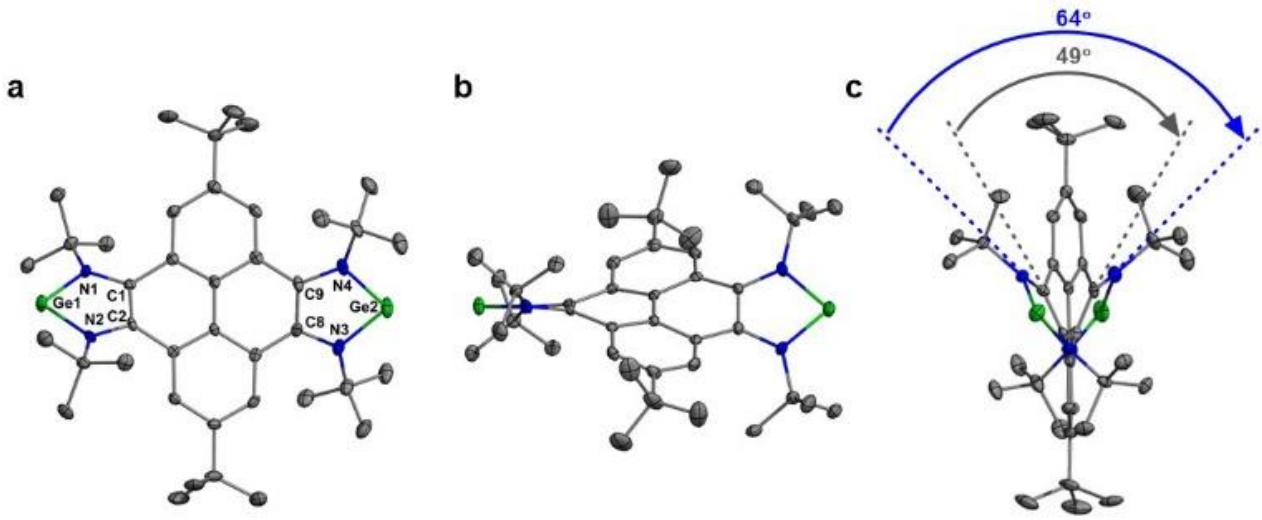

Figure 2.2. a) Pyrene-fused NHGe, b) view showing non-planarity of both the pyrene linker and N-heterocycle, and c) view down N atoms depicting twist angles. Thermal ellipsoids shown at 50% probability and H atoms were omitted for clarity. Selected bond lengths (Å) and angles (°): Ge1–N1: 1.871(3); Ge1–N2: 1.868(3); C1-C2-C8-C9: 49; N1-N2-N3-N4: 64.

In addition, the 64° N1-N2-N3-N4 twist angle is significantly larger than the reported 20-32° angles of phenyl-substituted heptacenes[168] and tetracene diimides.[151, 169] The severe degree of twisting in **2.2** is also much more substantial than the slight bow-shaped distortion observed in the bis-carbene-Ir compound with the same pyrene core.[166] The Ge1–N1 [1.871(3) Å] and Ge1–N2 [1.868(3) Å] bond lengths are within the range of reported Ge–N single bonds (1.833-2.118 Å).[40, 44-45]

2.3 Reactivity of Pyrene-Fused N-Heterocyclic Germylene

Due to the electrophilic nature of the germanium atoms, we were interested in how changes to the electronics would affect the twisting of the pyrene core. Lewis basic trimethyl phosphine

(PMe_3), 1,3-bis(2,6-diisopropylphenyl)imidazol-2-ylidene (IPr),[17] and (2,6-diisopropylphenyl)-4,4-diethyl-2,2-dimethyl-pyrrolidin-5-ylidene (^{Et2}CAAC)[170] were screened as possible donor ligands. However, no coordination to Ge was observed due to weak donor strength or sterics. Thus, the smaller, yet strongly *σ*-donating NHC, 1,3-diisopropyl-4,5-dimethylimidazol-2-ylidene (sIPr), was selected which readily coordinated to the electrophilic Ge atoms to afford compound **2.3** as a yellow solid in 41% yield (Scheme 2.2). In the ^{1}H NMR spectrum, a downfield shift in resonance from 1.85 to 1.99 ppm was observed for the protons on nitrogen bound *tert*-butyl groups. A broad singlet resonance at 6.68 ppm was attributed to the methine protons on the sIPr ligands. The significant downfield shift compared to 3.96 ppm for the free carbene supported coordination to the germylene.

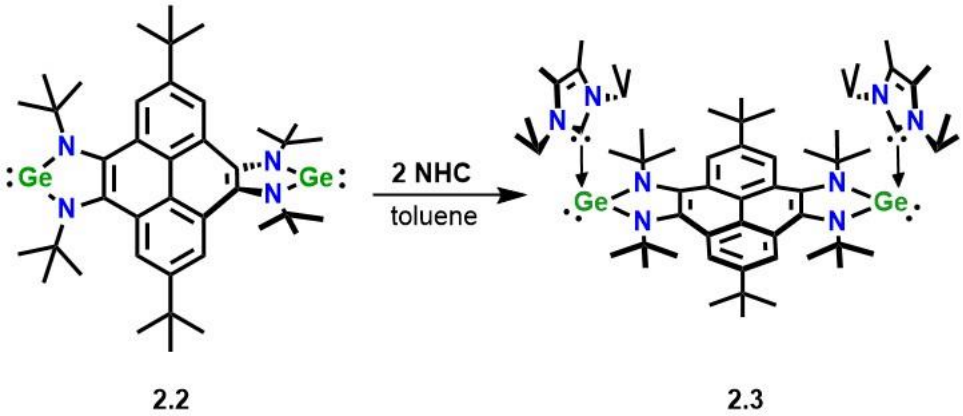

2.2 2.3

Scheme 2.2. Synthetic route to cis-sIPr coordinated bis-germylene complex.

Yellow block-shaped air- and moisture-sensitive single crystals of **2.3** sufficient for X-ray diffraction were grown from deuterated benzene. Interestingly, the structural distortion of **2.3** is completely different than **2.2** and coordination of the carbenes flatten out the end-to-end twisting (Figure 2.3a). Rather than an overall twisted structure, a negatively curved pyrene core with a bend angle of 141° is observed. A bend of the pyrene core to this extent is remarkable since there are no linkers distorting the planarity as shown in the bent tied-back pyrenophanes reported by

Bodwell.[157, 160, 171] Additionally, this concave shape is unique because the pyrene core is tilted out-of-plane towards the carbene ligands rather than away. Notably, the sIPr ligands add cis to each other on the same face of pyrene which induces an unusual out-of-plane distortion of the *tert*-butyl groups on the nitrogen atoms to accommodate steric repulsion. The cis-addition produces a pocket for a benzene solvent molecule and allows for interaction with the sIPr ligands in the solid-state packing diagram (Figure 2.3b). Twist angles are observed [C2-C1-C2'-C1' and N2-N1-N2'-N1' were 5° and 7° respectively] but significantly less than **2.2**. A torsion angle of 15° for the C21-Ge1-Ge1'-C21' atoms indicated that the sIPr ligands are nearly parallel to each other (Figure 2.3c). The Ge1–N1 (1.9430(14) Å) interaction is slightly longer than **2.2**. This was attributed to a decreased inductive effect of the nitrogen atoms as the empty *p*-orbital on the germanium atoms is now occupied by carbenes. The Ge1–C21 (2.1321(18) Å) bond length is within the reported range for typical Ge–C single bonds (1.965-2.192 Å).[172-174] An intermolecular interaction between one methyl group on the sIPr ligand to the ring of a neighboring molecule's carbene ligand is observed [Me---sIPr centroid = 3.43 Å] in the crystal packing diagram (Figure 2.3d).

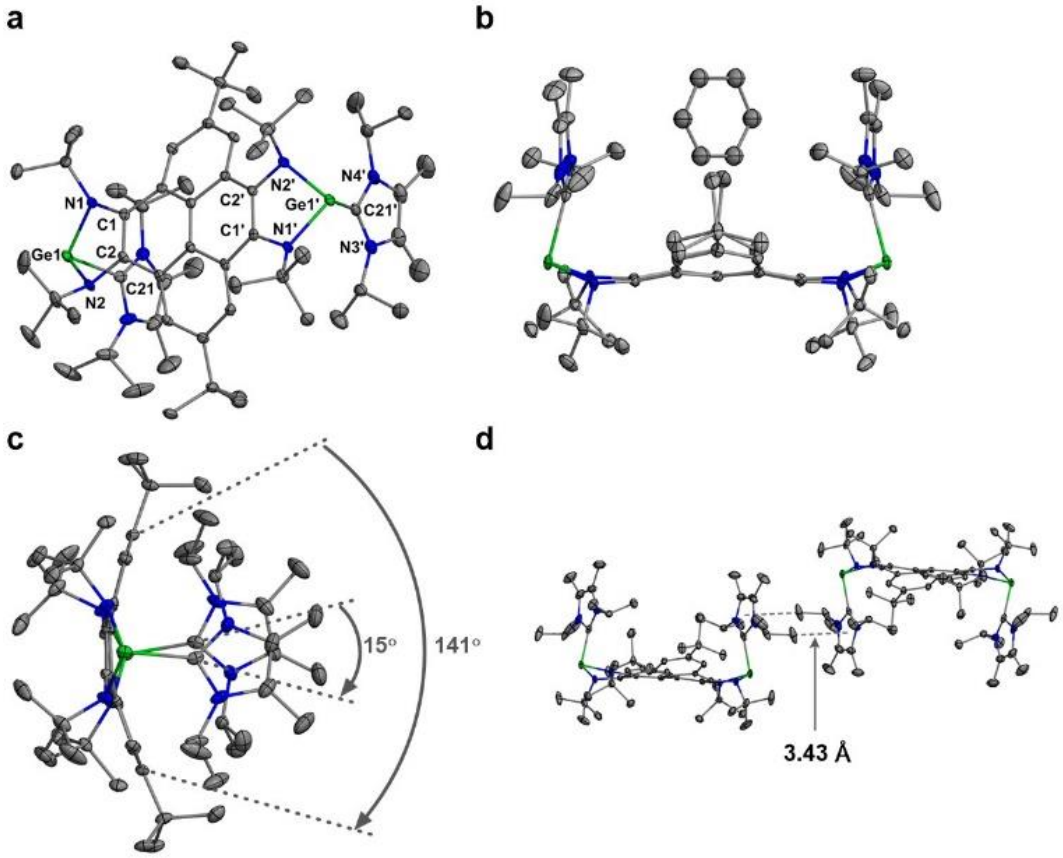

Figure 2.3. Molecular structure of **2.3**: a) cis-sIPr coordinated NHGe, b) top view with C_6D_6 molecule, c) sIPr side view, and d) crystal packing view with Me—sIPr centroid interaction. Thermal ellipsoids shown at 50% probability and H atoms were omitted for clarity. Selected bond lengths (Å) and angles (°): Ge1–N1: 1.9430(14); Ge1–N2: 1.9489(14); Ge1–C21: 2.1321(18); N4–C21: 1.359(2); N3–C21: 1.356(2); C2-C1-C2'-C1': 5; N2-N1-N2'-N1': 7; C21-Ge1-Ge1'-C21': 15.

2.4 Photophysical Properties of Pyrene-Fused N-Heterocyclic Germylenes

To gain insight into the absorption properties of **2.2** and **2.3** UV-vis studies were performed. Absorption maxima for **2.1-2.3** were exhibited at 369, 378, 384 nm respectively (Figure 2.4).

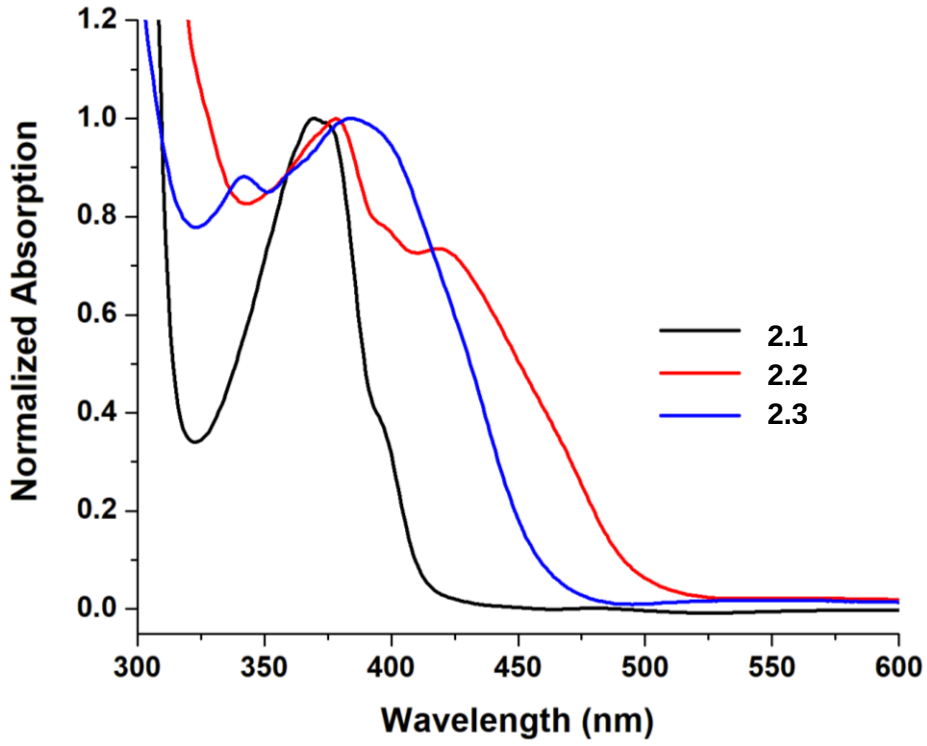

Figure 2.4. UV-vis absorption spectra of **2.1-2.3** in toluene at room temperature.

A slight bathochromic shift in λ_{max} was observed from **2.1** to **2.3**. In order to acquire a better understanding of the electronics, computations were performed at the B3LYP/BS1 level of theory. Based on TD-DFT, the λ_{max} of **2.2** was assigned to the $\pi \rightarrow$Ge $p + \pi^*$ transition, while the λ_{max} of **2.3** was assigned to the $\pi \rightarrow \pi^*$ transition. The broad shifts in the UV-vis spectra of **2.2** and **2.3** were attributed to fluxional behavior in solution, and the inversion barriers for twisting were further studied by computations (Figure A4.11-12). Analysis of MO results indicate that the HOMO for compounds **2.2** and **2.3** is mostly delocalized across the pyrene linker, with some

extension to the N atoms of the heterocycle (Figure 2.5). The LUMO in **2.2** is a Ge *p*-type orbital, while the LUMO in **2.3** is delocalized on pyrene. The Ge lone pair orbital of **2.2** is HOMO-4, which is consistent with the experimental observations. In **2.3**, the Ge lone pair is HOMO-2, due to enhanced nucleophilicity resulting from NHC coordination. Additional MOs and TD-DFT results are provided in Appendix IV (Figures A4.1-A4.3). To explore how the twisting of the structures affect the aromaticity of **2.2** and **2.3**, nucleus independent chemical shift (NICS(0)) calculations were conducted at the B3LYP/BS2 level of theory. NICS(0) values for the pyrene rings that link the NHGe heterocycles in **2.2** were less negative (-3.66 and -2.86) than **2.3** (–3.87 and –3.87) and free pyrene (-3.99 and -4.03), which supports decreased aromatic character due to twisting (Figure A4.8-10).

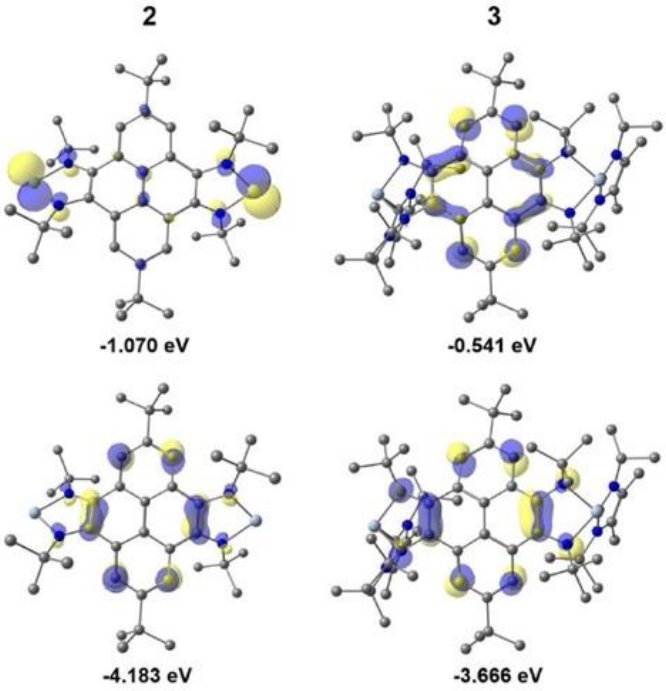

Figure 2.5. LUMO (top) and HOMO (bottom) orbital representations of **2.2** and **2.3** depicting the delocalization on pyrene.

2.5 Summary and Outlook

In conclusion, we have prepared the first examples of pyrene-fused N-heterocyclic germylenes. Notably, compounds **2** and **3** possess exceptional twist or bend angles as a result of unfavorable steric interactions between the pyrene core and the N-(*tert*-butyl) groups. We envision that these molecules can be utilized as functional building blocks for main-group element molecular materials chemistry where the Ge atoms participate in electron transfer or bind to other metals/element centers. We also expect that this new strategy will be successful for isolating distorted PAH compounds which incorporate other main-group elements and these studies are currently underway in our laboratory.

Future investigations in this area would need to explore the steric effects that larger N-substituents (e.g. phenyl or 2,6-diisopropylphenyl) would have on the structures of the pyrene-fused NHGes. Increasing the size of substituent bound to the N atoms is expected to result in more twisted and structurally distorted pyrene cores. Additionally, it would be important to explore pyrene-fused NHGes with smaller N-substituents (e.g. methyl or ethyl) in effort to flatten the pyrene core out. Furthermore, studies with a wider range of substrates would also give more insight into the reactivity profile of the pyrene-fused NHGes. For example, reactions between the pyrene-fused NHGe and transition metal carbonyl compounds would be important in order to compare with previously reported monomeric NHGes.[39]

Chapter Three: Pyrene- and Benzene-Fused N-Heterocyclic Boranes

Containing work that was originally published in:

Krantz, K. E.; Weisflog, S. L.; Frey, N. C.; Yang, W.; Dickie, D. A.; Webster, C. E.; Gilliard Jr., R. J., Planar, Stair-Stepped, and Twisted: Modulating Structure and Photophysics in Pyrene- and Benzene-Fused N-Heterocyclic Boranes. *Chem. Eur. J.* **2020,** *26*, 10072-10082.

3.1 Introduction to N-Heterocyclic Boranes

The dramatic increase in the synthesis of chemical compounds that contain *N*-heterocyclic borane (NHB) (C_2N_2B-R, also called diazaborole) moieties may be traced to the seminal discovery of boryllithium.[175-176] Since then, anionic NHBs[177] (i.e., boryl ligands) have been widely used as ligands in main-group[178-185] and transition metal chemistry,[186-190] particularly in the synthesis of compounds featuring new heteronuclear bonds. Additionally, diazaboroles and their polymeric analogues[191-192] have been synthesized for their photoluminescent properties potentially useful for optoelectronic devices.[193-195] Fusing multiple NHB units together in a "Janus-type" fashion, and thus adding an element of bifunctionality, has received significantly less attention. These types of compounds are extremely rare, mostly due to synthetic difficulty and thermodynamic instability.[196] Cowley and coworkers isolated a cationic pyracene-fused NHB that displayed multielectron redox behavior due to the ligand's ability to readily undergo reduction (Figure 3.1a).[197-198] More recently, Kinjo *et al.* reported boron-based tetraaminoethylene radical cations derived from the boryl-linked tetraazaolefin (Figure 3.1b).[199] Last year, Weber *et. al* isolated and structurally characterized a methylated benzene-fused bis(diazaborole) (Figure 3.1c).[200] Notably, this was the first example of a benzene-fused bis(diazaborole) that was characterized structurally by X-ray diffraction. However, photophysical data was unable to be obtained due to rapid decomposition of UV-vis samples. Other examples of fused-NHBs with benzene[201] and quinone[202] cores have been incorporated into field effect transistors, but their structural properties were not studied. Despite

these advances, a comprehensive study of both the structural and photophysical properties of fused-NHBs linked by polycyclic aromatic hydrocarbons (PAHs) is hitherto unknown.

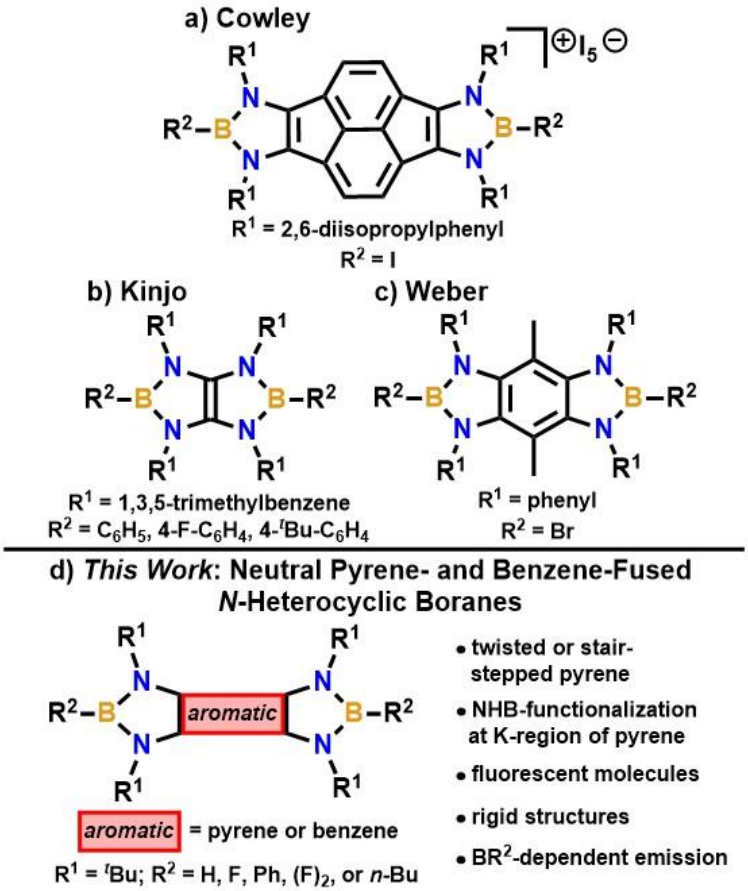

Figure 3.1. a) Pyracene-fused *N*-heterocyclic borane with redox properties; b) boryl-linked tetraazaolefin that oxidizes to the radical cation; c) methylated benzene-fused bis(diazaborole) d) This work: neutral pyrene- and benzene-fused *N*-heterocyclic boranes featuring structural distortions and luminescent properties.

Owing to boron's empty p_z-orbital, the incorporation of boron into aromatic systems can result in π-conjugation, important for inducing electronic properties useful in optoelectronics,[61, 203-205] sensor technology,[60, 62, 86-87, 206] and fluorescent dyes.[207-208] Pyrene, a blue-chromophore, has served as a ubiquitous building block in electronic devices.[46] In recent years, boron-doped pyrene-based molecules have become popular with main-group chemists, with the goal of understanding

structure-property relationships in new functional materials.[10, 58, 63, 209-219] For example, tethering boron to pyrene is known to reduce the LUMO energy and increase the acceptor character by lowering the energy needed for absorption and emission.[49, 209, 220-223] However, studies of compounds containing boron bound to pyrene have been limited due to challenging synthetic routes associated with modifying pyrene.[224-226] Indeed, functionalization at the K-region of pyrene often requires multi-step syntheses with low overall yields, and electrophilic substitution at the 1-, 3-, 6-, and 8-positions is preferred (i.e, where the HOMO lies).[46, 227-228] Recently, we have been exploring doping PAHs with boron,[99, 107, 123] and attaching main-group element fragments to the K-region of pyrene. This lead to the first pyrene-fused *N*-heterocyclic germylenes (NHGe), which display extremely twisted molecular structures.[229]

Herein we report the syntheses, molecular structures, photophysical properties, and extensive computational studies of pyrene- and benzene-fused NHBs (Figure 3.1d). Remarkably, the pyrene derivatives **3.2-3.4** and **3.11** are the first examples of compounds in which an NHB moiety is fused to the K-region of pyrene, and they display twisted or stair-stepped structures. In contrast, the benzene-fused compounds **3.6**-**3.9** are planar and possess tunable optical properties based on the electronics of the NHB moieties. It is noteworthy that these are the first fused-NHBs that exhibit fluorescent properties spanning the full visible spectrum.

3.2 Synthesis of Pyrene-Fused N-Heterocyclic Boranes

We began our studies by synthesizing a tetramine with sterically demanding *N*-(2,6-diisopropylphenyl) groups. However, due to low yields in the multi-step synthetic route we switched to the less bulky *N*-(*tert*-butyl) tetramine (**1**), prepared using a Buchwald-Hartwig amination (Scheme 3.1).[166] Dehydrogenation of **1** and BH_3•THF at 110 °C gave compound **2** as a pale-yellow solid in 77% yield. In the ^{1}H NMR spectrum, a downfield shift in the resonance (1.26

to 1.66 ppm) assigned to the *N*-(*tert*-butyl) protons represent the decrease in electron density at the nitrogen atoms, where the lone pairs fill the *p*-orbital of boron. A resonance was not observed in the $^{11}B\{^{1}H\}$ NMR spectrum, which was attributed to quadrupolar line broadening.

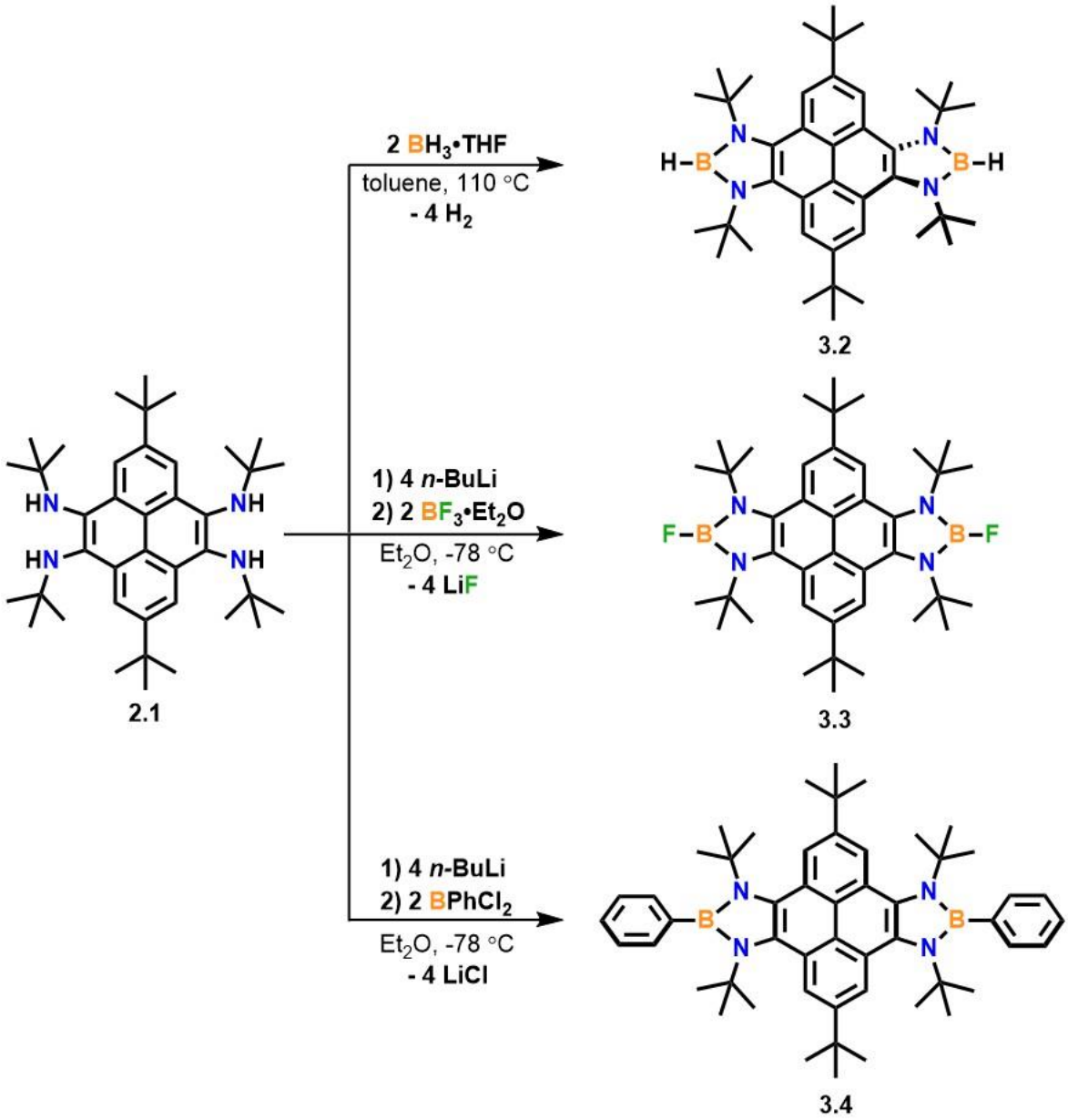

Scheme 3.1. Synthesis of pyrene-fused *N*-heterocyclic boranes.

Yellow plate-shaped air- and moisture-sensitive single crystals of **3.2** suitable for X-ray diffraction studies were obtained from a concentrated toluene solution at -37 °C. An overall twisted structure of **3.2** was observed, comparable to our pyrene-fused NHGe,[229] but with smaller "twist angles"[150] [C2–C2–C2′–C1′ (40°) and N2–N1–N2′–N1′ (52°)] (Figure 2.2a). However, the twist angles of **3.2** are still substantial compared to known pyrene-fused molecules which span two benzene rings (Figure 2.2b).[153, 158, 167]

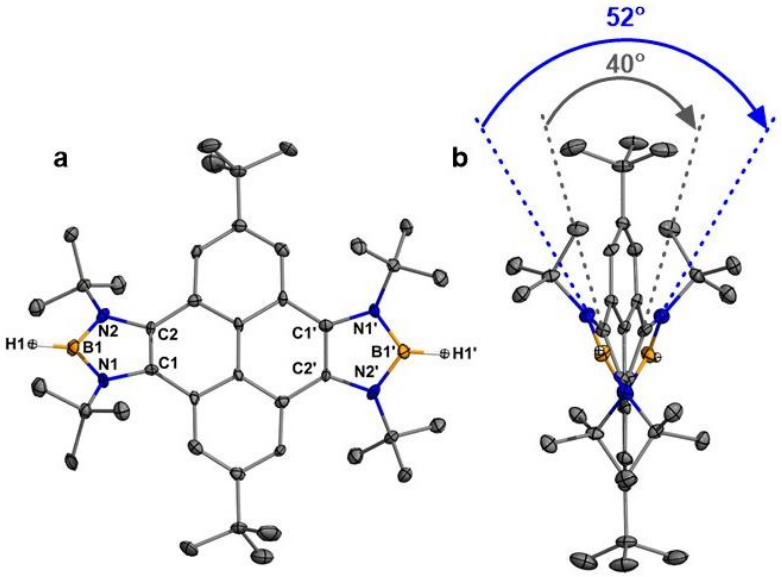

Figure 3.2. Molecular structure of **3.2**: a) front view, b) side view. Thermal ellipsoids shown at 50% probability and H atoms (except B-H) were omitted for clarity. Selected bond lengths (Å) and angles (°): B1–H1: 1.15(3); B1–N1: 1.421(7); B1–N2: 1.433(7); C2–C1–C2′–C1′: 40; N2–N1–N2′–N1′: 52.

Compound **3.3** was isolated by *in-situ* lithiation of **2.1** and subsequent salt elimination with BF_3•Et_2O to give a green solid in 32% yield (Scheme 3.1). A downfield shift in resonance from 1.26 to 1.79 ppm for the *N*-(*tert*-butyl) protons was observed in the ^{1}H NMR spectrum. In the $^{11}B\{^1H\}$ NMR spectrum, a broad singlet at 25.7 ppm was attributed to the two chemically equivalent boron atoms. In the ^{19}F NMR spectrum, two broad resonances separated by 0.06 ppm

(-125.64 and -125.70 ppm) were observed in approximately 20:80 ratio. These peaks were assigned to both ^{10}B (I = 3) and ^{11}B (I = 3/2) coupling to ^{19}F. However, due to rapid quadrupolar relaxation the coupling constants could not be determined.

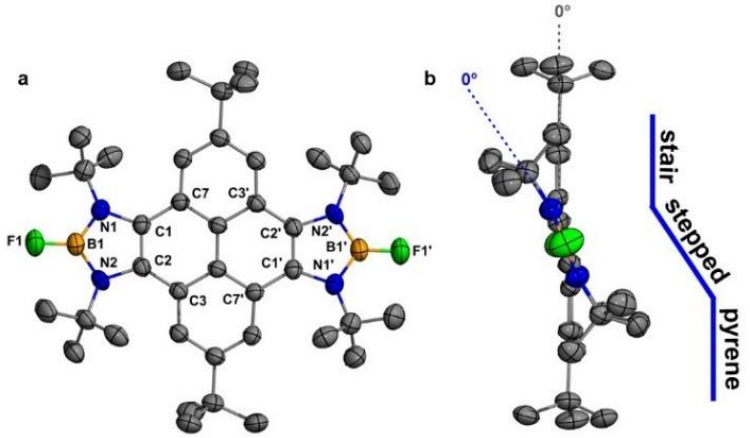

Figure 3.3. Molecular structure of **3.3**: a) front view, b) side view. Thermal ellipsoids shown at 50% probability and H atoms were omitted for clarity. Selected bond lengths (Å) and angles (°): B1–F1: 1.335(4); B1–N1: 1.419(5); B1–N2: 1.423(5); C1–C2–C1′–C2′: 0; N1-N2-N1′-N2′: 0, C3–C2–C1–C7: 20.

Pale green plate-shaped air- and moisture-sensitive single crystals of **3.3** suitable for X-ray studies were obtained from a concentrated toluene/hexane (1:1) mixture at -37 °C (Figure 3.3a). Unlike the twisted structure of **3.2**, 0° "twist angles" are observed, and the middle four rings of **3.3** are distorted out of plane in a stair-step fashion with a 20° C3–C2–C1–C7 torsion angle (Figure 3.3b). The 6-membered rings of pyrene not interacting with nitrogen atoms remain coplanar. It is noteworthy that **3.3** is the first structurally characterized NHB bearing a terminal boron monofluoride unit.

Lithiation and subsequent salt elimination of **2.1** with $PhBCl_2$ afforded a light orange solid of **3.4** in 47% yield (Scheme 3.1). The ^1H NMR spectrum showed a downfield shift in resonance from 1.26 to 1.61 ppm which integrated to 36, and was attributed to the *N*-(*tert*-butyl) protons. In

the $^{11}B\{^{1}H\}$ NMR, a broad singlet at 33.1 ppm was assigned to the two chemically equivalent boron atoms.

Yellow rod-shaped air- and moisture-sensitive single-crystals of **3.4** suitable for X-ray diffraction studies were obtained from a concentrated hexanes solution at -37 °C (Figure 3.4a). Compound **3.4** displayed a distorted pyrene core similar to **3.3** (Figure 3.4b), but with a larger torsion angle [28° for C3–C2–C1–C7 plane]. Additionally, the boron-bound phenyl rings are twisted away from the 5-membered rings, yielding a 60° C22–C21–B1–N2 torsion angle, while the geometry around the boron atoms remains trigonal planar.

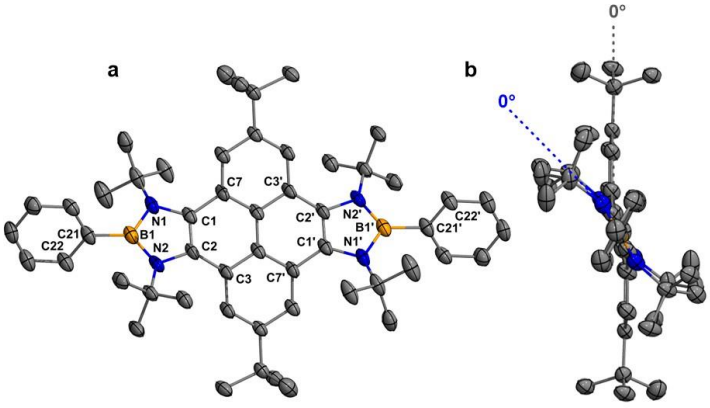

Figure 3.4. Molecular structure of **3.4**: a) front view, b) side view. Thermal ellipsoids shown at 50% probability. H atoms and co-crystallized solvent were omitted for clarity. Selected bond lengths (Å) and angles (°): B1–C21: 1.573(4); B1–N1: 1.453(4); B1–N2: 1.448(5); C1–C2–C1′–C2′: 0; N1–N2–N1′–N2′: 0, C3–C2–C1–C7: 28; C22–C21–B1–N2: 60.

3.3 Synthesis of Benzene-Fused N-Heterocyclic Boranes

We were then interested in obtaining fused boranes in which the entire molecule is planar, to study how the linker and topography of the structure affects the photophysical properties. Due to its tunable pH-dependent colorimetric properties, we targeted fused systems based on an *N*-alkyl substituted benzene tetramine.[230] Using the tetramine (**3.5**)[231] and similar reaction conditions used

for making compounds **3.2-3.4**, the benzene-fused compounds **3.6-3.8**, (Scheme 2) were synthesized in 62, 48, and 50% yields respectively. In the ^{1}H NMR spectra, a downfield shift from 1.29 to 1.65 (for **3.6**), 1.43 (for **3.7**), and 1.54 ppm (for **3.8**) for the N-*tert*-butyl protons were consistent with the formation new products. In the ^{11}B{^{1}H} NMR spectra, chemical shifts of 5.4 (for **3.7**), 28.4 (for **3.8**), 30.0 ppm (for **3.9**) were attributed to the chemically equivalent boron environments. Similar to **3.2,** no ^{11}B{^{1}H} NMR chemical shift was observed for **3.6** due to quadrupolar line broadening. In the ^{19}F NMR spectrum of **3.7**, a standard 1:1:1:1 quartet resonance was observed at -151.8 ppm which was attributed to the presence of two BF_2 units ($^{1}J_{BF}$ = 56.4 Hz). Compound **3.7** forms via loss of LiH after the first deprotonation due to the resonance structure that can be obtained when the nitrogen-based electrons are delocalized onto the benzene ring of **3.5**. The loss of LiH prohibits all four deprotonation events occurring, and accordingly, only two equivalents of LiF are eliminated. Though the specific reasons for the mechanistic differences between **3.3** and **3.7** are unclear, this underscores the ability of the two linking π-systems to facilitate the formation of diverse structural arrangements.

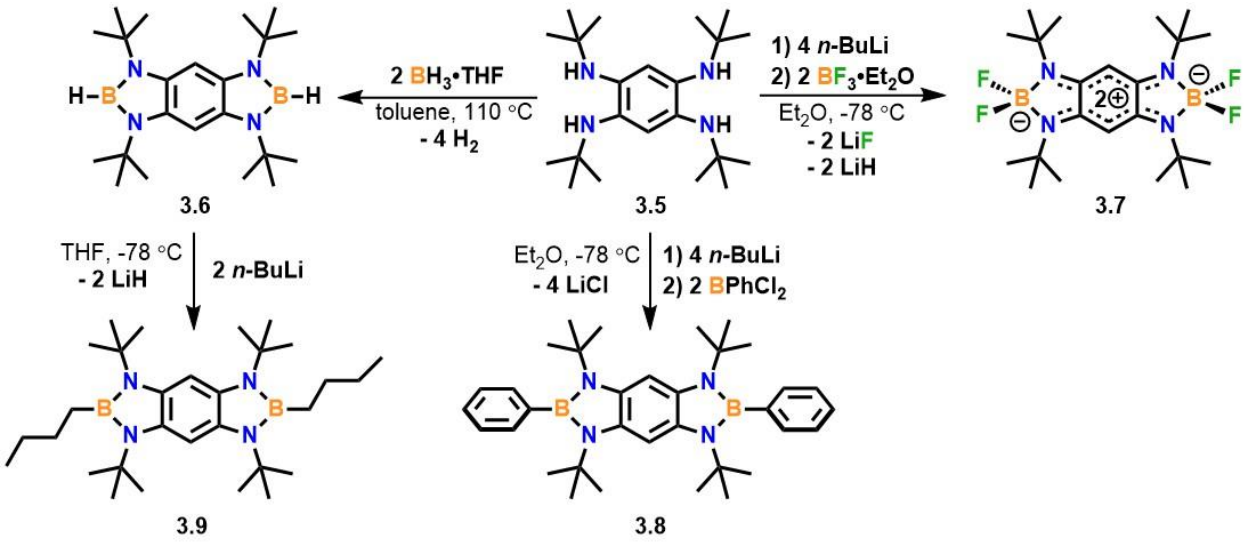

Scheme 3.2. Synthesis of benzene-fused *N*-heterocyclic boranes.

Air- and moisture-sensitive colorless rod-shaped crystals of **3.6** suitable for X-ray studies were obtained from a concentrated solution in toluene at 110 °C and subsequent cooling to room temperature (Figure 3.5a). Unlike **3.2**, compound **3.6** displayed a completely planar structure (Figure 3.5b). The B1–H1 [1.140(17) Å] bond lengths were comparable to those in **3.2** [1.15(3) Å].

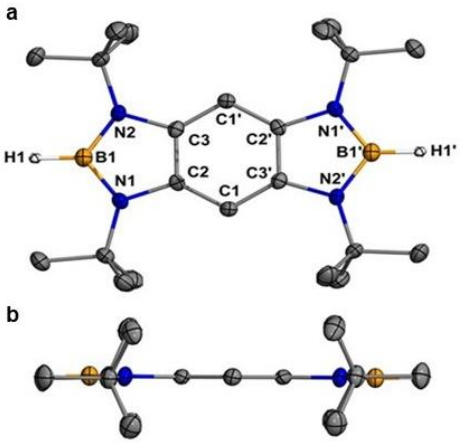

Figure 3.5. Molecular structure of **3.6**: a) front view, b) view showing planarity of benzene. Thermal ellipsoids shown at 50% probability and H atoms except for boron bound H were omitted for clarity. Selected bond lengths (Å): B1–H1: 1.140(17); B1–N1: 1.426(2); B1–N2: 1.426(2); N1–C2: 1.4166(18); C1–C2: 1.395(2); C1–C3′: 1.398(2).

Pink cube-shaped crystals of **3.7** suitable for X-ray studies were obtained from a concentrated THF solution at room temperature (Figure 3.6a). Similar to **3.6**, compound **3.7** displayed a planar structure (Figure 3.6b). The system, which indeed contains two BF_2 units, can be best described as a zwitterionic molecule with two positive charges delocalized over the benzene core and a negative charge localized on each boron atom. This interpretation is further supported by the bond lengths of C1–C2 [1.3968(12) Å] and C1–C3′ [1.5062(12) Å] which suggest that the π-electrons are delocalized across the N1–C1–C2–C3–N2 atoms and not within the central 6-membered ring. This description is also consistent with reported bis(boron difluoride) complex [$(BF_2)_2$(μ-4-EtAp)] (Ap = azophenine),[232] platinum *N',N',N'',N''*-diboronazophenine

complexes,[233] and the [(ttmgb)$(BF_2)_2$]$(BF_4)_2$ (ttmgb = 1,2,3,4-tetrakis(tetramethylguanidinyl)benzene) salt.[234] Additionally, the B–F bond lengths [1.3906(12) and 1.3853(12) Å] are slightly longer than the B1–F1 bond [1.335(4) Å] in the pyrene complex **3.3**.

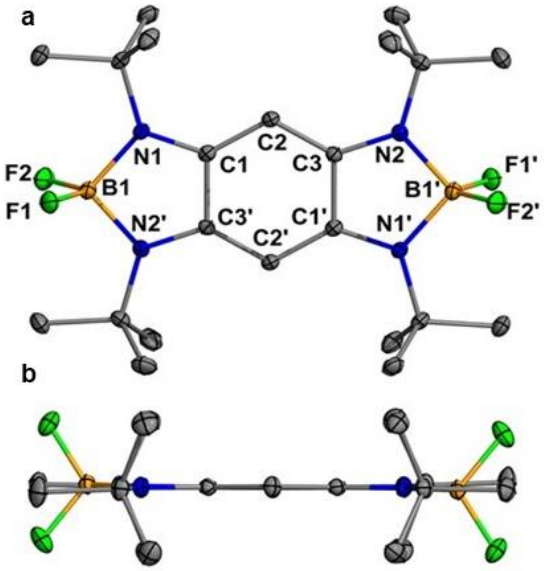

Figure 3.6. Molecular structure of **3.7**: a) front view, b) view showing planarity of benzene. Thermal ellipsoids shown at 50% probability and H atoms were omitted for clarity. Selected bond lengths (Å): B1–F1: 1.3906(12); B1–F2: 1.3853(12); B1–N1: 1.5690(13), B1–N2: 1.5678(13), C1–N1: 1.3266(11); C1–C2: 1.3968(12); C1–C3′: 1.5062(12).

Colorless plate-shaped single crystals of **3.8** suitable for X-ray studies were obtained from a concentrated toluene solution at -37 °C (Figure 3.6a). The molecular structure showed a planar benzene-fused NHB with orthogonal phenyl groups bound to boron (Figure 3.6b). In contrast to **3.4**, the phenyl groups in compound **3.8** are perpendicular to the boron plane, with a C13–C12–B1–N1 torsion angle of 93°.

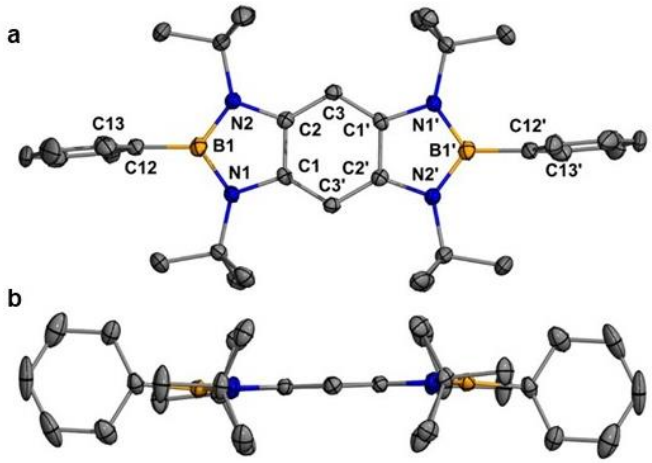

Figure 3.7. Molecular structure of **3.8**: a) front view, b) view showing planarity of benzene. Thermal ellipsoids shown at 50% probability and H atoms were omitted for clarity. Selected bond lengths (Å) and angles (°): B1–N1: 1.4436(19), B1–N2: 1.440(2), B1–C12: 1.609(6); C13–C12–B1–N1: 93.

Probing the acidity of compound **3.6** was then of interest, and we explored this by the addition of a strong base (Scheme 3.2). Two equivalents of *n*-butyllithium were added to a mixture of **3.6** in THF. The absence of a resonance in the ^{7}Li NMR spectrum supported the elimination of LiH rather than the formation of a tetracoordinate Li borate salt. Further analysis of the reaction revealed that the B–*H* substituent on **3.6** is more hydridic than acidic, and thus compound **3.9** was isolated as a white crystalline solid (50% isolated yield). A broad resonance at 30.0 ppm was observed in the ^{11}B{^{1}H} NMR spectrum which was very similar to the shift of **3.8** (28.4 ppm).

Plate-shaped colorless single crystals of **3.9** suitable for X-ray analysis were grown from a concentrated toluene solution at -37 °C (Figure 3.8a). Compound **3.9** exhibited a planar structure with the *n*-butyl groups oriented trans to each other (Figure 3.8b). The B1–C12 bond length [1.589(8) Å] was comparable to the B1–C12 bond [1.609(6) Å] of **3.8**.

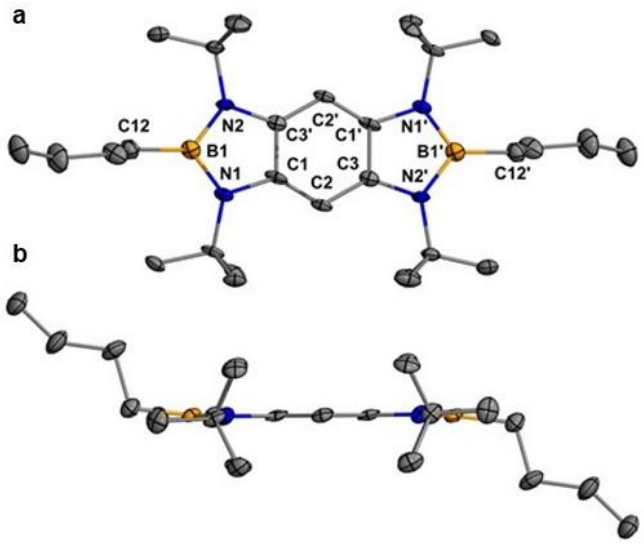

Figure 3.8. Molecular structure of **3.9**: a) front view, b) view showing planarity of benzene. Thermal ellipsoids shown at 50% probability and H atoms were omitted for clarity. Selected bond lengths (Å): B1–N1: 1.439(7), B1–N2: 1.460(7), B1–C12: 1.589(8).

3.4 Photophysical Properties of Fused NHBs

To gain insight into the photophysical properties of **3.2**-**3.4** and **3.6**-**3.9**, UV-vis and fluorescence studies were performed. Absorption maxima of **3.2**-**3.4** were exhibited at 395, 377, and 405 nm, respectively, assignable to π-π^* transitions (Figure 3.9a). Emission maxima for the pyrene-fused NHBs (**3.2**-**3.4**) were shown at 442, 456, and 457 nm, respectively (Figure 3.9b), which were all hypsochromically shifted with respect to the tetramine starting material (**2.1**). Due to the high contribution of the pyrene core in these excitations, they all emit blue fluorescence under UV-light. The benzene-fused molecules (**3.6**-**3.9**) have absorption maxima at 326, 384, 387,

and 320 nm, respectively, which were all assignable to π-π^* transitions (Figure 3.9c). Emission maxima for the benzene-fused NHBs (**3.6**-**3.9**) were shown at 346, 415, 489, and 350 nm, respectively, and were attributed to π^*-π transitions (Figure 3.9d). Compounds **3.7** and **3.8** were bathochromically shifted with respect to the tetramine starting material (**3.5**) while compounds **3.6** and **3.9** were hypsochromically shifted. In addition to the experimental studies, the electronic structure and transitions of the fused-NHBs were investigated by DFT calculations (B3LYP/BS1 level of theory), which supported the aforementioned assignments. (see Appendix 4 for details). In the benzene-fused NHBs, the color of emission varies significantly based on the substituent bound to boron. This major difference is due to the NHB rings contributing more hole to particle (**3.6**, 88%-30%, see Figure A4.33), while the NHB rings in the pyrene-fused compounds contribute much less (**3.2**, 49%-24%). Notably, **3.6**-**3.9** all emit in the NIR region (750 nm) which is promising for optoelectronic materials, specifically fluorescent probes.[235-236]

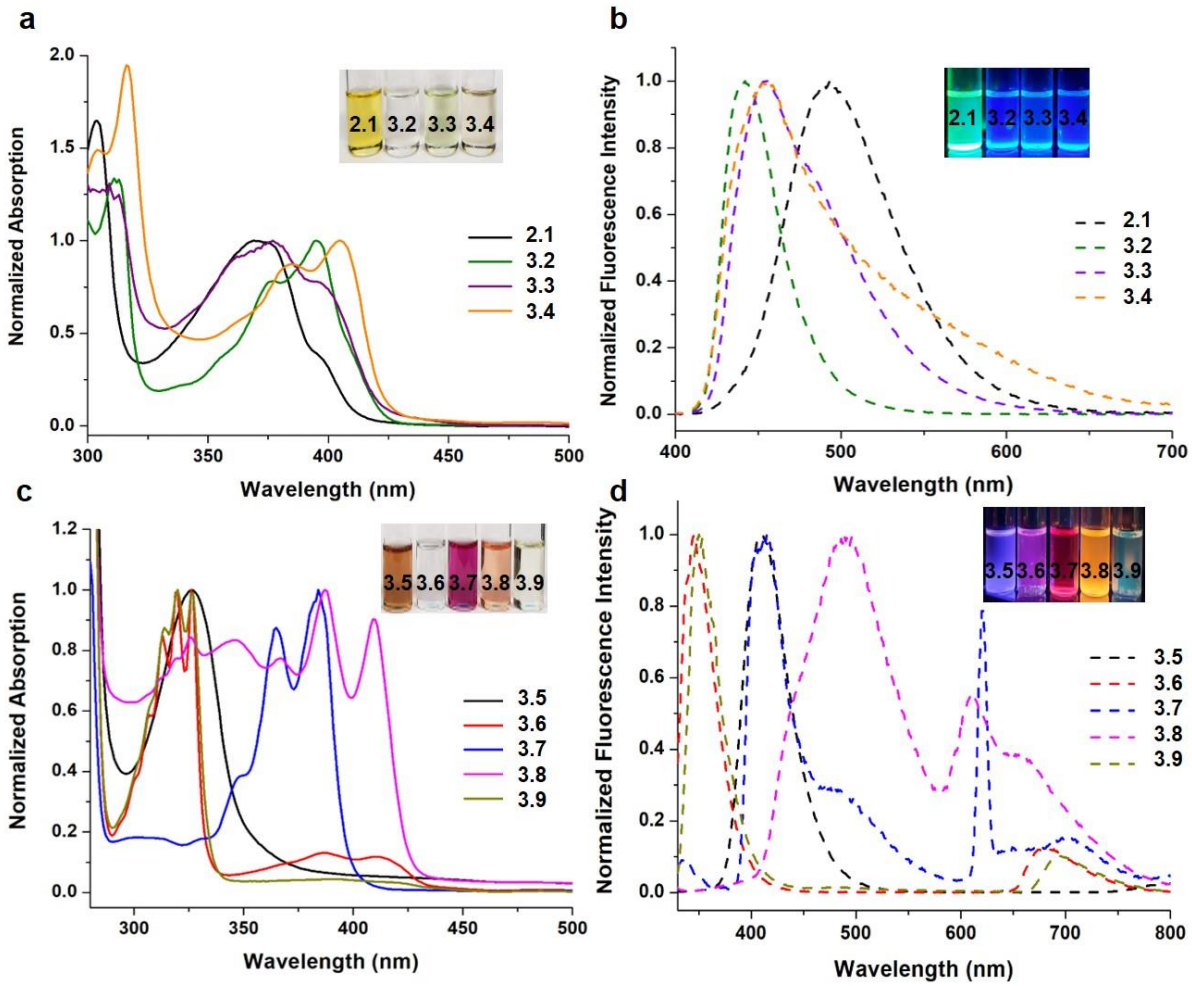

Figure 3.9. a) UV-vis absorption of **2.1, 3.2**-**3.4**; b) emission of **2.1, 3.2**-**3.4**; c) UV-vis absorption of **3.5**-**3.9**; d) emission of **3.6**-**3.9**. All samples were dissolved in toluene and ran at room temperature. Compounds **2.1, 3.2**-**3.4** were excited at 380 nm and **3.5**-**3.9** were excited at 310 nm.

3.5 Synthesis of Pyrene-Fused N-Heterocyclic Borane with Methyl Substituents

We then desired to explore the photophysical properties of a planar pyrene-fused NHB to test if the fluorescence could be tuned in a manner similar to the benzene-fused NHBs. Therefore, we replaced the *N*-(*tert*-butyl) substituents with less bulky *N*-methyl groups to limit steric interactions with the pyrene-C-*H*. Compound **3.10** was isolated in 45% yield via Buchwald-

Hartwig amination (see Appendix 1 for details). Lithiation of **3.10** and successive salt elimination with $PhBCl_2$ gave **3.11** as a yellow solid in 66% yield (Scheme 3.3).

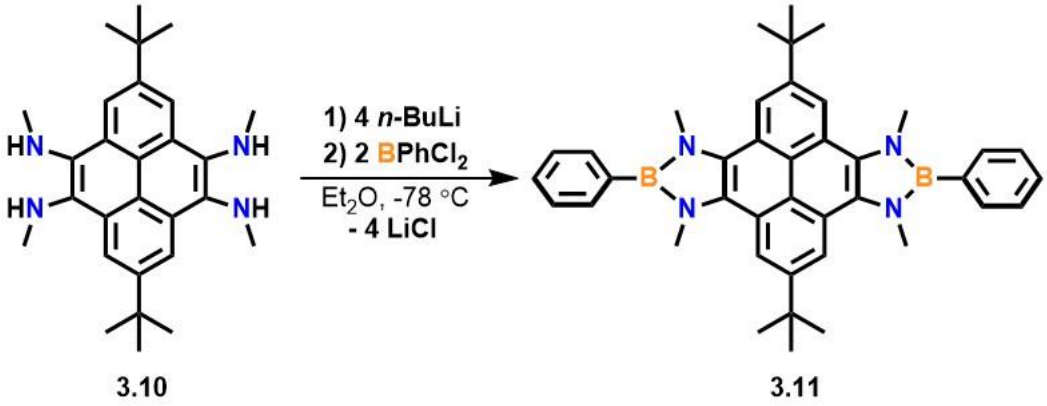

3.10 3.11

Scheme 3.3. Synthesis of pyrene-fused *N*-heterocyclic borane (N-methyl).

Yellow rod-shaped single crystals of **3.11** were obtained from a concentrated toluene/THF (10:1) mixture at room temperature (Figure 3.10a). As expected, the overall structure revealed a more planar pyrene core, albeit not completely flat (Figure 3.10b). Examination of the space-filling model (**Figure A3.11**) clearly shows that the methyl protons still interact with the hydrogen atoms on pyrene to yield a slight distortion from planarity. The C3-C2-C1-C7 torsion angle in **3.11** (11°) is significantly smaller than that in **3.4** (28°). The decrease in steric bulk at nitrogen also impacts the rotation of the B-Ph group. Consequently, compound **3.11** displayed the smallest torsion angle for the C20-C15-B1-N2 plane (49°) compared to the same angle in **3.4** (60°) and benzene-fused **3.8** (93°).

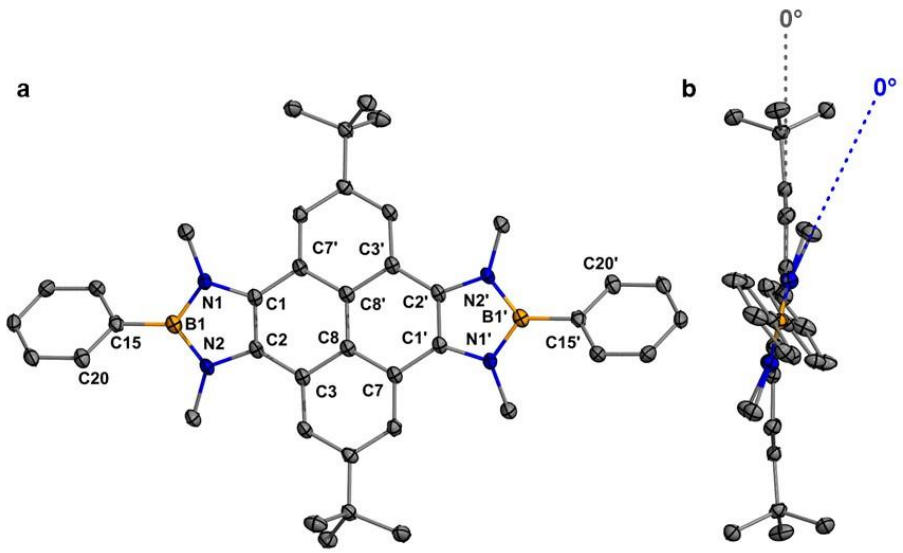

Figure 3.10. Molecular structure of **3.11**: a) front view, b) side view. Thermal ellipsoids shown at 50% probability and H atoms were omitted for clarity. Selected bond lengths (Å) and angles (°): B1–C15: 1.5669(19); B1–N1: 1.4291(18); B1–N2: 1.4272(18); C1–C2–C1′–C2′: 0; N1–N2–N1'–N2': 0, C3–C2–C1–C7: 11; C22–C21–B1–N2: 49.

The absorption (366 nm) and emission maxima (487 nm) of **3.10** were comparable to that of **2.1** (λ_{abs} = 369 nm, λ_{em} = 493 nm)[229] (Figure 3.11). Conversely, a significant difference in the appearance of the absorption and emission features of **3.11** (λ_{abs} = 392 nm, λ_{em} = 419 nm) was observed in contrast to **3.4**. Additionally, the emission maximum was substantially blue-shifted from **3.4**. Since the blue emission color of **3.11** is not drastically different from **3.2**-**3.4**, it supports the use of pyrene-based molecules as blue emitters in organic light emitting diodes. However, this also highlights the benefit of the benzene-fused materials (i.e., in terms of tunable optical by eye properties).

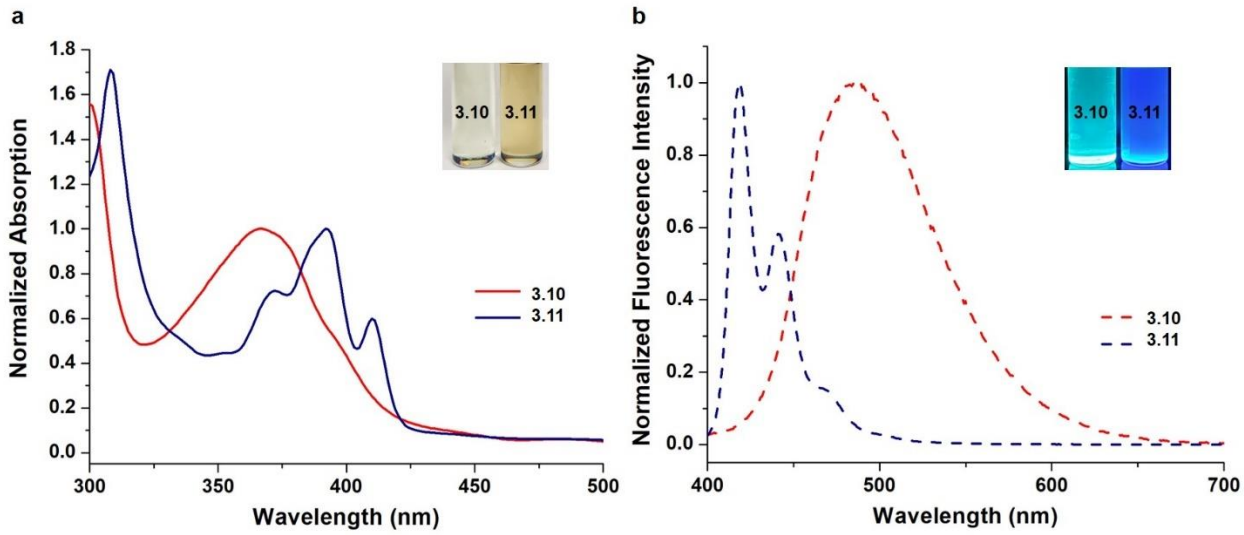

Figure 3.11. a) UV-vis absorption of **3.10** and **3.11**; b) emission of **3.10** and **3.11**. Samples were dissolved in toluene and run at room temperature. Compound **3.10** was excited at 365 nm and **3.11** was excited at 380 nm.

3.6 Computational Comparison of Pyrene- and Benzene-Fused NHBs

In the pyrene-fused molecules, the HOMO and LUMO are all delocalized throughout the pyrene core with minimal electron density at boron (Figure 3.12). However, benzene-fused **3.6**, **3.8**, and **3.9** all have HOMOs that are localized on boron and the benzene core (Figure 3.13). Nodal planes pass directly through the middle of the compounds, parallel to the boron atoms. In contrast, the HOMO and LUMO of compound **3.7** are delocalized on the carbon and nitrogen backbone with no localization on boron, which is consistent with its zwitterionic structure. Unlike **3.6** and **3.9**, the LUMO of compound **3.8** is localized on the outer phenyl rings rather than the boron atoms and benzene core. These results validate the boron-dependent electronics and the substantial difference in emission colors observed under UV light. In the pyrene-fused NHBs (**3.2-3.4,** and **3.11**) the frontier orbitals are only pyrene-based whereas the HOMO/LUMOs of the benzene-fused

NHBs (**3.6-3.9**) include the 5-membered boron heterocyclic rings. Notably, the LUMO of compound **3.8** is the only example where the frontier orbitals are extended to the boron-bound substituent outside of the ring (phenyl groups). Additionally, the fused NHBs possess large HOMO-LUMO gaps that cover a broad range of energies (2.88-4.84 eV) that could be promising for materials applications that require wide band gaps.[237-241]

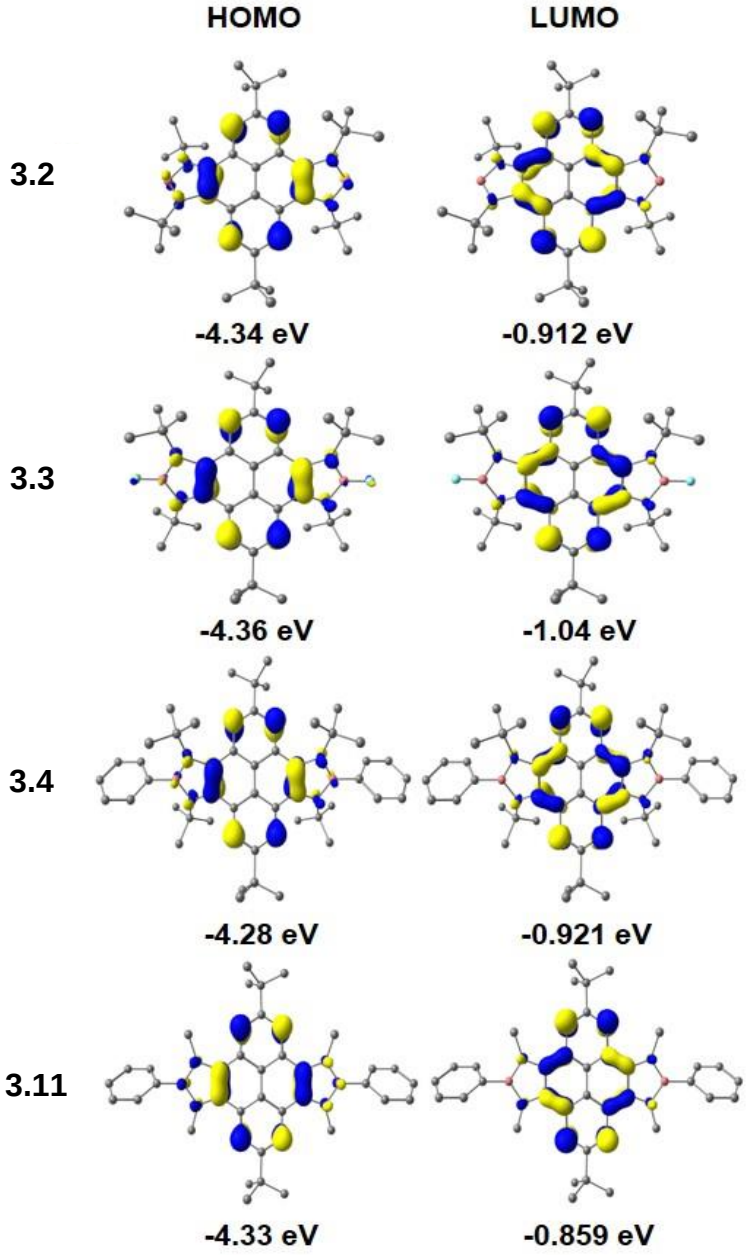

Figure 3.12. Frontier orbitals of pyrene-fused NHBs **3.2-3.4** and **3.11**.

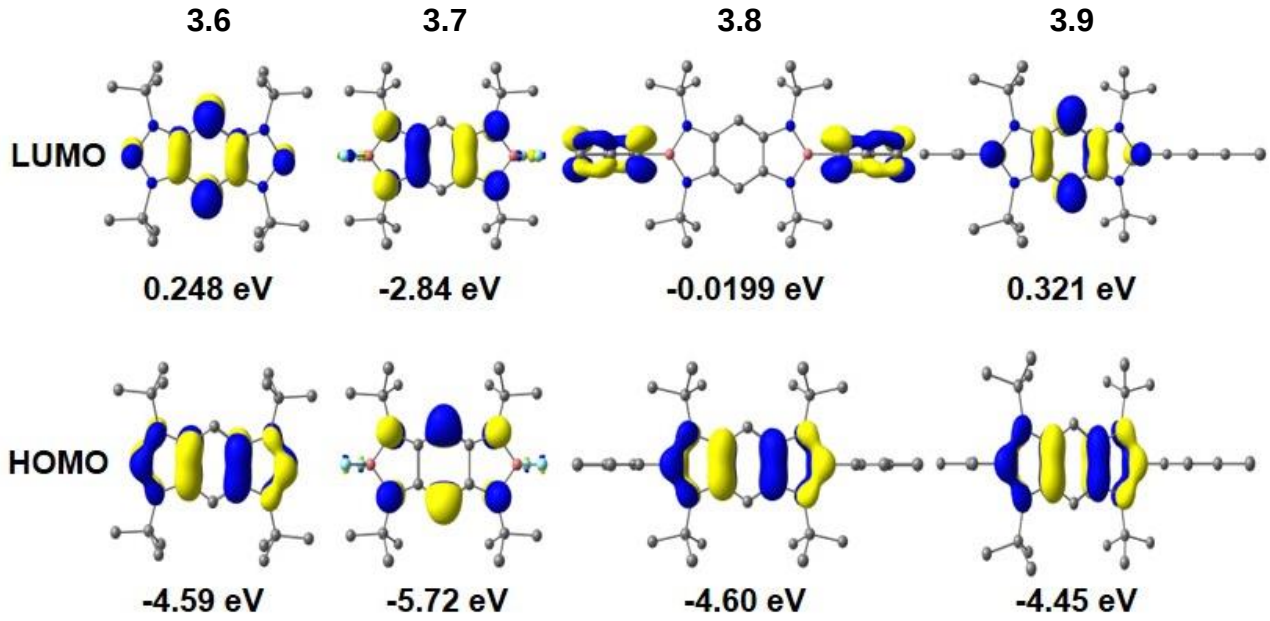

Figure 3.13. Frontier orbitals of benzene-fused NHBs **3.6**-**3.9**.

To further investigate the electronic contributions to aromaticity in the fused NHBs and how this was affected by structural distortions, Nucleus Independent Chemical Shifts (NICS(0)) were computed for each ring (Table 3.1). For the pyrene-fused NHBs, the NICS(0) values for **B/B'** and **C/C'** rings in the pyrene core are consistent across all compounds. As expected, the **C/C'** rings are the most aromatic in the pyrene core, and maintain their status as π-electron sextets as supported by Clar's theory.[242-243] However, the NICS(0) values for ring **A/A'**, the 5-membered boron-containing rings, change dramatically throughout all molecules. These changes can be attributed to the differences in the electronic and geometric structures influenced by nitrogen-alkyl group, boron-functional group, and the fused aromatic core. An overall trend of more negative values for the **A/A'** rings in the benzene-fused NHBs is observed in comparison to the pyrene-fused analogues (with the exception of **3.7**). This can be attributed to the electronic contribution and delocalization of the HOMO on the NHB in **3.6, 3.8,** and **3.9** unlike **3.2-3.4,** and **3.11.** Notably, the NICS(0) values for ring **A/A'** in **3.7** are significantly higher than those found in the other

compounds due to the borate drastically altering the electronics and removing all aromatic character from the center 6-membered ring (**E**). Consequently, the NICS(0) value for ring **E** in **3.7** is positive, a major contrast from any other molecule in this study. Compounds **3.6, 3.8,** and **3.9** all retain aromaticity in ring **E** as justified by the negative values.

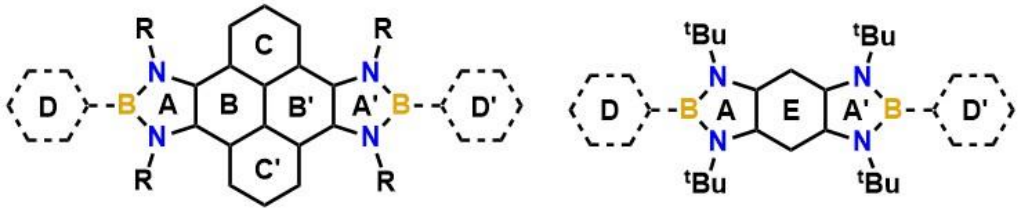

Table 3.1. NICS(0) values (B3LYP/BS2 level of theory) of compounds **3.2-3.11**.

Compound	A/A'	B/B'	C/C'	D/D'	E
3.2	-6.39	-4.95	-10.47	–	–
3.3	-5.80	-5.29	-10.78	–	–
3.4	-4.84	-4.44	-10.56	-7.09	–
3.6	-7.98	–	–	–	-11.77
3.7	-1.70	–	–	–	4.08
3.8	-7.56	–	–	-7.33	-11.44
3.9	-7.87	–	–	–	-11.51
3.10	–	-5.07	-11.65	–	–
3.11	-4.84	-4.44	-10.56	-7.09	–

3.7 Summary and Outlook

In conclusion, we have isolated, fully characterized, and investigated the photophysical properties of the first pyrene-fused NHBs, which display unique twisted or stair-stepped structures.

We have also compared them to structurally related benzene-fused materials, which are all planar. The tunable optical properties of the benzene-fused NHBs make them promising candidates for functional materials due to their emission in the near-infrared region. The structural properties of the fused-NHBs confirm that the aromatic core (pyrene vs. benzene) plays a significant role in the overall electronic structure of the molecules. We believe that these new synthetic routes to molecules that would otherwise be challenging to access, as well as the tunability of this system, will spark new research efforts regarding the use of these compounds as main-group functional materials. Moreover, similar strategies may be successful for unraveling the chemistry of distorted aromatic systems that incorporate other *p*-block elements and these efforts are currently underway in our laboratory.

Key future studies in this area include complete analysis of solid-state and solution-phase absolute quantum yields to gain a insight into the degree of luminescence compares within the pyrene-and benzene-fused NHBs. Additionally, it would be important to work towards isolating fused NHBs with halides (X = Cl, Br, or I) other than fluoride to render the B–X bond weaker. These species will be vital for extending the monomeric molecules into linearly fused polymeric materials. Furthermore, the ability to remove a halide from the boron atoms would allow for many new possibilities for potential reactivity studies.

Chapter Four: Carbene-Coordinated Borafluorene Monoanions

Containing work that was originally published in:

Wentz, K. E.; Molino, A.; Weisflog, S. L.; Kaur, A.; Dickie, D. A.; Wilson, D. J. D.; Gilliard Jr., R. J., Stabilization of the Elusive 9-Carbene-9-Borafluorene Monoanion. *Angew. Chem. Int. Ed.* **2021,** *60*, 13065-13072.

4.1 Introduction to Boryl Anions and Borafluorene Chemistry

Organoboranes are well-known as quintessential Lewis acids, a result of the empty p_z orbital at the boron center. However, with the appropriate ligand system, electron-deficient boron compounds can undergo chemical reduction; and the additional electrons transform these species into powerful nucleophiles. Indeed, since the seminal reports of boryllithium by Yamashita and Nozaki,[175-176, 185-186, 189-190, 244] boron-centered anions have become valuable synthons in organometallic chemistry, and have afforded the isolation of a wide range of unique boron–element chemical bonds[245-246] (element = s-, d-, p-block element) (Figure 4.1a). Very recently, Aldridge reported a boron complex that approaches the "naked" boryl anion (Figure 4.1a).[247] Despite the high reactivity of these types of compounds, they can be used *in situ* to generate boron species that cannot be prepared using higher oxidation state starting materials. For example, anionic organoboranes have been shown to activate the C=O, H–H, C_{sp}–H, O–O, and C–F bonds of catalytically relevant small molecules.[244, 246, 248-254] Braunschweig reported an N-heterocyclic carbene-stabilized borole anion which reacts with organotetrel halides via nucleophilic substitution or single-electron transfer.[255-256] While the donor-supported borole anion represents an example where the added electron density primarily resides in the p_z orbital of boron, the central 6π-electron C_4B ring is not conjugated by flanking phenyl rings. Therefore, less electron delocalization occurs throughout the π-system of free borole anions (*vide infra*).

The incorporation of boron into polycyclic aromatic hydrocarbon (PAH) systems has gained immense attention as a creative strategy for the development of chromogenic and light-emitting materials technologies.[58, 61-62] Recently, substantial progress has been made in the synthesis of boron-based heterocycles (Figure 4.1), and borafluorene has become a popular building block in molecular chemistry.[98, 257-259] Indeed, neutral borafluorene compounds have been used extensively as redox-flexible emissive materials[93-97] and polymer-based sensors.[60, 260-263]

Despite the widespread applications of borafluorene, and the profound interest in accessing novel redox chemistry, isolated examples of reduced borafluorene compounds are exceptionally rare. Understanding the chemistry of borafluorenes featuring low-valent boron centers is not only important for the advancement of redox-dependent device applications, but could also led to new materials with unique bonding or optical properties that would otherwise be inaccessible.

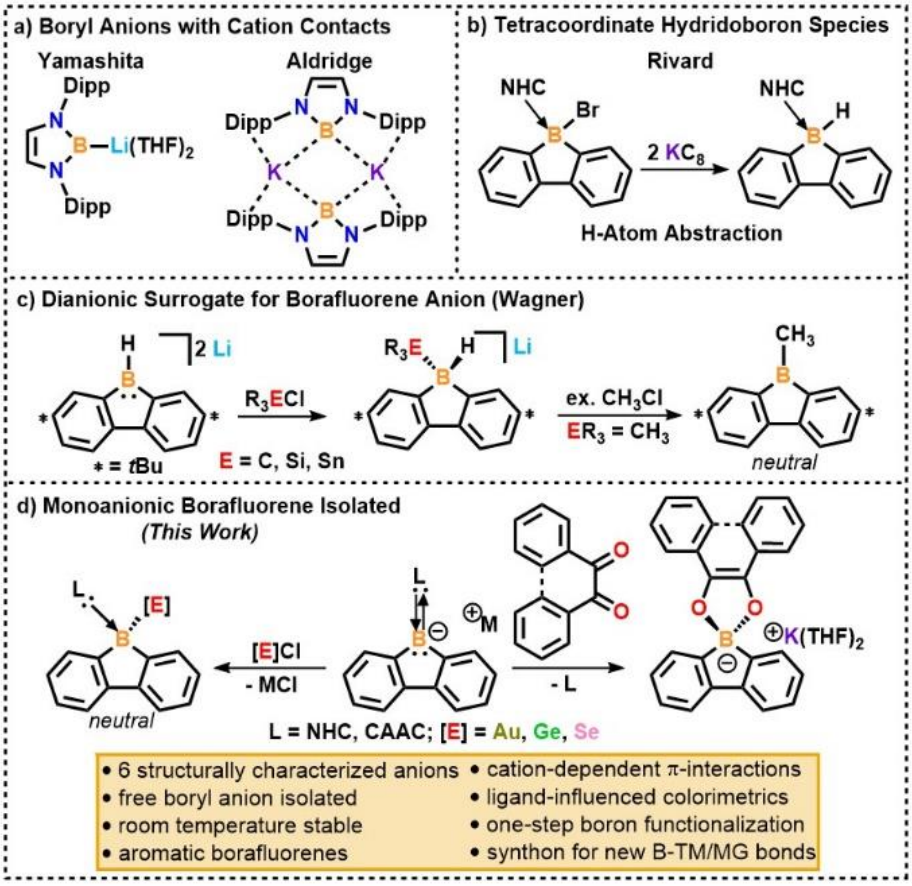

Figure 4.1. a) Reported boryl anions with cation contacts; b) hydrogen atom abstraction under reducing conditions; c) borafluorene dianion; and d) Lewis base-stabilized borafluorene monoanions (this work).

Recently, we have utilized carbenes to isolate a range of boracyclic materials,[99, 107] including the first examples of borafluorene radicals.[123] The successful synthesis of carbene-stabilized borafluorene radicals, and the appearance of reversible reduction waves in the cyclic voltammograms, led us to hypothesize that the elusive monoanionic borafluorene should be attainable under specific conditions. This compound type has been desired for years, but the increased reactivity of borafluorene anions compared to their neutral counterparts makes the synthesis quite challenging. It is noteworthy that Rivard and coworkers targeted the tricoordinate borafluorene anion by chemical reduction of the N-heterocyclic carbene (NHC)-9-bromo-9-borafluorene adduct (NHC-BF-Br). However, the tetracoordinate hydridoboron adduct (NHC-BF-H) was observed by ^{11}B NMR (confirmed by NMR spectral matching with NHC-BF-H isolated from the direct reaction of NHC-BF-Br and $LiAlH_4$). The reaction was reported to proceed via hydrogen atom abstraction, which highlights the high reactivity of the reduced species (Figure 4.1b).[102] Wagner et al. recently reported the synthesis of a borafluorene dianion bearing the non-sterically encumbered hydride ligand (Figure 4.1c).[264] Although this example represents a significant stride towards nucleophilic borafluorene, the existence of an isolable borafluorene monoanion remains elusive, and the chemical reactivity of reduced BFs as a building block for boron–element-containing materials is hitherto unknown.

Herein we report the synthesis, molecular structures, theoretical studies, and reactivity of NHC[16-20]- and CAAC[21-23, 265-266]-stabilized borafluorene monoanions (Figure 4.1d). Notably, these compounds represent the first successful two-electron reduction of carbene-supported 9-bromo-9-borafluorenes and the first isolation of the elusive 9-carbene-9-borafluorene monoanions. In addition, these anions react as nucleophilic boryl anions towards metal halides and ketones to generate new B–Au/Se/Ge/O bonded species that are unattainable using known starting materials.

Thus, 9-carbene-9-borafluorene monoanions are not only isolable, but they may be utilized as a chemical synthon.

4.2 Synthesis of 9-Carbene-9-Borafluorene Monoanions

Due to the reported challenges associated with the chemical reduction of NHC-coordinated (NHC = 1,3-bis(2,6-diisopropylphenyl)imidazol-2-ylidene) 9-bromo-9-borafluorene (Figure 4.1b),[102] we selected the CAAC (CAAC = 2,6-diisopropylphenyl)-4,4-diethyl-2,2-dimethyl-pyrrolidin-5-ylidene) analogue (CAAC-BF-Br) as a starting material, which was synthesized according to methods established by our laboratory.[102, 107] The addition of excess reducing agent [lithium naphthalenide (LiNp), sodium metal (Na), or potassium graphite (KC_8)] to a solution of **4.1** immediately resulted in a deep purple solution consistent with the previously reported CAAC-borafluorene radical.[123] Vigorous stirring at room temperature overnight produced a deep red solution, and the corresponding borafluorene anions **4.3-4.5** were obtained as deep red crystalline solids in 47-73% isolated yields (Scheme 4.1). The red solids are stable in solution at room temperature up to one week, and at least three months in the solid-state. Compounds **4.3-4.5** were characterized by their distinct downfield chemical shift [14.5 (**4.3**), 3.5 (**4.4**), and 1.5 ppm (**4.5**)] in the $^{11}B\{^1H\}$ NMR spectra, which was attributed to increased electron density and shielding at the boron center.

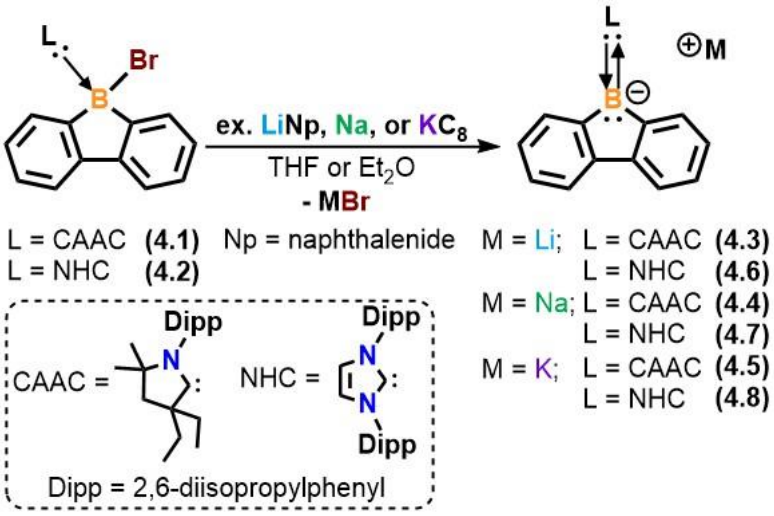

Scheme 4.1. Synthesis of Lewis base-stabilized borafluorene monoanions.

Due to the surprising storability of the CAAC-stabilized borafluorene anions, we sought to make direct comparisons with reactions to produce the NHC analogues, and speculated that cation effects, reaction conditions, and work-up method would be critical in their potential isolation. Compound **4.2** was reacted with the same reducing agents (LiNp, Na, KC_8), and during the course of the reaction, the solution remained deep purple in color, which would support the formation of a reduced species. Accordingly, deep indigo solids were obtained, which were identified as compounds **4.6-4.8** by X-ray crystallography, *vide infra* (60-79% isolated yields). While solutions of compounds **4.7** and **4.8** were stable to excess Na and K, for the LiNp reduction of **4.2**, excess reducing agent resulted in NHC ligand activation (Figure A3.11). As expected, the NHC-stabilized borafluorene anions were significantly less stable in solution than the CAAC analogues. We attribute the highly reactive nature of these compounds to the lower electrophilicity of NHCs, resulting in a more electron rich boron center. In fact, even after rigorous drying of NMR solvent, rapid conversion to the hydridoborafluorene product was supported by a doublet in the ^{11}B NMR spectra (-15.8 to -19.2 ppm). Thus, only NMR data for compound **4.8**, which was the most stable of the NHC analogues, is reported. Even in that case, sample prep required distillation of THF-d_8

over Na, storage over Na/K alloy overnight, and immediately completing NMR studies after **4.8** was dissolved. In the ^{11}B NMR spectrum of **4.8**, a singlet at 5.3 ppm was indicative of an anionic tricoordinate boron environment, in the range of CAAC compounds **4.3-4.5**. However, **4.6-4.8** can be stored in the solid state under an inert atmosphere for several weeks. The NMR challenges observed with the NHC compounds are consistent with reported boryl anions,[247] and thus highlights the value of CAAC compounds **4.3-4.5**.

In an effort understand the solid-state structures of the reduced borafluorenes, X-ray diffraction studies were performed. Red single crystals of **4.3-4.5** and violet crystals of **4.6-4.8** were obtained from concentrated diethyl ether solutions. The solid-state structures of the borafluorene anions varied drastically based on the ligand and cation (Figure 4.2).[267] Compounds **4.3** and **4.6** display solvated lithium cations with no contact to the central borafluorene ring. Generally, the solid-state structures of boryl anions have boron- and/or cation-π interactions and remarkably **4.3** and **4.6** represent examples of free boryl anions (Figure A3.18), with B---Li distances of 6.33 and 6.58 Å (>4.21 Å longer than the sum of the covalent radii (*R*(B-Li) = 2.12 Å)[268] and significantly longer than boryllithium (2.291 Å) (Figure 4.1a).[175] Conversely, the sodium cation of **4.4** was coordinated by two THF molecules, and maintained contact to the central 5-membered boron-containing ring [Na---centroid, 2.5109(13) Å]. In order to obtain a single crystal of **4.6** and **4.7**, one equivalent of 18−crown−6 was added to stabilize the Li and Na cations. Therefore, **4.7** displays a structure in which the sodium cation is encapsulated by 18−crown−6 and has no contact with the borafluorene unit [B---Na, 7.35 Å], (4.85 Å longer than the sum of the covalent radii (*R*(B–Na) = 2.50 Å).[268] When the syntheses of **4.5** and **4.8** are carried out in Et_2O, the crystals grown from that reaction display structures with no solvent contacts. Instead, the reduced borafluorene moieties are linked by potassium cations in a polymeric (for **4.5**) and

cyclohexameric (for **8**) fashion (Figure 4.3). In compound **4.5,** the potassium cations interact with the 5-membered boron-containing ring, forming a coordination polymer with K---centroid distances between 2.8721(18) and 2.9649(19) Å. In contrast, the primary interaction in compound **4.8** is between the potassium cation and the six-membered rings of the reduced borafluorene system and between the potassium and the 2,6-diisopropylphenyl rings on the NHC ligand. The K---centroid distances for these interactions span a larger range than those in **4.5**, measuring between 2.8032(15) – 3.4647(13) Å.

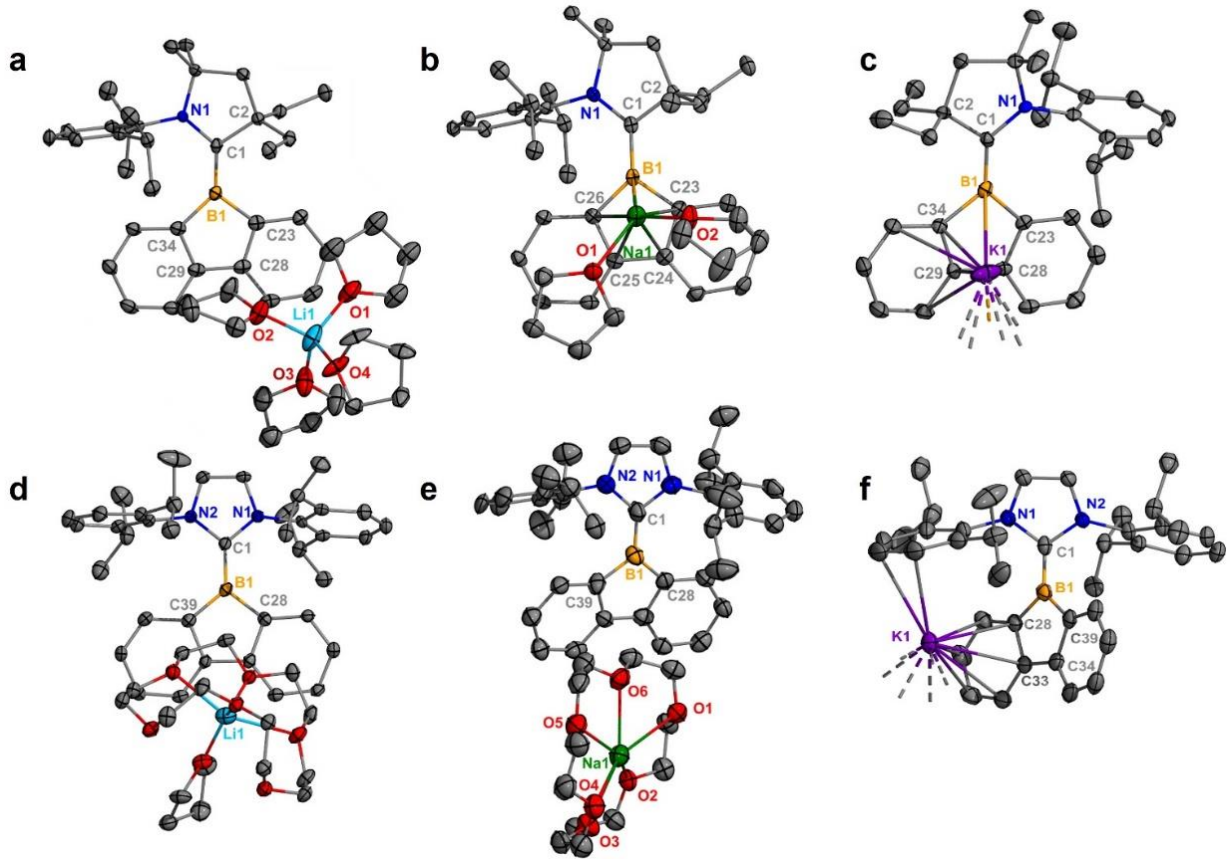

Figure 4.2. Molecular structures of CAAC-BF-anions [**4.3**(a), **4.4**(b), **4.5**(c)] and NHC-BF-anions [**4.6**(d), **4.7**(e), **4.8**(f)]. Thermal ellipsoids shown at 50% probability and H atoms were omitted for clarity.

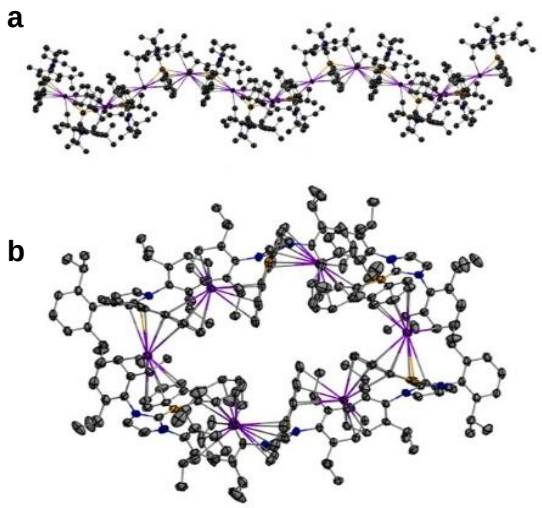

Figure 4.3. Solid state structures of **4.5** (a) and **4.8** (b) depicting polymeric and cyclohexameric structures.

In all of the Lewis base-stabilized borafluorene anions (**4.3-4.8**), the B1–C1 bond lengths [1.502(5)-1.527(4) Å] are significantly shorter than the reported borafluorenium ions [1.581(10) and 1.567(5) Å], radical species [1.551(2) and 1.550(2)], and neutral carbene-coordinated 9-bromo-9-borafluorenes [**4.1** = 1.640(4), and **4.2** = 1.639(3) Å] (Table 1).[102, 107, 123] The B1–C1 bond distances of the borafluorene anions are in range of reported B=C double bonds [1.45-1.58 Å].[105] Additionally, the boron atom in each anion occupies a distorted trigonal planar geometry as the angles range from 100.8-132.8°. Due to the superior π-accepting ability of CAAC, the B–C bonds in the central boron-containing ring were significantly longer in **4.3-4.5** [1.599(3)-1.621(5) Å] compared to **4.6-4.8** [1.533(4)- 1.576(11)Å]. Notably, the carbene ligand N-heterocycles are not coplanar with the borafluorene moiety, and the NHC analogues possess the largest interplanar angles (14-32°) while the CAAC anions had angles ranging from 7.5-14°.

Table 4.1. Selected bond distances obtained from crystallographic data and observed chemical shifts of the ^{11}B nuclei of compounds **4.3-4.14**.

Compound	B1–C1 (Å)	B–C_{endo} (Å)	B–C_{endo} (Å)	^{11}B (ppm)
4.3	1.506(3)	1.599(3)	1.614(3)	14.45
4.4	1.512(3)	1.606(3)	1.618(3)	3.51
4.5	1.502(5)	1.603(5)	1.621(5)	1.46
4.6	1.527(4)	1.575(4)	1.585(4)	-
4.7	1.513(11)	1.573(11)	1.576(11)	-
4.8	1.508(4)	1.533(4)	1.534(4)	5.29
4.9	1.555(8)	1.627(8)	1.644(8)	3.01
4.10	1.6186(14)	1.6337(14)	1.6578(14)	-10.75
4.11	1.635(7)	1.617(8)	1.630(8)	-5.40
4.12	1.601(4)	1.624(4)	1.640(4)	-3.42
4.13	-	1.6319(18)	1.6383(18)	13.71
4.14	-	1.56(3)	1.62(4)	16.27

The electronic structure and bonding of the bare anions $[L\text{-}BF]^-$ (L= CAAC, NHC) was investigated with DFT calculations. Computed geometries are in agreement with the X-ray structures, with B1−C1 bond distances of 1.501 Å (WBI = 1.153) for $[NHC\text{-}BF]^-$ and 1.502 Å (WBI = 1.381) for $[CAAC\text{-}BF]^-$. It is appropriate to compare the electronic structure of the anionic complexes with our previously reported carbene-stabilized borafluorene radicals.[123] The additional electron in the anion system results in a decrease in the B−$C_{(carbene)}$ bond distance (and increase in WBI). In both anion and radical complexes, the HOMO (SOMO for radical) is delocalized across the L-BF system (Figure 4.4), with significant B−$C_{(carbene)}$ π-bonding character. CM5 atomic charges yield negative charges on the boron atoms of -0.324e $[NHC\text{-}BF]^-$ and -0.302e $[CAAC\text{-}BF]^-$. The carbene C atom carries a positive charge, which is greater in the NHC system (0.195e) than in the CAAC system (0.081e).

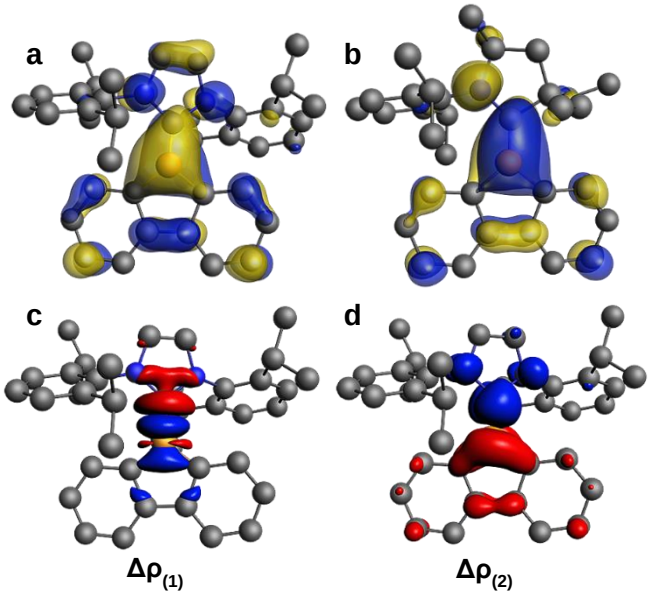

Figure 4.4. Plot of HOMO of (a) $[NHC\text{-}BF]^-$ and (b) $[CAAC\text{-}BF]^-$. EDA-NOCV deformation densities (c) Δρ(1) and (d) Δρ(2) associated with orbital interactions $\Delta E_{orb}(1)$ and $\Delta E_{orb}(2)$ for $[NHC\text{-}BF]^-$. Charge flow red→blue (isosurface = 0.003).

Energy decomposition analysis in combination with natural orbitals for chemical valence (EDA-NOCV) was performed in order to probe the $[L\text{-}BF]^-$ bond and to compare with the previously reported $[NHC\text{-}Borole]^-$ (Figure 4.4). Both donor-acceptor, and electron-sharing bonding models were explored. For the donor-acceptor model, fragments of singlet anion BF and neutral singlet L were examined, while triplet configurations for BF and L were used to model the electron-sharing model (Figure 4.5). Both models represent a B=C bonding motif.

Figure 4.5. Bonding models considered for EDA, a) Singlet fragment donor-acceptor model, b) Triplet fragment electron-sharing model.

The overall interaction energy (ΔE_{int}) between L and BF is greater for CAAC (-153.9 kcal/mol) than NHC (-132.4 kcal/mol) (Table 4.2). In comparison, ΔE_{int} for [NHC-Borole]$^-$ is -128.5 kcal/mol, which is indicative of a stronger B-C bond in the borafluorene systems. The preferred bonding model – either donor-acceptor or electron-sharing – is indicated by the smallest orbital interaction (ΔE_{orb}), which favors a donor-acceptor description of the B-C bond for [NHC-BF]$^-$, [CAAC-BF]$^-$ and [NHC-Borole]$^-$ (Table A4.25). In both complexes, dispersion interactions account for 12-14% of the total attractive interactions. For [NHC-BF]$^-$ there are nearly equal contributions from covalent (ΔE_{orb}, 50%) and electrostatic (ΔE_{elstat}, 43%) interactions, whereas [CAAC-BF]$^-$ has a larger covalent contribution (52%). NOCV analysis was utilized to decompose the attractive orbital interactions into pairwise orbital interactions (Figure 4.5). The largest orbital interaction in both [L-BF]$^-$ systems is σ-donation [L]→[BF]$^-$, which accounts for 53% of ΔE_{orb} in [NHC-BF]$^-$ and 50% in [CAAC-BF]$^-$. The second most significant orbital interaction is π-backdonation, accounting for 33% of ΔE_{orb} in [NHC-BF]$^-$ and 38% in [CAAC-BF]$^-$.

Table 4.2. EDA-NOCV results for [NHC-Borole]$^-$ and [L-BF]$^-$ (L = NHC, CAAC) at the B3LYP-D3(BJ)/TZTP level of theory for the donor-acceptor bonding model. Energies given in kcal mol^{-1}.

	[NHC-Borole]$^-$	[NHC-BF]$^-$	[CAAC-BF]$^-$
ΔE_{int}	-128.5	-132.4	-153.9
ΔE_{Pauli}	+216.8	+219.9	+223.1
ΔE_{elstat} [a]	-151.7 (44%)	-151.7 (43%)	-157.9 (42%)
ΔE_{orb} [a]	-165.5 (48%)	-176.7 (50%)	-198.1 (52%)
ΔE_{disp} [a]	-28.5 (8%)	-23.9 (7%)	-21.1 (6%)
$\Delta E_{orb(1)}$ [b] (σ)	-97.1 (59%)	-94.1 (53%)	-99.0 (50%)
$\Delta E_{orb(2)}$ [b] (π)	-46.9 (28%)	-58.2 (33%)	-75.4 (38%)
ΔE_{rest}	-21.5 (13%)	-24.4 (14%)	-23.7 (12%)

[a] Values in parentheses give the percentage contribution to the total attractive interactions $\Delta E_{elstat} + \Delta E_{orb} + \Delta E_{disp}$. [b] Values in parentheses give the percentage contribution to the total orbital interactions ΔE_{orb}.

The aromatic character of [L-BF]$^-$ was assessed using nucleus-independent chemical shifts (NICS) and through visualization of the anisotropy of the induced current density (AICD). Negative values of NICS(1) (calculated 1 Å perpendicular to the plane of the ring) are indicative of aromatic character (Figure 4.6). For reference, the NICS(1) value for the Ph groups of the BF moiety is approximately -24 ppm in both the [NHC-BF]$^-$ and [CAAC-BF]$^-$ complexes. Comparison of NICS(1) values for the neutral, cationic, and anionic BFs highlight the tunable electronic structure of the BF moiety. Our recently reported carbene-stabilized borafluorene cations exhibit 4π antiaromatic character.[107] The neutral radical [L-BF]$^\bullet$ complexes are nonaromatic with 5π-electrons and a positive NICS(1) value.[123] Reduction of these radicals affords the aromatic 6π-electron anion. The difference in magnitude of the NICS(1) value between the [NHC-BF]$^-$ and [CAAC-BF]$^-$ is due to the enhanced electron-donating ability of the in-plane σ lone-pair of CAAC over NHC that distorts the ring current. This is also observed in the NICS(1) values of the NHC (Table A4.28) whereby the magnitude of the shielding decreases going from the [NHC-BF]$^\bullet$ (-18.6 ppm) to the [NHC-BF]$^-$ (-9.7 ppm). The spin-density in [NHC-BF]$^\bullet$ was found to be localized to the N-C-B π-system, therefore a decrease in magnitude of the NICS(1) shielding for the NHC in the anion suggests further delocalization (enhanced π-interaction), which is consistent with results from EDA. Notably, the NICS(1) value for the boron-containing ring in [NHC-BF]$^-$ (-21.4 ppm) is significantly larger than the borole analogue (-10.1 ppm) due to the additive ring currents of the neighboring phenyl groups in [NHC-BF]$^-$, indicating a drastic increase in aromaticity. The dianion synthesized by Wagner *et al.*[264] was found to be a highly localized 6π-electron aromatic system, as a result of having no Lewis base to disrupt the uniformity of the ring current.

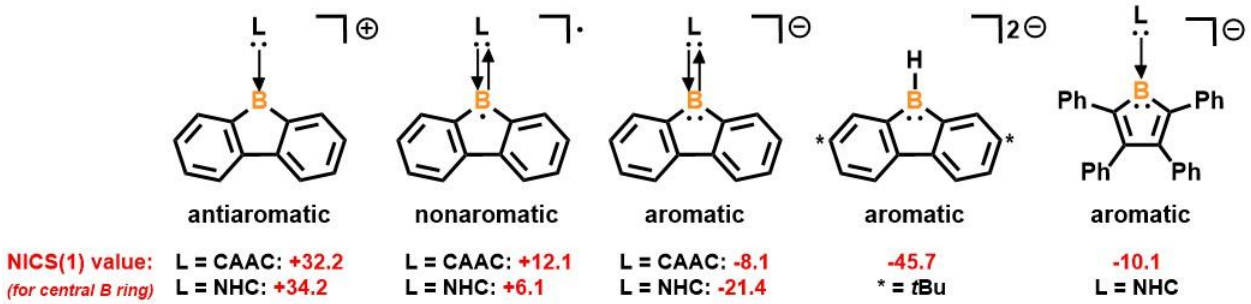

Figure 4.6. Calculated isotropic out-of-plane NICS(1)$_{ZZ}$ values (ppm) at the B3LYP-D3(BJ)/def2-TZVP level of theory.

ACID plots provide further insight into the aromatic character of [NHC-BF]$^-$ and [CAAC-BF]$^-$ in comparison with [NHC-Borole]$^-$ (Figure 4.7 and A4.40). All systems exhibit a diatropic (clockwise) aromatic π-electron circulation, with greater delocalization and uniformity of the current density vectors across boron of the BF complexes than that observed in [NHC-Borole]$^-$. The magnitude of the critical isosurface value (CIV) indicates the extent of delocalization between two atoms. The CIV for heterocylic B-C bonds was found to be 0.063, 0.058 and 0.056 for [NHC-BF]$^-$, [NHC-Borole]$^-$ and [CAAC-BF]$^-$ respectivly (for reference the CIV between two carbon atoms in benzene is 0.074). Both NICS and ACID results indicate that [NHC-BF]$^-$ exhibits greater aromatic character than [CAAC-BF$^-$] or [NHC-Borole]$^-$.

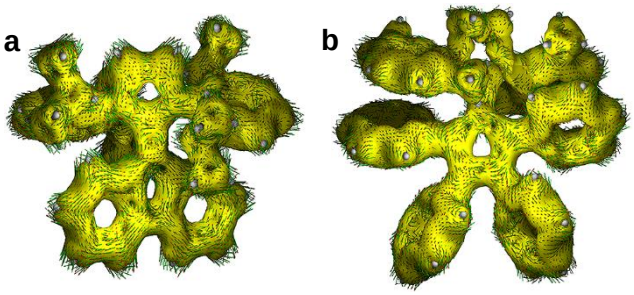

Figure 4.7. ACID plots of (a) [NHC-BF]$^-$ and (b) [NHC-Borole]$^-$ (isosurface = 0.03).

4.3 Reactivity of 9-Carbene-9-Boralfuorene Monoanions with Metal Halides

After isolating the borafluorene anions, we were interested in probing their ability to react as nucleophiles with various substrates. The addition of one equivalent of PPh_3AuCl, Et_3GeCl, or PhSeCl to **4.5** resulted in KCl salt elimination and afforded tetracoordinate compounds **4.9-4.11** in 41-58% yields (Scheme 4.2). In the $^{11}B\{^1H\}$ NMR spectra, chemical shifts at 3.0 (for **4.9**), -10.8 (for **4.10**), and -5.4 ppm (for **4.11**) were consistent with the structures containing a single boron-containing product. After adding one equivalent of Ph_3PAuCl to a solution of **8**, the crude ^1H NMR spectrum revealed a complex mixture of new products due to the highly reactive nature of **4.8** in solution. However, yellow crystals of **4.12** were obtained. The $^{11}B\{^1H\}$ NMR spectrum of the single crystals of **4.12** showed a signal at -3.4 ppm, which is similar to that of **4.9** (Scheme 4.2).

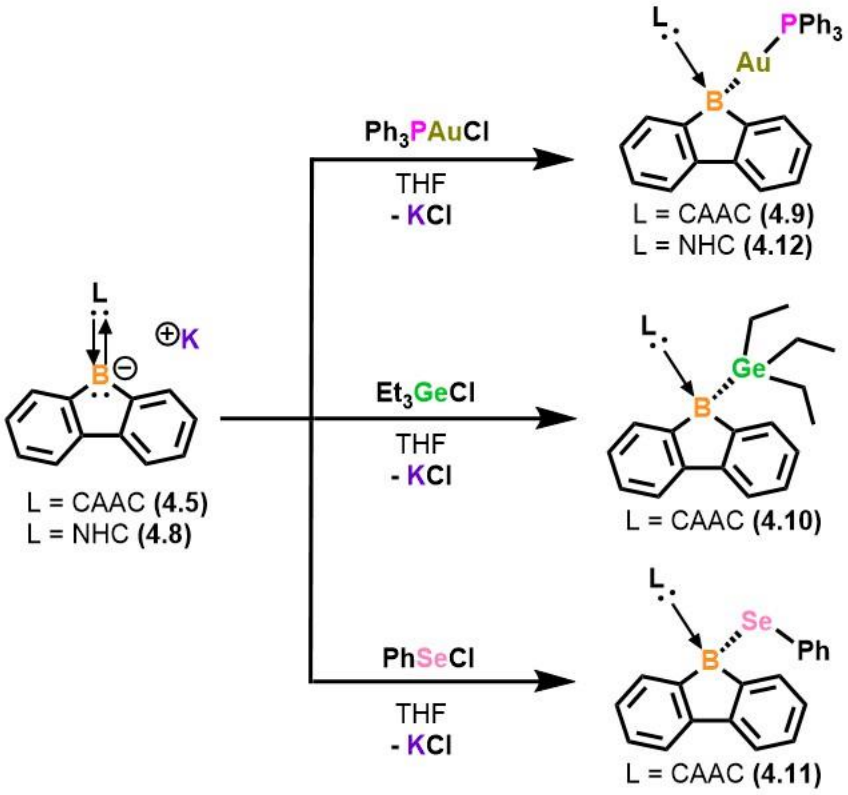

Scheme 4.2. Reactivity of borafluorene anions with transition metal and main-group halides.

Compounds **4.9-4.12** were characterized by X-ray crystallography, all of which displayed a tetracoordinate boron center (Figure 4.8). In all cases, the B1–C1 bond in **4.9-4.12** [1.555(8)-1.635(7)] was elongated in comparison to **4.5** and **4.8**. the B1–C1 interactions [**4.9**: 1.555(8) Å; **4.12**: 1.601(4) Å] were similar in both borafluorene-[gold] analogues. The bulky N-diisopropylphenyl substituents on NHC in **4.12** have the effect of distorting the planarity between the [L-BF]- system (N1-C1-B1-C23; 24.5° for **4.9** and 34.3° **4.12** respectively) thereby reducing the B1-C1 π-interaction. This same trend was observed computationally with interplanar angles of 21.5° (**4.9**) and 35.8° (**4.12**).

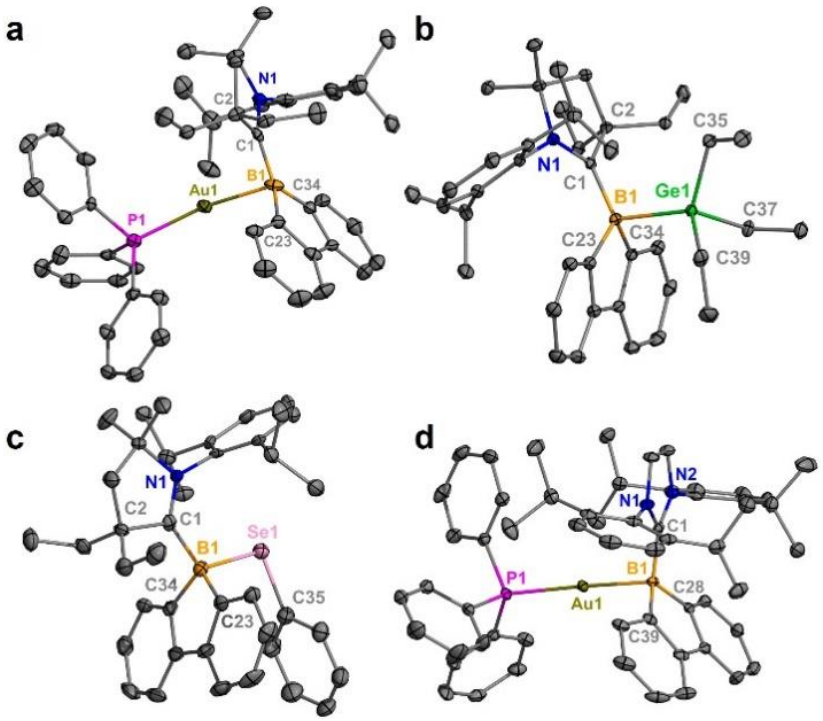

Figure 4.8. Molecular structures of reactivity products of **4.9-12** (a-d respectively). Thermal ellipsoids shown at 50% probability and H atoms were omitted for clarity. Selected bond lengths [Å] and angles [°]: **4.9**: B1–Au1 2.223(6), P1–Au1 2.2969(13), B1–Au1– P1 164.85(16); **4.10**: B1–Ge1 2.2079(10); **4.11**: B1–Se1 2.103(6), Se1–C35 1.926(5); **4.12**: B1–Au1 2.184(3), P1–Au1 2.3361(7), B1–Au1– P1 175.04(8).

4.4 Reactivity of 9-Carbene-9-Borafluorene Monoanions with Diketones

To understand the reactivity of the BF anions with unsaturated substrates, one equivalent of benzil was added to **5** or **8** in THF. An immediate loss of the deep colors was observed in addition to their solutions becoming fluorescent. Interestingly, the carbene ligands are displaced to yield the new spirocyclic compound **4.13** in 44% (**4.8**) and 58% (**4.5**) isolated yields (Scheme 3). In a similar fashion, one equivalent of 9,10-phenanthrenequinone was added to **4.5** in THF, which afforded compound **4.14** in 55% isolated yield. It is noteworthy that both of these reactions cleanly eliminate free carbene and essentially serves as a means to transfer $[BF]^-$ for the construction of complex heterocycles. Thus, the size of the ligand does not prohibit the formation of new B–centered materials. These reactions illustrate a clear difference in reactivity compared to the hydride-protected dianionic BF and highlights a potential benefit for the utilization of BF monoanions stabilized by neutral ligands. In addition, this novel reactivity with diketones showcases an instance in which the borafluorene monoanions can be transformed into O–B–O containing materials.[269] Spirocycles **4.13** and **4.14** were characterized by distinct downfield shifts in the $^{11}B\{^1H\}$ NMR spectra (13.7 ppm for **4.13**; 16.3 ppm for **4.14**), compared to **4.5** (1.5 ppm).

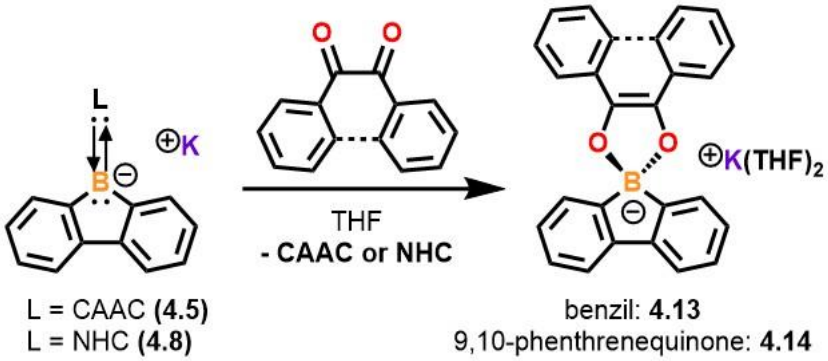

Scheme 4.3. Synthesis of O–B–O spirocyclic materials (**4.13** and **4.14**) from borafluorene anions.

Single crystals of **4.13** and **4.14** were obtained from concentrated THF/toluene mixtures at -37 °C. In contrast to the nucleophilic substitution products **4.9-4.12**, the boron atom in **4.13** and

4.14 remain anionic and maintain contact with the potassium cation (Figure 4.9). In **4.14** the phenanthrene moiety is planar, while the phenyl groups of **4.13** are not bound, and therefore twist out of plane. These O–B–O compounds also exist as a coordination polymers in the solid state (Figures A3.24 and A3.26).

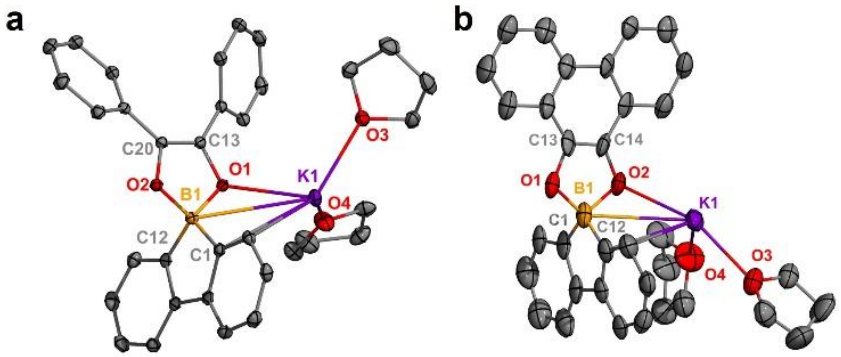

Figure 4.9. Molecular structures of **4.13** (a) and **4.14** (b). Thermal ellipsoids shown at 50% probability and H atoms were omitted for clarity. Selected bond lengths [Å]: 13: B1–O1 1.5103(15); B1–O2 1.5156(15); O1–C13 1.3796(14); O2–C20 1.3801(14); C13–C20 1.3565(16); 14: B1–O1 1.52(3); B1–O2 1.57(3); O1–C13 1.42(2); O2–C14 1.35(2); C13–C14 1.30(3).

The photophysical properties of compounds **4.13** and **4.14** were explored by UV/vis and fluorescence spectroscopy. Absorption maxima for **4.13** and **4.14** were exhibited at 411 nm and 374 nm respectively, with emission maxima for **4.13** and **4.14** red-shifted to 513 nm and 520 nm (Figure 4.10). Both spirocyclic boron heterocycles (**4.13** and **4.14**) display bright green fluorescence under UV light. Time-dependent density functional theory (TD-DFT, ωb97X/def2-SVP) analysis indicates that the first excited state (S_1) centred at 410 nm and 450 nm for **4.13** and **4.14**, respectively, correspond to $\pi \rightarrow \pi^*$ transitions on the benzil and phenanthrenequinone moieties (see ESI for plots of frontier molecular orbitals). Excited state

dynamics calculations reproduced the emission spectra with only the first root (S_1) for both compounds. This indicates that although the absorbance maxima for **4.14** is observed at 374 nm, an internal conversion process ($S_2 \rightarrow S_1$) results in a $\pi^* \rightarrow \pi$ emission ($S_1 \rightarrow S_0$) in accordance with Kasha's rule.[270] This was confirmed via experiment whereby excitation wavelengths at 370 nm and 450 nm result in the same emission spectra.

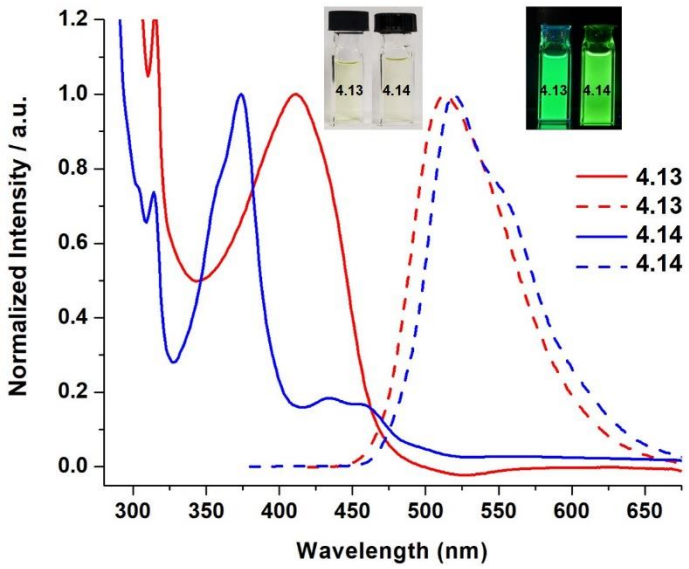

Figure 4.10. Normalized absorption (solid) and emission (dashed) spectra of **4.13** (red) and **4.14** (blue). Solutions were dissolved in THF and ran at room temperature. Compound **4.13** was excited at 410 nm and compound **4.14** was excited at 370 nm.

4.5 Summary and Outlook

We have synthesized and structurally characterized the first examples of borafluorene monoanions, and the first reduced borafluorenes isolated using neutral ligands−a feat that has proved extremely challenging. DFT calculations support the anionic character of the borafluorenes and the nucleophilicity was probed by various reactions with metal halides and diketones. Now

that a tricoordinate boron anion is "doped" within a rigid polycyclic aromatic hydrocarbon, these compounds are well-suited to be used as a building block for the synthesis of new materials. This is supported by the preliminary reactivity studies presented herein, including the synthesis of boron-element chemical bonds and spirocycles. Efforts to expand the reactivity of these anions towards other small molecule substrates and chemically inert bonds are currently under investigation in our laboratory.

Moving forward, it will be important to explore the reactivity of the borafluorene monoanions with lithium and sodium countercations (**4.3** and **4.4**). With the presence of smaller cations, it is expected that a new variety of borafluorene-containing products can be obtained. Additionally, it will be essential try to isolate borafluorene monoanions with a less π-accepting and more σ-donating carbene ligand (e.g. yilidic diaminocarbenes)[20, 271] than the CAAC and NHC ligands used in this study. By using these 6-membered yilidic diaminocarbenes to stabilize borafluorene monoanions, more electron-rich boron environments should be obtained than those of the CAAC-borafluorene monoanions. Additionally, due to the superior σ-donor ability of yilidic diaminocarbenes in comparison to the 5-membered NHCs studied herein, these new borafluorene monoanions should be more stable and easier to work with for develop a new reactivity profile.

Chapter Five: Boryl-Substituted Selenides and Diselenides

Containing work that was originally published in:

Wentz, K. E.; Molino, A.; Freeman, L. A.; Dickie, D. A.; Wilson, D. J. D.; Gilliard, R. J., Reactions of 9-Carbene-9-Borafluorene Monoanion and Selenium: Synthesis of Boryl-Substituted Selenides and Diselenides. *Inorg. Chem.* **2021,** *60*, 13941-13949.

5.1 Introduction to Group 13 Reactivity with Selenium

Traditional tricoordinate boranes, possessing an empty p_z-orbital, are well-known as Lewis acids due to their ability to readily accept an electron pair.[272] However, chemical reduction of these borane moieties generates a class of potent nucleophiles, which have been shown to activate various small molecules[176, 190, 244, 246, 248, 252-253, 264] and form numerous transition metal coordination complexes.[186-189] Low-coordinate, anionic group 13 element-centered heterocycles that feature a lone pair are isoelectronic to N-heterocyclic carbenes (NHC),[16-17, 273-275] however, they are stronger σ-donors and weaker π-acceptors.[177] Even though several studies on NHC-stabilized heavy chalcogens exist,[276-280] and the anionic group 13 analogues of NHC have been known for over two decades, the reactivity of these anions with heavy chalcogens has been limited to only two examples.[281-282]

Reactions with selenium give valuable insight into the electronics and redox behavior of a given molecular system because of its ability to exist in a variety of oxidation states.[283-287] In addition, selenides and diselenides are useful synthetic targets and play a vital role in the development of organic oxidations[288-289] and functionalized alkenes.[283-285, 287, 290-292] Owing to the poor solubility of elemental selenium in common organic solvents, most reactions involve the use of organochalogenide starting materials (e.g., Ph_2Se_2). One key account involving the N-heterocyclic gallyl (NHGa) anion activating the Se–Se bond of diphenyl diselenide was reported by Jones *et al.* wherein they isolated a [NHGa$(SePh)_2$] anion (Figure 5.1a).[282]In addition, Coles reacted the aluminyl anion {K[Al(NON^{Ar}]} with elemental selenium to generate a group 13 metal analogue of a carbonyl group, containing an Al=Se multiple bond (Figure 5.1b).[282] While several studies by Braunschweig involving the reactivity of NHC-borylene moieties and heavy chalcogens are known,[293-296] it was not until recently that anionic boryl heterocycles were shown to activate selenium. Kinjo demonstrated that aromatic diazaborinine can oxidatively add elemental selenium

across the 6-membered core to yield a heavier analogue of dibora-peroxide (Figure 5.1c).[297] Wagner and coworkers used a doubly-reduced diboraanthracene (DBA) dianion to cleave the $\sigma_{Se–Se}$ bond of Se_2Ph_2 to furnish the oxidized DBA as the first example of boron heterocycle mediated Se–Se bond activation (Figure 5.1d).[253]

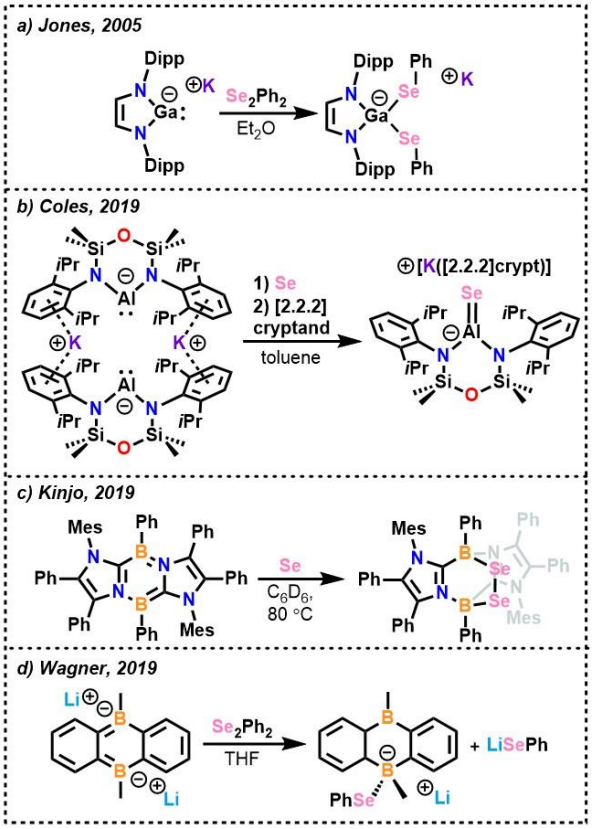

Figure 5.1. a) PhSe–SePh cleavage by N-heterocyclic gallyl anion; b) reaction of diboraanthracene dianion with Se_2Ph_2; c) activation of elemental selenium by diazaborinine; d) synthesis of a group 13 metal analogue of CO containing an Al=Se multiple bond.

Recently we isolated 9-carbene-9-borafluorene monoanions and described initial reactions with metal halides and diketones, which produced a series of new compounds with B–E bonds (E = Au, Se, Ge, and O).[298] We remain interested in gaining a deeper understanding of the reactivity trends for these boracyclic anions and herein we report reactions of 9-carbene-9-borafluorene

monoanion with elemental selenium and selenium-containing reagents. Notably, we have synthesized and structurally characterized the first examples of boryl-substituted selenides and diselenides.

5.2 Reactivity of 9-Carbene-9-Borafluorene Monoanion with Grey Selenium

After the addition of grey selenium powder to a solution of 9-CAAC-9-borafluorene monoanion (**4.5**) [CAAC = 2,6-diisopropylphenyl)-4,4-diethyl-2,2-dimethyl-pyrrolidin-5-ylidene][21-23] in THF, an immediate color change from deep red to orange was observed (Scheme 1). The crude ^{1}H NMR spectrum showed a mixture of various products which was supported by the appearance of four new ligand methine environments. Numerous reaction trials under similar conditions and multiple recrystallizations gave differing mixtures of single-crystals which were identified by X-ray crystallography (vide infra) as selenium-containing products **5.2-5.6** (Figure 5.2). In one instance, a few single-crystals were used to characterize compounds **5.2**-**5.4** via multinuclear NMR, however, it was not enough to establish bulk purity by elemental analysis. Surprisingly, in compounds **5.3** and **5.4**, migration of the *N*-Dipp group to the selenium was observed, while in **5.2**, the *N*-Dipp group was not a part of the structure. The isolation of these compounds is consistent with the formation of the potassium organoselenide **5.6**, which was isolated from the same reaction mixture, but has ether coordination due to additional workup procedures and crystallization conditions. In the unsymmetrical diselenide (**5.4**), the *N*-Dipp group stayed intact with the nitrogen atom and another Dipp group migrated to the second selenium atom. A sufficiently resolved ^{77}Se{^{1}H} chemical shift for compound **5.2** could not be observed. Due to the symmetry present in compound **5.3** only one selenium environment was observed at 0.2 ppm in the ^{77}Se{^{1}H} NMR spectrum. However, in the ^{77}Se{^{1}H} NMR spectrum of **5.4**, two resonances at 144 and 299 ppm correspond to the two chemically inequivalent selenium atoms.

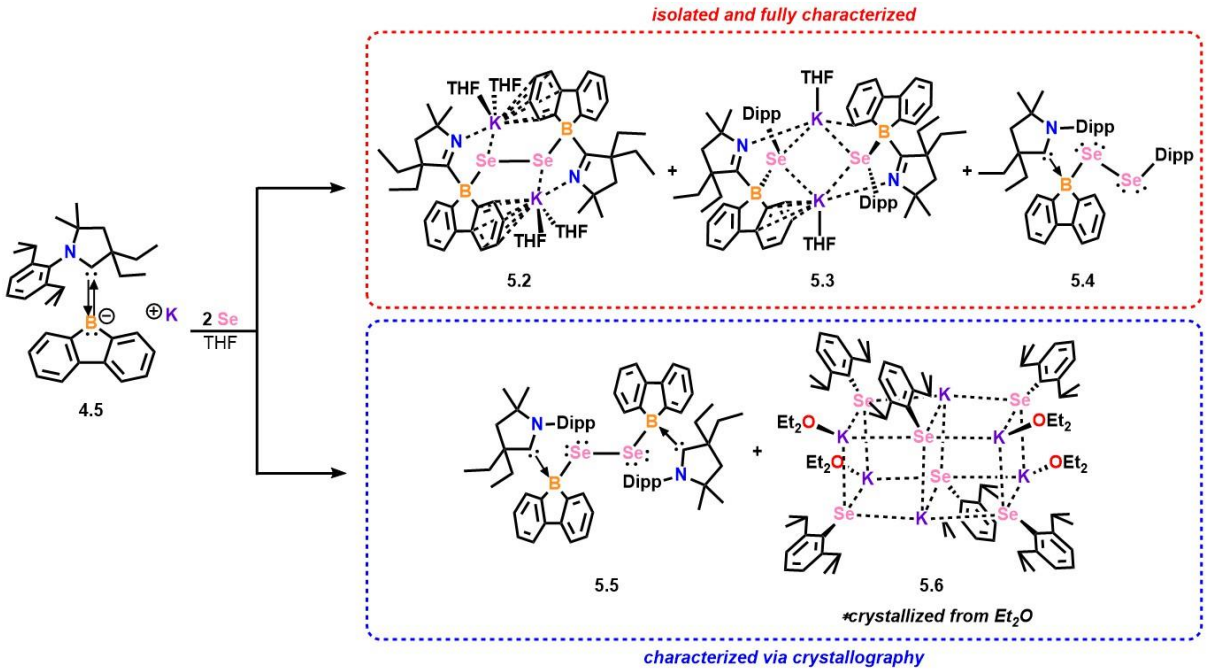

Scheme 5.1. Reaction of 9-CAAC-9-borafluorene monoanion and grey selenium yields multiple selenium-containing products.

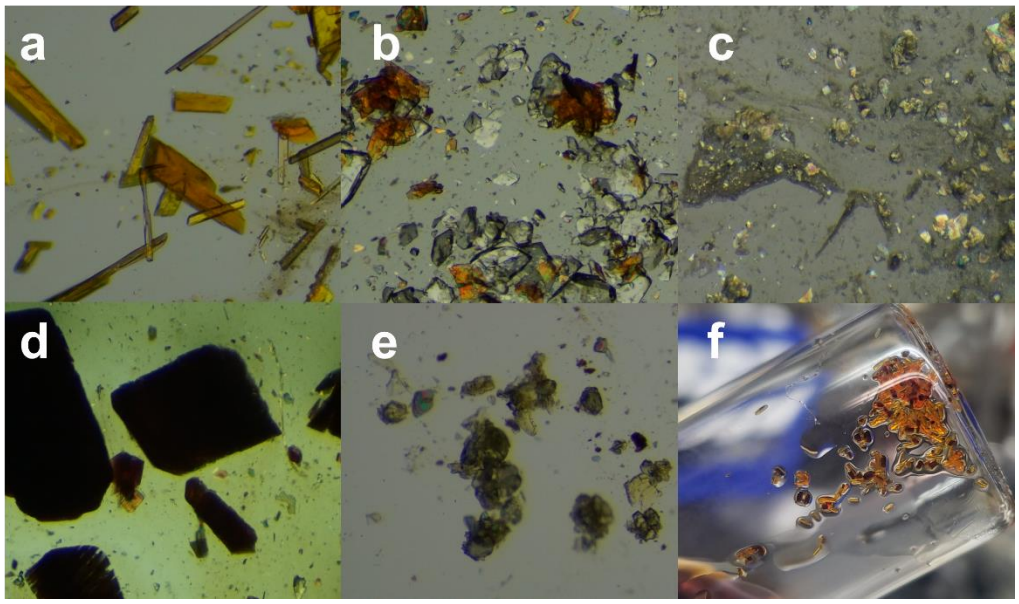

Figure 5.2. Digital images of the samples of single-crystals: a (**5.2**); b (mixture of **5.2** (orange) and **5.3** (colorless)); c (**5.4**); d (**5.5**); e (**5.6**); f (mixture of **5.2** (orange) and **5.5** (red)). Crystals of **a-e** are magnified by 40x on an optical microscope while **f** is not magnified.

Single-crystals of compounds **5.2**-**5.6** were grown and X-ray diffraction studies were performed to explore the structural properties of the selenium-containing products (Figure 3).[49] The molecular geometries of **5.2**, **5.4**, and **5.5** are all consistent with a trans-bent B–Se–Se–B core structure with torsion angles for B–Se–Se–B ranging from 146° (**5.4**) to 180° (**5.2** and **5.5**). The B-Se-Se angles are 103.92(18)° (**5.2**), 98.23(8)° (**5.4**), and 95.56(4)° (**5.5**), consistent with the presence of lone pairs on the Se atoms. Compounds **5.2**, **5.3**, and **5.6** have Se–K bonds ranging from 3.2174(14) to 3.303(2) Å, which are within the reported range of single bonds between selenium and potassium (Table 1).[267] The Se–Se bonds in compounds **5.2**, **5.4**, and **5.5** [2.3612(4)-2.3807(11) Å] are slightly shorter than the reported sum of the single bond covalent radii, *R*(Se–Se) = 2.40 Å.[268] In compound **5.3**, the distance between the two selenium atoms is 4.411 Å, which is significantly longer than the Se–Se bonds in **5.2**, **5.4**, and **5.5**, indicating that no significant Se-Se interaction exists in **5.3**.

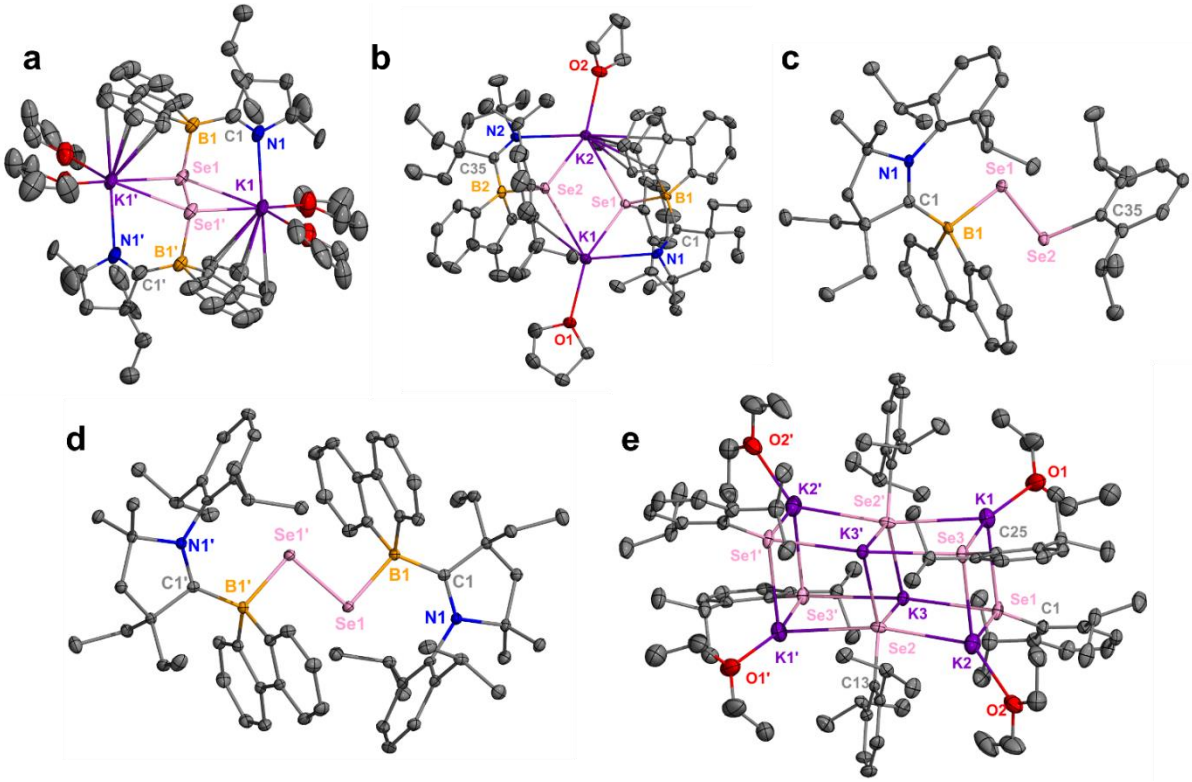

Figure 5.3. Molecular structures of **5.2**-**5.6** (**a**-**e**, respectively). Thermal ellipsoids set at 50% probability with H atoms and non-coordinated solvent omitted for clarity.

Table 5.1. Selected bond distances (Å) in compounds **5.2**-**5.8**.

Compound	B1–C1	C1–N1	B1–Se1	Se1–K1	Se1–Se1′/2
5.2	1.613(9)	1.301(8)	2.131(7)	3.2745(14)	2.3807(11)
5.3	1.627(8)	1.285(7)	2.126(6)	3.2174(14)	–
5.4	1.617(4)	1.312(4)	2.141(3)	–	2.3685(4)
5.5	1.634(2)	1.3139(17)	2.0937(15)	–	2.3612(4)
5.6	–	–	–	3.303(2)	–
5.7	1.624(4)	1.283(3)	2.129(3)	3.5103(6)	–
5.8	–	–	–	3.3326(5)	–

5.3 Effect on Reactivity in Presence of 18-crown-6

In order to decrease the number of products obtained from Se activation, 18-crown-6 was added to **4.5** to aid solubilization in non-polar solvent and to promote product stability. The potassium cation was encapsulated by the crown ether thereby rendering the borafluorene monoanion soluble in toluene. After the addition of one equivalent of selenium to the reaction mixture, the reaction was stirred for 20 hours and analysis of the resulting solid by a ^{1}H NMR experiment in C_6D_6 showed a new resonance at 4.22 ppm, which was assigned to the *N*-Dipp methine environment of **5.7** (Scheme 5.2). After reducing the volume of the solution and storing at -37 °C two different sizes of colorless crystals were obtained. The larger colorless blocks were determined to be **5.7** by X-ray crystallography while the smaller crystals were characterized as **5.8**. A ^{1}H NMR spectrum of crystalline **5.8** in THF-d_8, which was not soluble in the original C_6D_6 NMR sample, revealed a different methine environment at 4.64 ppm.

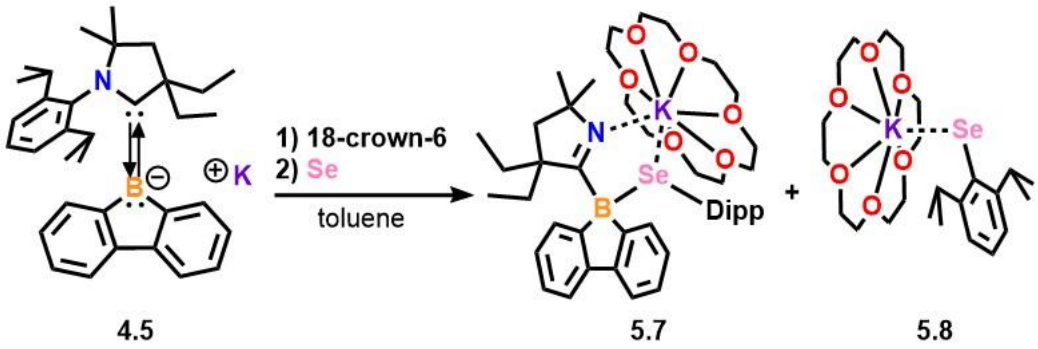

Scheme 5.2. Reaction of 9-CAAC-9-borafluorene monoanion and grey selenium in the presence of 18-crown-6 prohibits dimerization and yields boryl-substituted selenide and potassium organoselenide.

To compare the geometrical parameters of the selenium-containing products, single-crystals of **5.7** and **5.8** were grown and X-ray diffraction studies were performed (Figure 5.4). The

B1–Se1 bond distance of **5.7** [2.129(3) Å] is within the range of compounds **5.2**-**5.5** [2.094-2.141 Å] (Table 1). In **5.7**, the Se1–K1 bond distance is longer [3.5103(6) Å] than that of **5.8** [3.3326(5)], which suggests a weaker interaction in compound **5.7**. Theoretical studies were carried out to rationalize the observed Dipp migration from CAAC to Se in **5.7** (Figure 5.5). Nucleophilic attack of elemental selenium by **4.5** is energetically favorable, forming a selenolate anion intermediate (**Int1a**). A subsequent transition state (**TS1**) was located where the Dipp group is centered between the nitrogen and selenium atoms. The calculated barrier for Dipp migration is $\Delta G^{\ddagger}$ = +81 kJ mol^{-1}. Analysis of the bonding in **5.7** indicates that the most appropriate description of the CAAC structure is a single lone-pair on nitrogen and a double bond between N1 and C1 ($WBI_{N1\text{-}C1}$ = 1.81, WBI = Wiberg Bond Index). For comparison, the unmodified CAAC (with an *N*-Dipp group) possesses a C1–N1 single bond. The nature of the CAAC-boron interaction in **5.7** was investigated with energy decomposition analysis in combination with natural orbitals for chemical valence (EDA-NOCV), which indicated a slight preference for a donor-acceptor description (ΔE_{orb} = -187 kcal mol^{-1}) over an electron-sharing description (ΔE_{orb} = -200 kcal mol^{-1}), where the smaller magnitude of orbital interaction (ΔE_{orb}) indicates the preferred bonding description. However, the small difference in ΔE_{orb} for the two models indicates that either description could reasonably be employed. For consistency, throughout the paper an electron-sharing C–B bonding description has been used for compounds with the loss of Dipp (**5.2**, **5.3**, **5.7**), while a donor-acceptor C–B bonding interaction has been used for CAAC-based compounds (**5.4**, **5.5**).

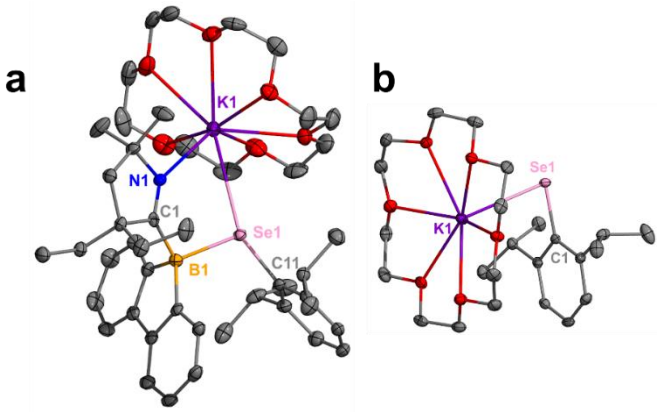

Figure 5.4. Molecular structures of **5.7** (a) and **5.8** (b). Thermal ellipsoids set at 50% probability with H atoms omitted for clarity.

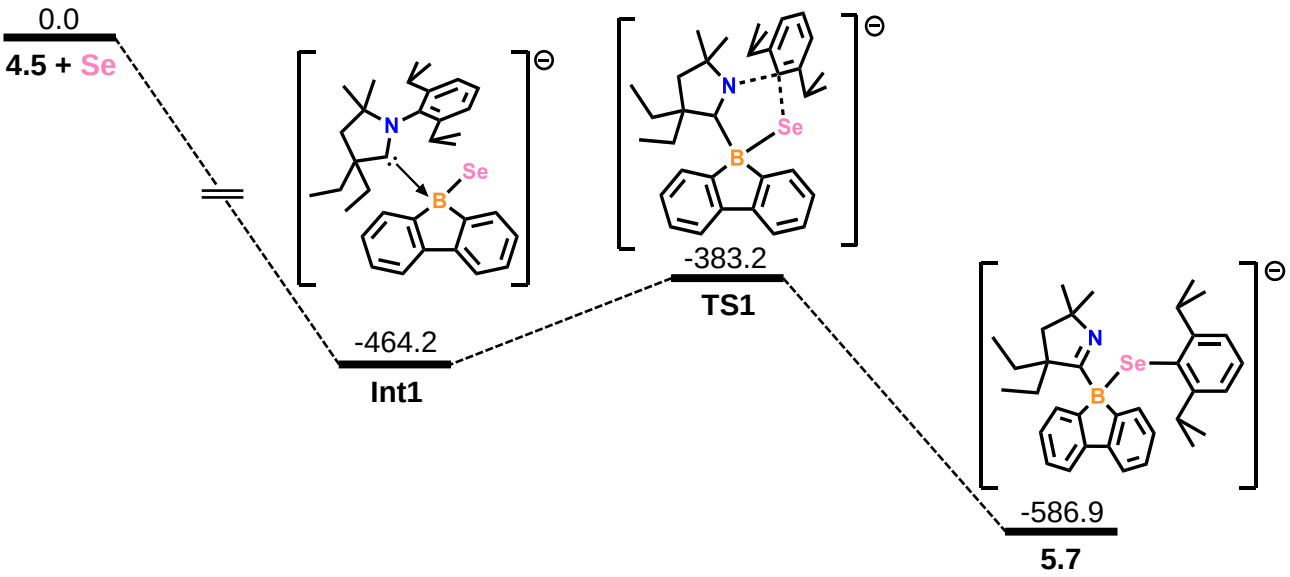

Figure 5.5. Calculated relative free energies (ΔG, kJ mol^{-1}) for the reaction of **4.5** and elemental selenium at the RI-SCS-MP2/def2-TZVP//B3LYP-D3(BJ)/def2-SVP (SMD, Toluene) level of theory.

5.4 Direct Synthesis of Boryl-Substituted Selenide

Due to the absence of Dipp migration in **5.5**, we were interested in devising a synthetic method to directly synthesize the boryl-substituted diselenide in higher yield as a single product. The addition of dichlorodiselenide (Se_2Cl_2) to a solution of **4.5** in THF produced **5.5** in 79% yield as a yellow solid (Scheme 5.3). A resonance at 3.16 ppm in the ^{1}H NMR spectrum was observed for the *N*-Dipp methine protons, while a singlet at -2.8 ppm in the ^{11}B NMR spectrum and a singlet at 16.5 ppm in the ^{77}Se NMR spectrum are consistent with the structure.

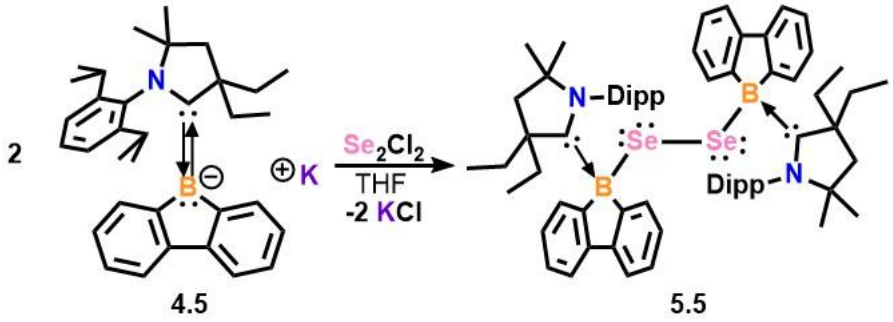

Scheme 5.3. Direct synthesis of boryl-substituted diselenide.

Theoretical calculations were also carried out to determine the mechanism for the formation of **5.5**. Typically, addition of electrophilic selenium to alkenes and diboranes proceed through a highly reactive seleniranium ion intermediate.[299-300] However, attempts to locate a seleniranium ion intermediate associated with addition across the B-$C^{carbene}$ bond in **4.5** were unsuccessful, despite a comprehensive search of the potential energy surface. It was subsequently proposed that a radical process was occurring via reduction of Se_2Cl_2 by **4.5**. To assess this hypothesis, a solution of the CAAC-borafluorene radical [BF = borafluorene][123] was reacted with Se_2Cl_2, which cleanly converted to **5.5** in 76% yield. We therefore propose that formation of **5** occurs via two successive radical additions to Se_2Cl_2 proceeding through a chlorodiselaneyl

intermediate **Int1b** (Scheme 5.4). Calculated free energies indicate that each step is favorable with an overall reaction ΔG_{rxn} = -473 kJ mol^{-1}. This type of single electron transfer is comparable to observations made by Braunschweig *et al.* with the anionic NHC-borole.[255-256]

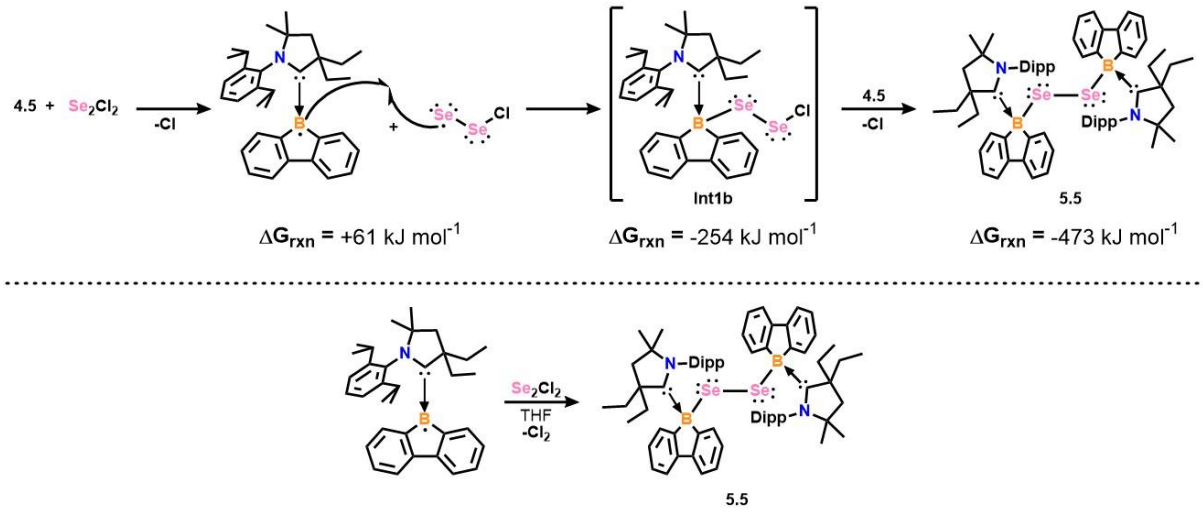

Scheme 5.4. Proposed mechanism for the direct synthesis of **5** (top). Calculated free energies (ΔG, kJ mol^{-1}) relative to reactants (RI-SCS-MP2/def2-TZVP//B3LYP-D3(BJ)/def2-SVP, (SMD, THF)). Reaction of CAAC-borafluorene radical with Se_2Cl_2 in THF also produces **5.5**.

The bonding and electronic structure of **5.5** was investigated with molecular orbital (MO), natural bond orbital (NBO), and EDA-NOCV. The HOMO and HOMO-1 of **5.5** are both π symmetric and localized to the diselenide moiety (Figure 6). NBO calculations reveal each selenium atom in **5.5** possesses two lone-pairs, with an Se−Se single bond (WBI = 0.93). Similarly, both B−Se bonds are single bonds (WBI = 0.90). The boron centers in **5.5** retain a large negative natural population analysis (NPA) charge relative to the selenium atoms (B = -0.119e, Se = -0.038e). To determine the nature of the CAAC-borafluorene-diselenide interaction in **5.5**, EDA-NOCV calculations were carried out with both electron-sharing and donor-acceptor bonding

descriptions (Table 5.2). The electron-sharing model used triplet fragments (triplet CAAC-borafluorene dimer with each CAAC-BF having one unpaired electron, and Se_2 in the $^3\Sigma_u^+$ state), while the donor-acceptor description utilized fragments of singlet CAAC-BF^+ dimer and singlet Se_2^{2-}. Numerical EDA-NOCV results indicate that an electron-sharing approach is the favored description (smaller magnitude ΔE_{orb} term). For the electron-sharing description, the total interaction energy (ΔE_{int}, -168.9 kcal mol^{-1}) is composed of almost equal contributions from covalent (ΔE_{orb}, 50%) and electrostatic (ΔE_{elstat}, 42%) interactions. The two most important pairwise orbital interactions arise from the singly-occupied in-phase (+,+) and out-of-phase (+,-) orbital interactions between boron and selenium (Figure 5.6). Both NBO and EDA-NOCV calculations indicate that the ligand-diselenide interaction is best described as covalent single bonds between boron and selenium.

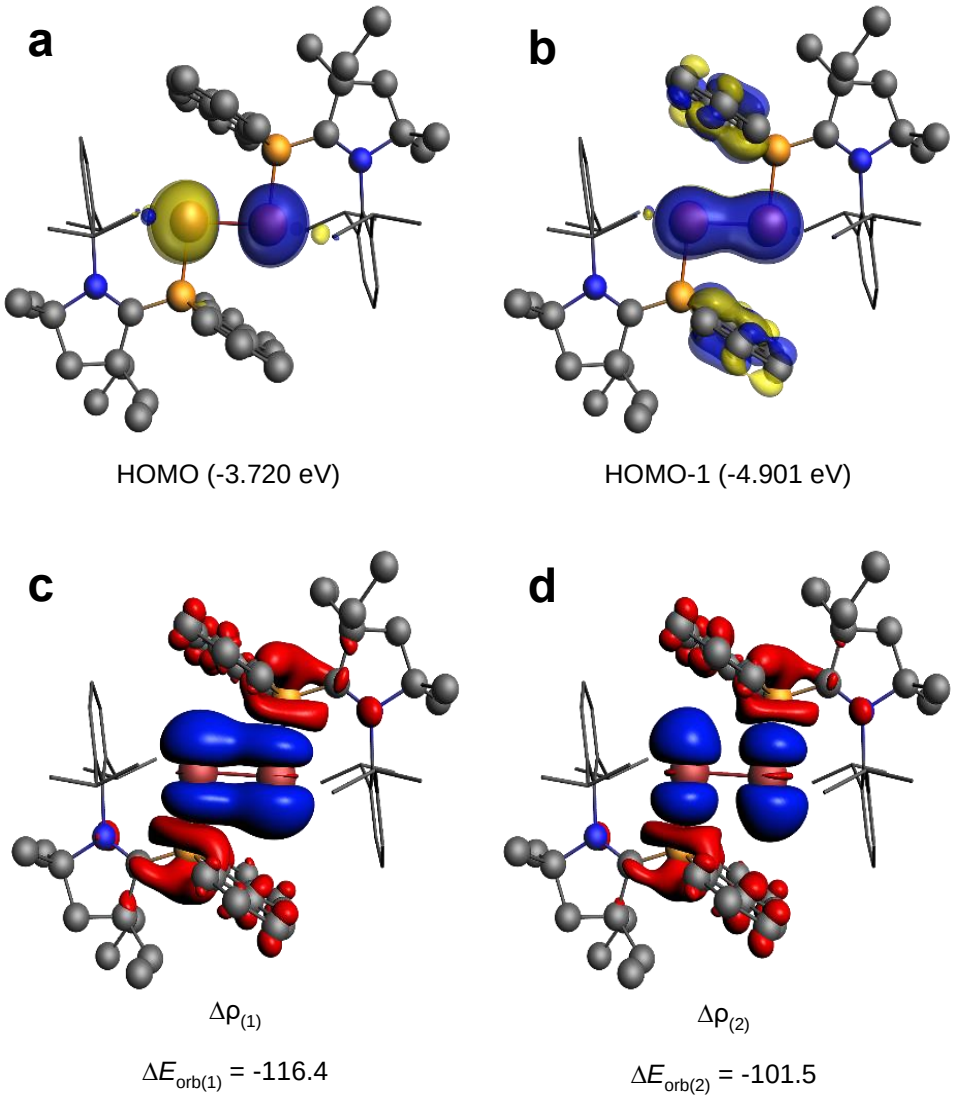

Figure 5.6. Plots of the HOMO (a) and HOMO-1 (b) of **5.5**. Deformation densities $\Delta\rho$ (c) and (d) of the pairwise orbital interactions for the electron-sharing model of **5.5**. The direction of charge flow for the deformation densities is red → blue. Associated interaction energies given in kcal mol^{-1}. Only the α-pair is shown, see ESI for β-pair. Hydrogen atoms omitted for clarity.

Table 5.2. EDA-NOCV results for **5.5** at the B3LYP-D3(BJ)/TZ2P//B3LYP-D3(BJ)/def2-SVP level of theory. Energies given in kcal mol^{-1}.

	2CAACBF (T) + Se_2 [$^3\Sigma_u^+$]	2[CAACBF]$^+$ (S) + [Se_2]$^{2-}$ [$^1\Sigma_u^+$]
ΔE_{Int}	-168.9	-419.5
ΔE_{Pauli}	+331.8	+406.0
ΔE_{elstat}[a]	-208.1 (42%)	-478.7 (58%)
ΔE_{orb}[a]	-252.4 (50%)	-306.5 (37%)
ΔE_{disp}[a]	-40.2 (8%)	-40.2 (5%)
$\Delta E_{orb(1)\ (+,-)}$[b]	-116.4 (46%)	-113.2 (37%)
$\Delta E_{orb(2)\ (+,+)}$[b]	-101.5 (40%)	-100.1 (33%)
$\Delta E_{orb(rest)}$	-34.5 (14%)	-93.2 (30%)

[a] Values in parentheses give the percentage contribution to the total attractive interactions $\Delta E_{elstat} + \Delta E_{orb} + \Delta E_{disp}$.

[b] Values in parentheses give the percentage contribution to the total orbital interactions ΔE_{orb}.

5.5 Summary and Outlook

We have reported the first reactivity study of the 9-carbene-9-boraafluorene monoanion and elemental selenium. While the reaction in THF produces multiple products, the reaction is controlled using toluene as a solvent with the addition of 18-crown-6, producing the boryl-substituted organoselenide. During the course of the reaction the Dipp group migrates from the carbene to selenium, and this process was modelled using density functional theory. While the reaction between 9-carbene-9-borafluorene monoanion and grey selenium yields **5.5** and multiple

side products, the boryl-substituted diselenide **5.5** was isolated on a preparative scale from a reaction of the monoanion and Se_2Cl_2. Theoretical modelling of this reaction supports a radical mechanism, which was assessed via an experimental reaction between CAAC-borafluorene radical and Se_2Cl_2, which cleanly gave compound **5.5**. This study highlights the fundamental reactivity of the 9-CAAC-9-borafluorene monoanion with chalcogen reagents, and investigations with small gaseous molecules are currently underway in our laboratory.

Future studies in this area would involve an exploration of the reactivity between the 9-CAAC-9-borafluorene monoanion with sulfur and tellurium as a means to unravel new chemistry with other elements in group 16. Additional experiments with the CAAC-borafluorene radical and elemental selenium would provide more insight into the mechanism of formation of the aforementioned Dipp-group migration products.

Chapter Six: Electron-Rich Borafluorene Monoanions

Containing work that was originally published in:

Wentz, K. E.; Molino, A.; Freeman, L. A.; Dickie, D. A.; Wilson, D. J. D.; Gilliard, R. J., Systematic Electronic and Structural Studies of 9-Carbene-9-Borafluorene Monoanions and Transformations into Luminescent Boron Spirocycles. *Submitted.*

6.1 Introduction to Cyclic Boryl Anions and Their Structural Diversity

Tricoordinate Lewis acidic boron complexes have long been utilized in synthetic chemistry as strong electrophilic reagents for the formation of new olefin polymers,[301-304] substituted aromatics,[305-307] and the functionalization of C–H bonds[308] which have all been essential in materials-relevant chemical synthesis. However, through chemical reduction reactions, boron-based compounds can be designed such that they become electron-rich nucleophiles. The initial reports on boron nucleophiles (or boryl anions)[175-176, 244, 246, 256, 264, 275, 298, 309] spawned new investigations into understanding the chemistry and reactivity of group 13 Lewis bases (Figure 6.1a). These compounds are isoelectronic to N-heterocyclic carbenes (NHC) but are weaker sigma-donors,[177] and are generally used for the formation of novel B–E bonds (E = transition metal, main-group element, or lanthanide). By stabilizing the E element in low oxidation states, reactivity occurring at the E atom or within the B–E bond can be explored.[185-187, 189, 245, 255, 310-312] Since the first isolation of the unsaturated boryllithium,[175] structurally unique boryl anions have been reported which have benzannulated backbones, and potassium cation interactions with the electron-rich boron atom.[244, 256, 313-317] Despite this class of compound being identified nearly 15 years ago, much less is known concerning the chemical reactivity of these species with small molecules compared to the chemistry of the related aluminyl anions,[282, 318-320] which is rapidly emerging. Because of the drastically different positioning and nature of the bonding within the ion pair (e.g., binding of weakly coordinating atoms, cation-π or other non-covalent interactions, fully charge-separated ions), diverse reactivity can occur. Accordingly, there is still a need for the realization and isolation of electronically and sterically different anionic boryl species as a means to probe reactivity and donor strength at the boron center, and their use as a platform for the development of novel boron-containing materials.

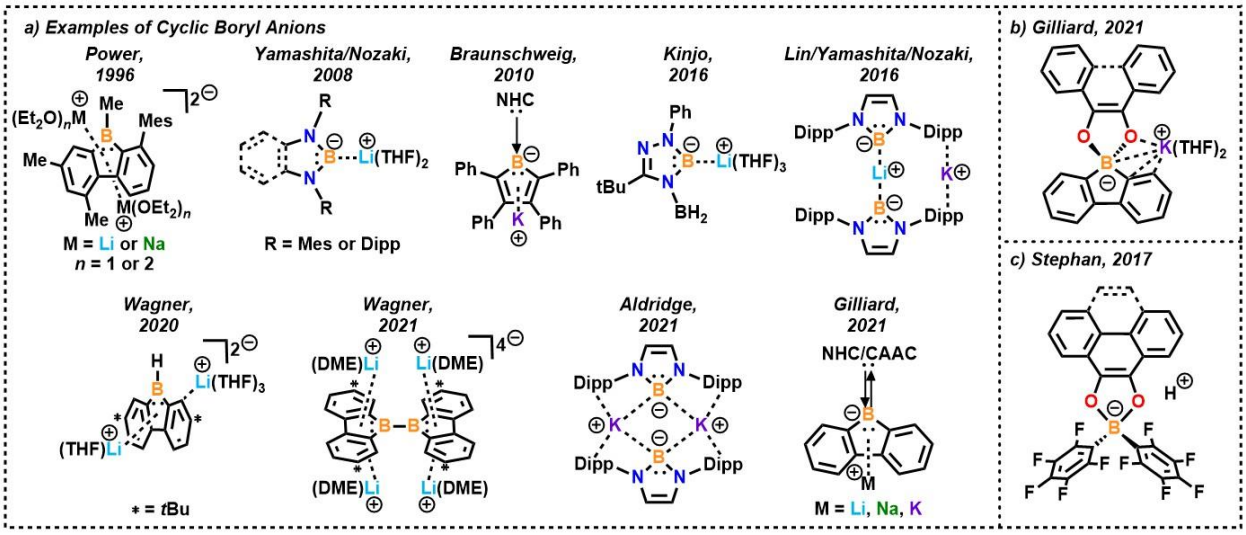

Figure 6.1. a) Examples of structurally unique cyclic boryl anions; b) Borafluorene-based spirocycles obtained from 9-carbene-9-borafluorene monoanion and diketones; c) R_2BO_2 zwitterions prepared via nucleophilic addition to Frustrated Lewis pair-stabilized boracyclic radicals.

Recently, we have been investigating the structure and bonding, reactivity, and materials properties 9-carbene-9-borafluorenes.[99, 107, 122-123, 311] While 9-borafluorene has become a popular building block in molecular chemistry,[98] studies of chemically reduced borafluorenes are still rare.[123, 264, 275, 298] We reported the formation of borafluorene-based spirocycles resulting from the reaction of diketones and 9-carbene-9-borafluorene monoanion (Figure 6.1b).[298] Although the electronic structures differ significantly, the R_2BO_2 moiety of our closed-shell compounds bear resemblance, in terms of connectivity, to open-shell boracyclic radicals and zwitterions synthesized by Stephan (Figure 1c).[269, 321] Most notably, the incorporation of borafluorene in the zwitterionic spirocycle produces fluorescent materials. In light of the novelty of the R_2BO_2 spirocyclic fragment, and luminescent properties that can be accessed, we sought to investigate reactions of borafluorene monoanions with other diketones in order to study their optical properties

in more detail. This resulted in a need to understand how the spatial arrangement of the alkali metal in 9-carbene-9-borafluorene monoanions affect chemical reactions and the crystallization of various products. Herein we report a study on the structural and electronic properties of [K][9-CAAC-9-borafluorene] complexes (**6.1**-**6.4**) (CAAC = cyclic(alkyl)(amino) carbene). Charge-separated [K(2.2.2-cryptand)][9-CAAC-9-borafluorene] is used as a building block for the synthesis of boron-oxygen heterocycles **6.5**-**6.6**. The optical properties of **6.5**-**6.6** demonstrate that changes in the alkali metal coordination environment in the spirocycles results in significant differences in the emission behavior and quantum yields.

6.2 Synthesis of Electron-Rich Borafluorene Monoanions

During our initial studies on the isolation and reactivity of 9-carbene-9-borafluorene monoanions, we often observed solvent- or cation-dependent stability differences and variations in the selectivity for specific products, even in cases where the carbene ligand and alkali metal cation were the same.[298, 311] To systematically investigate the possibility of different bonding modes of [K][9-CAAC-9-borafluorene monoanion] (CAAC = (2,6-diisopropylphenyl)-4,4-diethyl-2,2-dimethyl-pyrrolidin-5-ylidene;[21-22, 322] BF = borafluorene) and the role coordination environment plays in chemical reactions, we first sought to understand the solution-phase behavior of our previously reported [K][9-CAAC-9-BF] monoanion coordination polymer.[298] When **CAAC-BF-P** is dissolved in THF (Scheme 6.1), the $^{11}B\{^{1}H\}$ NMR spectrum shows a singlet at 1.5 ppm. Single crystal X-ray diffraction studies of **6.1** reveal a $[K(THF)_3]$[9-CAAC-9-BF] structure in which the K atom is binding to the central BF ring in an η^5-fashion. In contrast, when compound **6.1** is reacted with 18-crown-6, 2.2.2-cryptand, or phenanthroline, charge-separated ion pairs **6.2**-**6.4** are formed as red solids, which display downfield chemical shifts in the $^{11}B\{^{1}H\}$

NMR spectra (14.2 -15.4 ppm, THF-d_8). The significant differences in the ^{11}B NMR data suggest that the structure of **6.1** is persistent in solution (THF) and the boron center of **6.2**-**6.4** are more electron-rich.

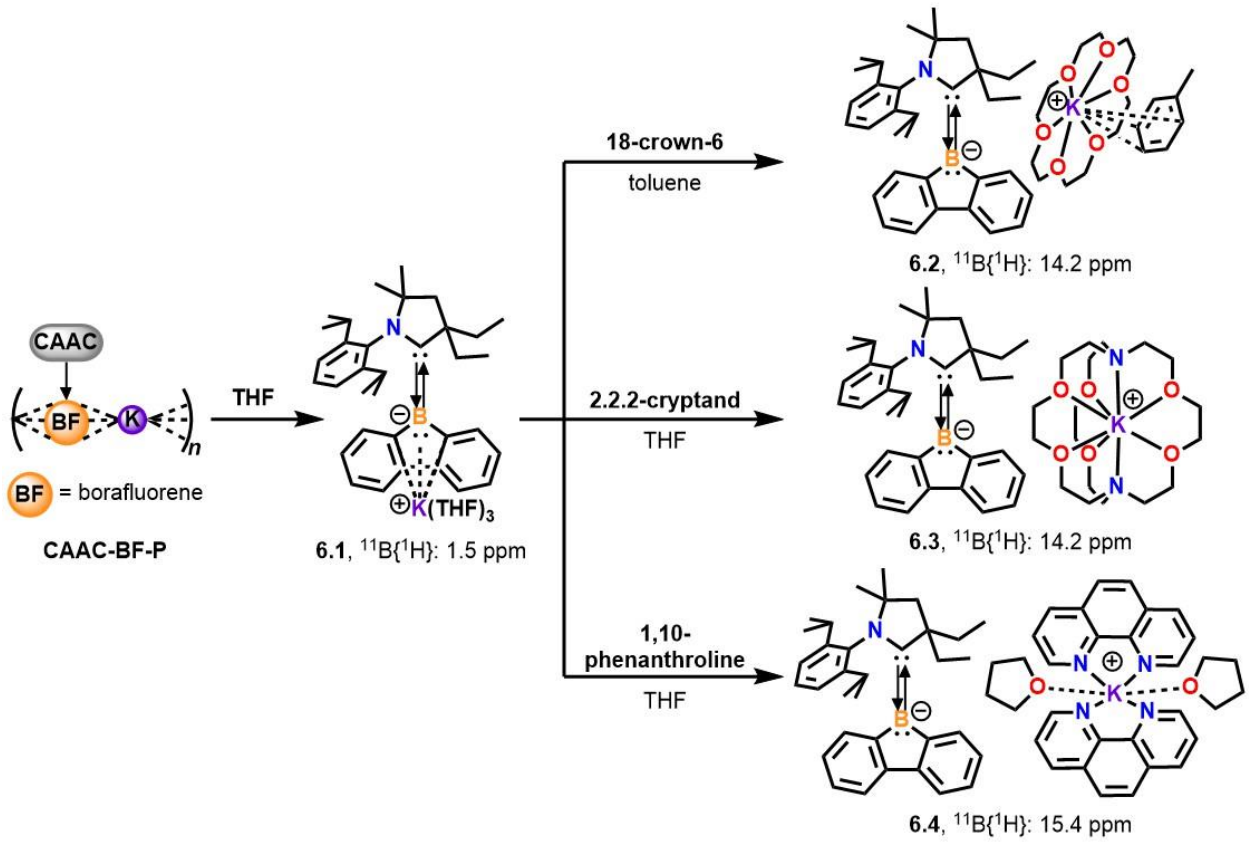

Scheme 6.1. Synthesis of [K][9-carbene-9-borafluorene] complexes (**6.1**-**6.4**).

Theoretical studies were performed to gain insight into the altered electronic properties of BF with respect to contact ion distance. Comparison of the calculated partial charges at boron and Wiberg bond indices (WBI) for B1-C1 in **6.1** (-0.119 e^-, WBI = 1.299) and **3** (-0.155, WBI=1.423) highlight the increased anionic character of the charge-separated species. Plots of the electrostatic potentials of **6.1** and **6.3** are shown in Figure 6.2, with large negative values in the regions surrounding boron in **6.3** compared to **6.1**. Calculated ^{11}B nuclear shielding values of **6.1** (1.89

ppm) and **6.3** (11.60 ppm) are in agreement with the observed experimental trends. Additionally, constrained scan calculations varying the potassium contact distance of **6.1** from the central BF ring resulted in an increasing downfield chemical shift (BF--K(3.1 Å) = 1.89 ppm, BF--K(6.6 Å) = 3.95 ppm) (Figure 6.2c).

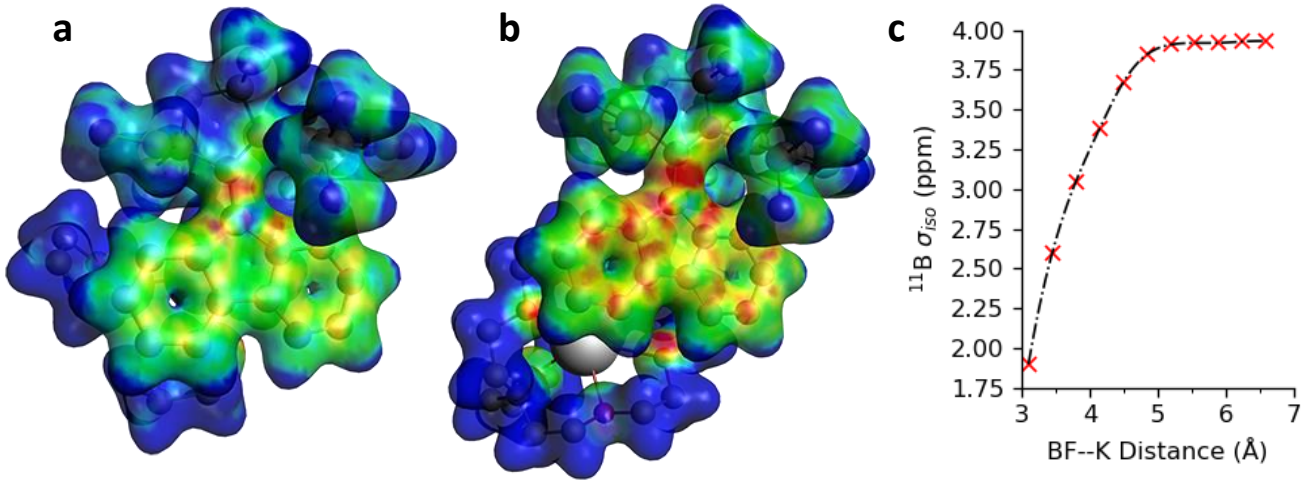

Figure 6.2. Plots of the electrostatic potential (ESP) of **6.1** (a) and **6.3** (b), B3LYP-D3(BJ)/TZ2P (COSMO, THF), isosurface from -2.5e-2 (red) to +8.0e-2 (blue). Plot of the calculated isotropic ^{11}B nuclear shielding of **6.1** with respect to BF--K(THF)$_3$ distance (TPSSh/pcSseg-2 (CPCM, THF)) (c).

Comparison of the single crystal X-ray diffraction data for **6.1**-**6.4** show that the bond metrics for **6.1** are similar to free boryl anions (**6.2**-**6.4)** in the solid state (Figure 6.3). The B1–C1 bond lengths for **6.1** [1.505(3)], **6.2** [1.519(7)], **6.3** [1.495(2)], and **6.4** [1.504(3)] are also similar to the previously reported **CAAC-BF-P** [1.502(5)],[298] and all indicate double bond character between the boron and carbon atoms.

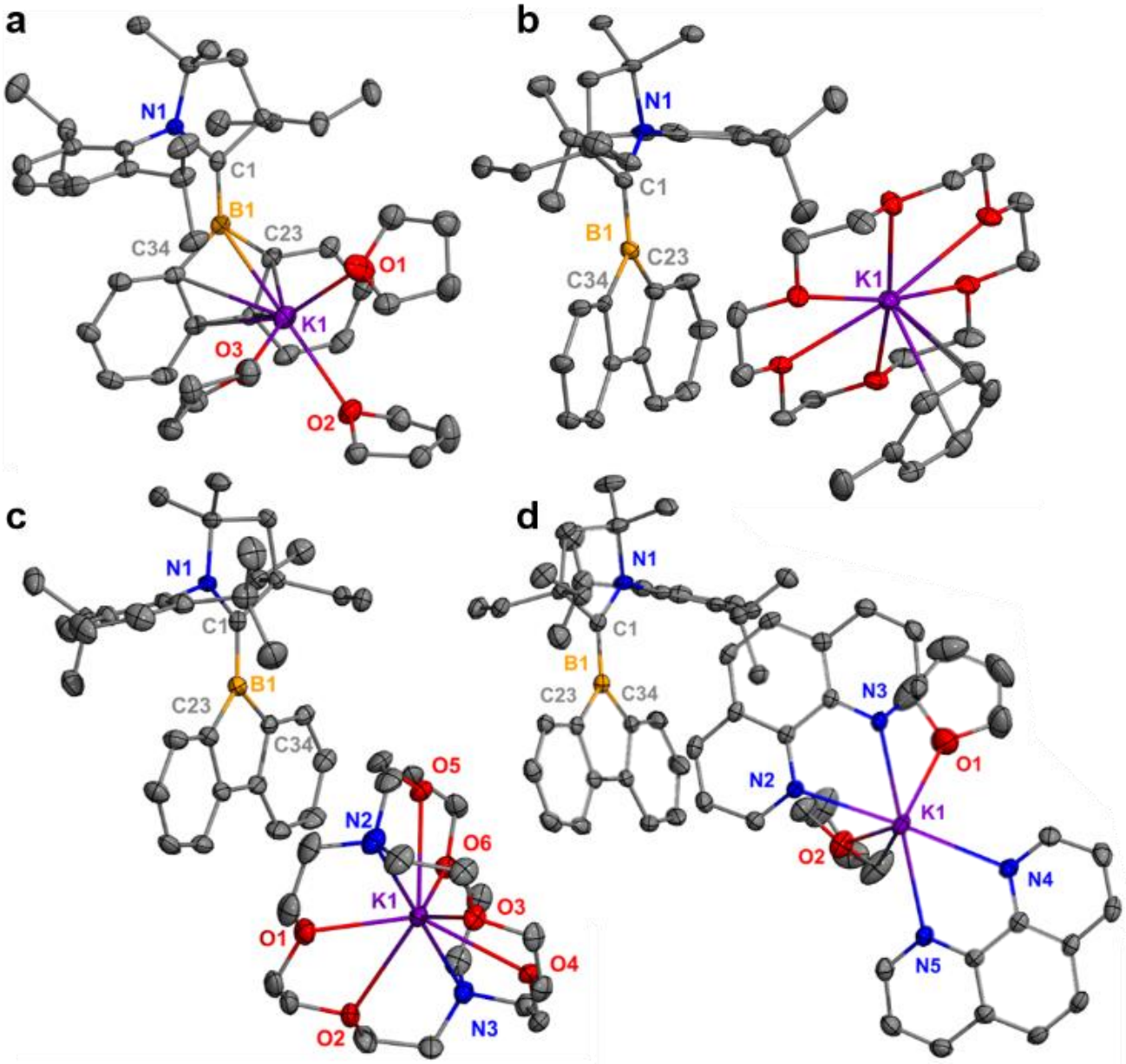

Figure 6.3. Molecular structures of **6.1** (a), **6.2** (b), **6.3** (c), and **6.4** (d). Hydrogen atoms omitted for clarity and thermal ellipsoids shown at 50% probability. Selected bond lengths [Å]: **6.1**: B1–C1 1.505(3), B1–C23 1.609(2), B1–C34 1.598(3), B1–K1 3.2363(19); **6.2**: B1–C1 1.519(7), B1–C23 1.586(8), B1–C34 1.617(8), B1---K1 5.911(6); **6.3**: B1–C1 1.495(2), B1–C23 1.601(2), B1–C34 1.616(2) B1---K1 6.891(2); **6.4**: B1–C1 1.504(3), B1–C23 1.607(3), B1–C34 1.600(3), B1---K1 8.095(2).

6.3 Reactivity of Charge Separated Borafluorene Monoanion with Diketones

Because of the drastic difference in electronics between **6.1** and **6.3**, we hypothesized that the use of the charge-separated borafluorene monoanion **6.3** as a starting material for reactions with 9,10-phenanthrenequinone and 1,10-phenanthroline-5,6-dione would generate borafluorene spirocycles with different photophysical properties. In order to ensure solvent-free potassium cations in reaction products, compound **6.3** was used for these studies. Upon addition of 9,10-phenanthrenequinone and 1,10-phenanthroline-5,6-dione to **6.3**, immediate color changes from deep red to orange were observed which were indicative of the formation of **6.5** and **6.6** (Scheme 6.2). In both cases, the CAAC ligand was displaced and borafluorene spirocycles **6.5** and **6.6** were characterized by distinct downfield chemical shifts in the ^{11}B NMR spectra at 16.2 and 16.6 ppm respectively.

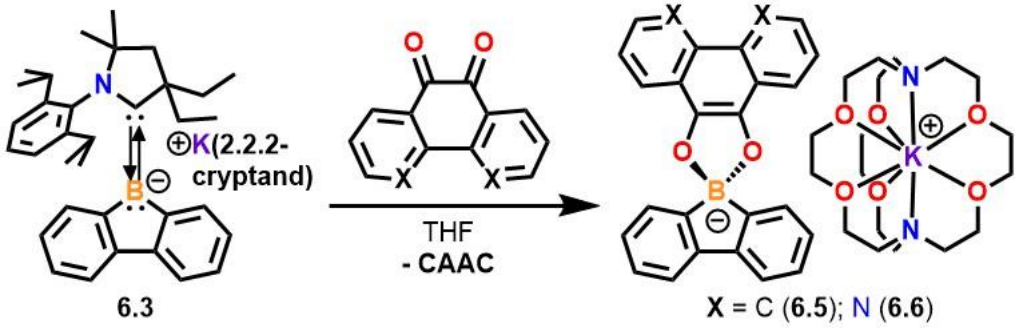

Scheme 6.2. Displacement of CAAC ligand by 9,10 phenanthrenequinone and 1,10-phenanthroline-5,6-dione to form spirocyclic borafluorenes **6.5** and **6.6**.

Yellow and orange air-stable single crystals of **6.5** and **6.6** were grown from concentrated solutions in THF with a couple drops of hexanes added. In both molecules, charge-separated boron-based spirocycles with no potassium contacts were observed, which differ from our previously reported borafluorene spirocycles that exist as coordination polymers (Figure 6.4).[298] Additionally, the B–O bonds of **6.5** and **6.6** range from 1.513(14) to 1.533(2) Å, and are close in length to the sum of the covalent radii (R(B–O) = 1.50 Å)[268] indicative of single bond character. The placement of the nitrogen atoms on **6.6** leaves a site for potential binding to other elements to generate mixed metal systems. Compound **6.6** is particularly interesting as 1,10-phenanthroline complexes have been used for various technologies including analytical probes.[323-325] Due to the higher quantum yields of **6.6** ($\Phi_{solution}$ = 4%) in comparison to the weakly luminescent parent phenanthroline ($\Phi_{solution}$ = 0.8%),[323] complexes similar to **6.6** should open up new possibilities in molecular materials applications.

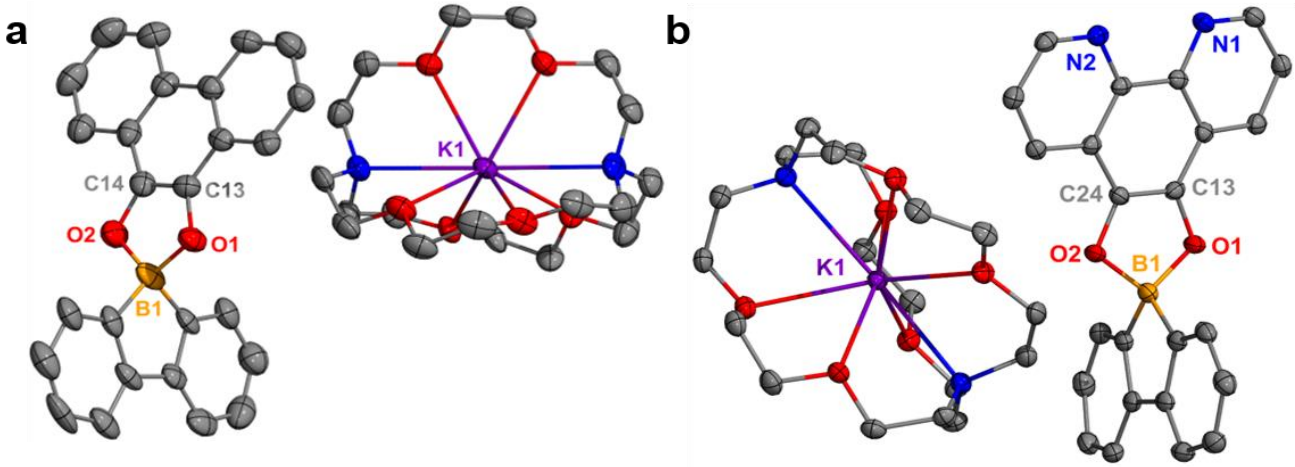

Figure 6.4. Molecular structures of **6.5** (a) and **6.6** (b). Hydrogen atoms omitted for clarity and thermal ellipsoids shown at 50% probability. Selected bond lengths [Å]: **6.5**: B1–O1 1.525(13), B1–O2 1.513(14), O1–C13 1.362(11), O2–C14 1.356(12), C13–C14 1.352(14). **6.6**: B1–O1 1.533(2), B1–O2 1.532(2), O1–C13 1.348(2), O2–C24 1.49(2), C13–C24 1.364(2).

Theoretical calculations were used to determine the possible mechanism for the formation of spirocycles **6.5** and **6.6**. Recently, we have shown that **6.1** may act as a single-electron donor with diselenides to undergo subsequent radical coupling.[311] The reactivity of quinones with electron-rich species has been reported to proceed via the same route, resulting in cyclization products similar to those described herein.[326-330] We first sought to model the electron-transfer pathway using broken-symmetry density functional theory. Single-electron transfer (SET) from the borafluorene monoanion (**BFA**) to 9,10-phenanthrenequinone forming open-shell singlet complex (**RC1**) was found to be energetically favorable relative to reactants (ΔG_{rxn} = -95 kJ mol^{-1}). An alternative nucleophilic addition pathway was also examined. All attempts to optimize an intermediate adduct with boron bound to one of the carbonyl carbons (Figure S18) reorganized to the boron oxygen adduct **Int1** (ΔG_{rxn} = -154 kJ mol^{-1}). No transition state could be located for the formation of **Int1**. A scan of the reaction energy surface of **Int1** on a series of B-O bond distances converged smoothly (Figure S19), suggesting that adduct formation may proceed through a shallow potential energy surface. Such shallow potential energy surfaces are commonly associated with radical or barrierless processes; however, barrierless adduct formation is not expected to occur due to the significant geometry reorganization between **BFA** and **Int1**. Although both SET and nucleophilic addition pathways are exergonic, given the previously reported reversible redox properties of **6.1**, we postulate adduct formation **Int1** proceeds through the radical coupling of **RC1**.[123, 311] Concerted intramolecular cyclization of **Int1** and loss of CAAC results in products **6.5** and **6.6** (Figure 6.5).

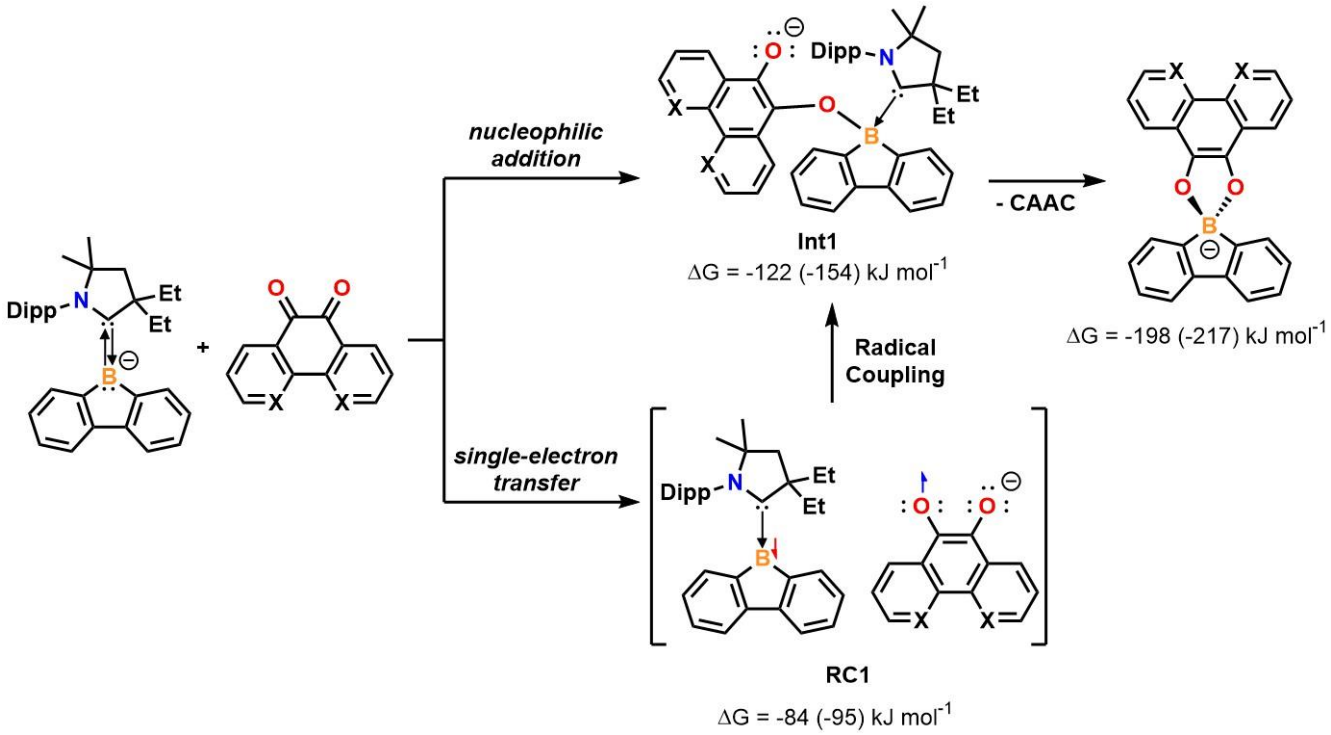

Figure 6.5. Proposed reactivity pathways for the synthesis of **6.5** and **6.6**. Calculated free energies (ΔG, kJ mol^{-1}) relative to reactants (B3LYP-D3(BJ)/def2-SVP (CPCM, THF)). Values in parentheses correspond to the reactivity of **BFA** with 1,10-phenanthroline-5,6-dione.

6.4 Photophysical Properties of Luminescent Borafluorene Spirocycles

In order to explore the photophysical properties of the borafluorene spirocycles, UV-vis, fluorescence, and quantum yield measurements were carried out. Absorption maxima for **6.5** and **6.6** are observed at 390 nm and 414 nm, respectively, with red-shifted emission wavelengths for **6.5** and **6.6** at 517 nm and 569 nm (Figure 6.6). These absorption and emission values are in line with what was observed for the previously reported potassium coordinated borafluorene spirocycles (**4.13** and **4.14**).[298] However, under UV light, **6.5** displays a bright green color while **6.6** is orange. Time-dependent density functional theory (ωB97X/def2-TZVP, CPCM(THF))

analysis indicates the the absorption maxima for **6.5** and **6.6** are associated with $\pi \rightarrow \pi^*$ transitions centered on the quinone moieties (Figures A4.46-A4.47).

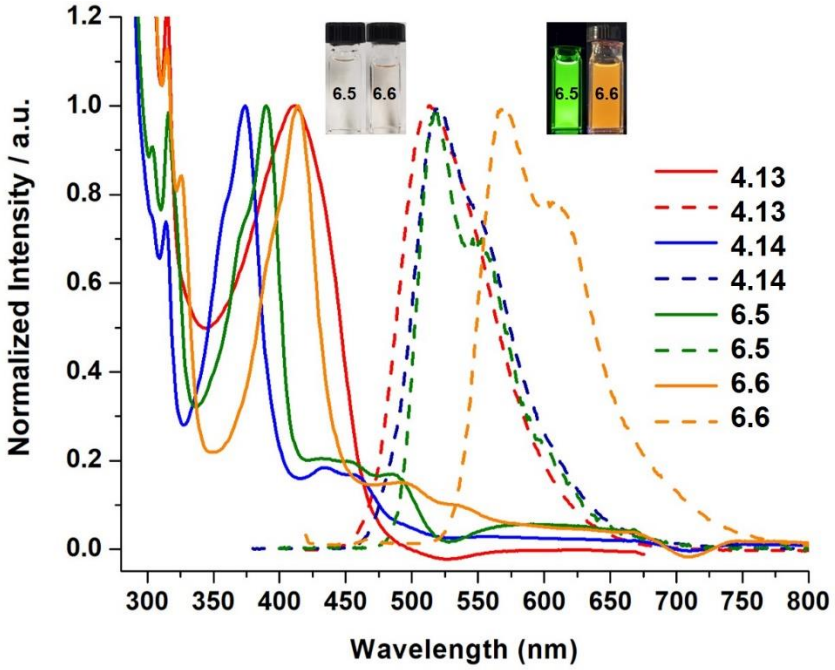

Figure 6.6. Normalized absorption (solid line) and emission (dashed line) spectra of **4.13** (red) **4.14** (blue), **6.5** (green), and **6.6** (orange). Samples were dissolved in THF and ran at room temperature. Compounds **4.13** and **6.6** were excited at 410 nm, **4.14** was excited at 370 nm, and **6.5** was excited at 390 nm.

To quantify luminescence, quantum yield studies were performed in the solution and solid-states of the borafluorene spirocycles. As expected, **4.14** has the highest QY in solution phase due to the more rigid structure than **4.13** (Table 6.1). However, compound **6.5** has a higher QY in the solid state than the solution phase due to crystal packing. These data clearly indicate that the nature of the K atom position play a role in the optical properties of the spirocycles.

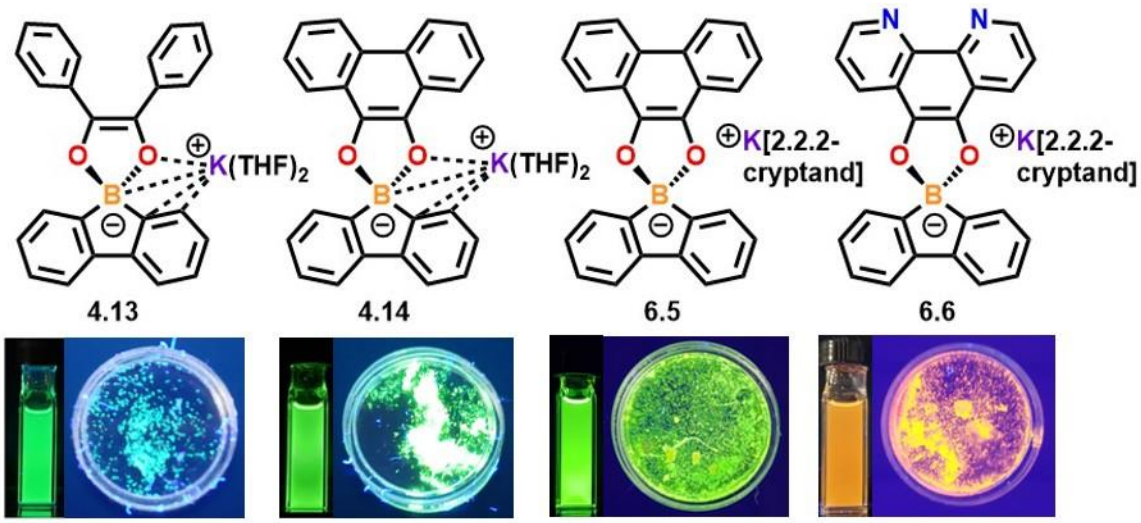

Table 6.1. Comparison of quantum yields in THF solutions and solid state.

Compound	$\Phi_F^{(solution)}$ / %[a]	$\Phi_F^{(solid)}$ / %[a]
4.13	9	1
4.14	37	6
6.5	1	15
6.6	4	3

[a]Absolute quantum yields determined using an integrating sphere. Digital images of solution and solid state luminescence are shown under 365 nm UV light.

6.5 Summary and Outlook

In summary, we report structurally different charge-separated 9-CAAC-9-borafluorene monoanions (**6.1**-**6.4**). Charge-separated compounds **6.2**-**6.4** with potassium counteranions captured by 18-crown-6, 2.2.2-cryptand, and 1,10-phenanthroline are significantly more electron-rich at the boron center which is supported by significant differences in the ^{11}B NMR chemical shifts. Theoretical modelling has provided evidence that the enhanced anionic character in compounds **6.2**-**6.4** is distance-dependent with the potassium counterions. The ability to easily tune the nucleophilicity of the boron atom of the 9-carbene-9-borafluorene monoanions is not only a way to modify the electronic structure of the anions but may also prove useful as a means to

control reaction pathways. Moreover, when reacting **6.3** with 9,10-phenanthrenequinone and 1,10-phenanthroline-5,6-dione, novel charge-separated boron spirocycles (**6.5** and **6.6**) are synthesized via carbene elimination, with computational mechanistic studies suggesting this reactivity proceeds via an electron-transfer mechanism. Compounds **6.5** and **6.6** display bright yellow and orange luminescence under UV light, and are air-stable in the solid state. Due to the absence of potassium interactions with the boron center in **6.5**, the crystal packing is affected, and the solid-state quantum yield (Φ_{solid} = 15%) is drastically higher than in the solution state ($\Phi_{solution}$ = 1%). The presence of nitrogen atoms on the phenanthroline moiety of **6.6** leads to a red-shifted emission color. Because of the open biding site, compounds similar to **6.6** may be useful in the preparation of other metal complexes. Additional reactivity studies with the charge-separated borafluorene monoanions and spirocycles are currently underway in our laboratory and will be reported in due course.

Studies in the future with other aromatic diketones will be imperative for expanding the emission properties to different wavelengths. Additional experiments to evaluate scalability and photophysical properties of the spirocycles as thin films will be key for fabrication into optoelectronic devices. Coordination reactions between **6.6** and metals will also be of interest to the materials, main-group, and inorganic chemistry communities. Specifically, studies with germanium, platinum, and iron will be explored for the development of new coordination complexes with fluorescent properties.

Chapter Seven: Trioxiborinanone and Dioxaborinanone

Containing work that was originally published in:

Wentz, K. E.; Molino, A.; Freeman, L. A.; Dickie, D. A.; Wilson, D. J. D.; Gilliard, R. J., Activation of Carbon Dioxide by 9-Carbene-9-Borafluorene Monoanion: Carbon Monoxide-Releasing Transformation of Trioxaborinanone to Luminescent Dioxaborinanone. *Manuscript in Preparation.*

7.1 Introduction to Activation of Carbon Dioxide by Boron-Based Species

Given the overabundance of greenhouse gases such as carbon dioxide (CO_2) in the Earth's atmosphere, scientists have been interested in understanding chemical transformations of these small molecules, and their modification into higher value chemical feedstocks.[331-333] Although the complete conversion of CO_2 into desirable materials is quite complex, a key first step is the activation of their inert chemical bonds. Because of the high thermodynamic stability of CO_2, reactive species are often required to break their strong bonds. Transition metal complexes have been widely used for the activation of these small molecules, but some of these elements remain costly and susceptible to potential supply chain issues.[334-336] Therefore, researchers are interested in designing inexpensive main-group compounds that can activate inert gases. However, due to the inherent disposition of energetically accessible molecular orbitals, the synthesis of suitable main-group compounds that interact with small molecules remain an ongoing challenge.

Owing to its ability to exist as both a strong electrophile or nucleophile, boron has been an element of choice for several small molecule activation studies.[252, 337] Elegant work by Kinjo and coworkers highlighted the ambiphilic nature of diazadiborinines in which one boron atom acts as a Lewis base and the other as a Lewis acid to undergo a [4+2] cycloaddition reaction with CO_2 (Figure 1a).[338-339] Yamashita and Nozaki reported that the reaction of the Lewis basic boryllithium with carbon dioxide, followed by protonation yields a borylcarboxylic acid (Figure 1a).[244] Stephen has shown that the combination of a frustrated phosphine---borane Lewis pair results in the reversible insertion of carbon dioxide (Figure 1b).[340-341] Most recently, Braunschweig demonstrated that nonpolar B=B double bonds can activate CO_2 to form novel dibora-β-lactones and diboraoxetanones.[342] In contrast, introducing a diboracumulene with partial triple bond character to carbon dioxide results in the formation of a dioxaborinanone (Figure 1c).[343] Although

these examples represent significant strides in main- group chemistry, studies of boryl anions activating small molecules are still limited.[244, 252, 264, 344]

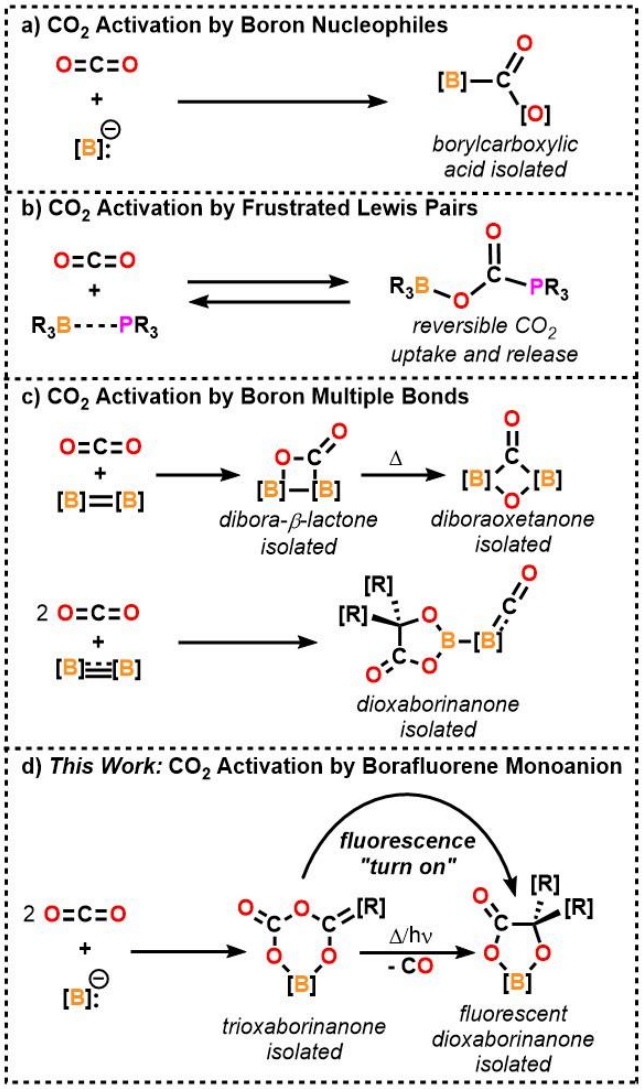

Figure 7.1. a) Boron nucleophiles react with CO_2 to form borylcarboxylic acid; b) CO_2 capture by Frustrated Lewis Pairs; c) activation of CO_2 by nonpolar double multiple bonds; d) *This Work*: synthesis of trioxaborinanone by borafluorene monoanion activation of CO_2, and elimination of CO to form the fluorescent dioxaborinanone.

Due to the reduced, electron-rich nature of 9-carbene-9-borafluorene monoanions that were recently isolated by our laboratory,[298, 311] we hypothesized that they would be a suitable platform

for small molecule activation chemistry. Herein, we report the reactions of the 9-CAAC-9-borafluorene monoanion with CO_2 (CAAC = (2,6-diisopropylphenyl)-4,4-diethyl-2,2-dimethyl-pyrrolidin-5-ylidene)[21-22, 322] (Figure 1d). Notably, the activation of CO_2 produces the first example of a trioxaborinanone. Thermolysis or photolysis of trioxaborinanone results in CO release to yield a luminescent dioxaborinanone. Carbon monoxide is essential physiologically as a messenger for various neurological pathways, however is fatal if inhaled in high concentrations.[345] Accordingly, materials which can deliver stoichiometric amounts of CO in a controlled manner [e.g., carbon monoxide releasing molecules (CORMs)] have gained significant attention for anti-inflammatory therapies and other medicinal applications.[346-349] Furthermore, it is rare for the products yielded from the CO_2 activation to be heterocyclic materials with desirable luminescent responses.

7.2 Synthesis of Trioxaborinanone and Dioxaborinanone

We began our studies by pressurizing a solution of CAAC-borafluorene monoanion (**6.1**) to 50 psi with carbon dioxide and an immediate color change from deep red to yellow was observed. A crude ^{1}H NMR spectrum of the solid obtained from the reaction showed the formation of a complex mixture of intractable products. However, when 18-crown-6 was added to a solution of **6.1** before pressurizing with CO_2, the 6-membered trioxaborinanone (**7.2**) was cleanly isolated as a colorless solid in 71% yield. Heating a solution of **7.2** in toluene to 70 °C for 18 hours results in CO release and the air-stable 5-membered dioxaborinanone (**7.3**) was obtained in 55% isolated yield. Photolysis of **2** under UV light also promotes CO release to form **3** and the CAAC-CO_2 adduct, albeit with free CAAC and unidentified species as minor products (2:1 ratio, **3**:CAAC-CO_2). Compounds **2** and **3** are characterized by distinct $^{11}B\{^{1}H\}$ NMR chemical shifts at 8.0 and

11.8 ppm, respectively. Analysis of the heterocycles by infrared spectroscopy indicates that **7.2** and **7.3** exhibit C=O stretching bands at 1693 and 1690 cm^{-1}, respectively.

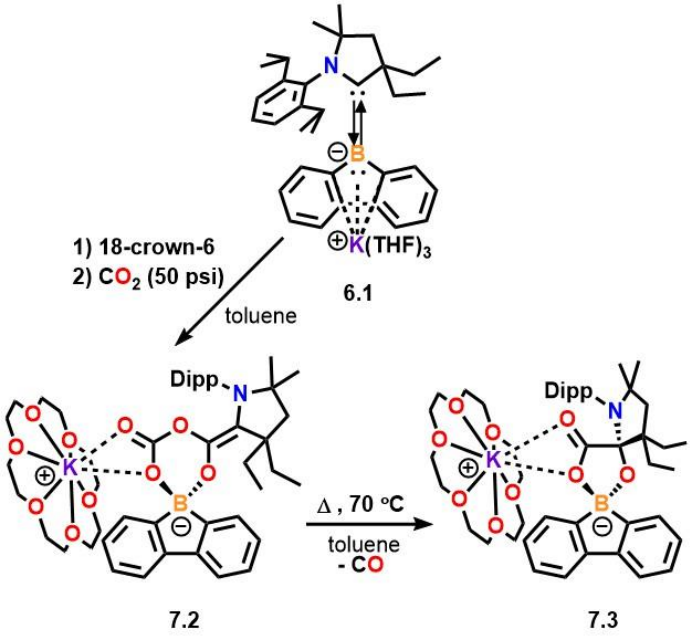

Scheme 7.1. Reaction of **6.1** with CO_2 yields new 6-membered trioxaborinanone (**7.2**). Heating a solution of **7.2** releases CO and produces 5-membered dioxaborinanone (**7.3**).

7.3 Structural Properties of Trioxaborinanone and Dioxaborinanone

In the solid state, both **7.2** and **7.3** feature unique structures with spirocyclic cores containing boron and oxygen heteroatoms (Figure 7.2). Although spirocyclic molecules have received great attention in drug discovery for their three dimensionality, spirocycles featuring heteroatoms have historically been less explored.[350-354] Remarkably, compound **7.3** possesses two spirocyclic moieties, which both contain oxygen atoms. In addition, **7.3** adopts an unusual structure by which the oxidized carbene carbon forms a spirocycle, representing one of only a few examples.[343, 355-358] The 5-membered ring of **7.3** is planar while the 6-membered ring of **7.2** is puckered. The B1–O1 and B1–O3 bond lengths of **7.2** are 1.478(4) Å and 1.535(3) Å respectively and are close to the sum of the covalent radii (R(B–O) = 1.50 Å)[268] for a single bond. In the 6-

membered ring of **7.2** the endocyclic C–O bond lengths range from 1.298(3) to 1.410(3) Å while the length of the exocyclic C2–O4 bond is significantly shorter [1.210(3) Å] and indicative of double bond character. In compound **7.3**, the B–O bond lengths [1.5429(18) Å and 1.4746(17) Å] are comparable to those of **7.2**.

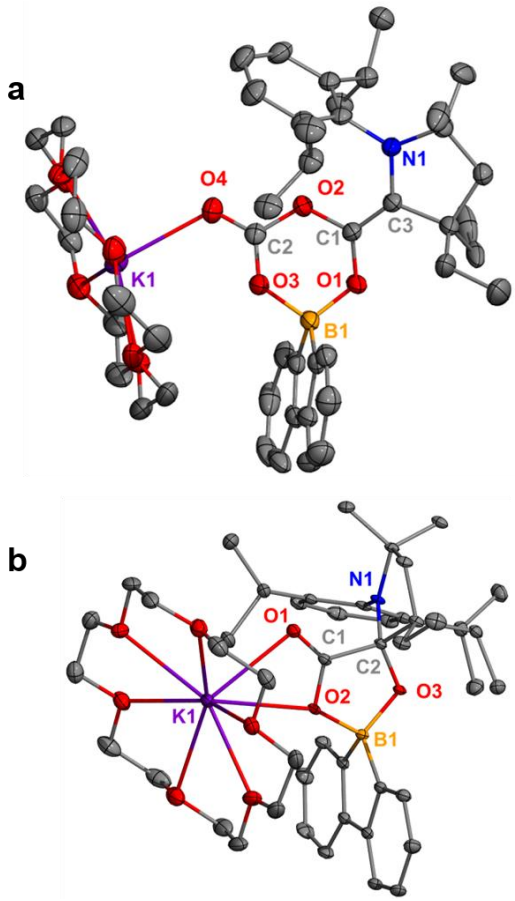

Figure 7.2. Molecular structures of **7.2** (a) and **7.3** (b). Hydrogen atoms omitted for clarity and thermal ellipsoids shown at 50% probability. Selected bond lengths [Å]: 2: B1–O1 1.478(4), B1–O3 1.535(3), C1–O1 1.350(3), C1–O2 1.410(3), C2–O2 1.351(3), C2–O3 1.298(3), C2–O4 1.210(3), C1–C3 1.340(4); 3: B1–O2 1.5429(18), B1–O3 1.4746(17), C1–O1 1.2223(17), C1–O2 1.3113(16), C1–C2 1.5517(18), C2–O3 1.3945(16).

7.4 Mechanism for the Formation of Trioxaborinanone

The mechanism for the formation of **7.2** was investigated using density functional theory (Figure 7.3). The addition of electron-rich boron **6.1** to the carbon center of CO_2 forms borylcarboxylate adduct **Int1**. The nature of the formation of **Int1**, described by **TS1**, was further examined using energy decomposition analysis in conjunction with the natural orbitals for chemical valence method (EDA-NOCV). The boron center in **TS1** adopts sp^3 hybridization. The highest occupied fragment orbital describes a lone-pair centered at boron, with the complimentary π* lowest occupied fragment orbital on bent CO_2. The resultant NOCV identifies charge-transfer from boron to the carbon atom of CO_2, indicating the initial adduct formation proceeds via nucleophilic addition (Figure 7.4). The CO_2 adduct undergoes a concerted migration from boron to the carbene carbon forming *β*-lactone intermediate **Int2**. The calculated barrier height for the [2+2] cycloaddition of CO_2 to the B-Carbene bond of 1 forming the β-lactone intermediate similar to that observed in Braunschweig's diboranes,[342] was found to be energetically unfavorable ($\Delta G^{\ddagger}$=+216.4 kJ mol^{-1}). This observation highlights the π nucleophilic character of boron in **1** as predicted by the donor-acceptor bonding interactions between borafluorene and CAAC.[298] Dissociation of the boron-carbene bond in **Int2** yields **Int3** possessing a nucleophilic site at the singly coordinated oxygen. **Int3** readily undergoes nucleophilic addition with CO_2 (**Int4**) and subsequent intramolecular cyclization to form **7.2** (ΔG_{rxn} = -68.2 kJ mol^{-1}).

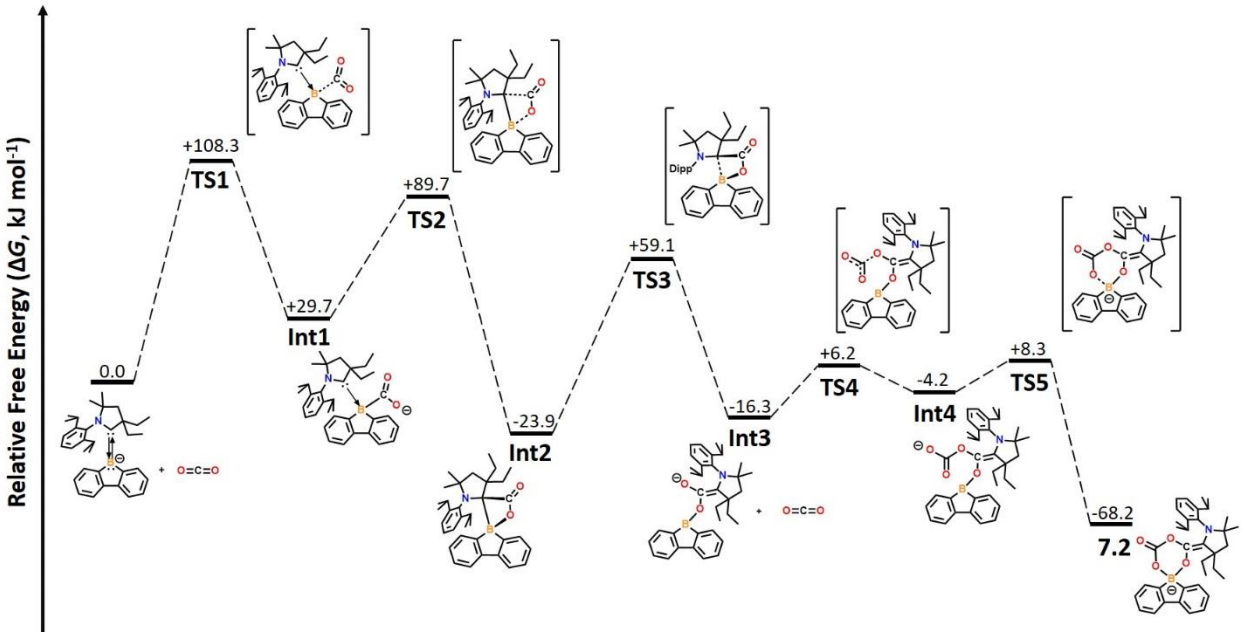

Figure 7.3. Calculated relative free energies (ΔG, kJ mol^{-1}) for the reaction of **6.1** with CO_2 to form **7.2** at the B3LYP-D3(BJ)/def2-TZVP//B3LYP-D3(BJ)/def2-SVP (SMD, Toluene) level of theory. All thermochemical values computed at 298.15 K and 3.4 atm.

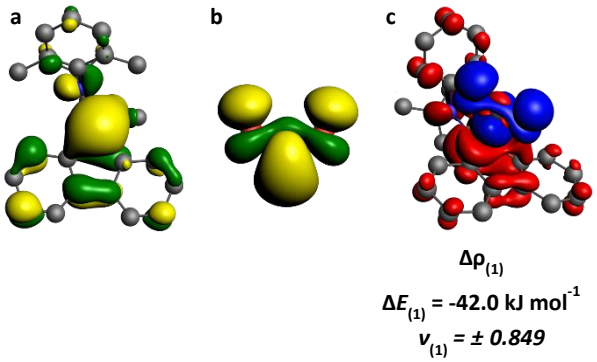

Figure 7.4. Plots of the reactant fragment orbitals for **TS1** (a) and (b). Plot of the deformation density $\Delta\rho_{(1)}$ (c) indicating charge flow between NOCVs for TS1 and the associated contribution to the total orbital interaction ($\Delta E_{(1)}$, kJ mol^{-1}). Eigenvalue $v_{(1)}$ quantifies the amount of transferred electron density (red: charge depletion, blue: charge accumulation), isosurface = 0.001.

7.5 Photophysical Properties of Luminescent Dioxaborinanone

Spirocyclic **7.2** can be considered among carbon monoxide-releasing molecules (CORMs) that are important for their ability to deliver specific amounts CO, reducing the risk of CO poisoning.[348-349] Monitoring the reaction of **7.2** to **7.3** by ^{1}H NMR indicates that after 2 hrs of heating compound **7.2** at 60 °C in THF-d_8, it is completely converted to **7.3** and CAAC-CO_2[359] (2:1 ratio, **7.3**:CAAC-CO_2). It is noteworthy that dioxaborinanone **7.2** emits blue light under UV excitation. Therefore, compound **7.2** is an especially promising CORM with the ability to deliver CO under both thermal or photochemical conditions with a simultaneous optical response (i.e., fluorescence turn-on due to the formation of **7.3**). The absorption maximum for **7.3** in THF was observed at 318 nm, with a red shifted emission maximum at 352 nm (Figure 7.5). In order to quantify luminescence, an absolute quantum yield of 7% in solution was determined for **7.3**. Theoretical modelling of the electronic excitations for **7.3** at the CAM-B3LYP-D3(BJ)/def2-TZVP(-f) level of theory identifies the lowest energy transition to be a mixed HOMO→LUMO (44%) and HOMO-1→LUMO (34%) configuration. These transitions describe π→π* transitions centered on the borafluorene moiety with minor charge-transfer character from CAAC to borafluorene (Figure A4.48).

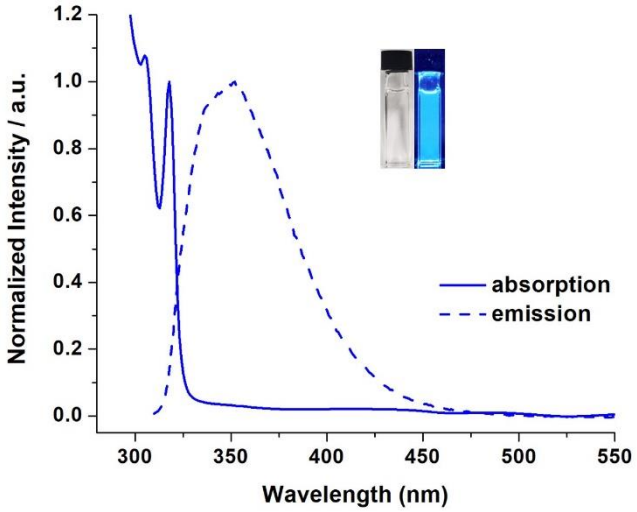

Figure 7.5. Normalized absorption (solid line) and emission (dashed line) spectra of **7.3**. Solutions were dissolved in THF and ran at room temperature, and excited at 300 nm.

7.6 Summary and Outlook

In conclusion, we report the first structurally authenticated example of a trioxaborinanone (**7.2**), which was synthesized from the activation of CO_2 by the 9-CAAC-9-borafluorene monoanion. Notably, compound **7.2** functions as a CO releasing molecule when heated or irradiated, and forms the luminescent dioxaborinanone (**7.3**) via loss of CO. Thus, a fluorescent response is initiated, and can be observed optically when one equivalent of CO is released. Theoretical mechanistic studies reveal the reactivity of 9-CAAC-9-borafluorene monoanion with CO_2 proceeds via a nucleophile addition pathway. Other studies to investigate the reactivity of the 9-carbene-9-borafluorene monoanions with different small molecules are currently underway in our laboratory.

Future studies in this area include reactions with carbon disulfide to investigate if any differences in bonding and structure exist with a heavier analogue of carbon dioxide. Additional experiments with other solvents for the reaction would be screened to gain a better understanding of what temperature and reaction time is needed for complete CO release. For CORM applications,

it is essential to deliver pure CO quickly, therefore the shortest reaction time is ideal. It is also necessary to examine the role the potassium interaction plays on the formation of the CO_2 inserted product, thus experiments with compound **6.3** instead of **6.2** will be vital.

Appendix I – Experimental Details

General Procedures

All experiments were carried out under an inert atmosphere of argon using an MBRAUN LABmaster glovebox equipped with a -37 °C freezer. The solvents were purified by distillation over sodium and benzophenone. THF-d_8 for NMR experiments was purified by distillation over sodium and stored over Na/K under an inert atmosphere. CD_3CN was purified by distillation over CaH_2. Glassware was oven-dried at 190 °C overnight. The NMR spectra were recorded at room temperature on a Varian 600 MHz spectrometer. Proton and carbon chemical shifts are reported in ppm and referenced using the residual proton and carbon signals of the deuterated solvent (^{1}H: C_6D_6 - δ = 7.16; ^{13}C: C_6D_6 - δ = 128.1; ^{1}H: THF-d_8 - δ = 3.58; ^{13}C: THF-d_8 - δ = 67.6; ^{1}H: CD_3CN - δ = 1.94; ^{13}C: CD_3CN - δ = 118.3), while lithium, boron, fluorine, phosphorus, and selenium chemical shifts are referenced to external standards (^{7}Li: 9.7 M LiCl in D_2O - δ = 0.0; ^{11}B: BF_3•Et_2O - δ = 0.0; ^{19}F: C_6F_6 - δ = 164.9 ; ^{31}P: 85% H_3PO_4 in H_2O - δ = 0.0; ^{77}Se: Ph_2Se_2 in C_6D_6 - δ = 459). Due to the borosilicate NMR probe, a large broad peak is observed at approximately 25 to -25 ppm in the ^{11}B NMR spectra. Reactions with CO_2 were carried out in Fisher-Porter reaction vessels with gas that was dried over P_2O_5 for 4 hrs. The UV-visible and fluorescence spectra were recorded on a Cary 60 UV-vis Spectrophotometer and a Cary Eclipse Fluorescence Spectrophotometer. Sample solutions were prepared in toluene or THF in 1 cm square air-free quartz cuvettes. Absolute fluorescence quantum yields were obtained using a Hamamatsu C11347-11 Quantaurus-QY Absolute PL Quantum Yield Spectrometer. Samples were prepared in the glovebox using quartz petri dishes (single crystals) or 1 cm square quartz cuvettes (solutions). The solutions were prepared in THF and the data was collected with absorbance values less than 0.1. Elemental analyses were performed on a Perkin-Elmer 2400 Series II analyzer. 18-crown-6 was

purchased from Sigma Aldrich and was recrystallized from minimal toluene at -37 °C and dried under reduced pressure before use. All other chemicals were purchased from Sigma Aldrich or Strem Chemicals and used as received. The 1,3-bis(2,6-diisopropylphenyl)imidazolium chloride (IPr•HCl)[17], 4,5,9,10-tetrabromo-2,7-ditert-butylpyrene,[56] 4,5,9,10-tetrabromo-2,7-di-tert-butylpyrene,[56] and 1,3-diisopropyl-4,5-dimethylimidazol-2-ylidene (sIPr),[170] **2.1**,[166, 229] **4.1**,[107] **4.2**,[102] and CAAC-BF•[123] were prepared according to the literature procedures.

Chapter Two

*Synthesis of **2.1***

In a 50 mL flask, 1,3-bis(2,6-diiso-propylphenyl)imidazolium chloride (IPr•HCl, 0.471 g, 1.11 mmol), [$Pd(OAc)_2$] (0.124 g, 0.554 mmol), and NaO*t*Bu (0.160 g, 1.66 mmol) were stirred in 20 mL of toluene at room temperature for 1 hr until a clear orange solution was observed. In a Schlenk tube 4,5,9,10-tetrabromo-2,7-di-tert-butylpyrene (5.00 g, 7.91 mmol) and NaO*t*Bu (3.65 g, 38.0 mmol) were dissolved in anhydrous toluene (100 mL). The previous solution was added to the Schlenk tube, and tert-butylamine (3.99 mL, 38.0 mmol) was added under positive argon pressure. The resulting dark orange solution was stirred at 110 °C for 16 hrs. The mixture was cooled to room temperature and filtered over Celite®. The solvent was removed from the filtrate to leave a dark orange solid. The crude solid was washed with hexanes (3 x 20 mL) to yield the pure yellow product (4.41 g, 93% yield). Colorless block-shaped crystals suitable for X-ray diffraction studies were obtained from a concentrated hexane solution at -37 °C. ^{1}H NMR (600 MHz, C_6D_6, 298 K) δ = 8.85 (s, 4H, CH_{pyr}), 4.23 (br. s, 4H, N*H*), 1.65 (s, 18H, C(CH_3)$_3$), 1.26 ppm (s, 36H, N(C(CH_3)$_3$). ^{13}C{^{1}H} NMR (150.90 MHz, C_6D_6, 298 K) δ = 146.3, 136.9, 132.1, 120.8, 119.6, 56.0, 35.9, 32.3, 31.8 ppm.

*Synthesis of **2.2***

Compound **2.1** (1.00 g, 1.67 mmol) was dissolved in freshly distilled Et_2O (10 mL) in a 100 mL Schlenk flask to yield a yellow solution. *n*-BuLi (2.5 M in hexanes, 2.84 mL, 7.02 mmol) was added dropwise under argon at -78 °C, and a color change to red was observed. The reaction was slowly warmed to room temperature and stirred for 22 hrs. The solvent was removed under reduced pressure, and the orange residue was redissolved in toluene (60 mL). $GeCl_2$•dioxane (0.774 g, 3.34

mmol) was added, and the reaction was stirred for 17 hrs. The mixture was filtered over Celite® to leave a dark orange filtrate. The solvent was removed from the filtrate under reduced pressure to leave a dark orange solid. The crude solid was washed with hexane (3 x 10 mL) to leave the pure orange compound **2.2** (0.517 g, 46% yield). Yellow rod-shaped crystals suitable for X-ray diffraction studies were obtained from a concentrated toluene solution at -37 °C. ^{1}H NMR (600 MHz, C_6D_6, 298 K) δ = 8.50 (s, 4H, CH_{pyr}), 1.85 (s, 36H, N(C(CH_3)$_3$)) 1.59 ppm (s, 18H, C(CH_3)$_3$). ^{13}C{^{1}H} NMR (150.90 MHz, C_6D_6, 298 K) δ = 143.7, 136.8, 126.7, 117.2, 116.3, 59.3, 37.5, 36.4, 32.6 ppm. Anal. Calcd for $C_{40}H_{58}Ge_2H_4$: C, 64.91; H, 7.90; N, 7.57%. Found: C, 64.38; H, 8.14; N, 7.24%.

*Synthesis of **2.3***

To a solution of compound **2.2** (0.200 g, 0.270 mmol) in toluene (25 mL), sIPr (0.0974 g, 0.540 mmol) was added. After addition, the reaction was stirred at room temperature for 3.5 hrs. The yellow precipitate was then collected through filtration and washed with hexane (3 x 5 mL), and the remaining solid was dried under reduced pressure to yield compound **2.3** (0.122 g, 41% yield). Yellow block-shaped crystals suitable for X-ray diffraction were obtained from a concentrated NMR sample in C_6D_6. ^{1}H NMR (600 MHz, C_6D_6, 298 K) δ = 8.57 (s, 4H, CH_{pyr}), 6.68 (br. s, 4H, CH(CH$_3$)$_2$), 1.99 (s, 36H, N(C(CH_3)$_3$)), 1.72 (s, 18H, C(CH_3)$_3$), 1.49 (s, 12H, CCH_3), 1.05 ppm (s, 24H, CH(CH_3)$_2$). ^{13}C{^{1}H} NMR (150.90 MHz, C_6D_6, 298 K) δ = 188.4, 141.9, 120.1, 119.3, 111.8, 58.4, 48.4, 36.2, 35.8, 33.0, 21.4, 9.8 ppm.

Chapter Three

*Synthesis of **3.2***

To a solution of compound **2.1** (0.300 g, 0.501 mmol) in toluene (15 mL), BH_3•THF (1 M in THF, 1.75 mL, 1.75 mmol) was added under argon. The yellow slurry was heated to 110 °C for 2 days until a yellow solution was observed. The reaction was cooled to room temperature and the pale-yellow solid was collected via filtration and washed with hexanes (5 mL) and the remaining solid was dried under reduced pressure to leave compound **3.2** (0.239 mg, 77% yield). ^{1}H NMR (600 MHz, C_6D_6, 298 K) δ = 8.83 (s, 4H, CH_{pyr}), 1.88 (s, 36H, $N(C(CH_3)_3)$), 1.66 ppm (s, 18H, $C(CH_3)_3$). Unable to observe the BH due to the quadrupolar effect. $^{13}C\{^{1}H\}$ NMR (150.90 MHz, C_6D_6, 298 K) δ = 132.3, 129.3, 125.7, 125.2, 117.5, 54.5, 34.8, 32.6, 30.2 ppm. $^{11}B\{^{1}H\}$ NMR (C_6D_6, 192.55 MHz): No shift was observed. Anal. Calcd for $C_{40}H_{60}B_2N_4$: C, 77.67; H, 9.78; N, 9.06%. Found: C, 77.18; H, 9.75; N, 9.02%.

*Synthesis of **3.3***

To a -78 °C solution of compound **2.1** (0.200 mg, 0.334 mmol) in Et_2O (20 mL), *n*-BuLi (2.5 M in hexanes, 0.560 mL, 1.40 mmol) was added slowly. The orange solution was slowly warmed to room temperature and stirred for 20 hrs. The reaction mixture was cooled to -78 °C, and BF_3• Et_2O (0.0825 mL, 0.668 mmol) was added. The reaction was slowly warmed to room temperature and the light green solution was stirred at room temperature for 22 hrs. The solvent was removed under reduced pressure, and the product was extracted from the green residue with toluene (30 mL). The mixture was filtered over Celite® to remove LiF salt. The solvent was removed from the filtrate to leave a crude green solid. The solid was washed with hexanes (3 x 5 mL) to leave compound **3.3** as a light green solid (0.0698 g, 32% yield). Single crystals were obtained via 1:1 mixture of

toluene/hexane at -37 °C. ^{1}H NMR (600 MHz, C_6D_6, 298 K) δ = 8.57 (s, 4H, CH_{pyr}), 1.79 (s, 36H, N(C(CH_3)$_3$)), 1.60 ppm (s, 18H, C(CH_3)$_3$). ^{13}C{^{1}H} NMR (150.90 MHz, C_6D_6, 298 K) δ = 144.0, 131.0, 125.5, 117.2, 116.8, 55.1, 36.1, 33.2, 32.4 ppm. ^{11}B{^{1}H} NMR (C_6D_6, 192.55 MHz): δ 25.7 ppm. ^{19}F NMR (C_6D_6, 564.69 MHz): δ -125.7 ppm (d, *J* = 33.9 Hz, 1F).

*Synthesis of **3.4***

To a -78 °C solution of compound **2.1** (500 mg, 0.835 mmol) in Et_2O (20 mL), *n*-BuLi (2.5 M in hexanes, 1.40 mL, 3.51 mmol) was added slowly. The orange solution was slowly warmed to room temperature and stirred for 17 hrs. The solvent was removed under reduced pressure and the orange residue was dissolved in toluene (50 mL), and $PhBCl_2$ (0.218 mL, 1.67 mmol) was added slowly. The reaction was stirred at room temperature for 21 hrs. The red mixture was filtered over Celite® to remove LiCl salt, and the solvent was removed from the filtrate to leave a crude red solid. The solid was washed with hexane (3 x 5 mL) to leave compound **3.4** as a pale orange solid (303.8 mg, 47% yield). ^{1}H NMR (600 MHz, C_6D_6, 298 K) δ = 8.65 (s, 4H, CH_{pyr}), 7.96 (d, 4H, *o*-Ph*H*), 7.37 (t, 4H, *m*-Ph*H*), 7.29 (t, 2H, *p*-Ph*H*), 1.64 (s, 18H, C(CH_3)$_3$), 1.61 ppm (s, 36H, N(C(CH_3)$_3$)). ^{13}C{^{1}H} NMR (150.90 MHz, C_6D_6, 298 K) δ = 144.1, 134.6, 134.3, 126.4, 116.7, 116.0, 56.4, 36.2, 35.2, 32.4 ppm. ^{11}B{^{1}H} NMR (C_6D_6, 192.55 MHz): δ 33.1 ppm.

*Synthesis of **3.5***

Synthesis of compound **3.5** was modified from the reported literature.[231] In a Schlenk tube 1,3-bis(2,6-diiso-propylphenyl)imidazolium chloride (IPr•HCl, 0.189 g, 0.444 mmol), [$Pd(OAc)_2$] (0.0513 g, 0.229 mmol), and NaO*t*Bu (0.0646 g, 0.673 mmol) were stirred in toluene (30 mL) at

room temperature until a clear orange solution was observed. 1,2,4,5-tetrabromobenzene (5.00 g, 12.7 mmol) and NaO*t*Bu (5.98 g, 62.2 mmol) were then added to the orange solution. Under positive argon pressure, *tert*-butylamine (5.61 mL, 53.3 mmol) was added, and the resulting orange mixture was heated to 110 °C for 15 hrs. The mixture was cooled to room temperature and filtered over Celite® to remove NaBr salt. The solvent was removed from the filtrate to leave a brown solid. The crude solid was washed with hexane (3 x 20 mL) to leave compound **3.5** as a tan solid (3.93 g, 85% yield). ^{1}H NMR (600 MHz, C_6D_6, 298 K) δ = 6.68 (s, 2H, CH_{benz}), 3.61 (s, 4H, N*H*), 1.29 ppm (s, 36H, N(C(CH_3)$_3$).

*Synthesis of **3.6***

To a solution of compound **3.5** (1.00 g, 2.76 mmol) in toluene (100 mL), BH_3•THF (1 M in THF, 5.79 mL, 5.79 mmol) was added dropwise. The resulting yellow mixture was heated to 110 °C for 2 days. The mixture was then cooled to room temperature and the product was collected via filtration. The solid was washed with hexane (3 x 5 mL) to leave compound **3.6** as a white crystalline solid (0.650 g, 62% yield). Single crystals suitable for X-ray studies were grown from a refluxing toluene solution and slow cooling to room temperature. ^{1}H NMR (600 MHz, C_6D_6, 298 K) δ = 7.66 (s, 2H, CH_{benz}), 1.65 ppm (s, 36H, N(C(CH_3)$_3$). Unable to observe the B*H* due to quadrupolar effect. ^{13}C{^{1}H} NMR (150.90 MHz, C_6D_6, 298 K) δ = 130.7, 100.6, 67.8, 52.4, 30.9 ppm. ^{11}B{^{1}H} NMR (C_6D_6, 192.55 MHz): No shift was observed. Anal. Calcd for $C_{22}H_{40}B_2N_4$: C, 69.14; H, 10.55; N, 14.66%. Found: C, 68.64; H, 10.62; N, 14.54%.

*Synthesis of **3.7***

To a -78 °C solution of compound **3.5** (0.200 g, 0.552 mmol) in THF (40 mL) *n*-BuLi (2.5 M in hexanes, 0.927 mL, 2.32 mmol) was added slowly. The red solution was slowly warmed to room temperature and stirred for 20 hrs. The solution was cooled to -78 °C, and BF_3• Et_2O (0.136 mL, 1.10 mmol) was added. The dark purple solution was stirred at room temperature for 24 hrs. The solvent was removed under reduced pressure, and the product was extracted from the purple solid residue with toluene (40 mL). The mixture was filtered over Celite® to remove LiF salts. The solvent was removed from the filtrate to leave a crude purple solid. The solid was recrystallized from a concentrated THF solution at room temperature to leave compound **3.7** as a purple crystalline solid (120 mg, 48% yield). ^{1}H NMR (600 MHz, C_6D_6, 298 K) δ = 5.43 (s, 2H, CH_{benz}), 1.43 ppm (s, 36H, N(C(CH_3)$_3$). ^{13}C{^{1}H} NMR (150.90 MHz, C_6D_6, 298 K) δ = 155.9, 128.9, 55.2, 29.0, 28.3 ppm. ^{11}B{^{1}H} NMR (C_6D_6, 192.55 MHz): δ 5.4 ppm. ^{19}F NMR (C_6D_6, 564.69 MHz): δ -151.8 ppm (q, J = 56.4 Hz, 2F). Anal. Calcd for $C_{22}H_{38}B_2F_4N_4$: C, 57.92; H, 8.40; N, 12.28%. Found: C, 58.03; H, 8.46; N, 11.84%.

*Synthesis of **3.8***

To a -78 °C solution of compound **3.5** (0.500 g, 1.38 mmol) in Et_2O (40 mL), *n*-BuLi (1.6 M in hexanes, 3.62 mL, 5.79 mmol) was added slowly. The red solution was slowly warmed to room temperature and stirred for 20 hrs. The solvent was removed under reduced pressure and the red solid residue was dissolved in toluene (40 mL), and $PhBCl_2$ (0.365 mL, 2.76 mmol) was then added. The reaction was stirred at room temperature for 24 hrs. The reaction mixture was filtered over Celite® to remove LiCl salt. The solvent was removed from the filtrate to leave a crude pink solid. The solid was washed with hexane (3 x 5 mL) to leave compound **3.8** as a light pink solid

(0.373 g, 51% yield). Single crystals suitable for X-ray studies were obtained from a concentrated toluene solution at -37 °C. ^{1}H NMR (600 MHz, C_6D_6, 298 K) δ = 7.81 (s, 2H, CH_{benz}), 7.56 (d, 4H, *o*-Ph*H*), 7.20 (m, 6H, *m*-Ph*H*/*p*-Ph*H* overlapped), 1.54 ppm (s, 36H, N(C(CH_3)$_3$)). ^{13}C{^{1}H} NMR (150.90 MHz, C_6D_6, 298 K) δ = 133.9, 130.1, 127.3, 127.0, 102.8, 54.5, 32.4 ppm. ^{11}B{^{1}H} NMR (C_6D_6, 192.55 MHz): No shift was observed, hidden behind probe.

*Synthesis of **3.9***

To a -78 °C mixture of compound **3.6** (0.200 g, 0.5233 mmol) in THF (20 mL), *n*-BuLi (1.6 M in hexanes, 0.719 mL, 1.15 mmol) was added slowly. The resulting green mixture was warmed to room temperature and stirred for 4 hrs. The solvent was removed under reduced pressure to leave a green residue. The product was extracted with toluene (5 mL) and recrystallized at -37 °C to leave compound **3.9** as a white crystalline solid (0.130 g, 50% yield). ^{1}H NMR (600 MHz, C_6D_6, 298 K) δ = 7.64 (s, 2H, CH_{benz}), 1.77 (s, 36H, N(C(CH_3)$_3$), 1.73 (t, 4H, CH_2CH$_2$CH$_2$CH$_3$), 1.68 (m, 4H, CH$_2$CH_2CH$_2$CH$_3$), 1.50 (m, 4H, CH$_2$CH$_2$CH_2CH$_3$), 1.02 ppm (t, 6H, CH$_2$CH$_2$CH$_2$CH_3). ^{13}C{^{1}H} NMR (150.90 MHz, C_6D_6, 298 K) δ = 129.9, 103.0, 54.4, 32.1, 31.8, 26.6, 14.3 ppm. ^{11}B{^{1} NMR (C_6D_6, 192.55 MHz): 30.0 ppm. Anal. Calcd for $C_{30}H_{56}B_2N_4$: C, 72.88; H, 11.42; N, 11.33%. Found: C, 72.41; H, 11.42; N, 11.16%.

*Synthesis of **3.10***

In a Schlenk tube 1,3-bis(2,6-diiso-propylphenyl)imidazolium chloride (IPr•HCl, 0.0861 g, 0.202 mmol), [Pd(OAc)$_2$] (0.0227 g, 0.101 mmol), and NaO*t*Bu (0.0292 g, 0.304 mmol) were stirred in toluene (40 mL) at room temperature until a clear orange solution was observed. 4,5,9,10-

tetrabromo-2,7-ditert-butylpyrene (0.914 g, 1.45 mmol) and NaO*t*Bu (0.667 g, 6.94 mmol) were then added to the orange solution. Under positive argon pressure, methylamine (2 M in THF, 3.47 mL, 6.94 mmol) was added, and the resulting tan mixture was heated to 110 °C for 18 hrs. The mixture was cooled to room temperature and filtered over Celite® to remove NaBr salt. The solvent was removed from the filtrate to leave a brown solid. The crude solid was washed with hexane (3 x 5 mL) to leave compound **3.10** as an orange solid (0.281 g, 45% yield). ^{1}H NMR (600 MHz, C_6D_6, 298 K) δ = 8.43 (s, 4H, CH_{pyr}), 4.02 (q, 4H, N*H*), 2.28 (d, 12H, NCH_3), 1.60 ppm (s, 18H, C(CH_3)$_3$). ^{13}C{1H} NMR (150.90 MHz, C_6D_6, 298 K) δ = 147.8, 137.0, 129.0, 120.6, 116.5, 37.4, 35.6, 32.3 ppm.

*Synthesis of **3.11***

To a -78 °C solution of compound **3.10** (200 mg, 0.464 mmol) in Et_2O (40 mL), *n*-BuLi (1.6 M in hexanes, 1.22 mL, 1.95 mmol) was added slowly. The dark red solution was slowly warmed to room temperature and stirred for 20 hrs. The solvent was removed under reduced pressure and the red residue was dissolved in toluene (40 mL), and $PhBCl_2$ (0.121 mL, 0.929 mmol) was added slowly. The reaction was stirred at room temperature for 27 hrs. The dark yellow mixture was filtered over Celite® to remove LiCl salt, and the solvent was removed from the filtrate. The crude yellow-green solid was washed with hexanes (3 x 5 mL) to leave compound **3.11** as a yellow solid (184 mg, 66% yield). Single crystals suitable for X-ray studies were obtained from a concentrated toluene/THF mixture (10:1) at room temperature. ^{1}H NMR (600 MHz, C_6D_6, 298 K) δ = 9.05 (s, 4H, CH_{pyr}), 7.73 (d, 4H, *o*-Ph*H*), 7.46 (t, 4H, *m*-Ph*H*), 7.38 (t, 2H, *p*-Ph*H*), 3.94 (s, 12H, NCH_3), 1.63 ppm (s, 18H, C(CH_3)$_3$). ^{13}C{^{1}H} NMR (150.90 MHz, C_6D_6, 298 K) δ = 146.1, 136.0, 135.1,

129.7, 128.8, 128.4, 126.1, 117.8, 113.4, 35.8, 35.7, 32.2 ppm. $^{11}B\{^{1}H\}$ NMR (C_6D_6, 192.55 MHz): δ 29.8 ppm.

Chapter Four

*Synthesis of **4.3***

In a 100 mL Schlenk flask, Li metal (24.9 mg, 3.58 mmol) and naphthalene (9.18 mg, 0.0716 mmol) were stirred in THF (40 mL) at room temperature for 40 minutes until a deep green solution was observed. Compound **4.1** (200 mg, 0.358 mmol) was then added and the reaction immediately became purple in color. The reaction was stirred at room temperature for 18 hrs, during which the solution became deep red in color. The solvent was removed under reduced pressure and the product was extracted with Et_2O (30 mL). The deep red mixture was filtered through a 0.45 μm PTFE syringe filter and the solvent was removed to leave the product as a deep red solid (131 mg, 47% yield). Single crystals were grown from a concentrated solution in Et_2O at -37 °C. ^{1}H NMR (600 MHz, THF-d_8, 298 K) δ = 7.91 (d, 1H, Ar*H*), 7.47 (d, 1H, Ar*H*), 7.34 (d, 1H, Ar*H*), 7.22 (t, 1H, Ar*H*), 7.10 (d, 2H, Ar*H*), 6.67 (t, 1H, Ar*H*), 6.48 (t, 1H, Ar*H*), 6.29 (t, 1H, Ar*H*), 6.00 (t, 1H, Ar*H*), 4.72 (d, 1H, Ar*H*), 3.70 (hept, 2H, C*H*$(CH_3)_2$), 2.54 (q, 2H, C*H*$_2$CH$_3$), 2.37 (q, 2H, C*H*$_2$CH$_3$) 2.02 (s, 2H, C*H*$_2$), 1.18 (s, 6H, C*H*$_3$), 1.17 (d, 6H, CH(C*H*$_3$)$_2$), 1.08 (t, 6H, CH$_2$C*H*$_3$), 0.82 ppm (d, 6H, CH(C*H*$_3$)$_2$); ^{13}C{^{1}H} NMR (151 MHz, THF-d_8, 298 K) δ = 153.9 (Ar*C*), 144.6 (Ar*C*), 144.2 (Ar*C*), 143.8 (Ar*C*), 143.3(Ar*C*), 134.2 (Ar*C*), 133.2 (Ar*C*), 126.7 (Ar*C*), 124.7 (Ar*C*), 121.7 (Ar*C*), 121.0 (Ar*C*), 117.2 (Ar*C*), 116.9 (Ar*C*), 116.3 (Ar*C*), 116.2 (Ar*C*), 68.4 (O*C*H$_2$CH$_2$), 65.5 (OCH$_2$CH$_2$), 53.0 (N*C*), 51.0 (*C*$_q$), 32.0 (*C*H$(CH_3)_2$), 31.6 (*C*H$(CH_3)_2$), 29.6 (CH$_2$*C*H$_3$), 27.2 (CH$_2$*C*H$_3$), 26.5 (*C*H$_3$), 25.0 (*C*H$_2$), 10.9 ppm (CH(*C*H$_3$)$_2$); ^{11}B NMR (193 MHz, THF-d_8, 298 K) δ = 14.45 ppm; ^{7}Li NMR (233 MHz, THF-d_8, 298 K) δ = 1.26 ppm.

*Synthesis of **4.4***

To a solution of compound **4.1** (200 mg, 0.358 mmol) in THF (40 mL), Na metal (18.1 mg, 0.788 mmol) was added. The reaction was stirred at room temperature for 23 hrs. The deep red solution was filtered through a 0.45 μm PTFE syringe filter, and the solvent was removed under reduced pressure. Red crystals were obtained from a concentrated Et_2O/hexanes (10:1) mixture at room temperature (129 mg, 55% yield). ^{1}H NMR (600 MHz, THF-d_8, 298 K) δ = 7.91 (d, 1H, Ar*H*), 7.43-7.37 (m, 3H, Ar*H*), 7.09 (td, 2H, Ar*H*), 7.01 (t, 1H, Ar*H*), 6.96 (t, 1H, Ar*H*), 6.92 (m, 2H, Ar*H*), 6.87 (t, 1H, Ar*H*), 4.82 (hept, 1H, C*H*$(CH_3)_2$), 4.00 (s, 1H, C*H*$_2$), 3.71 (hept, 1H, C*H*$(CH_3)_2$), 2.47 (s, 1H, C*H*$_2$), 1.62 (d, 3H, CH(C*H*$_3)_2$), 1.45 (s, 3H, C*H*$_3$), 1.36 (d, 3H, CH(C*H*$_3)_2$), 1.29 (dd, 6H, CH(C*H*$_3)_2$), 1.09 (q, 2H, C*H*$_2$CH$_3$), 0.86 (s, 3H, C*H*$_3$), 0.71 (t, 3H, CH$_2$C*H*$_3$), 0.67 (q, 2H, C*H*$_2$CH$_3$), 0.37 ppm (t, 3H, CH$_2$C*H*$_3$); ^{13}C{^{1}H} NMR (151 MHz, THF-d_8, 298 K) δ = 183.1 (Ar*C*), 179.3 (Ar*C*), 152.6 (Ar*C*), 151.5 (Ar*C*), 149.6 (Ar*C*), 149.1 (Ar*C*), 132.7 (Ar*C*), 132.7 (Ar*C*), 130.9 (Ar*C*), 126.1 (Ar*C*), 126.0 (Ar*C*), 126.0 (Ar*C*), 125.9 (Ar*C*), 124.9 (Ar*C*), 124.7 (Ar*C*), 118.9 (Ar*C*), 118.9 (Ar*C*), 68.4 (O*C*H$_2$CH$_2$), 62.6 (O*C*H$_2$CH$_2$), 50.7 (N*C*), 49.8 (*C*$_q$), 47.4 (*C*H$(CH_3)_2$), 33.6 (*C*H$(CH_3)_2$), 32.7 (*C*H$_2$CH$_3$), 32.2 (*C*H$_2$CH$_3$), 30.1 (CH$_2$*C*H$_3$), 30.0 (CH$_2$*C*H$_3$), 27.9 (CH(*C*H$_3)_2$), 27.5 (CH(*C*H$_3)_2$), 26.8 (*C*H$_3$), 26.6 (*C*H$_3$), 25.0 (*C*H$_2$), 11.1 (CH(*C*H$_3)_2$), 10.3 ppm (CH(*C*H$_3)_2$); ^{11}B NMR (193 MHz, THF-d_8, 298 K) δ = 3.51 ppm.

*Synthesis of **4.5***

To a solution of compound **4.1** (1.34 g, 2.40 mmol) in THF (100 mL), KC_8 (0.973 g, 7.20 mmol) was added and the solution immediately turned purple in color. The reaction was stirred at room temperature for 23 hrs. The deep red reaction mixture was filtered over Celite® to remove graphite,

and the solvent was removed from the filtrate under reduced pressure. The crude solid was washed with Et_2O (3 x 30 mL) to leave the pure product as a red crystalline solid (0.904 g, 73% yield). Single crystals suitable for X-ray crystallography were obtained from the combined and concentrated Et_2O washes at -37 °C. ^{1}H NMR (600 MHz, THF-d_8, 298 K) δ = 8.02 (d, 1H, Ar*H*), 7.66 (d, 2H, Ar*H*), 7.52 (d, 1H, Ar*H*), 7.30 (t, 1H, Ar*H*), 7.17 (d, 2H, Ar*H*), 6.84 (t, 1H, Ar*H*), 6.66 (t, 1H, Ar*H*), 6.45 (t, 1H, Ar*H*), 6.13 (t, 1H, Ar*H*), 4.81 (d, 1H, Ar*H*) 3.59 (hept, 2H, C*H*$(CH_3)_2$), 2.52 (m, 2H, C*H*$_2$CH$_3$), 2.41 (m, 2H, C*H*$_2$CH$_3$), 2.07 (s, 2H, C*H*$_2$), 1.21 (m, 12H, CH$_3$/CH(C*H*$_3$)$_2$), 1.11 (m, 6H, CH$_2$C*H*$_3$), 0.81 ppm (d, 6H, CH(C*H*$_3$)$_2$); ^{13}C{^{1}H} NMR (151 MHz, THF-d_8, 298 K) δ = 183.2 (Ar*C*), 152.6 (Ar*C*), 151.4 (Ar*C*), 149.0 (Ar*C*), 149.0 (Ar*C*), 147.4 (Ar*C*), 133.0 (Ar*C*), 131.4 (Ar*C*), 126.0 (Ar*C*), 125.8 (Ar*C*), 125.8 (Ar*C*), 125.8 (Ar*C*), 124.7 (Ar*C*), 124.7 (Ar*C*), 124.7 (Ar*C*), 119.0 (Ar*C*), 119.0 (Ar*C*), 62.5 (O*C*H$_2$CH$_2$), 50.0 (N*C*), 47.5 (*C*$_q$), 33.7 (*C*H(CH$_3$)$_2$), 33.7 (*C*H(CH$_3$)$_2$), 32.7 (*C*H$_2$CH$_3$), 32.7 (*C*H$_2$CH$_3$), 32.3, 30.1 (CH$_2$*C*H$_3$), 30.0 (CH$_2$*C*H$_3$), 27.9 (CH(*C*H$_3$)$_2$), 27.5 (CH(*C*H$_3$)$_2$), 27.1 (*C*H$_3$), 26.7 (*C*H$_2$), 11.1 (CH(*C*H$_3$)$_2$), 10.3 ppm (CH(*C*H$_3$)$_2$); ^{11}B NMR (193 MHz, THF-d_8, 298 K) δ = 1.46 ppm. Anal. Calcd for $C_{34}H_{43}BKN$•3/2(Et_2O): C, 75.64; H, 8.87; N, 2.26%. Found: C, 75.27; H, 8.50; N, 2.65%.

*Synthesis of **4.6***

In a 100 mL Schlenk flask, Li metal (6.58 mg, 0.958 mmol) and naphthalene (12.2 mg, 0.0948 mmol) were stirred in THF (40 mL) at room temperature for 20 minutes until a deep green solution was observed. Compound **4.2** (300 mg, 0.474 mmol) was then added and the reaction immediately became deep blue in color. The reaction was stirred at room temperature for 23 hrs, during which the solution became deep yellow-brown in color. The solvent was removed under reduced pressure and the product was extracted with Et_2O (20 mL). The mixture was filtered through a 0.45 μm

PTFE syringe filter, and the solvent was removed to leave the product as a deep brown solid (257 mg, 79% yield). 18-crown-6 (125 mg, 0.474 mmol) was added to a concentrated solution of **4.6** in Et_2O to yield single crystals suitable for X-ray studies. Dark blue single crystals were grown from a concentrated solution in Et_2O at -37 °C. Due to the highly reactive nature of **4.6** and rapid conversion to the hydridoborafluorene product we relied on X-ray studies for characterization. ***Note:** For the LiNp reduction of **4.2**, excess reducing agent resulted in NHC ligand activation and a mixture of products were observed from which a molecule showing loss of the N-diisopropylphenyl group on NHC was crystallized and characterized via X-ray crystallography (Figure A3.11). Thus, stoichiometric amounts (2 eq.) of LiNp were used for the isolation of **4.6**.

*Synthesis of **4.7***

To a solution of compound **4.2** (200 mg, 0.316 mmol) in THF (40 mL), Na metal (21.8 mg, 0.948 mmol) was added. The reaction was stirred at room temperature for 22 hrs. The solvent was removed under reduced pressure and the product was extracted with Et_2O (40 mL). The deep purple mixture was filtered through a 0.45 μm PTFE syringe filter, and the solvent was removed under reduced pressure. 18-crown-6 ether (83.5 mg, 0.316 mmol) was added to yield single crystals suitable for X-ray studies. Deep purple crystals were obtained from a concentrated Et_2O solution at -37 °C (136 mg, 60% yield). Due to the highly reactive nature of **4.7** and rapid conversion to the hydridoborafluorene product we relied on X-ray studies for characterization.

*Synthesis of **4.8***

To a solution of compound **4.2** (2.00 g, 3.16 mmol) in THF (125 mL), KC_8 (1.28 g, 9.48 mmol) was added and the solution immediately turned blue in color. The reaction was stirred at room temperature for 25 hrs. The deep indigo reaction mixture was filtered over Celite® to remove the graphite and the solvent was removed from the filtrate under reduced pressure. The crude solid was washed with hexanes (3 x 20 mL) to leave the pure product as a deep indigo solid (1.20 g, 64% yield). Deep purple single crystals were obtained from a concentrated Et_2O solution at -37 °C. ^{1}H NMR (600 MHz, THF-d_8, 298 K) δ = 7.55 (d, 2H, Ar*H*), 7.28 (t, 2H, Ar*H*), 7.21(d, 4H, Ar*H*), 6.43 (s, 2H, Ar*H*), 6.27 (2, 2H, Ar*H*), 6.06 (t, 2H, Ar*H*), 5.91 (d, 2H, Ar*H*), 3.66 (hept, 4H, C*H*(CH_3)$_2$), 1.19 (d, 12H, CH(C*H*$_3$)$_2$), 0.97 ppm (d, 12H, CH(C*H*$_3$)$_2$); ^{13}C{^{1}H} NMR (151 MHz, THF-d_8, 298K) δ = 185.1 (Ar*C*), 149.3 (Ar*C*), 141.8 (Ar*C*), 136.6 (Ar*C*), 128.7 (Ar*C*), 128.4 (Ar*C*), 125.0 (Ar*C*), 121.2 (Ar*C*), 119.6 (Ar*C*), 117.8 (Ar*C*), 113.4 (Ar*C*), 29.4 (*C*H(CH_3)$_2$), 25.0 (CH(*C*H_3)$_2$), 23.4 ppm (CH(*C*H_3)$_2$); ^{11}B{^{1}H} NMR (193 MHz, THF-d_8, 298 K) δ = 7.20 ppm.

*Synthesis of **4.9***

To a solution of compound **4.5** (100 mg, 0.193 mmol) in THF (25 mL), PPh_3AuCl (95.6 mg, 0.193 mmol) was added. The deep red solution immediately turned orange in color. The reaction was stirred at room temperature for 1.5 hrs, and then the solvent was removed under reduced pressure. The yellow solid product was washed with Et_2O (20 mL), and collected via filtration. The pure product was further dried under reduced pressure to leave compound **4.9** as a yellow solid (105 mg, 58% yield). Yellow plate-shaped single crystals were grown from a concentrated Et_2O solution at room temperature. ^{1}H NMR (600 MHz, THF-d_8, 298 K) δ = 8.10 (d, 1H, Ar*H*), 7.61 (d, 1H,

Ar*H*), 7.52 (d, 1H, Ar*H*), 7.39 (tq, 3H, Ar*H*), 7.35 (t, 1H Ar*H*), 7.30 (tt, 7H, Ar*H*), 7.25 (m, 6H, Ar*H*), 5.13 (d, 1H, Ar*H*), 3.63 (hept, 1H, C*H*(CH_3)$_2$), 3.44 (hept, 1H, C*H*(CH_3)$_2$), 2.86 (m, 1H, C*H*$_2$$CH_3$), 2.77 (m, 1H, C*H*$_2$$CH_3$), 2.42 (m, 1H, C*H*$_2$$CH_3$), 2.15 (m, 2H, C*H*$_2$$CH_3$/C*H*$_2$), 1.99 (d, 1H, C*H*$_2$), 1.65 (s, 3H, C*H*$_3$), 1.14 (d, 3H, CH(C*H*$_3$)$_2$), 1.10 (m, 6H, CH(C*H*$_3$)$_2$/ CH_2C*H*$_3$), 1.04 (d, 3H, CH(C*H*$_3$)$_2$) 0.91 (s, 3H, C*H*$_3$), 0.71 (t, 3H, CH_2C*H*$_3$), 0.26 ppm (d, 3H, CH(C*H*$_3$)$_2$); ^{13}C{^{1}H} NMR (151 MHz, THF-d$_8$, 298K) δ = 183.7 (Ar*C*), 152.0 (Ar*C*), 149.2 (Ar*C*), 147.5 (Ar*C*), 146.7 (Ar*C*), 140.2 (Ar*C*), 135.2 (Ar*C*), 135.1 (Ar*C*), 134.7 (Ar*C*), 133.7 (Ar*C*), 132.8 (Ar*C*), 132.5 (Ar*C*), 131.7 (Ar*C*), 131.7 (Ar*C*), 129.8 (Ar*C*), 129.7 (Ar*C*), 128.8 (Ar*C*), 126.3 (Ar*C*), 126.0 (Ar*C*), 124.2 (Ar*C*), 123.2 (Ar*C*), 123.2 (Ar*C*), 123.0 (Ar*C*), 119.1 (Ar*C*), 118.0 (Ar*C*), 69.5 (N*C*), 56.7 (*C*$_q$), 49.8 (*C*H(CH_3)$_2$), 39.8 (*C*H(CH_3)$_2$), 32.9 (*C*$H_2$$CH_3$), 31.2 (*C*$H_2$$CH_3$), 29.7 ($CH_2$*C*$H_3$), 29.5 ($CH_2$*C*$H_3$), 28.9 (*C*$H_3$), 26.1 (*C*$H_3$), 25.2 (*C*$H_2$), 24.5 (CH(*C*$H_3$)$_2$), 11.5 (CH(*C*$H_3$)$_2$), 11.0 ppm (CH(*C*$H_3$)$_2$); ^{11}B{^{1}H} NMR (193 MHz, THF-d$_8$, 298 K) δ = 3.01 ppm; ^{31}P{^{1}H} NMR (243 MHz, THF-d$_8$, 298 K) δ = 39.77 ppm. Anal. Calcd for $C_{56}H_{68}AuBNOP$: C, 66.74; H, 6.25; N, 1.50%. Found: C, 66.38; H, 6.25; N, 1.66%.

*Synthesis of **4.10***

In a Schlenk tube, **4.5** (50.0 mg, 0.0966 mmol) was dissolved in THF (4 mL), and Et_3GeCl (0.0160 mL, 0.0966 mmol) was added. The reaction was heated to 70 °C for 24 hrs, and then the solvent was removed under reduced pressure. The product was extracted with Et_2O (4 mL) and KCl was removed via 0.45 μm PTFE syringe filter. The filtrate was concentrated under reduced pressure and pink single crystals were obtained at room temperature (25.4 mg, 41% yield). ^{1}H NMR (600 MHz, THF-d$_8$, 298 K) δ = 7.50 (d, 2H, Ar*H*), 7.32 (t, 1H, Ar*H*), 7.13 (d, 2H, Ar*H*), 7.04 (d, 2H,

Ar*H*), 6.86 (t, 2H, Ar*H*), 6.63 (t, 2H, Ar*H*), 3.09 (b-hept, 2H, C*H*$_2$CH$_3$), 2.69 (hept, 2H, C*H*$_2$CH$_3$), 2.27 (s, 2H, CH$_2$), 1.90 (hept, 2H, C*H*(CH$_3$)$_2$), 1.38 (s, 6H, C*H*$_3$), 1.16 (d, 12H, CH(C*H*$_3$)$_2$/CH$_2$C*H*$_3$), 0.79 (d, 6H, CH(C*H*$_3$)$_2$), 0.47 ppm (br-s, 15H, Ge(C*H*$_2$C*H*$_3$); ^{13}C{^{1}H} NMR (151 MHz, THF-d$_8$, 298K) δ = 147.6 (Ar*C*), 147.1 (Ar*C*), 137.5 (Ar*C*), 134.5 (Ar*C*), 130.5 (Ar*C*), 126.6 (Ar*C*), 124.5 (Ar*C*), 124.1 (Ar*C*), 118.9 (Ar*C*), 79.3 (N*C*), 62.8 (*C*$_q$), 45.6 (*C*H(CH$_3$)$_2$), 33.0 (*C*H$_2$CH$_3$), 30.8 (*C*H$_2$CH$_3$), 29.9 (CH$_2$*C*H$_3$), 26.7 (*C*H$_3$), 11.6 (CH(*C*H$_3$)$_2$) 10.5 (Ge*C*H$_2$CH$_3$), 10.1 ppm (GeCH$_2$*C*H$_3$); ^{11}B{^{1}H} NMR (193 MHz, THF-d$_8$, 298 K) δ = -10.75 ppm. Anal. Calcd for C$_{40}$H$_{58}$BGeN: C, 75.50; H, 9.19; N, 2.20%. Found: C, 75.75; H, 9.24; N, 2.24%.

*Synthesis of **4.11***

In a 50 mL Schlenk flask, **4.5** (80.0 mg, 0.155 mmol) was dissolved in THF (10 mL), and then PhSeCl (29.6 mg, 0.155 mmol) was added. The deep red solution immediately turned yellow in color. The reaction was stirred at room temperature for 1 hr. The solvent was removed under reduced pressure and the product was extracted with Et$_2$O (25 mL). KCl and other insoluble solids were removed via 0.45 μm PTFE syringe filter. The yellow filtrate was concentrated under reduced pressure and colorless single crystals were obtained at room temperature (42.8 mg, 44% yield). ^{1}H NMR (600 MHz, THF-d$_8$, 298 K) δ = 7.60 (d, 1H, Ar*H*), 7.54 (d, 1H, Ar*H*), 7.58 (m, 2H, Ar*H*), 7.40 (m, 2H, Ar*H*), 7.34 (d, 1H, Ar*H*), 7.19 (m, 1H, Ar*H*), 7.09 (t, 1H, Ar*H*), 7.02 (d, 1H, Ar*H*), 6.98 (t, 1H, Ar*H*), 6.93 (t, 1H, Ar*H*), 6.85 (t, 1H, Ar*H*), 6.52 (t, 1H, Ar*H*), 6.22 (t, 1H, Ar*H*), 5.98 (t, 1H, Ar*H*), 3.28 (hept, 1H, C*H*(CH$_3$)$_2$), 3.16 (hept, 1H, C*H*(CH$_3$)$_2$), 2.07 (s, 1H, C*H*$_2$), 2.05 (d, 3H, CH(C*H*$_3$)$_2$), 2.01 (s, 1H, C*H*$_2$), 1.65 (d, 3H, CH(C*H*$_3$)$_2$), 1.47 (m, 10H, CH(C*H*$_3$)$_2$/C*H*$_3$/ C*H*$_2$CH$_3$), 1.39 (m, 1H, C*H*$_2$CH$_3$), 1.35 (s, 3H, C*H*$_3$), 1.27 (m, 1H, C*H*$_2$CH$_3$), 1.19 (m, 1H, C*H*$_2$CH$_3$), 0.63 ppm (m, 6H, CH$_2$C*H*$_3$); ^{13}C{^{1}H} NMR (151 MHz, THF-d$_8$, 298K) δ = 149.3 (Ar*C*),

149.0 (Ar*C*), 147.5 (Ar*C*), 145.7 (Ar*C*), 137.8 (Ar*C*), 133.3 (Ar*C*), 132.9 (Ar*C*), 131.3 (Ar*C*), 130.0 (Ar*C*), 127.1 (Ar*C*), 126.6 (Ar*C*), 126.5 (Ar*C*), 126.3 (Ar*C*), 125.7 (Ar*C*), 125.7 (Ar*C*), 124.6 (Ar*C*), 120.1 (Ar*C*), 119.5 (Ar*C*), 81.4 (Ar*C*), 80.9 (Ar*C*), 66.5 (Ar*C*), 64.2 (Ar*C*), 63.4 (N*C*), 42.2 (C_q), 41.4 ($CH(CH_3)_2$), 34.8 ($CH(CH_3)_2$), 34.4 (CH_2CH_3), 30.6 (CH_2CH_3), 30.5 (CH_2CH_3), 29.9 (CH_2CH_3), 29.6 (CH_2), 28.9 (CH_3), 28.4 (CH_3), 26.5 ($CH(CH_3)_2$), 15.9 ($CH(CH_3)_2$), 11.6 ($CH(CH_3)_2$), 11.6 ppm ($CH(CH_3)_2$); $^{11}B\{^1H\}$ NMR (193 MHz, THF-d_8, 298 K) δ = -5.40 ppm. Anal. Calcd for $C_{40}H_{48}NBSe$: C, 75.95; H, 7.65; N, 2.21%. Found: C, 75.97; H, 8.09; N, 2.29%.

*Synthesis of **4.12***

To a solution of compound **4.8** (50.0 mg, 0.0845 mmol) in THF (4 mL), PPh_3AuCl was then added. The deep purple solution immediately turned green in color. The reaction was then mixed at room temperature for 2 hrs. The insoluble solids were then removed through a 45 μm PTFE syringe filter. The solvent was removed from the filtrate to yield an inseparable mixture of **4.12** and other unidentifiable products. Single crystals of **4.12** were obtained from a concentrated Et_2O solution at -37 °C. ^1H NMR (600 MHz, THF-d_8, 298 K) δ = 7.37 (m, 4H, Ar*H*), 7.32 (m, 9H, Ar*H*), 7.27 (m, 6H, Ar*H*), 7.12 (d, 4H, Ar*H*), 6.98 (s, 2H, Ar*H*), 6.60 (t, 2H, Ar*H*), 6.22 (t, 2H, Ar*H*), 6.04 (d, 2H, Ar*H*), 3.04 (hept, 4H, $CH(CH_3)_2$), 1.02 (d, 12H, $CH(CH_3)_2$), 0.66 ppm (d, 12H, $CH(CH_3)_2$); $^{13}C\{^1H\}$ NMR (151 MHz, THF-d_8, 298K) δ = 174.9 (Ar*C*), 135.6 (Ar*C*), 134.8 (Ar*C*), 131.0 (Ar*C*), 130.3 (Ar*C*), 129.4 (Ar*C*), 125.0 (Ar*C*), 124.1 (Ar*C*), 121.8 (Ar*C*), 117.9 (Ar*C*), 30.1 ($CH(CH_3)_2$), 25.5 ($CH(CH_3)_2$), 22.9 ppm ($CH(CH_3)_2$); $^{11}B\{^1H\}$ NMR (193 MHz, THF-d_8, 298 K) δ = -3.42 ppm; ^{31}P NMR (243 MHz, THF-d_8, 298 K) δ = 45.64 ppm.

*Synthesis of **4.13***

To a solution of compound **4.5** (80.0 mg, 0.155 mmol) in THF (4 mL), benzil (32.5 mg, 0.155 mmol) was added. The deep red solution immediately turned yellow-green in color, and was stirred at room temperature for 1.5 hrs. The solvent was removed under reduced pressure, and the crude yellow solid was precipitated out of a concentrated toluene/hexanes mixture (2 mL toluene: couple drops of hexanes) at room temperature. Yellow block-shaped single crystals were grown from a toluene/THF (1:1) mixture at room temperature (50.3 mg, 58% yield). Compound **4.13** can also be obtained following the same procedure, but starting from compound **4.8** the yield is 44%. ^{1}H NMR (600 MHz, THF-d_8, 298 K) δ = 7.55 (dt, 4H, Ar*H*), 7.51 (d, 2H, Ar*H*), 7.46 (d, 2H, Ar*H*), 7.11 (t, 4H, Ar*H*), 7.04 (td, 2H, Ar*H*), 6.97 ppm (m, 4H, Ar*H*); ^{13}C{^{1}H} NMR (151 MHz, THF-d_8, 298K) δ = 149.7, 139.4, 138.2, 131.3, 128.4 (Ar*C*), 127.3 (Ar*C*), 127.1 (Ar*C*), 25.6 (Ar*C*), 119.0 (Ar*C*), 68.4 (O*C*H$_2$CH$_2$), 26.6 ppm (OCH$_2$*C*H$_2$); ^{11}B{^{1}H} NMR (193 MHz, THF-d_8, 298 K) δ = 13.71 ppm. Anal. Calcd for $C_{34}H_{34}BKO_4$: C, 73.38; H, 6.16%. Found: C, 73.63; H, 6.04%.

*Synthesis of **4.14***

To a solution of **4.5** (100 mg, 0.193 mmol) in THF (10 mL), 9,10-phenanthrenequionone (40.2 mg, 0.193 mmol) was then added. The deep red solution immediately lost its darkness and turned red in color. The reaction was stirred at room temperature for 5.5 hrs. The solvent was removed under reduced pressure, and the crude solid was washed with Et_2O (10 mL), redissolved in THF (2 mL), and precipitated out with hexanes (5 mL). The pure yellow solid was collected via filtration (58.8 mg, 55% yield). Yellow needle-shaped single crystals were grown from a toluene/THF (1:1) mixture at -37 °C. ^{1}H NMR (600 MHz, THF-d_8, 298 K) δ = 8.66 (d, 2H, Ar*H*), 7.91 (d, 2H, Ar*H*),

7.54 (d, 2H, Ar*H*), 7.33 (m, 6H, Ar*H*), 7.09 (t, 2H, Ar*H*), 6.94 ppm (t, 2H, Ar*H*); $^{13}C\{^{1}H\}$ NMR (151 MHz, THF-d_8, 298K) δ = 185.9 (Ar*C*), 149.7 (Ar*C*), 145.3 (Ar*C*), 131.2 (Ar*C*), 127.8 (Ar*C*), 127.3 (Ar*C*), 126.1 (Ar*C*), 126.0 (Ar*C*), 125.7 (Ar*C*), 123.8 (Ar*C*), 121.8 (Ar*C*), 121.0 (Ar*C*), 119.3 (Ar*C*), 68.4 (O*C*H_2*C*H_2), 26.5 ppm (OCH_2*C*H_2); ^{11}B NMR (193 MHz, THF-d_8, 298 K) δ = 16.27 ppm. Anal. Calcd for $C_{26}H_{16}BKO_2$•1/2(THF): C, 74.02; H, 4.44%. Found: C, 74.21; H, 4.06%.

Chapter Five

*Synthesis of **5.2-5.6***

In a vial, compound **4.5** (92.0 mg, 0.178 mmol) was dissolved in THF (4 mL) and Se powder (28.1 mg, 0.355 mmol) was then added. The deep red solution immediately turned orange in color and was stirred at room temperature for 2.5 hrs. The insoluble solids were then removed via filtration through a 0.45 μm PTFE syringe filter. The solvent was removed under reduced pressure and a crude solid containing a mixture of **5.2-5.6** was isolated. Numerous recrystallizations from a THF solution with a couple drops of hexanes yielded differing ratios of **5.2-5.4** which were fully characterized via multinuclear NMR. Compounds **5.5** and **5.6** were identified by X-ray crystallography.

Compound 5.2: ^{1}H NMR (600 MHz, THF-d_8, 298 K) δ = 7.58 (d, *J* = 7.4 Hz, 4H, Ar*H*), 7.51 (d, *J* = 6.7 Hz, 4H, Ar*H*), 7.02 (td, *J* = 7.3 Hz, 4H, Ar*H*), 6.91 (td, *J* = 7.1 Hz, 4H, Ar*H*), 3.62 (m, 8H, OC*H*$_2$CH$_2$), 1.77 (m, 8H, OCH$_2$C*H*$_2$), 1.25 (s, 4H, C*H*$_2$), 1.18 (s, 12H, (C*H*$_3$)$_2$), 0.86 (dq, *J* = 14.7, 7.3 Hz, 4H, C*H*$_2$CH$_3$), 0.69 (dq, 14.6, 7.3 Hz, 4H, C*H*$_2$CH$_3$), 0.46 (t, 7.4 Hz, 12H, CH$_2$C*H*$_3$) ppm; ^{13}C{^{1}H} NMR (151 MHz, THF-d_8, 298 K) δ = 186.1, 147.8, 131.6, 125.4, 125.3, 119.8, 72.1, 68.4, 45.1, 31.9, 31.9, 26.6, 11.0 ppm; ^{11}B{^{1}H} NMR (193 MHz, THF-d_8, 298 K) No resonance was observed; ^{77}Se{^{1}H} NMR (114 MHz, THF-d_8, 298 K) No resonance was observed. Anal. Calcd for $C_{60}H_{84}B_2K_2N_2O_4Se$: C, 63.05; H, 6.35; N, 2.45%. Found: C, 62.83; H, 6.56; N, 2.48%.

Compound 5.3: ^{1}H NMR (600 MHz, THF-d_8, 298 K) δ = 7.35 (d, *J* = 7.3 Hz, 4H, Ar*H*), 7.31 (d, *J* = 7.1 Hz, 4H, Ar*H*), 6.83 (td, 7.3, 1.3 Hz, 4H, Ar*H*), 6.76 (td, 7.2, 1.1 Hz, 4H, Ar*H*), 6.69 (t, 7.5 Hz, 2H, Ar*H*), 6.58 (d, *J* = 7.6 Hz, 4H, Ar*H*), 3.74 (hept, *J* = 6.8 Hz, 4H, C*H*(CH$_3$)$_2$), 3.62 (m, 4H, OC*H*$_2$CH$_2$), 1.77 (m, 4H, OCH$_2$C*H*$_2$), 1.33 (s, 4H, C*H*$_2$), 1.30 (s, 12H, (C*H*$_3$)$_2$), 1.14 (m, 4H,

C*H*$_2$CH$_3$), 0.91 (m, 4H, C*H*$_2$CH$_3$), 0.81 (d, *J* = 6.8 Hz, 24H, CH(C*H*$_3$)$_2$), 0.57 ppm (t, *J* = 7.4 Hz, 12H, CH$_2$C*H*$_3$); ^{13}C{^{1}H} NMR (151 MHz, THF-d$_8$, 298 K) δ = 184.1, 154.1, 149.3, 136.4, 132.3, 125.9, 125.3, 125.0, 121.8, 119.1, 72.3, 68.4, 44.9, 34.5, 32.1, 31.5, 26.6, 24.7, 24.4, 10.8 ppm; ^{11}B{^{1}H} NMR (193 MHz, THF-d$_8$, 298 K) No resonance was observed; ^{77}Se{^{1}H} NMR (114 MHz, THF-d$_8$, 298 K) δ = 0.18 ppm. Elemental analysis could not be obtained due to the difficulty in separating 3 from the mixture of crystals (Figure S13).

Compound 5.4: ^{1}H NMR (600 MHz, THF-d$_8$, 298 K) δ = 7.61 (m, 4H, Ar*H*), 7.39 (t, *J* = 7.7 Hz, 1H, Ar*H*), 7.27 (d, *J* = 7.7 Hz, 2H, Ar*H*), 7.10 (td, *J* = 7.4, 1.2 Hz, 2H, Ar*H*), 7.02 (td, *J* = 7.3, 1.2 Hz, 2H, Ar*H*), 6.88 (t, *J* = 7.6 Hz, 1H, Ar*H*), 6.70 (d, *J* = 7.6 Hz, 2H, Ar*H*), 3.17 (m, 4H, C*H*(CH$_3$)$_2$), 2.05 (s, 2H, C*H*$_2$), 1.86 (d, *J* = 7.6 Hz, 6H, CH(C*H*$_3$)$_2$), 1.41 (m, 12H, CH(C*H*$_3$)$_2$/(C*H*$_3$)$_2$), 1.20 (m, 4H, C*H*$_2$CH$_3$), 0.78 (d, *J* = 6.8 Hz, 12H, CH(C*H*$_3$)$_2$), 0.65 ppm (t, *J* = 7.5 Hz, 6H, CH$_2$C*H*$_3$); ^{13}C{^{1}H} NMR (151 MHz, THF-d$_8$, 298 K) δ = 185.9, 154.9, 149.9, 147.8, 133.5, 131.5, 128.6, 126.6, 126.1, 122.9, 119.6, 80.8, 64.2, 42.2, 34.7, 34.5, 30.6, 29.9, 29.3, 26.3, 25.1, 11.6 ppm; ^{11}B{^{1}H} NMR (193 MHz, THF-d$_8$, 298 K) δ = -7.86 ppm; ^{77}Se{^{1}H} NMR (114 MHz, THF-d$_8$, 298 K) δ = 299.0, 143.7 ppm. Elemental analysis could not be obtained due to the difficulty in separating **5.3** from the mixture of crystals (Figure A2.77).

*Direct Synthesis of **5.5***

In a vial, **4.5** (50 mg, 0.0966 mmol) was dissolved in THF (5 mL), and Se$_2$Cl$_2$ (0.1 M in THF, 0.483 mL, 0.0483 mmol) was slowly added dropwise. The brick red mixture was stirred at room temperature for 4 hrs. The insoluble red solids were removed via a 0.45 μm PTFE syringe filter and the solvent was removed from the yellow filtrate to leave compound **5.5** (42.5 mg, 79% yield).

^{1}H NMR (600 MHz, THF-d_8, 298 K) δ = 7.55 (d, *J* = 7.5 Hz, 4H, Ar*H*), 7.47 (d, *J* = 7.2 Hz, 4H, Ar*H*), 7.41 (t, *J* = 8.4 Hz, 2H, Ar*H*), 7.35 (d, *J* = 8.0 Hz, 4H, Ar*H*), 7.09 (td, *J* = 7.4, 1.0 Hz, 4H, Ar*H*), 6.98 (td, *J* = 7.3, 1.0 Hz, 4H, Ar*H*), 3.17 (hept, *J* = 6.5 Hz, 4H, C*H*(CH_3)$_2$), 2.02 (s, 4H, C*H*$_2$), 1.65 (d, *J* = 6.6 Hz, 12H, CH(C*H*$_3$)$_2$), 1.47 (d, *J* = 6.5 Hz, 12H, CH(C*H*$_3$)$_2$), 1.36 (m, 16H, C*H*$_2$CH$_3$/(C*H*$_3$)$_2$), 1.19 (m, 4H, C*H*$_2$CH$_3$), 0.63 ppm (t, *J* = 7.5 Hz, 12H, CH$_2$C*H*$_3$); ^{13}C{^{1}H} NMR (151 MHz, THF-d_8, 298 K) δ = 185.6, 169.8, 149.3, 145.7, 135.6, 132.9, 130.0, 127.1, 126.5, 125.7, 120.1, 81.4, 41.4, 34.4, 30.5, 29.6, 28.4, 11.6 ppm; ^{11}B{^{1}H} NMR (193 MHz, THF-d_8, 298 K) δ = -2.84 ppm; ^{77}Se{^{1}H} NMR (114 MHz, THF-d_8, 298 K) No resonance was observed. Anal. Calcd for $C_{69}H_{90}B_2N_2Se_2$: C, 73.53; H, 8.05; N, 2.49%. Found: C, 73.45; H, 7.75; N, 2.48%.

*Synthesis of **5.5** from CAAC-BF•*

In a vial, CAAC-BF• (50.0 mg, 0.105 mmol) was dissolved in THF (4 mL), and Se_2Cl_2 (4.32 μL, 0.0522 mmol) was then added. The deep purple solution immediately turned orange in color and was stirred at room temperature for 4 hrs. The insoluble solids were removed via a 0.45 μm PTFE syringe filter and the solvent was removed from the orange filtrate. A ^{1}H NMR spectrum showed full conversion to **5.5** (44.3 mg, 76% yield).

*Synthesis of **5.7** and **5.8***

In a vial, compound **4.5** (100 mg, 0.193 mmol) was suspended in toluene (8 mL), and 18-crown-6 (51.0 mg, 0.193 mmol) was added. Upon addition, compound **4.5** fully dissolved in toluene and after 5 mins of stirring, grey Se powder (15.3 mg, 0.193 mmol) was then added. The reaction was stirred at room temperature for 20 hrs. The solvent was concentrated to ~1 mL and stored at -37 °C to yield two sizes of colorless block shaped crystals. The large colorless blocks are the major

product, compound **5.7** (70.2 mg, 42% yield) and the smaller crystals are the minor product, compound **5.8**. Compound **5.7** can be purified by washing the mixture of crystals with small amounts of toluene. Only a few crystals of **5.8** could be isolated for NMR characterization.

Compound 5.7: ^{1}H NMR (600 MHz, C_6D_6, 298 K) δ = 7.88 (d, *J* = 7.4 Hz, 2H, Ar*H*), 7.83 (d, *J* = 7.1 Hz, 2H, Ar*H*), 7.29 (td, *J* = 7.3, 1.3 Hz, 2H, Ar*H*), 7.16 (m, 2H, Ar*H*), 7.05 (m, 3H, Ar*H*), 4.22 (hept, „*J* = 6.8 Hz, 2H, C*H*$(CH_3)_2$), 3.17 (s, 24H, 18-c-6–C*H*$_2$), 1.67 (m, 2H, C*H*$_2$CH$_3$) 1.55 (s, 2H, C*H*$_2$), 1.47 (s, 6H, (C*H*$_3$)$_2$), 1.35 (m, 2H, C*H*$_2$CH$_3$), 1.24 (d, *J* = 6.8 Hz, 12H, CH(C*H*$_3$)$_2$), 0.91 ppm (t, *J* = 7.4 Hz, 6H, CH$_2$C*H*$_3$); ^{13}C{^{1}H} NMR (151 MHz, C_6D_6, 298 K) δ = 153.8, 149.5, 137.7, 132.6, 125.6, 124.7, 121.8, 119.0, 71.8, 69.5, 67.7, 44.7, 34.3, 31.8, 31.2, 25.1, 10.8 ppm; ^{11}B{^{1}H} NMR (193 MHz, C_6D_6, 298 K) No resonance was observed; ^{77}Se NMR (114 MHz, C_6D_6, 298 K) δ = 16.5 ppm. Anal. Calcd for $C_{46}H_{67}BKNO_6Se$: C, 64.33; H, 7.86; N, 1.63%. Found: C, 64.29; H, 7.86; N, 1.69%.

Compound 5.8: ^{1}H NMR (600 MHz, THF-d_8, 298 K) δ = 6.63 (d, *J* = 7.4 Hz, 2H, Ar*H*), 6.52 (t, *J* = 7.4 Hz, 1H, Ar*H*), 4.64 (hept, *J* = 6.9 Hz, 2H, C*H*$(CH_3)_2$), 3.58 (s, 24H, 18-c-6–C*H*$_2$), 1.14 ppm (d, *J* = 6.9 Hz, 12H, CH(C*H*$_3$)$_2$; ^{13}C{^{1}H} NMR (151 MHz, THF-d_8, 298 K) δ = 183.9, 151.8, 120.4, 118.8, 71.2, 35.1, 24.4 ppm; ^{77}Se NMR (114 MHz, THF-d_8, 298 K) δ = 17.4 ppm. Elemental analysis was not obtained for **5.8** due to the small amount produced, therefore we relied on NMR studies for purity.

Chapter Six

*Synthesis of **6.2***

In a vial, **4.5** (25.0 mg, 0.0483 mmol) and 18-crown-6 (12.8 mg, 0.0483 mmol) were dissolved in toluene (5 mL). The solution was then filtered through a 0.45 μm PTFE syringe filter to remove any residual solids. Dark red rod-shaped crystals were obtained and further dried under vacuum (13.3 mg, 35% yield). ^{1}H NMR (600 MHz, THF-d_8, 298 K) δ = 7.90 (d, *J* = 7.4 Hz, 1H, Ar*H*), 7.49 (d, *J* = 8.4 Hz, 1H, Ar*H*), 7.36 (d, *J* = 7.5 Hz, 1H, Ar*H*), 7.22 (t, *J* = 7.7 Hz, 1H, Ar*H*), 7.10 (d, *J* = 7.7 Hz, 2H, Ar*H*), 6.69 (t, *J* = 7.4 Hz, 1H, Ar*H*), 6.50 (t, *J* = 7.0 Hz, 2H, Ar*H*), 6.29 (t, *J* = 7.0 Hz, 1H, Ar*H*), 6.00 (t, *J* = 8.0 Hz, 1H, Ar*H*), 4.75 (d, *J* = 8.4 Hz, 1H, Ar*H*), 3.68 (hept, *J* = 7.0 Hz, 2H, C*H*$(CH_3)_2$), 3.24 (s, 24H, 18-c-6), 2.52 (m, 2H, C*H*$_2$$CH_3$), 2.38 (m, 2H, C*H*$_2$$CH_3$), 2.01 (s, 2H, C*H*$_2$) 1.17 (m, 12H, CH(C*H*$_3$)$_2$/(C*H*$_3$)$_2$), 1.08 (t, *J* = 7.3 Hz, 6H, CH_2C*H*$_3$), 0.81 ppm (d, *J* = 6.6 Hz, 6H, CH(C*H*$_3$)$_2$); ^{13}C{^{1}H} NMR (151 MHz, THF-d_8, 298K) δ = 153.9, 144.2, 133.2, 126.8, 124.7, 121.7, 121.0, 117.6, 117.0, 116.6, 116.3, 71.1, 53.06, 51.00, 32.0, 31.7, 29.7, 27.2, 11.0 ppm; ^{11}B{^{1}H} NMR (193 MHz, THF-d_8, 298 K) δ = 14.2 ppm. Anal. Calcd for $C_{53}H_{75}BKNO_6$: C, 72.99; H, 8.67; N, 1.61%. Found: C, 72.88; H, 8.66; N, 1.70%.

*Synthesis of **6.3***

In a vial, **4.5** (25.0 mg, 0.0483 mmol) and 2.2.2 cryptand (18.2 mg, 0.0483 mmol) were dissolved in toluene (5 mL). The solution was then filtered through a 0.45 μm PTFE syringe filter to remove any residual solids. The deep red solution was concentrated to ~2 mL under reduced pressure, and stored at room temperature for recrystallization. Dark red block shaped crystals were obtained and further dried under vacuum (34.3 mg, 79% yield). ^{1}H NMR (600 MHz, THF-d_8, 298 K) δ = 7.90

(d, *J* = 7.9 Hz, 1H, Ar*H*), 7.51 (d, *J* = 8.3 Hz, 1H, Ar*H*), 7.37 (d, *J* = 8.5 Hz, 1H, Ar*H*), 6.68 (t, *J* = 7.9 Hz, 1H, Ar*H*), 6.51 (t, *J* = 7.0 Hz, 1H, Ar*H*), 6.30 (t, *J* = 7.0 Hz, 1H, Ar*H*), 6.00 (t, *J* = 8.0 Hz, 1H, Ar*H*), 4.75 (d, *J* = 7.9 Hz, 1H, Ar*H*), 3.69 (hept, *J* = 6.7 Hz, 2H, C*H*$(CH_3)_2$), 3.23 (m, 24H, crypt), 2.53 (m, 2H, C*H*$_2$CH$_3$), 2.39 (m, 2H, C*H*$_2$CH$_3$), 2.23 (br s, 12H, crypt), 2.02 (s, 2H, C*H*$_2$), 1.18 (m, 12H, CH(C*H*$_3$)$_2$/(C*H*$_3$)$_2$), 1.09 (t, *J* = 7.3 Hz, 6H, CH$_2$C*H*$_3$), 0.83 ppm (d, *J* = 6.6 Hz, 6H, CH(C*H*$_3$)$_2$); $^{13}C\{^1H\}$ NMR (151 MHz, THF-d$_8$, 298K) δ = 154.0, 138.6, 134.1, 133.2, 129.8, 129.1, 126.8, 126.2, 124.7, 121.7, 121.2, 121.1, 117.7, 117.0, 116.6, 116.4, 71.3, 68.5, 65.6, 54.7, 53.0, 51.0, 32.0, 31.7, 29.7, 27.3, 11.0 ppm; $^{11}B\{^1H\}$ NMR (193 MHz, THF-d$_8$, 298 K) δ = 14.2 ppm. Anal. Calcd for $C_{52}H_{79}BKN_3O_6$: C, 70.01; H, 8.93; N, 4.71%. Found: C, 70.06; H, 9.20; N, 4.61%.

Synthesis of ***6.4***

In a vial, **4.5** (50.0 mg, 0.0966 mol) was dissolved in THF (4 mL), and 1,10-phenanthroline (34.8 mg, 0.193 mmol) was then added. The reaction was stirred at room temperature for 4 hrs. A few drops of hexanes were added to the solution and after storage at -37 °C red needle-shaped single crystals were obtained (55.0 mg, 56%). ^{1}H NMR (600 MHz, THF-*d*$_8$) δ 8.72 (d, *J* = 2.7 Hz, 4H, Ar*H*), 8.24 (br s, 4H, Ar*H*) 8.03 (d, *J* = 7.5 Hz, 1H), 7.78 (s, 4H, Ar*H*) 7.49 (m, 6H, Ar*H*), 7.28 (t, *J* = 7.7 Hz, 1H, Ar*H*), 7.13 (d, *J* = 8.0 Hz, 2H, Ar*H*), 6.79 (t, *J* = 8.0 Hz, 1H, Ar*H*), 6.55 (t, *J* = 7.2 Hz, 1H, Ar*H*), 6.41 (t, *J* = 7.7 Hz, 1H, Ar*H*), 6.16 (t, *J* = 7.9 Hz, 1H, Ar*H*), 4.84 (d, *J* = 7.8 Hz, 1H, Ar*H*), 3.62 (m, 8H, OC*H*$_2$CH$_2$), 2.51 (m, 2H, C*H*$_2$CH$_3$), 2.37 (m, 2H, C*H*$_2$CH$_3$), 2.01 (s, 2H, C*H*$_2$), 1.77 (m, 8H, OCH$_2$C*H*$_2$), 1.16 (m, 12H, CH(C*H*$_3$)$_2$/(C*H*$_3$)$_2$), 1.01 (t, *J* = 7.3 Hz, 6H, CH$_2$C*H*$_3$), 0.76 (d, *J* = 6.6 Hz, 6H, CH(C*H*$_3$)$_2$); $^{13}C\{^1H\}$ NMR (151 MHz, THF-d$_8$, 298K) δ = 185.8, 153.6, 150.96, 147.3, 137.1, 134.5, 133.3, 127.6, 127.3, 125.0, 122.4, 121.8, 118.3, 117.6,

117.3, 117.0, 111.2, 99.9, 50.5, 32.0, 31.6, 29.7, 27.0, 24.8, 10.8; $^{11}B\{^{1}H\}$ NMR (193 MHz, THF-d_8, 298 K) δ = 15.4 ppm. Anal. Calcd for $C_{66}H_{75}BKN_5O_2$: C, 77.70; H, 7.41; N, 6.86%. Found: C, 77.48; H, 7.70; N, 6.72%.

*Synthesis of **6.5***

In a vial, **4.5** (50.0 mg, 0.0966 mmol) and 2.2.2 cryptand (36.4 mg, 0.0966 mmol) were dissolved in THF (5 mL), and 9,10-phenanthrenequinone (20.1 mg, 0.0966 mmol) was then added. The deep red solution immediately turned orange in color and was stirred at room temperature for 2 hrs. During that time, yellow fluorescent crystals precipitated out of solution. The yellow crystals were collected via filtration, washed with hexanes (5 mL), and dried under reduced pressure (53.2 mg, 70% yield). Single crystals were grown from a concentrated THF solution and with a few drops of hexanes added. ^{1}H NMR (600 MHz, THF-d_8, 298 K) δ = 8.57 (d, *J* = 8.2 Hz, 2H, Ar*H*), 7.99 (dd, *J* = 8.1, 1.4 Hz, 2H, Ar*H*), 7.42 (d, *J* = 7.6 Hz, 2H, Ar*H*), 7.30 (m, 4H, Ar*H*), 7.16 (ddd, *J* = 8.2, 6.7, 1.3 Hz, 2H, Ar*H*), 6.96 (td, *J* = 7.4, 1.3 Hz, 2H, Ar*H*), 6.83 (td, *J* = 7.1, 0.9 Hz, 2H, Ar*H*), 3.45 (s, 12H, crypt), 3.38 (m, 12H, crypt), 2.38 (m, 12H, crypt). $^{13}C\{^{1}H\}$ NMR (151 MHz, THF-d_8, 298K) δ = 183.9, 131.5, 126.5, 126.4, 125.0, 123.4, 121.8, 120.6, 118.4, 118.2, 71.4, 68.6, 54.9 ppm. $^{11}B\{^{1}H\}$ NMR (193 MHz, THF-d_8, 298 K) δ = 16.2 ppm. Anal. Calcd for $C_{44}H_{52}BKN_2O_8$: C, 67.17; H, 6.66; N, 3.56%. Found: C, 66.95; H, 6.95; N, 3.26%.

*Synthesis of **6.6***

In a vial, **4.5** (50.0 mg, 0.0966 mmol) and 2.2.2 cryptand (36.4 mg, 0.0966 mmol) were dissolved in THF (4 mL). 1,10-phenanthroline-5,6-dione (20.3 mg, 0.0966 mmol) was then added. The deep

red solution quickly turned orange in color and was stirred at room temperature for 4 hrs. The insoluble solids were removed via filtration through a 0.45 μm PTFE syringe filter. A few drops of hexanes were added to the filtrate and orange single crystals were grown at room temperature after slow evaporation (38.4 mg, 50%). ^{1}H NMR (600 MHz, THF-d_8, 298 K) δ = 8.68 (dd, *J* = 4.1, 1.8 Hz, 2H, Ar*H*), 8.28 (dd, *J* = 8.1, 1.8 Hz, 2H, Ar*H*), 7.43 (d, *J* = 7.5 Hz, 2H, Ar*H*), 7.30 (m, 2H, Ar*H*), 6.99 (td, *J* = 7.4, 1.3 Hz, 2H, Ar*H*), 6.84 (td, *J* = 7.1, 1.0 Hz, 2H, Ar*H*), 3.45 (s, 12H, crypt), 3.39 (m, 12H, crypt), 2.39 ppm (m, 12H, crypt). ^{13}C NMR (151 MHz, THF-d_8, 298 K) δ = 149.9, 145.9, 144.2, 141.9, 131.3, 128.3, 126.8, 126.5, 121.3, 118.5, 71.4, 68.6, 54.9 ppm. ^{11}B{^{1}H} NMR (193 MHz, THF-d_8, 298 K) δ = 16.6 ppm. Anal Calcd for $C_{42}H_{50}BKN_4O_8$•1/2(hexanes): C, 64.89; H, 7.02; N, 6.73%. Found: C, 65.00; H, 6.74; N, 6.48%.

Chapter Seven

*Synthesis of **7.2***

In a Fisher-Porter reaction vessel, **4.5** (200 mg, 0.386 mmol) and 18-crown-6 (102 mg, 0.386 mmol) were dissolved in toluene (10 mL) and pressurized to 50 psi with CO_2 (dried over P_2O_5). The deep red solution immediately turned yellow in color. The solution was then filtered through a 0.45 μm PTFE syringe filter. Colorless crystals were grown from the toluene solution at -37 °C (238 mg, 71% yield). ^{1}H NMR (600 MHz, THF-d_8, 298 K) δ = 7.41 (d, *J* = 7.5 Hz, 1H, Ar*H*), 7.35 (d, *J* = 7.3 Hz, 1H, Ar*H*), 7.22 (d, *J* = 7.4 Hz, 1H, Ar*H*), 7.13 (t, *J* = 6.7 Hz, 2H, Ar*H*), 7.05 (m, 1H, Ar*H*), 6.97 (td, *J* = 7.4, 1.3 Hz, 1H, Ar*H*), 6.89 (m, 2H, Ar*H*), 6.77 (m, 2H, Ar*H*), 3.61 (m, 1H, C*H*(CH_3)$_2$), 3.36 (m, 1H, C*H*(CH_3)$_2$), 3.24 (s, 24H, 18-crown-7), 2.05 (dq, *J* = 13.6, 6.3 Hz, 2H, C*H*$_2$CH$_3$), 1.94 (s, 1H, C*H*$_2$), 1.88 (s, 1H, C*H*$_2$), 1.76 (m, 1H, C*H*$_2$CH$_3$), 1.67 (m, 1H, C*H*$_2$CH$_3$), 1.28 (dd, *J* = 6.7, 4.6 Hz, 6H, CH(C*H*$_3$)$_2$), 1.14 (s, 3H, (C*H*$_3$)$_2$), 1.09 (m, 9H, (C*H*$_3$)$_2$/CH(C*H*$_3$)$_2$), 0.83 (t, *J* = 7.3 Hz, 6H, CH$_2$C*H*$_3$); ^{13}C{^{1}H} NMR (151 MHz, THF-d_8, 298K) δ = 152.5, 151.1, 150.1, 140.5, 137.1, 131.2, 127.0, 126.6, 126.4, 123.9, 118.6, 116.6, 70.8, 63.3, 48.8, 47.9, 32.3, 31.0, 29.3, 26.6, 10.5 ppm; ^{11}B{^{1}H} NMR (193 MHz, THF-d_8, 298 K) δ = 8.0 ppm. Anal. Calcd for $C_{48}H_{67}BKNO_{10}$: C, 66.42; H, 7.78; N, 1.61%. Found: C, 66.21; H, 7.88; N, 1.60%.

*Synthesis of **7.3***

In a Schlenk tube, **7.2** (75.0 mg, 0.0864 mmol) was dissolved in toluene (8 mL) and heated to 70 °C for 18 hrs. After cooling to room temperature, the insoluble solids were filtered off through a 0.45 μm PTFE syringe filter. The filtrate was evaporated to dryness, and colorless crystals were grown from a 2:1 mixture of toluene/THF at room temperature (38.9 mg, 55% yield). ^{1}H NMR

(600 MHz, THF-d_8, 298 K) δ = 7.53 (d, *J* = 6.4 Hz, 1H, Ar*H*), 7.27 (d, *J* = 7.2 Hz, 1H, Ar*H*), 7.19 (m, 2H, Ar*H*), 7.14 (d, *J* = 7.4 Hz, 1H, Ar*H*), 7.01 (dd, *J* = 7.0, 2.5 Hz, 1H, Ar*H*), 6.90 (td, *J* = 7.3, 1.3 Hz, 1H, Ar*H*), 6.85 (td, *J* = 7.2, 1.2 Hz, 1H, Ar*H*), 6.70 (td, *J* = 7.3, 1.3 Hz, 1H), 6.34 (td, *J* = 7.2, 1.1 Hz, 1H, Ar*H*), 4.96 (d, *J* = 7.1 Hz, 1H, Ar*H*), 4.16 (sept, *J* = 6.7 Hz, 1H, C*H*(CH_3)$_2$), 3.89 (sept, *J* = 6.7 Hz, 1H, C*H*(CH_3)$_2$), 3.30 (s, 24H, 18-crown-6), 2.62 (m, 1H, C*H*$_2$$CH_3$), 2.29 (m, 2H, C*H*$_2$$CH_3$/C*H*$_2$), 1.97 (m, 1H, C*H*$_2$$CH_3$), 1.91 (d, *J* = 12.0 Hz, 1H, C*H*$_2$), 1.68 (m, 1H, C*H*$_2$$CH_3$), 1.32 (s, 3H, ($CH_3$)$_2$), 1.22 (d, *J* = 6.7 Hz, 3H, CH(CH_3)$_2$), 1.09 (m, 15H, CH(CH_3)$_2$/CH_2C*H*$_3$/(CH_3)$_2$), 0.73 (d, *J* = 6.5 Hz, 3H, CH(CH_3)$_2$); $^{13}C\{^1H\}$ NMR (151 MHz, THF-d_8, 298K) δ = 185.7, 182.8, 156.9, 154.9, 151.2, 149.1, 138.4, 132.2, 132.1, 127.1, 126.6, 126.2, 125.9, 125.7, 124.8, 118.3, 117.3, 105.1, 70.9, 60.7, 51.9, 49.4, 34.0, 31.1, 30.1, 29.6, 29.0, 29.0, 28.5, 26. 6, 117, 11.2; $^{11}B\{^1H\}$ NMR (193 MHz, THF-d_8, 298 K) δ = 11.8 ppm. Anal. Calcd for $C_{47}H_{67}BKNO_9$: C, 67.21; H, 8.04; N, 1.67%. Found: C, 67.21; H, 8.33; N, 1.70%.

Appendix II – Spectral Data

Chapter Two:

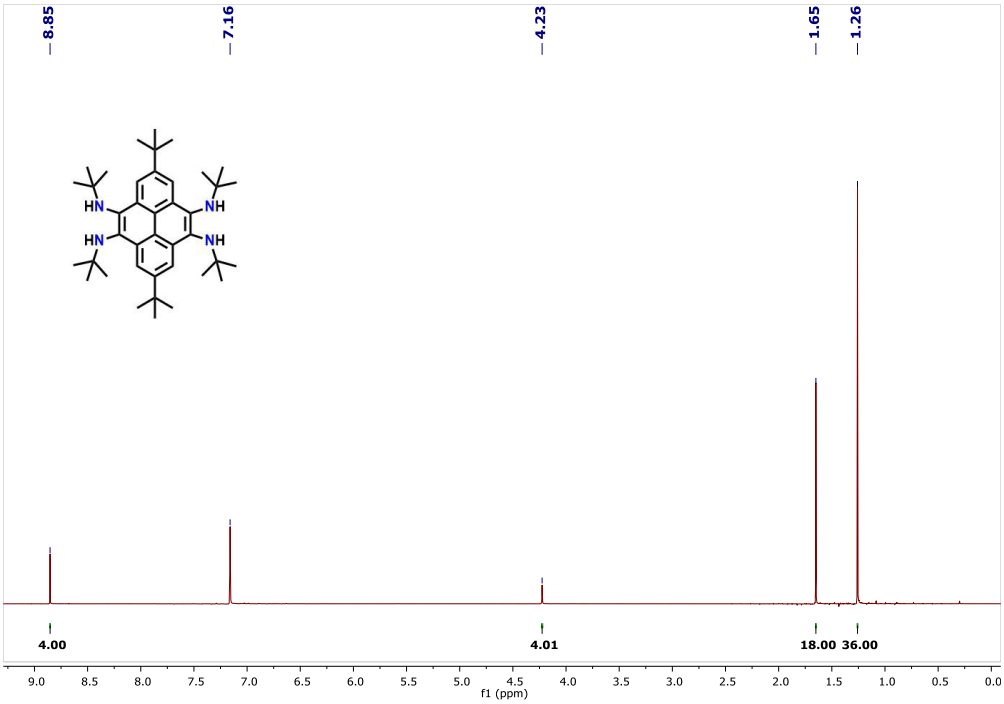

Figure A2.1. ^{1}H NMR spectrum (600 MHz, C_6D_6, 298 K) of **2.1**.

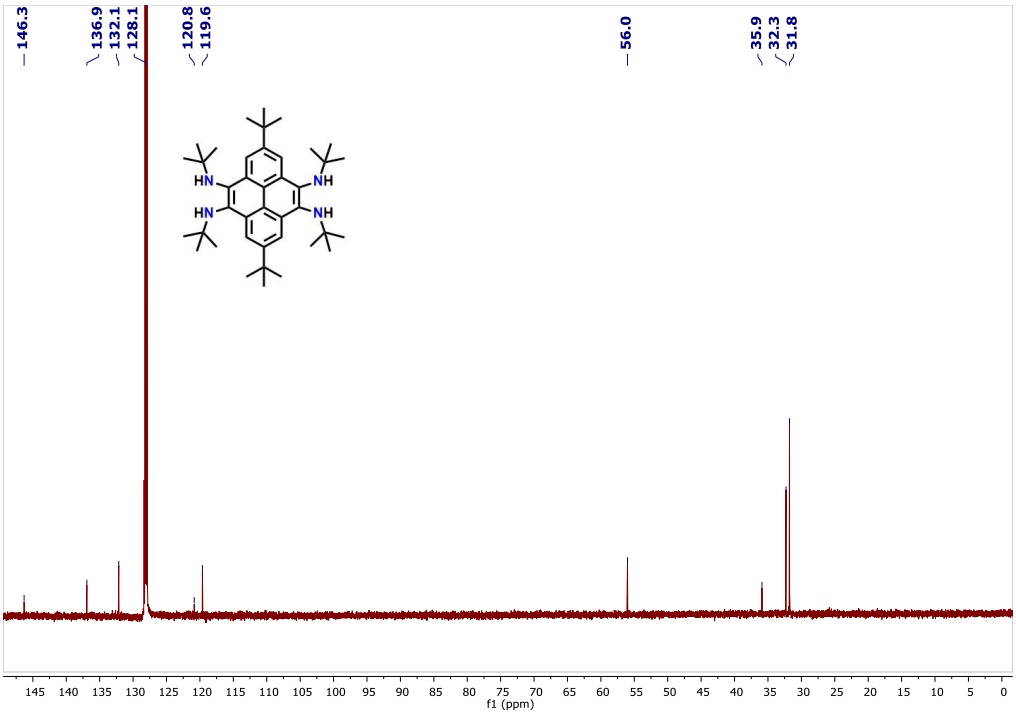

Figure A2.2. $^{13}C\{^{1}H\}$ NMR spectrum (151 MHz, C_6D_6, 298 K) of **2.1**.

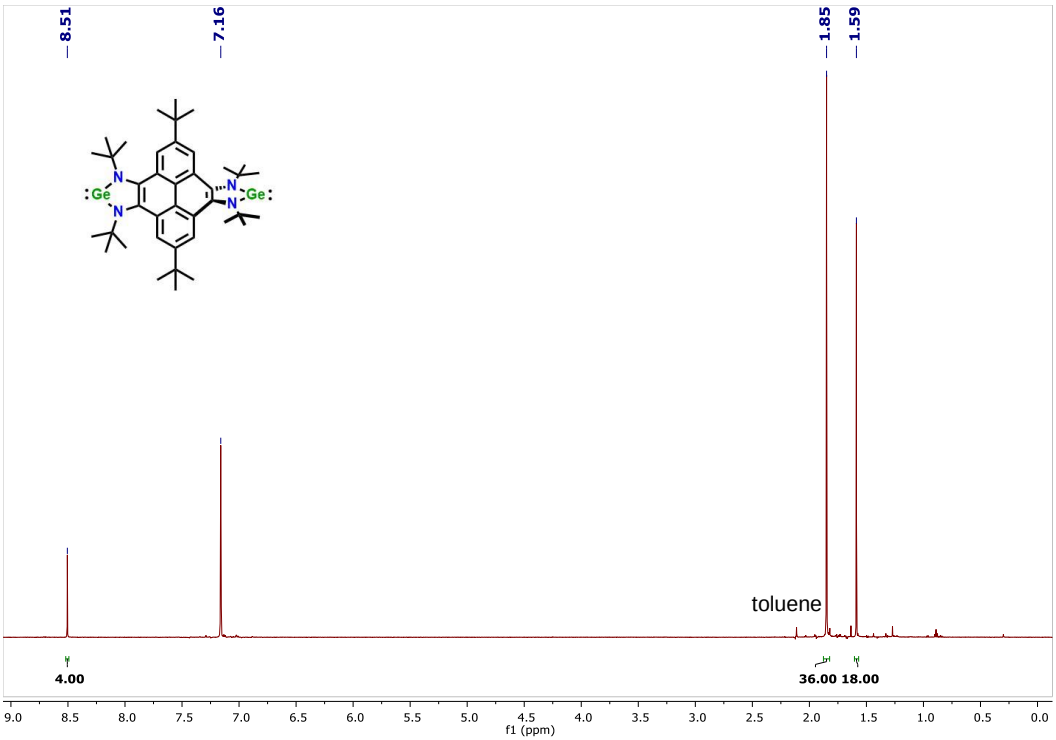

Figure A2.3. ^{1}H NMR spectrum (600 MHz, C_6D_6, 298 K) of **2.2**.

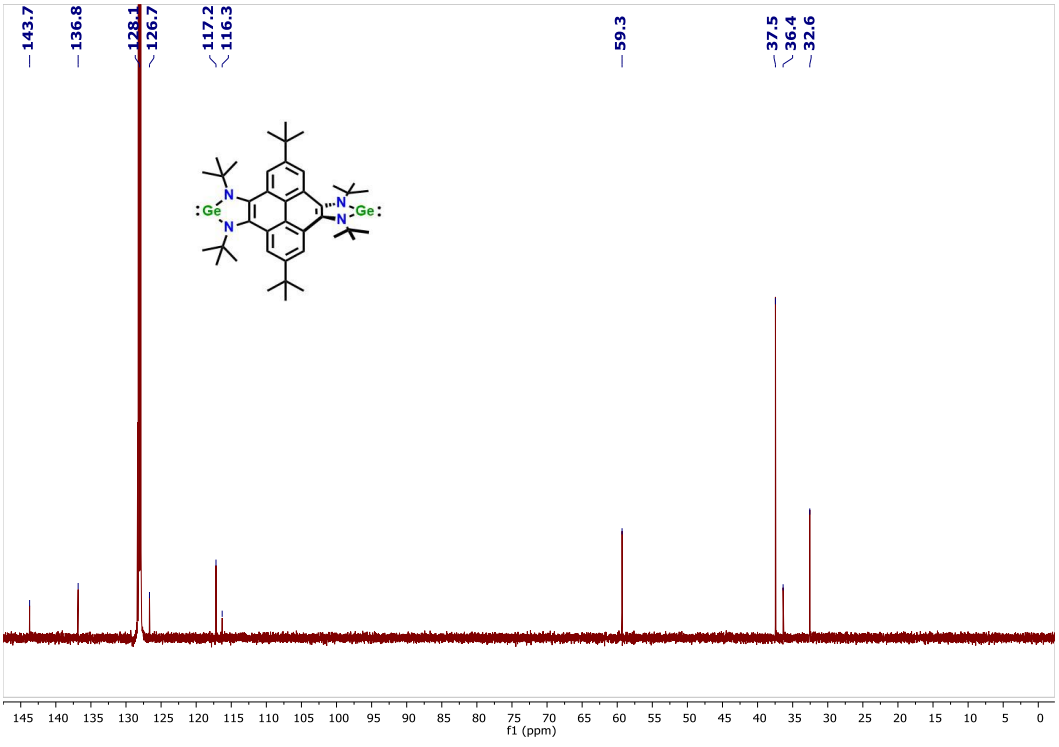

Figure A2.4. $^{13}C\{^{1}H\}$ NMR spectrum (151 MHz, C_6D_6, 298 K) of **2.2**.

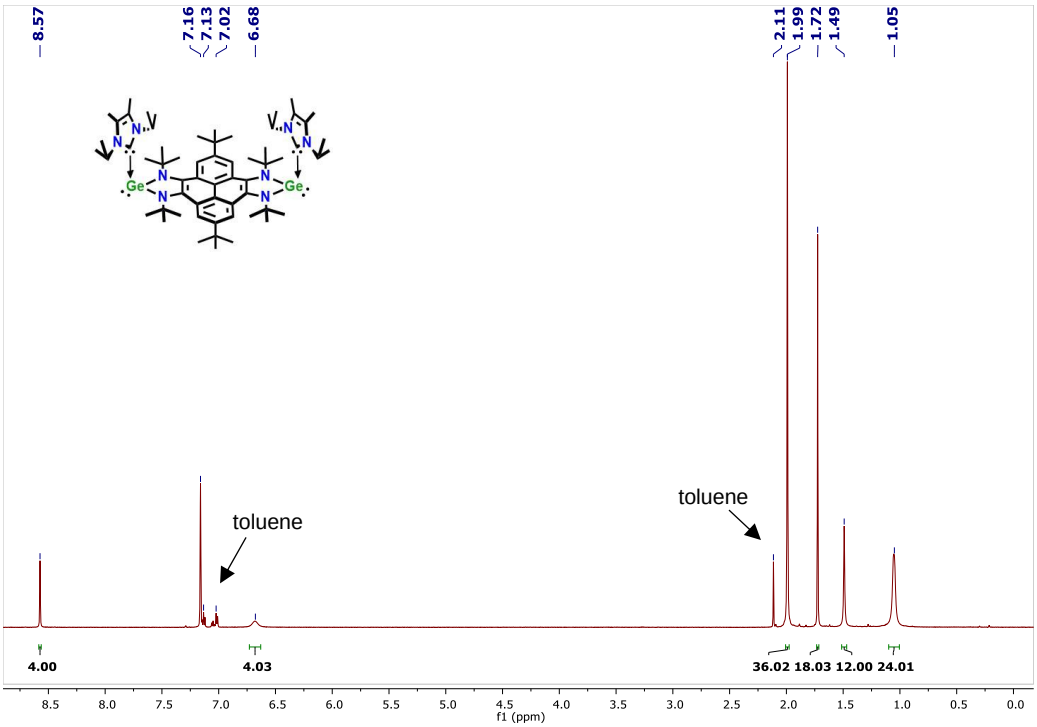

Figure S2.5. ^{1}H NMR spectrum (600 MHz, C_6D_6, 298 K) of **2.3**.

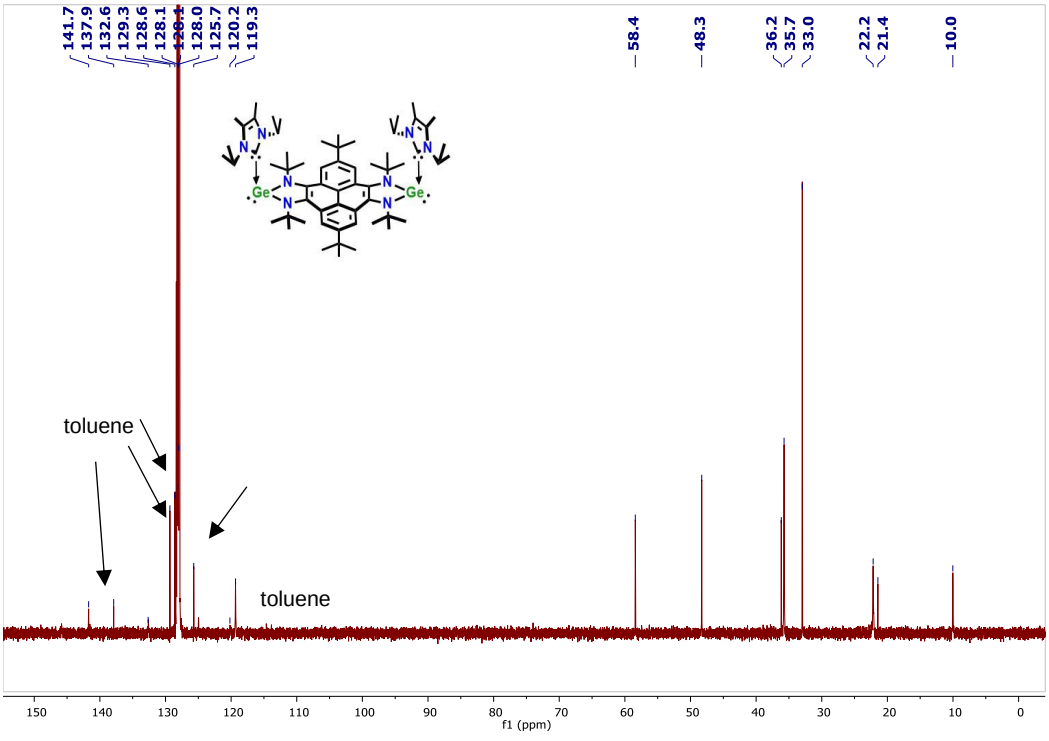

Figure A2.6. $^{13}C\{^{1}H\}$ NMR spectrum (151 MHz, C_6D_6, 298 K) of **2.3**.

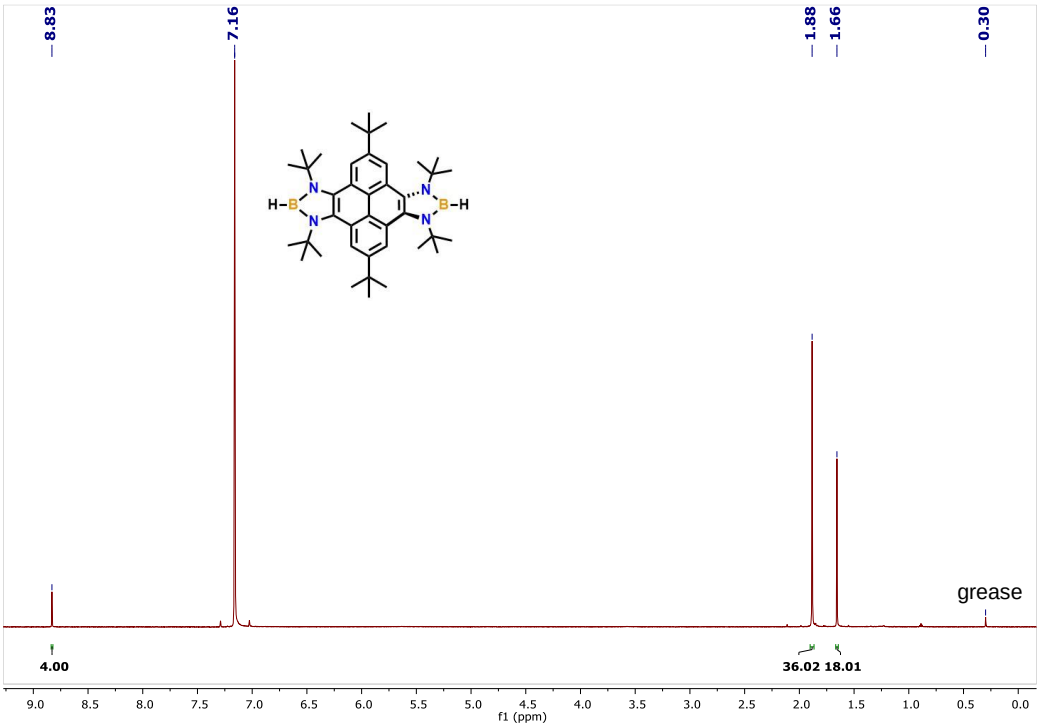

Figure A2.7. ^{1}H NMR spectrum (600 MHz, C_6D_6, 298 K) of **3.2**.

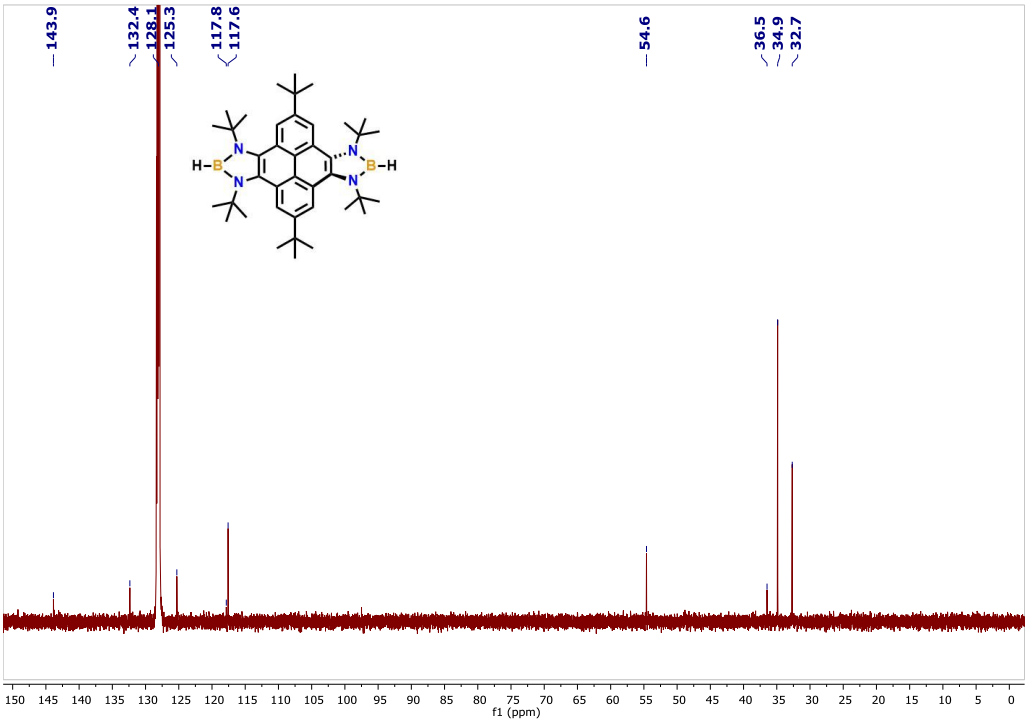

Figure A2.8. ^{13}C{^{1}H} NMR spectrum (151 MHz, C_6D_6, 298 K) of **3.2**.

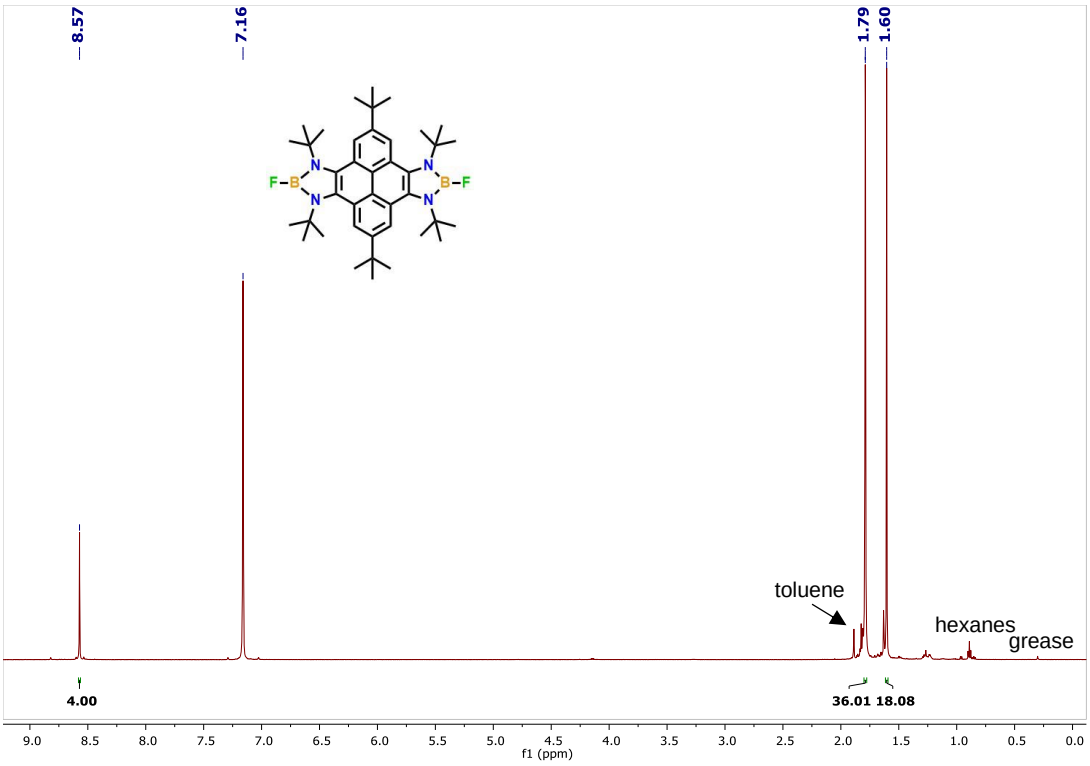

Figure A2.9. ^{1}H NMR spectrum (600 MHz, C_6D_6, 298 K) of **3.3**.

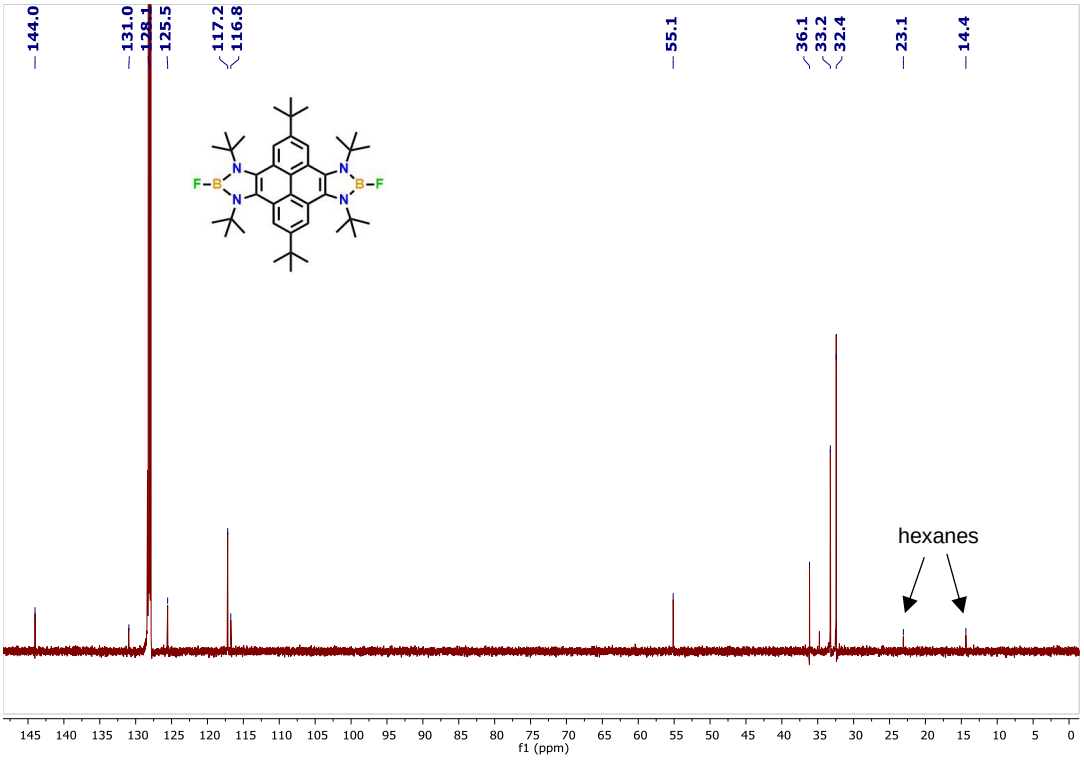

Figure A2.10. $^{13}C\{^{1}H\}$ NMR spectrum (151 MHz, C_6D_6, 298 K) of **3.3**.

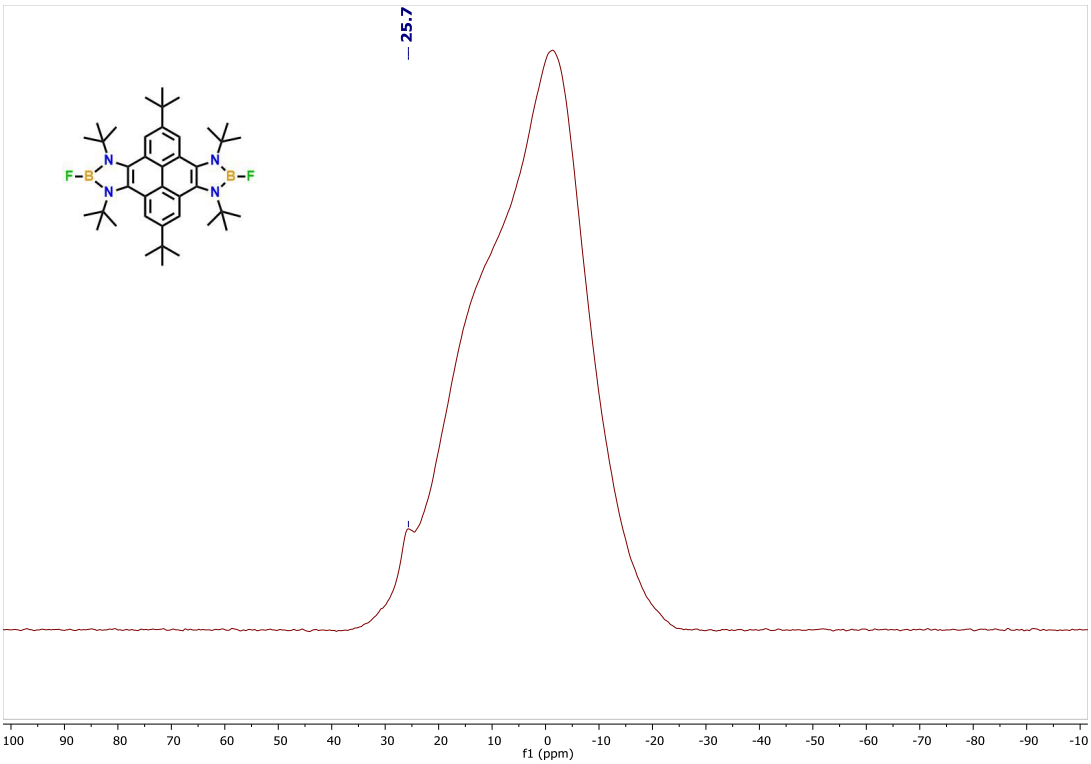

Figure A2.11. $^{11}B\{^{1}H\}$ NMR spectrum (192.55 Hz, C_6D_6, 298 K) of **3.3**.

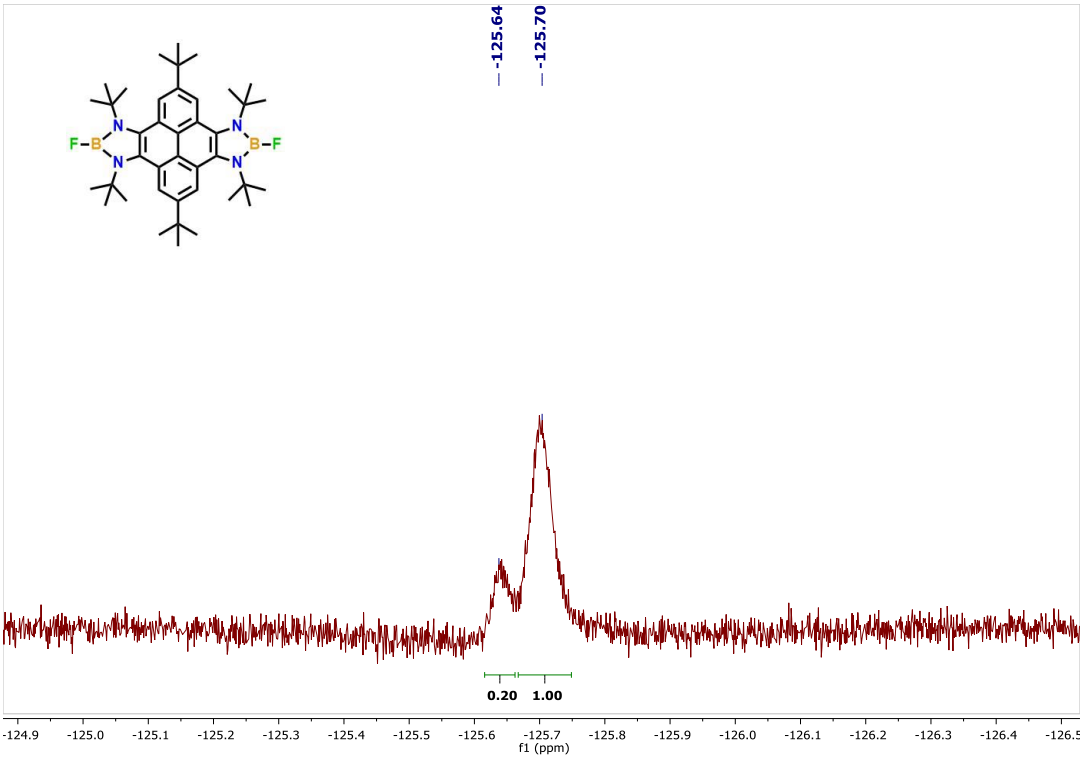

Figure A2.12. ^{19}F NMR spectrum (564.69 Hz, C_6D_6, 298 K) of **3.3**.

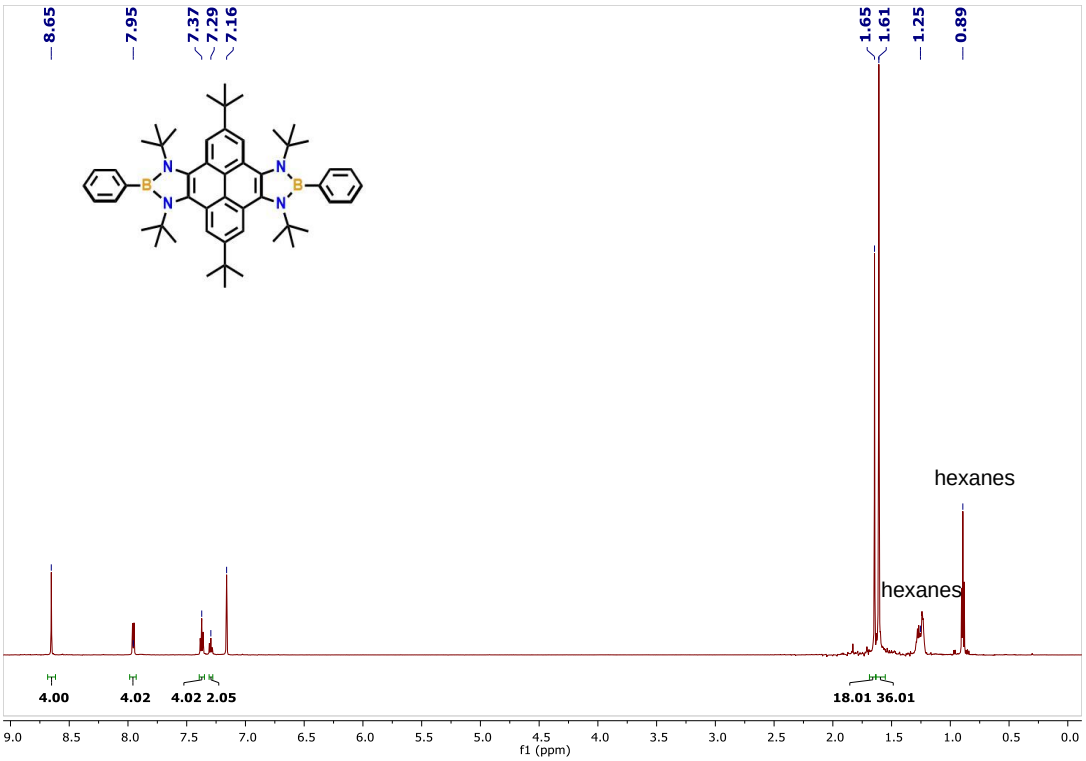

Figure A2.13. ^{1}H NMR spectrum (600 MHz, C_6D_6, 298 K) of **3.4**.

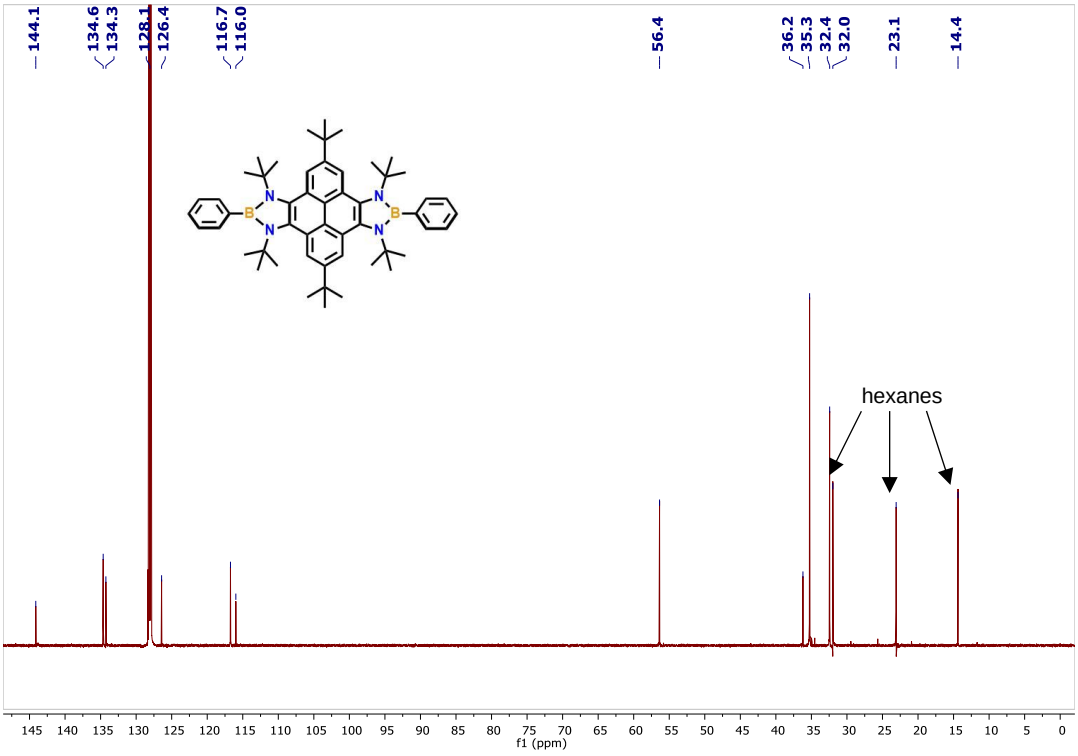

Figure A2.14. ^{13}C{^{1}H} NMR spectrum (151 MHz, C_6D_6, 298 K) of **3.4**.

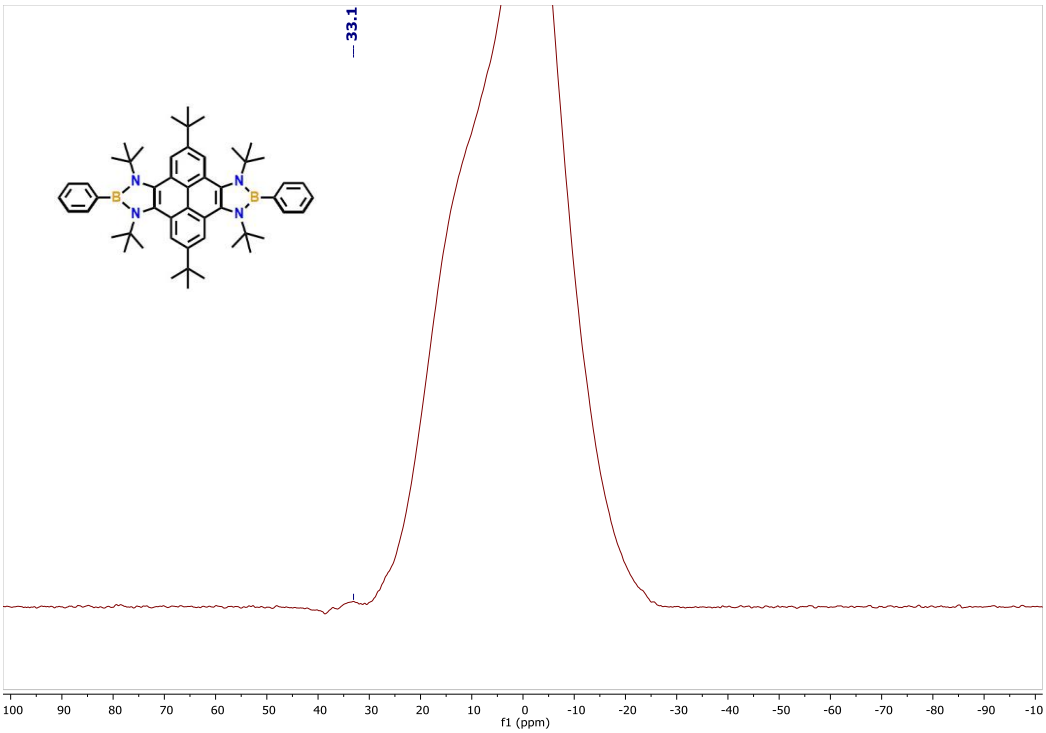

Figure A2.15. $^{11}B\{^{1}H\}$ NMR spectrum (192.55 Hz, C_6D_6, 298 K) of **3.4**.

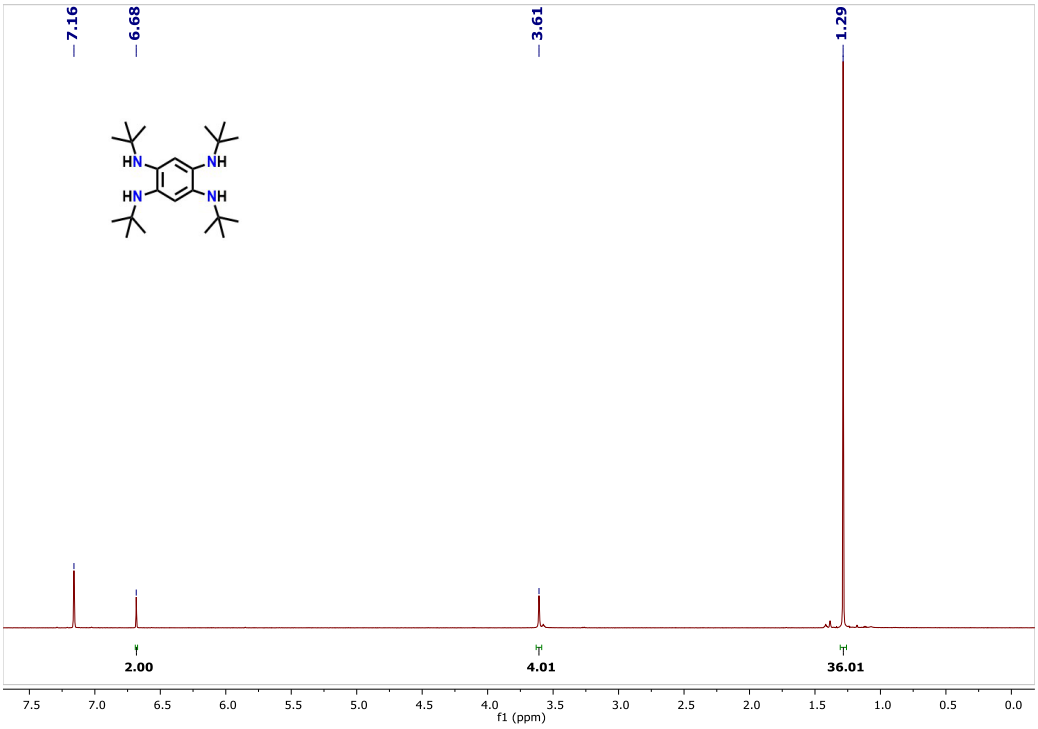

Figure A2.16. ^{1}H NMR spectrum (600 MHz, C_6D_6, 298 K) of **3.5**.

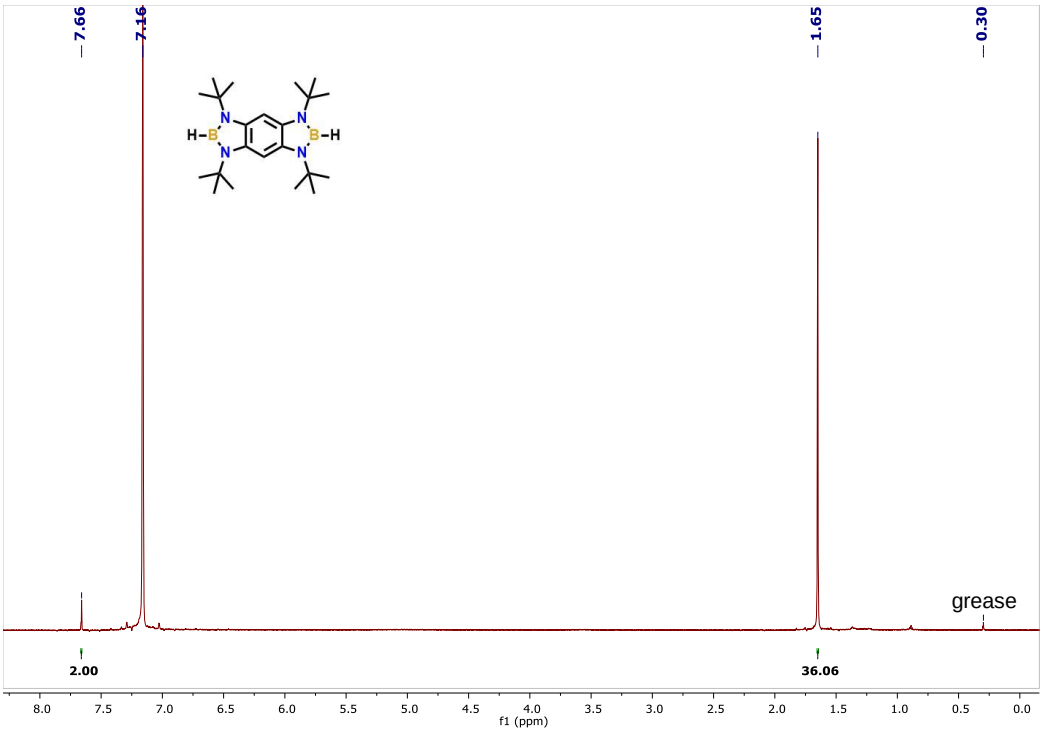

Figure A2.17. ^{1}H NMR spectrum (600 MHz, C_6D_6, 298 K) of **3.6**.

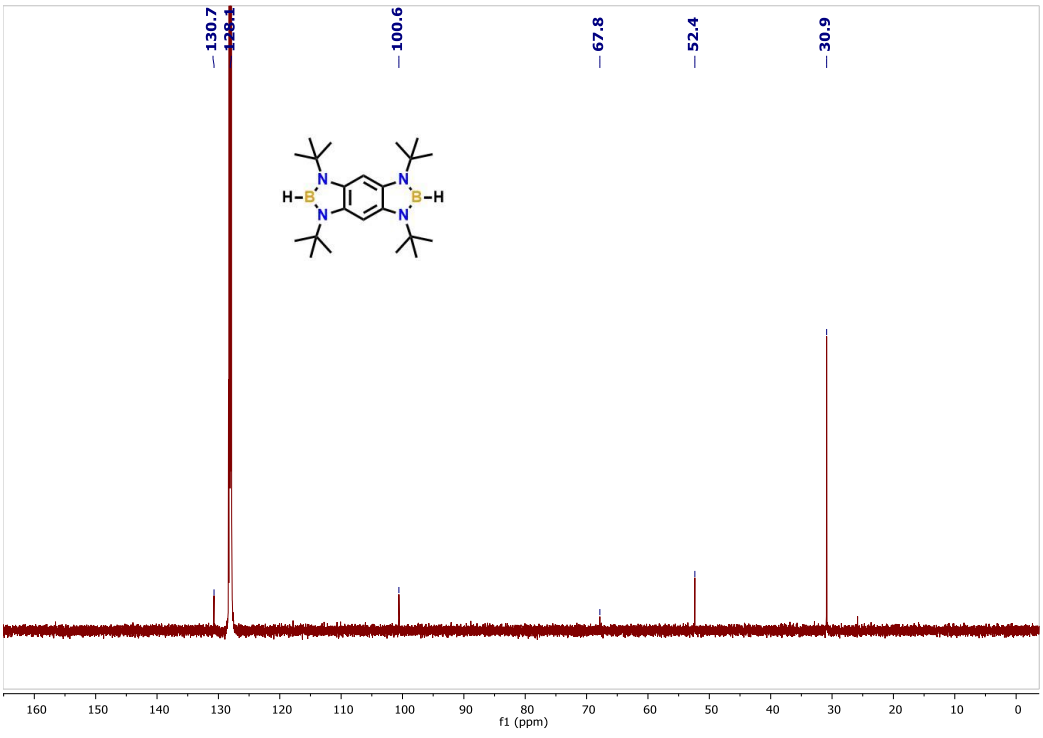

Figure A2.18. ^{13}C{^{1}H} NMR spectrum (151 MHz, C_6D_6, 298 K) of **3.6**.

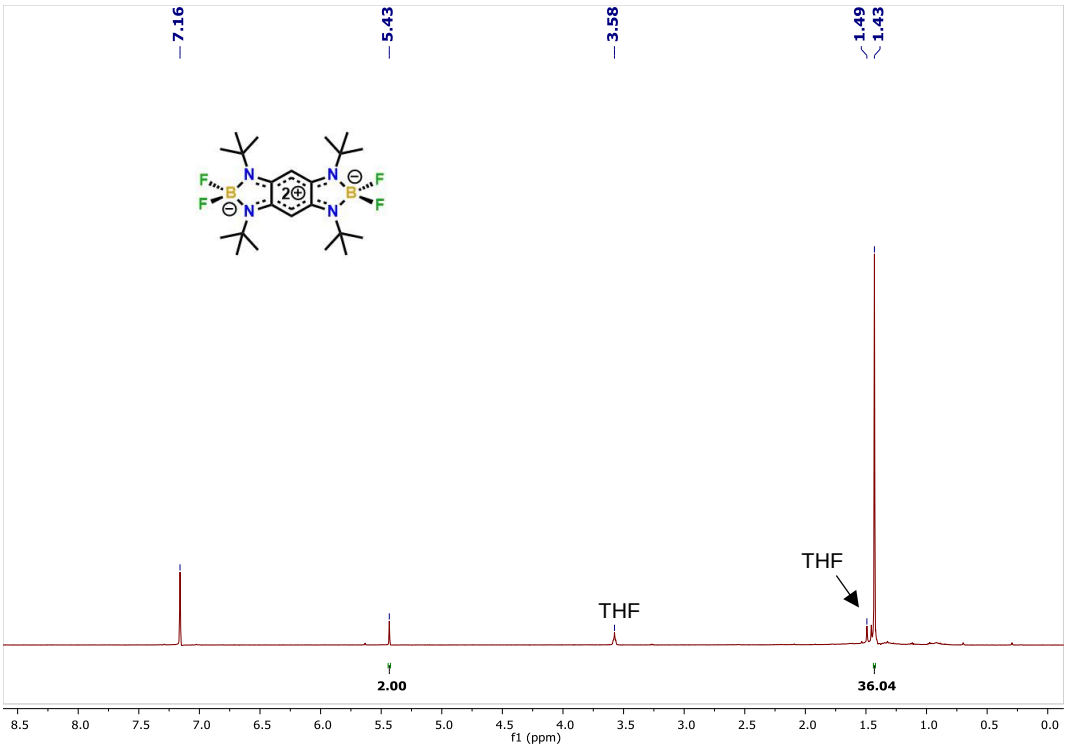

Figure A2.19. ^{1}H NMR spectrum (600 MHz, C_6D_6, 298 K) of **3.7**.

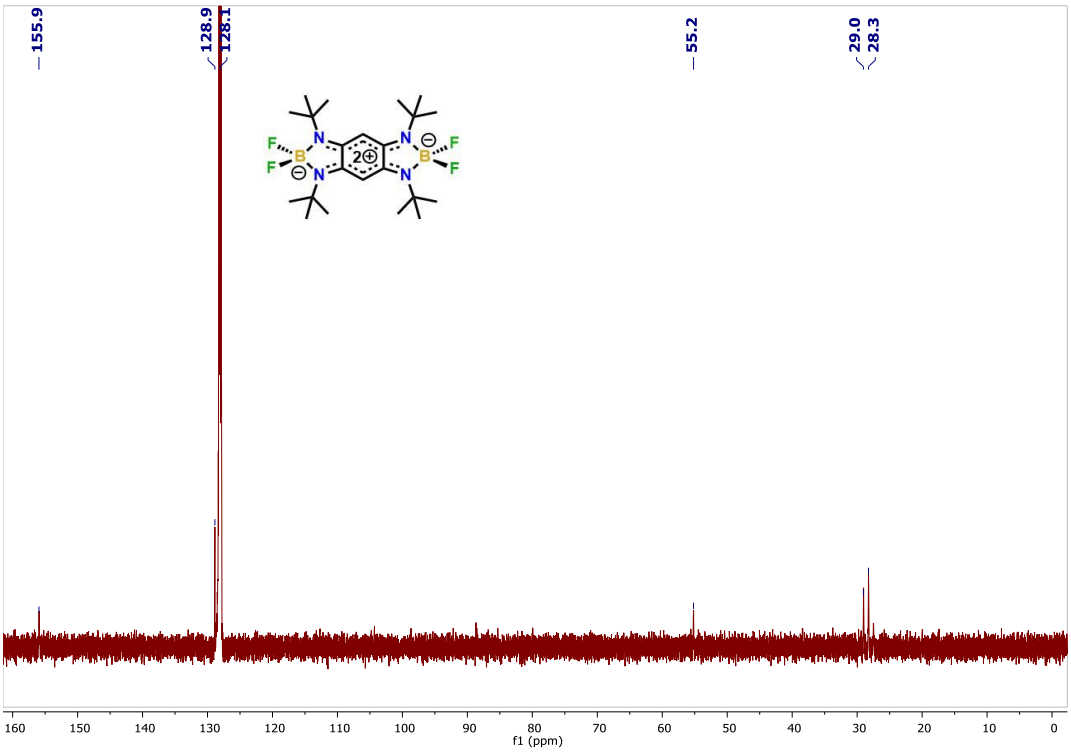

Figure A2.20. ^{13}C{^{1}H} NMR spectrum (151 MHz, C_6D_6, 298 K) of **3.7**.

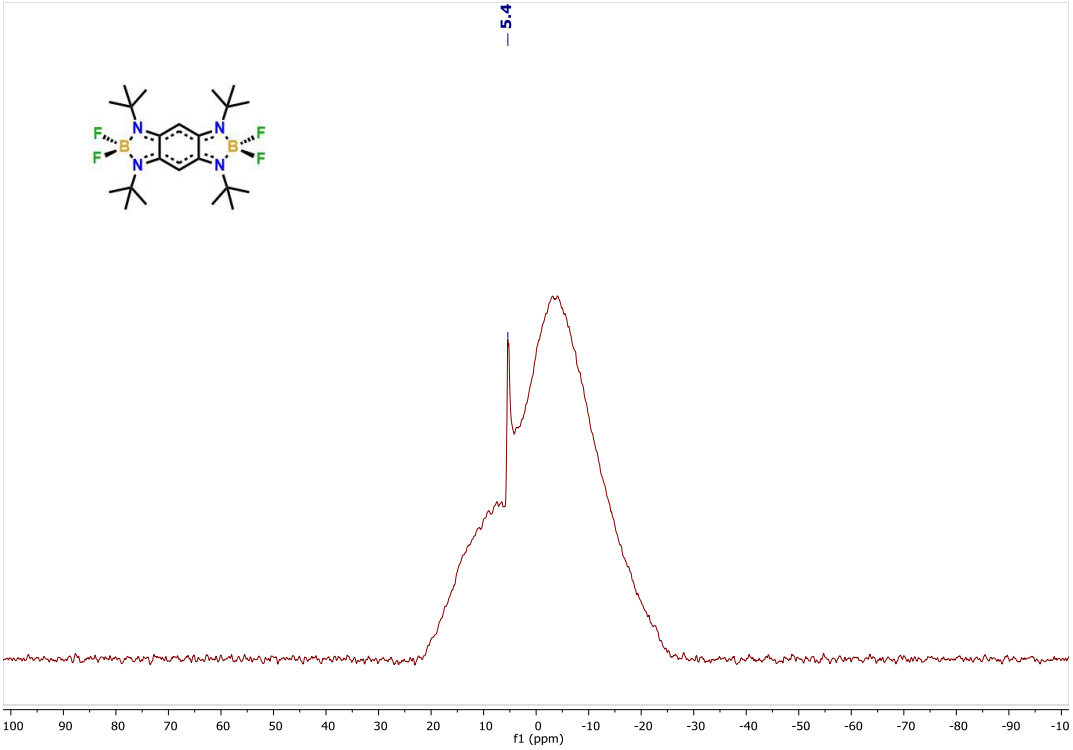

Figure A2.21. $^{11}B\{^{1}H\}$ NMR spectrum (192.55 Hz, C_6D_6, 298 K) of **3.7**.

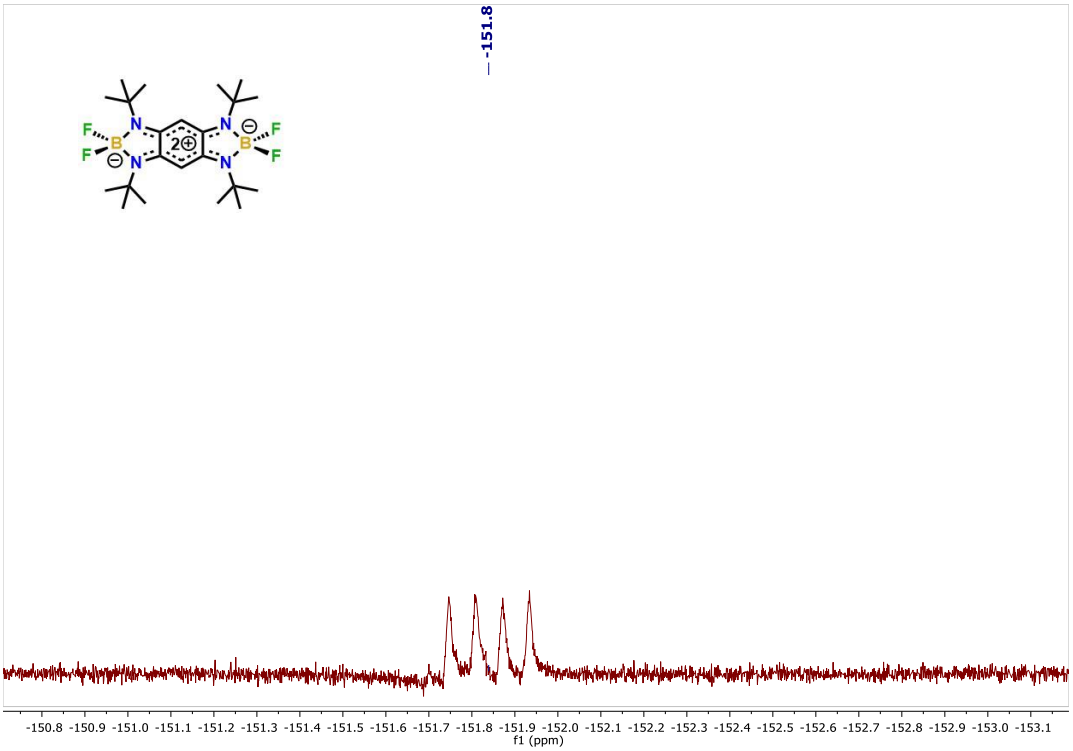

Figure A2.21. ^{19}F NMR spectrum (564.69 Hz, C_6D_6, 298 K) of **3.7**.

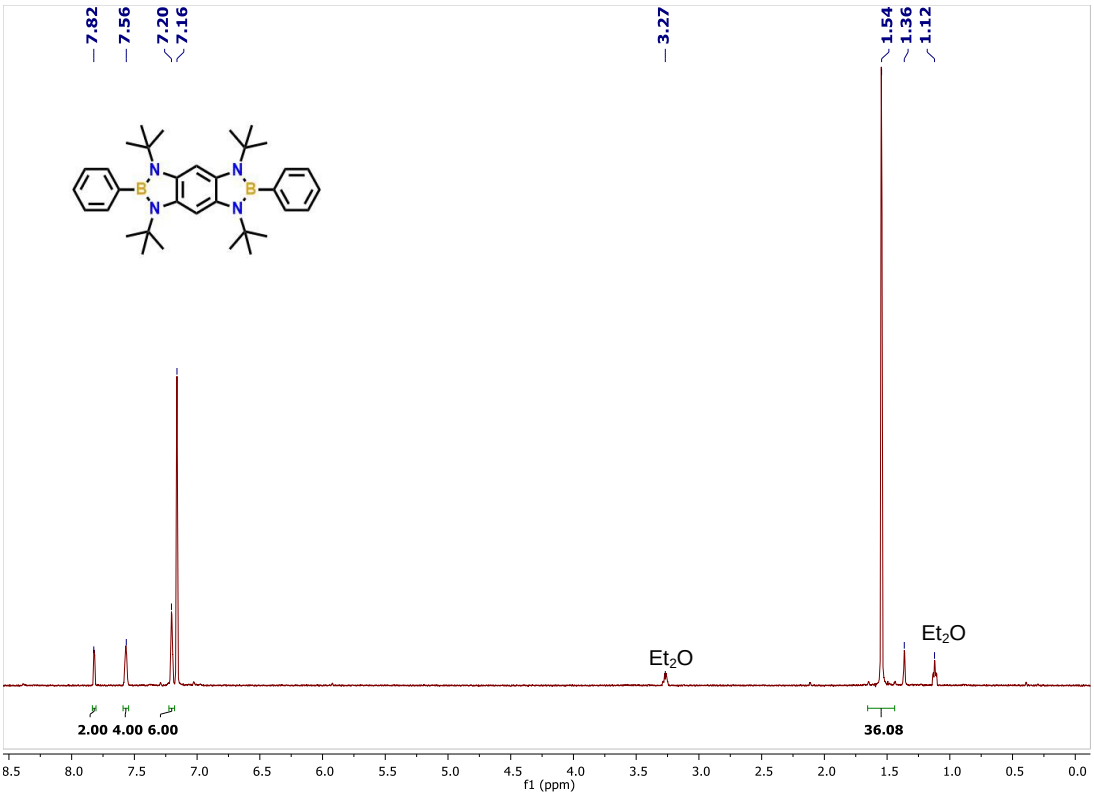

Figure A2.22. ^{1}H NMR spectrum (600 MHz, C_6D_6, 298 K) of **3.8**.

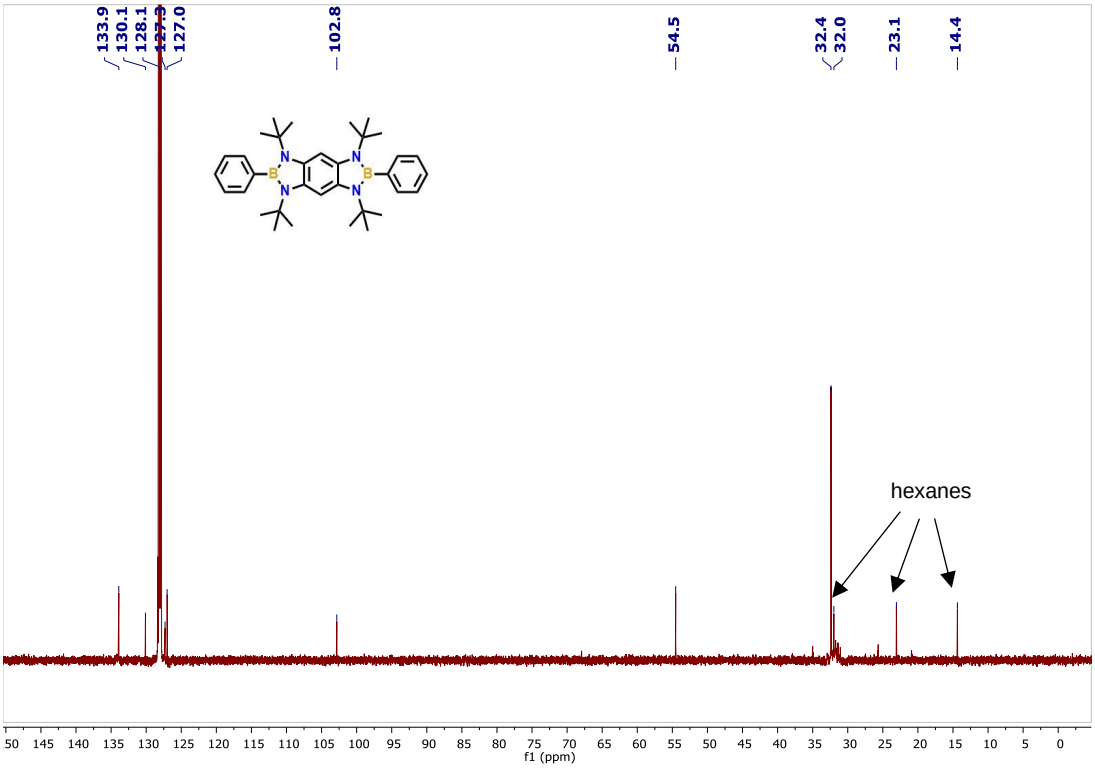

Figure A2.23. $^{13}C\{^{1}H\}$ NMR spectrum (151 MHz, C_6D_6, 298 K) of **3.8**.

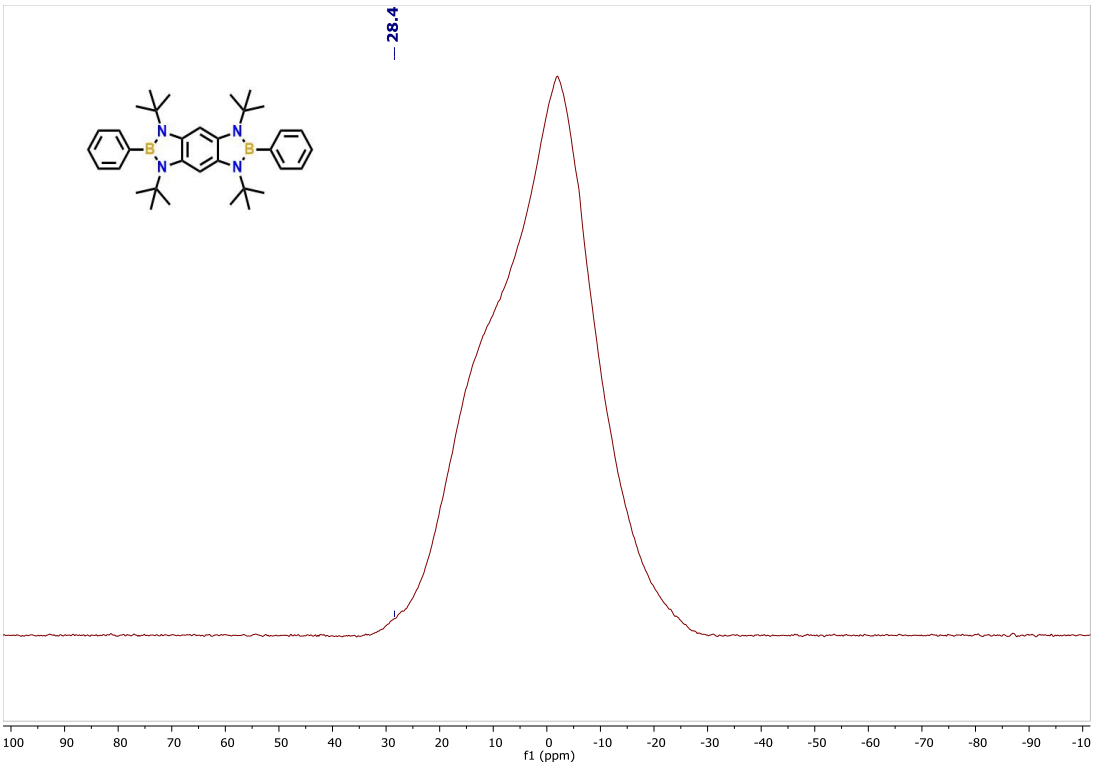

Figure A2.24. $^{11}B\{^{1}H\}$ NMR spectrum (192.55 Hz, C_6D_6, 298 K) of **3.8**.

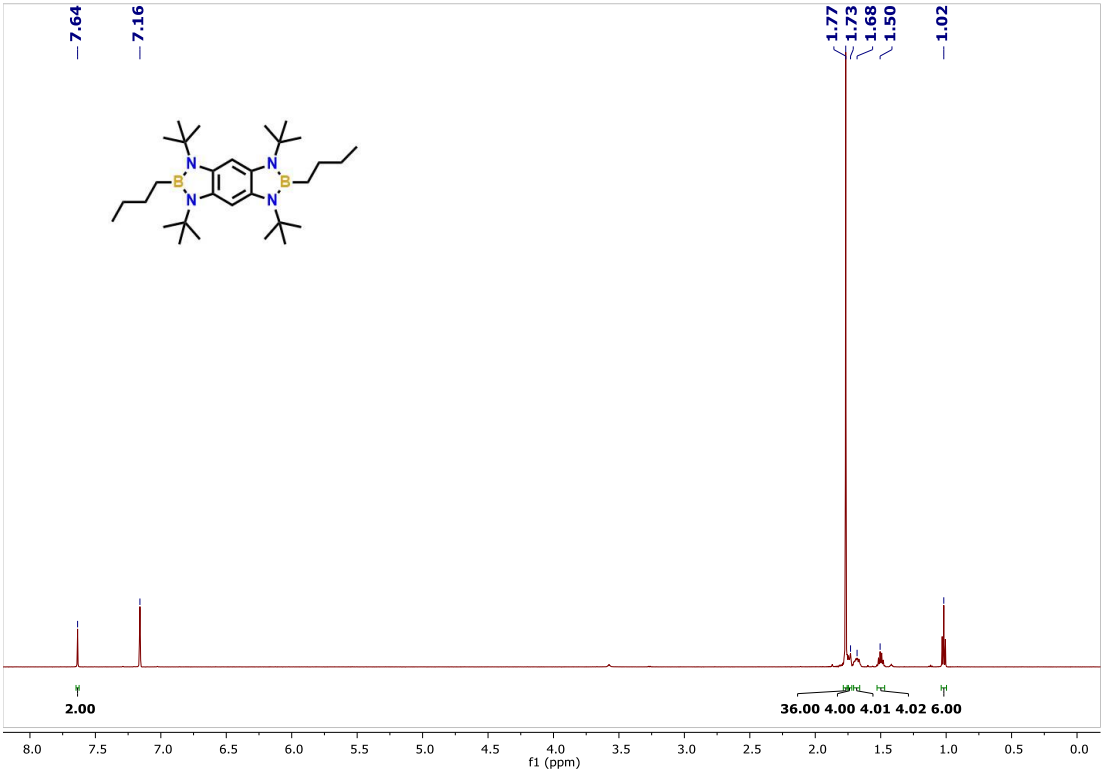

Figure A2.24. ^{1}H NMR spectrum (600 MHz, C_6D_6, 298 K) of **3.9**.

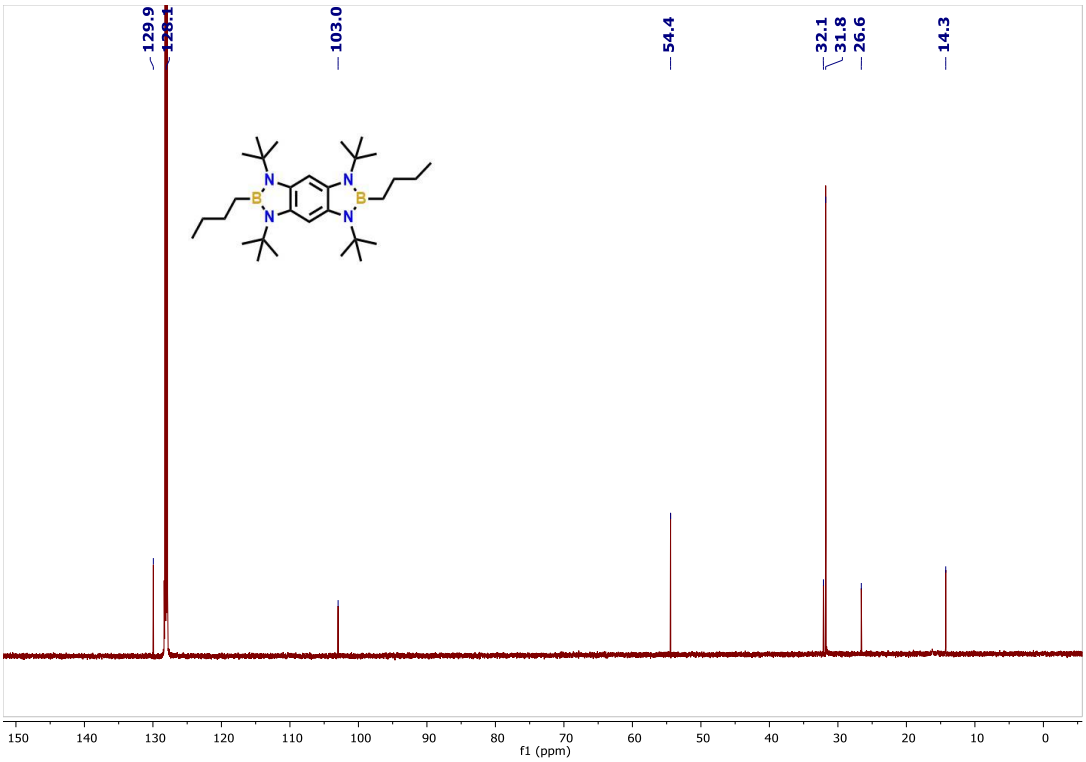

Figure A2.25. $^{13}C\{^{1}H\}$ NMR spectrum (151 MHz, C_6D_6, 298 K) of **3.9**.

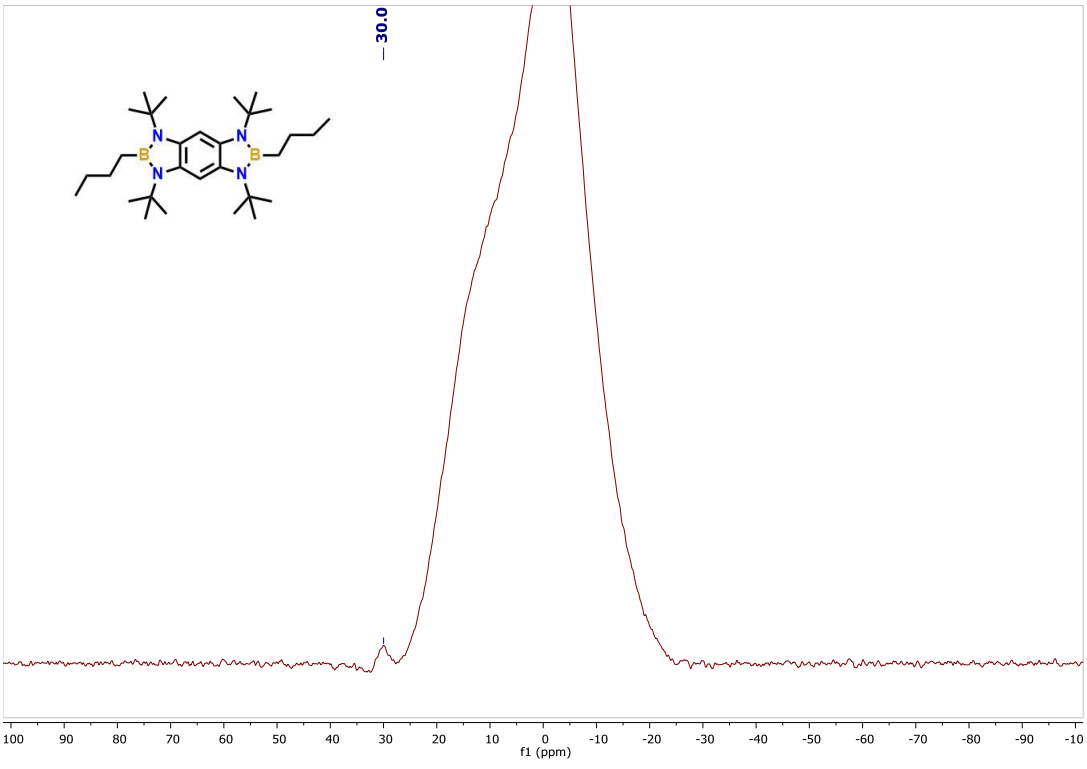

Figure A2.26. $^{11}B\{^{1}H\}$ NMR spectrum (192.55 Hz, C_6D_6, 298 K) of **3.9**.

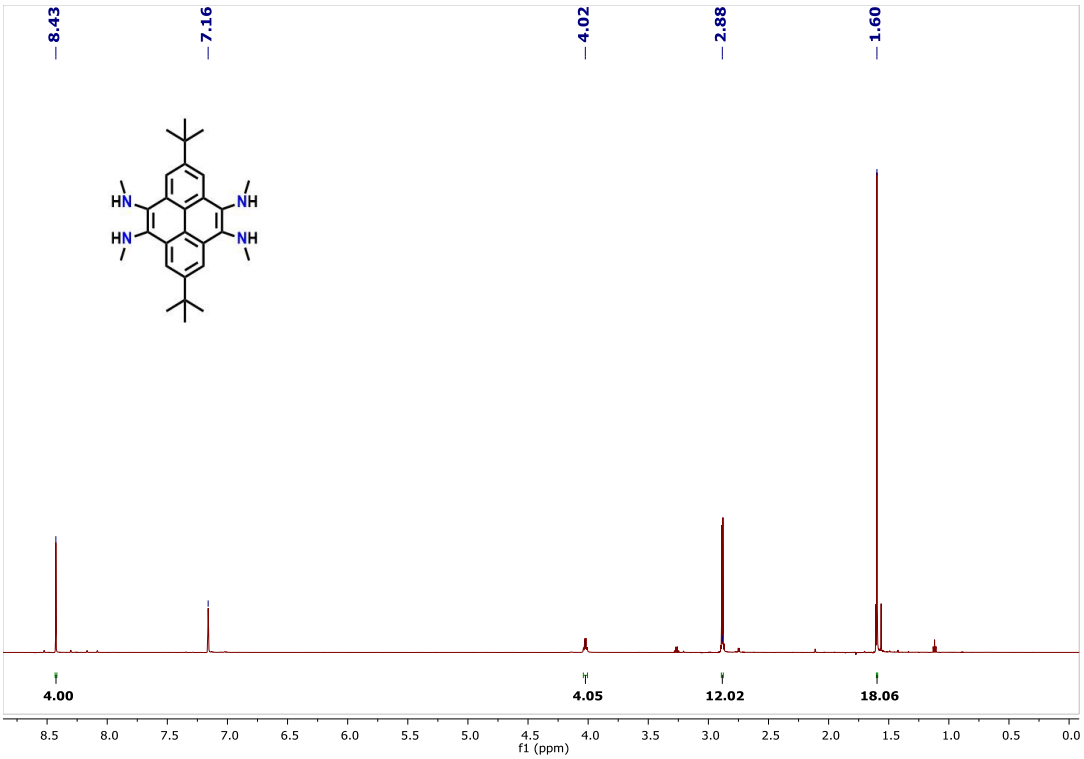

Figure A2.27. ^{1}H NMR spectrum (600 MHz, C_6D_6, 298 K) of **3.10**.

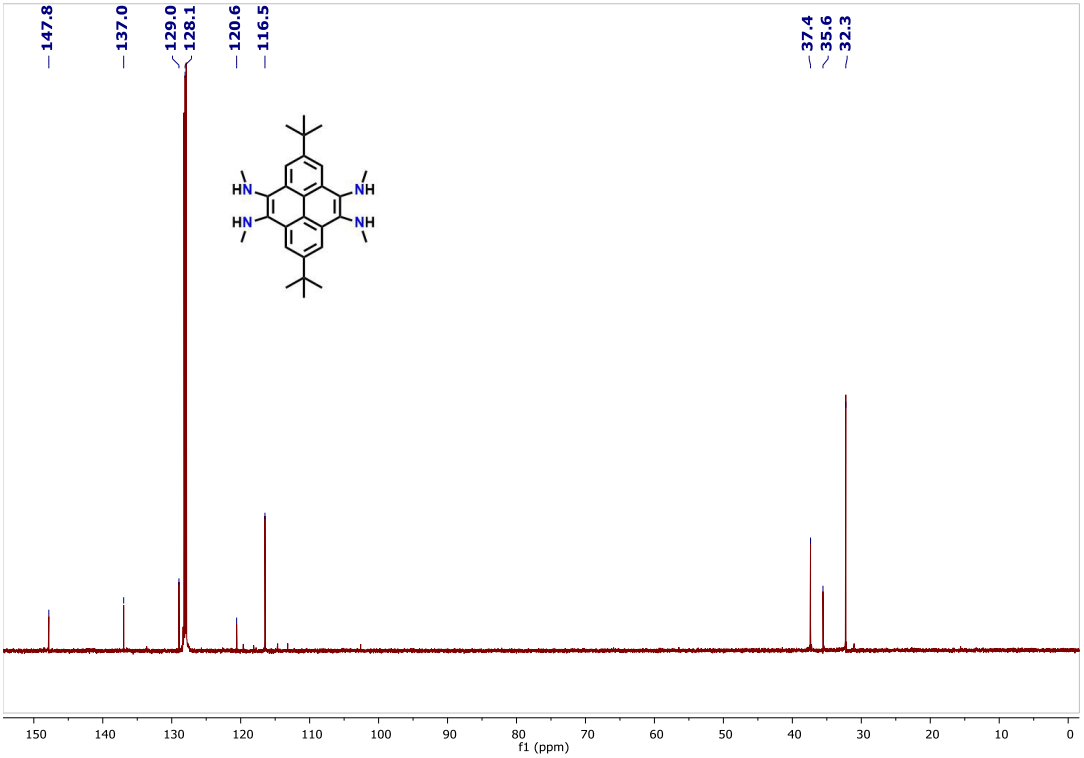

Figure A2.28. $^{13}C\{^{1}H\}$ NMR spectrum (151 MHz, C_6D_6, 298 K) of **3.10**.

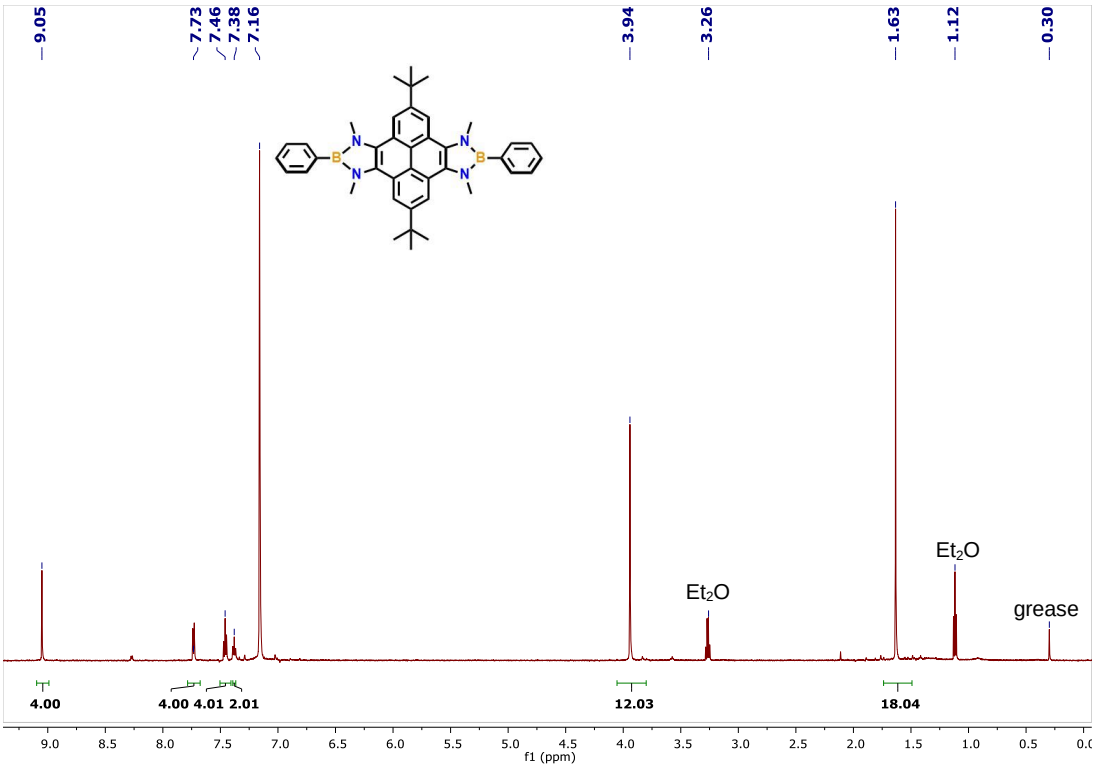

Figure A2.29. ^{1}H NMR spectrum (600 MHz, C_6D_6, 298 K) of **3.11**.

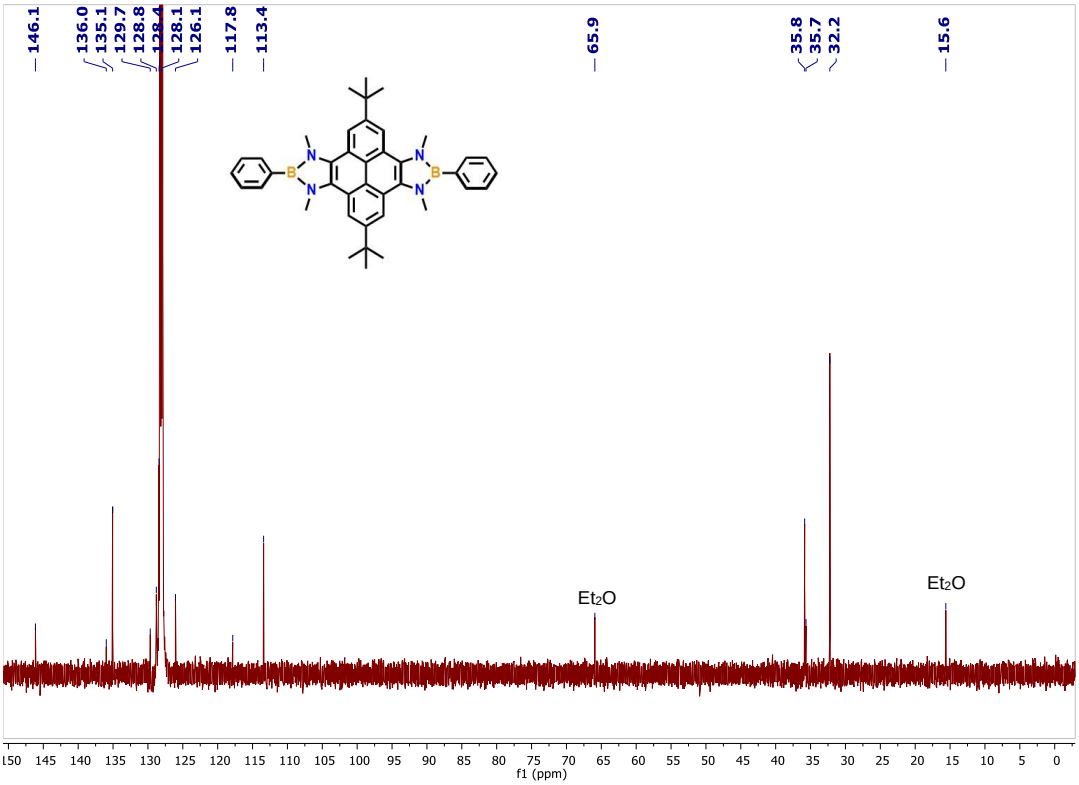

Figure A2.30. $^{13}C\{^{1}H\}$ NMR spectrum (151 MHz, C_6D_6, 298 K) of **3.11**.

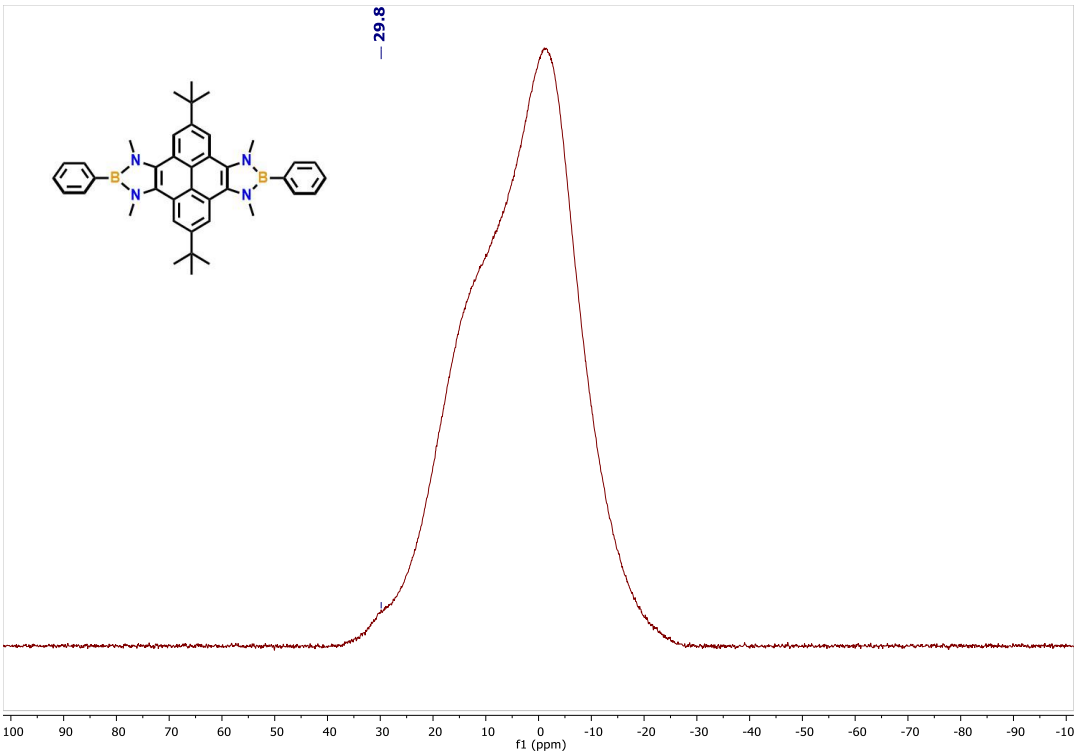

Figure A2.31. $^{11}B\{^{1}H\}$ NMR spectrum (192.55 Hz, C_6D_6, 298 K) of **3.11**.

Chapter Four:

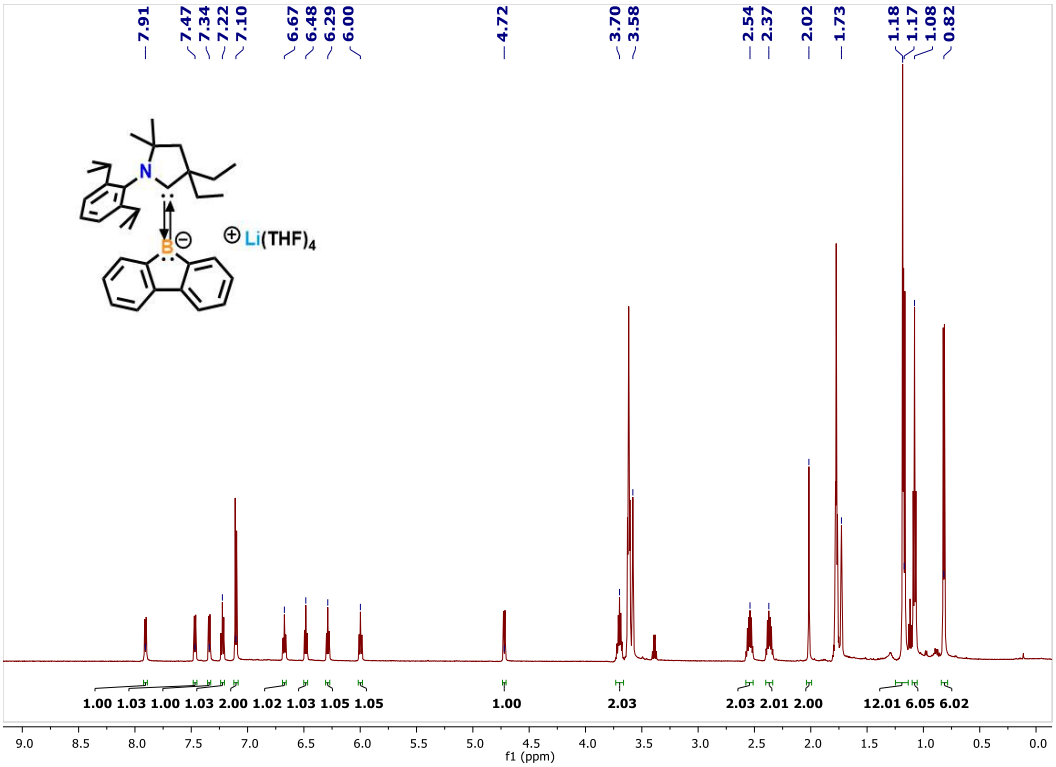

Figure A2.32. ^{1}H NMR spectrum (600 MHz, THF-d_8, 298 K) of **4.3**.

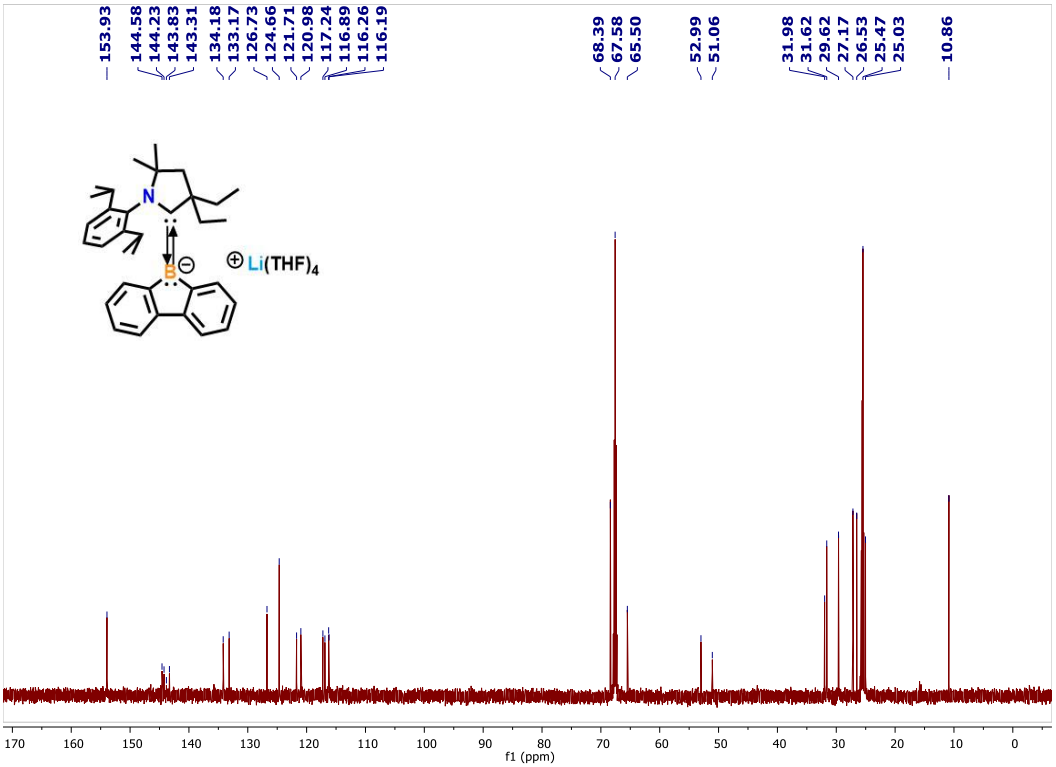

Figure A2.33. ^{13}C{^{1}H} NMR spectrum (151 MHz, THF-d_8, 298K) of **4.3**.

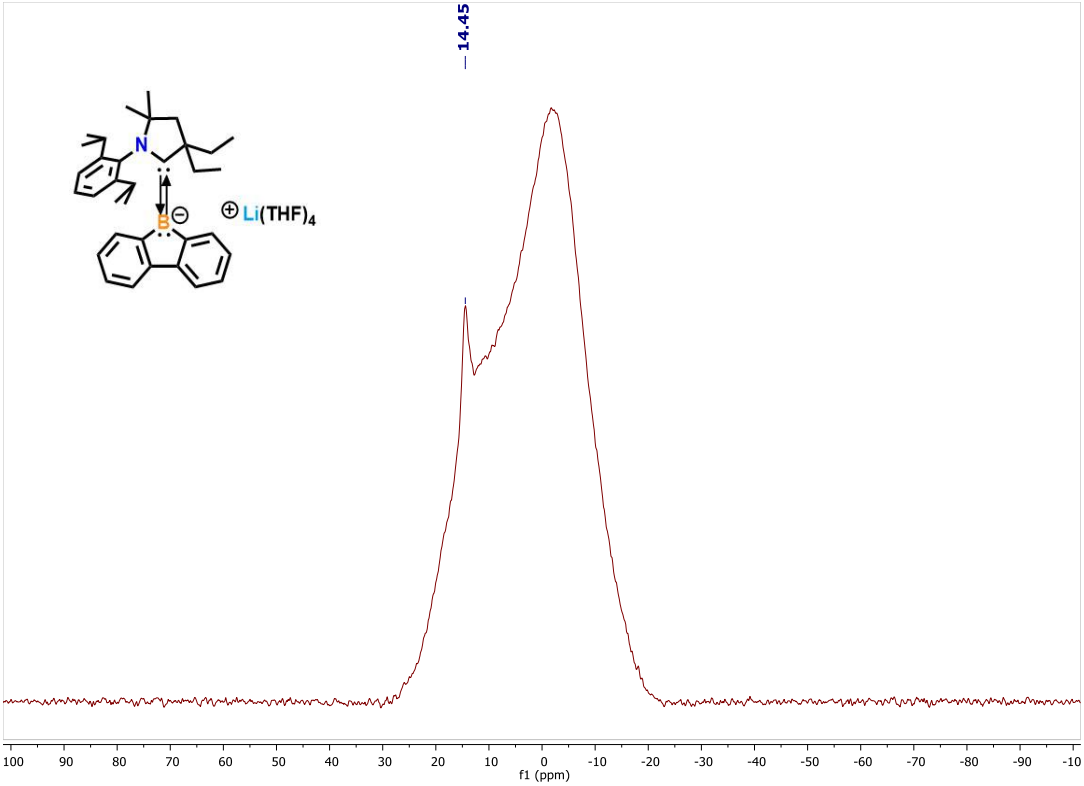

Figure A2.34. ^{11}B NMR spectrum (193 MHz, THF-d_8, 298 K) of **4.3**.

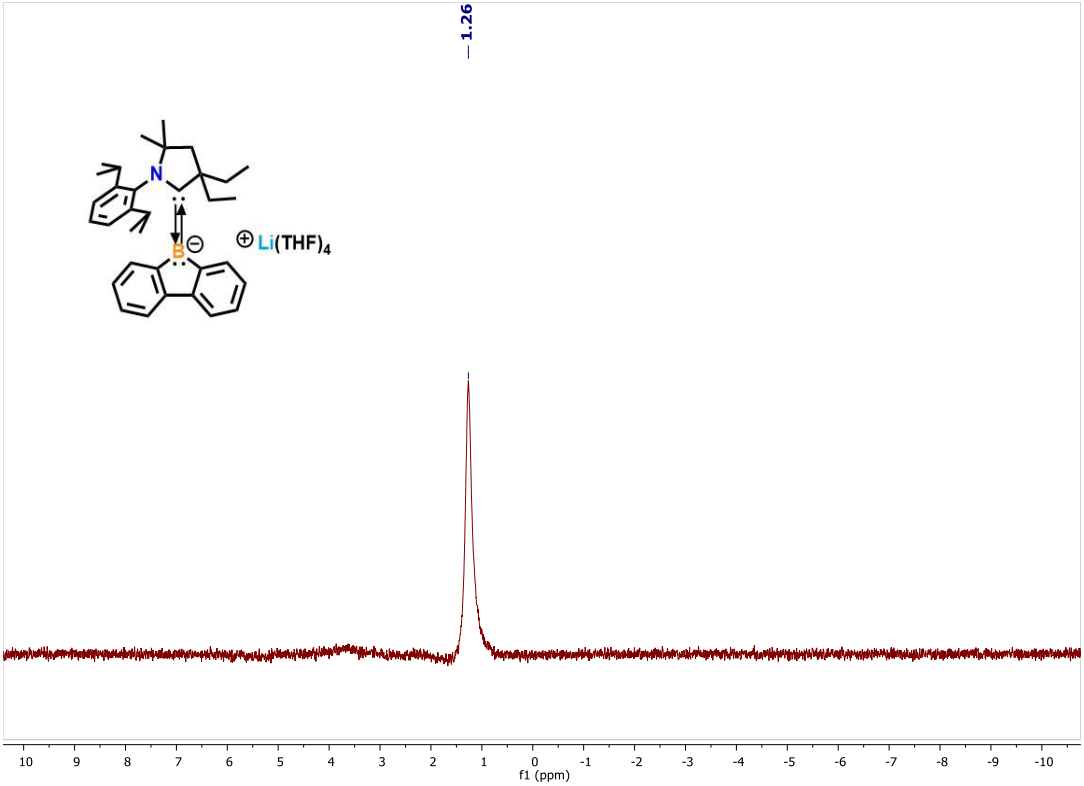

Figure A2.35. ^{7}Li NMR spectrum (233 MHz, THF-d_8, 298 K) of **4.3**.

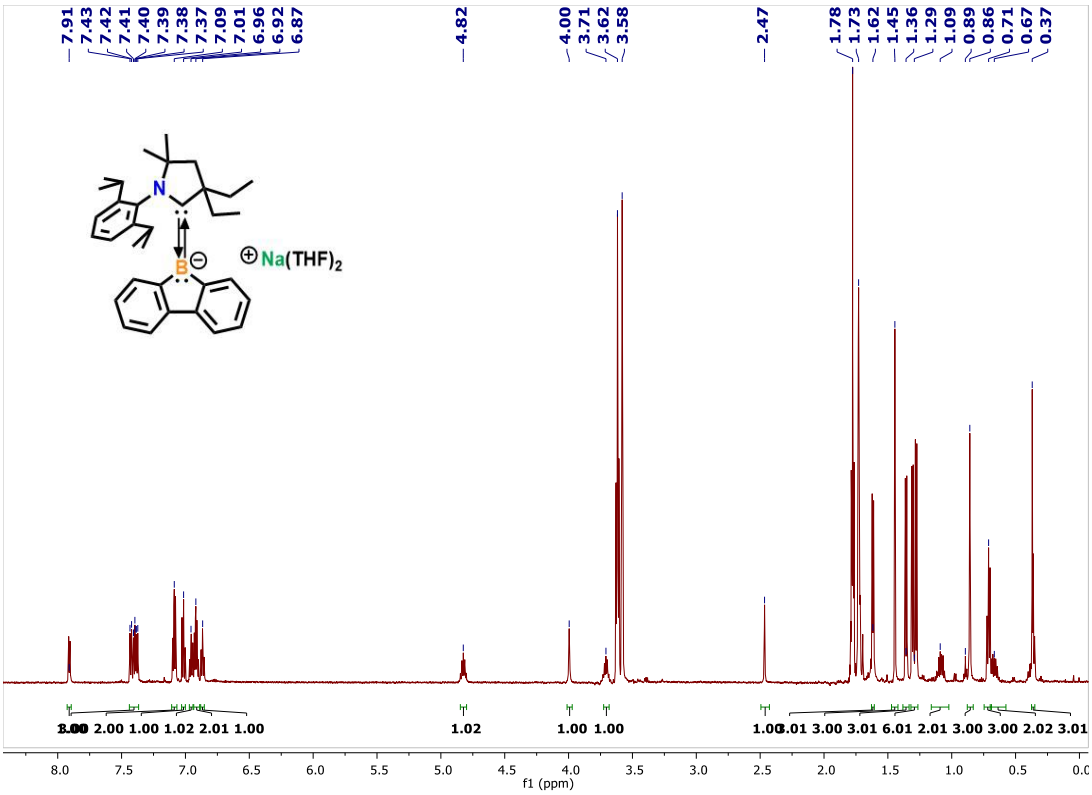

Figure A2.36. ^{1}H NMR spectrum (600 MHz, THF-d_8, 298 K) of **4.4**.

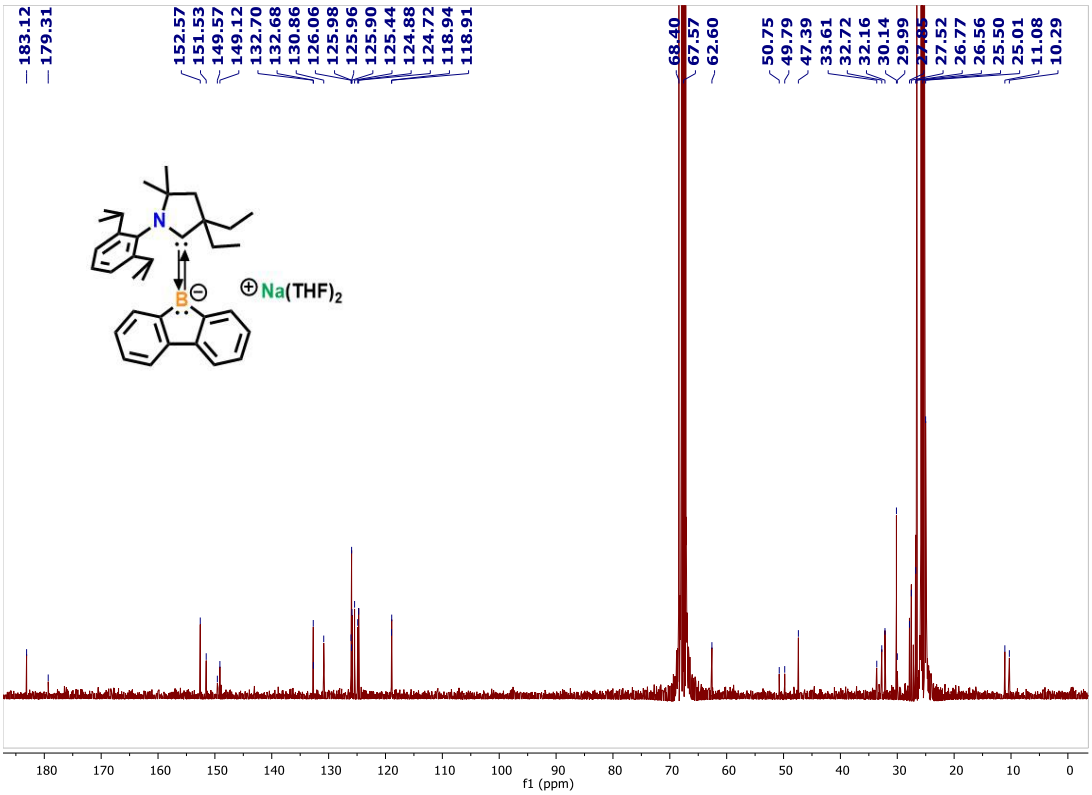

Figure A2.37. $^{13}C\{^{1}H\}$ NMR spectrum (151 MHz, THF-d_8, 298K) of **4.4**.

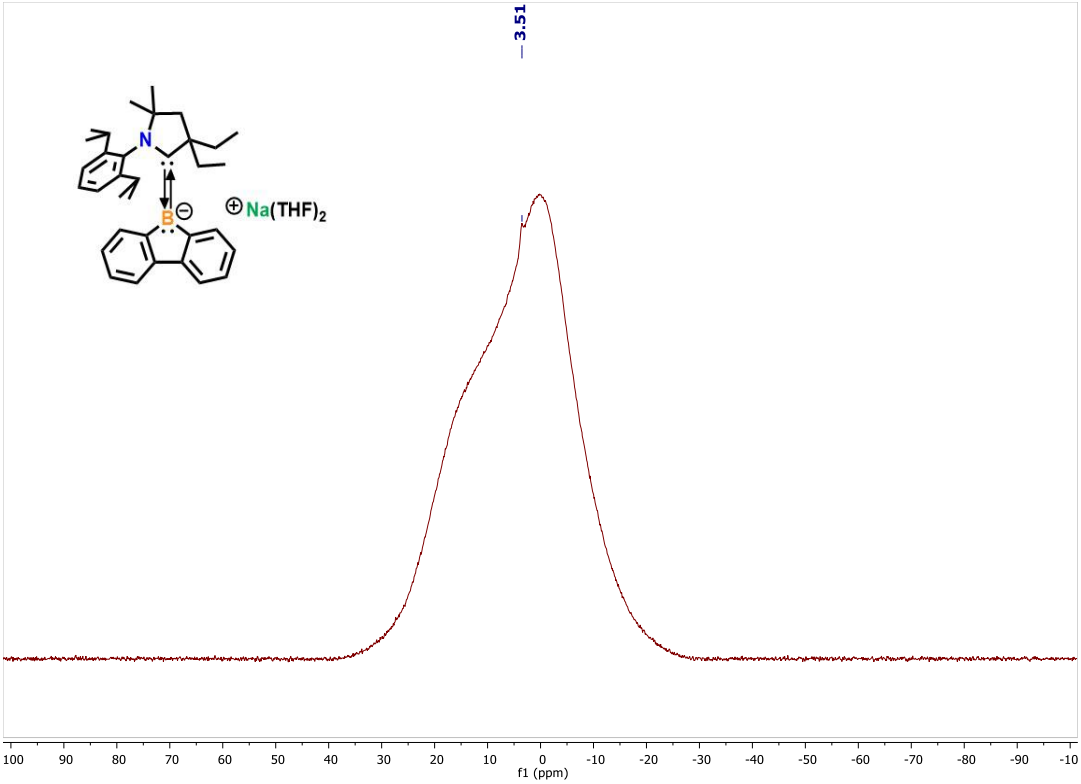

Figure A2.38. ^{11}B NMR spectrum (193 MHz, THF-d_8, 298 K) of **4.4**.

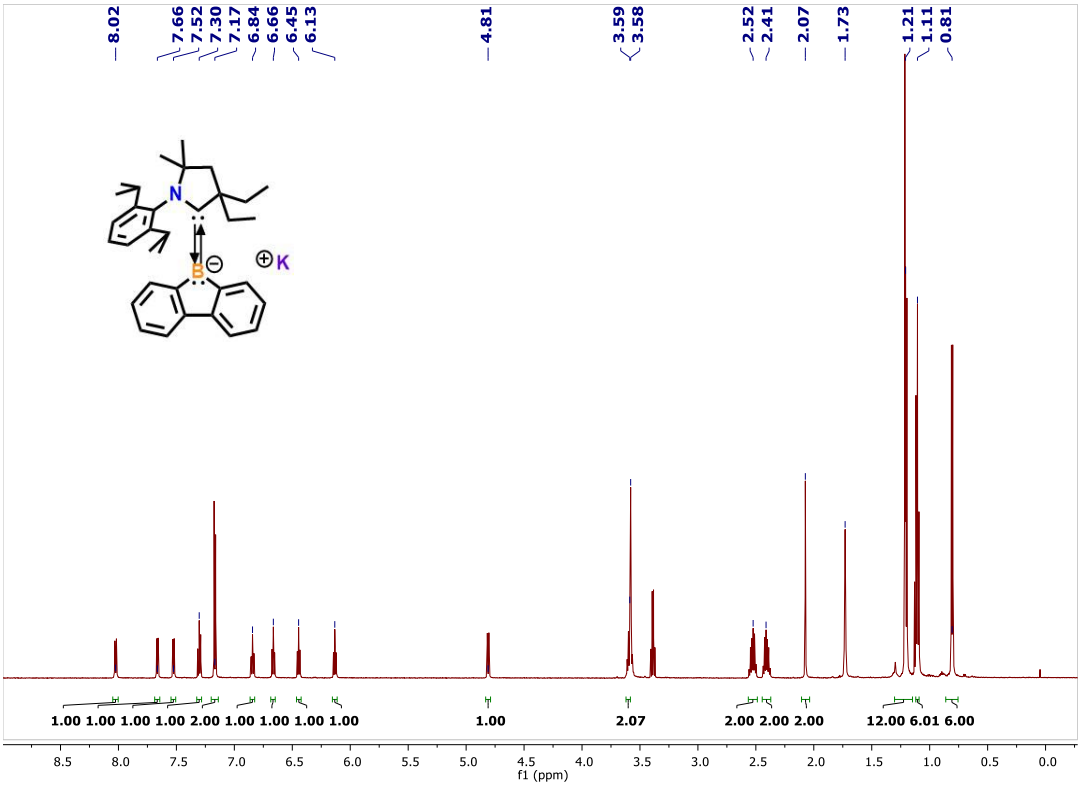

Figure A2.39. ^{1}H NMR spectrum (600 MHz, THF-d_8, 298 K) of **4.5**

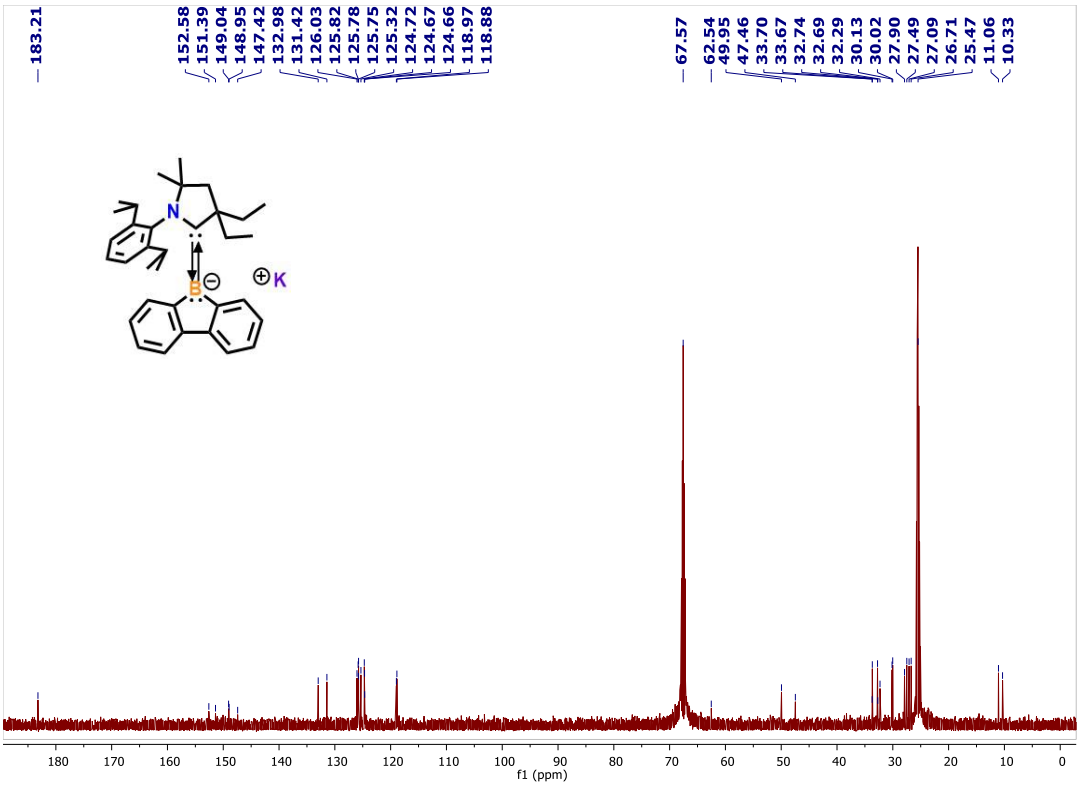

Figure A2.40. $^{13}C\{^{1}H\}$ NMR spectrum (151 MHz, THF-d_8, 298K) of **4.5**.

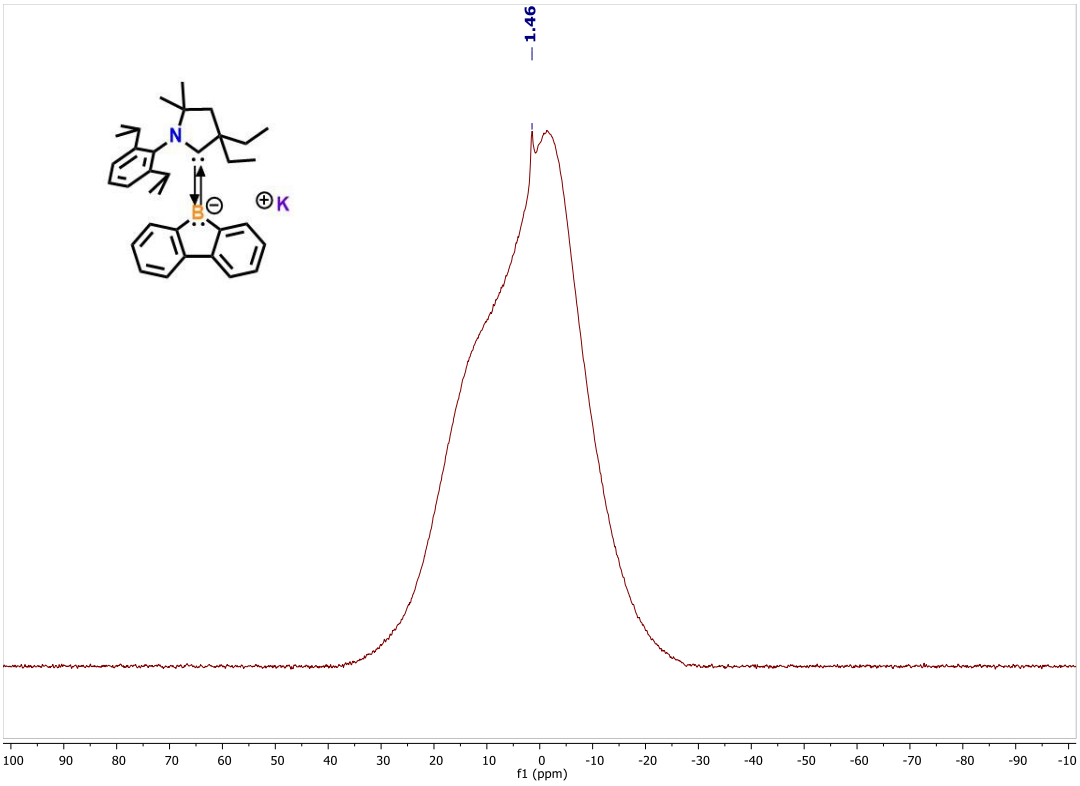

Figure A2.41. ^{11}B NMR spectrum (193 MHz, THF-d_8, 298 K) of **4.5**.

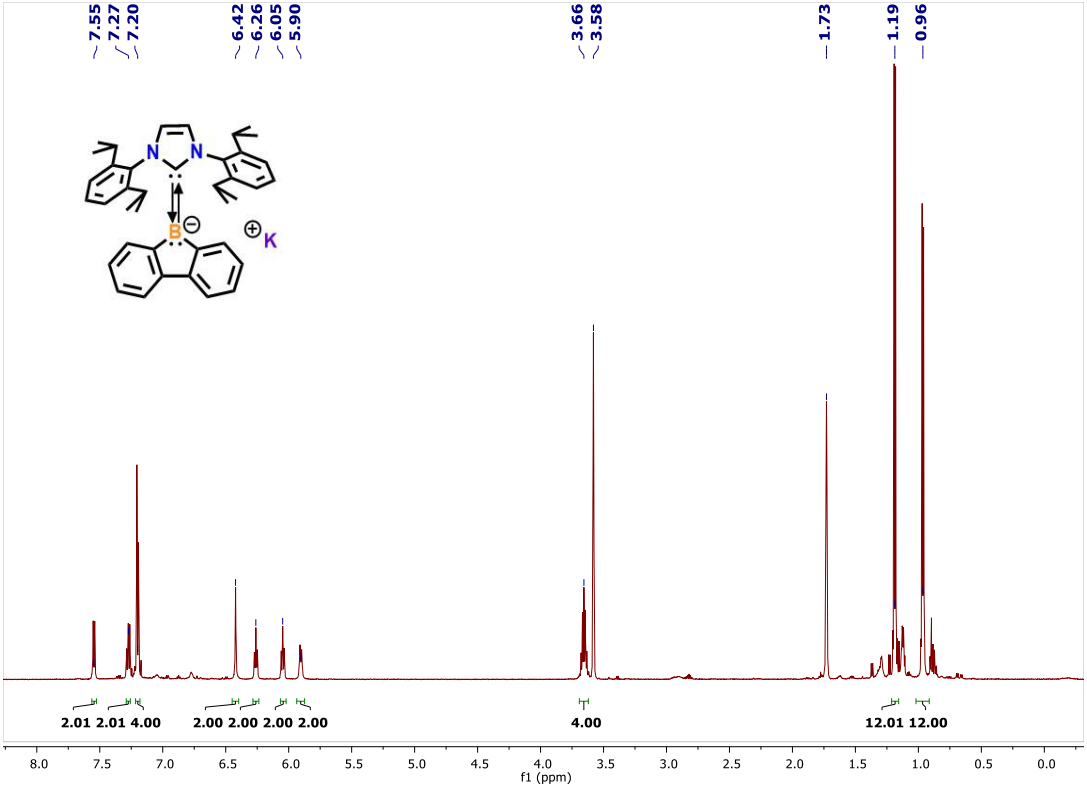

Figure A2.42. ^{1}H NMR spectrum (600 MHz, THF-d_8, 298 K) of **4.8**.

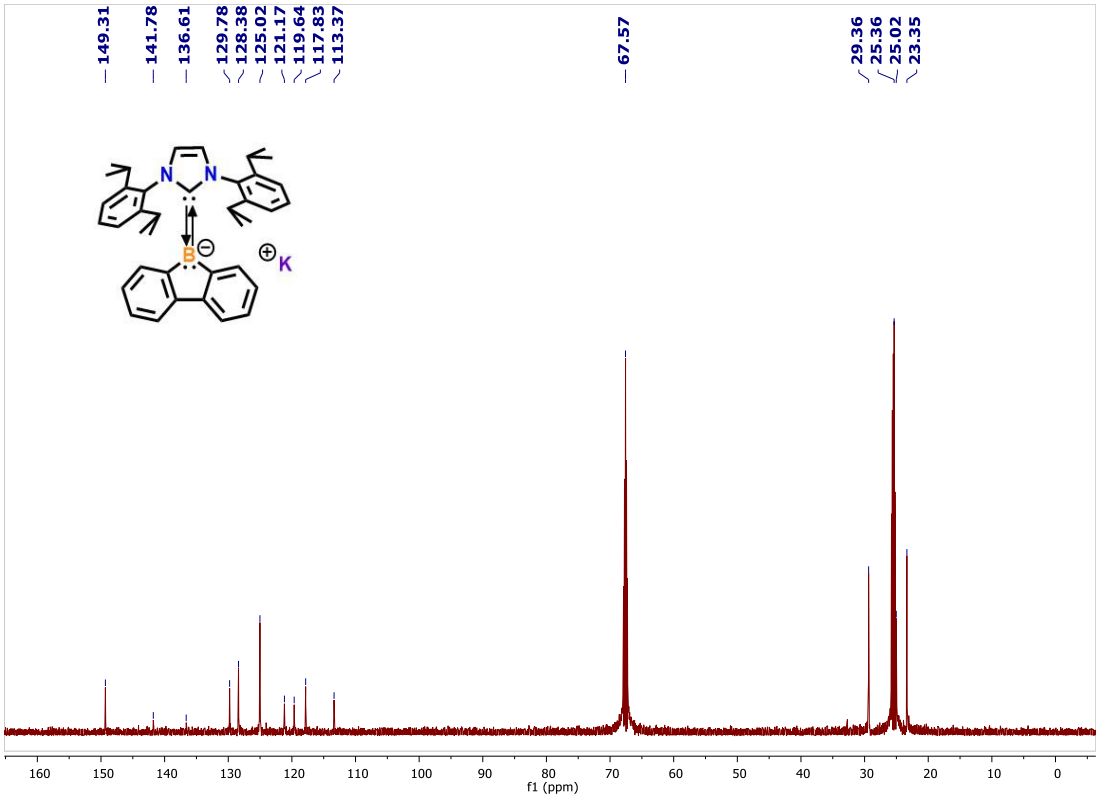

Figure A2.43. ^{13}C{^{1}H} NMR spectrum (151 MHz, THF-d_8, 298K) of **4.8**.

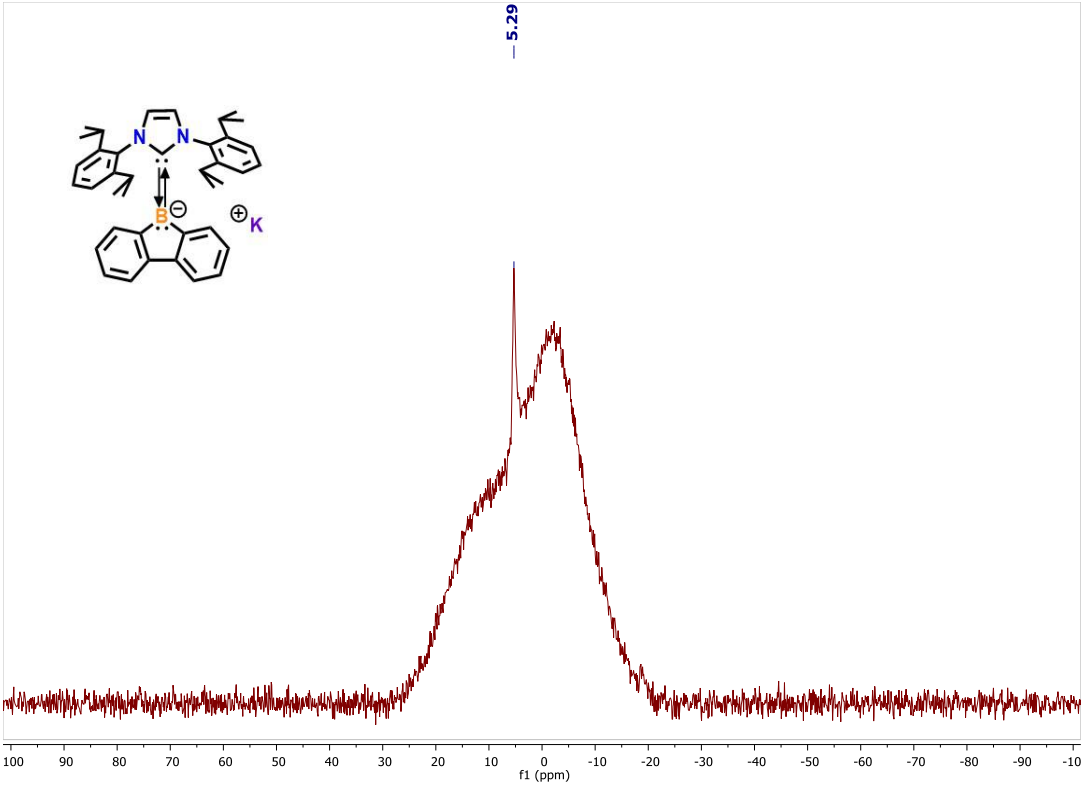

Figure A2.43. ^{11}B NMR spectrum (193 MHz, THF-d_8, 298 K) of **8**.

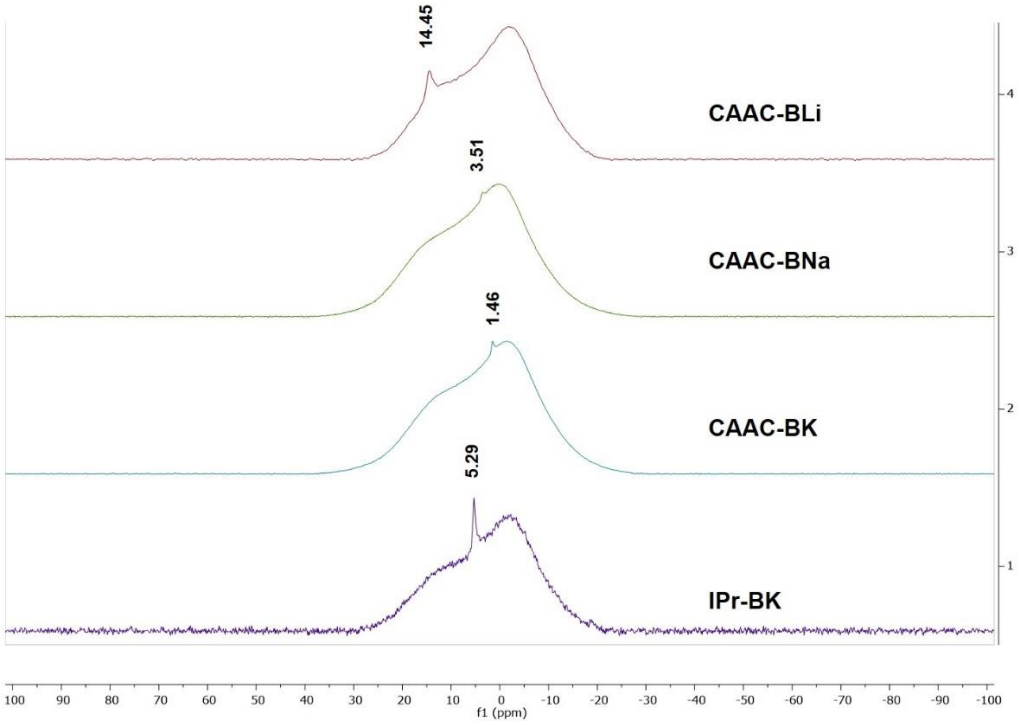

Figure A2.44. Stacked ^{11}B NMR spectra of borafluorene anions **4.3-4.5** and **4.8**.

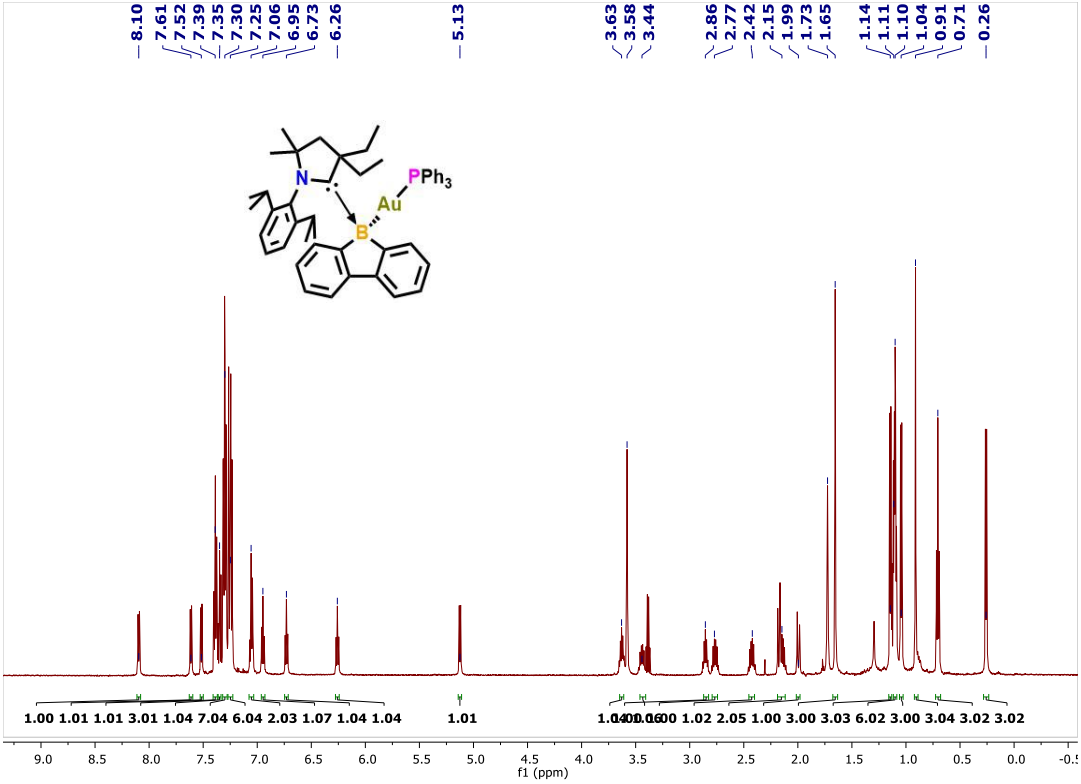

Figure A2.45. ^{1}H NMR spectrum (600 MHz, THF-d_8, 298 K) of **4.9**.

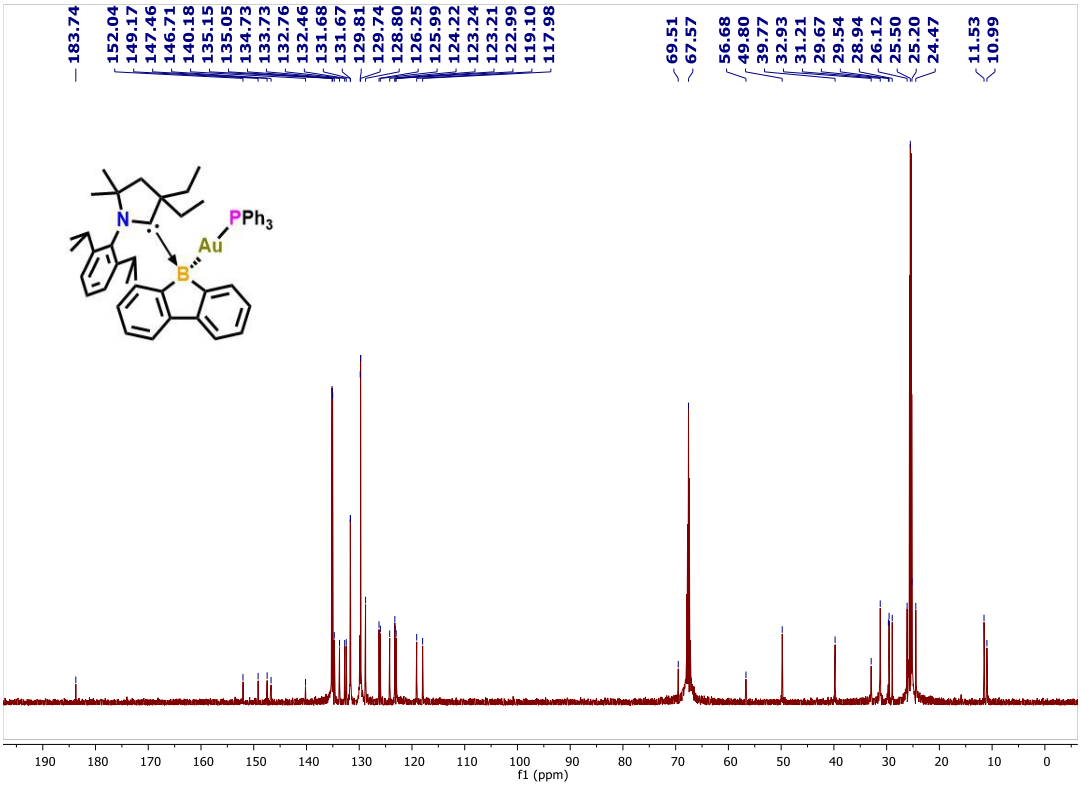

Figure A2.46. ^{13}C{^{1}H} NMR spectrum (151 MHz, THF-d_8, 298K) of **4.9**.

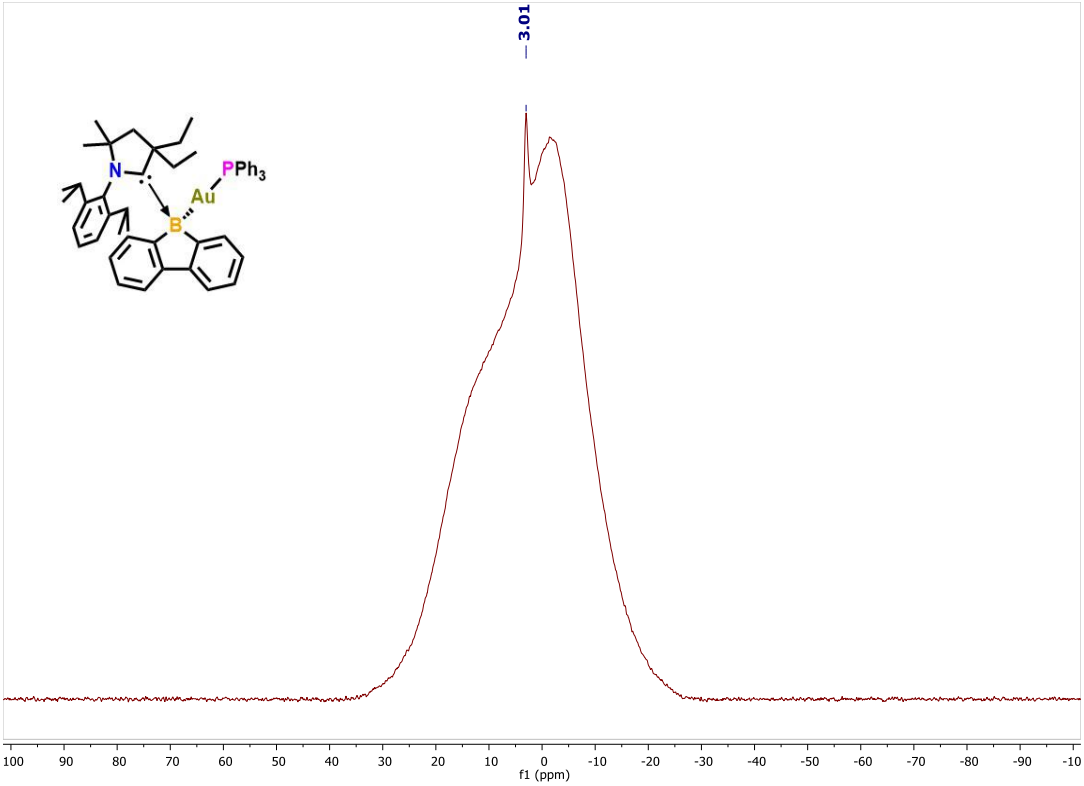

Figure A2.47. ^{11}B NMR spectrum (193 MHz, THF-d_8, 298 K) of **4.9**.

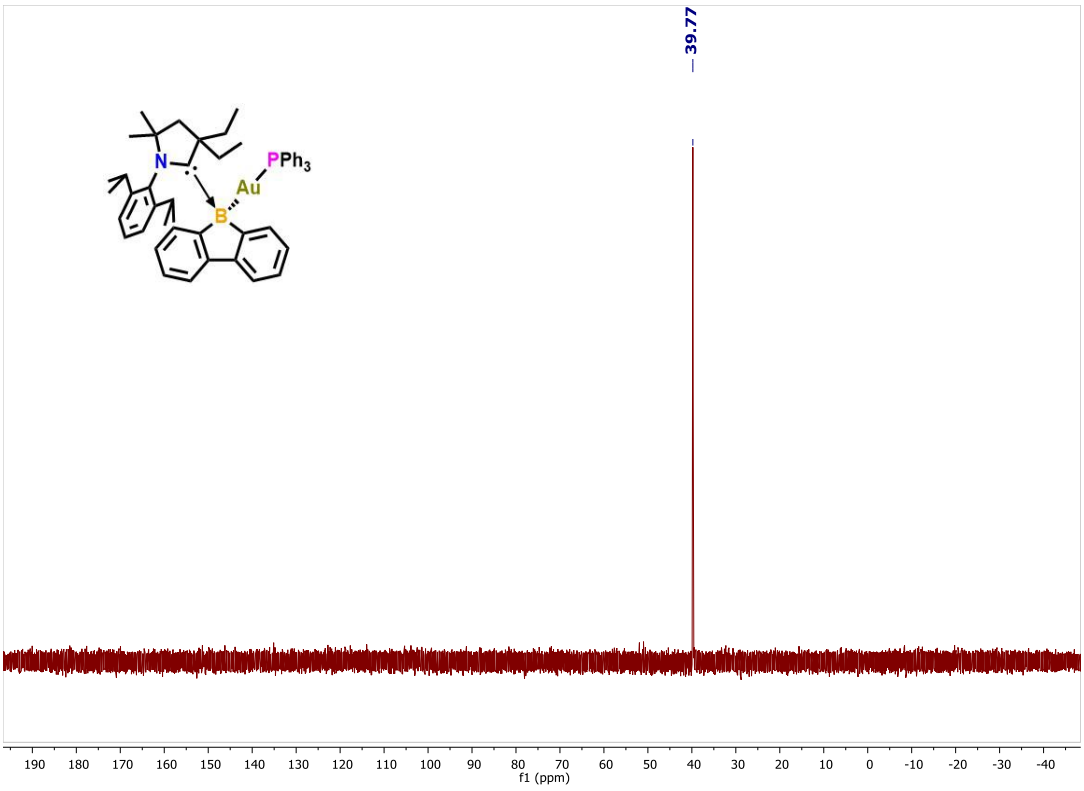

Figure A2.48. ^{31}P NMR spectrum (243 MHz, THF-d_8, 298 K) of **4.9**.

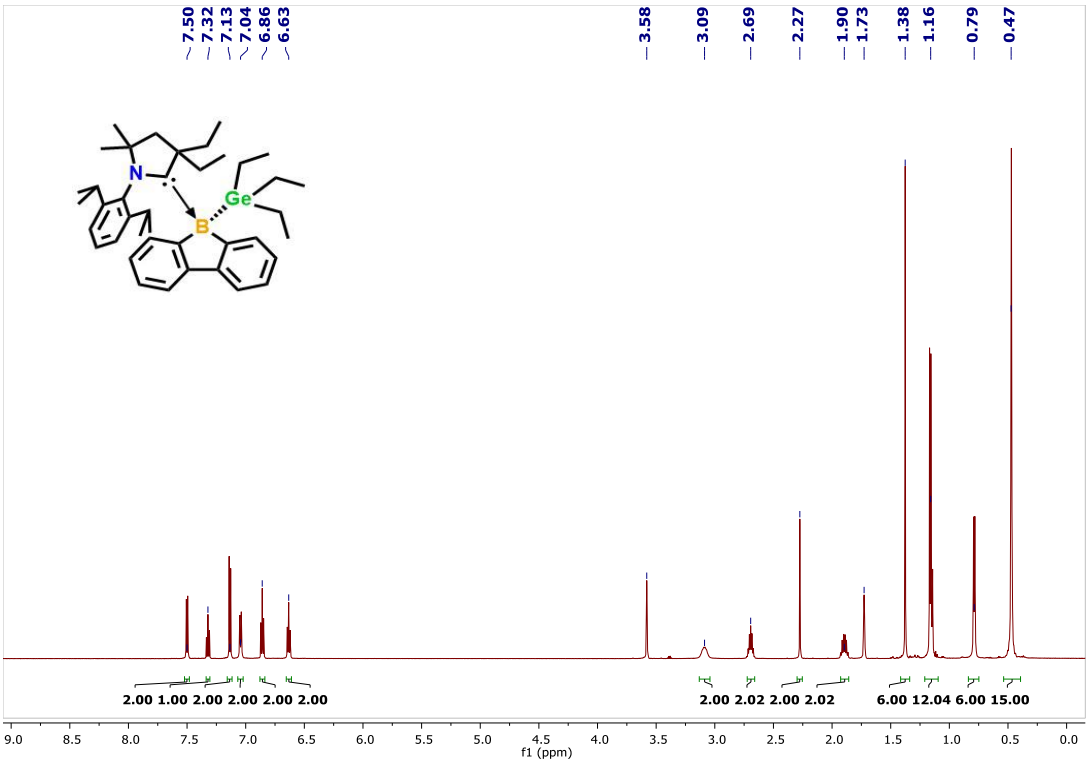

Figure A2.49. ^{1}H NMR spectrum (600 MHz, THF-d_8, 298 K) of **4.10**.

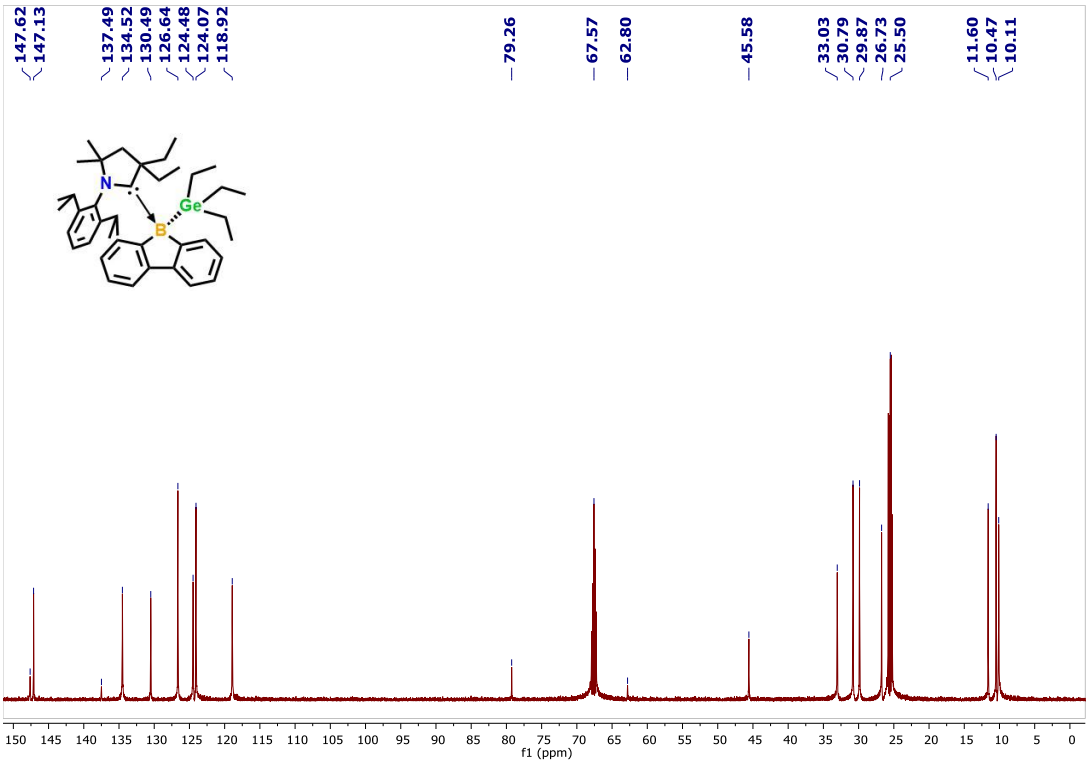

Figure A2.50. ^{13}C{^{1}H} NMR spectrum (151 MHz, THF-d_8, 298K) of **4.10**.

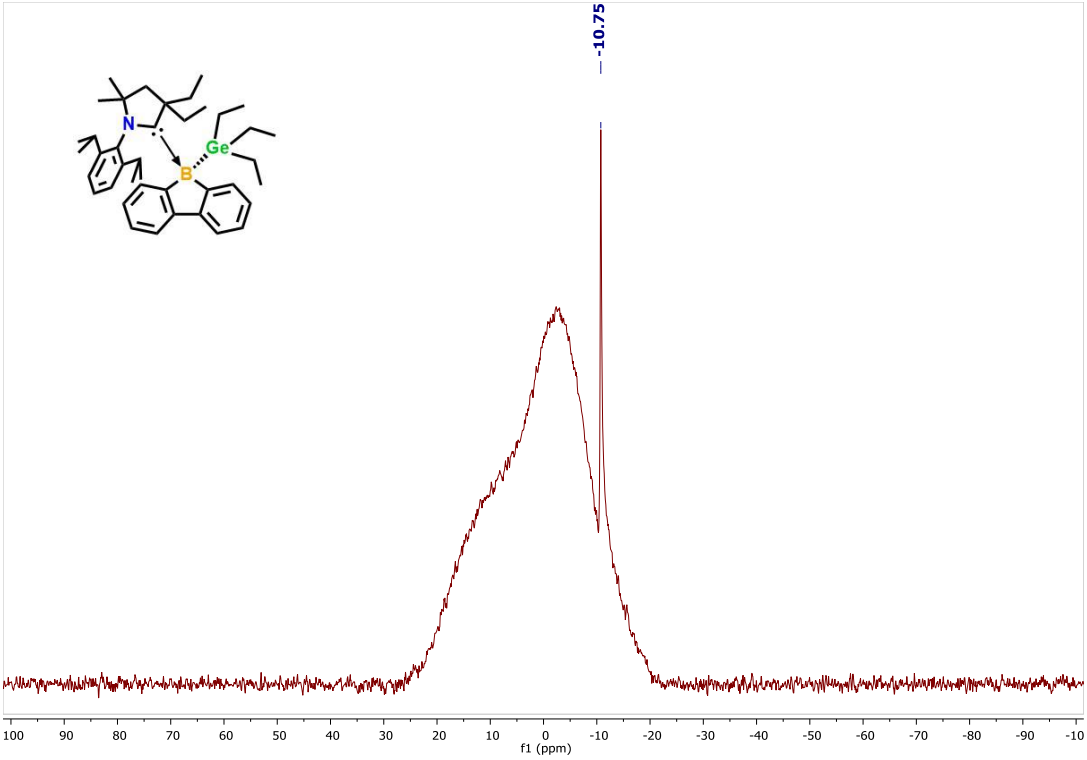

Figure A2.51. $^{11}B\{^{1}H\}$ NMR spectrum (193 MHz, THF-d_8, 298 K) of **4.10**.

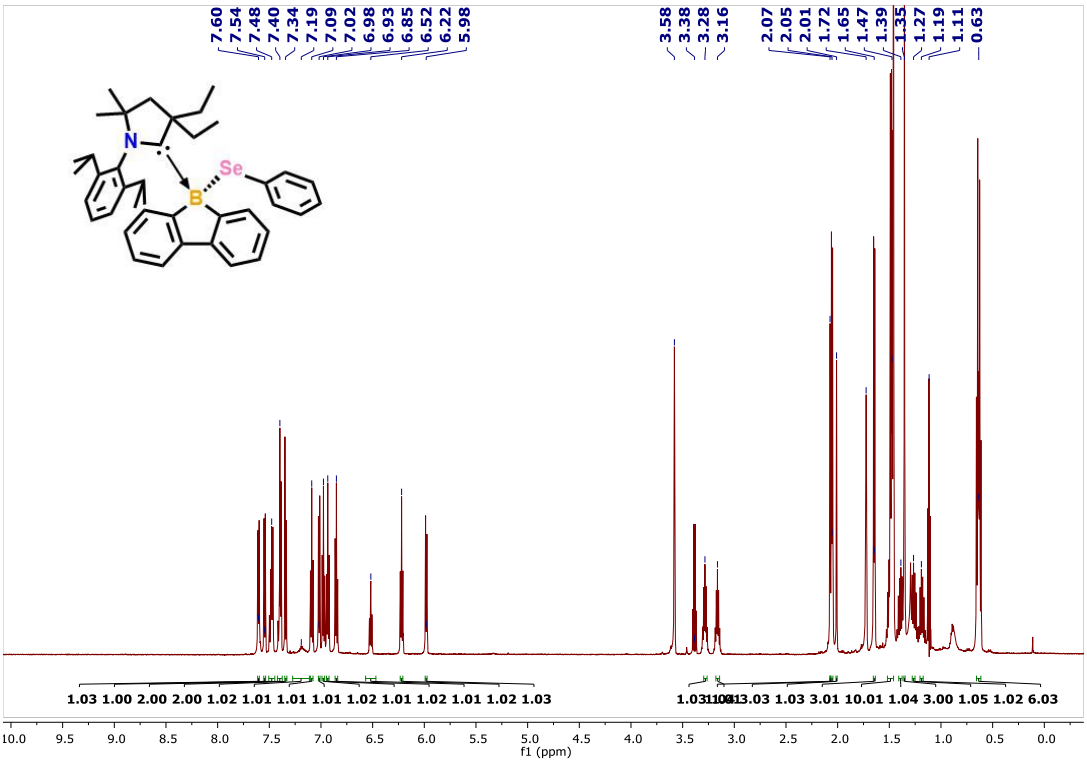

Figure A2.52. ^{1}H NMR spectrum (600 MHz, THF-d_8, 298 K) of **4.11**.

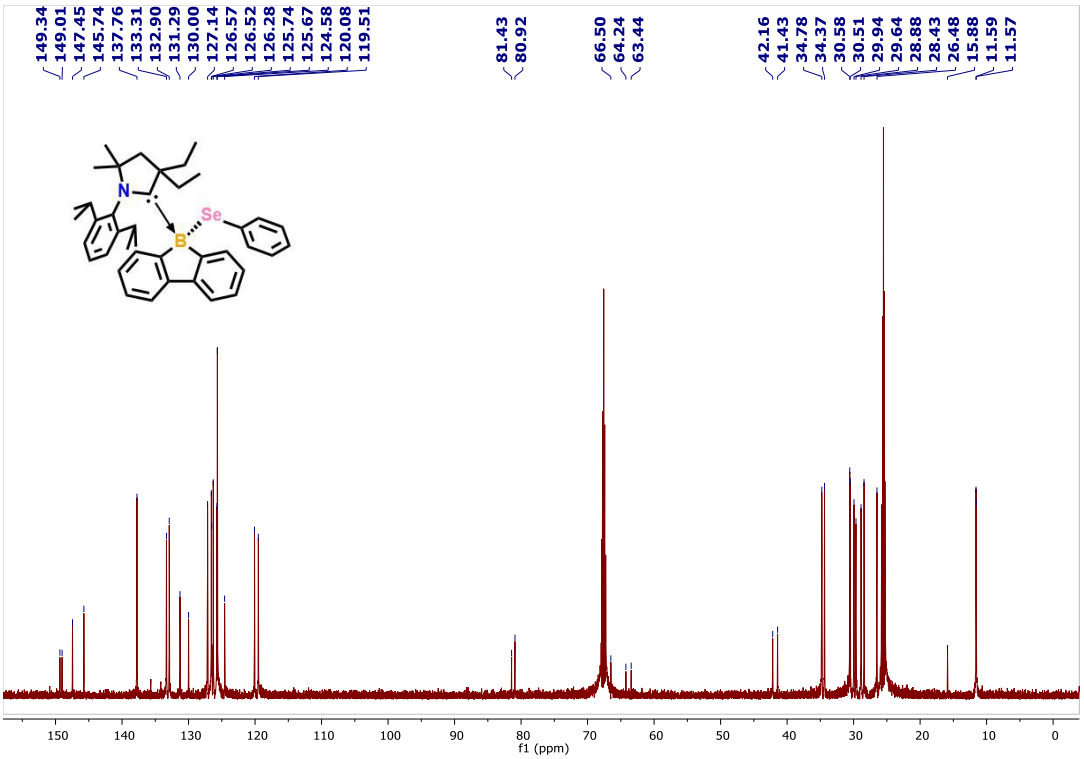

Figure A2.53. $^{13}C\{^{1}H\}$ NMR spectrum (151 MHz, THF-d_8, 298K) of **4.11**.

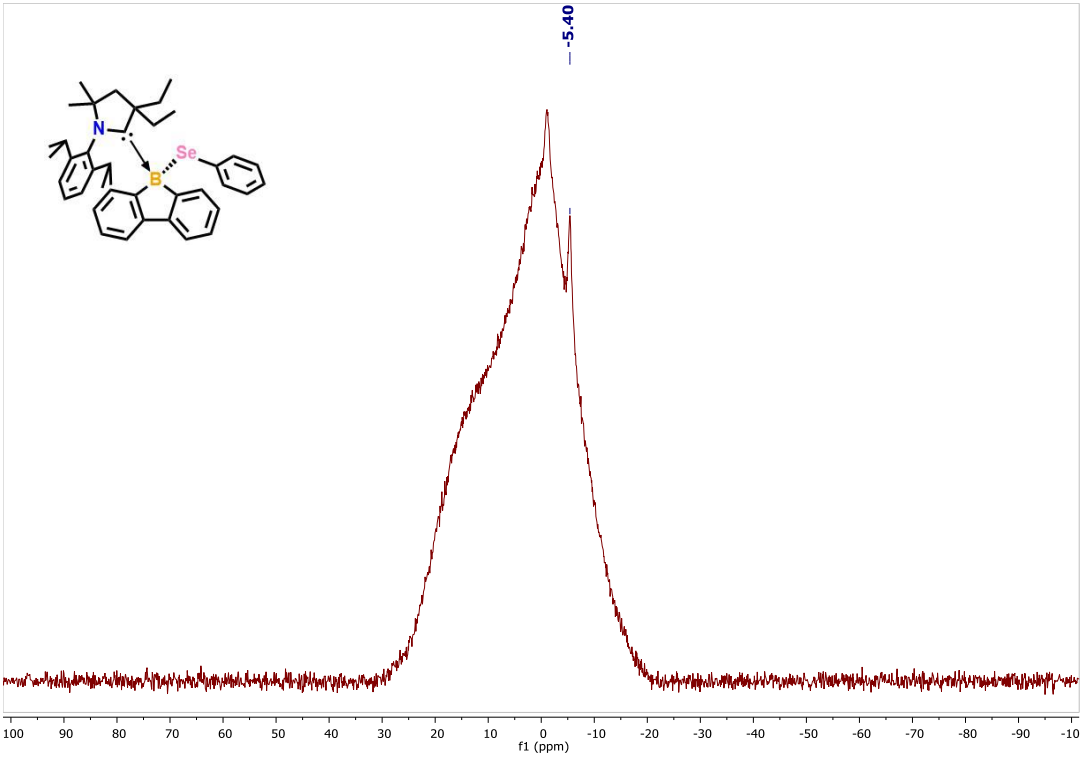

Figure A2.54. ^{11}B NMR spectrum (193 MHz, THF-d_8, 298 K) of **4.11**.

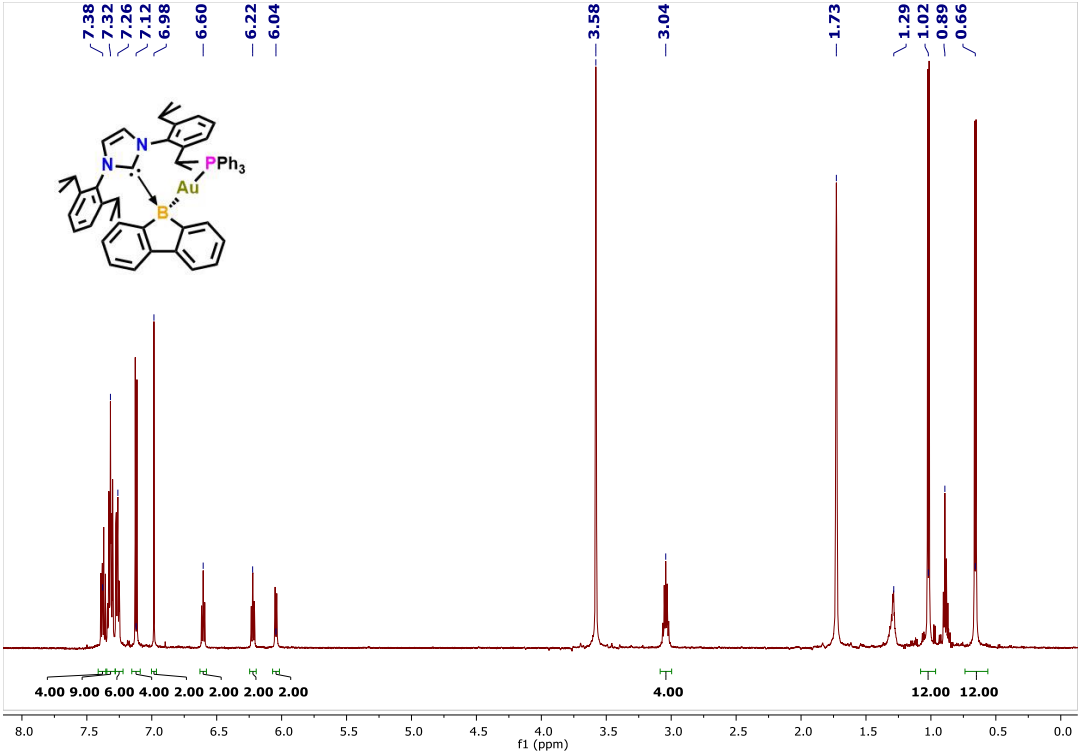

Figure A2.55. ^{1}H NMR spectrum (600 MHz, THF-d_8, 298 K) of **4.12**.

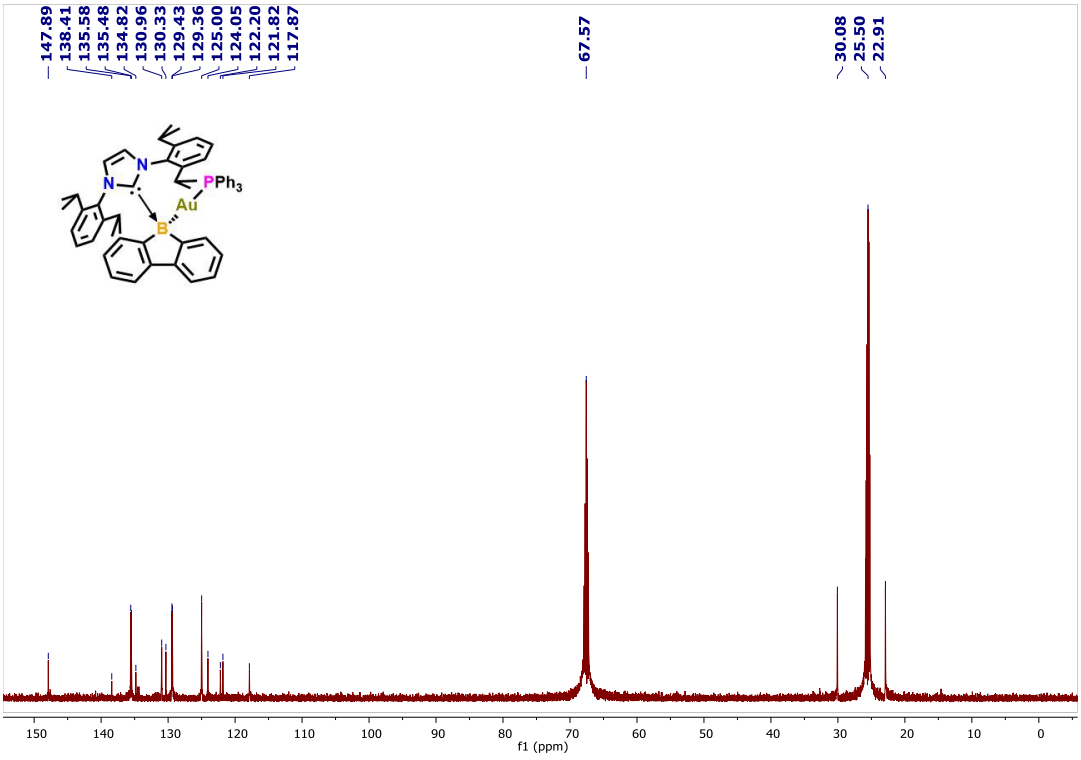

Figure A2.56. ^{13}C{^{1}H} NMR spectrum (151 MHz, THF-d_8, 298K) of **4.12**.

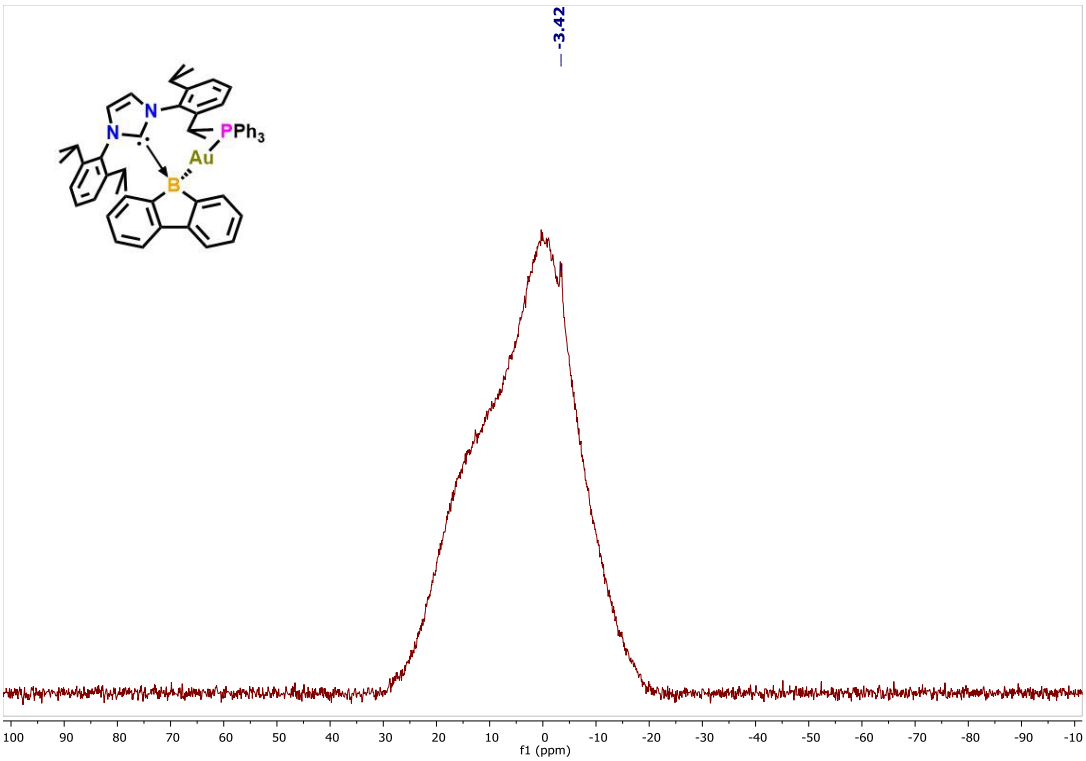

Figure A2.57. ^{11}B NMR spectrum (193 MHz, THF-d_8, 298 K) of **4.12**.

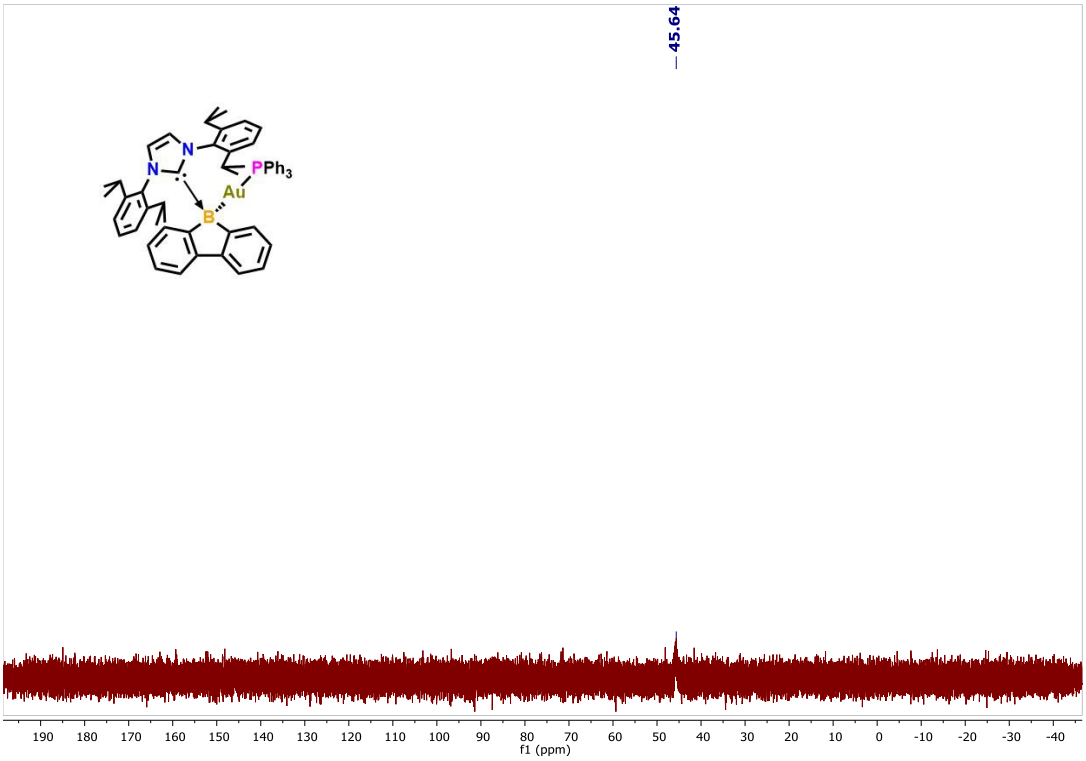

Figure A2.58. ^{31}P NMR spectrum (243 MHz, THF-d_8, 298 K) of **4.12**.

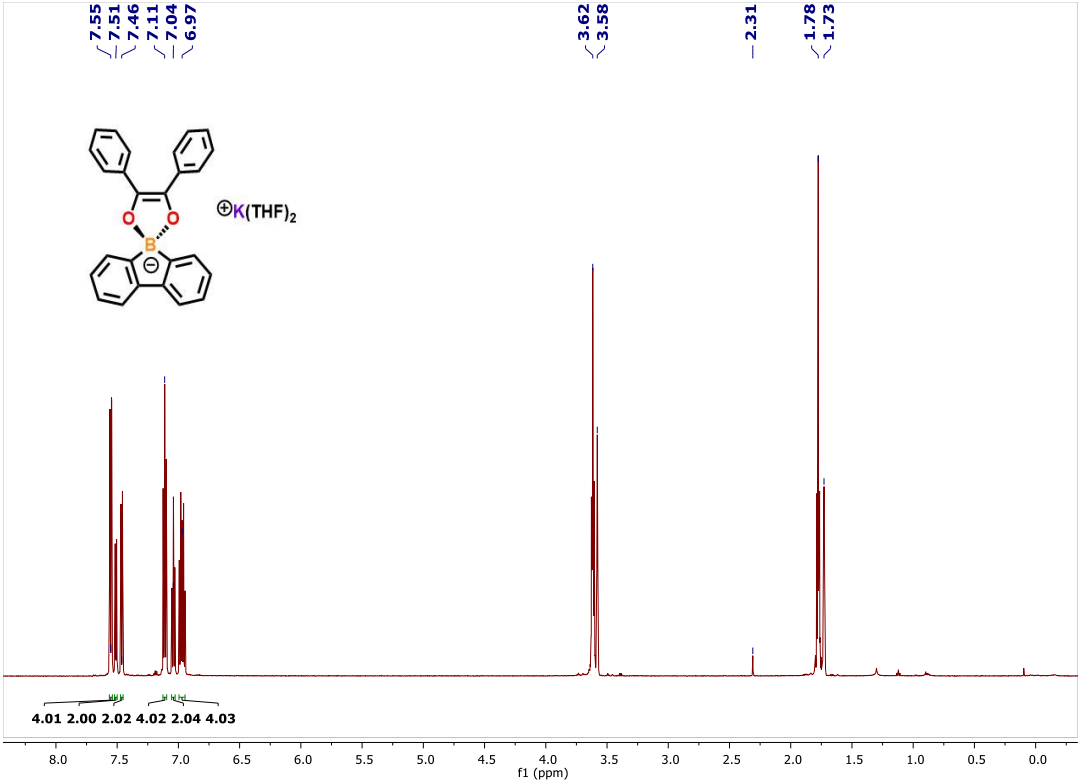

Figure A2.59. ^{1}H NMR spectrum (600 MHz, THF-d_8, 298 K) of **4.13**.

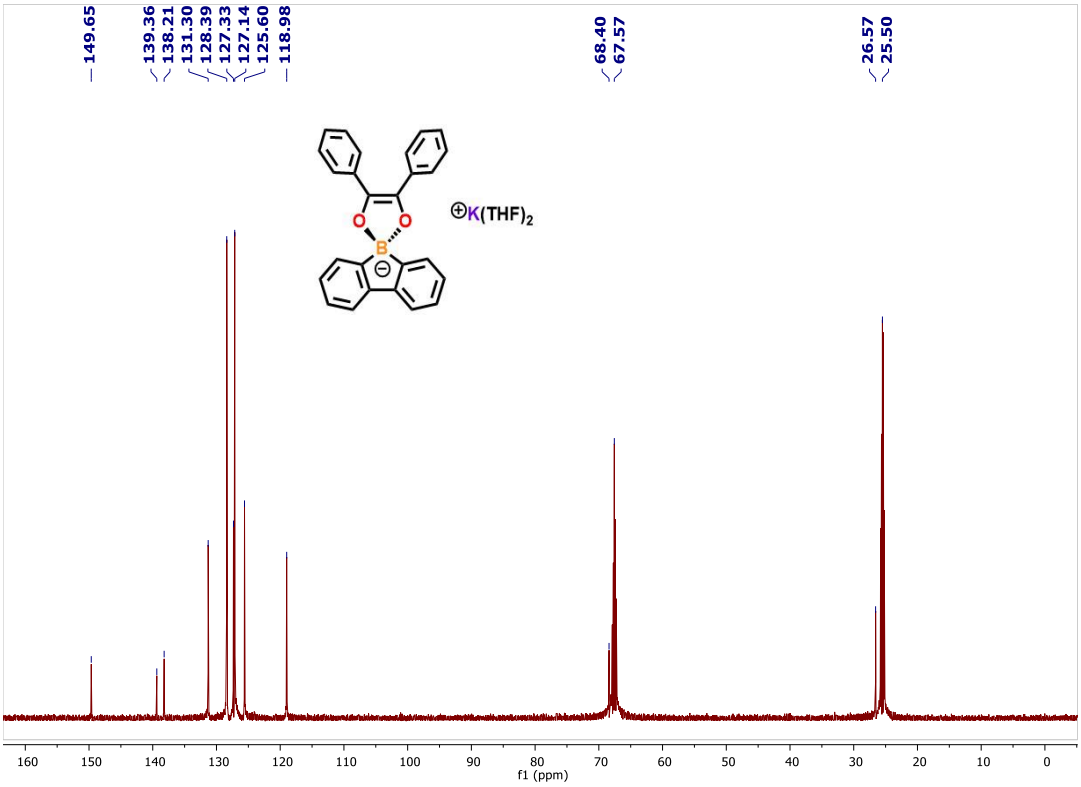

Figure A2.60. ^{13}C{^{1}H} NMR spectrum (151 MHz, THF-d_8, 298K) of **4.13**.

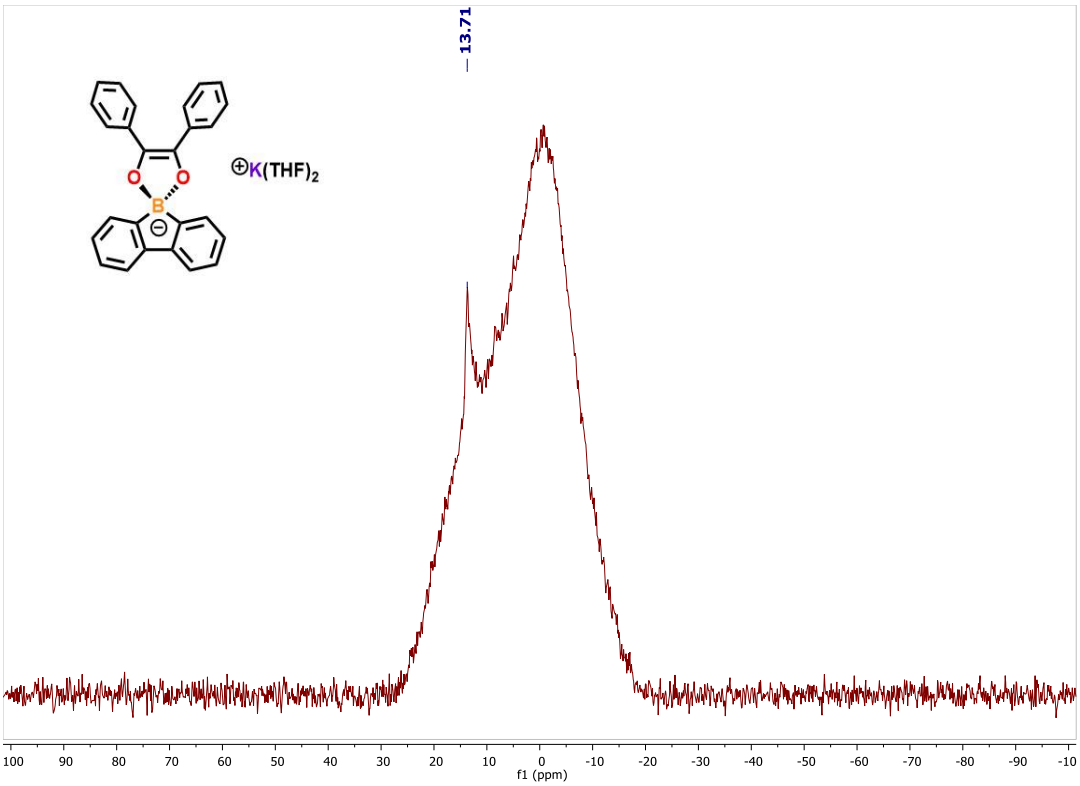

Figure A2.61. $^{11}B\{^{1}H\}$ NMR spectrum (193 MHz, THF-d_8, 298 K) of **4.13**.

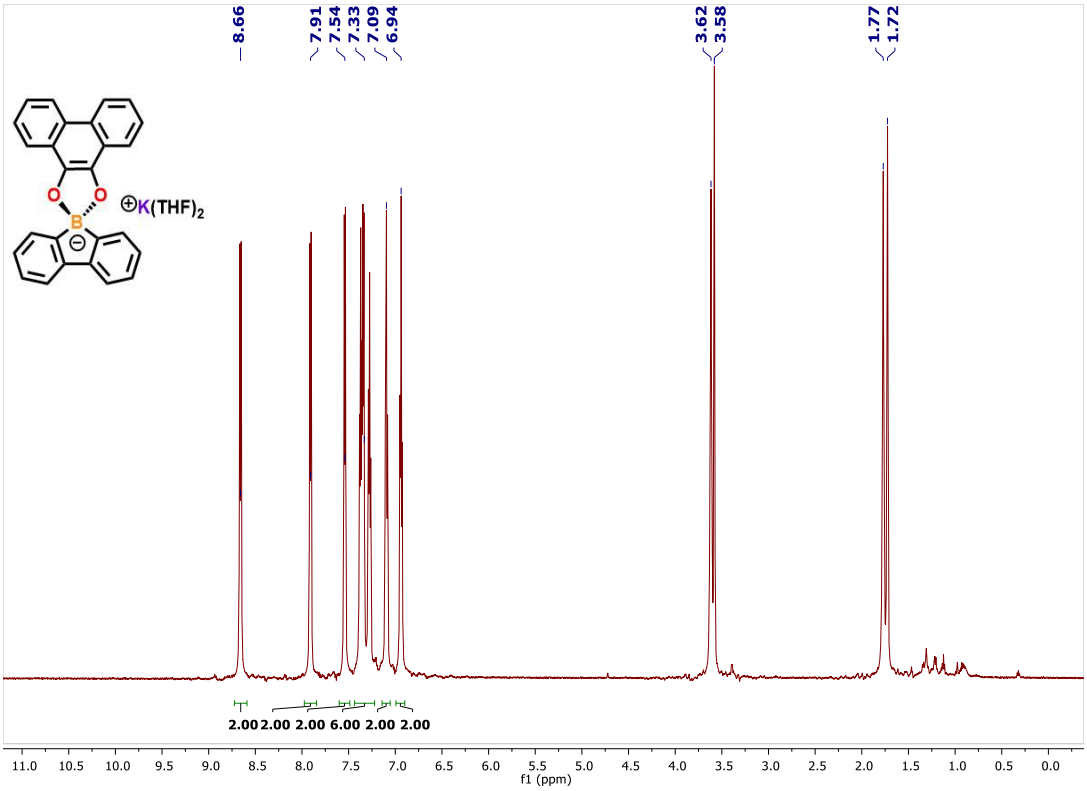

Figure A2.62. ^{1}H NMR spectrum (600 MHz, THF-d_8, 298 K) of **4.14**.

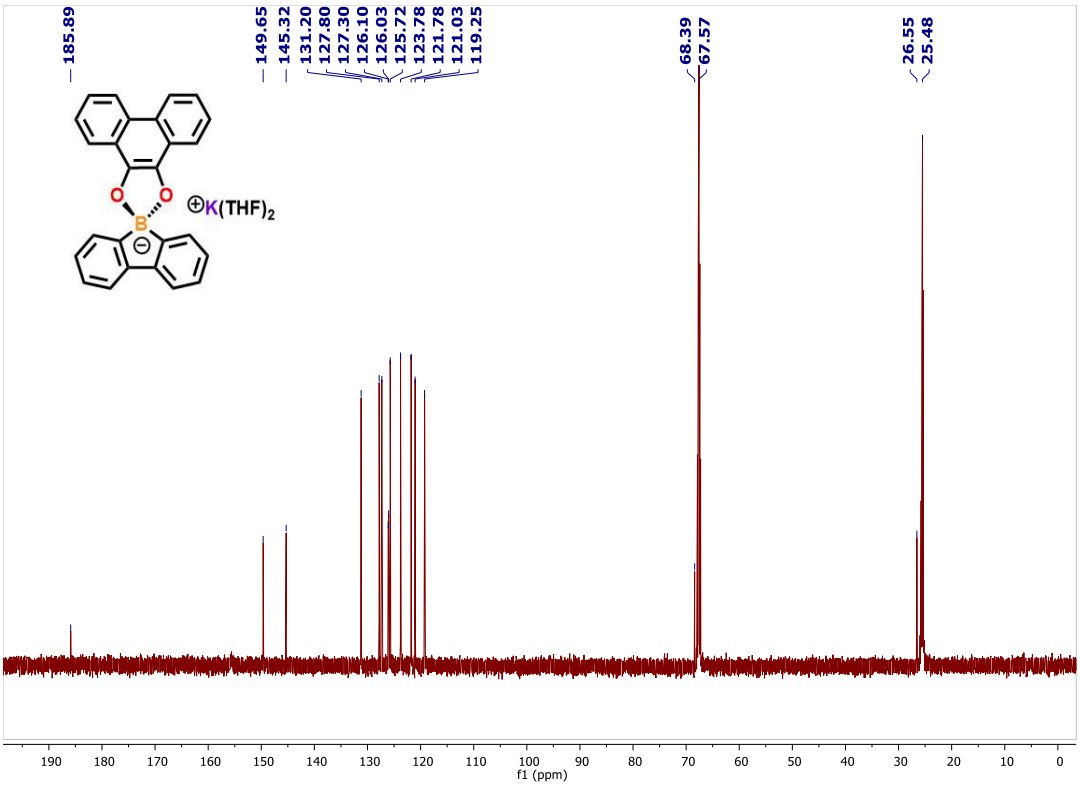

Figure A2.63. $^{13}C\{^{1}H\}$ NMR spectrum (151 MHz, THF-d_8, 298K) of **4.14**.

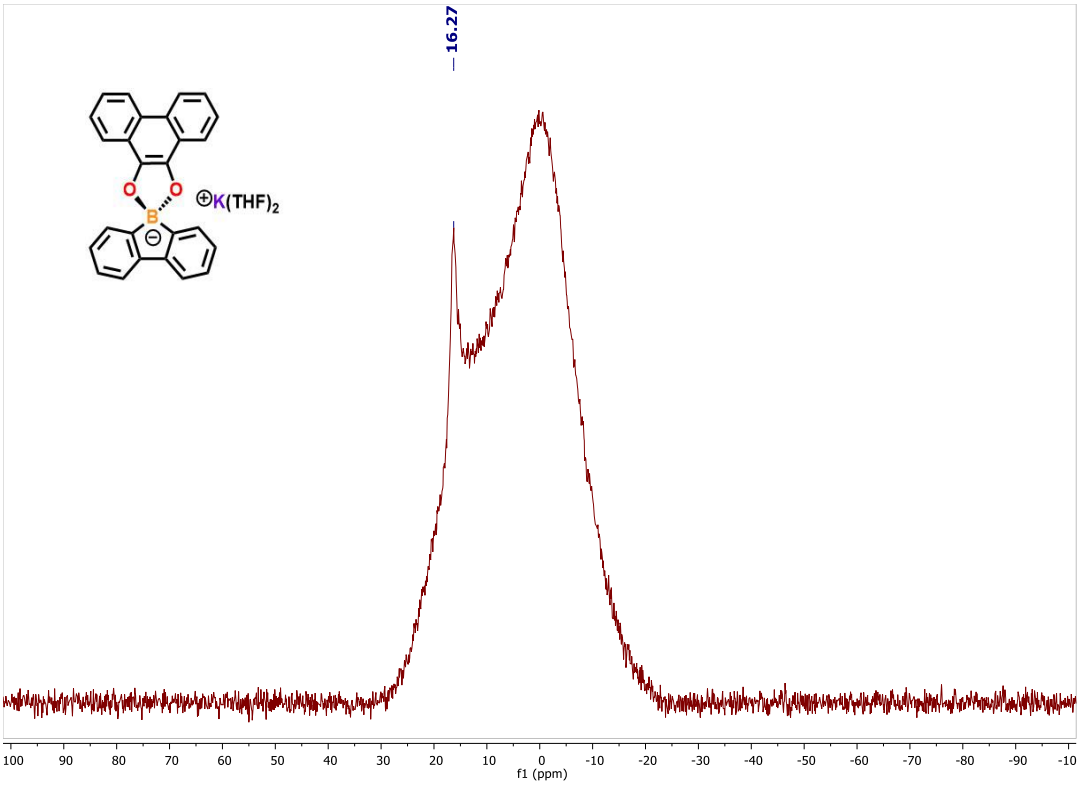

Figure A2.64. ^{11}B NMR spectrum (193 MHz, THF-d_8, 298 K) of **4.14**.

Chapter Five:

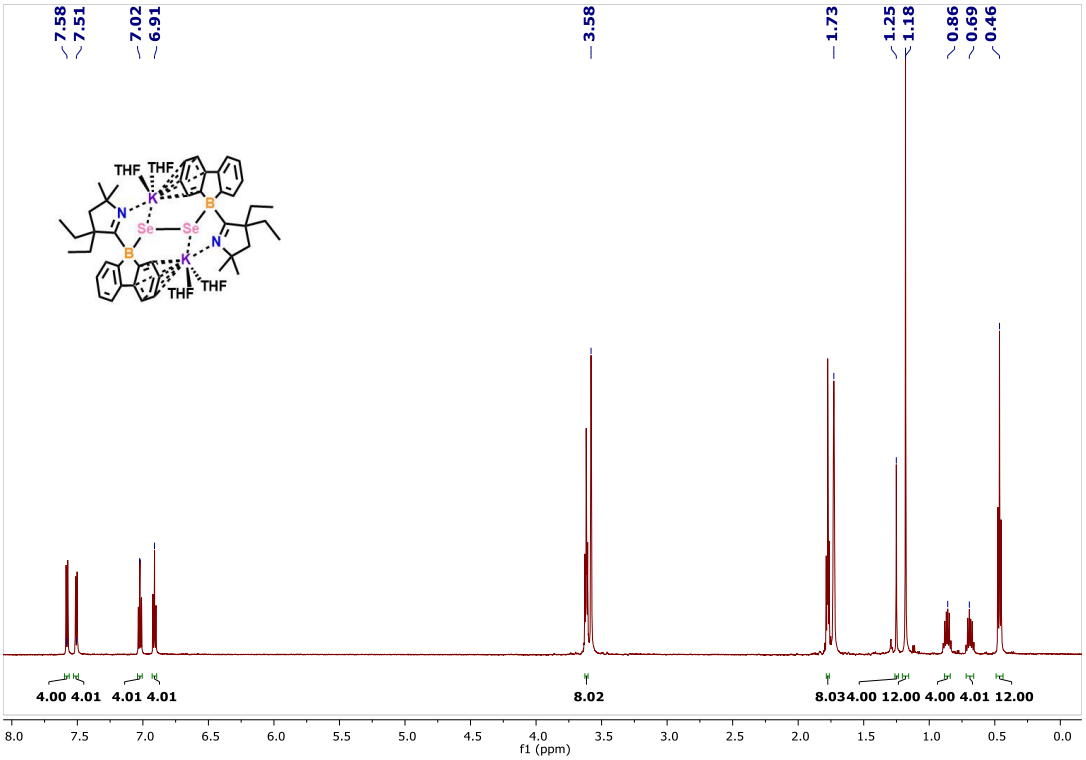

Figure A2.65. ^{1}H NMR spectrum (600 MHz, THF-d_8, 298 K) of **5.2**.

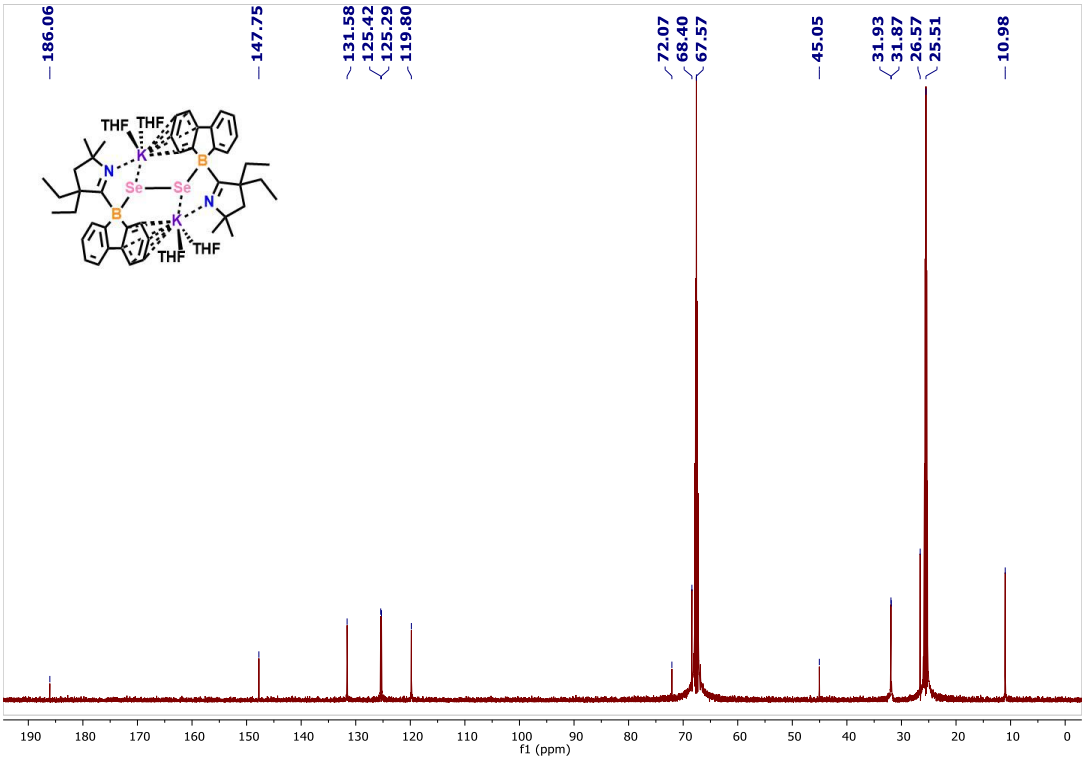

Figure A2.66. ^{13}C{^{1}H} NMR spectrum (151 MHz, THF-d_8, 298 K) of **5.2**.

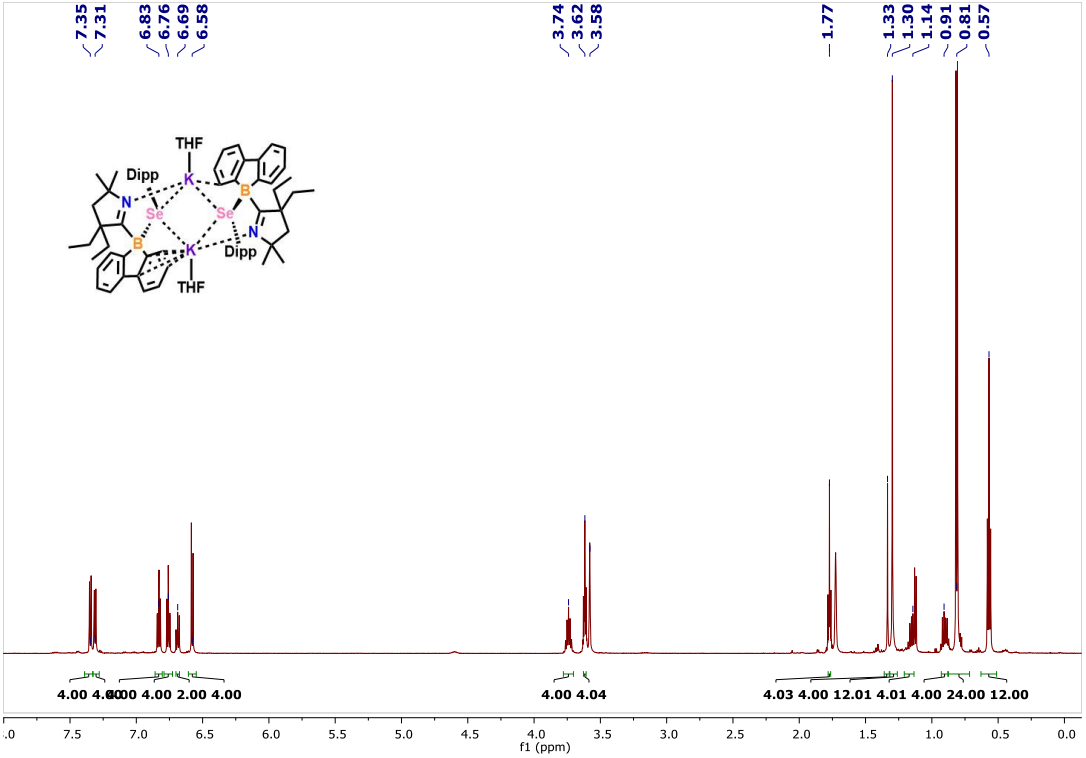

Figure A2.67. ^{1}H NMR spectrum (600 MHz, THF-d_8, 298 K) of **5.3**.

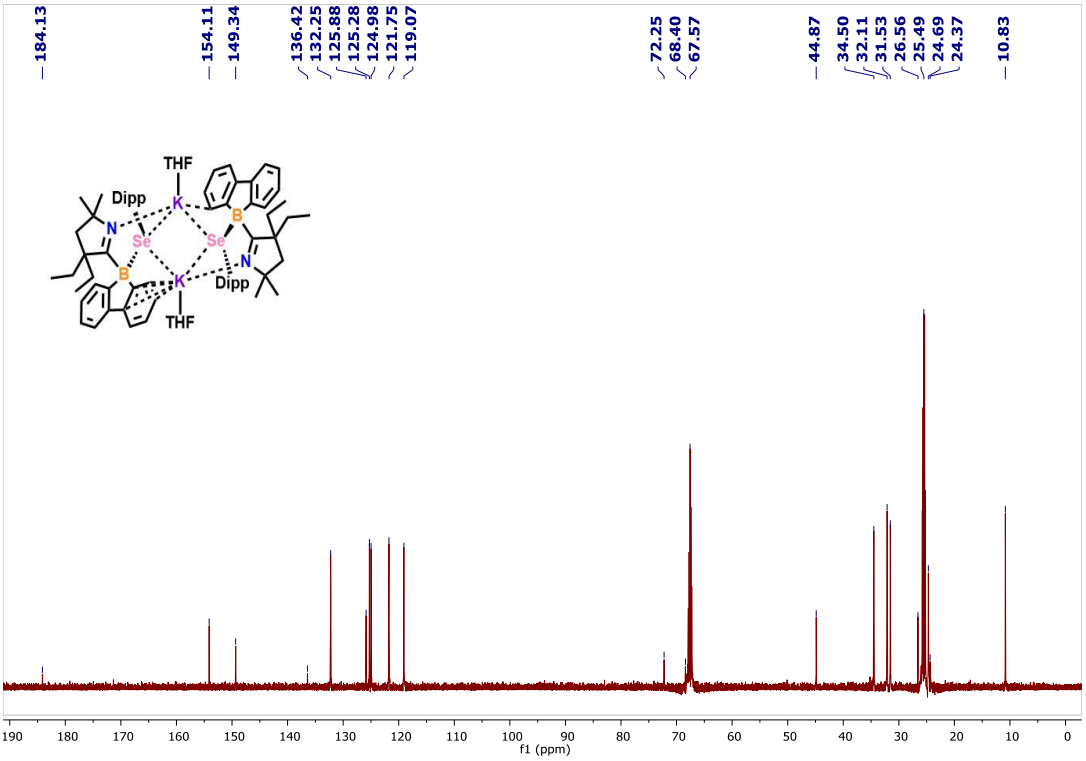

Figure A2.68. ^{13}C{^{1}H} NMR spectrum (151 MHz, THF-d_8, 298 K) of **5.3**.

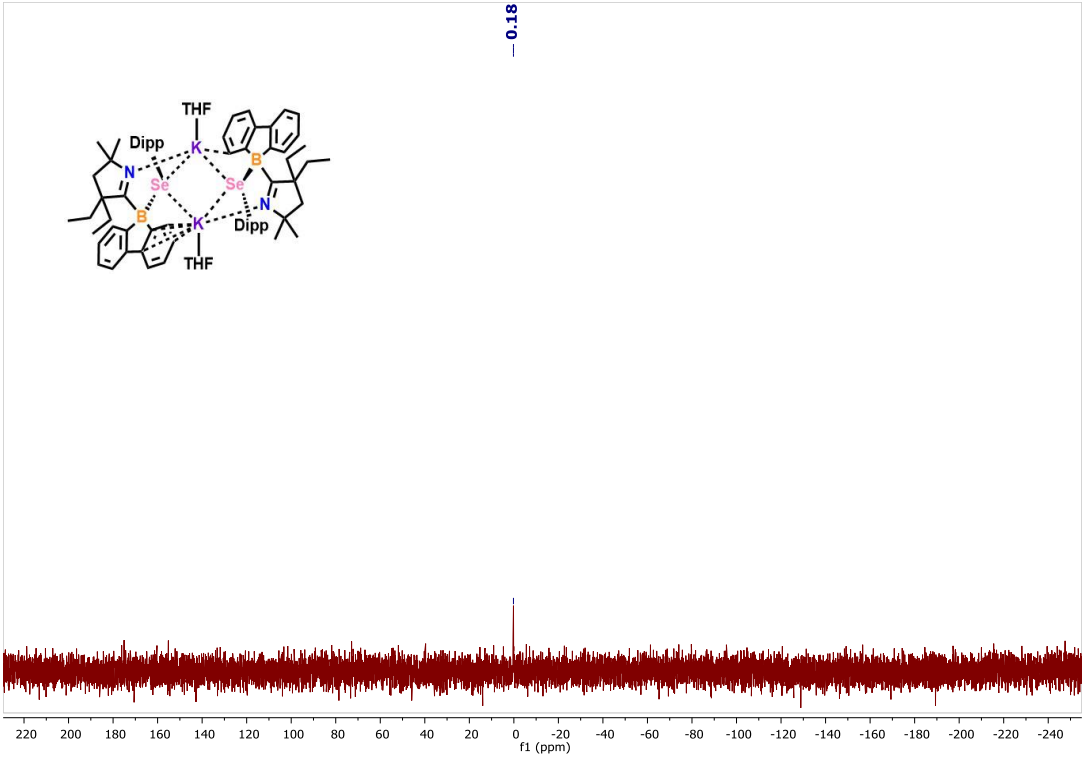

Figure A2.69. $^{77}Se\{^{1}H\}$ NMR spectrum (114 MHz, THF-d_8, 298K) of **5.3**.

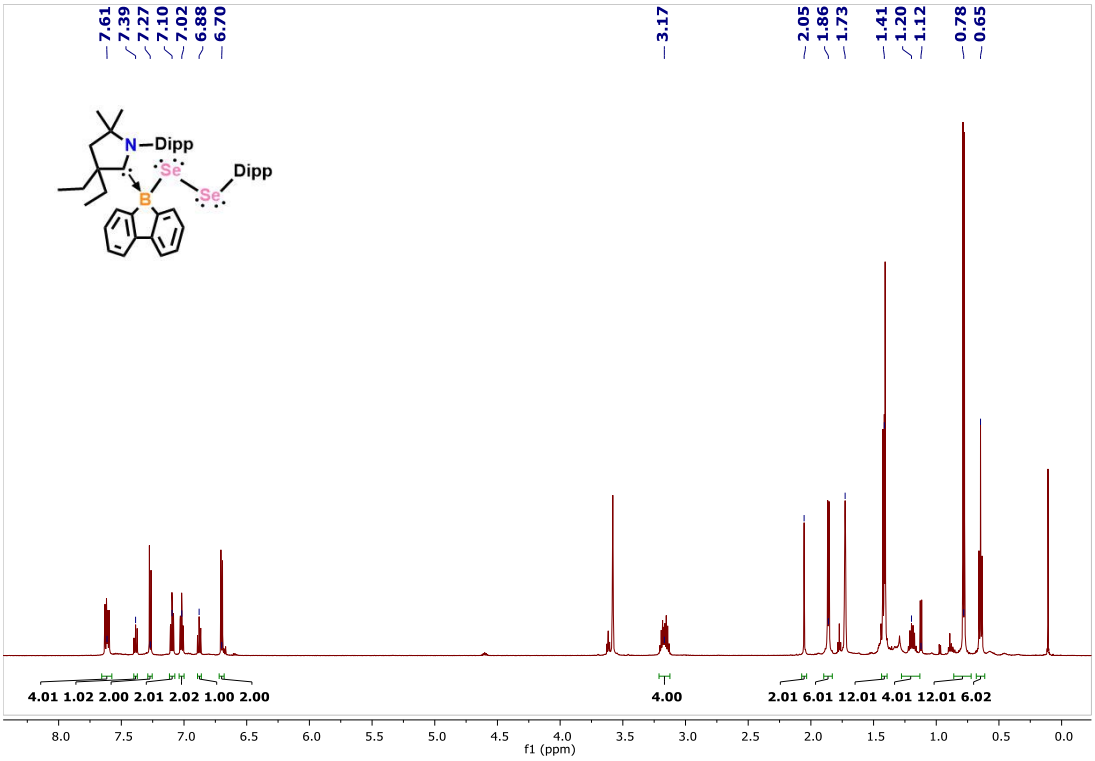

Figure A2.70. ^{1}H NMR spectrum (600 MHz, THF-d_8, 298 K) of **5.4**.

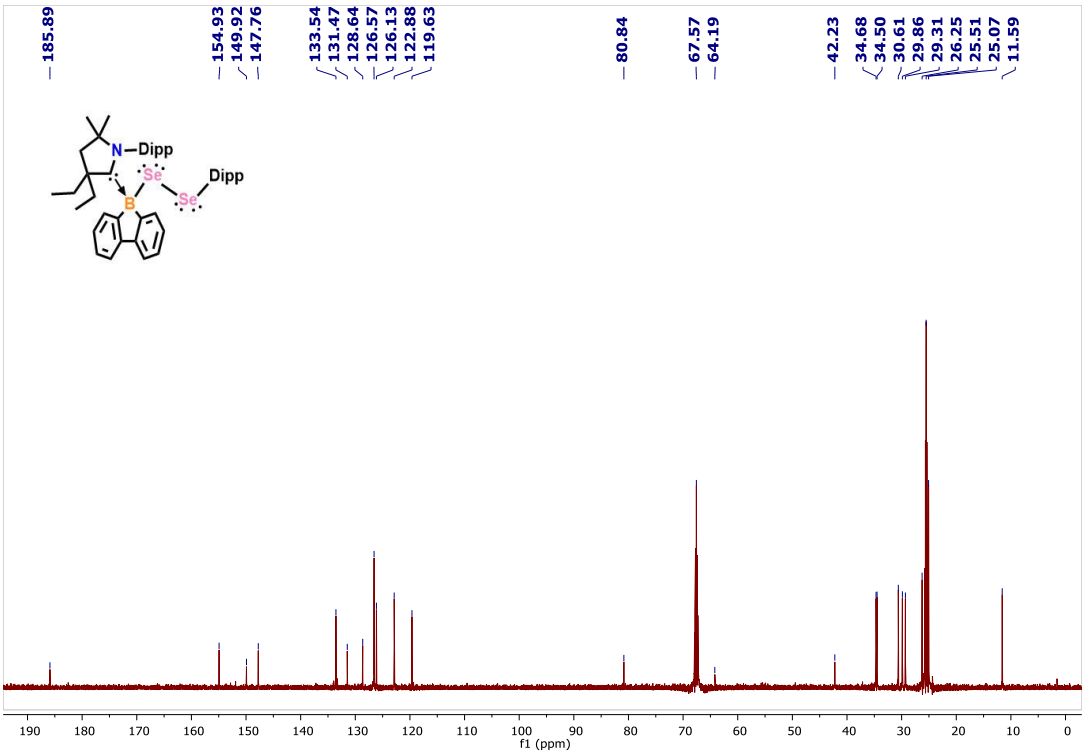

Figure A2.71. $^{13}C\{^{1}H\}$ NMR spectrum (151 MHz, THF-d_8, 298 K) of **5.4**.

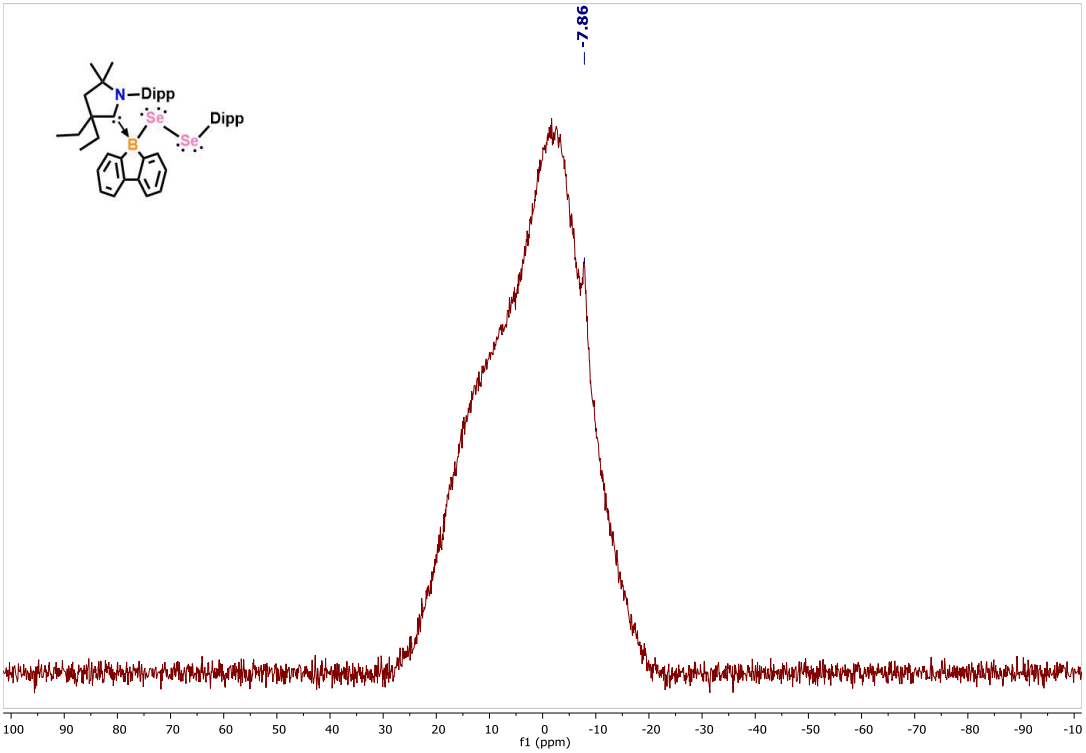

Figure A2.72. $^{11}B\{^{1}H\}$ NMR spectrum (193 MHz, THF-d_8, 298 K) of **5.4**.

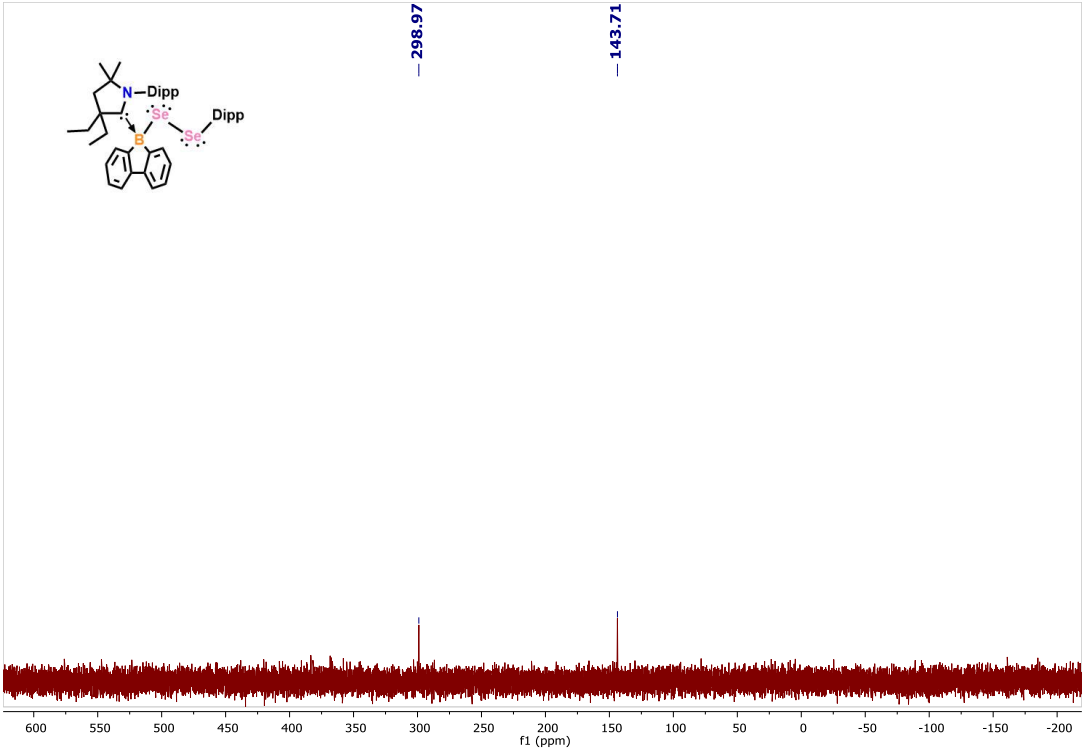

Figure A2.73. $^{77}Se\{^{1}H\}$ NMR spectrum (114 MHz, THF-d_8, 298K) of **5.4**.

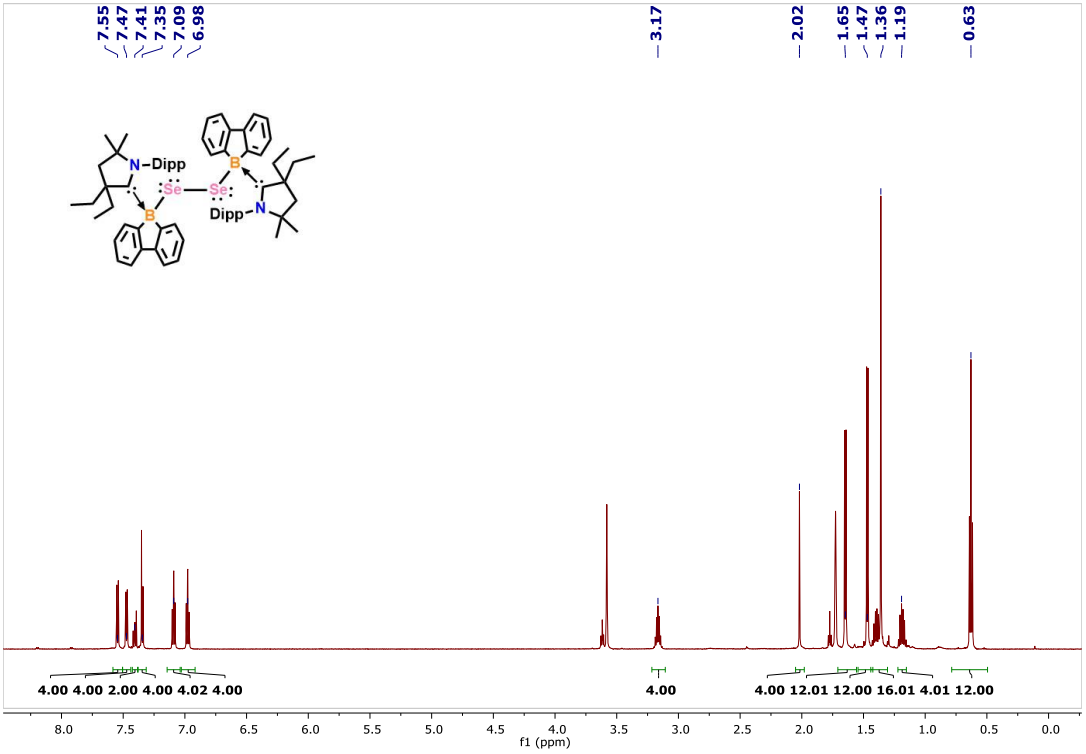

Figure A2.74. ^{1}H NMR spectrum (600 MHz, THF-d_8, 298 K) of **5.5**.

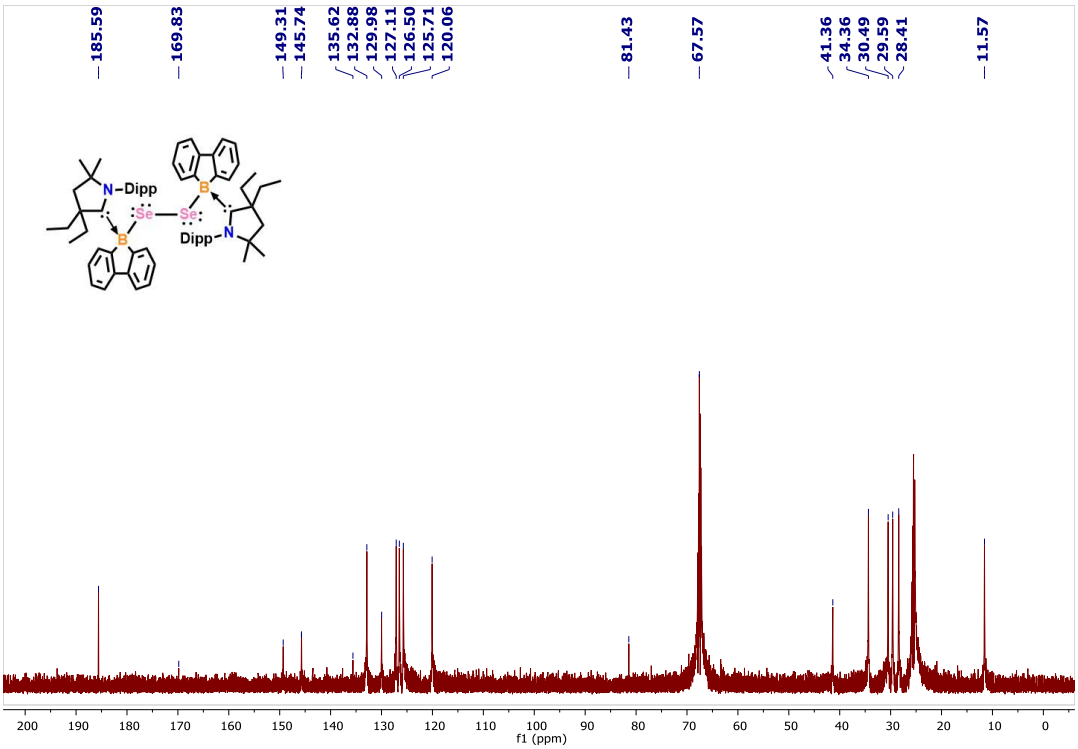

Figure A2.75. ^{13}C NMR spectrum (151 MHz, THF-d_8, 298 K) of **5.5**.

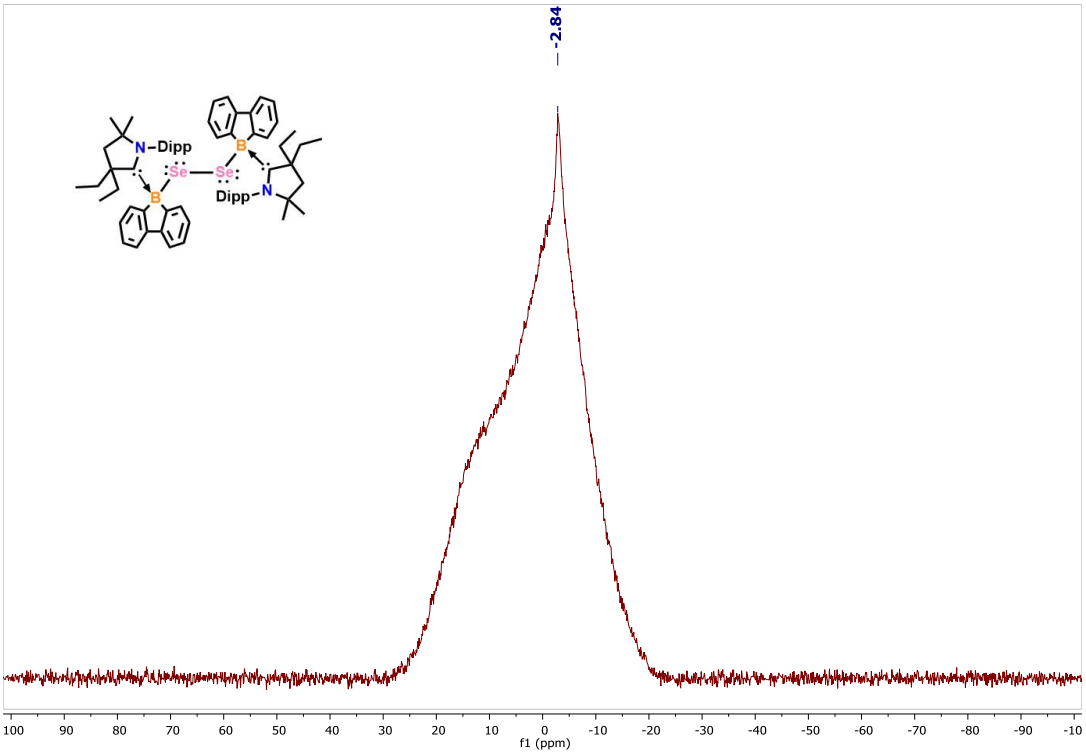

Figure A2.76. $^{11}B\{^1H\}$ NMR spectrum (193 MHz, THF-d_8, 298 K) of **5.5**.

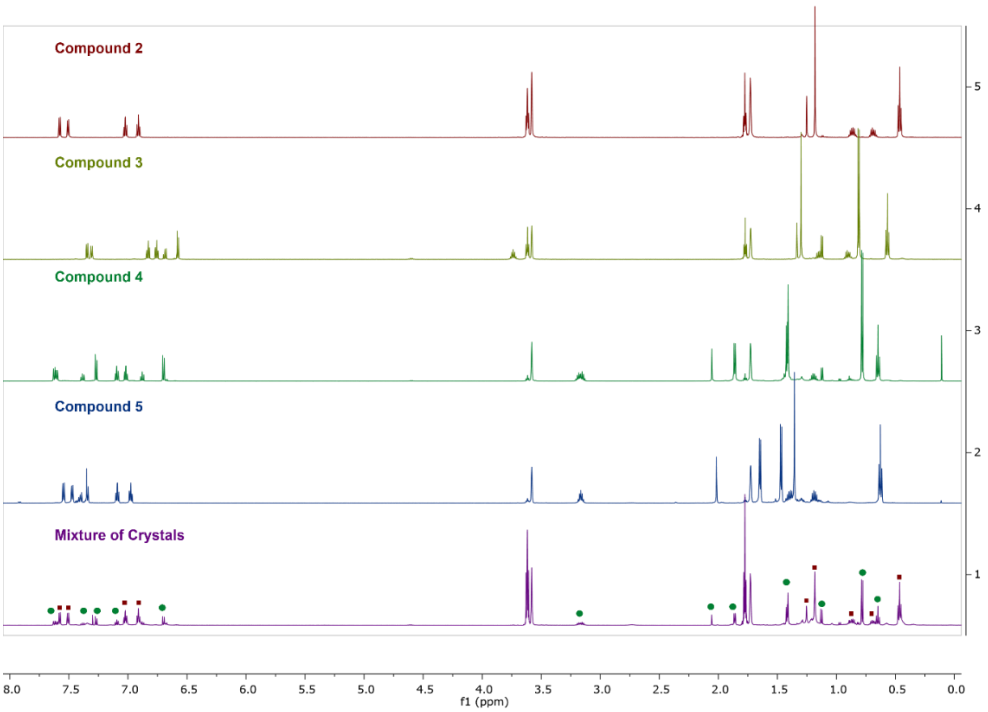

Figure A2.77. Stacked ^{1}H NMR spectra of compounds **5.2-5.5** and a mixture of the single crystals grown from THF at -37 °C (bottom).

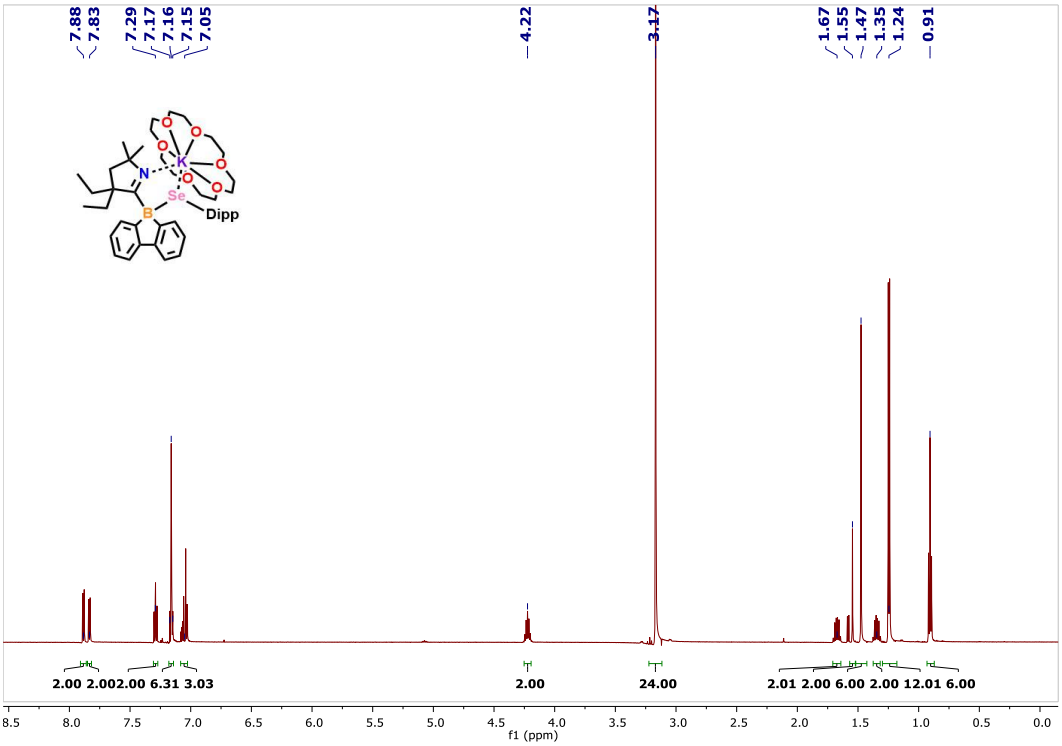

Figure A2.78. ^{1}H NMR spectrum (600 MHz, C_6D_6, 298 K) of **5.7**.

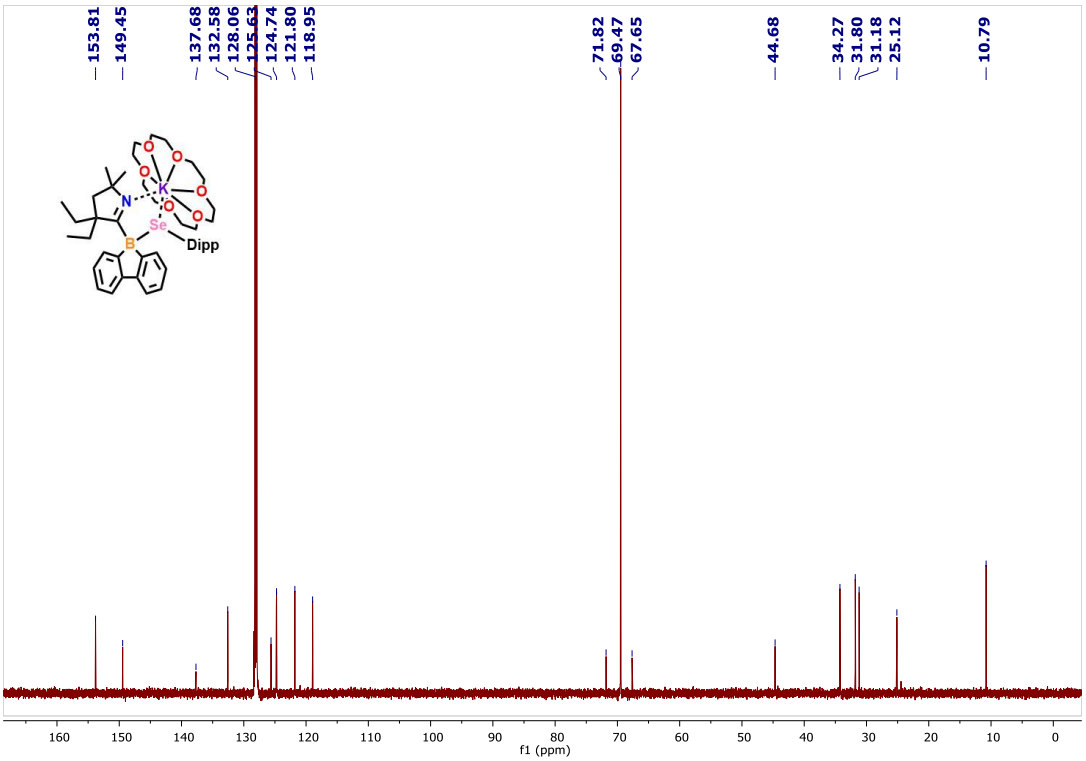

Figure A2.79. $^{13}C\{^{1}H\}$ NMR spectrum (151 MHz, C_6D_6, 298 K) of **5.7**.

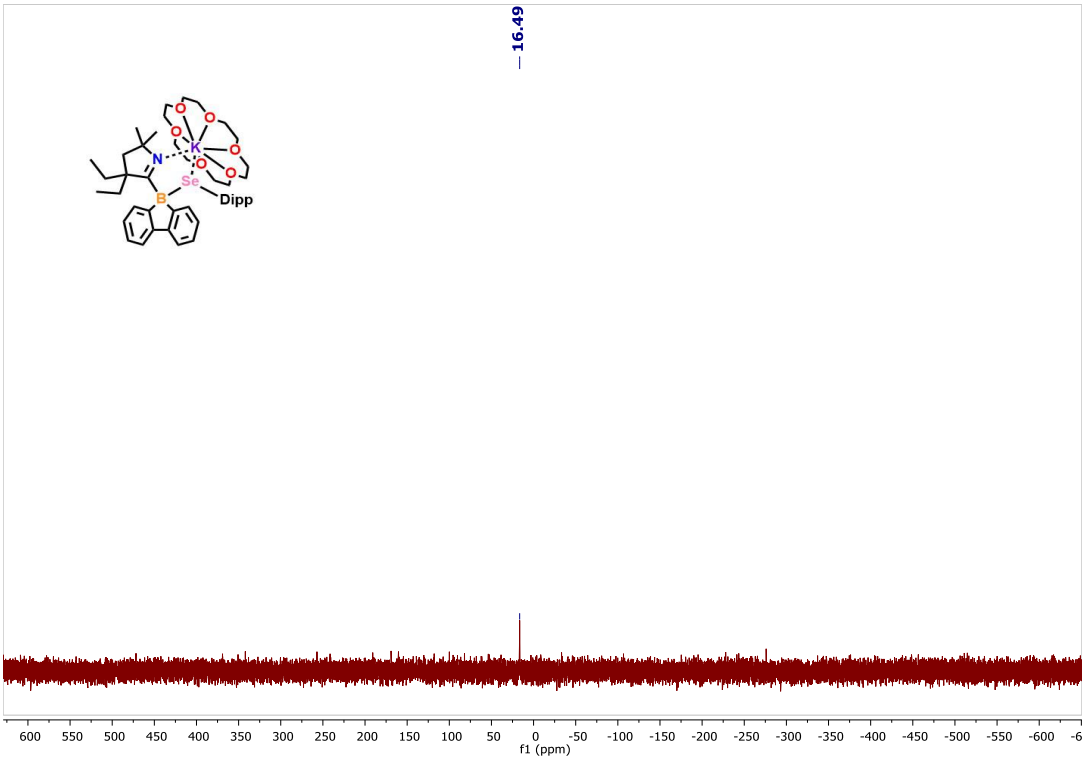

Figure A2.80. $^{77}Se\{^{1}H\}$ NMR spectrum (114 MHz, C_6D_6, 298 K) of **5.7**.

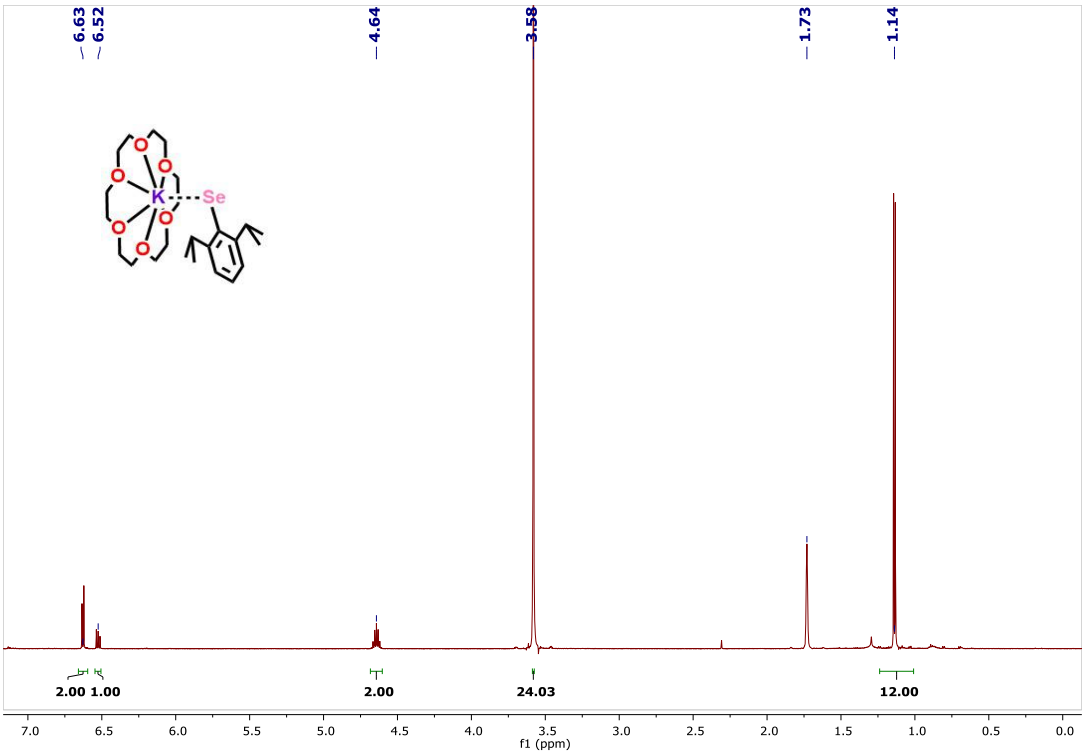

Figure A2.81 ^{1}H NMR spectrum (600 MHz, THF-d_8, 298 K) of **5.8**.

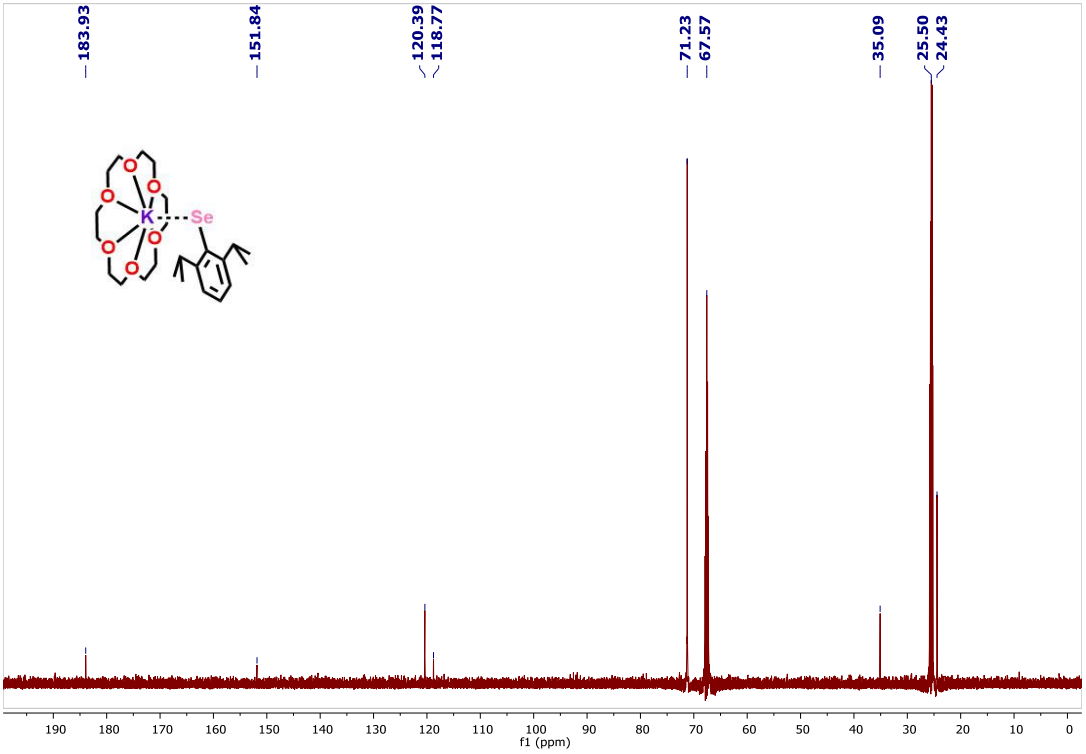

Figure A2.82. ^{13}C{^{1}H} NMR spectrum (151 MHz, THF-d_8, 298 K) of **5.8**.

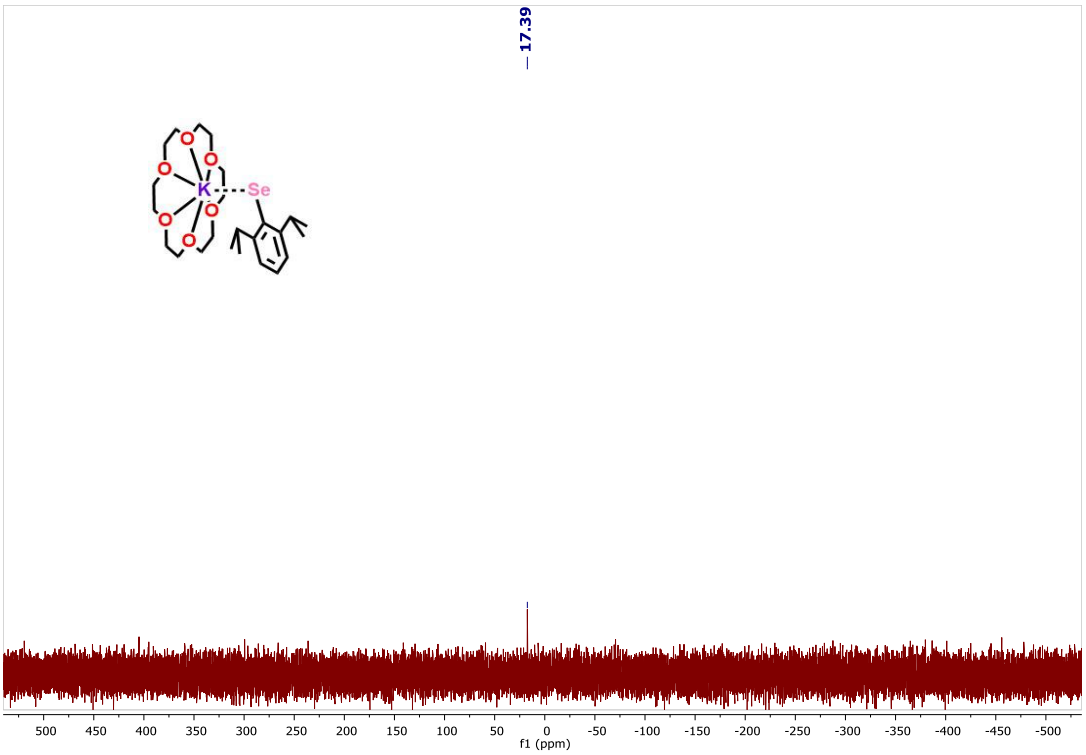

Figure A2.83. $^{77}Se\{^{1}H\}$ NMR spectrum (114 MHz, THF-d_8, 298K) of **5.8**.

Chapter Six:

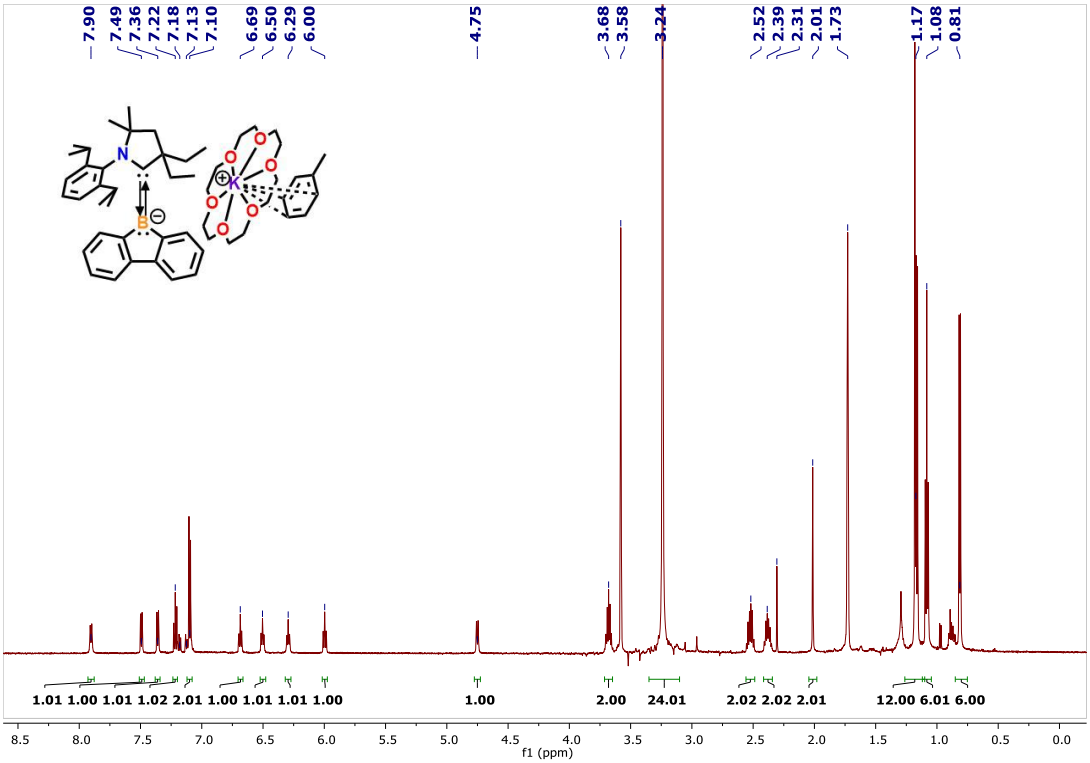

Figure A2.84. ^{1}H NMR (600 MHz, THF-d_8, 298 K) of **6.2**.

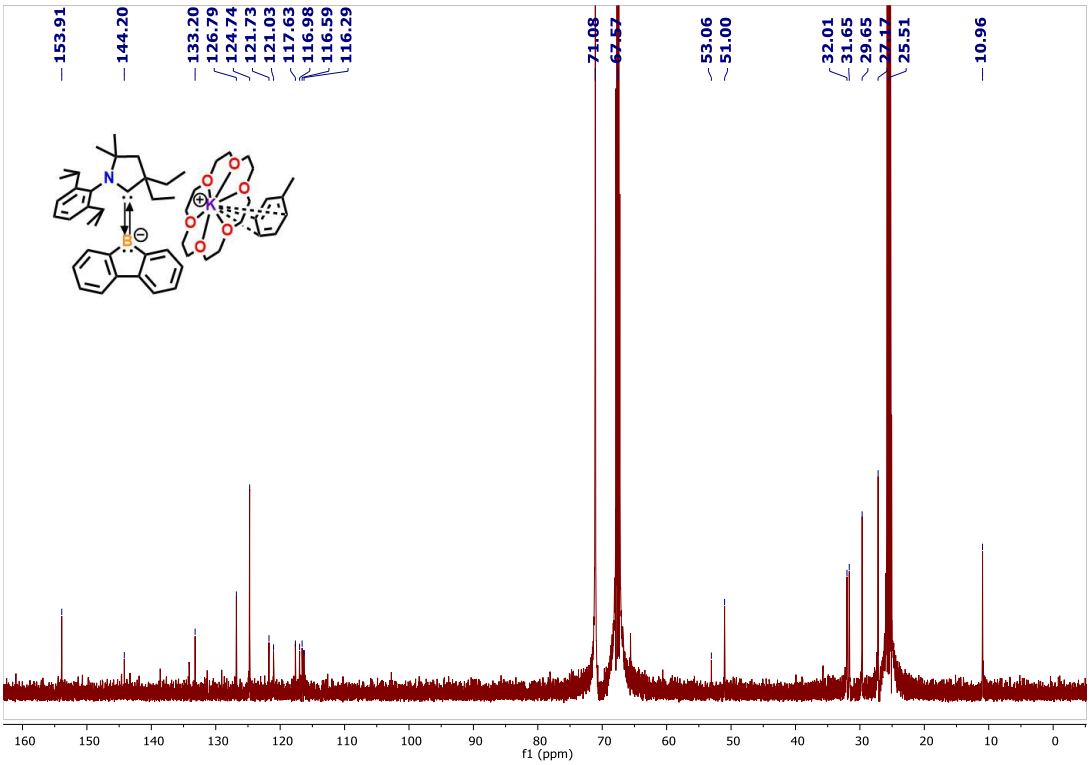

Figure A2.85. ^{13}C{^{1}H} NMR (151 MHz, THF-d_8, 298K) of **6.2**.

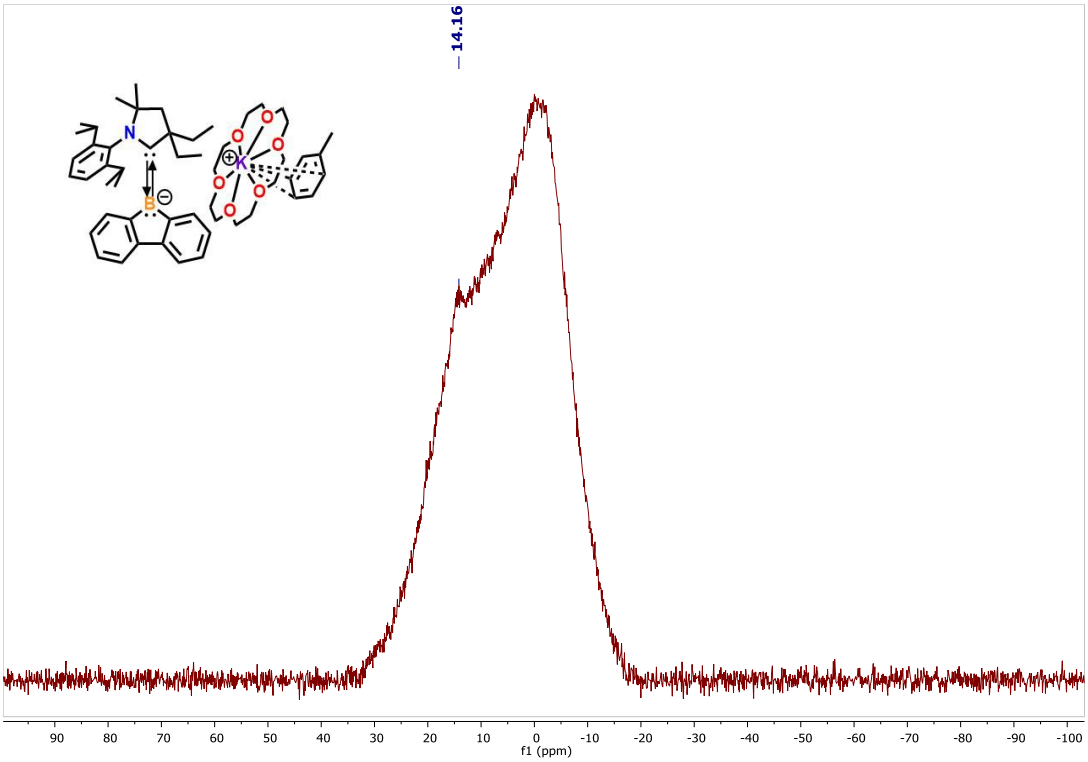

Figure A2.86. $^{11}B\{^{1}H\}$ NMR (193 MHz, THF-d_8, 298 K) of **6.2**.

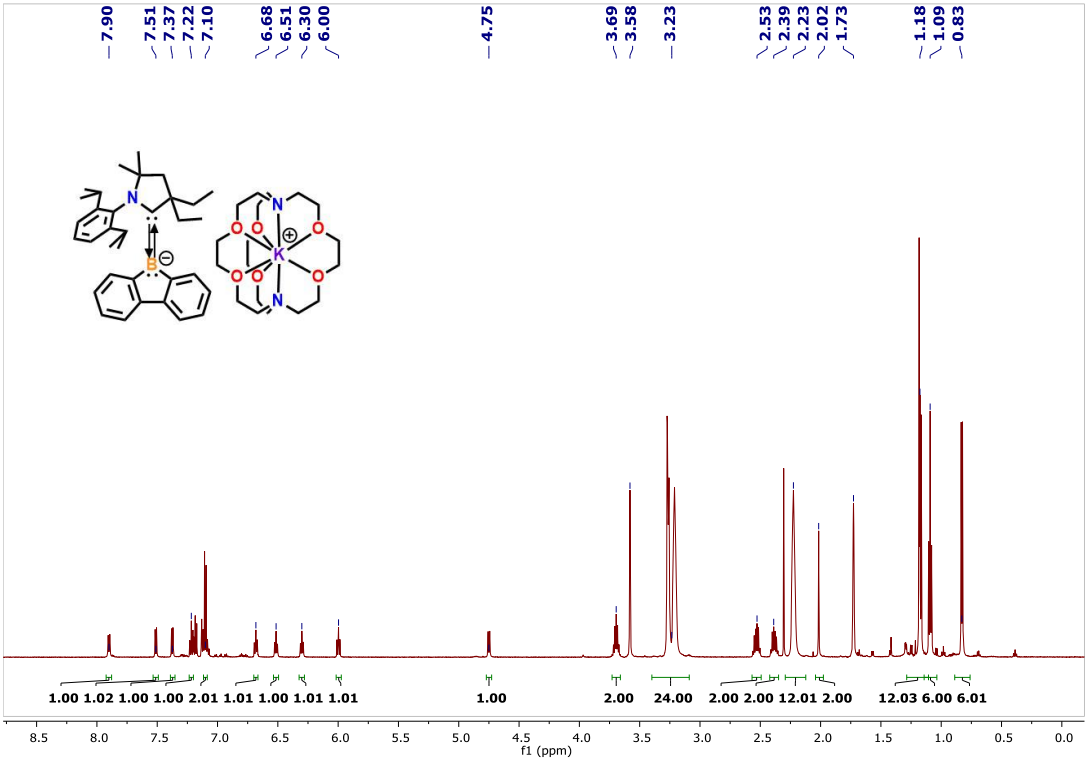

Figure A2.87. ^{1}H NMR (600 MHz, THF-d_8, 298 K) of **6.3**.

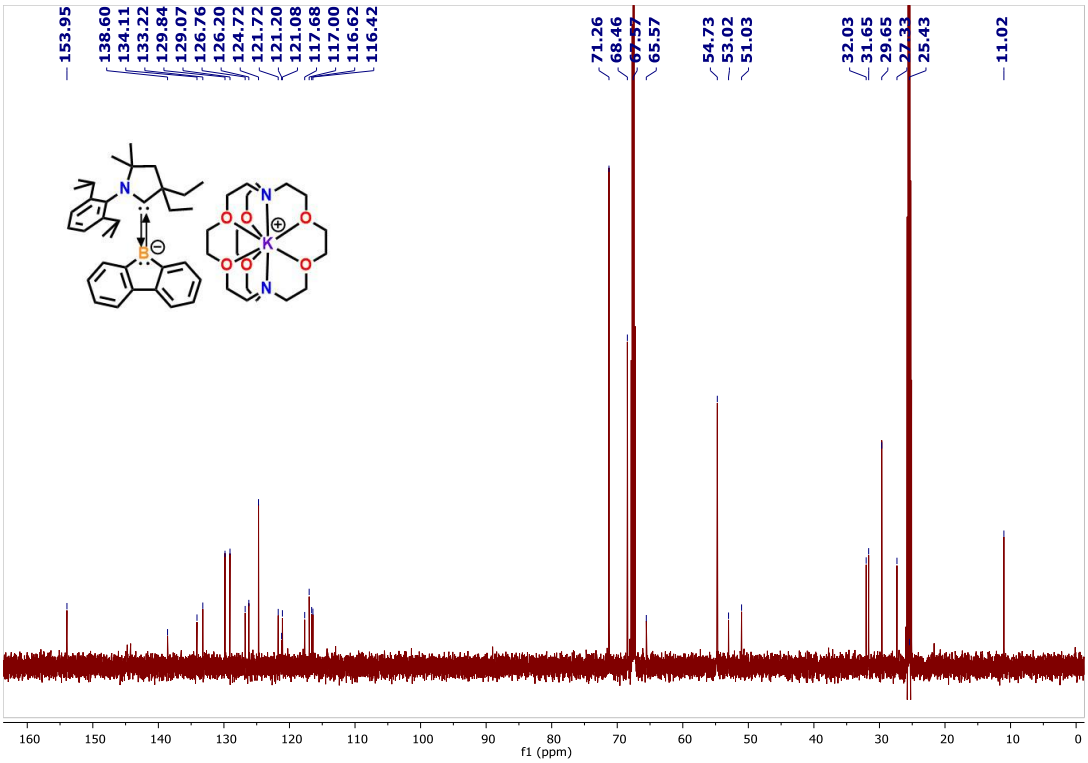

Figure A2.88. $^{13}C\{^{1}H\}$ NMR (151 MHz, THF-d_8, 298K) of **6.3**.

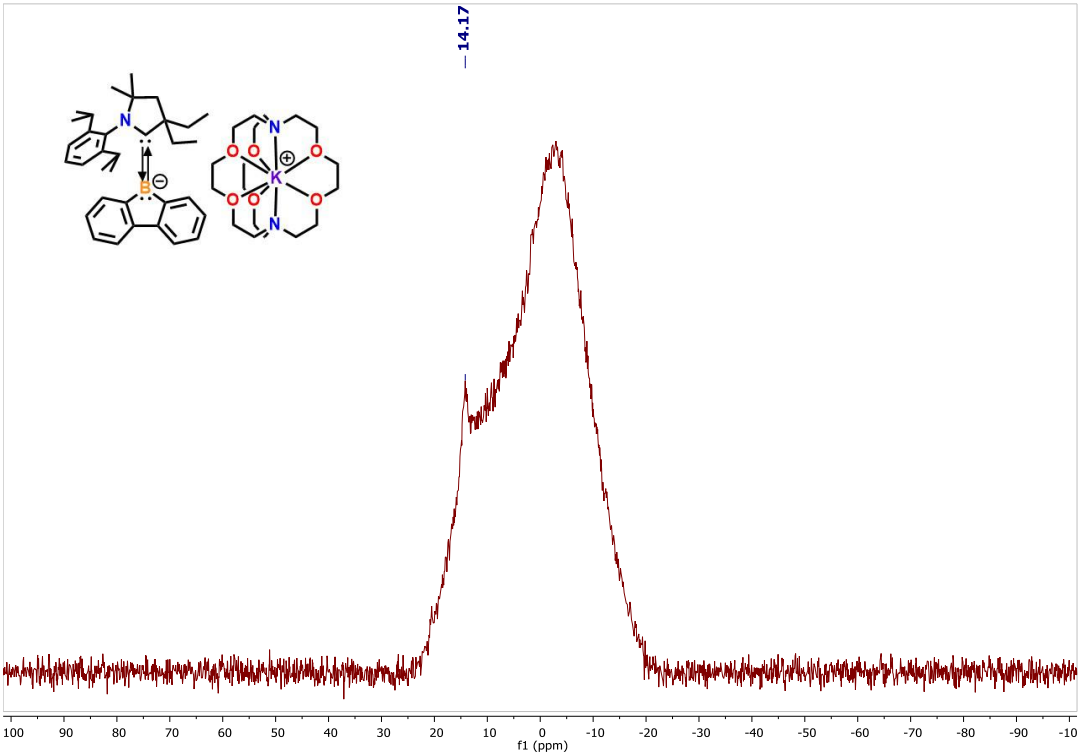

Figure A2.89. $^{11}B\{^{1}H\}$ NMR (193 MHz, THF-d_8, 298 K) of **6.3**.

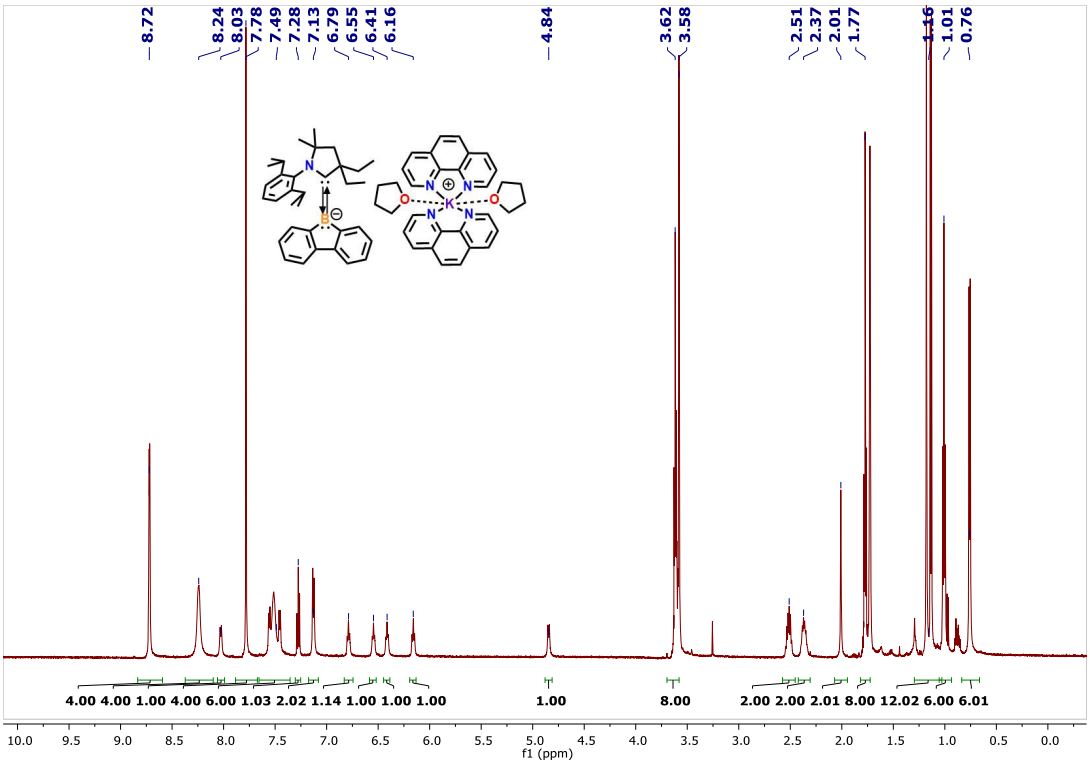

Figure A2.90. ^{1}H NMR (600 MHz, THF-d_8, 298 K) of **6.4**.

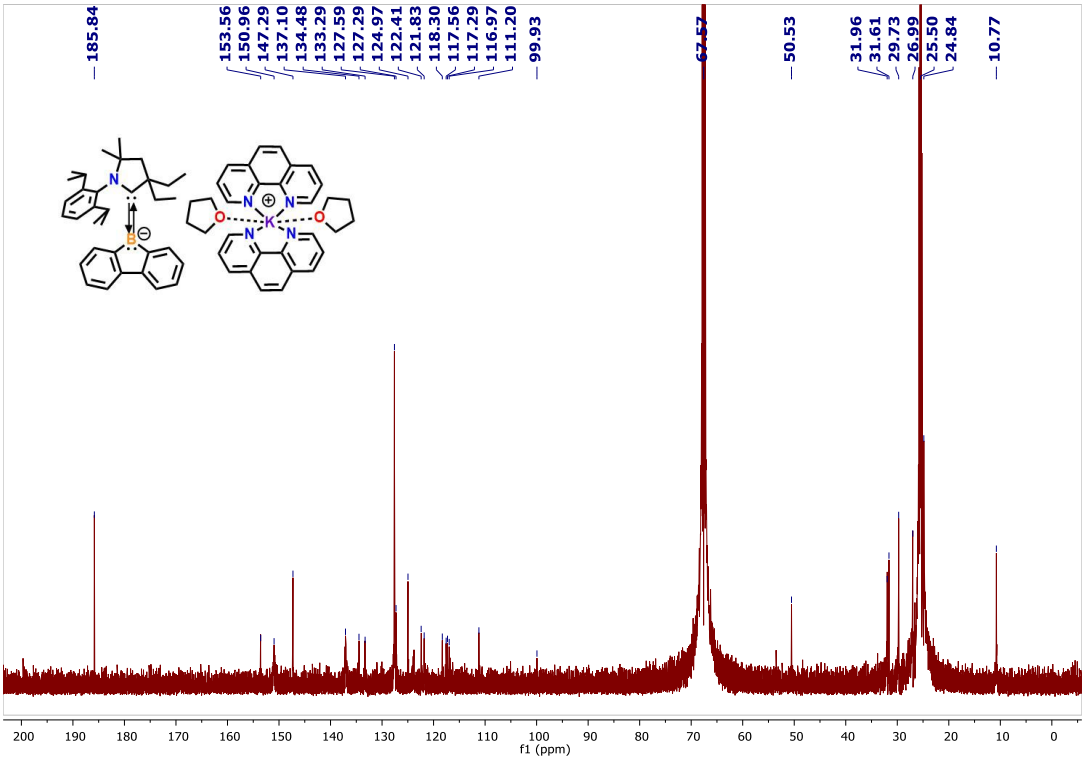

Figure A2.91. ^{13}C{^{1}H} NMR (151 MHz, THF-d_8, 298K) of **6.4**.

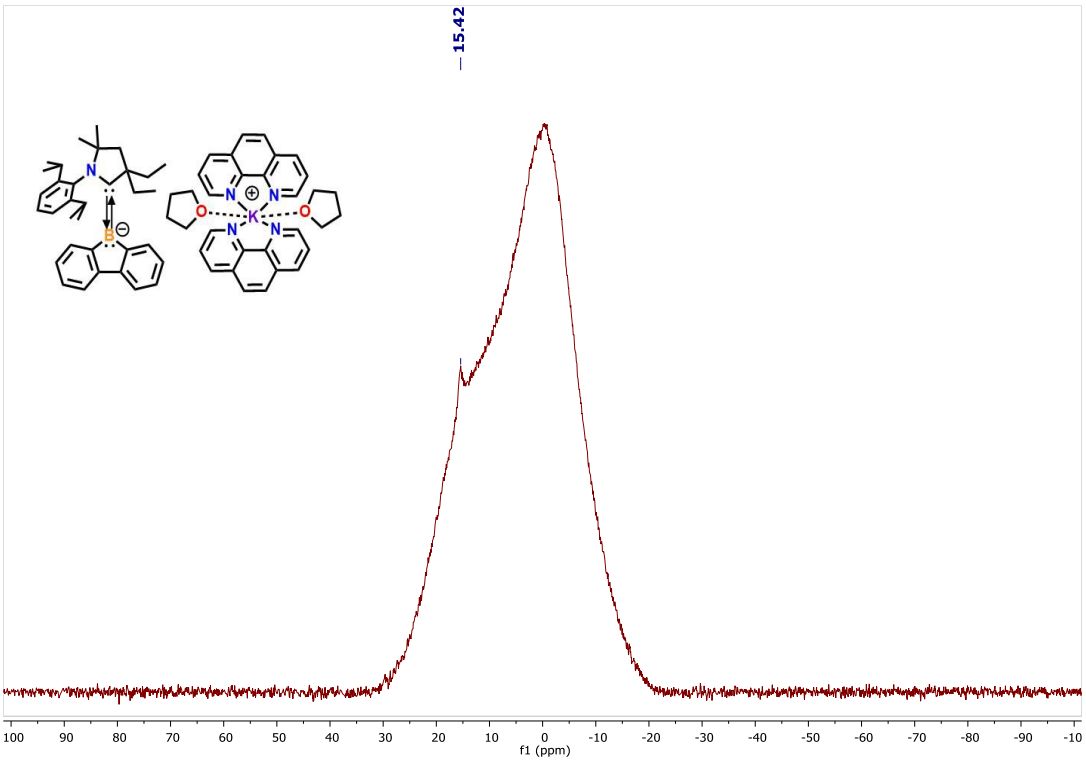

Figure A2.92. $^{11}B\{^{1}H\}$ NMR (193 MHz, THF-d_8, 298 K) of **6.4**.

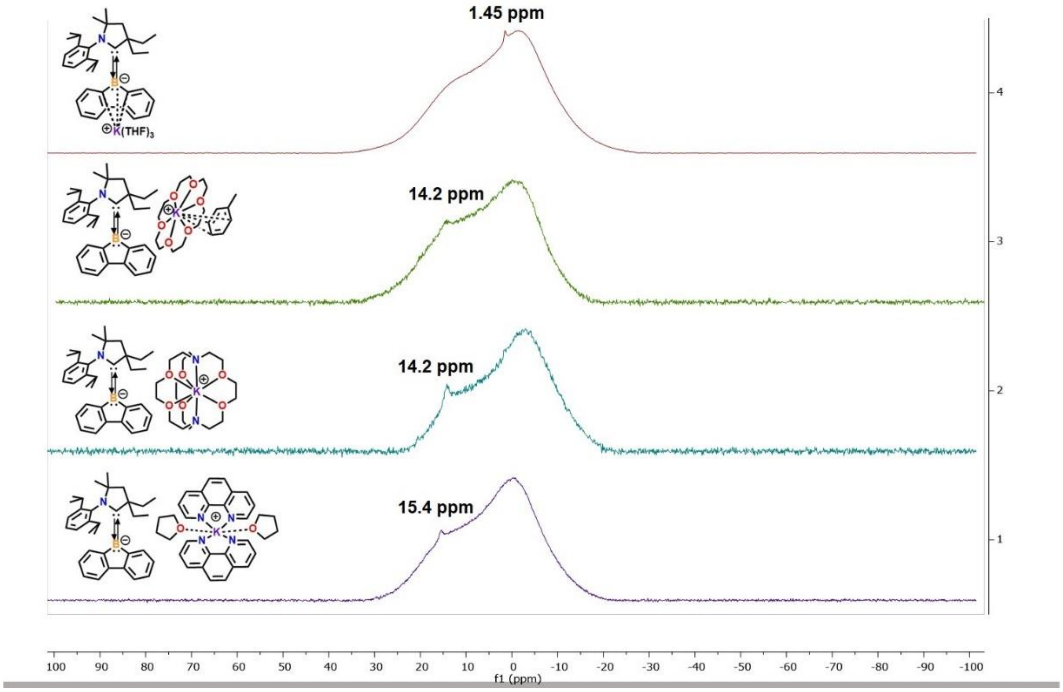

Figure A2.93. Stacked $^{11}B\{^{1}H\}$ NMR spectra of **4.5, 6.2-6.4**.

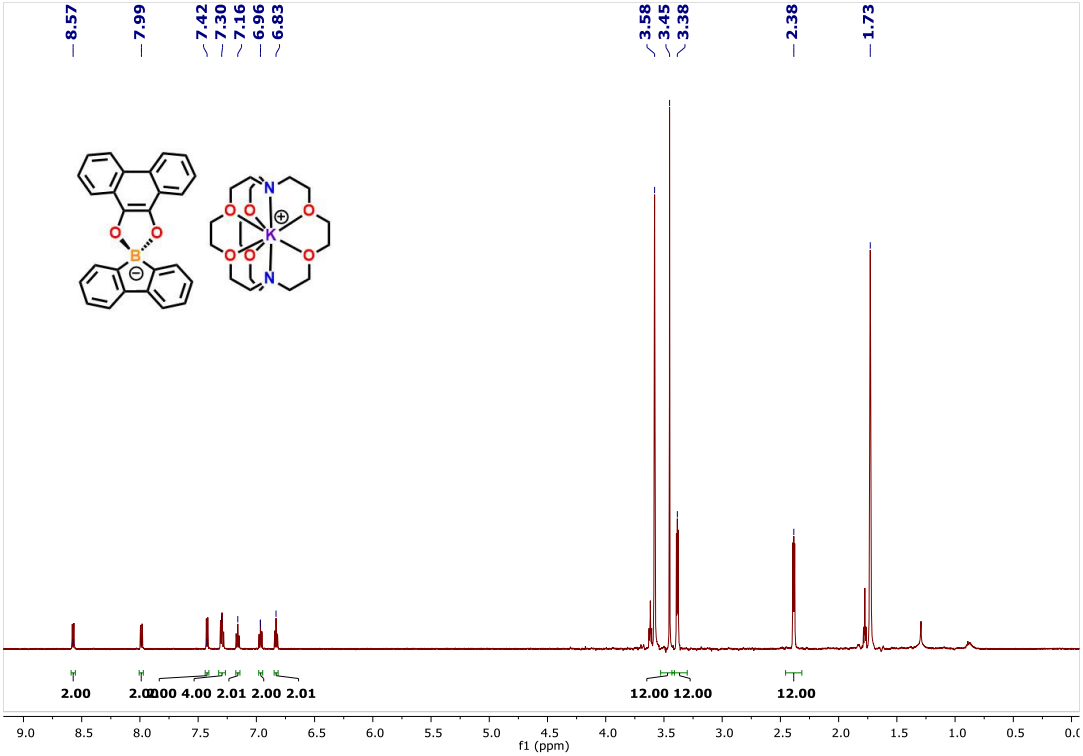

Figure A2.94. ^{1}H NMR (600 MHz, THF-d_8, 298 K) of **6.5**.

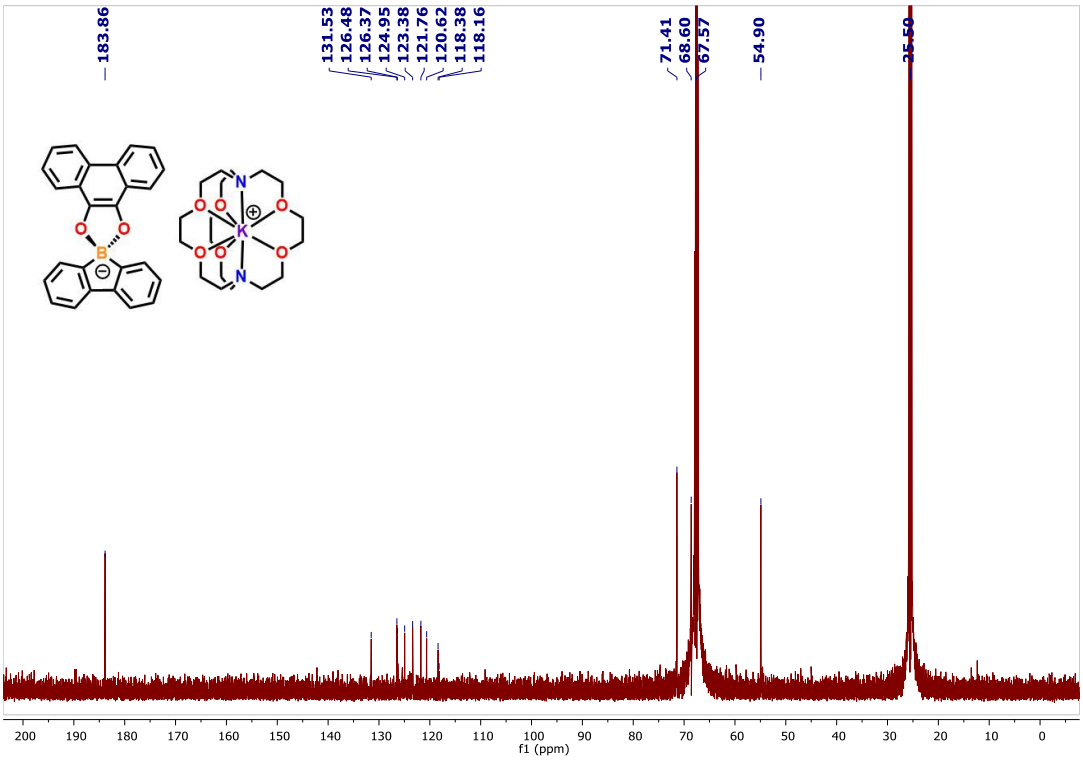

Figure A2.95. ^{13}C{^{1}H} NMR (151 MHz, THF-d_8, 298K) of **6.5**.

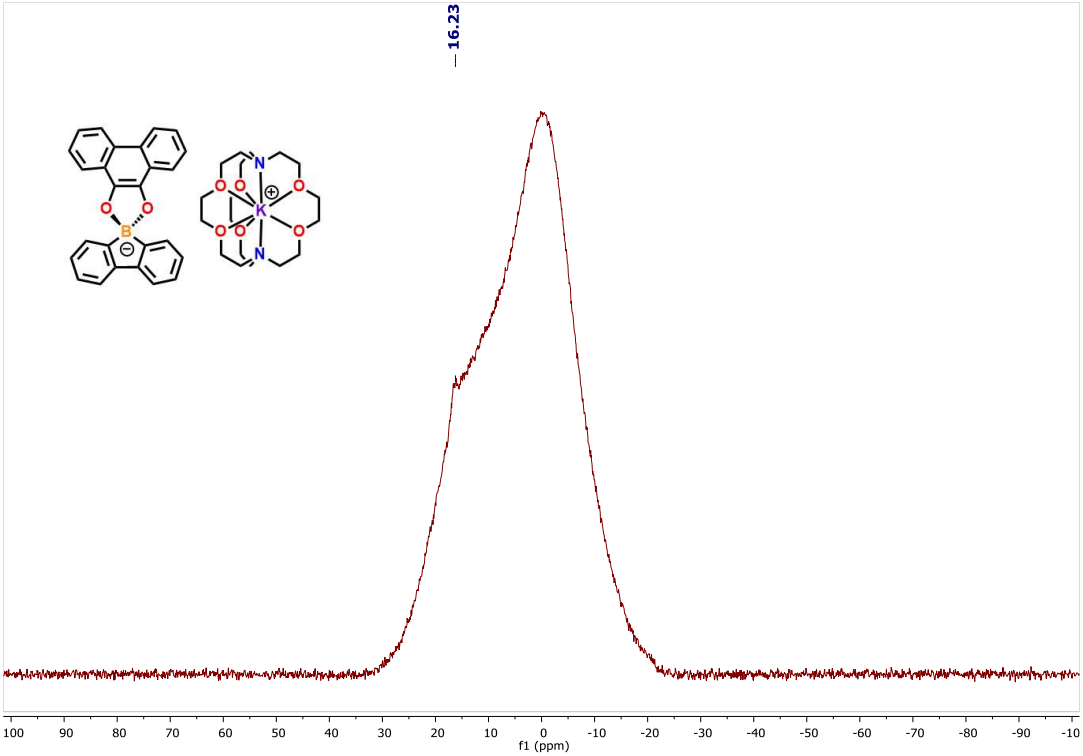

Figure A2.96. $^{11}B\{^{1}H\}$ NMR (193 MHz, THF-d_8, 298 K) of **6.5**.

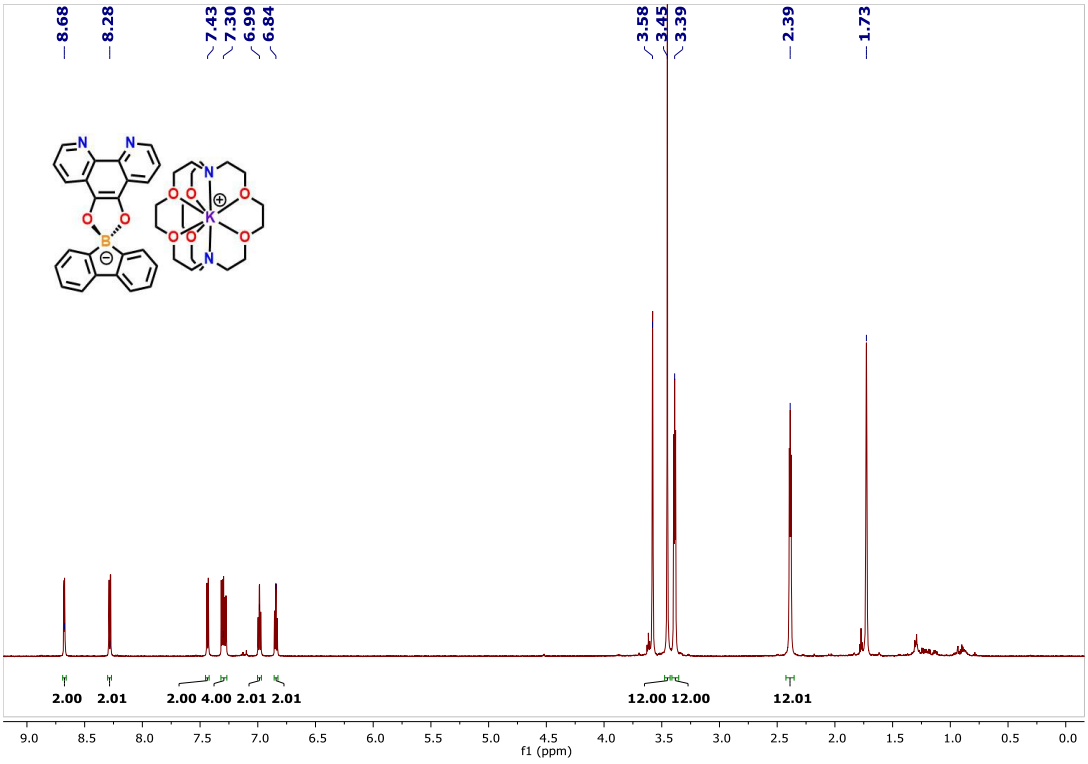

Figure A2.97. ^{1}H NMR (600 MHz, THF-d_8, 298 K) of **6.6**.

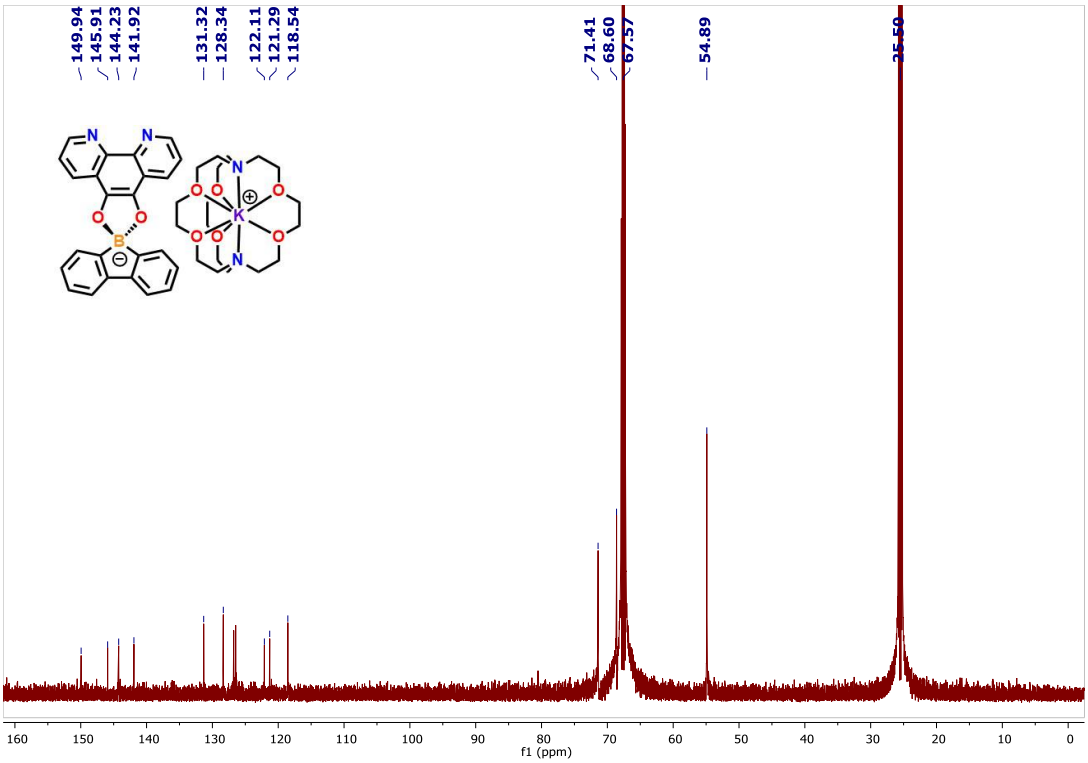

Figure A2.98. $^{13}C\{^{1}H\}$ NMR (151 MHz, THF-d_8, 298K) of **6.6**.

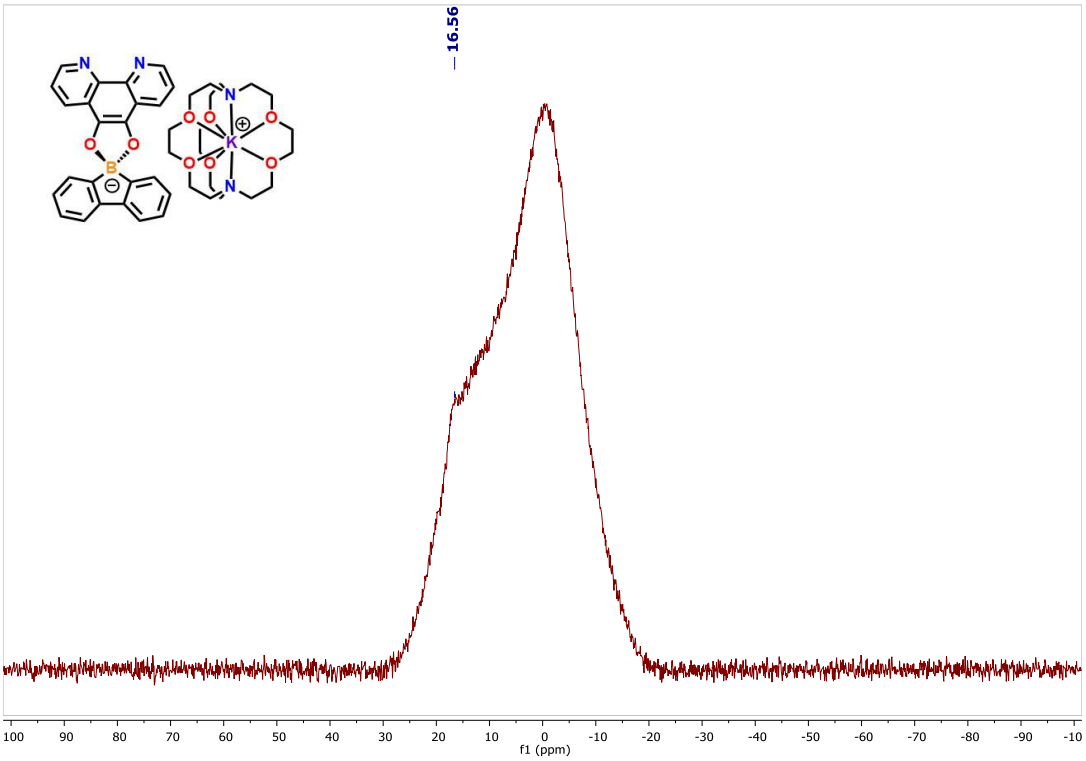

Figure A2.99. $^{11}B\{^{1}H\}$ NMR (193 MHz, THF-d_8, 298 K) of **6.6**.

Chapter Seven:

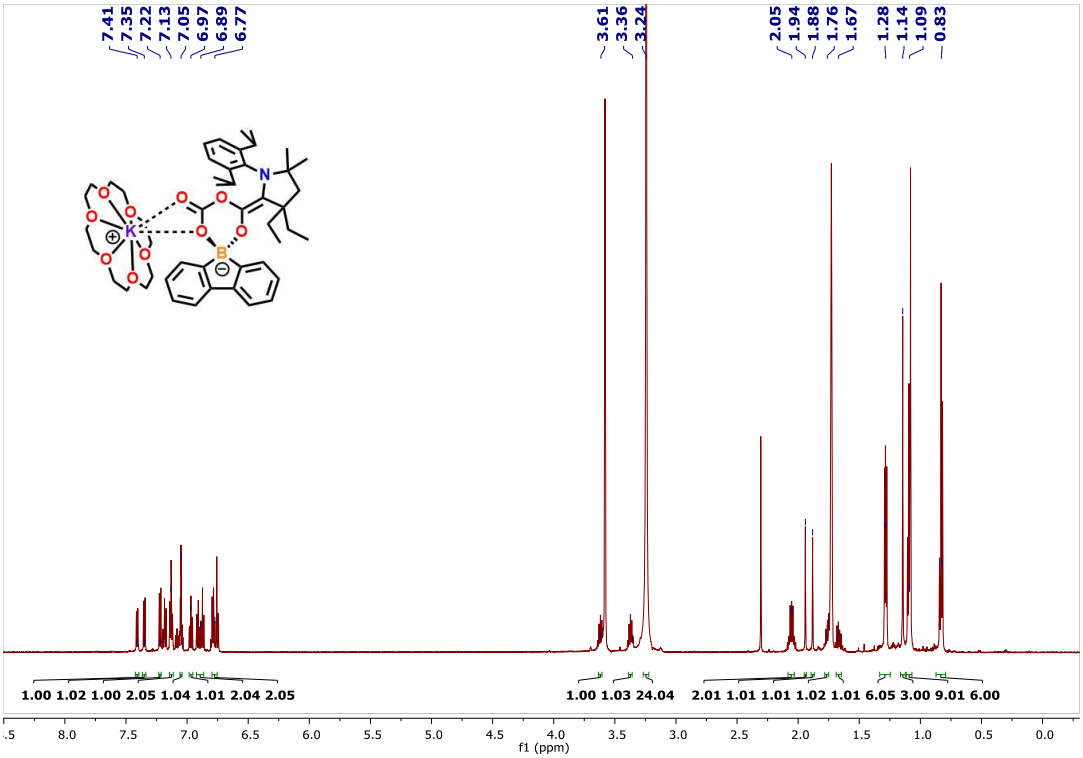

Figure A2.100. ^{1}H NMR (600 MHz, THF-d_8, 298 K) of **7.2**.

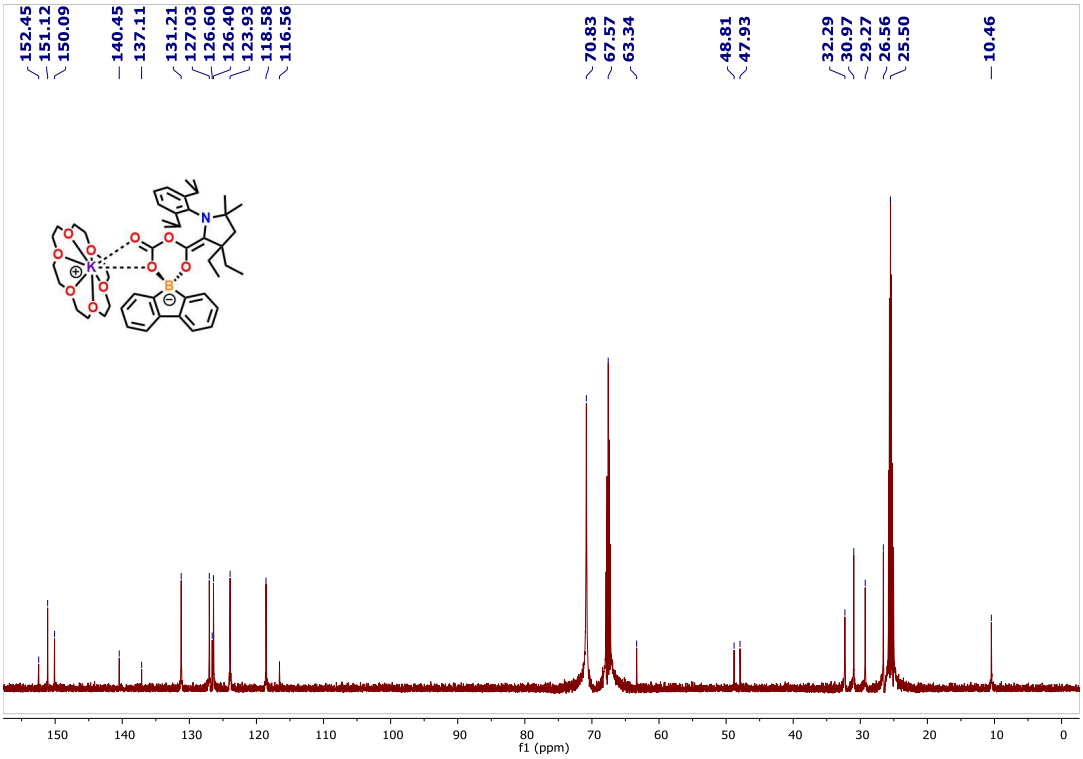

Figure A2.101. $^{13}C\{^{1}H\}$ NMR (151 MHz, THF-d_8, 298K) of **7.2**.

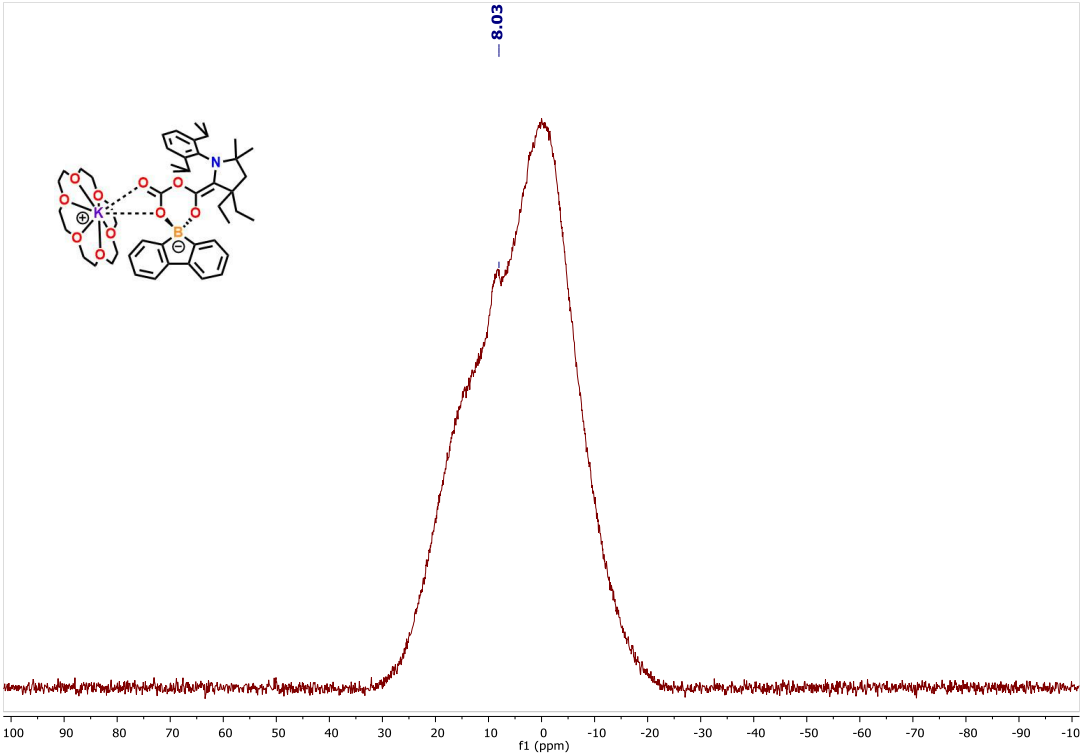

Figure A2.102. $^{11}B\{^{1}H\}$ NMR (193 MHz, THF-d_8, 298 K) of **7.2**.

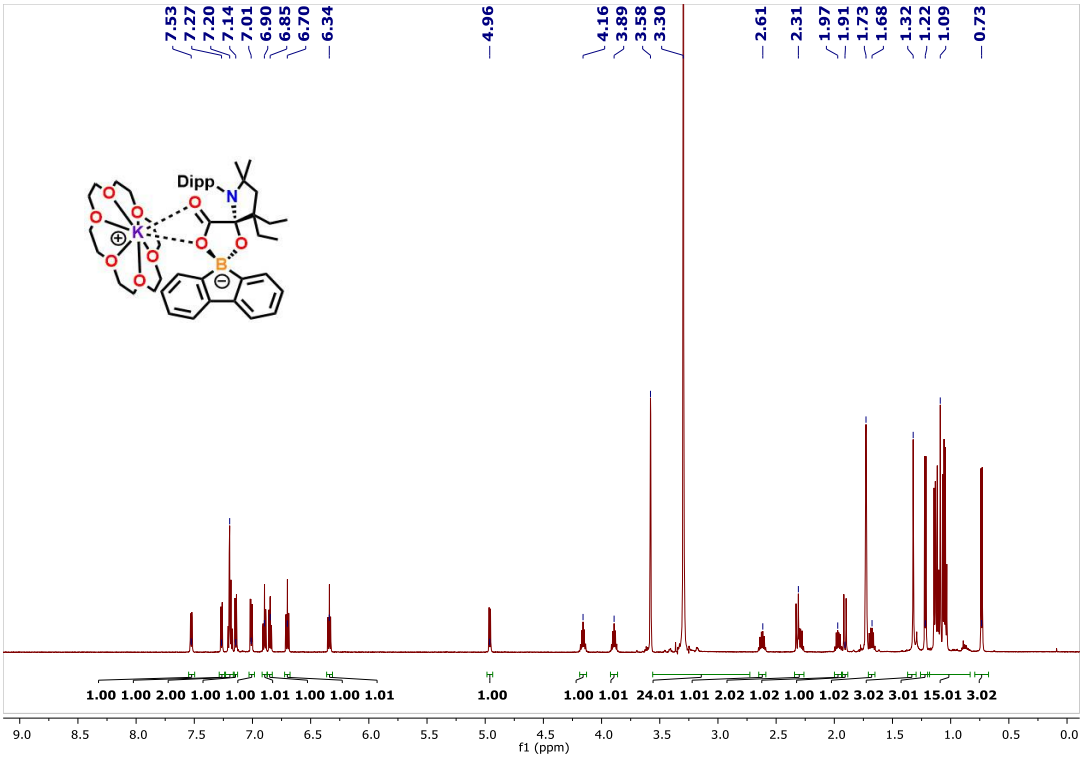

Figure A2.103. ^{1}H NMR (600 MHz, THF-d_8, 298 K) of **7.3**.

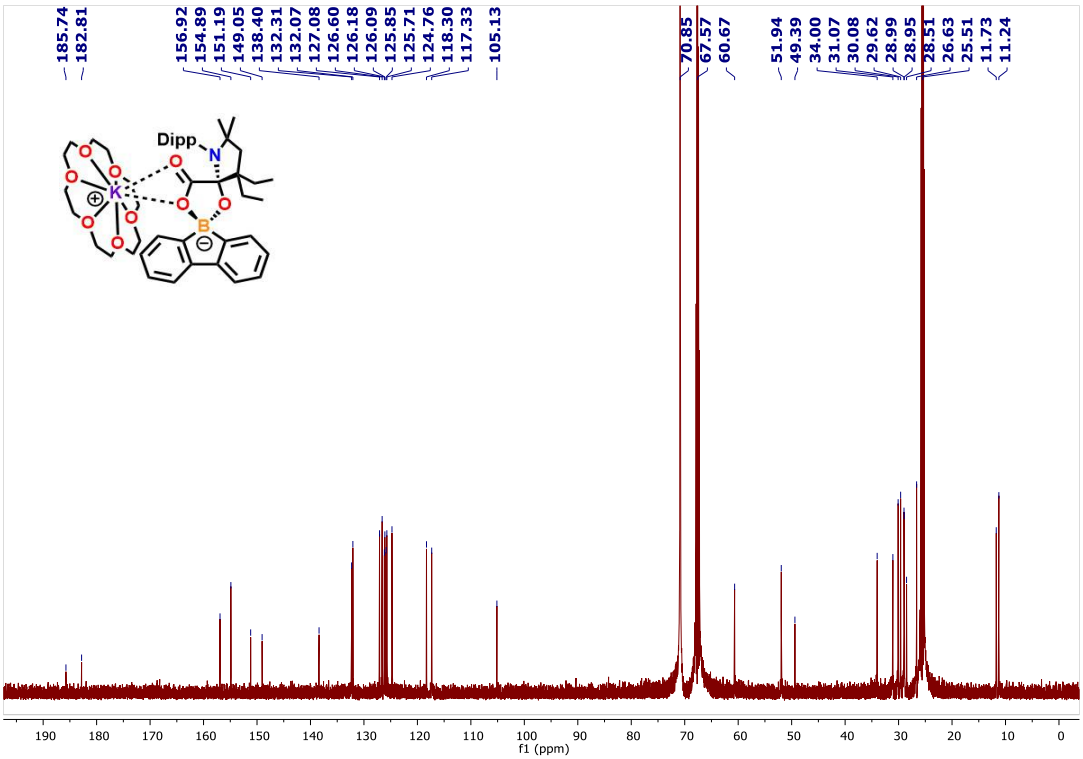

Figure A2.104. $^{13}C\{^{1}H\}$ NMR (151 MHz, THF-d_8, 298K) of **7.3**.

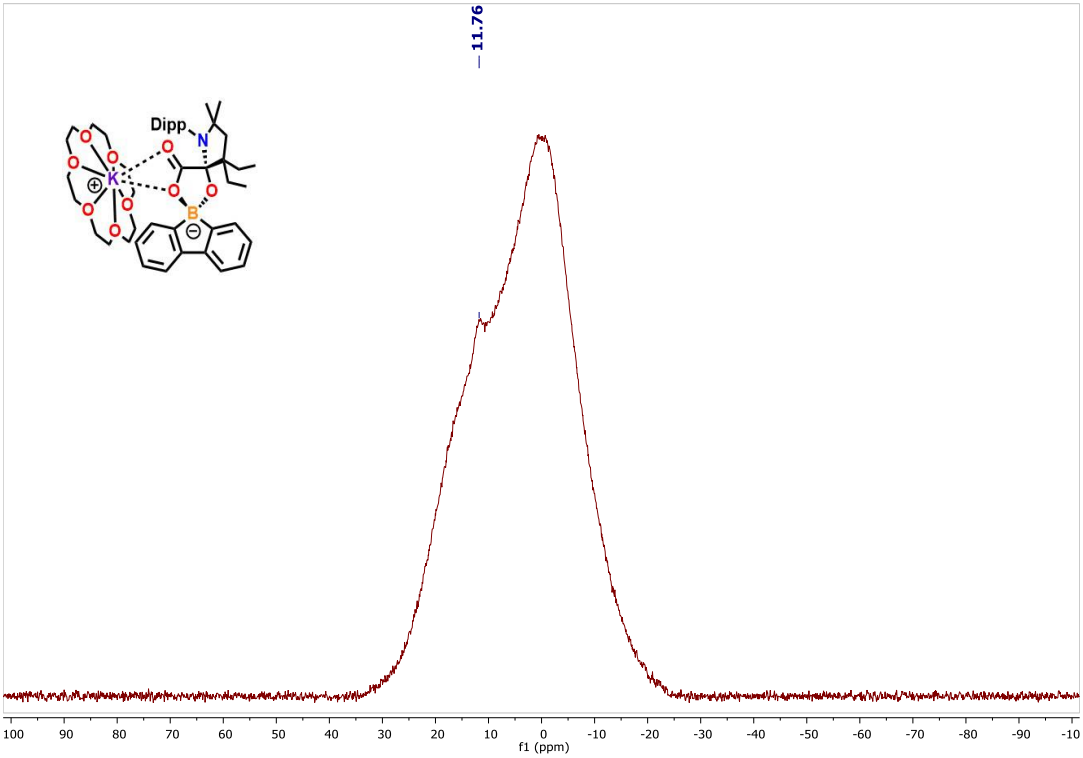

Figure A2.105. $^{11}B\{^{1}H\}$ NMR (193 MHz, THF-d_8, 298 K) of **7.3**.

Appendix III – Molecular Structures

Chapter Two

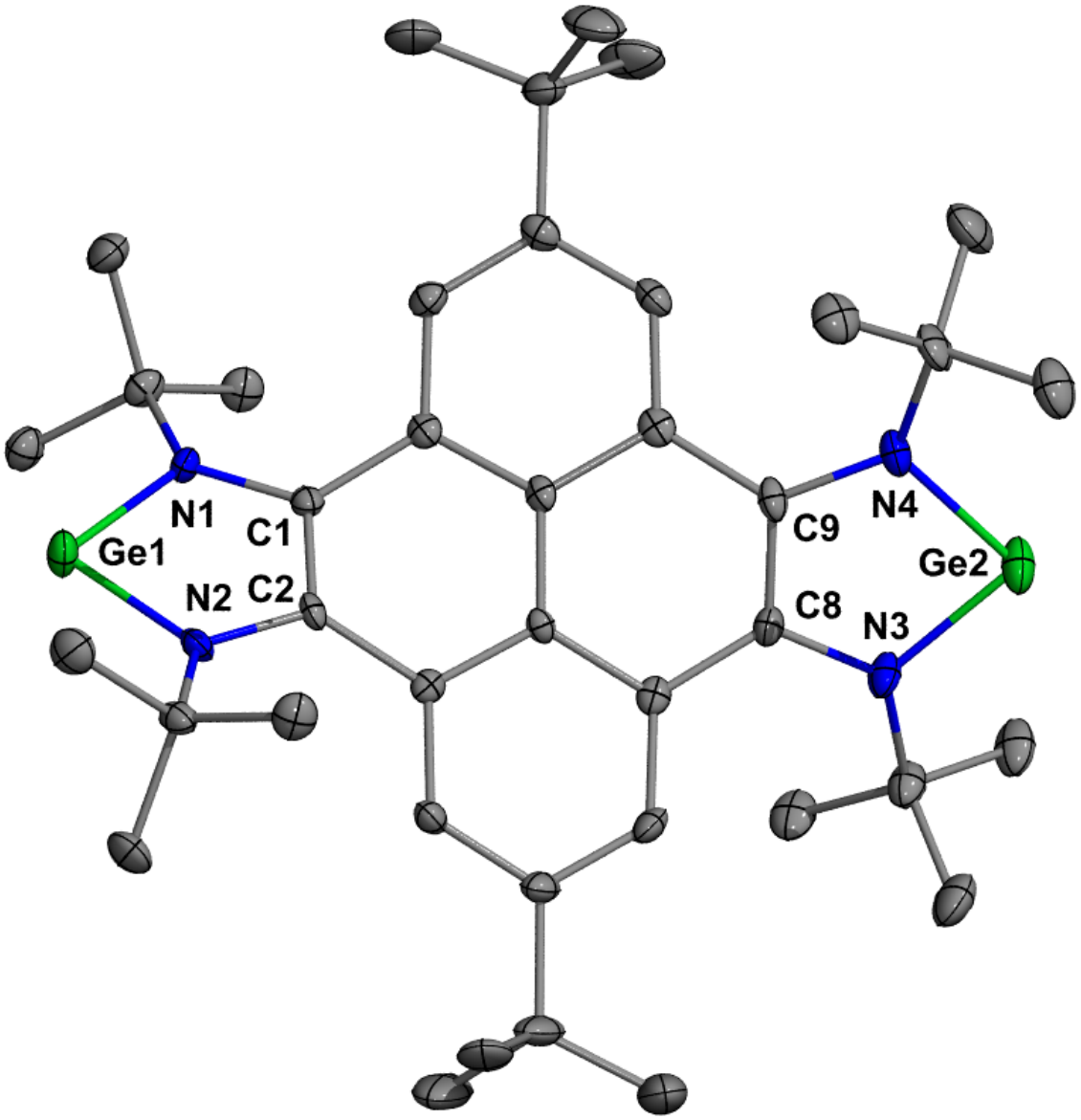

Figure A3.1. Molecular structure of **2.2**. Thermal ellipsoids shown at 50% probability and H atoms were omitted for clarity. Selected bond lengths (Å) and angles (°): Ge1–N1: 1.871(3); Ge1–N2: 1.868(3); C1-C2-C8-C9: 49; N1-N2-N3-N4: 64.

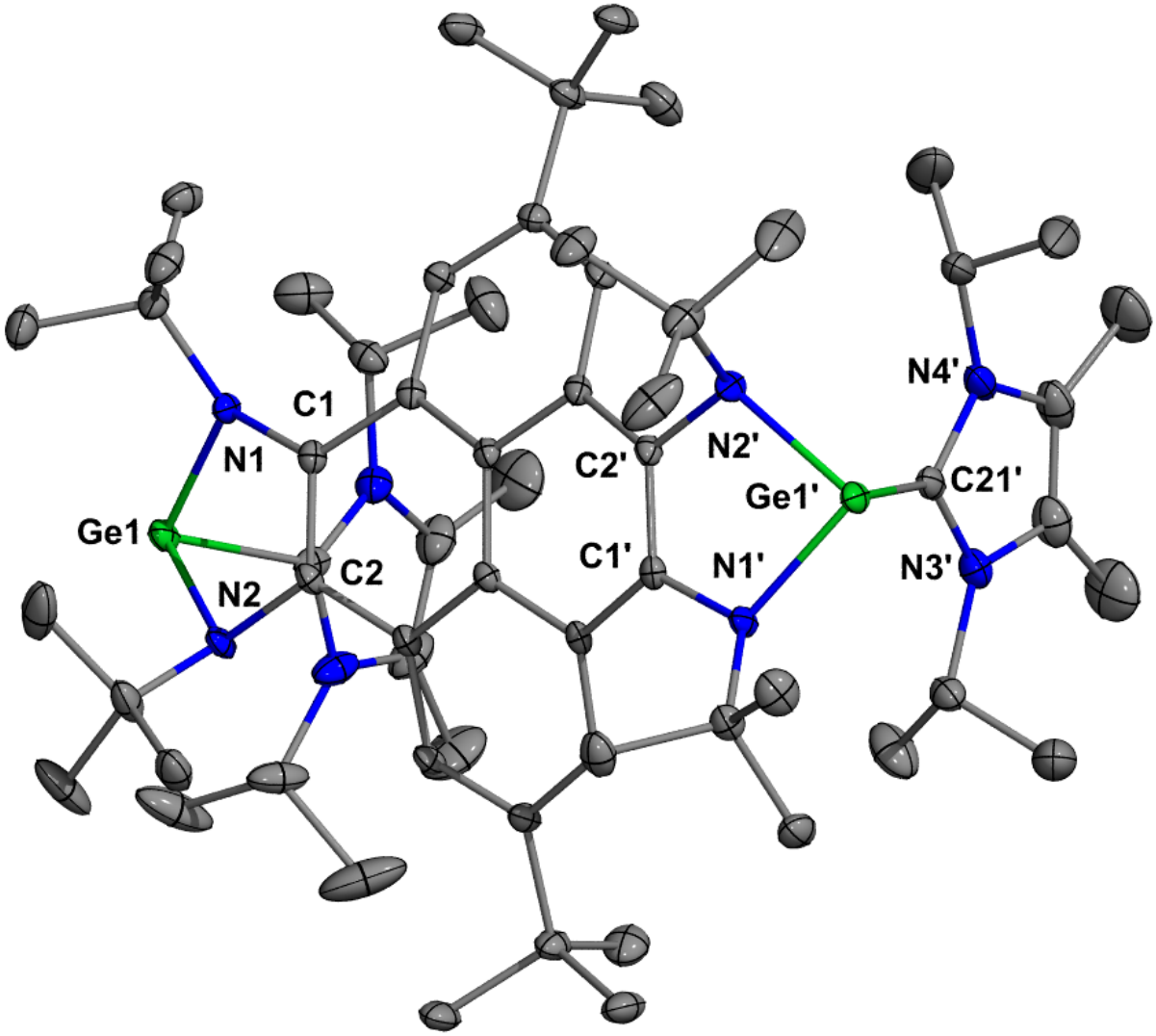

Figure A3.2. Molecular structure of **2.3.** Thermal ellipsoids shown at 50% probability and H atoms were omitted for clarity. Selected bond lengths (Å) and angles (°): Ge1–N1: 1.9430(14); Ge1–N2: 1.9489(14); Ge1–C21: 2.1321(18); N4–C21: 1.359(2); N3–C21: 1.356(2); C2-C1-C2'-C1': 5; N2-N1-N2'-N1': 7; C21-Ge1-Ge1'-C21': 15.

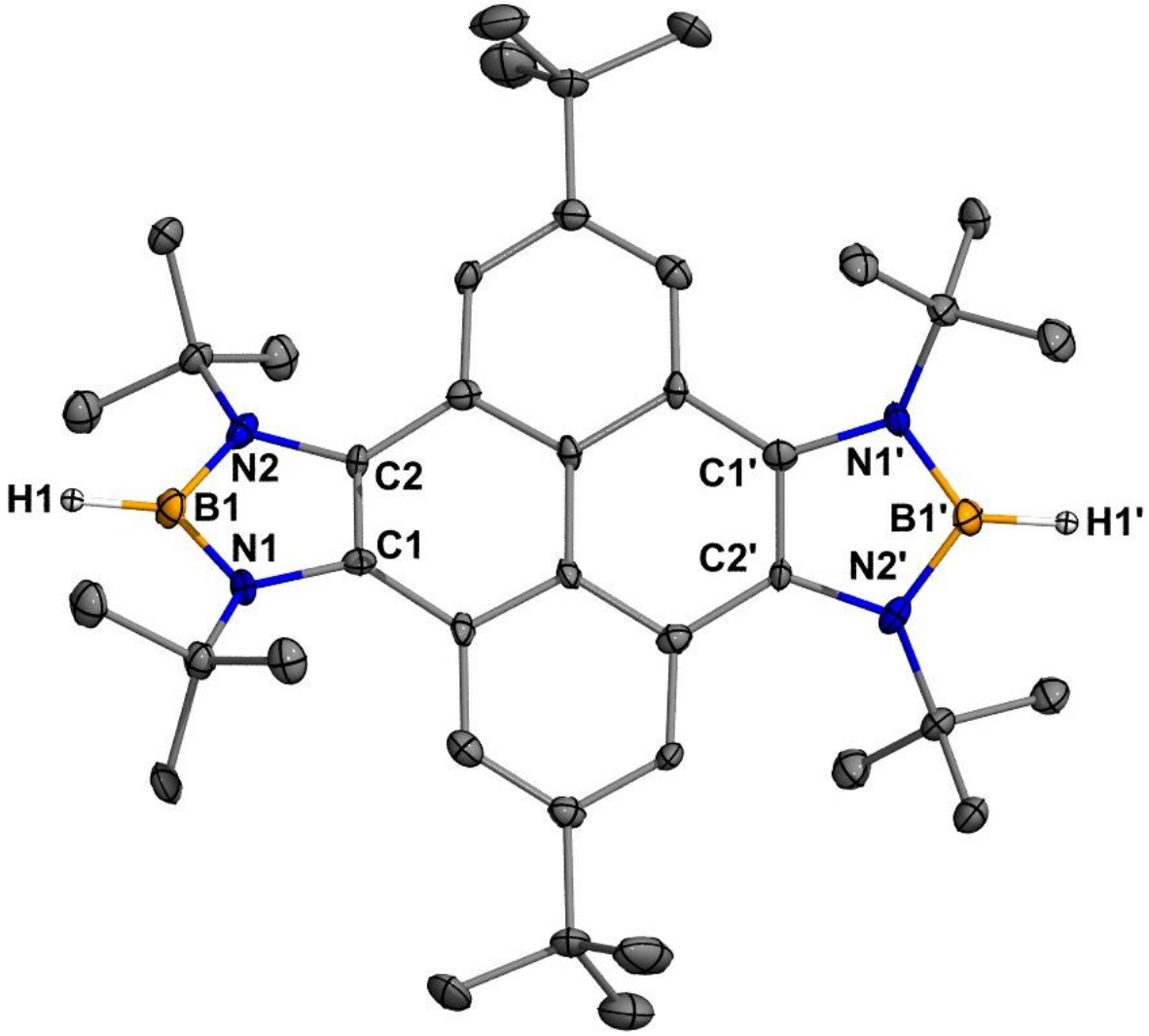

Figure A3.3. Molecular structure of **3.2**. Thermal ellipsoids shown at 50% probability and H atoms (except B-H) were omitted for clarity. Selected bond lengths (Å) and angles (°): B1–H1: 1.15(3); B1–N1: 1.421(7); B1–N2: 1.433(7); C2–C1–C2′–C1′: 40; N2–N1–N2′–N1′: 52.

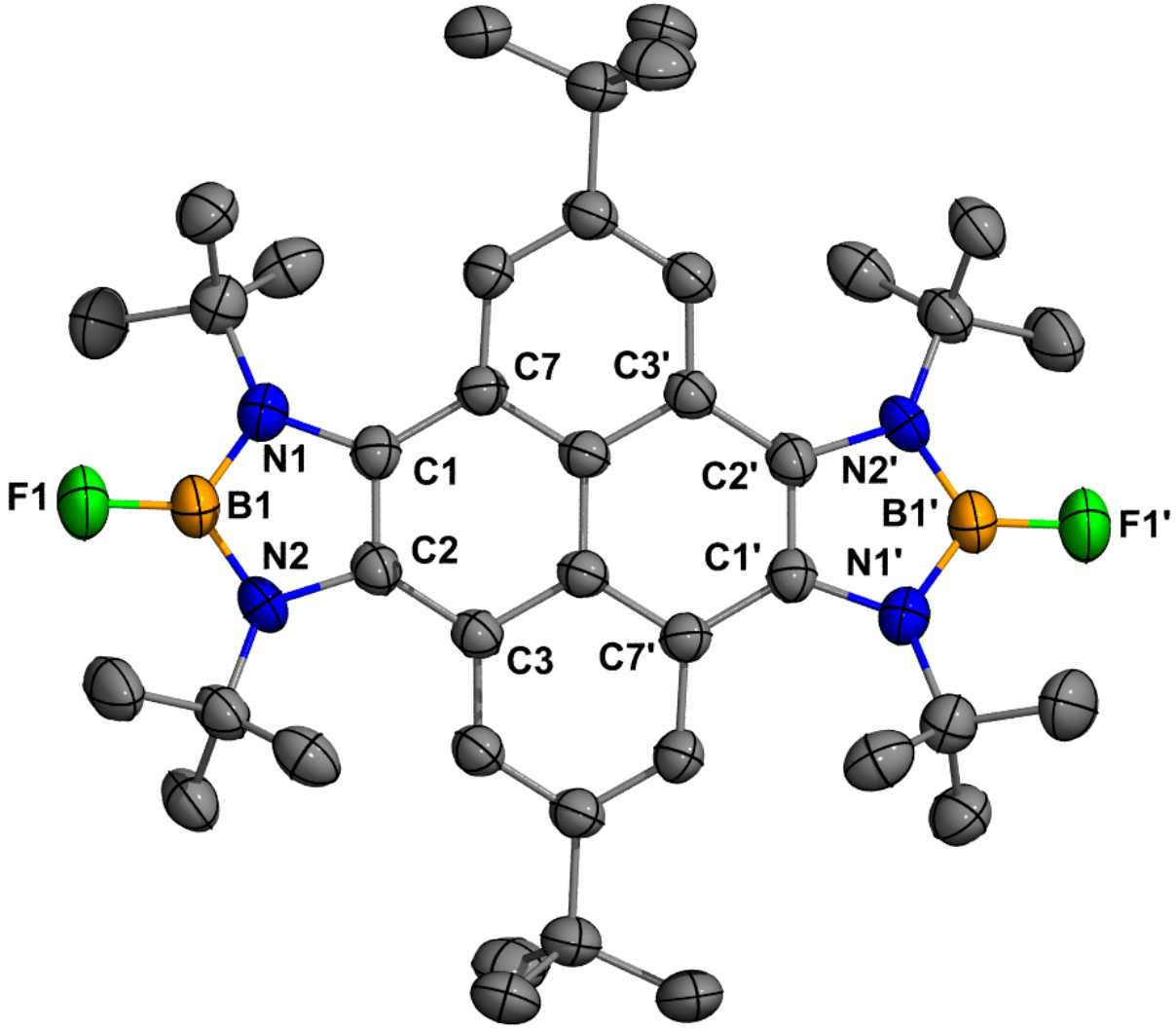

Figure A3.4. Molecular structure of **3.3**. Thermal ellipsoids shown at 50% probability and H atoms were omitted for clarity. Selected bond lengths (Å) and angles (°): B1–F1: 1.335(4); B1–N1: 1.419(5); B1–N2: 1.423(5); C1–C2–C1′–C2′: 0; N1-N2-N1′-N2′: 0, C3–C2–C1–C7: 20.

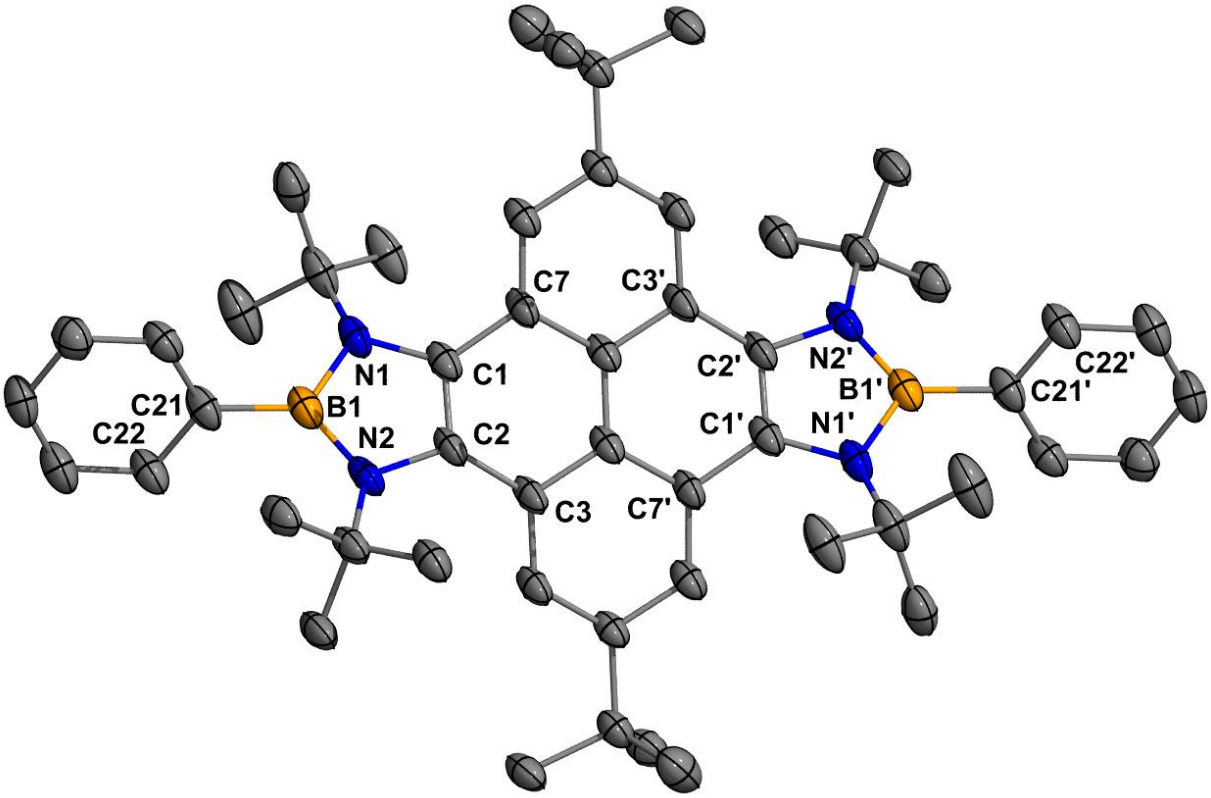

Figure A3.5. Molecular structure of **3.4**. Thermal ellipsoids shown at 50% probability. H atoms and co-crystallized solvent were omitted for clarity. Selected bond lengths (Å) and angles (°): B1–C21: 1.573(4); B1–N1: 1.453(4); B1–N2: 1.448(5); C1–C2–C1′–C2′: 0; N1–N2–N1′–N2′: 0, C3–C2–C1–C7: 28; C22–C21–B1–N2: 60.

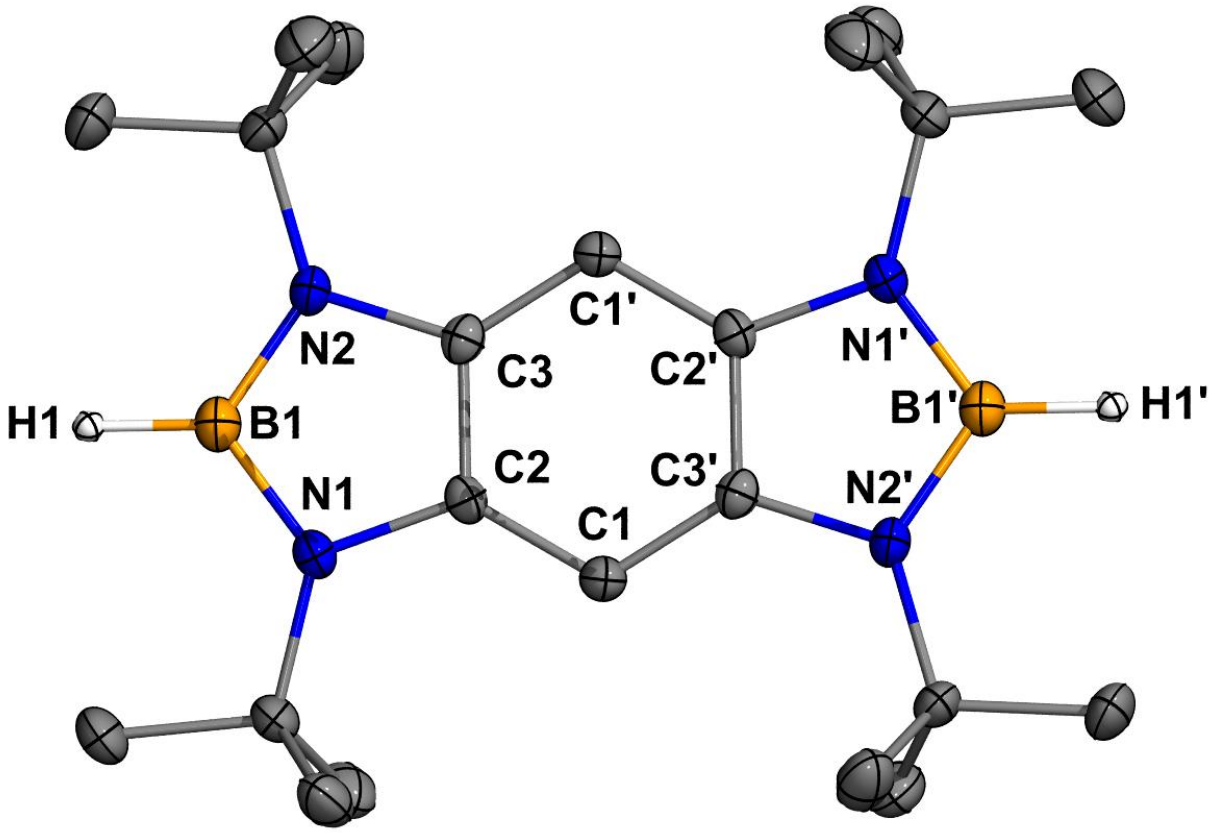

Figure A3.6. Molecular structure of **3.6**. Thermal ellipsoids shown at 50% probability and H atoms except for boron bound H were omitted for clarity. Selected bond lengths (Å): B1–H1: 1.140(17); B1–N1: 1.426(2); B1–N2: 1.426(2); N1–C2: 1.4166(18); C1–C2: 1.395(2); C1–C3′: 1.398(2).

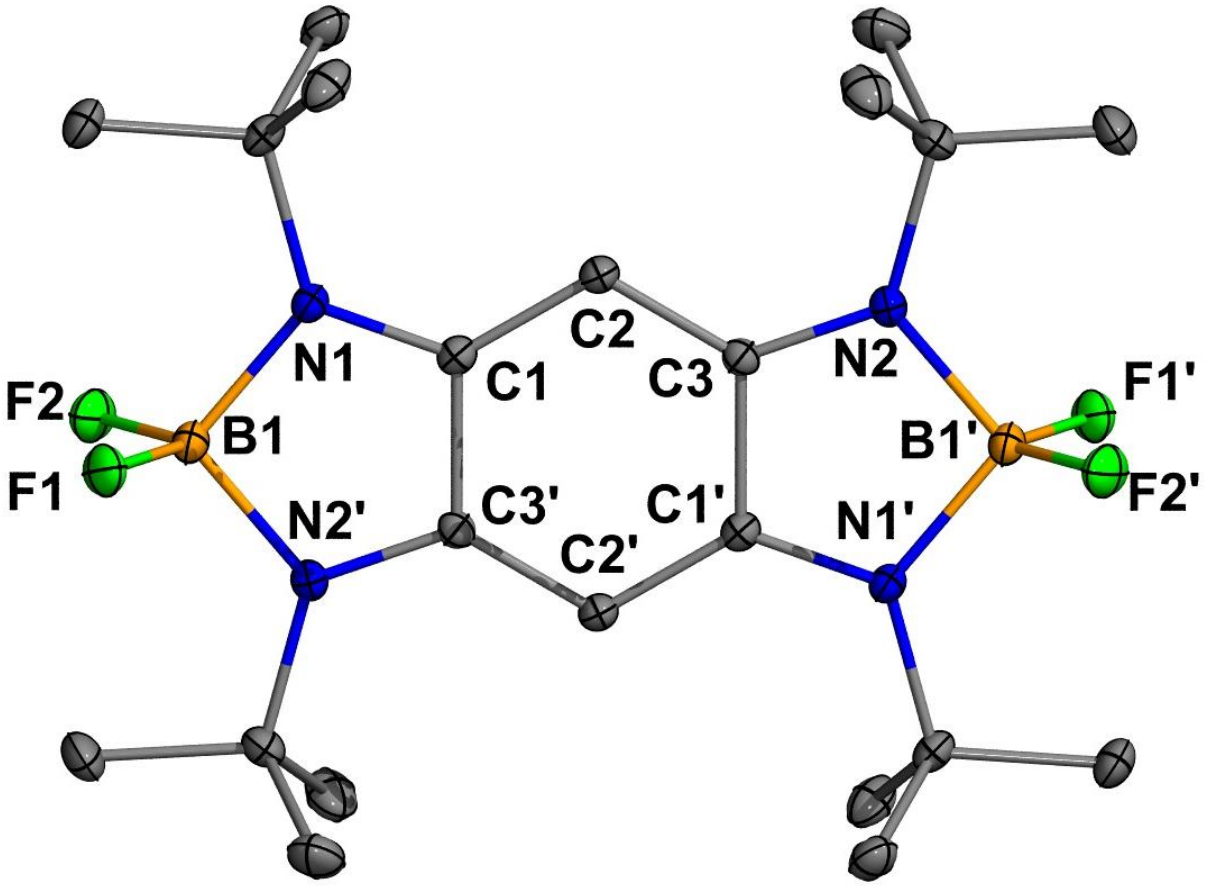

Figure A3.7. Molecular structure of **3.7**. Thermal ellipsoids shown at 50% probability and H atoms were omitted for clarity. Selected bond lengths (Å): B1–F1: 1.3906(12); B1–F2: 1.3853(12); B1–N1: 1.5690(13), B1–N2: 1.5678(13), C1–N1: 1.3266(11); C1–C2: 1.3968(12); C1–C3′: 1.5062(12).

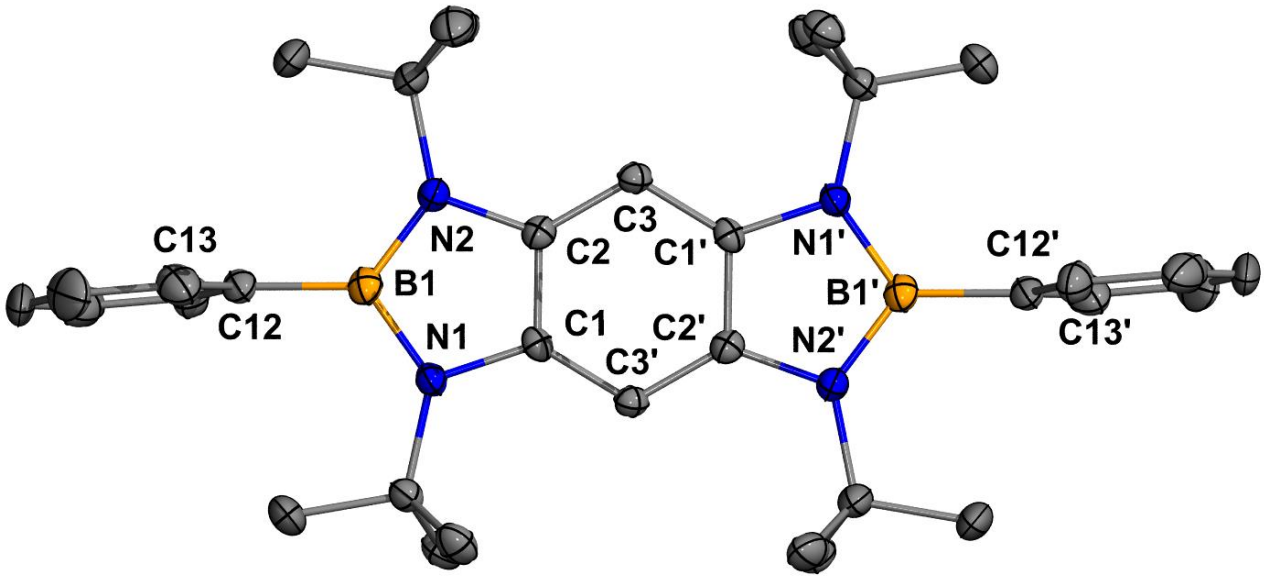

Figure A3.8. Molecular structure of **3.8**. Thermal ellipsoids shown at 50% probability and H atoms were omitted for clarity. Selected bond lengths (Å) and angles (°): B1–N1: 1.4436(19), B1–N2: 1.440(2), B1–C12: 1.609(6); C13–C12–B1–N1: 93.

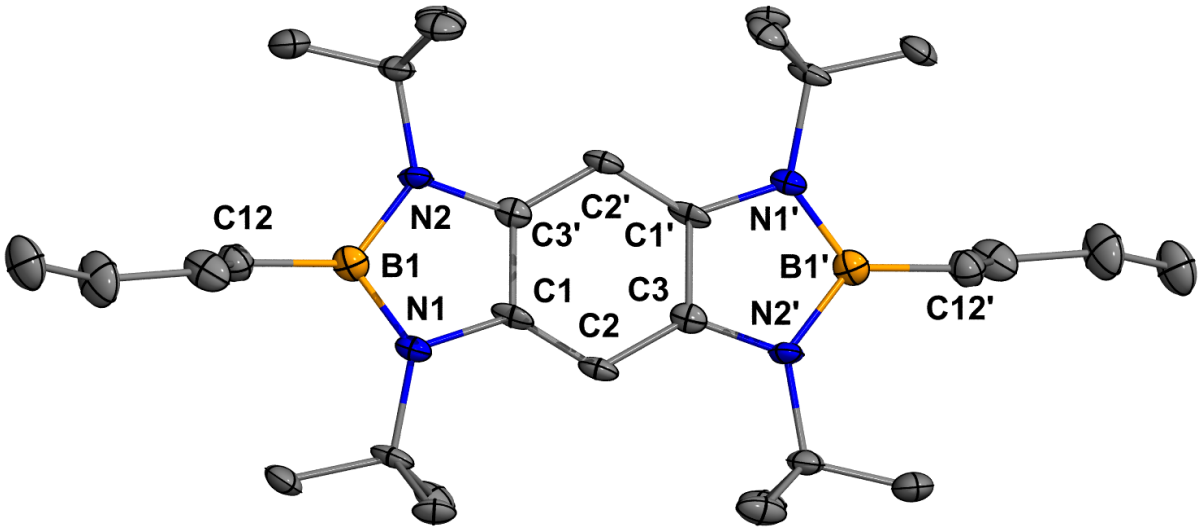

Figure A3.9. Molecular structure of **3.9**. Thermal ellipsoids shown at 50% probability and H atoms were omitted for clarity. Selected bond lengths (Å): B1–N1: 1.439(7), B1–N2: 1.460(7), B1–C12: 1.589(8).

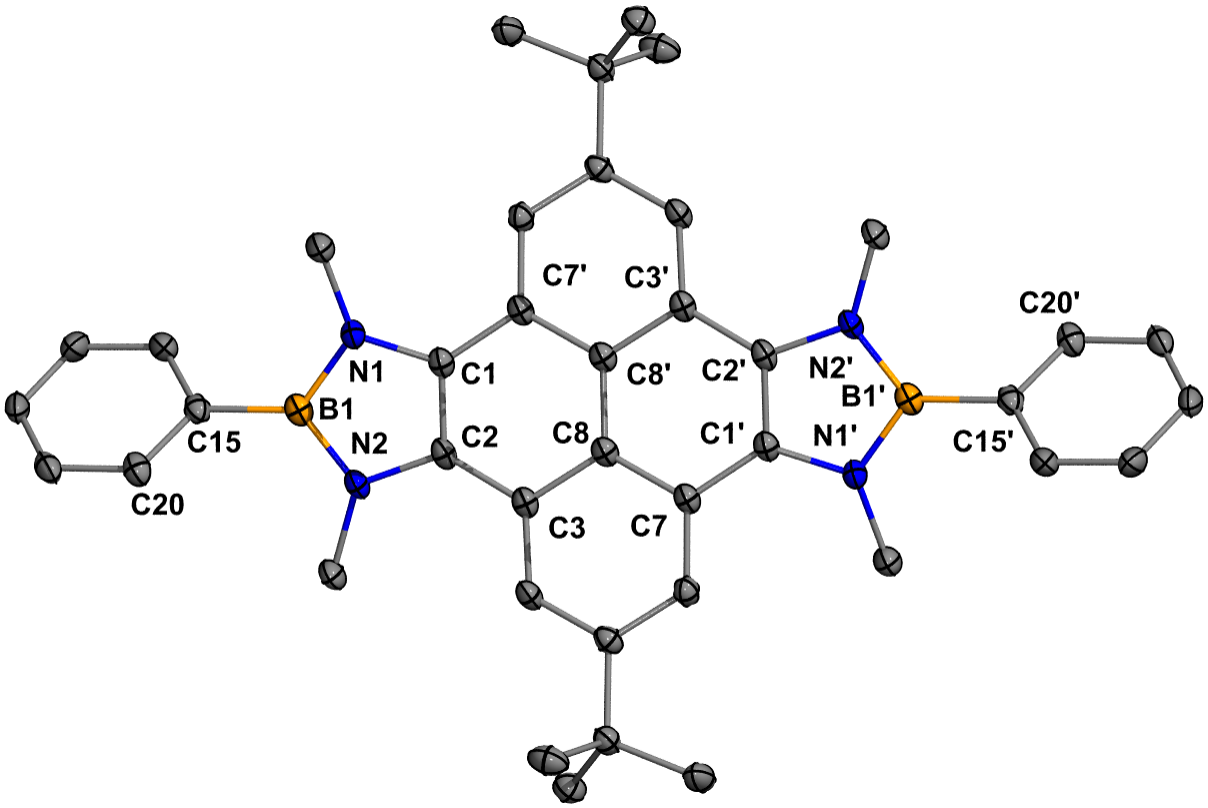

Figure A3.10. Molecular structure of **3.11**. Thermal ellipsoids shown at 50% probability and H atoms were omitted for clarity. Selected bond lengths (Å) and angles (°): B1–C15: 1.5669(19); B1–N1: 1.4291(18); B1–N2: 1.4272(18); C1–C2–C1′–C2′: 0; N1–N2–N1'–N2': 0, C3–C2–C1–C7: 11; C22–C21–B1–N2: 49.

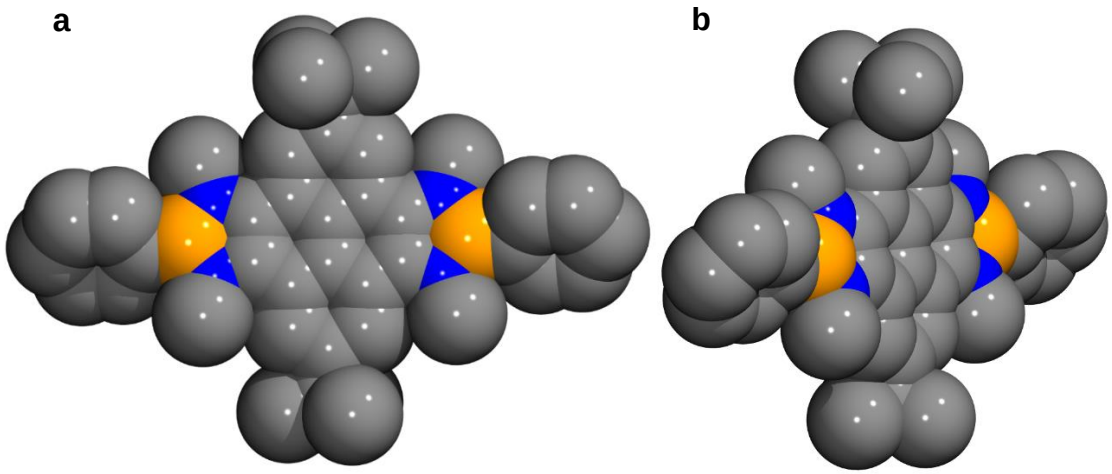

Figure A3.11. a) Space-filling model of **3.11** with H atoms omitted and b) different perspective showing *N*-methyl steric clash with pyrene ring.

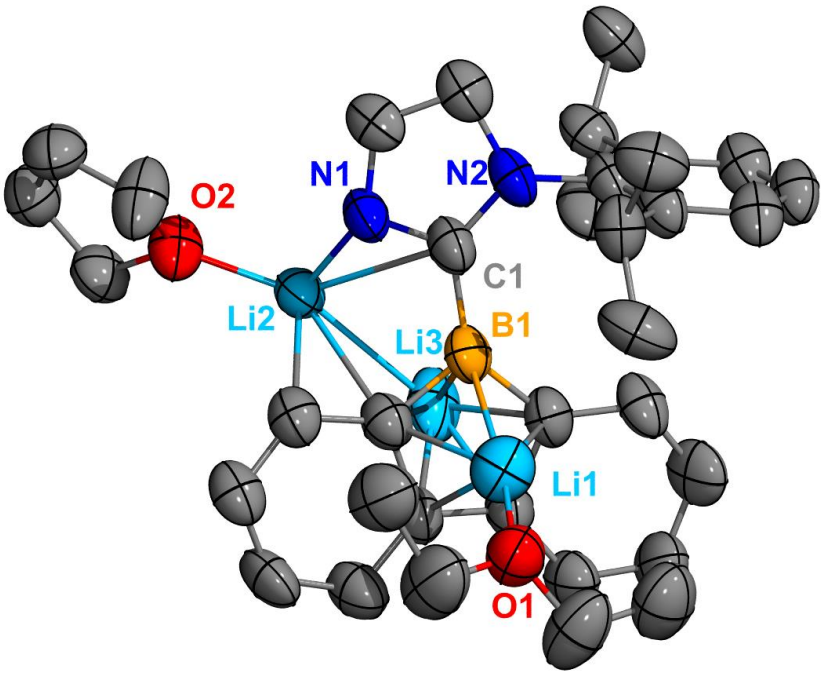

Figure A3.12. Molecular structure of ligand activation product obtained from reduction of **4.2** with excess Li-naphthalenide.

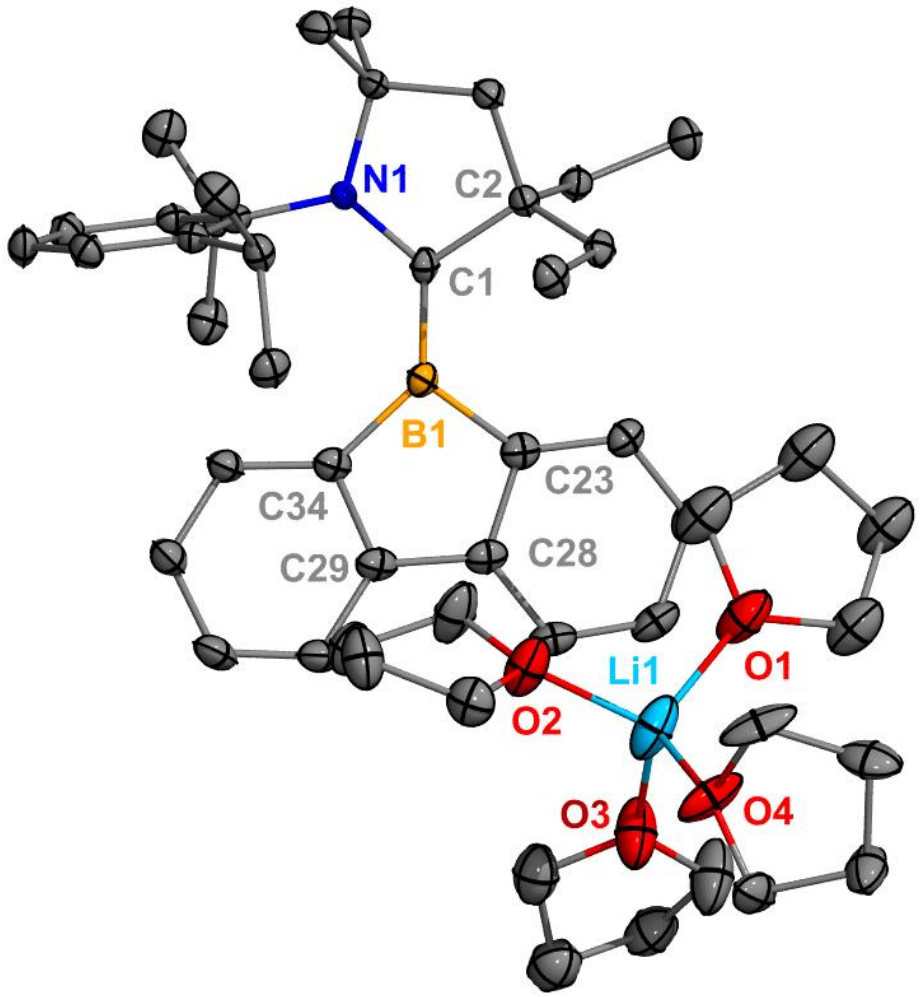

Figure A3.13. Molecular structure of **4.3**. Thermal ellipsoids shown at 50% probability and H atoms were omitted for clarity. Selected bond lengths (Å) and angles (°): B1–C1: 1.506(3); B1–C23: 1.614(3); B1–C34: 1.599(3).

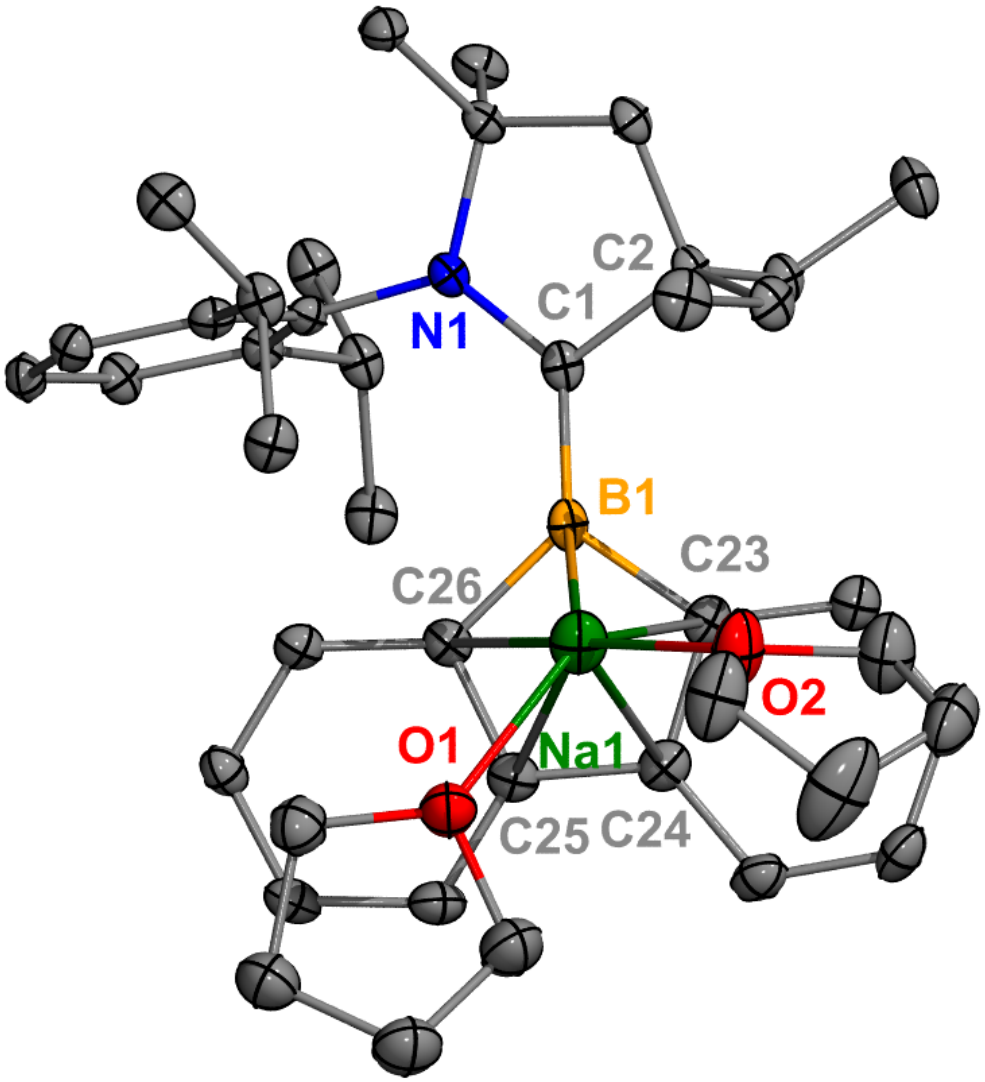

Figure A3.14. Molecular structure of **4.4.** Thermal ellipsoids shown at 50% probability and H atoms were omitted for clarity. Selected bond lengths (Å) and angles (°): B1–C1: 1.512(3); B1–C23: 1.618(3); B1–C26: 1.606(3).

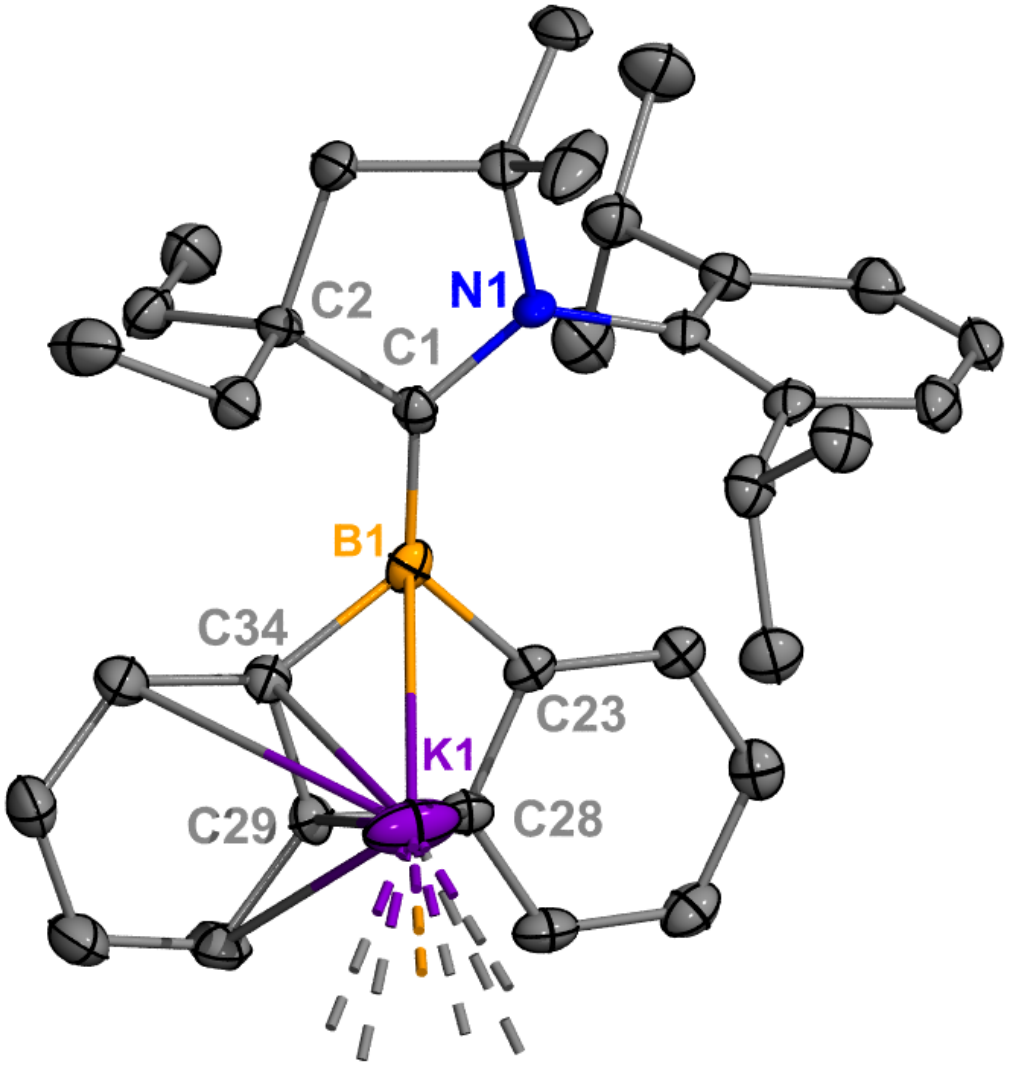

Figure A3.15. Molecular structure of **4.5.** Thermal ellipsoids shown at 50% probability and H atoms were omitted for clarity. Selected bond lengths (Å) and angles (°): B1–C1: 1.502(5); B1–C23: 1.603(5); B1–C34: 1.621(5).

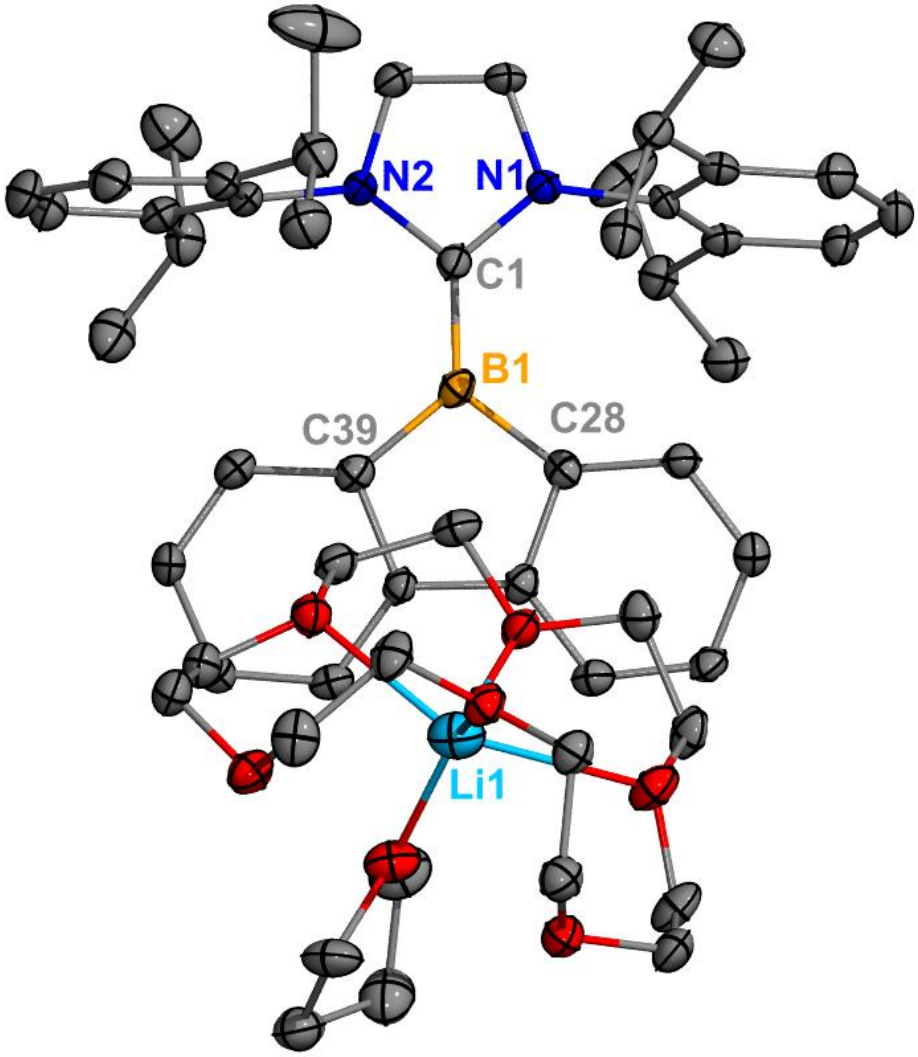

Figure A3.16. Molecular structure of **4.6.** Thermal ellipsoids shown at 50% probability and H atoms were omitted for clarity. Selected bond lengths (Å) and angles (°): B1–C1: 1.527(4); B1–C28: 1.585(4); B1–C39: 1.575(4).

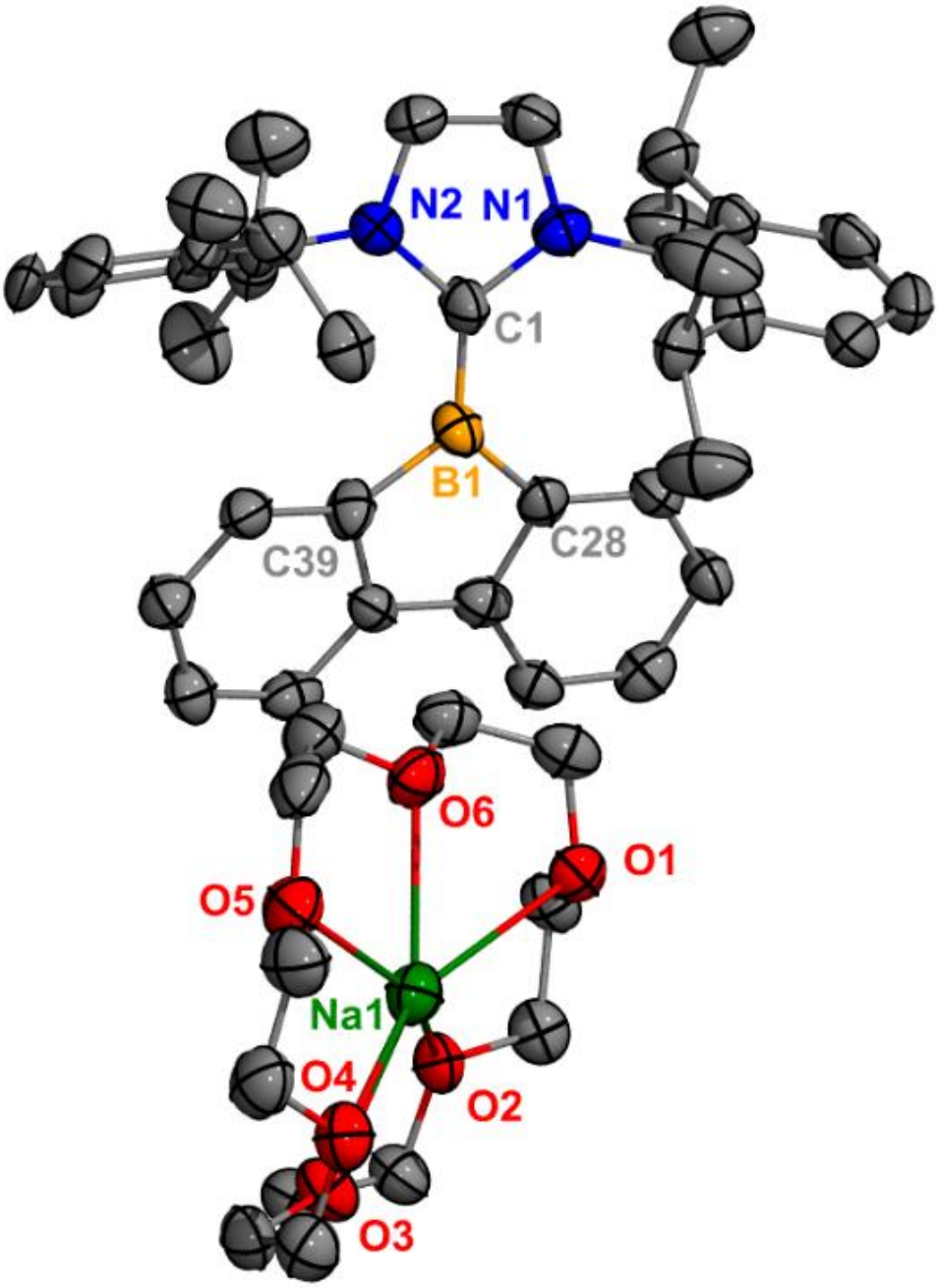

Figure A3.17. Molecular structure of **4.7.** Thermal ellipsoids shown at 50% probability and H atoms were omitted for clarity. Selected bond lengths (Å) and angles (°): B1–C1: 1.513(11) B1–C28: 1.576(11); B1–C39: 1.573(11).

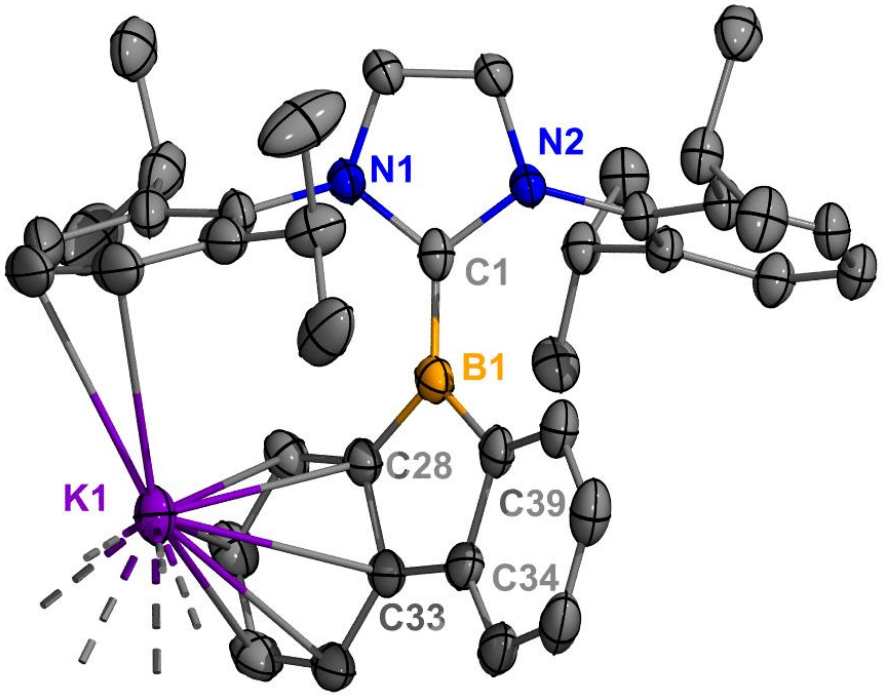

Figure A3.18. Molecular structure of **4.8.** Thermal ellipsoids shown at 50% probability and H atoms were omitted for clarity. Selected bond lengths (Å) and angles (°): B1–C1: 1.508(4); B1–C28: 1.534(4); B1–C34: 1.533(4).

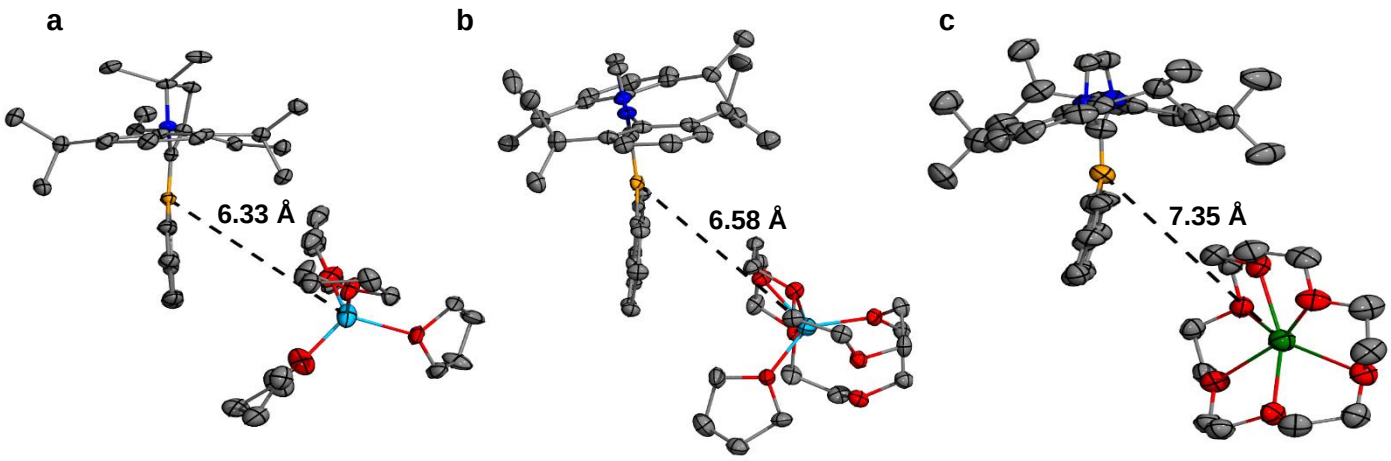

Figure A3.19. Charge separated borafluorene anions **4.3** (a), **4.6** (b), and **4.7** (c) with their B—M bond lengths shown.

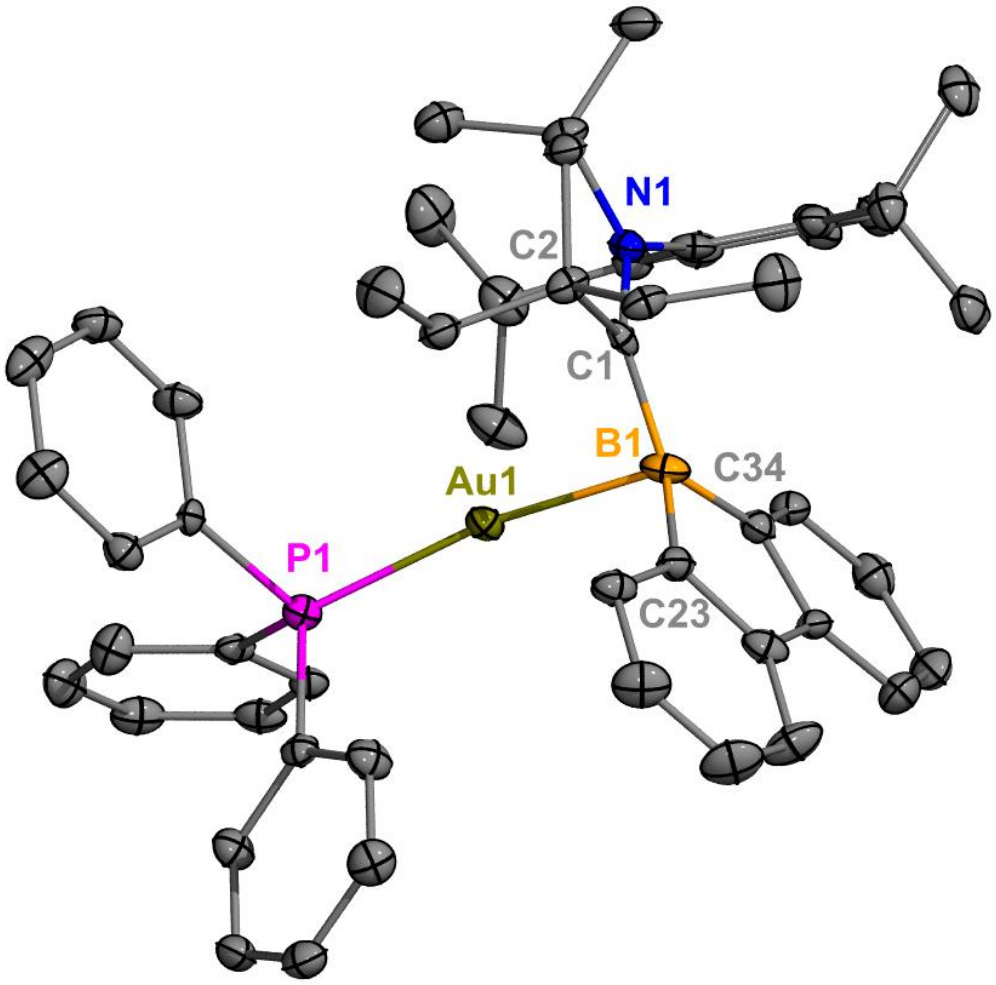

Figure A3.20. Molecular structure of **4.9.** Thermal ellipsoids set at 50 % probability and H atoms were omitted for clarity. Selected bond lengths [Å] and angles [°]: B1–C1: 1.555(8); B1–Au1 2.223(6), P1–Au1 2.2969(13); B1-Au1-P1 164.85(16).

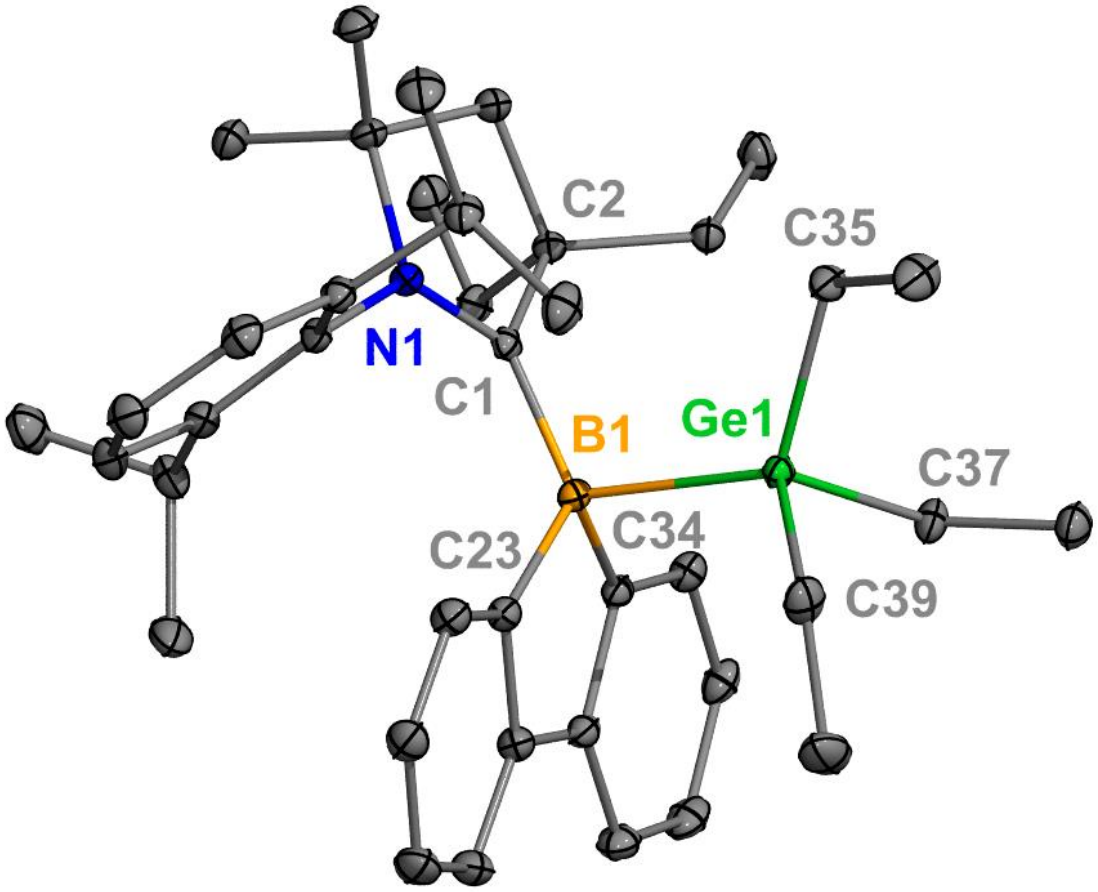

Figure A3.21. Molecular structure of **4.10.** Thermal ellipsoids set at 50 % probability and H atoms were omitted for clarity. Selected bond lengths [Å]: B1–C1: 1.6186(14); B1–Ge1 2.2079(10).

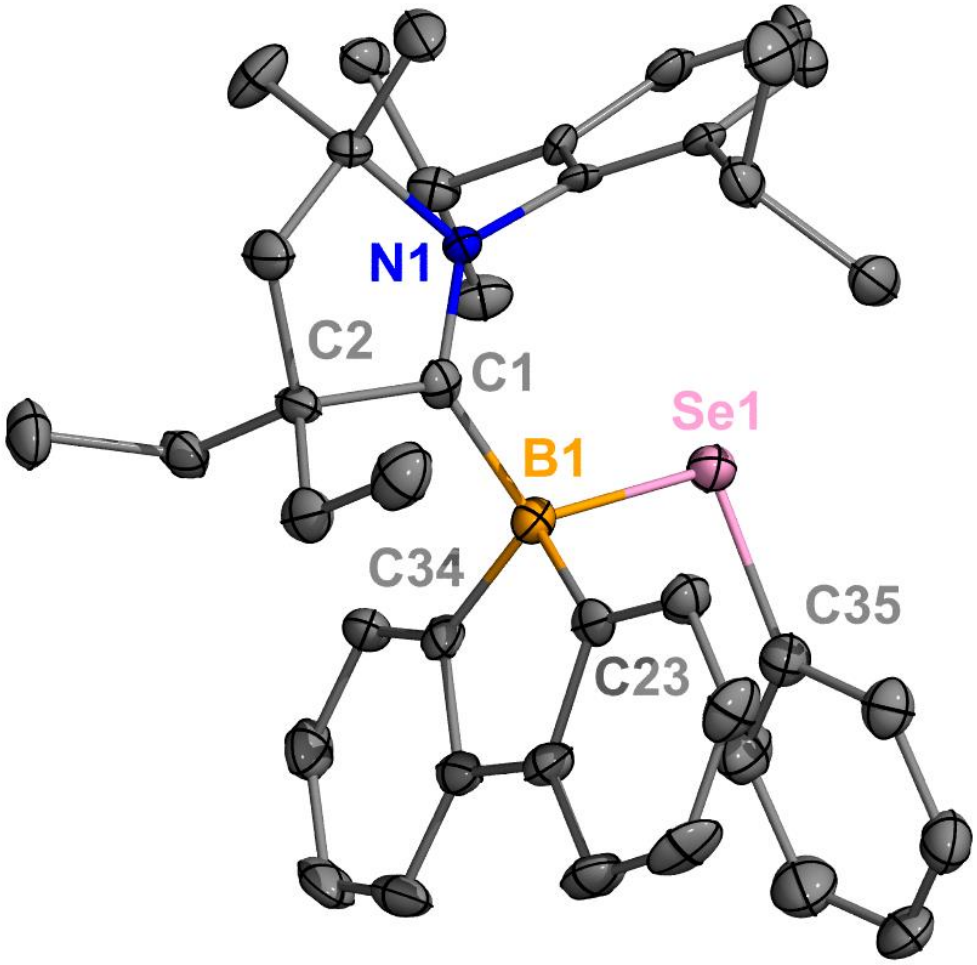

Figure A3.22. Molecular structure of **4.11.** Thermal ellipsoids set at 50 % probability and H atoms were omitted for clarity. Selected bond lengths [Å]: B1–C1: 1.635(7); B1–Se1 2.103(6); Se1–C35 1.926(5).

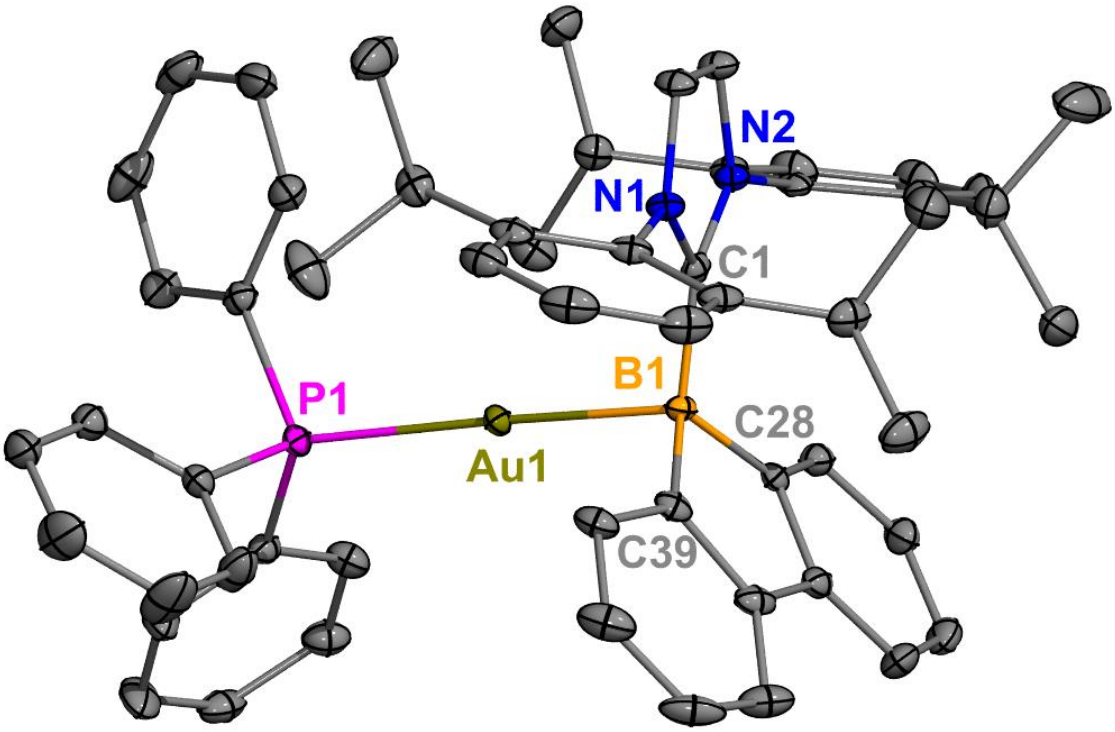

Figure A3.23. Molecular structure of **4.12.** Thermal ellipsoids set at 50 % probability and H atoms were omitted for clarity. Selected bond lengths [Å] and angles [°]: B1–C1: 1.601(4); B1–Au1 2.184(3); P1–Au1 2.3361(7); B1-Au1-P1 175.04(8).

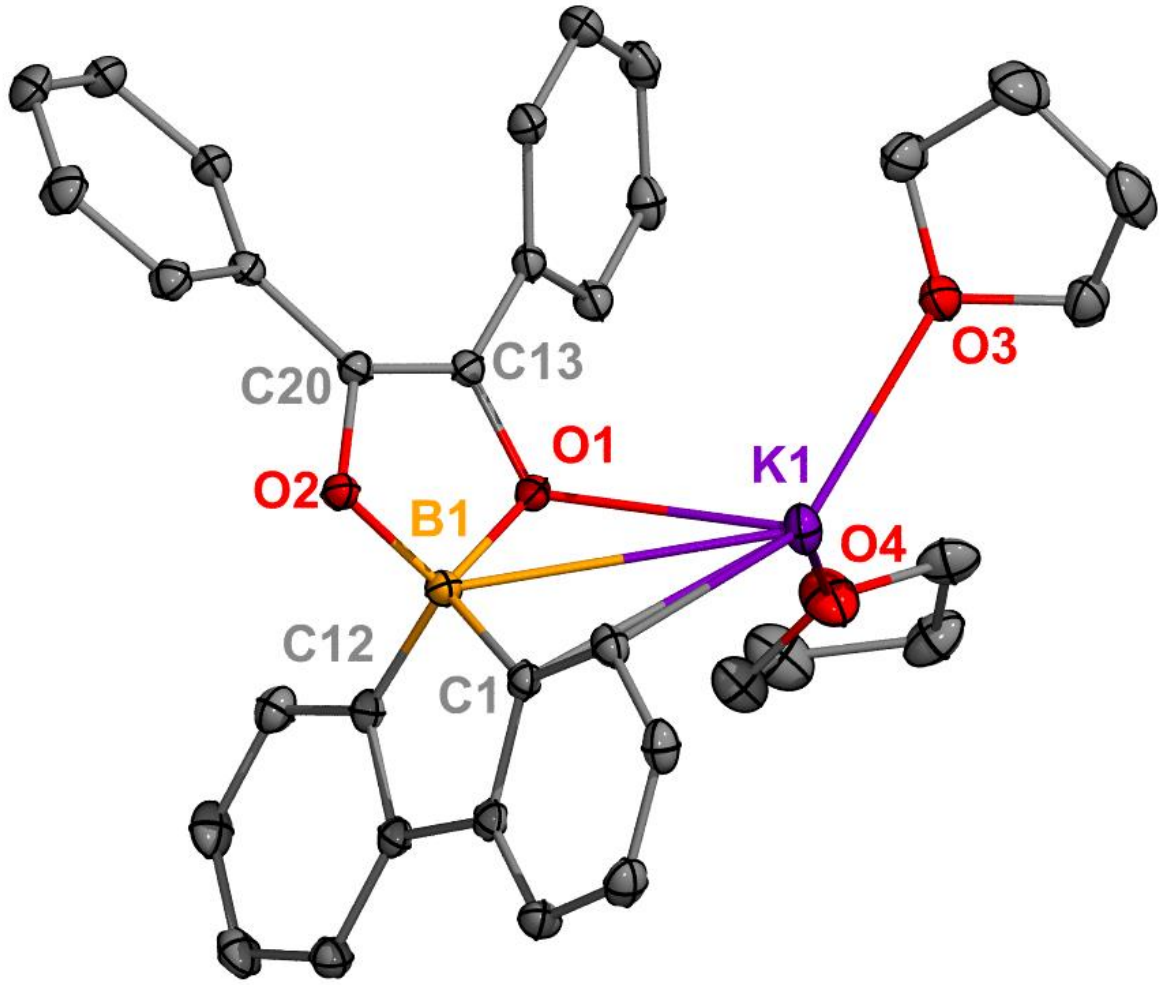

Figure A3.24. Molecular structures of **4.13**. Thermal ellipsoids set at 50 % probability and H atoms were omitted for clarity. Selected bond lengths [Å]: B1–O1: 1.5103(15); B1–O2: 1.5156(15); O1–C13: 1.3796(14); O2–C20: 1.3801(14); C13–C20: 1.3565(16).

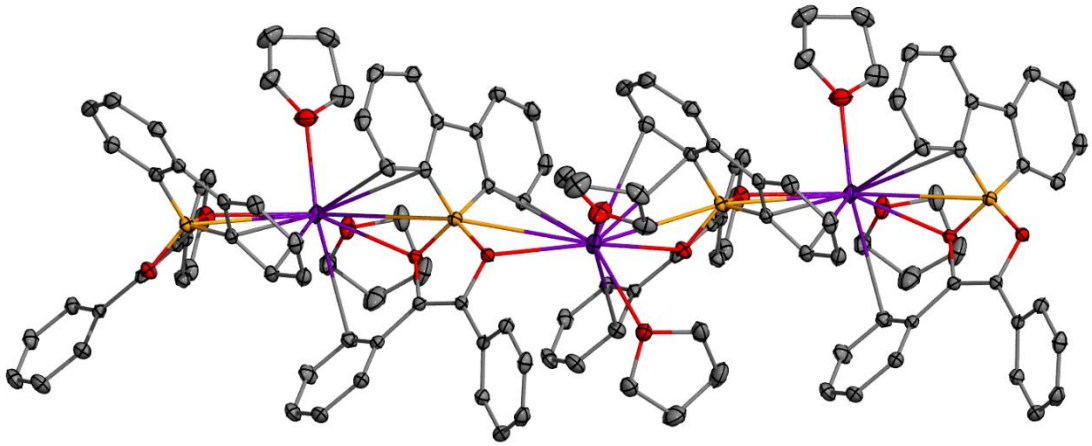

Figure A3.25. Coordination polymer of **4.13**.

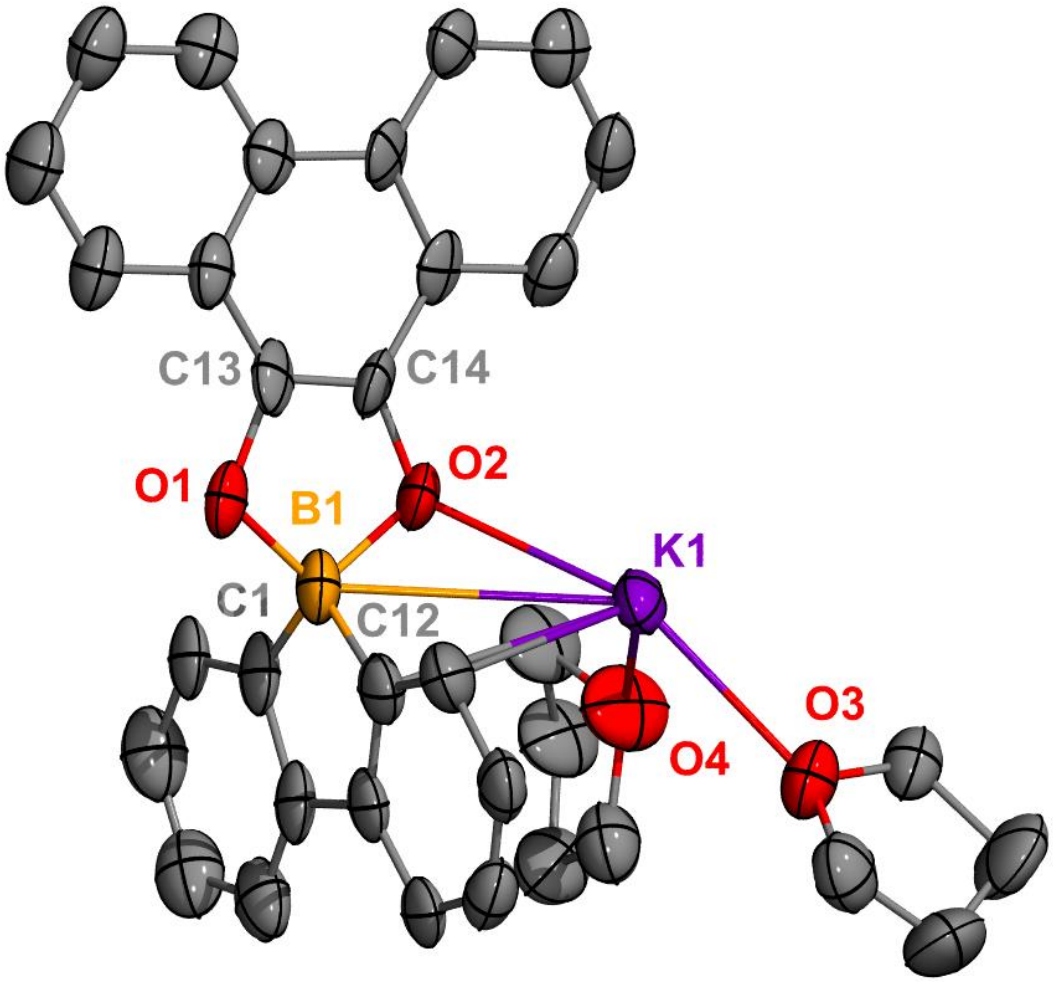

Figure A3.26. Molecular structures of **4.14**. Thermal ellipsoids set at 50 % probability and H atoms were omitted for clarity. Selected bond lengths [Å]: B1–O1: 1.52(3); B1–O2: 1.57(3); O1–C13: 1.42(2); O2–C14: 1.35(2); C13–C14: 1.30(3).

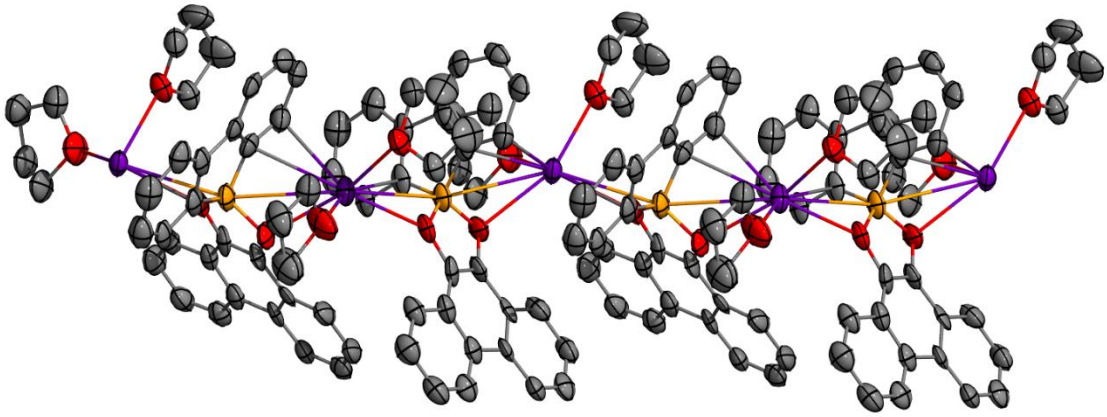

Figure A3.27. Coordination polymer of **4.14**.

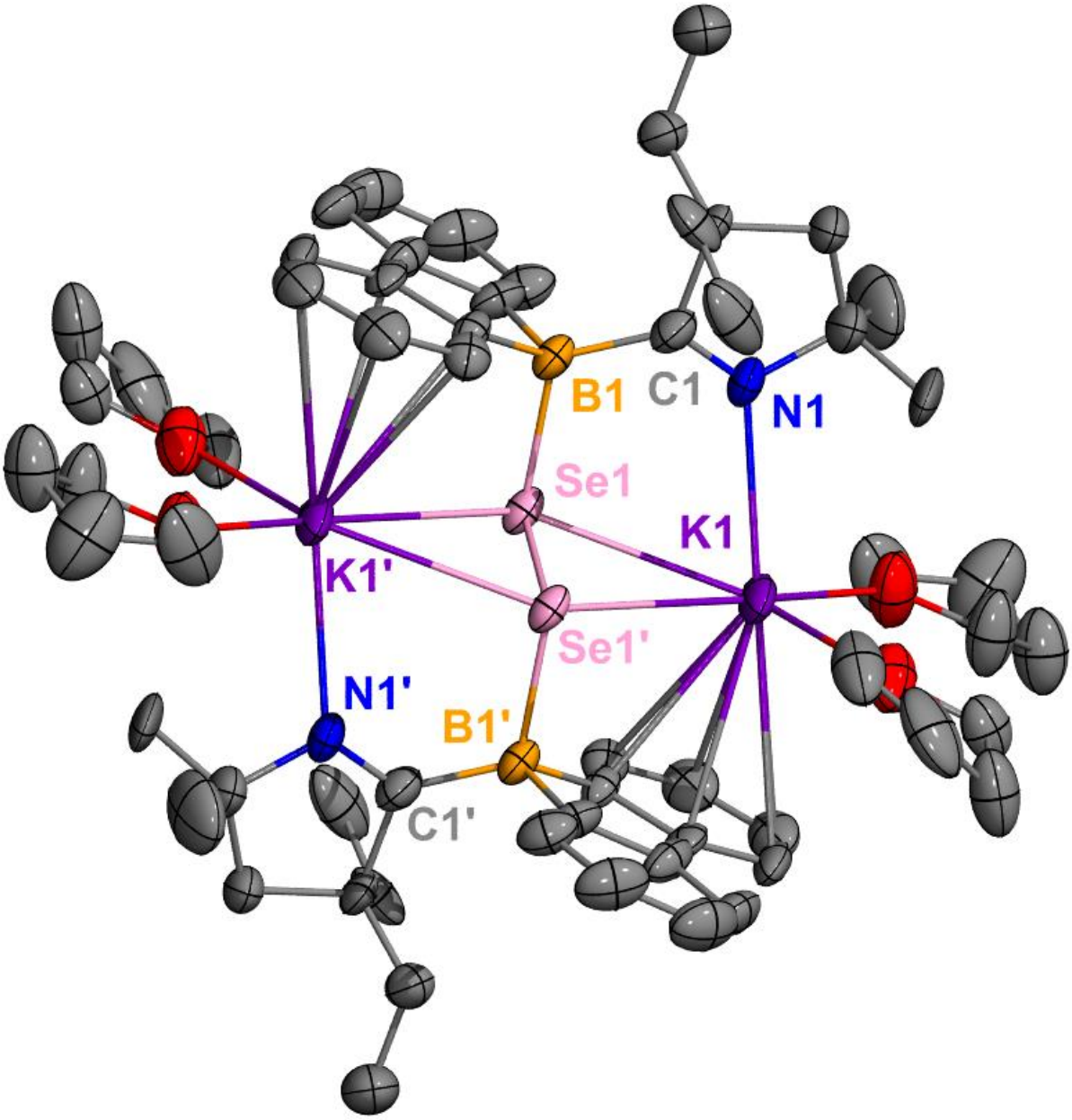

Figure A3.28. Molecular structure of **5.2**. Thermal ellipsoids set at 50% probability with H atoms and non-coordinated solvent omitted for clarity. Selected bond lengths [Å]: B1–C1: 1.613(9); C1–N1: 1.301(8); B1–Se1: 2.131(7); Se1–K1 3.2745(14); Se1–Se1´ 2.3807(11).

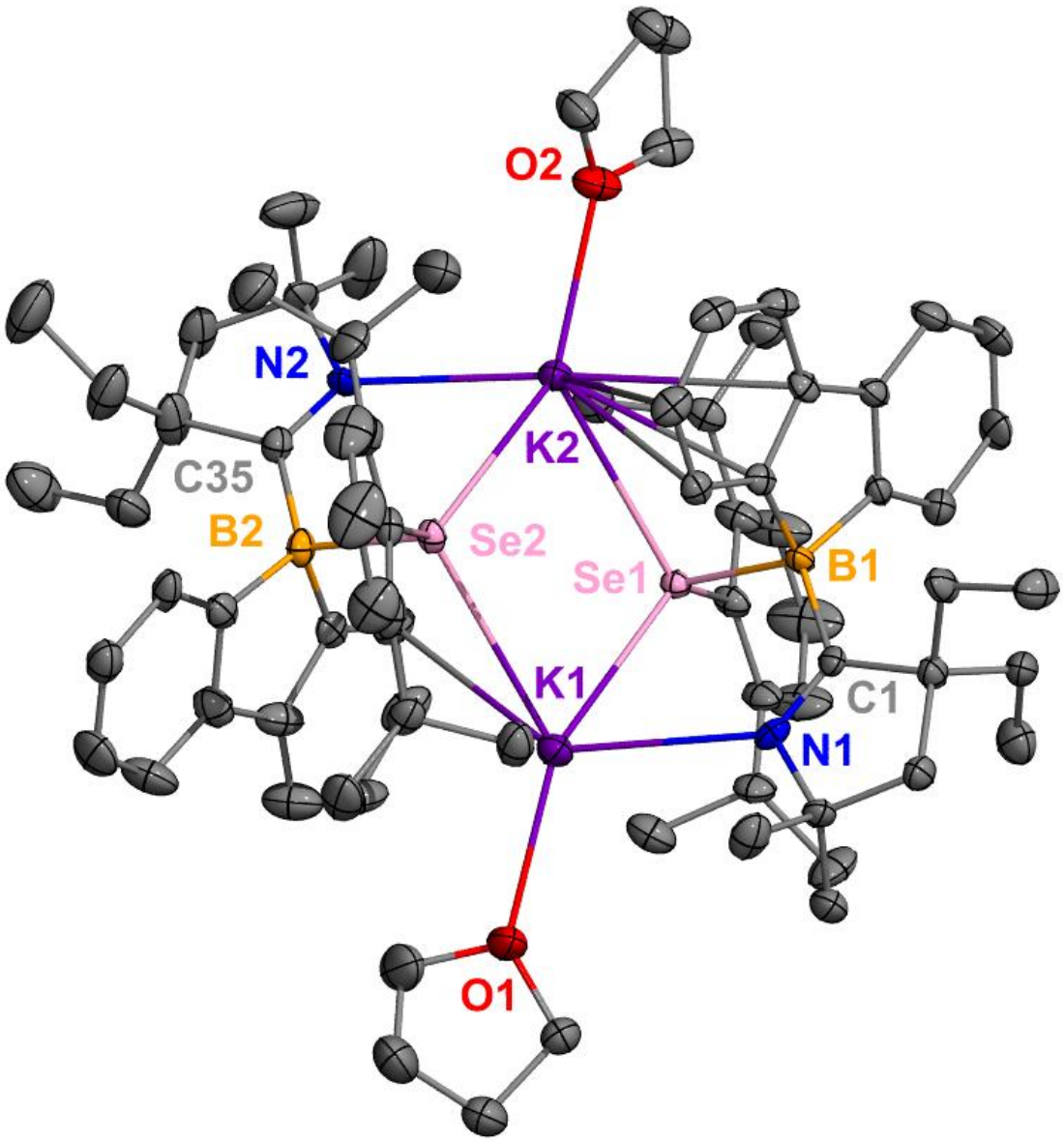

Figure A3.29. Molecular structure of **5.3**. Thermal ellipsoids set at 50% probability with H atoms and non-coordinated solvent omitted for clarity. Selected bond lengths [Å]: B1–C1: 1.627(8); C1–N1: 1.285(7); B1–Se1: 2.126(6); Se1–K1 3.2174(14).

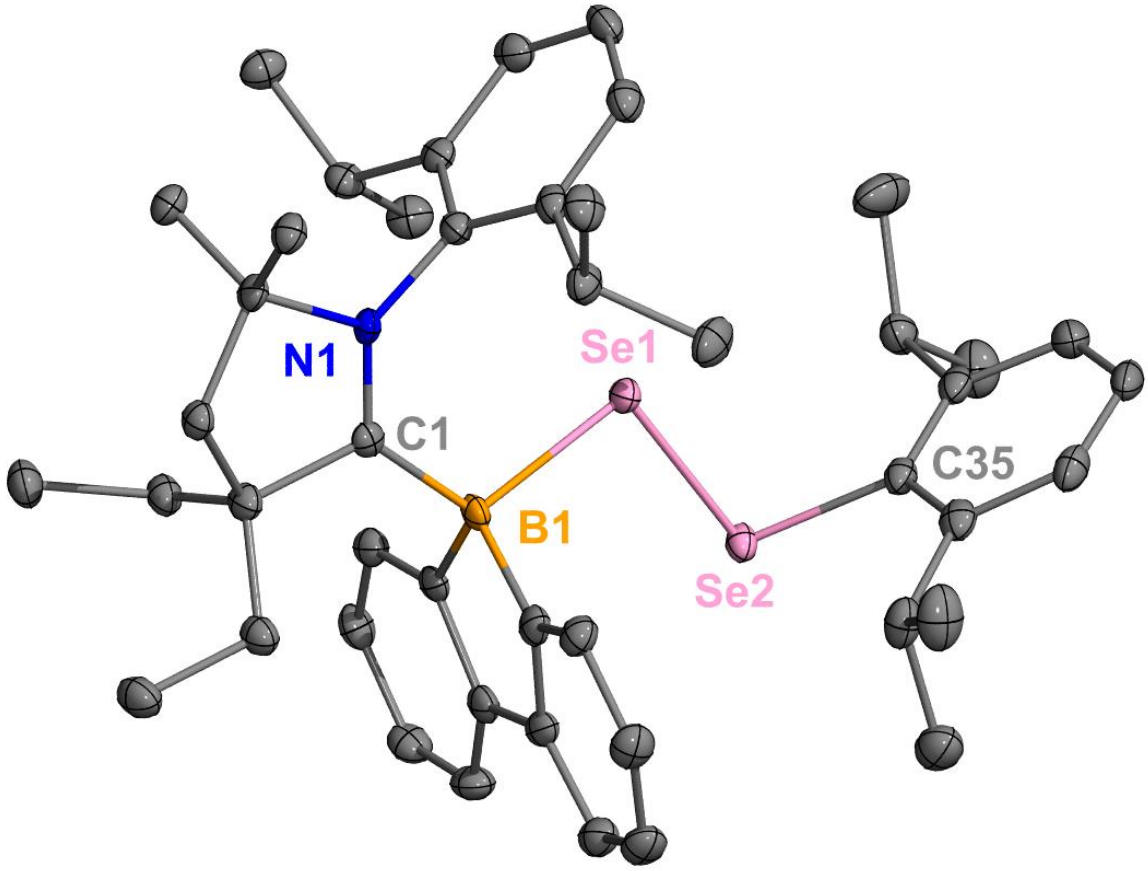

Figure A3.30. Molecular structure of **5.4**. Thermal ellipsoids set at 50% probability with H atoms and non-coordinated solvent omitted for clarity. Selected bond lengths [Å]: B1–C1: 1.613(9); C1–N1: 1.301(8); B1–Se1: 2.131(7); Se1–K1 3.2745(14); Se1–Se1´ 2.3807(11).

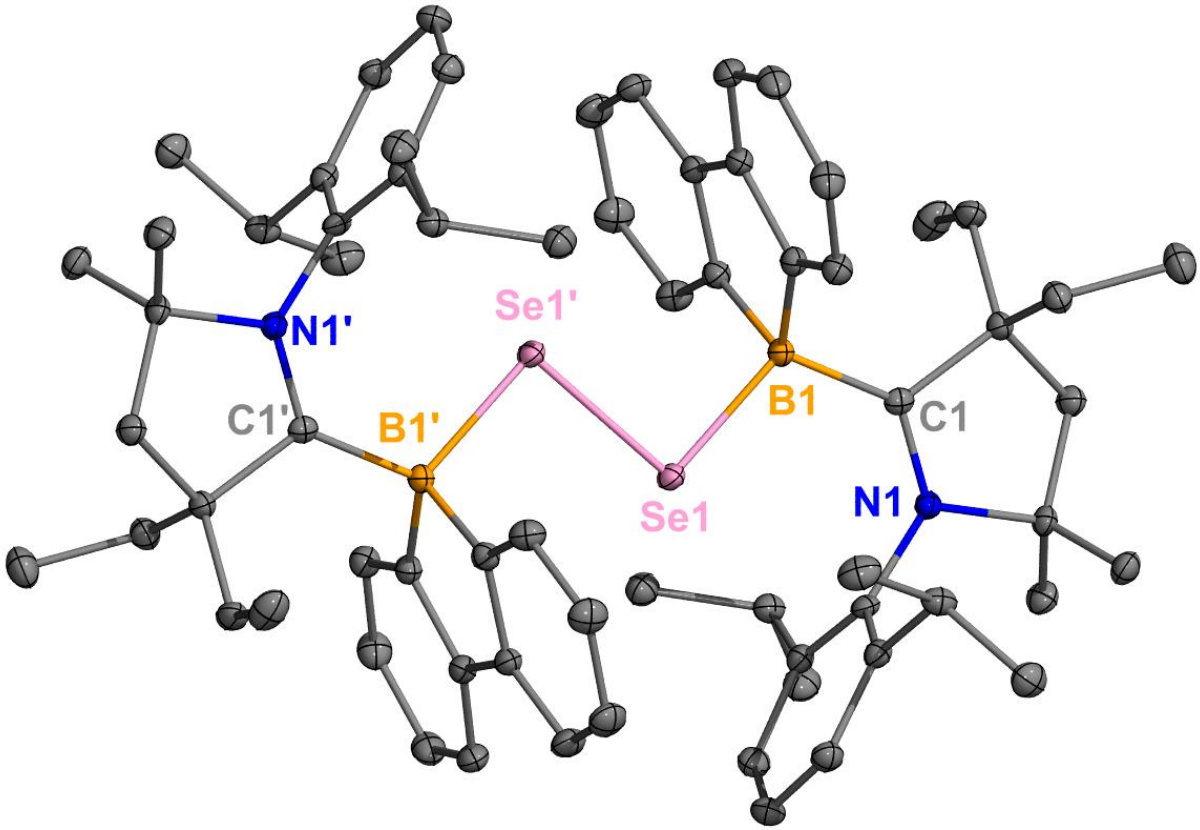

Figure A3.31. Molecular structure of **5.5**. Thermal ellipsoids set at 50% probability with H atoms and non-coordinated solvent omitted for clarity. Selected bond lengths [Å]: B1–C1: 1.634(2); C1–N1: 1.3139(17); B1–Se1: 2.0937(15); Se1–Se1′ 2.3612(4).

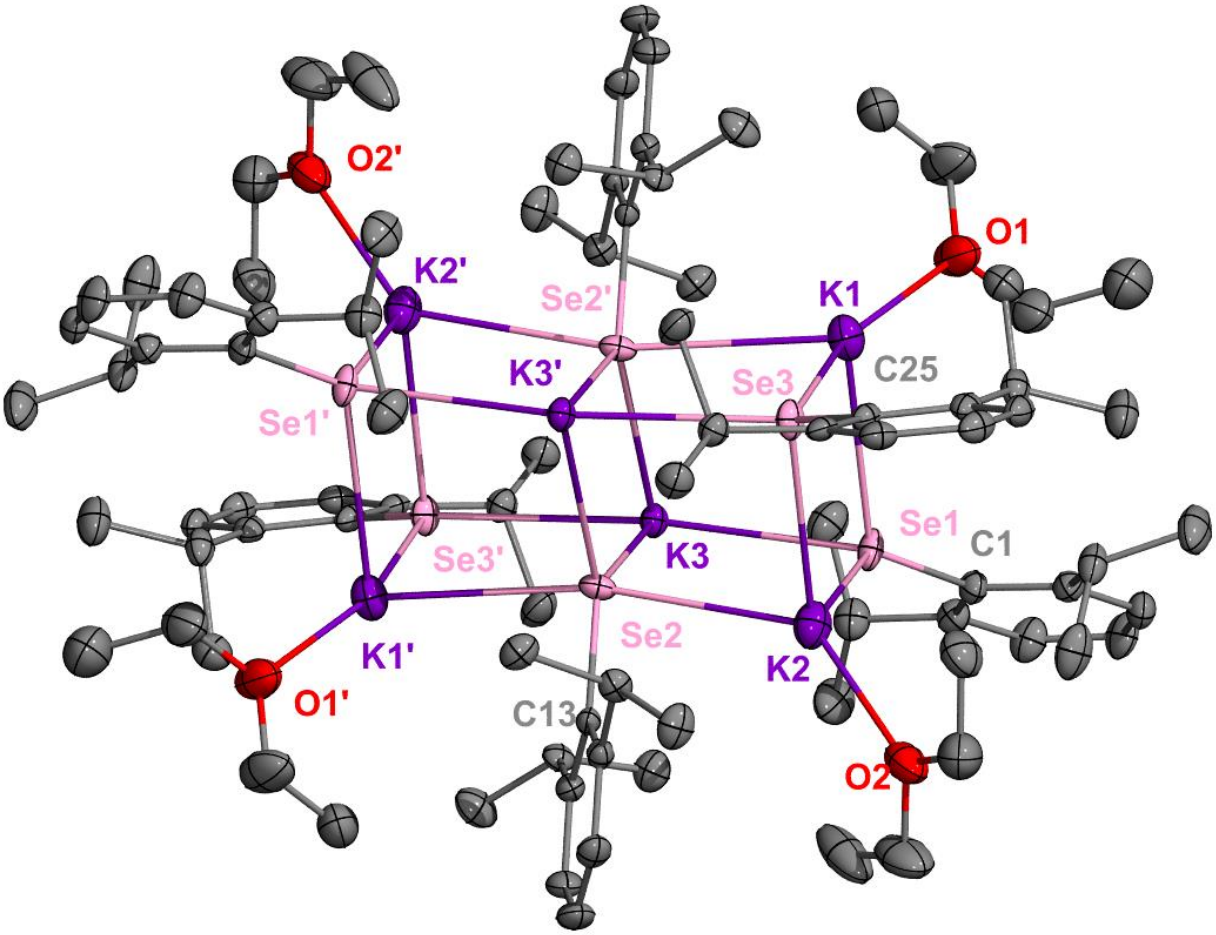

Figure A3.32. Molecular structure of **5.6**. Thermal ellipsoids set at 50% probability with H atoms and non-coordinated solvent omitted for clarity. Selected bond lengths [Å]: Se1–K1: 3.303(2).

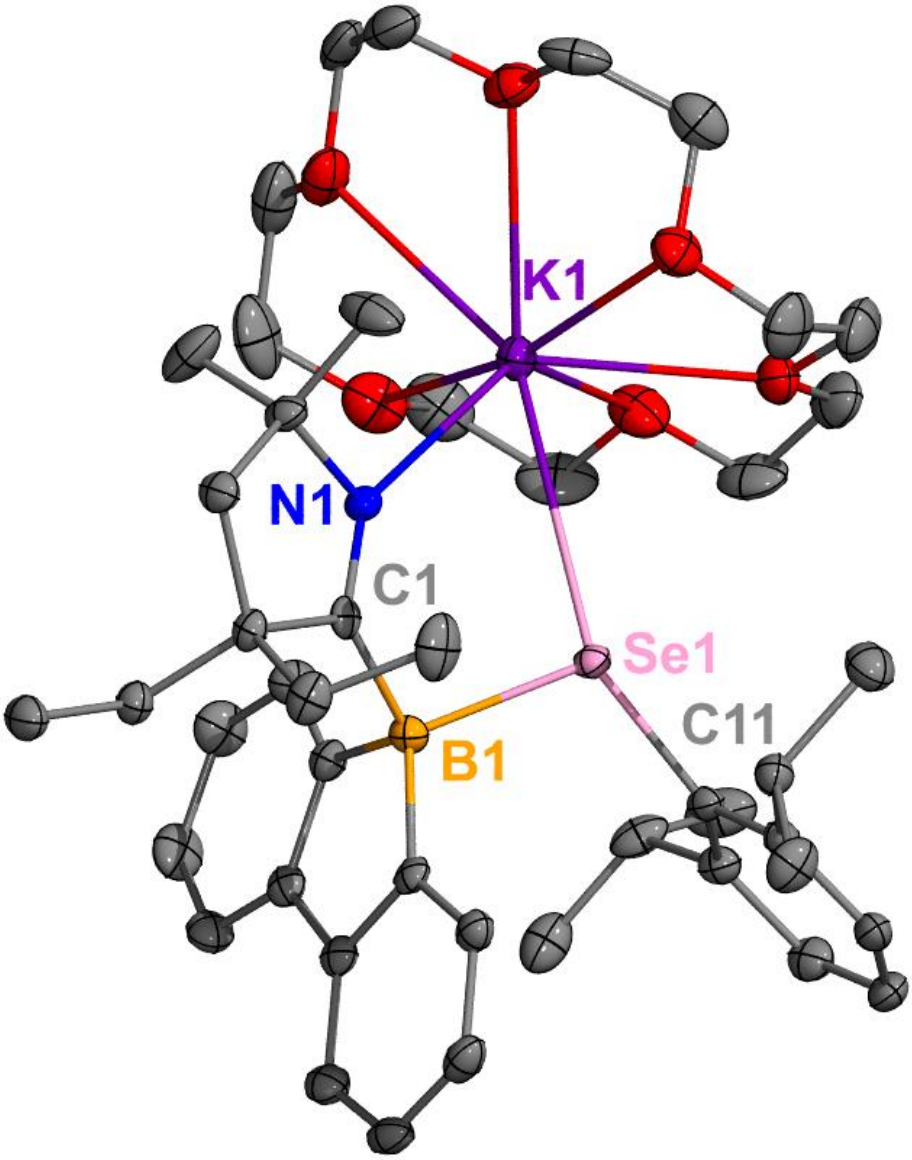

Figure A3.33. Molecular structure of **5.7**. Thermal ellipsoids set at 50% probability with H atoms and non-coordinated solvent omitted for clarity. Selected bond lengths [Å]: B1–C1: 1.624(4); C1–N1: 1.283(3); B1–Se1: 2.129(3); Se1–K1 3.5103(6).

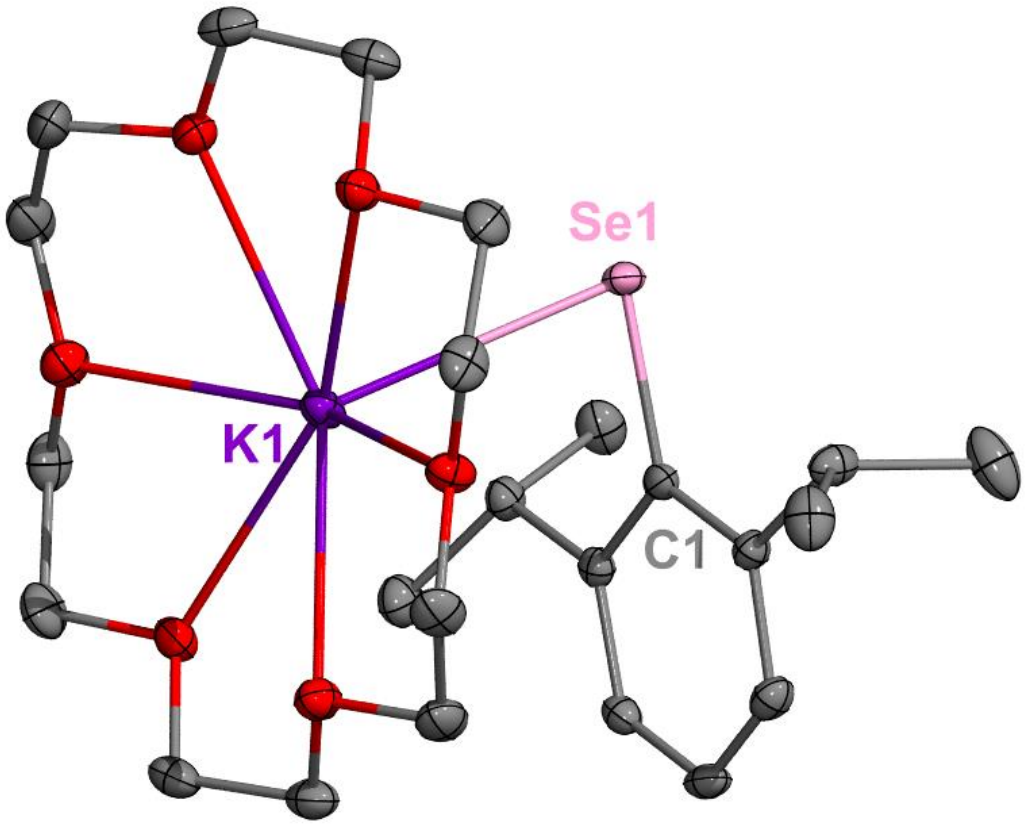

Figure A3.34. Molecular structure of **5.8**. Thermal ellipsoids set at 50% probability with H atoms and non-coordinated solvent omitted for clarity. Selected bond lengths [Å]: Se1–K1 3.3326(5).

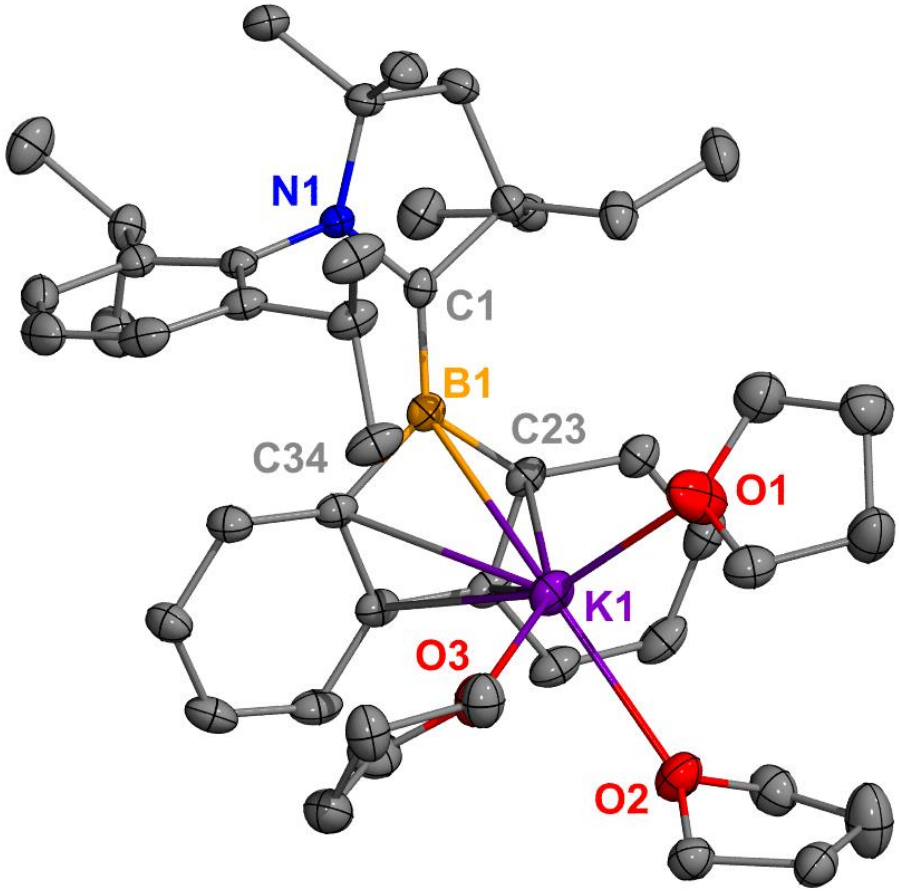

Figure A3.35. Molecular structure of **6.1**. Thermal ellipsoids set at 50% probability with H atoms and non-coordinated solvent omitted for clarity. Selected bond lengths [Å]: B1–C1 1.505(3); B1–C23 1.609(2); B1–C34 1.598(3); B1–K1 3.2363(19). **CCDC Deposition Number 2157309**

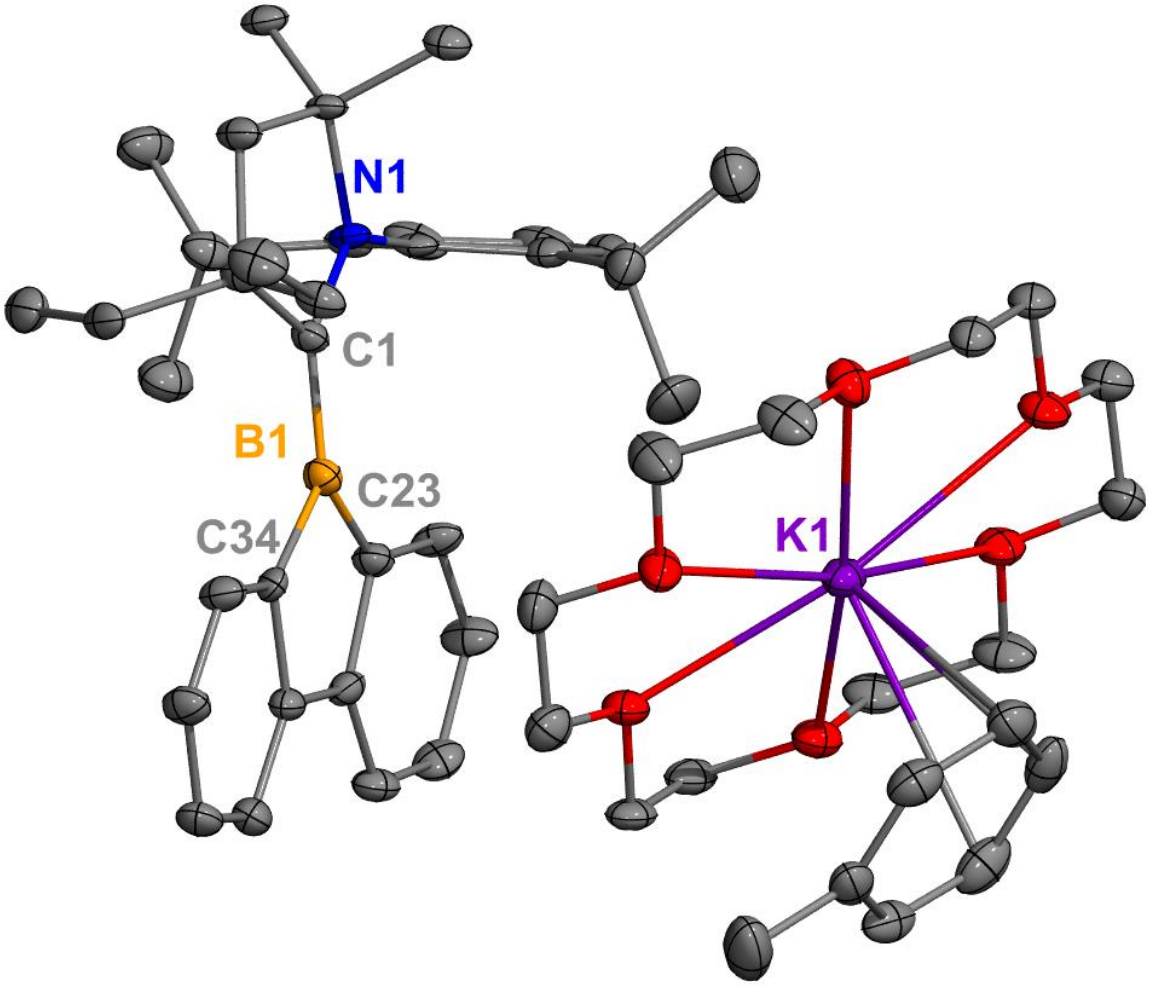

Figure A3.36. Molecular structure of **6.2**. Thermal ellipsoids set at 50% probability with H atoms and non-coordinated solvent omitted for clarity. Selected bond lengths [Å]: B1–C1 1.519(7); B1–C23 1.586(8); B1–C34 1.617(8); B1---K1 5.911(6). **CCDC Deposition Number 2157310**

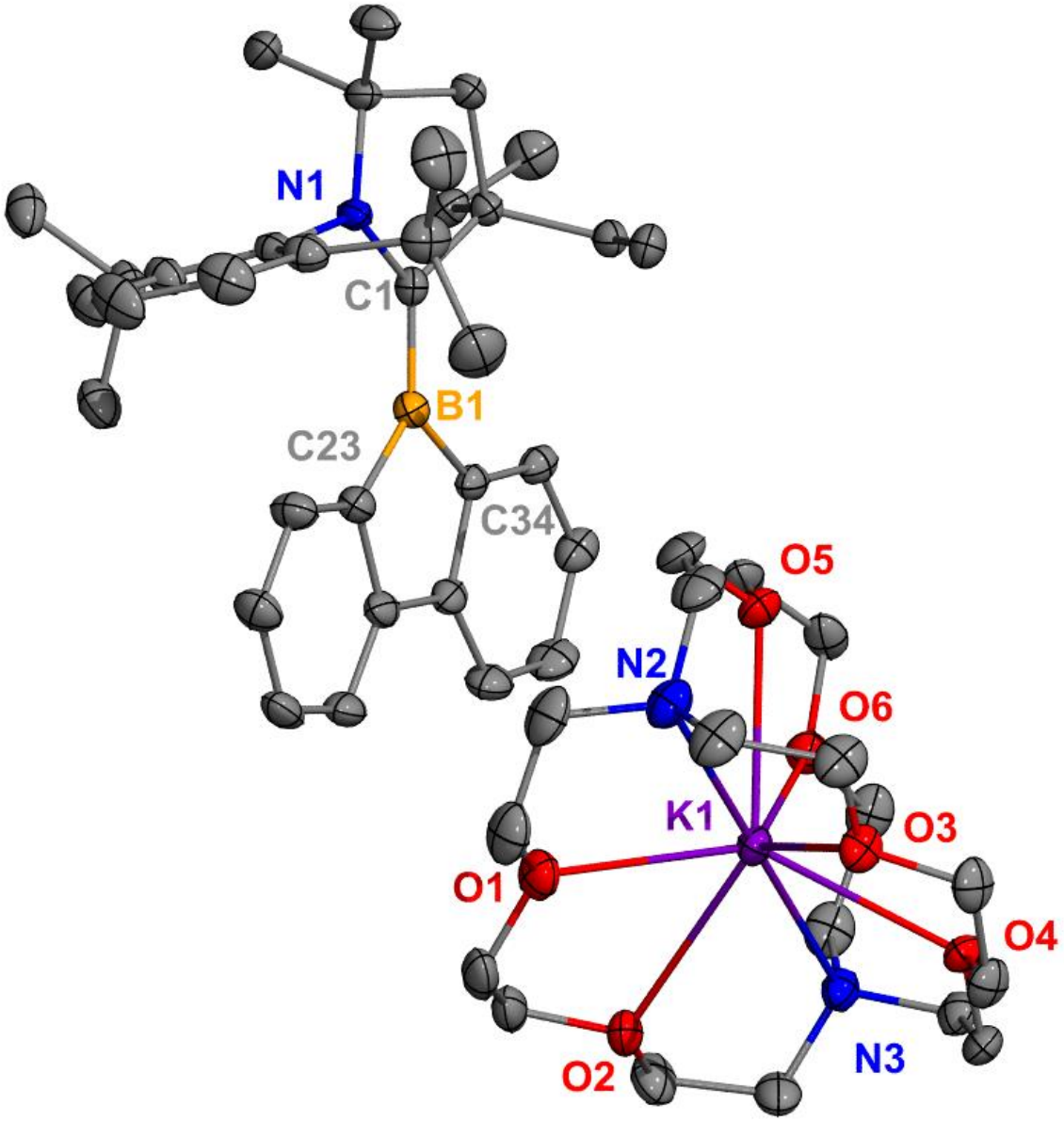

Figure A3.37. Molecular structure of **6.3**. Thermal ellipsoids set at 50% probability with H atoms and non-coordinated solvent omitted for clarity. Selected bond lengths [Å]: B1–C1 1.495(2); B1–C23 1.601(2); B1–C34 1.616(2); B1---K1 6.891(2). **CCDC Deposition Number 2157311**

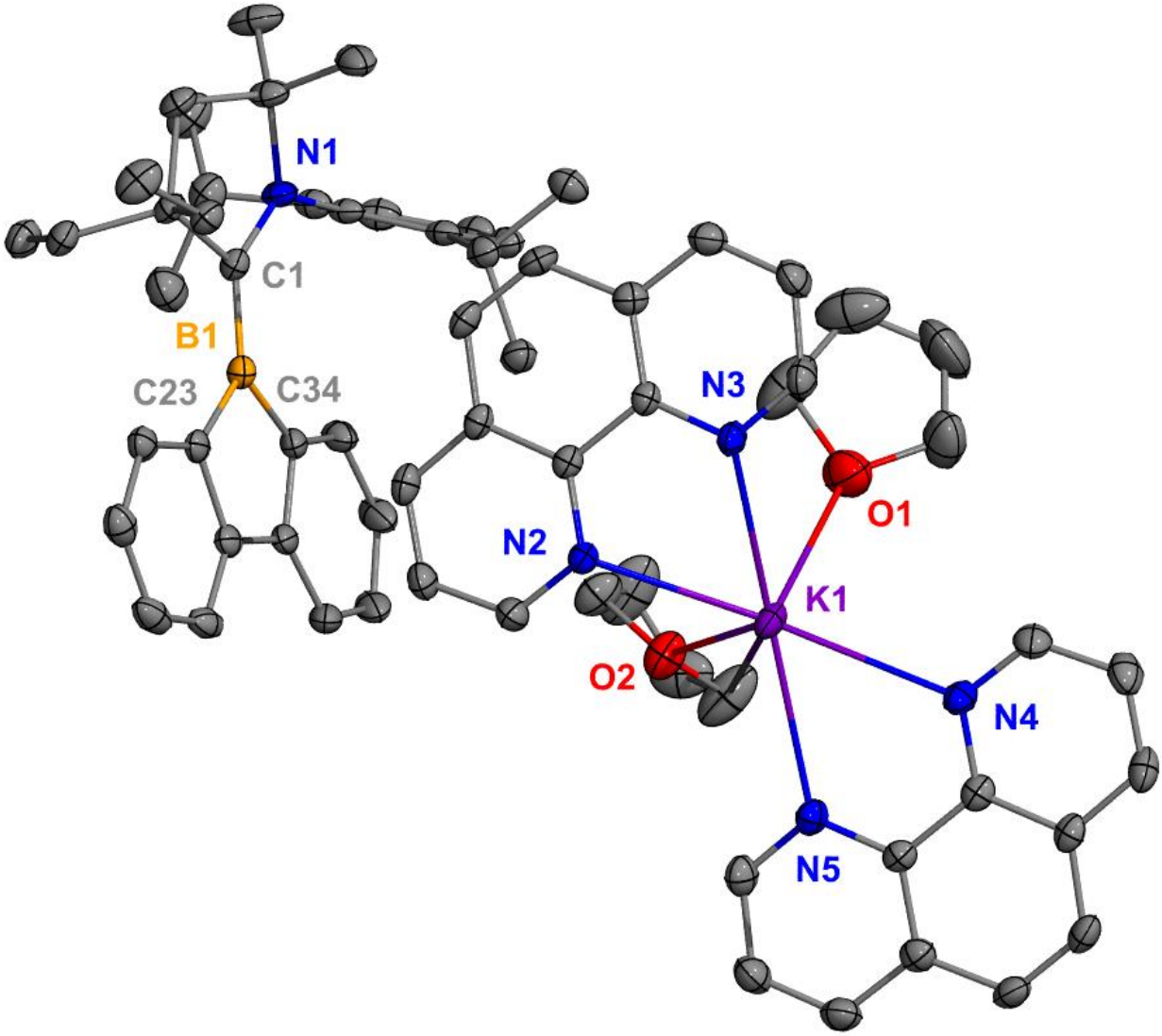

Figure A3.38. Molecular structure of **6.4**. Thermal ellipsoids set at 50% probability with H atoms and non-coordinated solvent omitted for clarity. Selected bond lengths [Å]: B1–C1 1.504(3); B1–C23 1.607(3); B1–C34 1.600(3); B1---K1 8.095(2). **CCDC Deposition Number 2157312**

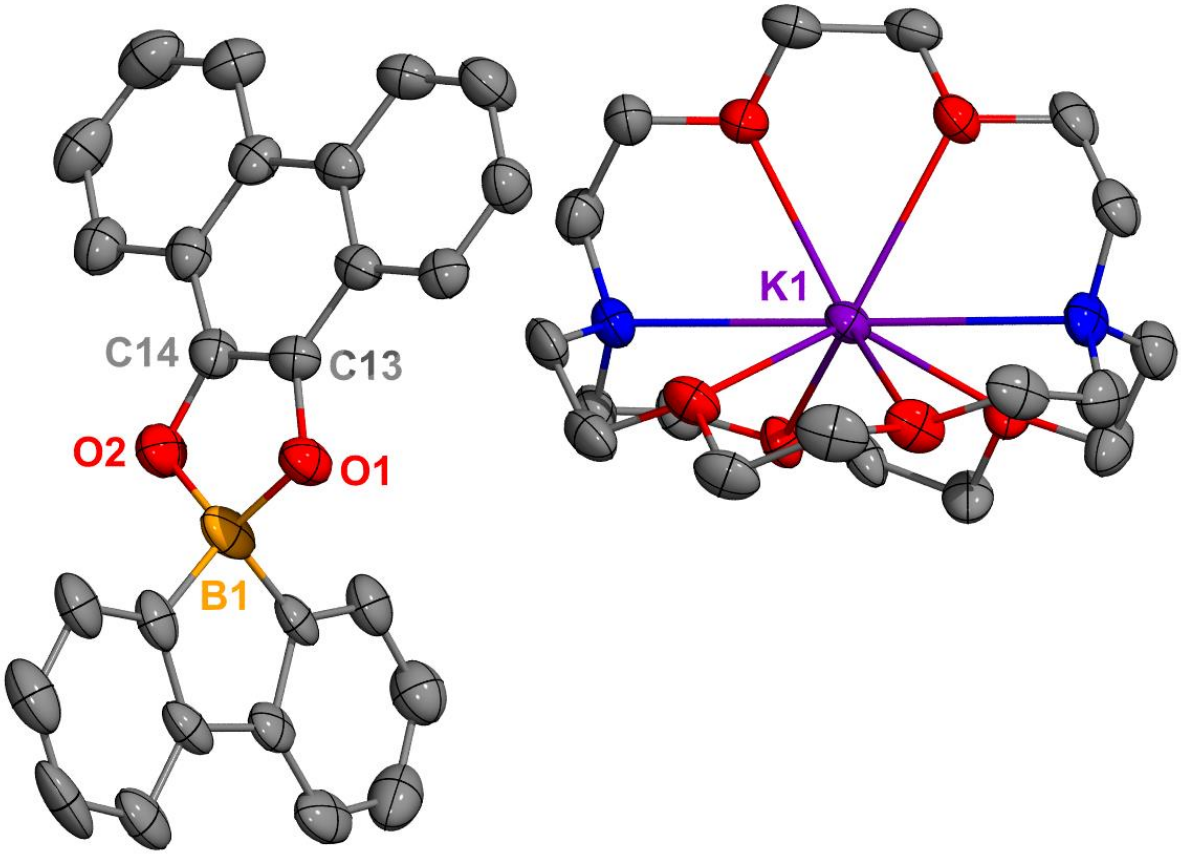

Figure A3.39. Molecular structure of **6.5**. Thermal ellipsoids set at 50% probability with H atoms and non-coordinated solvent omitted for clarity. Selected bond lengths [Å]: B1–O1 1.525(13); B1–O2 1.513(14); O1–C13 1.362(11); O2–C14 1.356(12); C13–C24 1.352(14). **CCDC Deposition Number 2157313**

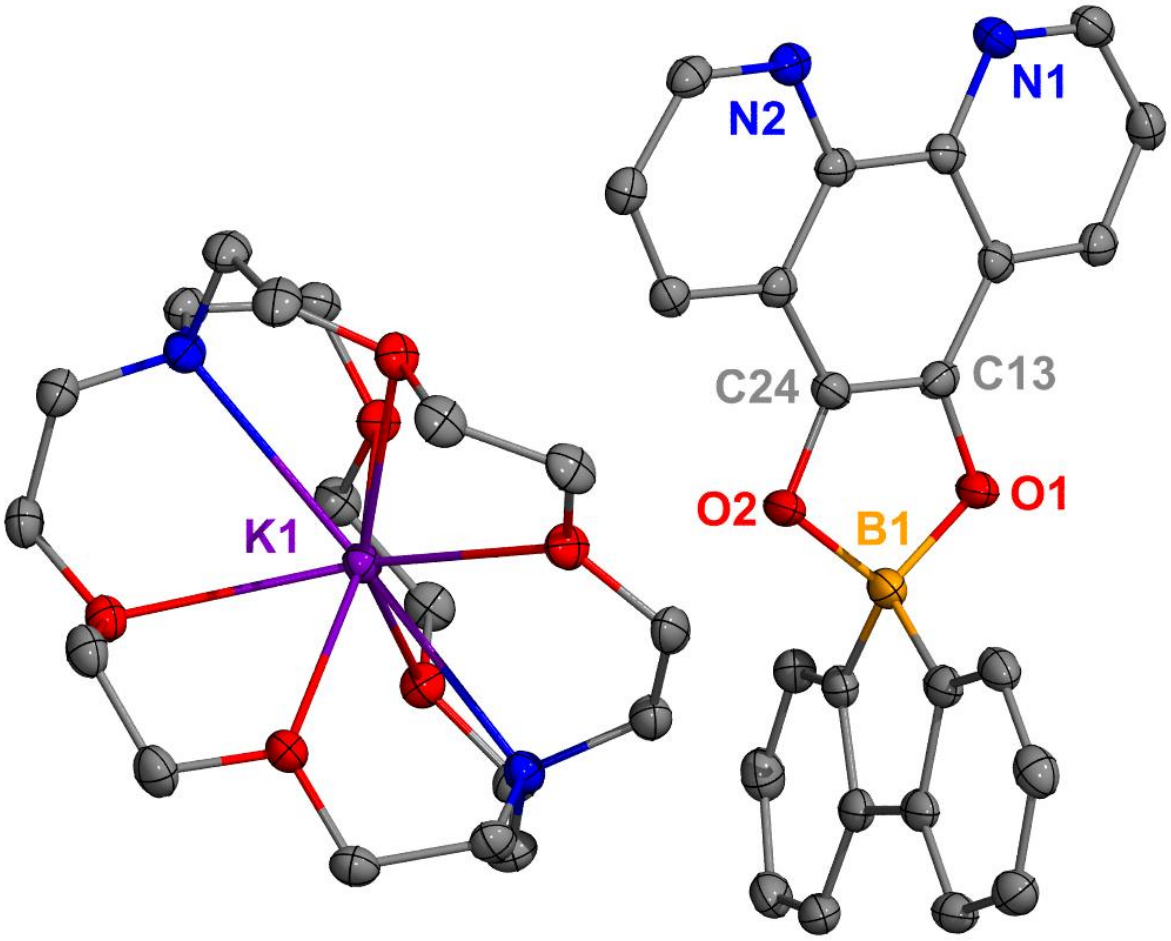

Figure A3.40. Molecular structure of **6.6**. Thermal ellipsoids set at 50% probability with H atoms and non-coordinated solvent omitted for clarity. Selected bond lengths [Å]: B1–O1 1.533(2), B1–O2 1.532(2), O1–C13 1.348(2), O2–C24 1.49(2), C13–C24 1.364(2). **CCDC Deposition Number 2157314**

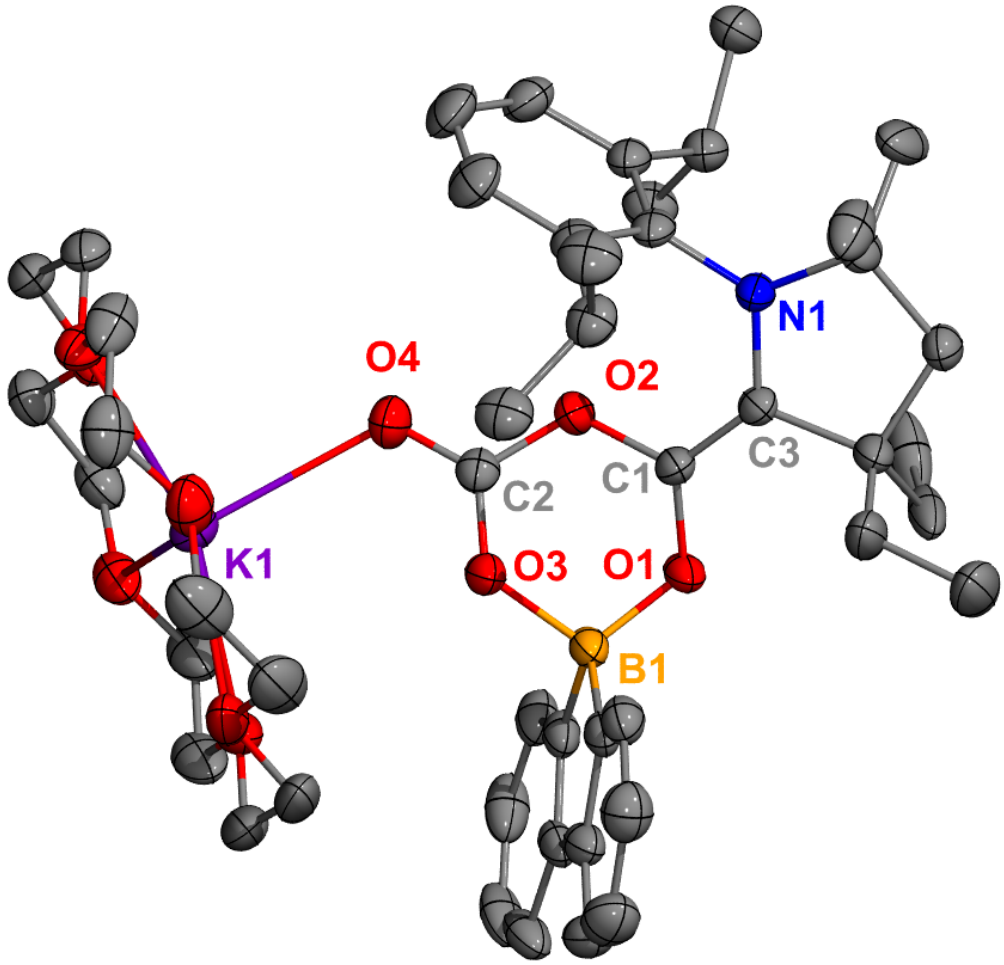

Figure A3.41. Molecular structure of **7.2**. Thermal ellipsoids set at 50% probability with H atoms and non-coordinated solvent omitted for clarity. Selected bond lengths [Å]: B1–O1 1.478(4), B1–O3 1.535(3), C1–O1 1.350(3), C1–O2 1.410(3), C2–O2 1.351(3), C2–O3 1.298(3), C2–O4 1.210(3), C1–C3 1.340(4). **CCDC Deposition Number 2166590**

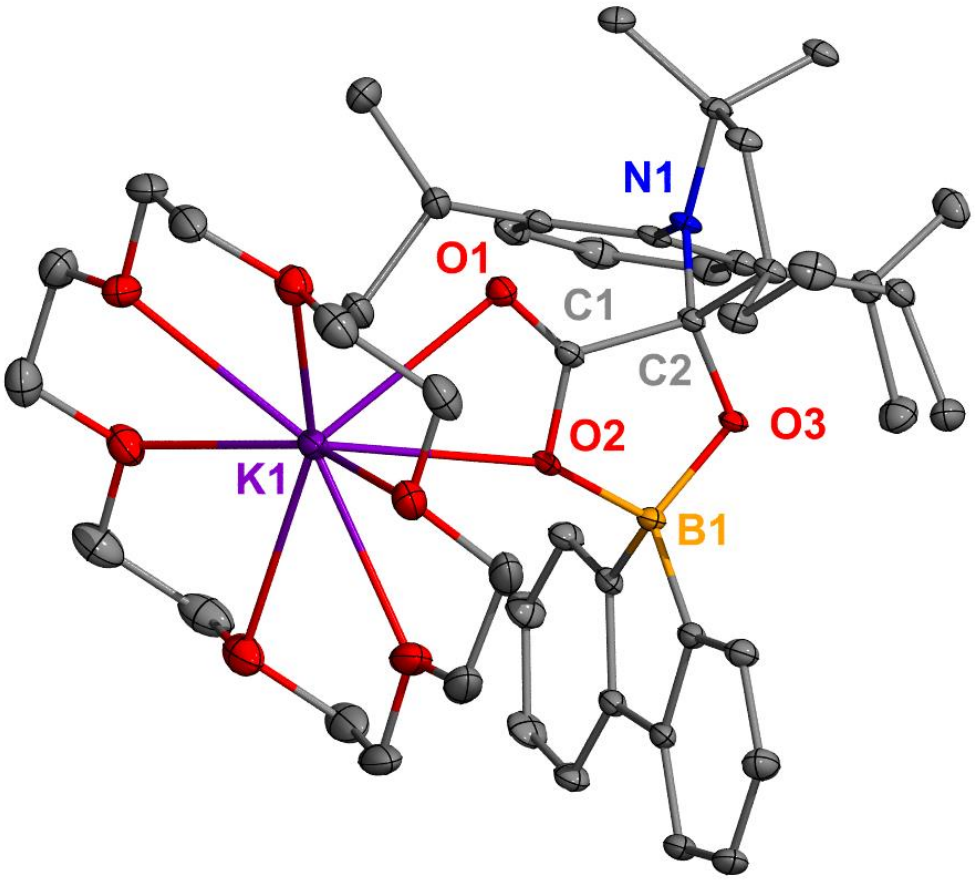

Figure A3.42. Molecular structure of **7.3**. Thermal ellipsoids set at 50% probability with H atoms and non-coordinated solvent omitted for clarity. Selected bond lengths [Å]: B1–O2 1.5429(18), B1–O3 1.4746(17), C1–O1 1.2223(17), C1–O2 1.3113(16), C1–C2 1.5517(18), C2–O3 1.3945(16). **CCDC Deposition Number 2166591**

Appendix IV – Computational Details

Chapter Two and Three

All computational data reported herein were obtained, analyzed, and prepared by Nathan Frey and Edwin Webster at Mississippi State University in Mississippi. Further information on TD-DFT excitation outputs, overlayed simulated absorption spectra, natural transition orbitals, calculated NICS values for other PAH systems, and details on the fluxionality of the twisted systems can be found in the original manuscripts.[229, 360] The starting geometries of compounds **2.2** and **2.3** were extracted from the X-ray crystal structures. Hydrogen positions were optimized using the Universal Force Field (UFF) freezing the location of all other atoms. The geometry of structure of **2.1** was generated from the molecular geometry of compound **2.2** from the X-ray crystal structure (the valency of the four amine nitrogens were satisfied with hydrogen atoms) and subsequently optimizing the structure at the B3LYP/BS1 level of theory. All computations were carried out using Gaussian 16 Revision B.01. Nucleus-Independent Chemical Shift (NICS) values[361] were computed for each aromatic ring of the compounds by computing gas phase magnetic shielding tensors of ghost atoms placed at the centroid of each ring [NICS(0)] using the Gauge Independent Atomic Orbital (GIAO)[362] method at the B3LYP/BS2 level of theory.[363-364] To simulate absorption and emission spectra using TD-DFT, the first twenty vertical transitions were computed for corresponding optimized geometries of each compound with B3LYP/BS1 (for absorption) and TD-B3LYP/BS1 (for emission).[365] Simulated absorption and emission spectra were obtained using an in-house Fortran program by convoluting the computed excitation energies and oscillator strengths with a Gaussian line-shape and a broadening of 20 nm. Orbital pictures were generated using Chemcraft with a contour value of 0.05.

Chapter Two

Frontier Molecular Orbitals

MO 166 LUMO –0.03729 Ha

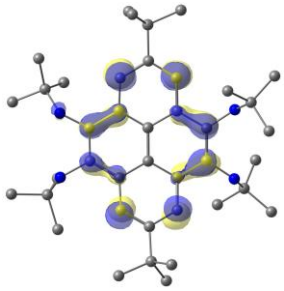

MO 165 HOMO –0.16233 Ha

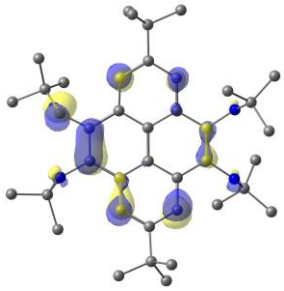

Figure A4.1. Frontier orbitals for the DFT-optimized geometry of **2.1**.

MO 168 LUMO –0.03933 Ha

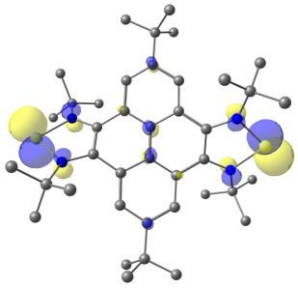

MO 167 HOMO –0.15373 Ha

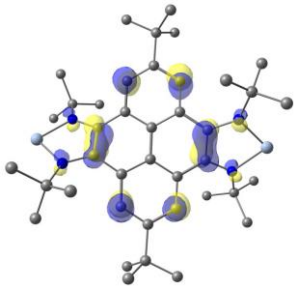

MO 163 HOMO – 4 –0.23229 Ha

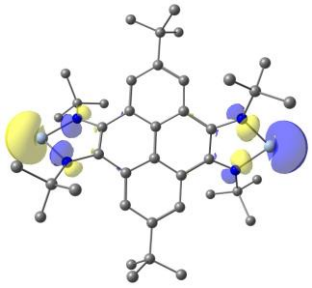

MO 162 HOMO – 5 –0.23563 Ha

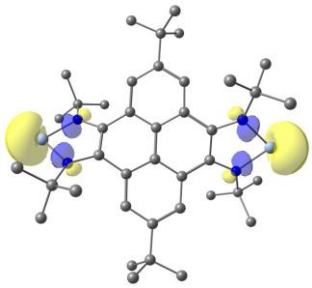

Figure A4.2. Selected molecular orbitals for the DFT-optimized geometry of **2.2**.

MO 268 LUMO –0.01988 Ha

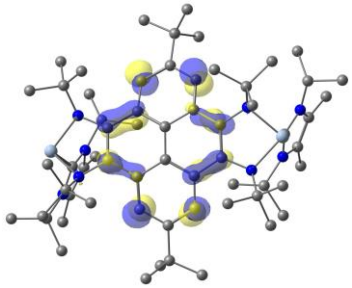

MO 267 HOMO –0.13473 Ha

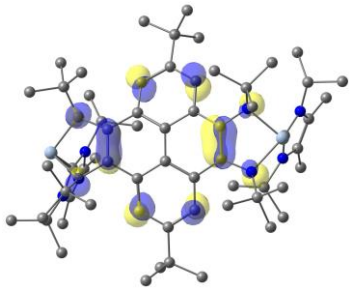

MO 265 HOMO – 2 –0.16555 Ha

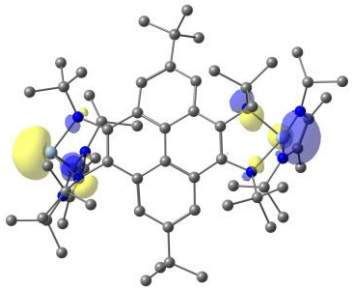

MO 264 HOMO – 3 –0.16776 Ha

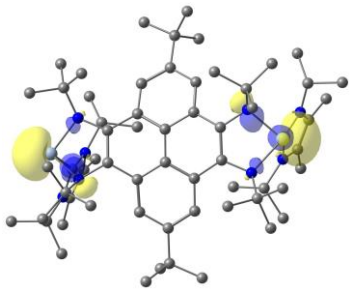

Figure A4.3. Selected molecular orbitals for the DFT-optimized geometry of **2.3**.

Simulated UV-vis Spectra

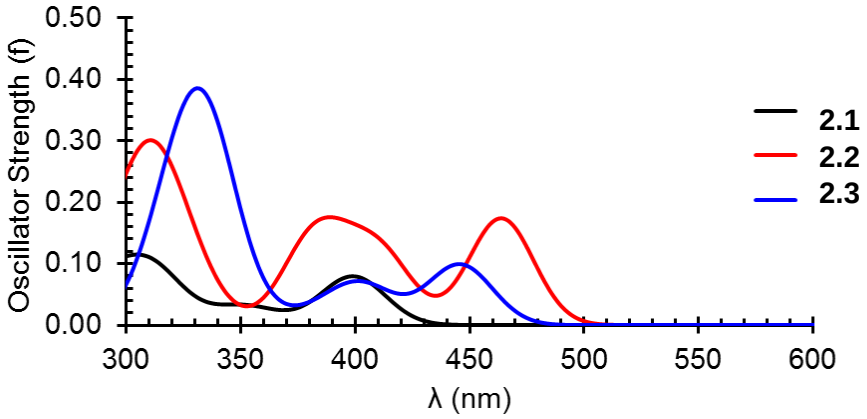

Figure A4.4. Simulated UV-vis absorption spectra of **2.1**-**2.3**.

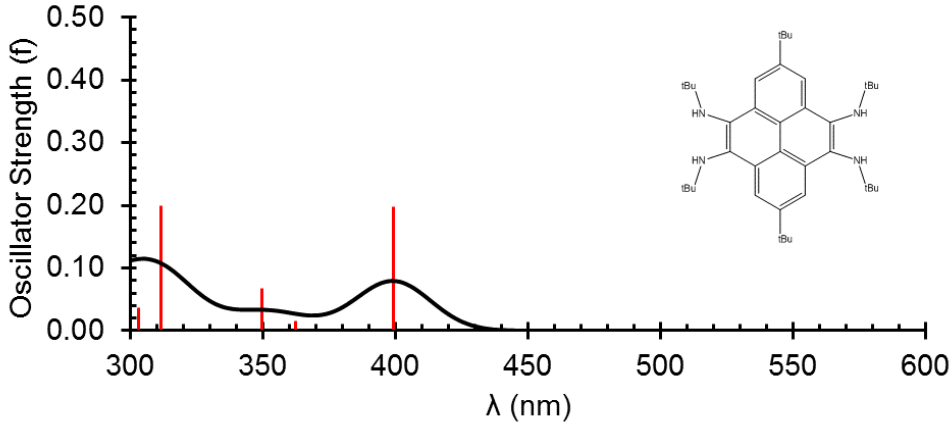

Figure A4.5. Simulated UV-vis absorption spectrum from TDDFT excitations for **2.1**.

Table A4.1. Electronic transitions for the calculated transitions of **2.1** and their orbital contributions.

λ (nm)	Character	% NTO Contribution
399	$\pi \rightarrow \pi^*$	96%
350	$\pi \rightarrow \pi^*$	90%
312	$\pi \rightarrow \pi^*$	59%
	$\pi \rightarrow \pi^*$	37%

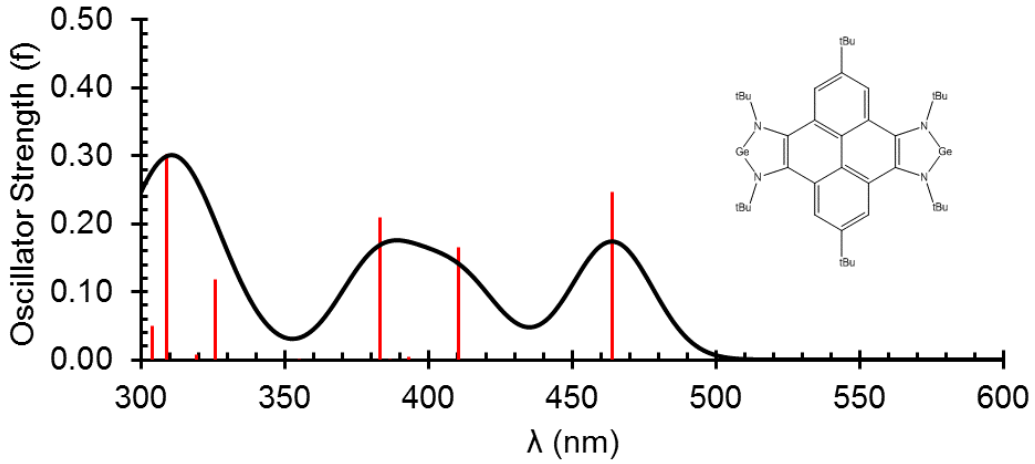

Figure A4.6. Simulated UV-vis absorption spectrum from TDDFT excitations for **2.2**.

Table A4.2. Electronic transitions for the calculated transitions of **2.2** and their orbital contributions.

λ (nm)	Character	% NTO Contribution
464	$\pi \rightarrow$ Ge $p + \pi^*$	98%
411	$\pi \rightarrow \pi^*$	92%
383	$\pi \rightarrow$ Ge $p + \pi^*$	99%
309	$\pi \rightarrow \pi^*$	52%
	$\pi \rightarrow \pi^*$	41%

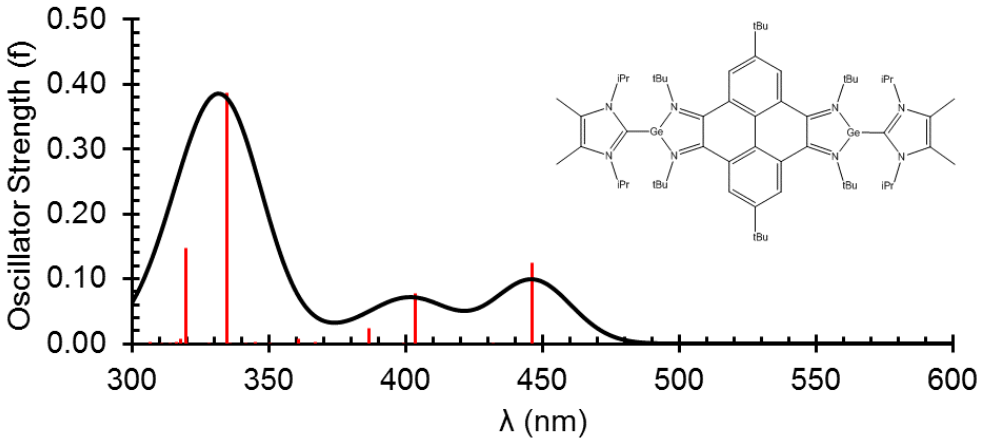

Figure A4.7. Simulated UV-vis absorption spectrum from TDDFT excitations for compound **2.3**.

Table A4.3. Electronic transitions for the calculated transitions of **2.3** and their orbital contributions.

λ (nm)	Character	% NTO Contribution
446	$\pi \rightarrow \pi^*$	96%
404	$\pi \rightarrow \pi^*$	87%
335	$\pi \rightarrow \pi^*$	81%

Nucleus Independent Chemical Shifts NICS(0) values (B3LYP/BS2)

	2.1
Bq^2	–3.89
Bq^3	–10.66
Bq^4	–3.95
Bq^5	–10.45

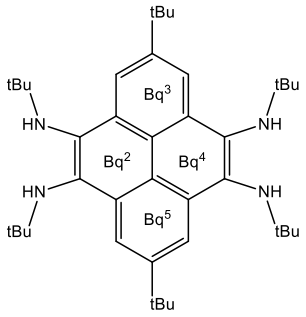

Figure A4.8. NICS(0) values for **2.1**.

	2.2	**2.2-H**
Bq^1	–5.90	–7.91
Bq^2	–3.66	–4.91
Bq^3	–9.98	–11.52
Bq^4	–2.86	–4.92
Bq^5	–9.99	–11.52
Bq^6	–5.83	–7.91

(Expt) and computed distances of Ge-N bond given in Å.

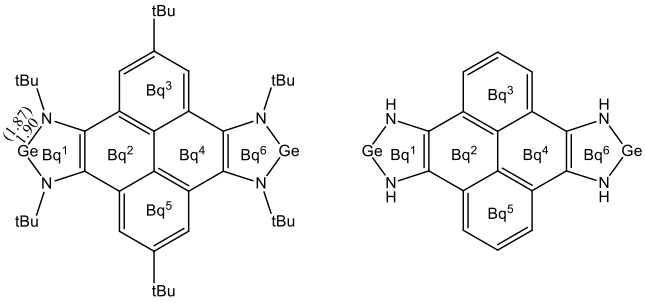

Figure A4.9. NICS(0) values for **2.2** and **2.2-H** (where *tert*-butyl groups were replaced with hydrogens).

	2.3	**2.3-H**
Bq^1	–0.56	–2.57
Bq^2	–3.87	–5.20
Bq^3	–10.26	–10.45
Bq^4	–3.87	–5.10
Bq^5	–10.26	–10.27
Bq^6	–0.56	–2.44
Bq^7	–11.83	–12.51
Bq^8	–11.83	–12.49

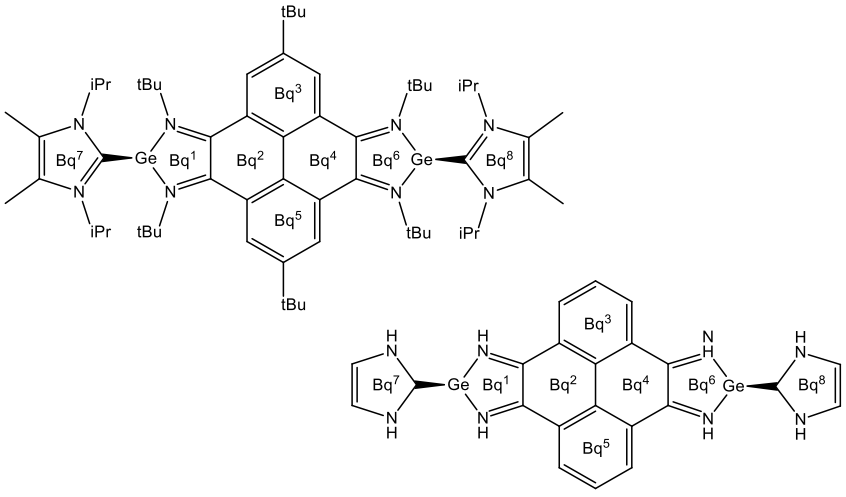

Figure A4.10. NICS(0) values for **2.3** and **2.3-H** (where *iso*-propyl and *tert*-butyl groups were replaced with hydrogens).

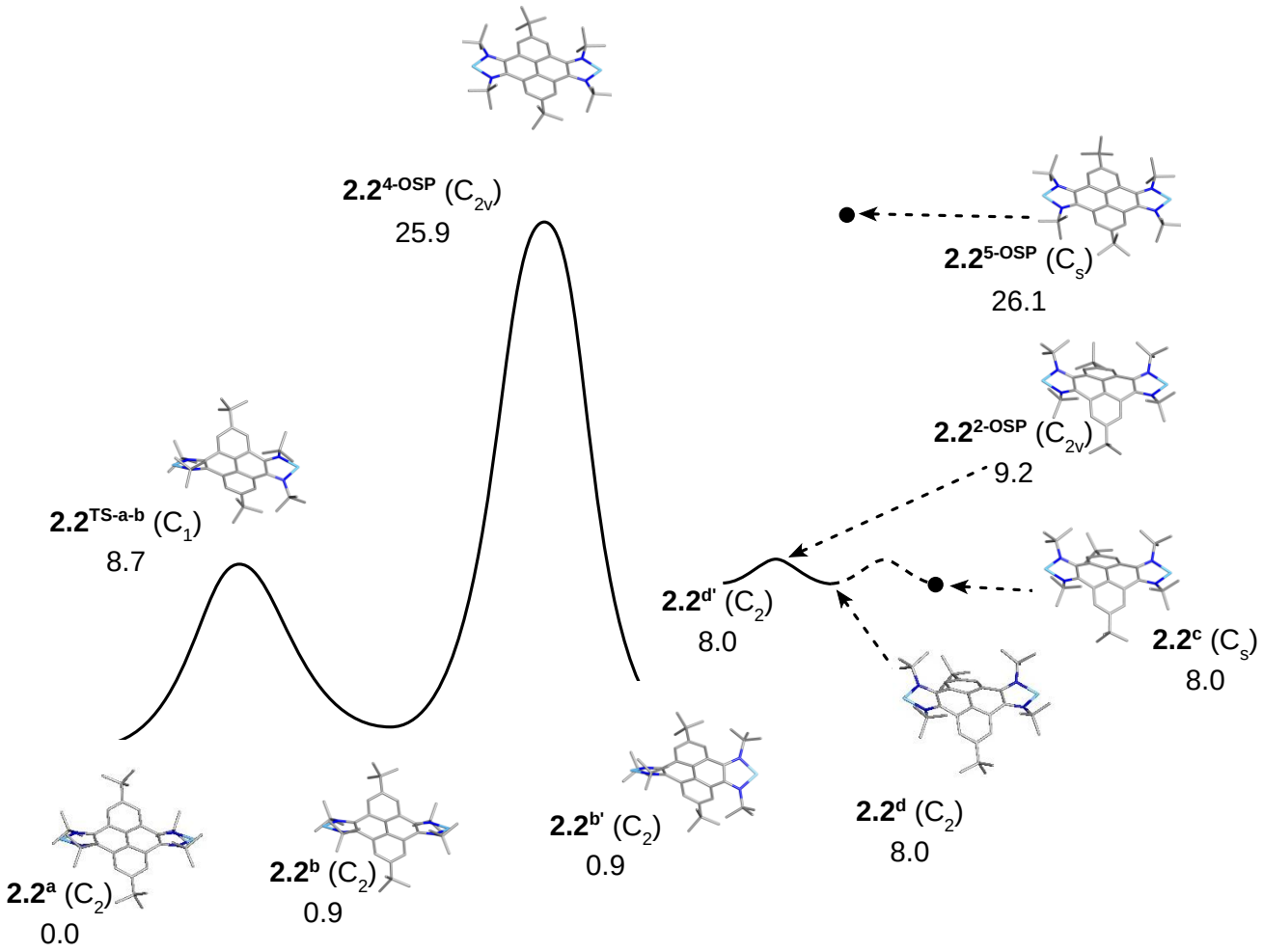

Figure A4.11. Potential Energy Surface (ΔE_e) for **2.2**. All energies reported in kcal mol^{-1}.

The potential energy surface above depicts various fluxional and higher-energy processes for compound **2**. The two lowest-energy structures for compound **2.2** are **2.2^{a}** and **2.2^{b}**. Structures **2.2^{a}** and **2.2^{b}** are connected by a low-energy transition state **2.2$^{TS\text{-}a\text{-}b}$**. While both **2.2^{a}** and **2.2^{b}** are C_2 symmetric, **2.2^{a}** has the same "twisting" of the germylene units where those units are staggered as observed in the geometry of the X-ray crystal structure. In **2.2^{b}**, the germylene units are eclipsed, i.e., they are rotating in the same direction. Structures **2.2^{b}** and **2.2$^{b'}$** are mirror images that are connected by a high-energy C_{2v}-symmetric fourth-order saddle point (**2.2$^{4\text{-}OSP}$**). Structures **2.2^{c}** and **2.2^{d}** are relatively low-energy C_s- and C_2-symmetric local minima, respectively, that buckle the pyrene core to form bowl-shaped structures, as opposed to the twisting of the pyrene in **2.2^{a}**. The only difference between **2.2^{c}** and **2.2^{d}** is a low-energy *t*-butyl rotation. It is notable that the structure of **2.2^{c}** is similar to the Ge-pyrene core part of the geometry of **2.3$^{6\text{-}OSP}$**. Two other higher-order saddle points (**2.2$^{2\text{-}OSP}$** and **2.2$^{5\text{-}OSP}$**) exist, and the relative energy of **2.2$^{2\text{-}OSP}$** is only 9.2 kcal mol^{-1} above the lowest energy structure **2.2^{a}**. Structure **2.2$^{2\text{-}OSP}$** connects mirror image enantiomers of **2.2^{d}** and **2.2$^{d'}$**. Structure **2.2$^{5\text{-}OSP}$** is 26.1 kcal mol^{-1} above **2.2^{a}**.

.

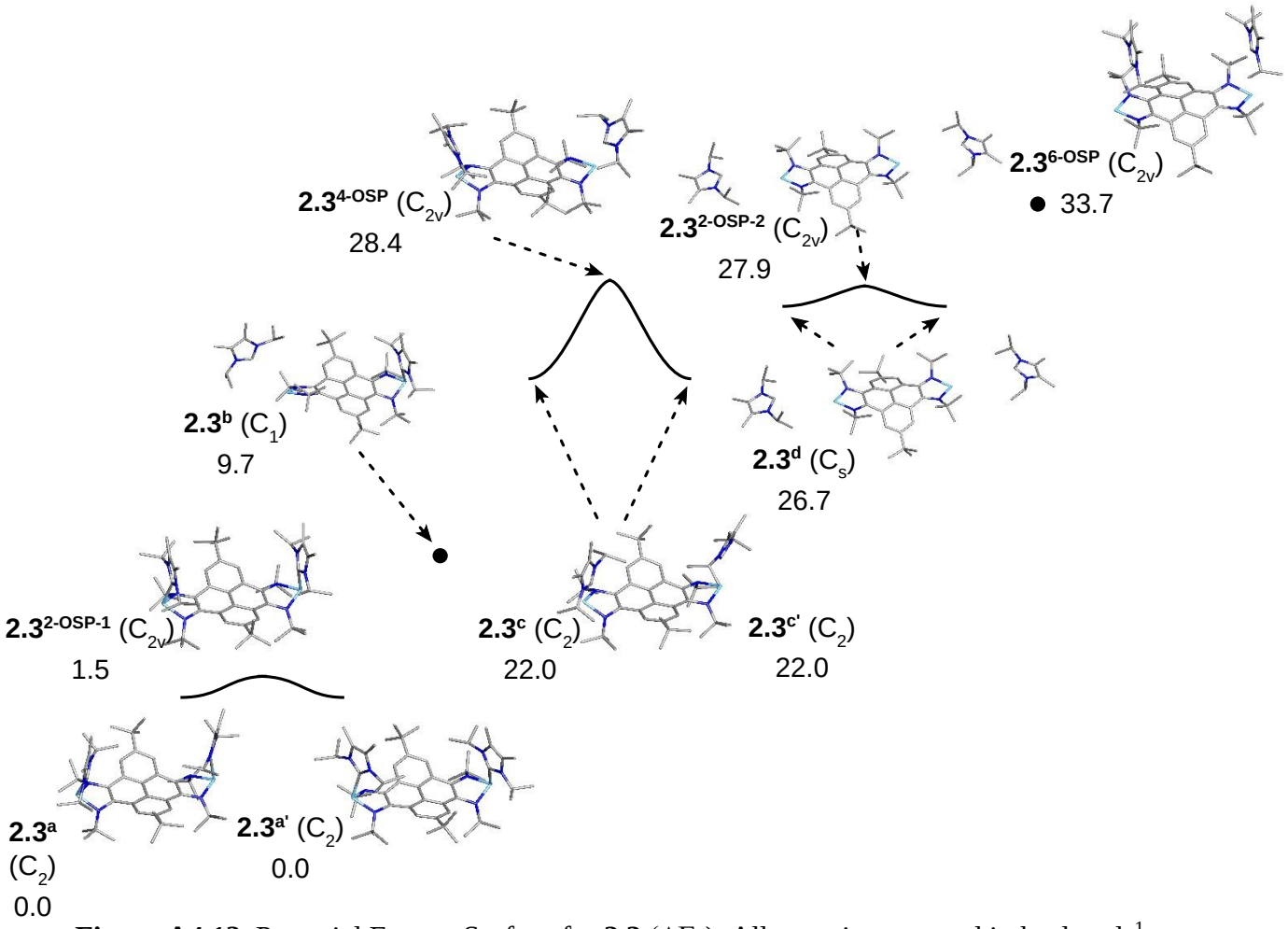

Figure A4.12. Potential Energy Surface for **2.3** (ΔE_e). All energies reported in kcal mol^{-1}.

The potential energy surface above depicts various fluxional and higher-energy processes for compound **2.3**. The lowest-energy structure for compound **2.3** is **2.3^{a}**, which has C_{NHC}-Ge distances of 2.21 Å. Structure **2.3$^{2\text{-}OSP\text{-}1}$** is a low-energy C_{2v}-symmetric second-order saddle point that connects two enantiomeric C_2 structures (**2.3^{a}** and **2.3$^{a'}$**). Structure **2.3^{b}** is C_1-symmetric where one of the NHCs has significantly lengthened away from the Ge-pyrene core (C_{NHC}-Ge distance of 4.12 Å), while the other NHC remains bound to the second germylene (C_{NHC}-Ge distance of 2.21 Å). Structures **2.3^{c}** and **2.3$^{c'}$** are high-energy local minimum enantiomers (C_{NHC}-Ge distances of 2.51 Å) that are connected through a fourth-order saddle point (**2.3$^{4\text{-}OSP}$** in which the Ge-C_{NHC} distances are 2.56 Å) by the double rotation of the NHCs about the Ge-C_{NHC} bond. Structure **2.3^{d}** is a C_s-symmetric structure in which both NHCs are significantly lengthened away from the Ge-pyrene core (C_{NHC}-Ge distances of 5.68 Å). A high-energy second-order saddle point (**2.3$^{2\text{-}OSP\text{-}2}$**) connects two equivalent structures of **2.3^{d}** through a motion of *t*-butyl rotation. Structure **2.3$^{6\text{-}OSP}$** is a C_{2v}-symmetric high-energy sixth-order saddle point with significantly lengthened C_{NHC}-Ge distances of 5.59 Å. Interestingly, the geometry of the Ge-pyrene core in **2.3$^{6\text{-}OSP}$** has a strong resemblance to the geometry observed in **2.2^{d}**.

Chapter Three

Frontier Molecular Orbitals

MO 118 LUMO –0.04153 Ha

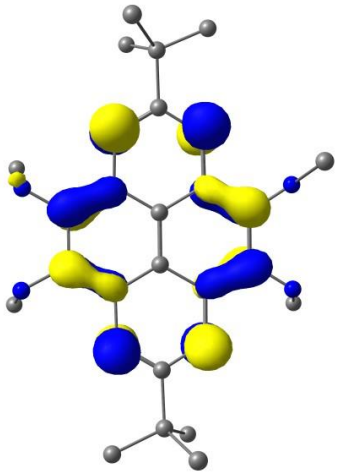

MO 117 LUMO –0.17243 Ha

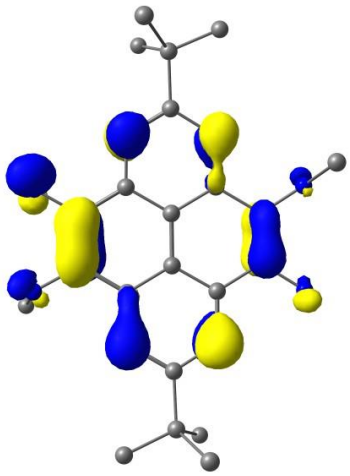

Figure A4.13. Selected molecular orbitals for the DFT-optimized geometry of **3.10**.

Simulated UV-vis and Fluorescence Spectra

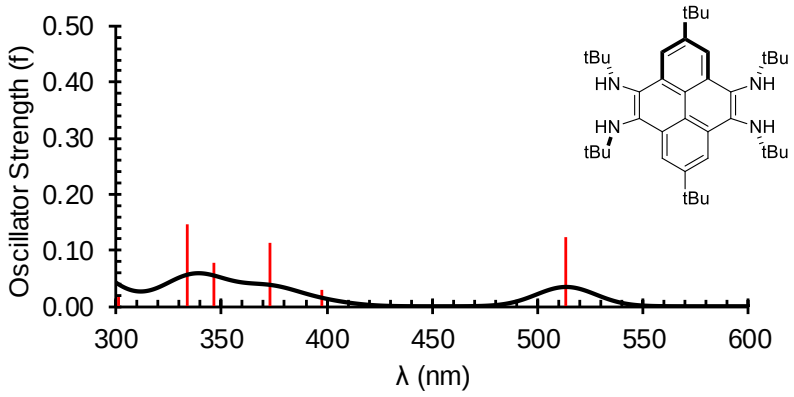

Figure A4.14. Simulated emission spectrum from TDDFT excitations for **2.1**.

Table A4.4. Electronic transitions for the calculated transitions for the emission of **2.1** and their orbital contributions.

λ (nm)	Character	% NTO Contribution
513	$\pi^* \rightarrow \pi$	95%

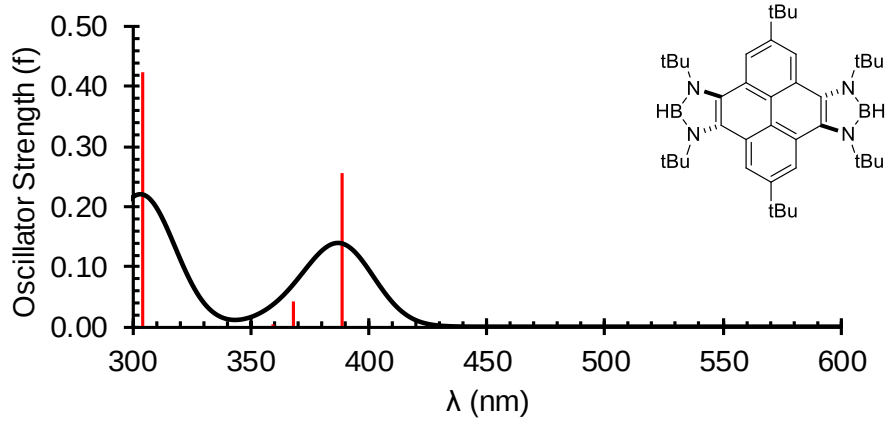

Figure A4.15. Simulated absorption spectrum from TDDFT excitations for **3.2**.

Table A4.5. Electronic transitions for the calculated transitions for the absorption of **3.2** and their orbital contributions.

λ (nm)	Character	% NTO Contribution
389	$\pi \rightarrow \pi^*$	93%
304	$\pi \rightarrow \pi^*$	73%
	$\pi \rightarrow \pi^*$	22%

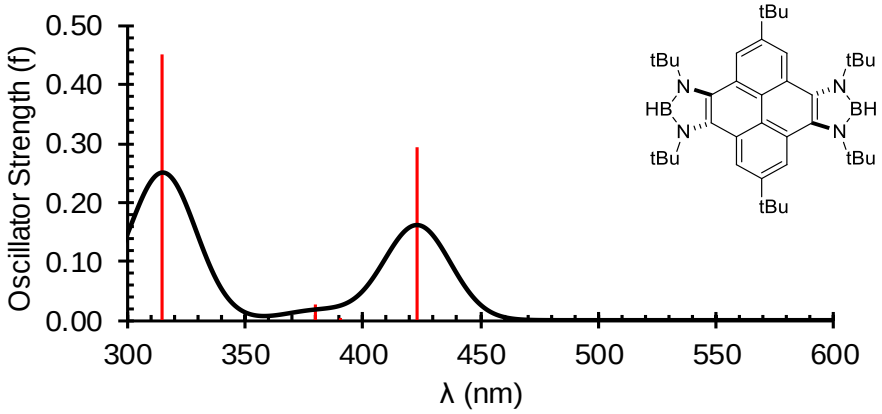

Figure A4.16. Simulated emission spectrum from TDDFT excitations for compound **3.2**.

Table A4.6. Electronic transitions for the calculated transitions for the emission of **3.2** and their orbital contributions.

λ (nm)	Character	% NTO Contribution
423	$\pi^* \rightarrow \pi$	95%
315	$\pi^* \rightarrow \pi$	68%
	$\pi^* \rightarrow \pi$	26%

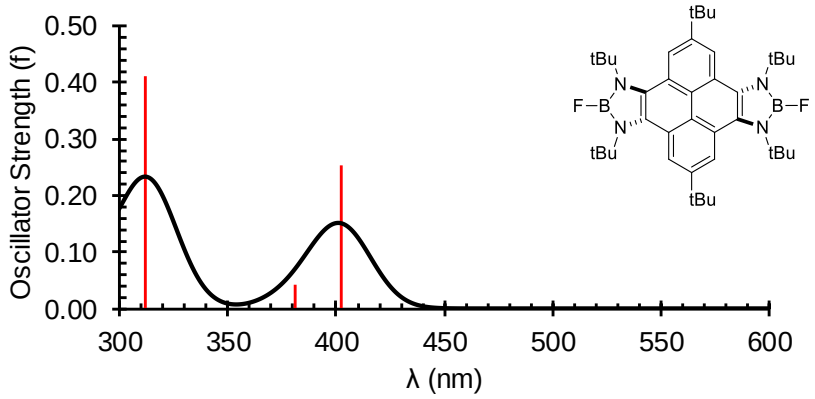

Figure A.17. Simulated UV-vis absorption spectrum from TDDFT excitations for compound **3.3**.

Table A4.7. Electronic transitions for the calculated transitions for the absorption of **3.3** and their orbital contributions.

λ (nm)	Character	% NTO Contribution
402	$\pi \rightarrow \pi^*$	94%
312	$\pi \rightarrow \pi^*$	73%
	$\pi \rightarrow \pi^*$	22%

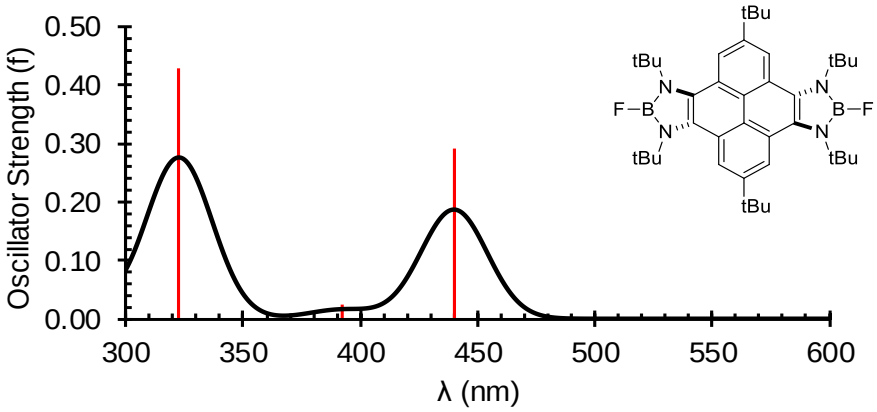

Figure A4.18. Simulated emission spectrum from TDDFT excitations for compound **3.3**.

Table A4.8. Electronic transitions for the calculated transitions for the emission of **3.3** and their orbital contributions.

λ (nm)	Character	% NTO Contribution
440	$\pi^* \rightarrow \pi$	96%
323	$\pi^* \rightarrow \pi$	69%
	$\pi^* \rightarrow \pi$	27%

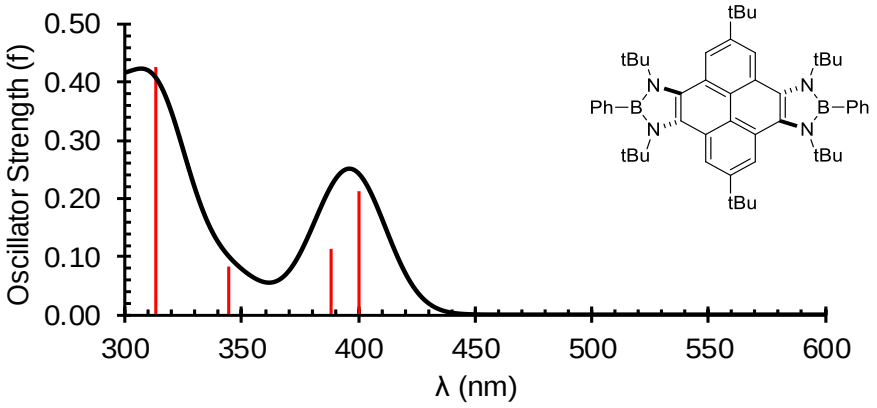

Figure A4.19. Simulated UV-vis absorption spectrum from TDDFT excitations for compound **3.4**.

Table A4.9. Electronic transitions for the calculated transitions for the absorption of **3.4** and their orbital contributions.

λ (nm)	Character	% NTO Contribution
400	$\pi \rightarrow \pi^*$	93%
313	$\pi \rightarrow \pi^*$	67%
	$\pi \rightarrow \pi^*$	27%

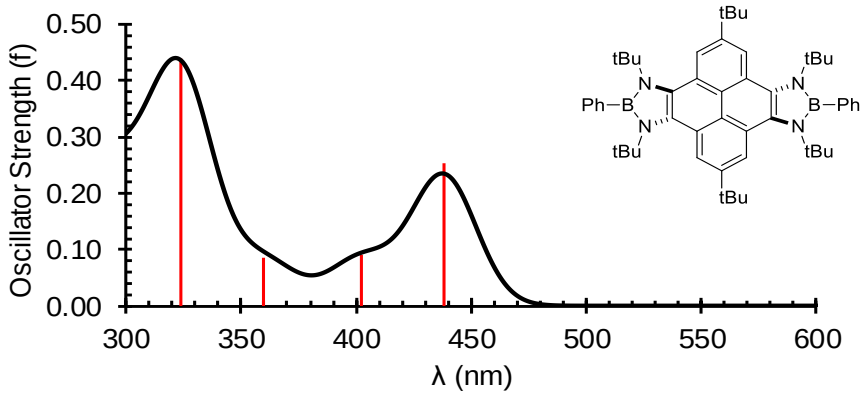

Figure A4.20. Simulated emission spectrum from TDDFT excitations for compound **3.4**.

Table A4.10. Electronic transitions for the calculated transitions for the emission of **3.4** and their orbital contributions.

λ (nm)	Character	% NTO Contribution
438	$\pi^* \rightarrow \pi$	95%
328	$\pi^* \rightarrow \pi$	61%
	$\pi^* \rightarrow \pi$	33%

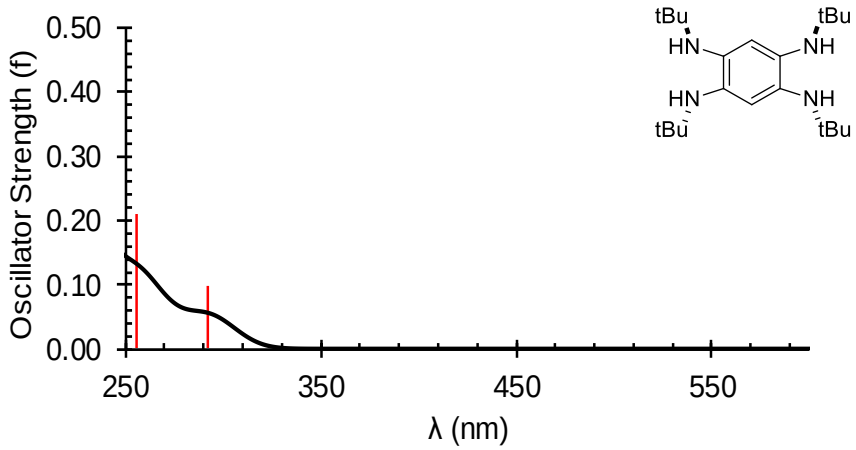

Figure A4.21. Simulated UV-vis absorption spectrum from TDDFT excitations for **3.5.**

Table A4.11. Electronic transitions for the calculated transitions for the absorption of **3.5** and their orbital contributions.

λ (nm)	Character	% NTO Contribution
292	$\pi/p \rightarrow \pi^*$	88%

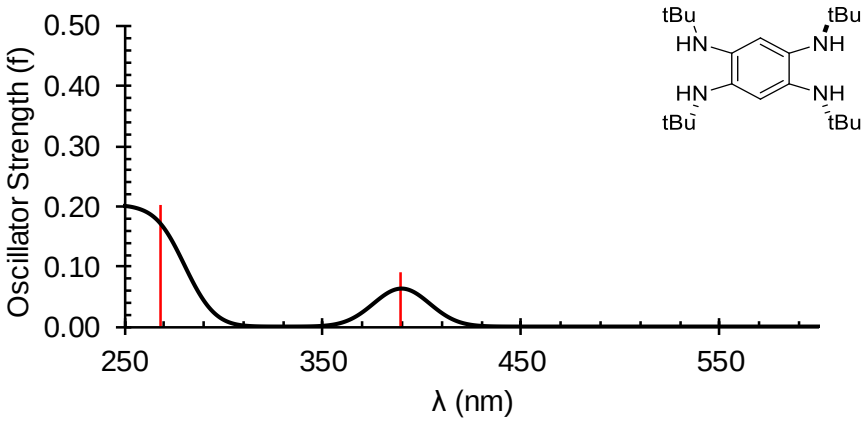

Figure A4.22. Simulated emission spectrum from TDDFT excitations for **3.5**.

Table A4.12. Electronic transitions for the calculated transitions for the emission of **3.5** and their orbital contributions.

λ (nm)	Character	% NTO Contribution
390	$\pi^* \rightarrow \pi$	98%

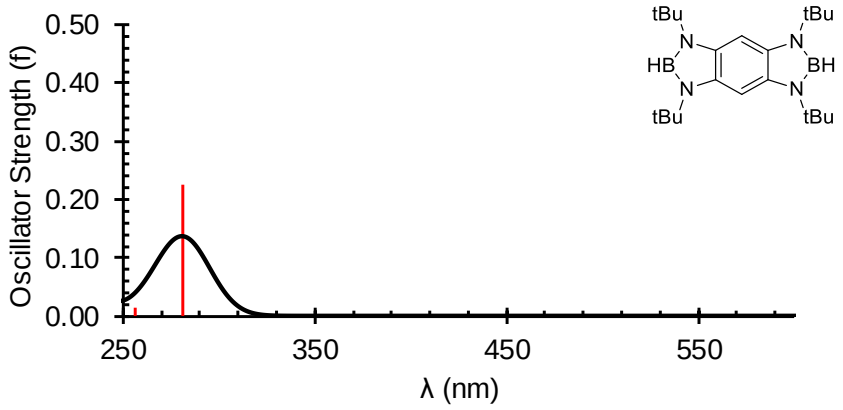

Figure A4.23. Simulated UV-vis absorption spectrum from TDDFT excitations for **3.6**.

Table A4.13. Electronic transitions for the calculated transitions for the absorption of **3.6** and their orbital contributions.

λ (nm)	Character	% NTO Contribution
285	$\pi \rightarrow \pi^*$	91%

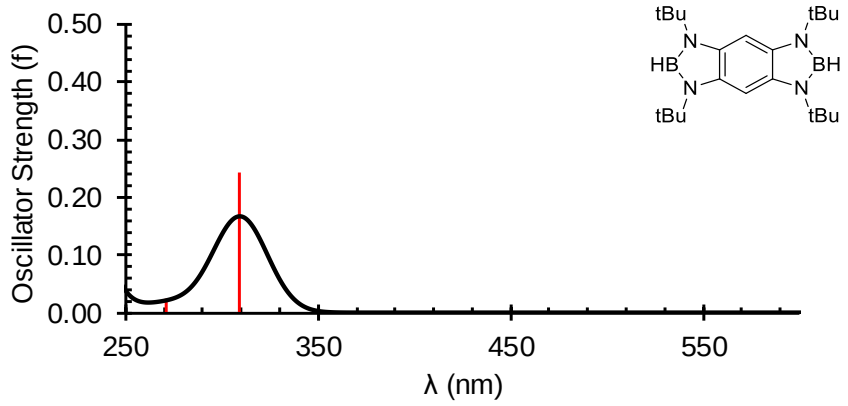

Figure A4.24. Simulated emission spectrum from TDDFT excitations for **3.6**.

Table A4.14. Electronic transitions for the calculated transitions for the emission of **3.6** and their orbital contributions.

λ (nm)	Character	% NTO Contribution
309	$\pi^* \rightarrow \pi$	93%

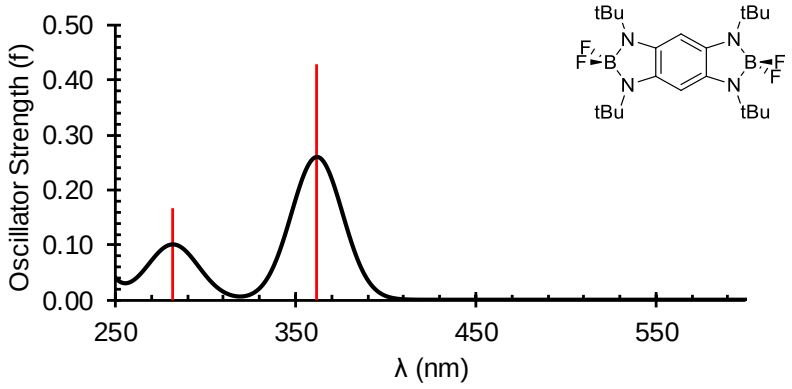

Figure A4.25. Simulated UV-vis absorption spectrum from TDDFT excitations for **3.7**.

Table A4.15. Electronic transitions for the calculated transitions for the absorption of **3.7** and their orbital contributions.

λ (nm)	Character	% NTO Contribution
362	$p \rightarrow \pi^*$	94%
282	$\pi \rightarrow \pi^*$	99%

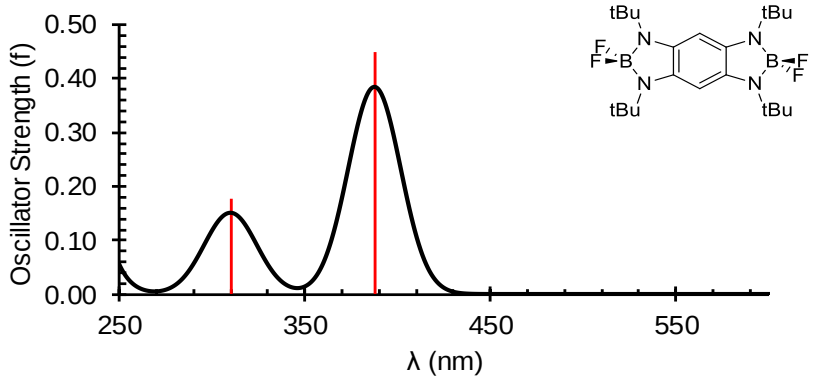

Figure A4.26. Simulated emission spectrum from TDDFT excitations for **3.7**.

Table A4.16. Electronic transitions for the calculated transitions for the emission of **3.7** and their orbital contributions.

λ (nm)	Character	% NTO Contribution
388	$\pi^* \rightarrow p$	96%
310	$\pi^* \rightarrow \pi$	99%

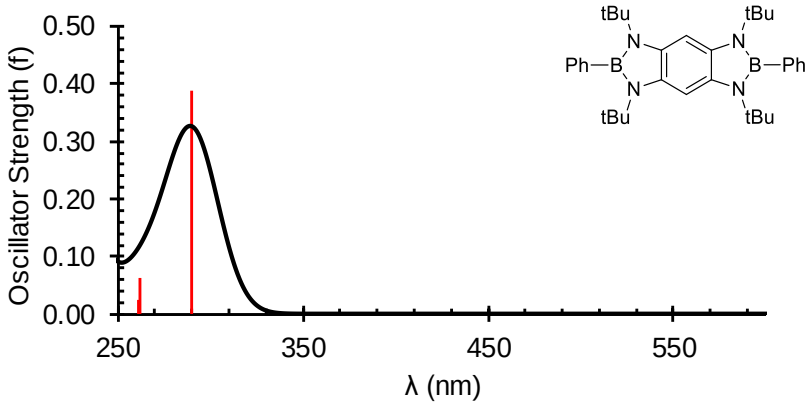

Figure A4.27. Simulated UV-vis absorption spectrum from TDDFT excitations for **3.8**.

Table A4.17. Electronic transitions for the calculated transitions for the absorption of **3.8** and their orbital contributions.

λ (nm)	Character	% NTO Contribution
290	$\pi \rightarrow \pi^*$	91%

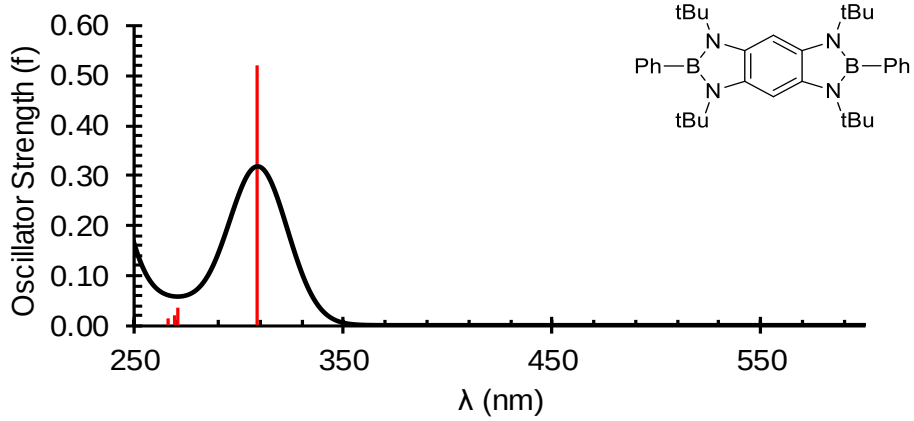

Figure A4.28. Simulated emission spectrum from TDDFT excitations for **3.8**.

Table A4.18. Simulated emission spectrum from TDDFT excitations for **3.8**.

λ (nm)	Character	% NTO Contribution
309	$\pi^* \rightarrow \pi$	93%

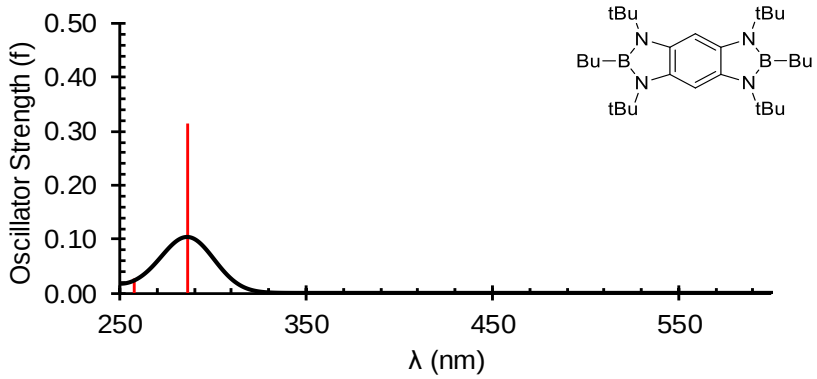

Figure A4.29. Simulated absorption spectrum from TDDFT excitations for **3.9**.

Table A4.19. Electronic transitions for the calculated transitions for the absorption of **3.9** and their orbital contributions.

λ (nm)	Character	% NTO Contribution
286	$\pi \rightarrow \pi^*$	91%

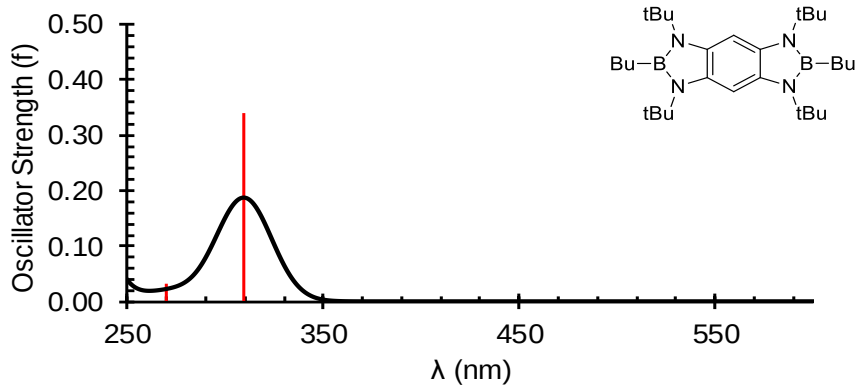

Figure A4.30. Simulated emission spectrum from TDDFT excitations for **3.9**.

Table A4.20. Electronic transitions for the calculated transitions for the emission of **3.9** and their orbital contributions.

λ (nm)	Character	% NTO Contribution
309	$\pi^* \rightarrow \pi$	93%

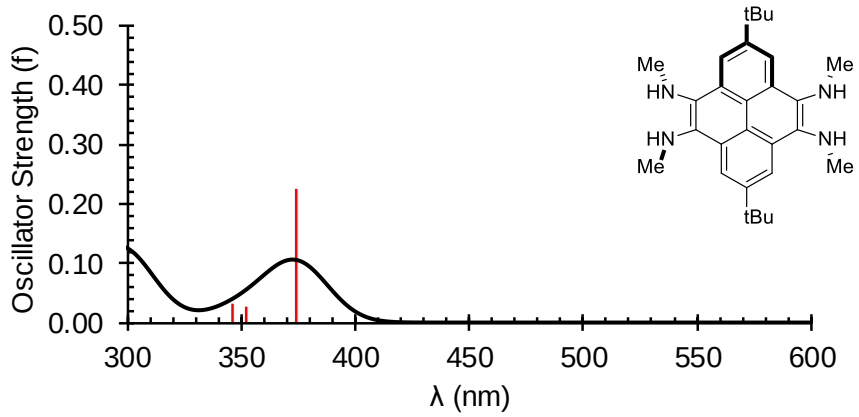

Figure A4.31. Simulated absorption spectrum from TDDFT excitations for **3.10**.

Table A4.21. Electronic transitions for the calculated transitions for the absorption of **3.10** and their orbital contributions.

λ (nm)	Character	% NTO Contribution
374	$\pi \rightarrow \pi^*$	94%

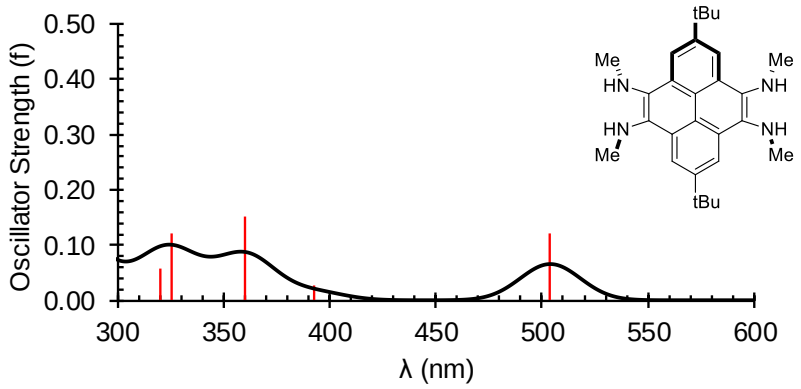

Figure A4.32. Simulated emission spectrum from TDDFT excitations for **3.10**.

Table A4.22. Electronic transitions for the calculated transitions for the emission of **3.10** and their orbital contributions.

λ (nm)	Character	% NTO Contribution
504	$\pi^* \rightarrow \pi$	99%

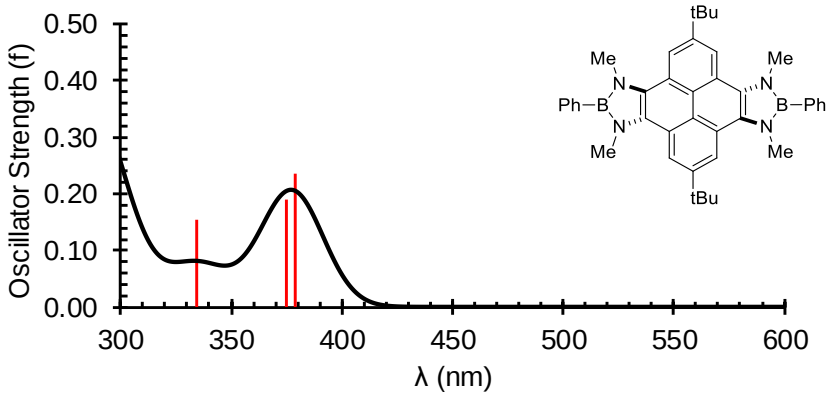

Figure A4.33. Simulated absorption spectrum from TDDFT excitations for **3.11**.

Table A4.23. Electronic transitions for the calculated transitions for the absorption of **3.11** and their orbital contributions.

λ (nm)	Character	% NTO Contribution
379	$\pi \rightarrow \pi^*$	92%
375	$\pi \rightarrow \pi^*$	87%

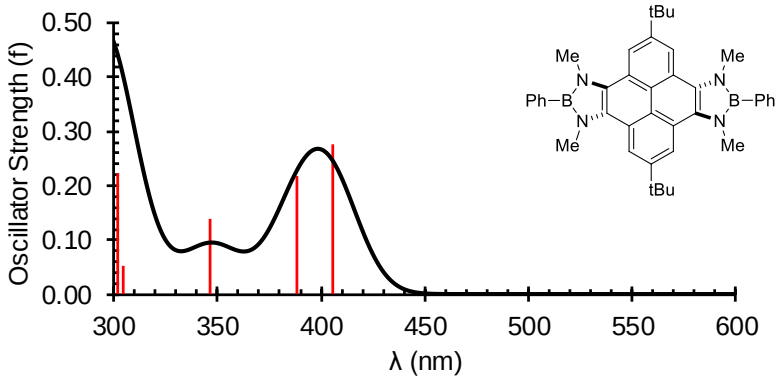

Figure A4.34. Simulated emission spectrum from TDDFT excitations for **3.11**.

Table A4.24 Electronic transitions for the calculated transitions for the emission of **3.11** and their orbital contributions.

λ (nm)	Character	% NTO Contribution
405	$\pi^* \rightarrow \pi$	94%
388	$\pi^* \rightarrow \pi$	88%

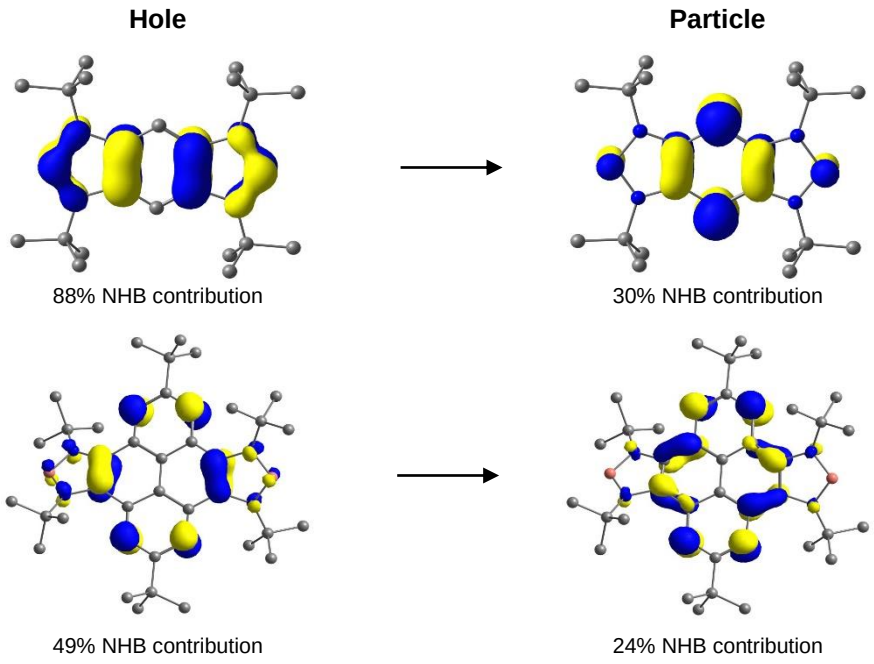

Figure A4.35. Hole-particle contributions in compounds **3.6** (top) and **3.2** (bottom), depicting more contribution of NHB in benzene-fused molecules than pyrene-fused analogues.

Chapters Four-Seven

All computational data reported herein were obtained, analyzed, and prepared by Andrew Molino and David Wilson at LaTrobe University in Melbourne, Australia. Further information on calculated atomic coordinates, bond distances, WBI values, and Mulliken charges, can be found in the original manuscripts.[298, 311] All calculations were performed using ADF2020.102 unless noted. Geometry optimizations were carried out with the B3LYP density functional utilizing the TZ2P basis set.[366] Grimme's D3 dispersion with Becke-Johnson damping was included, labelled D3(BJ).[367-368] Harmonic vibrational frequencies were calculated analytically at the same level of theory in order to characterize the stationary points as minima on the potential energy surface. All optimizations included solvent effects using the conductor like screening model of solvation (COSMO) with parameters for Toluene ($\varepsilon = 7.4257$). Nucleus-independent chemical shift (NICS) calculations were performed using the Aroma plug-in package and run using Gaussian16 at the B3LYP-D3(BJ)/def2-TZVP//B3LYP-D3(BJ)/TZ2P level of theory.[369] Excited state dynamic (ESD) calculations were performed using Orca 4.2.1 at the ωb97X-D3/def2-SVPD level of theory. ACID plots were generated using ACID 3.0.2.

Chapter Four

Energy Decomposition Analysis

Table A4.25. EDA-NOCV results [L-Bf]$^-$ (L=NHC, CAAC) at the B3LYP-D3(BJ)/TZ2P level of theory for the electron sharing bonding model. Energy values given in kcal mol^{-1}.

		Fragments	
Energy Terms	**Orbital Interaction**	**[Bf]$^-$ (Triplet Anion) + NHC (Triplet)**	**[Bf]$^-$ (Triplet Anion) + CAAC (Triplet)**
ΔE_{int}		-194.3	-169.4
ΔE_{Pauli}		+374.1	+299.2
ΔE_{elstat}[a]		-244.9 (43%)	-214.3 (46%)
ΔE_{orb}[a]		-299.6 (53%)	-233.3 (50%)
ΔE_{disp}[a]		-23.3 (4%)	-21.1 (4%)
$\Delta E_{orb(1)}$[b]	**[Bf]-[L] σ-electron sharing**	-206.6 (69%)	-168.4 (72%)
$\Delta E_{orb(2)}$[b]	**[Bf]-[L] π-electron sharing**	-59.2 (20%)	-39.9 (17%)
ΔE_{rest}		-33.9 (11%)	-25.0 (11%)

[a] The values in parentheses give the percentage contribution to the total attractive interactions $\Delta E_{elstat} + \Delta E_{orb} + \Delta E_{disp}$.
[b] The values in parentheses give the percentage contribution to the total orbital interactions $\Delta E_{orb.}$

Table A4.26. EDA-NOCV results [NHC-Borole]$^-$ at the B3LYP-D3(BJ)/TZ2P//B3LYP/6-31G(d) level of theory for the donor-acceptor and electron sharing bonding models. Energy values given in kcal mol-1.

		Fragments	
Energy Terms	**Orbital Interaction**	**Donor-Acceptor**	**Electron-sharing**
		[Borole]$^-$ (Singlet) + NHC (Singlet)	**[Borole]$^-$ (Triplet) + NHC (Triplet)**
ΔE_{int}		-128.5	-196.2
ΔE_{Pauli}		+216.8	+368.6
ΔE_{elstat}[a]		-151.7 (44%)	-236.9 (42%)
ΔE_{orb}[a]		-165.5 (48%)	-299.8 (53%)
ΔE_{disp}[a]		-28.5 (8%)	-28.1 (5%)
$\Delta E_{orb(1)}$[b]	**[Bf]-[L] σ**	-97.1 (59%)	-212.5 (71%)
$\Delta E_{orb(2)}$[b]	**[Bf]-[L] π**	-46.9 (28%)	-55.4 (18%)
ΔE_{rest}		-21.5 (13%)	-31.8 (11%)

[a] The values in parentheses give the percentage contribution to the total attractive interactions $\Delta E_{elstat} + \Delta E_{orb} + \Delta E_{disp}$.
[b] The values in parentheses give the percentage contribution to the total orbital interactions $\Delta E_{orb.}$

Natural Orbitals of Chemical Valence

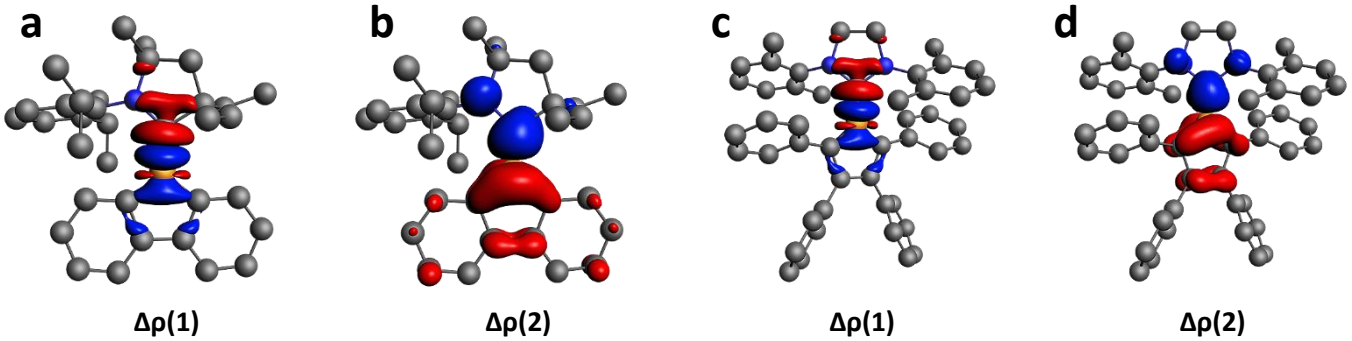

Figure A4.36. EDA-NOCV deformation densities (a/c) Δρ(1) and (b/d) Δρ(2) associated with orbital interactions $\Delta E_{orb}(1)$ and $\Delta E_{orb}(2)$ for [CAAC-BF]$^{-}$ and [NHC-Borole]$^{-}$. Charge flow red→blue (isosurface = 0.003).

Excited State Dynamics

Absorbance

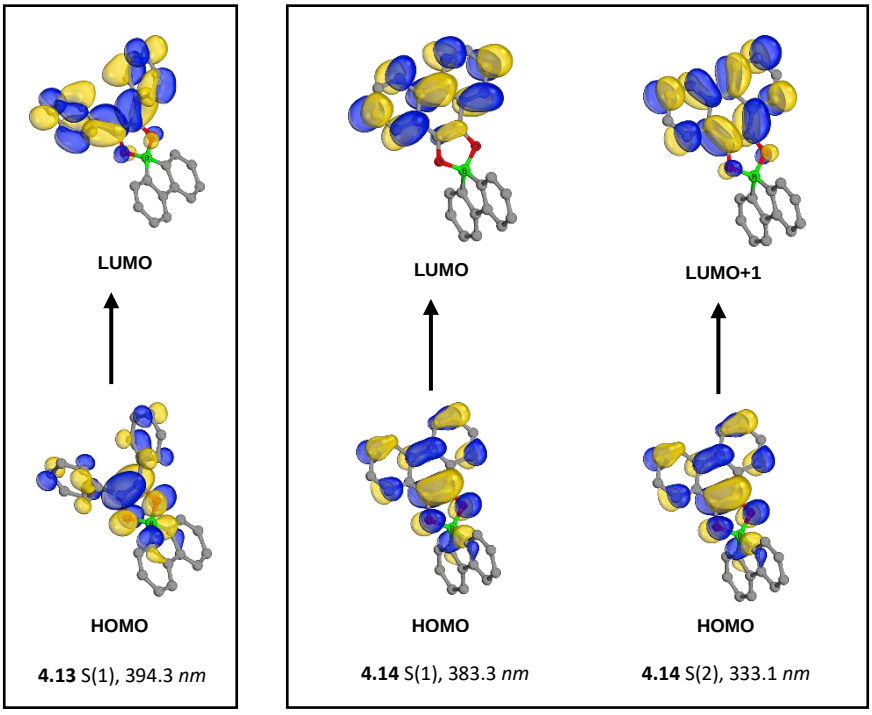

Figure A4.37. Frontier molecular orbitals of **4.13** and **4.14** calculated at the ωb97X-D3/def2-SVPD level of theory. Isovalue = 0.0200.

Table A4.27. Calculated vertical transition energies (ωB97X-D3/def2-SVPD//B3LYP-D3(BJ)/TZ2P).

	State	Energy (eV)	Fosc.	Orbital Transitions	Assignment
4.13	**S(1)**	3.144	3.74×10^{-1}	S(1) = 97 → 98, n = 0.97	HOMO → LUMO (π → π*)
4.14	**S(1)**	3.235	6.99×10^{-2}	S(1) = 96 → 97, n = 0.90	HOMO → LUMO (π → π*)
	S(2)	3.723	2.35×10^{-1}	S(2) = 96 → 98, n = 0.87	HOMO → LUMO+1 (π → π*)

Emission

Emission spectra were simulated using the excited state hessian S(1) computed at the ωB97X-D3/def2-SVPD level of theory. The potential energy surface was approximated using the vertical gradient (VG) model. For compound **4.13** only the S(1) (394.3 nm) state was evaluated, while for **4.14** the S(1) (383.3 nm) and S(2) (333.1 nm) excited states were evaluated as a multi-state spectrum.

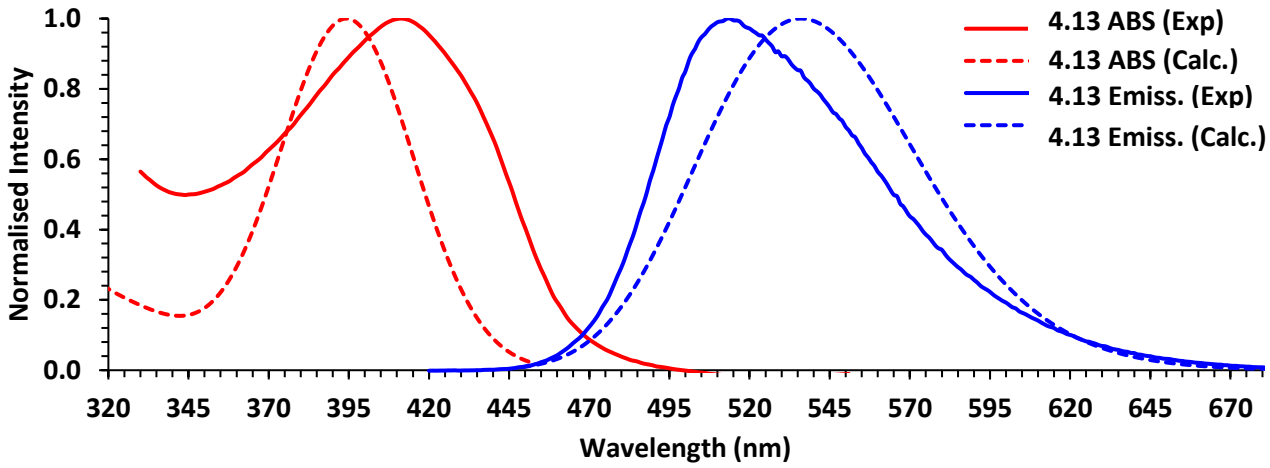

Figure A4.38. Calculated absorbance and emission spectra for **4.13**.

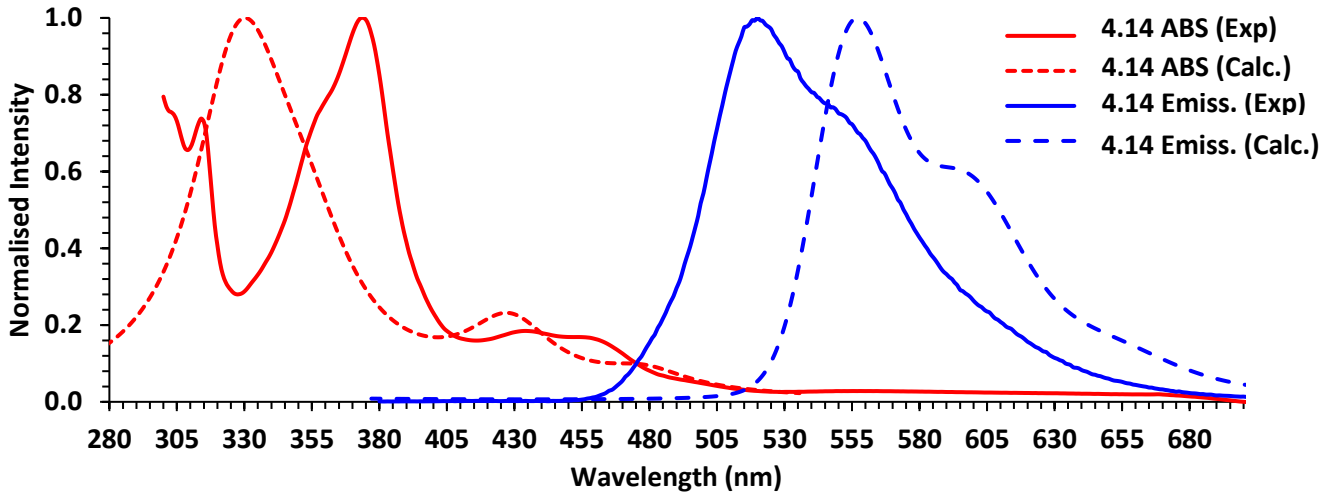

Figure A4.39. Calculated absorbance and emission spectra for **4.14**.

Nucleus Independent Shift Calculations

Table A4.28. Calculated isotropic out-of-plane NICS(1)$_{ZZ}$ values (ppm) at the B3LYP/def2-TZVP (SMD, THF) level of theory.

Compound	B Ring	Ph Ring	L[a]
[NHC-BF]$^{+}$	+34.2	-8.8	-26.4
[CAAC-BF]$^{+}$	+32.2	-11.3	NA
[NHC-BF]$^{\bullet}$	+6.0	-17.8	-18.6
[CAAC-BF]$^{\bullet}$	+12.1	-18.6	NA
[NHC-BF]$^{-}$	-21.4	-23.9	-9.7
[CAAC-BF]$^{-}$	-8.1	-23.1	NA
[NHC-Borole]$^{-}$	-10.1	NA	-8.8
[H-BF]$^{2-}$	-45.7	-20.4	NA

[a] NICS(1)ZZ values only available for planar rings ±15˚.

Additional ACID Plots

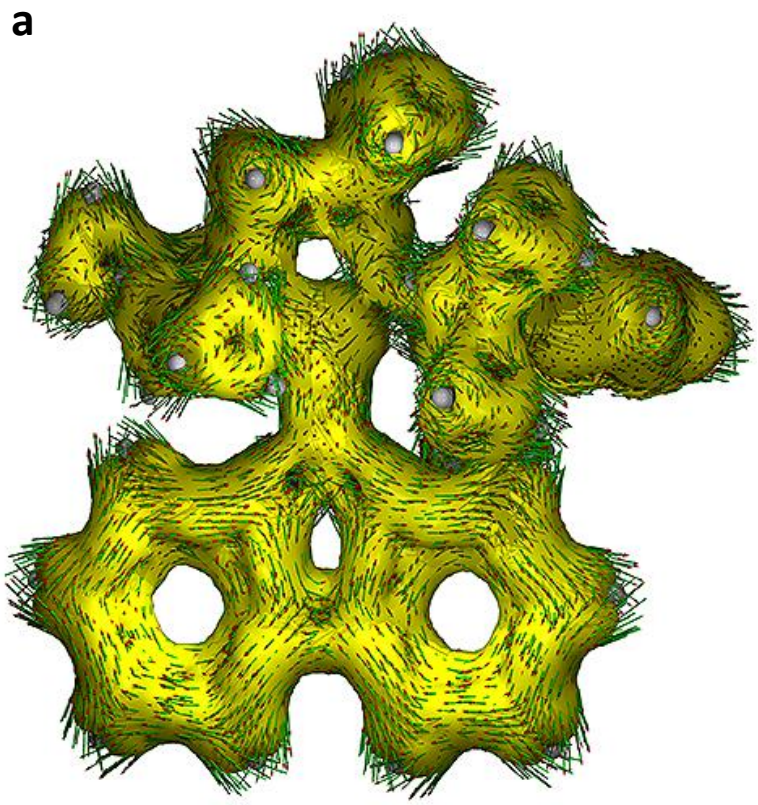

Figure A4.40. ACID plot for $[CAAC\text{-}BF]^{-}$. Isosurface = 0.03.

Chapter Five

Energy Decomposition Analysis

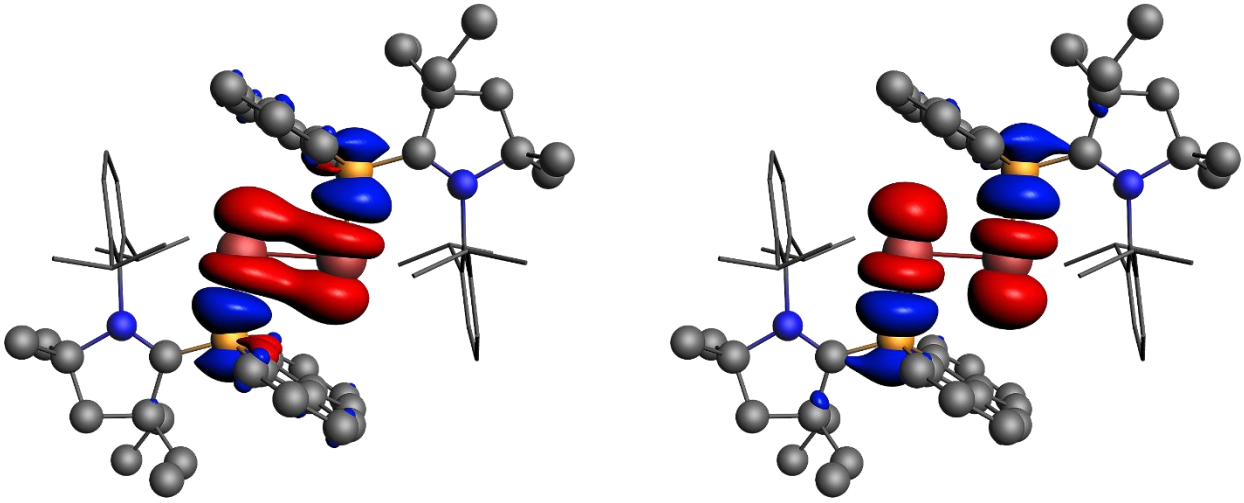

Figure A4.41. Plots of the β-pair deformation densities Δρ for **5.5**. Hydrogen atoms omitted for clarity.

Table A4.29. Additional RI-MP2/def2-TZVP//B3LYP-D3(BJ)/def2-SVP (SMD, THF) calculated energies for the proposed formation of **5.5**, and Dipp migration in **5.7**.

	ΔG (kJ mol^{-1})	
Reaction	RI-MP2/def2-TZVP	RI-SCS-MP2/def2-TZVP
1 + Se_2Cl_2 → [CAACBF]$^{\cdot}$ + $SeCl_2$ + Cl^-	+87.8	+61.3
1 + Se_2Cl_2 → [CAACBF-$SeCl_2$] + Cl^-	-259.5	-254.0
(2)1 + Se_2Cl_2 → 5 + 2Cl^-	-504.2	-472.5
1 + Se → [CAACBF-Se]$^-$	-421.6	-464.2
1 + Se → [CAACBF-Se-Dipp]	-563.3	-586.9
[CAACBF-Se]$^-$ → TS1	+64.4	+81.0
[CAACBF-Se]$^-$ → [CAACBF-Se-Dipp]	-103.5	-114.9

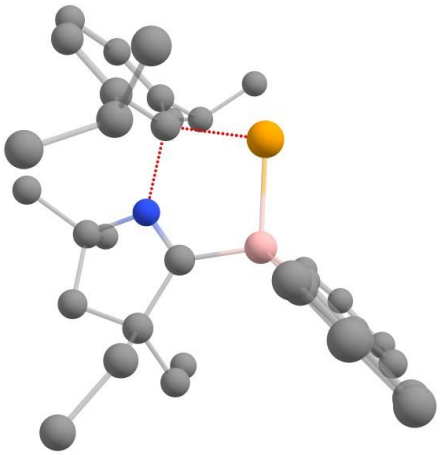

Figure A4.42. Calculated transition state for N-Dipp migration to selenium forming **5.7**. Hydrogen atoms omitted for clarity.

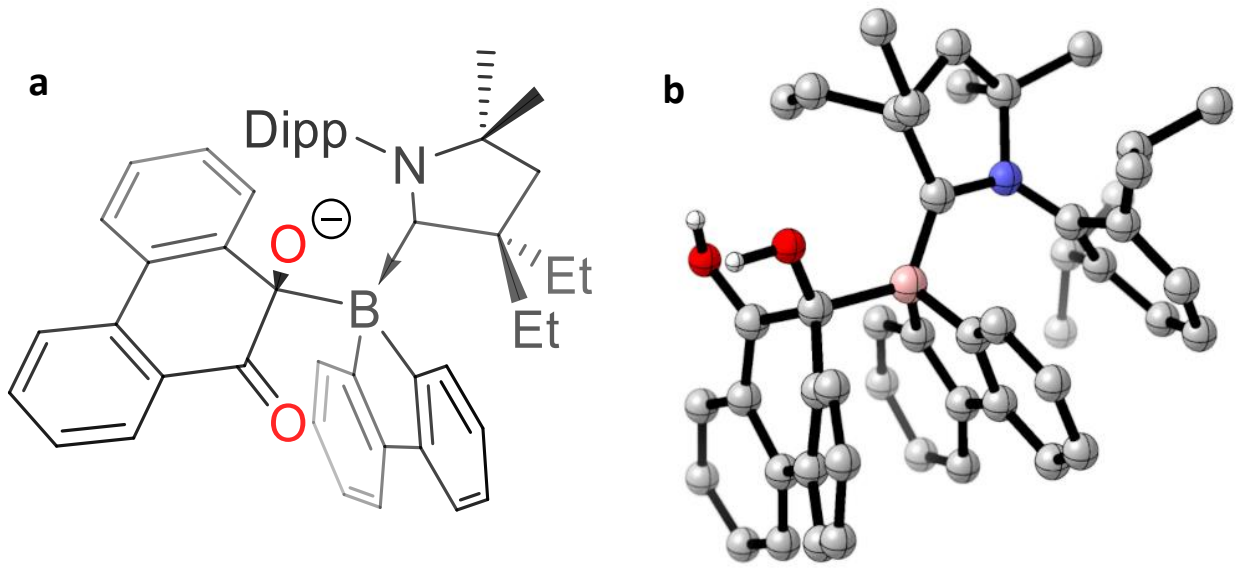

Figure A4.43. a) Intermediate structure (**Int1a**) for the nucleophilic addition of **BFA** to one of the carbonyl carbons of 9,10-phenanthrenequinone. b) Stable intermediate **Int1a** could only be located with protonated oxygen atoms (simulated acidic conditions).

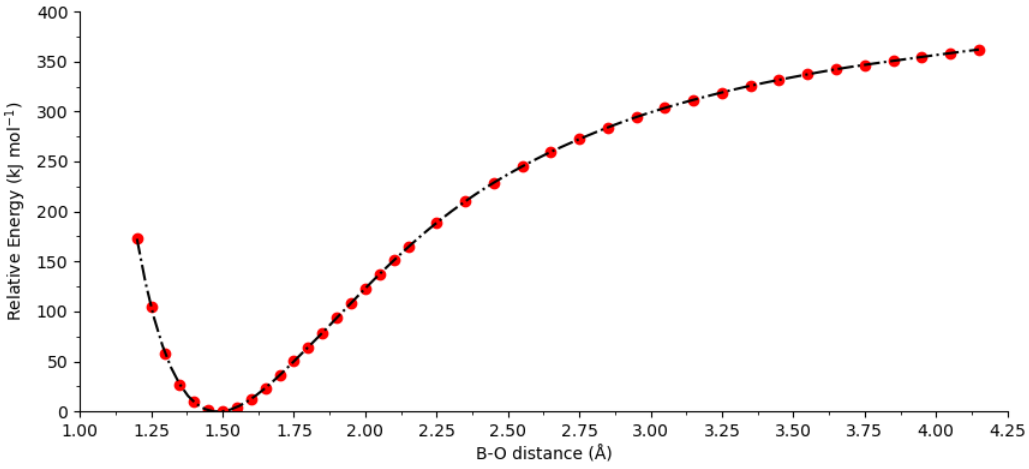

Figure A4.44. Scan of the potential energy surface for the adduct formation of **Int1**. Calculations were performed at ± 0.05 Å from the equilibrium bond distance.

Table A4.30. Mullikan spin populations for the triplet and open-shell singlet (OSS) reactant complexes.

[BFA phenanthrene-9,10-dione]	RC1 (Anion, Triplet)	RC1 (Anion, Open-Shell Singlet)
B(1)	+0.368997	+0.367111
O(1)	+0.253177	-0.251917
O(2)	+0.241448	-0.236243
[BFA phenanthrene-9,10-dione]		
B(1)	+0.382838	+0.295316
O(1)	+0.249130	-0.212418
O(2)	+0.243944	-0.178443

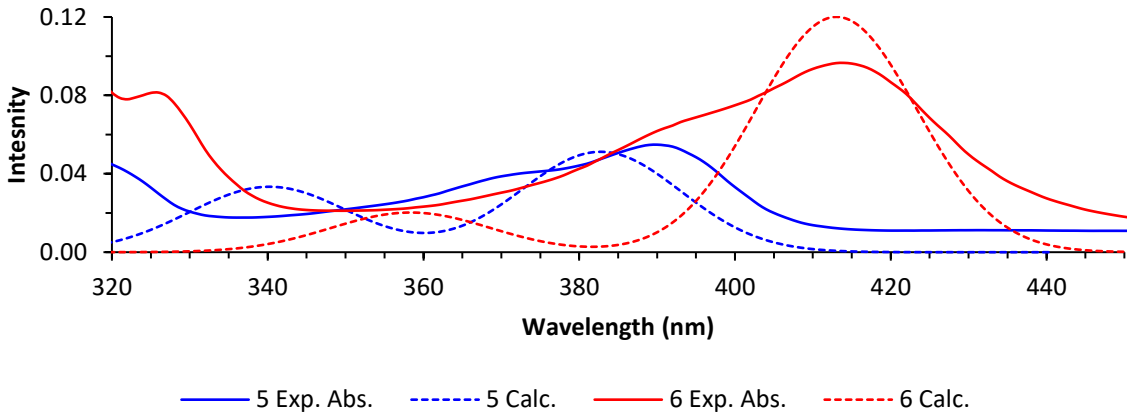

Figure A4.45. Comparison of the theoretical and experimental absorption spectra of **5.5** and **5.6**. Electronic transition energies corrected by –0.02 eV to account for systematic errors.

Table A4.31. Calculated vertical excitation energies of **6.5** and **6.6** at the ωB97X/def2-TZVP (CPCM, THF) level of theory.

6.5	Wavelength (nm)	f	Excitation
S_1	380.4	0.149455358	HOMO→LUMO
S_2	338.4	0.097171308	HOMO→LUMO+1
S_3	321.1	0.000888937	HOMO→LUMO+2
6.6			
S_1	410.3	0.282976974	HOMO→LUMO
S_2	356.3	0.047672609	HOMO→LUMO+1
S_3	311.4	0.000000007	HOMO→LUMO+2

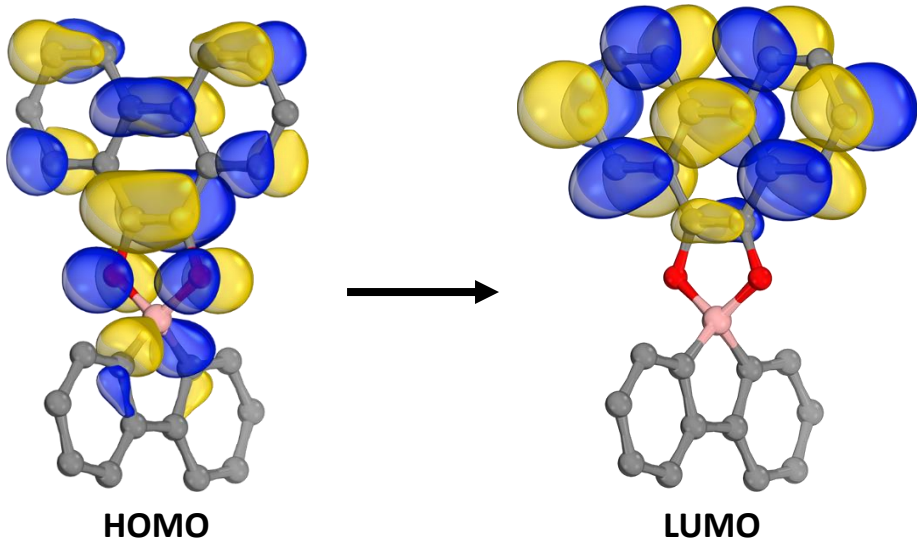

Figure A4.46. Plot of the S_1 HOMO→LUMO transition of **6.5** ωB97X/def2-TZVP (CPCM, THF).

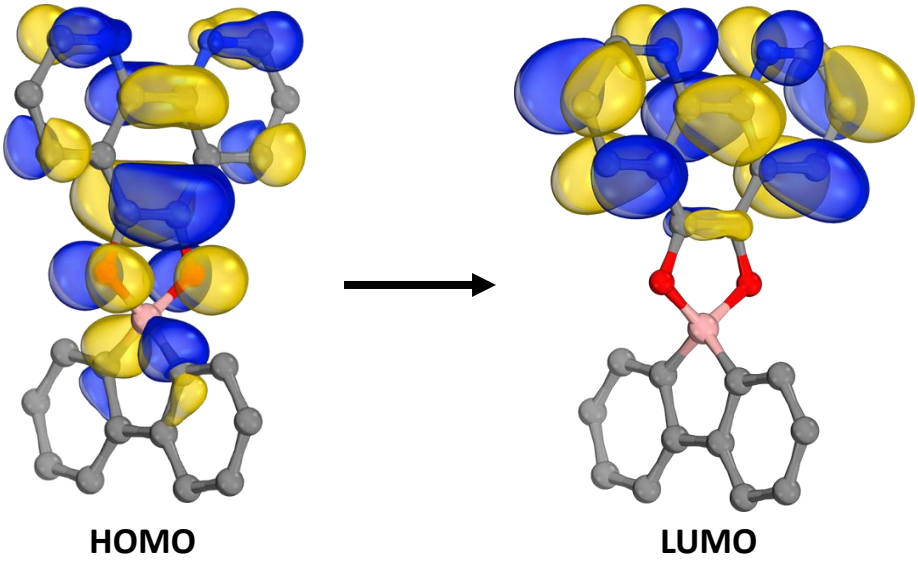

Figure A4.47. Plot of the S_1 HOMO→LUMO transition of **6.6** ωB97X/def2-TZVP (CPCM, THF).

Chapter Seven

EDA-NOCV

Table A4.32. EDA-NOCV results for **TS1** calculated at the B3LYP-D3(BJ)/TZ2P/B3LYP-D3(BJ)/def2-SVP level of theory. Reactants used as fragments in the neutral singlet electronic configurations.

	Energy (kcal mol^{-1})
ΔE_{int}	-29.0
ΔE_{Pauli}	+77.5
ΔE_{elstat}[a]	-44.1 (41.5%)
ΔE_{orb}[a]	-51.2 (48.1%)
ΔE_{disp}[a]	-11.1 (10.5%)
$\Delta E_{orb(1)}$[b] B(LP) → CO_2 π*	-42.0 (82.0%)
$\Delta E_{orb(rest)}$	-9.2 (18.0%)

[a] The values in parentheses give the percentage contribution to the total attractive interactions $\Delta E_{elstat} + \Delta E_{orb} + \Delta E_{disp}$.
[b] The values in parentheses give the percentage contribution to the total orbital interactions ΔE_{orb}.

TD-DFT and ESD

Table A4.33. Calculated TD-DFT excitations for the first 5 singlet excited states of **7.2**.

State	**Energy (nm)**	***f***	**$\lvert\langle i\lvert\mu\rvert j\rangle\rvert^2$**	**Transition**
S_1	268.2	0.3399	3.0004	HOMO→LUMO, HOMO-1→LUMO
S_2	262.9	0.0990	0.8563	HOMO-1→LUMO+1
S_3	258.1	0.0058	0.0492	HOMO→LUMO+2
S_4	250.1	0.0317	0.2610	HOMO-2→LUMO
S_5	241.0	0.0029	0.0233	HOMO→LUMO+4

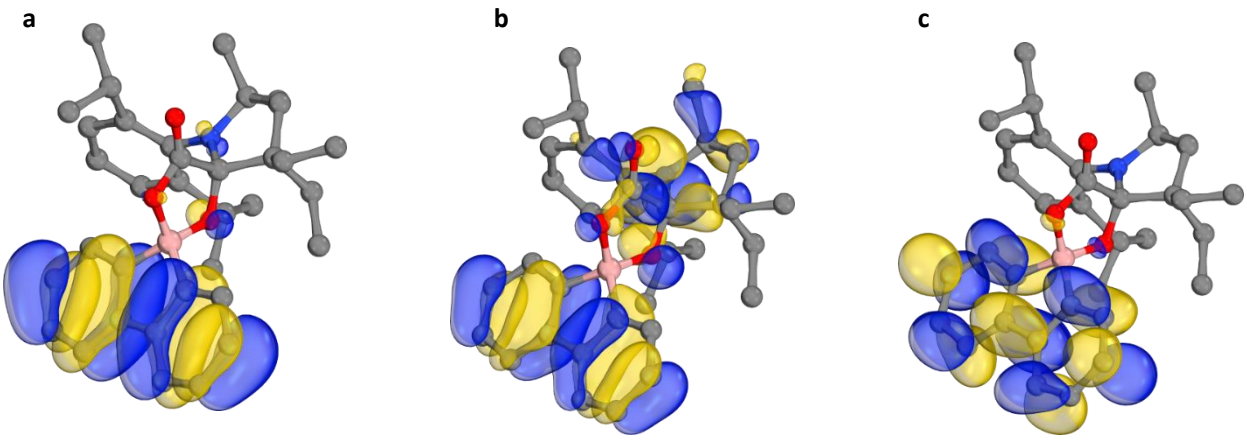

Figure A4.48. HOMO-1 (a), HOMO (b) and LUMO(c) of **7.2** calculated at the CAM-B3LYP-D3(BJ)/def2-TZVP(-f).

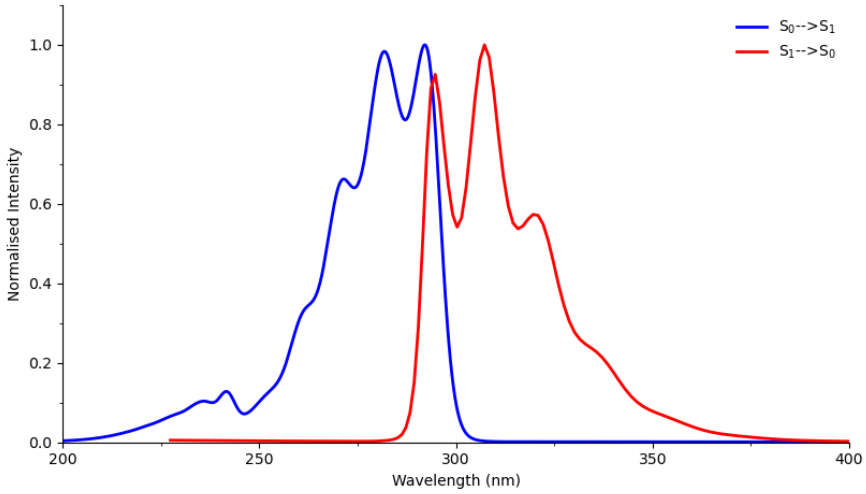

Figure A4.49. Calculated adiabatic transitions for the $S_0 \rightarrow S_1$ and $S_1 \rightarrow S_0$ electronic transitions for **7.2**. CAM-B3LYP-D3(BJ)/def2-TZVP(-f) (σ = 300 cm^{-1}).

References

1. Baumgartner, T.; Jakle, F., *Main Group Strategies towards Functional Hybrid Materials*. John Wiley & Sons Ltd: 2018.
2. Wang, Y.; Xie, Y.; Wei, P.; King, R. B.; Schaefer, H. F.; von R. Schleyer, P.; Robinson, G. H., A Stable Silicon(0) Compound with a Si=Si Double Bond. *Science* **2008,** *321*, 1069-1071.
3. Hadlington, T. J.; Hermann, M.; Li, J.; Frenking, G.; Jones, C., Activation of H2 by a Multiply Bonded Amido–Digermyne: Evidence for the Formation of a Hydrido–Germylene. *Angew. Chem. Int. Ed.* **2013,** *52*, 10199-10203.
4. Stender, M.; Phillips, A. D.; Wright, R. J.; Power, P. P., Synthesis and Characterization of a Digermanium Analogue of an Alkyne. *Angew. Chem. Int. Ed.* **2002,** *41*, 1785-1787.
5. Power, P. P., Silicon, germanium, tin and lead analogues of acetylenes. *Chem. Commun.* **2003**, 10.1039/B212224C, 2091-2101.
6. Mizuhata, Y.; Sasamori, T.; Tokitoh, N., Stable Heavier Carbene Analogues. *Chem. Rev.* **2009,** *109*, 3479-3511.
7. Melen, R. L., Frontiers in molecular p-block chemistry: From structure to reactivity. *Science* **2019,** *363*, 479-484.
8. Priegert, A. M.; Rawe, B. W.; Serin, S. C.; Gates, D. P., Polymers and the p-block elements. *Chem. Soc. Rev.* **2016,** *45*, 922-953.
9. Parke, S. M.; Narreto, M. A. B.; Hupf, E.; McDonald, R.; Ferguson, M. J.; Hegmann, F. A.; Rivard, E., Understanding the Origin of Phosphorescence in Bismoles: A Synthetic and Computational Study. *Inorg. Chem.* **2018,** *57*, 7536-7549.
10. Stępień, M.; Gońka, E.; Żyła, M.; Sprutta, N., Heterocyclic Nanographenes and Other Polycyclic Heteroaromatic Compounds: Synthetic Routes, Properties, and Applications. *Chem. Rev.* **2017,** *117*, 3479-3716.
11. Fagan, P. J.; Nugent, W. A., Synthesis of main group heterocycles by metallacycle transfer from zirconium. *J. Am. Chem. Soc.* **1988,** *110*, 2310-2312.
12. Yan, X.; Xi, C., Conversion of Zirconacyclopentadienes into Metalloles: Fagan–Nugent Reaction and Beyond. *Acc. Chem. Res.* **2015,** *48*, 935-946.
13. Braunschweig, H.; Dömling, M.; Kachel, S.; Kelch, H.; Kramer, T.; Krummenacher, I.; Lenczyk, C.; Lin, S.; Lin, Z.; Possiel, C.; Radacki, K., Abnormal Tin–Boron Exchange in the Attempted Synthesis of a Borylated Borole. *Chem. Eur. J.* **2017,** *23*, 16167-16170.
14. Chivers, T., Halogen exchange in reactions of boron halides with o-(trifluoromethyl)-phenyltrimethyl derivatives of silicon and tin. *Can. J. Chem.* **1970,** *48*, 3856-3859.
15. Hermeke, J.; Mewald, M.; Irran, E.; Oestreich, M., Chemoselective Tin–Boron Exchange Aided by the Use of Dummy Ligands at the Tin Atom. *Organometallics* **2014,** *33*, 5097-5100.
16. Arduengo, A. J.; Harlow, R. L.; Kline, M., A stable crystalline carbene. *J. Am. Chem. Soc.* **1991,** *113*, 361-363.
17. Arduengo, A. J.; Krafczyk, R.; Schmutzler, R.; Craig, H. A.; Goerlich, J. R.; Marshall, W. J.; Unverzagt, M., Imidazolylidenes, imidazolinylidenes and imidazolidines. *Tetrahedron* **1999,** *55*, 14523-14534.
18. Hopkinson, M. N.; Richter, C.; Schedler, M.; Glorius, F., An overview of N-heterocyclic carbenes. *Nature* **2014,** *510*, 485-496.
19. Huynh, H. V., Electronic Properties of N-Heterocyclic Carbenes and Their Experimental Determination. *Chem. Rev.* **2018,** *118*, 9457-9492.
20. Nesterov, V.; Reiter, D.; Bag, P.; Frisch, P.; Holzner, R.; Porzelt, A.; Inoue, S., NHCs in Main Group Chemistry. *Chem. Rev.* **2018,** *118*, 9678-9842.
21. Melaimi, M.; Jazzar, R.; Soleilhavoup, M.; Bertrand, G., Cyclic (Alkyl)(amino)carbenes (CAACs): Recent Developments. *Angew. Chem. Int. Ed.* **2017,** *56*, 10046-10068.
22. Soleilhavoup, M.; Bertrand, G., Cyclic (Alkyl)(Amino)Carbenes (CAACs): Stable Carbenes on the Rise. *Acc. Chem. Res.* **2015,** *48*, 256-266.

23. Soleilhavoup, M.; Bertrand, G., Stable Carbenes, Nitrenes, Phosphinidenes, and Borylenes: Past and Future. *Chem* **2020,** *6*, 1275-1282.
24. Wang, G.; Freeman, L. A.; Dickie, D. A.; Mokrai, R.; Benkő, Z.; Gilliard Jr., R. J., Isolation of Cyclic(Alkyl)(Amino) Carbene–Bismuthinidene Mediated by a Beryllium(0) Complex. *Chem. Eur. J.* **2019,** *25*, 4335-4339.
25. Wang, G.; Walley, J. E.; Dickie, D. A.; Pan, S.; Frenking, G.; Gilliard, R. J., A Stable, Crystalline Beryllium Radical Cation. *J. Am. Chem. Soc.* **2020,** *142*, 4560-4564.
26. Avarmaa, K.; Klemettinen, L.; O'Brien, H.; Taskinen, P.; Jokilaakso, A., Critical Metals Ga, Ge and In: Experimental Evidence for Smelter Recovery Improvements. *Minerals* **2019,** *9*, 367.
27. Goto, A.; Zushi, H.; Hirai, N.; Wakada, T.; Tsujii, Y.; Fukuda, T., Living Radical Polymerizations with Germanium, Tin, and Phosphorus Catalysts − Reversible Chain Transfer Catalyzed Polymerizations (RTCPs). *J. Am. Chem. Soc.* **2007,** *129*, 13347-13354.
28. Guo, J.; Haquette, P.; Martin, J.; Salim, K.; Thomas, C. M., Replacing Tin in Lactide Polymerization: Design of Highly Active Germanium-Based Catalysts. *Angew. Chem. Int. Ed.* **2013,** *52*, 13584-13587.
29. Rittinghaus, R. D.; Tremmel, J.; Růžička, A.; Conrads, C.; Albrecht, P.; Hoffmann, A.; Ksiazkiewicz, A. N.; Pich, A.; Jambor, R.; Herres-Pawlis, S., Undiscovered Potential: Ge Catalysts for Lactide Polymerization. *Chem. Eur. J.* **2020,** *26*, 212-221.
30. Allred, A. L.; Rochow, E. G., Electronegativities of carbon, silicon, germanium, tin and lead. *J. Inorg. Nucl.* **1958,** *5*, 269-288.
31. Selina, A. A.; Karlov, S. S.; Zaitseva, G. S., Metallocanes of group 14 elements. 1. Derivatives of silicon and germanium. (Review). *Chem. Heterocycl. Compd.* **2006,** *42*, 1518-1556.
32. Zheng, F.; Tan, S.-E.; Yanamoto, Y.; Shida, N.; Nishiyama, H.; Inagi, S.; Tomita, I., Preparation of a germole-containing π-conjugated polymer by the Te–Li exchange reaction of a tellurophene-containing polymer. *NPG Asia Mater.* **2020,** *12*, 41.
33. Liu, Y.; Ballweg, D.; Müller, T.; Guzei, I. A.; Clark, R. W.; West, R., Chemistry of the Aromatic 9-Germafluorenyl Dianion and Some Related Silicon and Carbon Species. *J. Am. Chem. Soc.* **2002,** *124*, 12174-12181.
34. Shynkaruk, O.; He, G.; McDonald, R.; Ferguson, M. J.; Rivard, E., Modular Synthesis of Spirocyclic Germafluorene–Germoles: A New Family of Tunable Luminogens. *Chem. Eur. J.* **2016,** *22*, 248-257.
35. Nakamura, M.; Ooyama, Y.; Hayakawa, S.; Nishino, M.; Ohshita, J., Synthesis of Poly(dithienogermole)s. *Organometallics* **2016,** *35*, 2333-2338.
36. Nagendran, S.; Roesky, H. W., The Chemistry of Aluminum(I), Silicon(II), and Germanium(II). *Organometallics* **2008,** *27*, 457-492.
37. Tokitoh, N.; Okazaki, R., Recent topics in the chemistry of heavier congeners of carbenes. *Coord. Chem. Rev.* **2000,** *210*, 251-277.
38. Zhang, S.-H.; So, C.-W., Synthesis and Characterization of an Amidinate-Stabilized Bisgermylene Oxide and Sulfide. *Organometallics* **2011,** *30*, 2059-2062.
39. Asay, M.; Jones, C.; Driess, M., N-Heterocyclic Carbene Analogues with Low-Valent Group 13 and Group 14 Elements: Syntheses, Structures, and Reactivities of a New Generation of Multitalented Ligands. *Chem. Rev.* **2011,** *111*, 354-396.
40. Herrmann, W. A.; Denk, M.; Behm, J.; Scherer, W.; Klingan, F.-R.; Bock, H.; Solouki, B.; Wagner, M., Stable Cyclic Germanediyls ("Cyclogermylenes"): Synthesis, Structure, Metal Complexes, and Thermolyses. *Angew. Chem. Int. Ed. Engl.* **1992,** *31*, 1485-1488.
41. Meller, A.; Pfeiffer, J.; Noltemeyer, M., Aza- und Thia-2-germa(II)-indane und entsprechende 2,2′-Spirobi(2-germaindane). *Z. Anorg. Allg. Chem.* **1989,** *572*, 145-150.
42. Pfeiffer, J.; Maringgele, W.; Noltemeyer, M.; Meller, A., Reaktionen von Germylenen mit Aziden: Iminogermane, Azidogermane, Tetrazagermole und Hexaazadigermadispirododecane. *Chemische Berichte* **1989,** *122*, 245-252.

43. Zabula, A. V.; Hahn, F. E.; Pape, T.; Hepp, A., Preparation and Coordination Chemistry of Bidentate Benzimidazoline-2-germylenes. *Organometallics* **2007,** *26*, 1972-1980.
44. Krupski, S.; Dickschat, J. V.; Hepp, A.; Pape, T.; Hahn, F. E., Synthesis and Characterization of Rigid Ditopic N-Heterocyclic Benzobisgermylenes and -stannylenes. *Organometallics* **2012,** *31*, 2078-2084.
45. Zhong, F.; Yang, X.; Shen, L.; Zhao, Y.; Ma, H.; Wu, B.; Yang, X.-J., Multinuclear Alkali Metal Complexes of a Triphenylene-Based Hexamine and the Transmetalation to Tris(N-heterocyclic tetrylenes) (Ge, Sn, Pb). *Inorg. Chem.* **2016,** *55*, 9112-9120.
46. Figueira-Duarte, T. M.; Müllen, K., Pyrene-Based Materials for Organic Electronics. *Chem. Rev.* **2011,** *111*, 7260-7314.
47. Chercka, D.; Yoo, S.-J.; Baumgarten, M.; Kim, J.-J.; Müllen, K., Pyrene based materials for exceptionally deep blue OLEDs. *J. Mater, Chem. C* **2014,** *2*, 9083-9086.
48. Lo, M. Y.; Zhen, C.; Lauters, M.; Jabbour, G. E.; Sellinger, A., Organic−Inorganic Hybrids Based on Pyrene Functionalized Octavinylsilsesquioxane Cores for Application in OLEDs. *J. Am. Chem. Soc.* **2007,** *129*, 5808-5809.
49. Zhou, Y.; Kim, J. W.; Kim, M. J.; Son, W.-J.; Han, S. J.; Kim, H. N.; Han, S.; Kim, Y.; Lee, C.; Kim, S.-J.; Kim, D. H.; Kim, J.-J.; Yoon, J., Novel Bi-Nuclear Boron Complex with Pyrene Ligand: Red-Light Emitting as well as Electron Transporting Material in Organic Light-Emitting Diodes. *Org. Lett.* **2010,** *12*, 1272-1275.
50. Zhang, H.; Wang, Y.; Shao, K.; Liu, Y.; Chen, S.; Qiu, W.; Sun, X.; Qi, T.; Ma, Y.; Yu, G.; Su, Z.; Zhu, D., Novel butterfly pyrene-based organic semiconductors for field effect transistors. *Chem. Commun.* **2006**, 10.1039/B515433B, 755-757.
51. Zhao, D.; Wu, Q.; Cai, Z.; Zheng, T.; Chen, W.; Lu, J.; Yu, L., Electron Acceptors Based on α-Substituted Perylene Diimide (PDI) for Organic Solar Cells. *Chem. Mater.* **2016,** *28*, 1139-1146.
52. Li, S.-S.; Jiang, K.-J.; Yu, C.-C.; Huang, J.-H.; Yang, L.-M.; Song, Y.-L., A 2,7-pyrene-based dye for solar cell application. *New J. Chem.* **2014,** *38*, 4404-4408.
53. Bernhardt, S.; Kastler, M.; Enkelmann, V.; Baumgarten, M.; Müllen, K., Pyrene as Chromophore and Electrophore: Encapsulation in a Rigid Polyphenylene Shell. *Chem. Eur. J.* **2006,** *12*, 6117-6128.
54. Hu, J.; Zhang, D.; Harris, F. W., Ruthenium(III) Chloride Catalyzed Oxidation of Pyrene and 2,7-Disubstitued Pyrenes: An Efficient, One-Step Synthesis of Pyrene-4,5-diones and Pyrene-4,5,9,10-tetraones. *J. Org. Chem.* **2005,** *70*, 707-708.
55. Yamato, T.; Fujimoto, M.; Miyazawa, A.; Matsuo, K., Selective preparation of polycyclic aromatic hydrocarbons. Part 5.1 Bromination of 2,7-di-tert-butylpyrene and conversion into pyrenoquinones and their pyrenoquinhydrones. *J. Chem. Soc. Perkin Trans. 1* **1997**, 10.1039/A606200H, 1201-1208.
56. Wu, Z. H.; Huang, Z. T.; Guo, R. X.; Sun, C. L.; Chen, L. C.; Sun, B.; Shi, Z. F.; Shao, X.; Li, H.; Zhang, H. L., 4,5,9,10-Pyrene Diimides: A Family of Aromatic Diimides Exhibiting High Electron Mobility and Two-Photon Excited Emission. *Angew. Chem. Int. Ed.* **2017,** *56*, 13031-13035.
57. Duret, G.; Quinlan, R.; Bisseret, P.; Blanchard, N., Boron chemistry in a new light. *Chem. Sci.* **2015,** *6*, 5366-5382.
58. Entwistle, C. D.; Marder, T. B., Boron Chemistry Lights the Way: Optical Properties of Molecular and Polymeric Systems. *Angew. Chem. Int. Ed.* **2002,** *41*, 2927-2931.
59. Huang, Z.; Wang, S.; Dewhurst, R. D.; Ignat'ev, N. V.; Finze, M.; Braunschweig, H., Boron: Its role in energy related research and applications. *Angew. Chem. Int. Ed. n/a*.
60. Jäkle, F., Advances in the Synthesis of Organoborane Polymers for Optical, Electronic, and Sensory Applications. *Chem. Rev.* **2010,** *110*, 3985-4022.
61. Mellerup, S. K.; Wang, S., Boron-Doped Molecules for Optoelectronics. *Trends Chem.* **2019,** *1*, 77-89.
62. Ji, L.; Griesbeck, S.; Marder, T. B., Recent developments in and perspectives on three-coordinate boron materials: a bright future. *Chem. Sci.* **2017,** *8*, 846-863.
63. Piers, W. E.; Bourke, S. C.; Conroy, K. D., Borinium, Borenium, and Boronium Ions: Synthesis, Reactivity, and Applications. *Angew. Chem. Int. Ed.* **2005,** *44*, 5016-5036.

64. Yin, X.; Liu, J.; Jäkle, F., Electron-Deficient Conjugated Materials via p–π* Conjugation with Boron: Extending Monomers to Oligomers, Macrocycles, and Polymers. *Chem. Eur. J.* **2021,** *27*, 2973-2986.
65. Chen, X.-L.; Jia, J.-H.; Yu, R.; Liao, J.-Z.; Yang, M.-X.; Lu, C.-Z., Combining Charge-Transfer Pathways to Achieve Unique Thermally Activated Delayed Fluorescence Emitters for High-Performance Solution-Processed, Non-doped Blue OLEDs. *Angew. Chem. Int. Ed.* **2017,** *56*, 15006-15009.
66. Hudson, Z. M.; Wang, X.; Wang, S., Triarylboron-Functionalized Metal Complexes for OLEDs. In *Organometallics and Related Molecules for Energy Conversion*, Wong, W.-Y., Ed. Springer Berlin Heidelberg: Berlin, Heidelberg, 2015, 10.1007/978-3-662-46054-2_8pp 207-239.
67. Lee, H.; Jana, S.; Kim, J.; Lee, S. U.; Lee, M. H., Donor–Acceptor-Appended Triarylboron Lewis Acids: Ratiometric or Time-Resolved Turn-On Fluorescence Response toward Fluoride Binding. *Inorg. Chem.* **2020,** *59*, 1414-1423.
68. Lee, Y. H.; Park, S.; Oh, J.; Shin, J. W.; Jung, J.; Yoo, S.; Lee, M. H., Rigidity-Induced Delayed Fluorescence by Ortho Donor-Appended Triarylboron Compounds: Record-High Efficiency in Pure Blue Fluorescent Organic Light-Emitting Diodes. *ACS Appl. Mater. Interfaces* **2017,** *9*, 24035-24042.
69. Lee, Y. H.; Park, S.; Oh, J.; Woo, S.-J.; Kumar, A.; Kim, J.-J.; Jung, J.; Yoo, S.; Lee, M. H., High-Efficiency Sky Blue to Ultradeep Blue Thermally Activated Delayed Fluorescent Diodes Based on Ortho-Carbazole-Appended Triarylboron Emitters: Above 32% External Quantum Efficiency in Blue Devices. *Adv. Opt. Mater.* **2018,** *6*, 1800385.
70. Liu, Y.; Xie, G.; Wu, K.; Luo, Z.; Zhou, T.; Zeng, X.; Yu, J.; Gong, S.; Yang, C., Boosting reverse intersystem crossing by increasing donors in triarylboron/phenoxazine hybrids: TADF emitters for high-performance solution-processed OLEDs. *J. Mater, Chem. C* **2016,** *4*, 4402-4407.
71. Suzuki, K.; Kubo, S.; Shizu, K.; Fukushima, T.; Wakamiya, A.; Murata, Y.; Adachi, C.; Kaji, H., Triarylboron-Based Fluorescent Organic Light-Emitting Diodes with External Quantum Efficiencies Exceeding 20 %. *Angew. Chem. Int. Ed.* **2015,** *54*, 15231-15235.
72. Huang, J.; Li, Y., BN Embedded Polycyclic π-Conjugated Systems: Synthesis, Optoelectronic Properties, and Photovoltaic Applications. *Front. Chem.* **2018,** *6*.
73. Dosso, J.; Tasseroul, J.; Fasano, F.; Marinelli, D.; Biot, N.; Fermi, A.; Bonifazi, D., Synthesis and Optoelectronic Properties of Hexa-peri-hexabenzoborazinocoronene. *Angew. Chem. Int. Ed.* **2017,** *56*, 4483-4487.
74. Hatakeyama, T.; Hashimoto, S.; Seki, S.; Nakamura, M., Synthesis of BN-Fused Polycyclic Aromatics via Tandem Intramolecular Electrophilic Arene Borylation. *J. Am. Chem. Soc.* **2011,** *133*, 18614-18617.
75. Lorenzo-García, M. M.; Bonifazi, D., Renaissance of an Old Topic: From Borazines to BN-doped Nanographenes. *Chimia Int. J. Chem.* **2017,** *71*, 550-557.
76. Morgan, M. M.; Piers, W. E., Efficient synthetic methods for the installation of boron–nitrogen bonds in conjugated organic molecules. *Dalton Trans.* **2016,** *45*, 5920-5924.
77. Scholz, A. S.; Massoth, J. G.; Bursch, M.; Mewes, J.-M.; Hetzke, T.; Wolf, B.; Bolte, M.; Lerner, H.-W.; Grimme, S.; Wagner, M., BNB-Doped Phenalenyls: Modular Synthesis, Optoelectronic Properties, and One-Electron Reduction. *J. Am. Chem. Soc.* **2020,** *142*, 11072-11083.
78. Tasseroul, J.; Lorenzo-Garcia, M. M.; Dosso, J.; Simon, F.; Velari, S.; De Vita, A.; Tecilla, P.; Bonifazi, D., Probing Peripheral H-Bonding Functionalities in BN-Doped Polycyclic Aromatic Hydrocarbons. *J. Org. Chem.* **2020,** *85*, 3454-3464.
79. Wang, X.-Y.; Zhuang, F.-D.; Wang, R.-B.; Wang, X.-C.; Cao, X.-Y.; Wang, J.-Y.; Pei, J., A Straightforward Strategy toward Large BN-Embedded π-Systems: Synthesis, Structure, and Optoelectronic Properties of Extended BN Heterosuperbenzenes. *J. Am. Chem. Soc.* **2014,** *136*, 3764-3767.
80. Wang, X.-Y.; Zhuang, F.-D.; Wang, X.-C.; Cao, X.-Y.; Wang, J.-Y.; Pei, J., Synthesis, structure and properties of C3-symmetric heterosuperbenzene with three BN units. *Chem. Commun.* **2015,** *51*, 4368-4371.

81. Lee, G.-H.; Yu, Y.-J.; Cui, X.; Petrone, N.; Lee, C.-H.; Choi, M. S.; Lee, D.-Y.; Lee, C.; Yoo, W. J.; Watanabe, K.; Taniguchi, T.; Nuckolls, C.; Kim, P.; Hone, J., Flexible and Transparent MoS2 Field-Effect Transistors on Hexagonal Boron Nitride-Graphene Heterostructures. *ACS Nano* **2013,** *7*, 7931-7936.
82. Marconcini, P.; Cresti, A.; Triozon, F.; Fiori, G.; Biel, B.; Niquet, Y.-M.; Macucci, M.; Roche, S., Atomistic Boron-Doped Graphene Field-Effect Transistors: A Route toward Unipolar Characteristics. *ACS Nano* **2012,** *6*, 7942-7947.
83. Meric, I.; Dean, C. R.; Petrone, N.; Wang, L.; Hone, J.; Kim, P.; Shepard, K. L., Graphene Field-Effect Transistors Based on Boron–Nitride Dielectrics. *Proc. IEEE* **2013,** *101*, 1609-1619.
84. Wang, L.; Wu, B.; Chen, J.; Liu, H.; Hu, P.; Liu, Y., Monolayer Hexagonal Boron Nitride Films with Large Domain Size and Clean Interface for Enhancing the Mobility of Graphene-Based Field-Effect Transistors. *Adv. Mater.* **2014,** *26*, 1559-1564.
85. DeRosa, C. A.; Seaman, S. A.; Mathew, A. S.; Gorick, C. M.; Fan, Z.; Demas, J. N.; Peirce, S. M.; Fraser, C. L., Oxygen Sensing Difluoroboron β-Diketonate Polylactide Materials with Tunable Dynamic Ranges for Wound Imaging. *ACS Sensors* **2016,** *1*, 1366-1373.
86. Liu, K.; Lalancette, R. A.; Jäkle, F., B–N Lewis Pair Functionalization of Anthracene: Structural Dynamics, Optoelectronic Properties, and O2 Sensitization. *J. Am. Chem. Soc.* **2017,** *139*, 18170-18173.
87. Liu, K.; Lalancette, R. A.; Jäkle, F., Tuning the Structure and Electronic Properties of B–N Fused Dipyridylanthracene and Implications on the Self-Sensitized Reactivity with Singlet Oxygen. *J. Am. Chem. Soc.* **2019,** *141*, 7453-7462.
88. Kubo, Y.; Eguchi, D.; Matsumoto, A.; Nishiyabu, R.; Yakushiji, H.; Shigaki, K.; Kaneko, M., Boron–dibenzopyrromethene-based organic dyes for application in dye-sensitized solar cells. *J. Mater. Chem. A* **2014,** *2*, 5204-5211.
89. Morse, G. E.; Gantz, J. L.; Steirer, K. X.; Armstrong, N. R.; Bender, T. P., Pentafluorophenoxy Boron Subphthalocyanine (F5BsubPc) as a Multifunctional Material for Organic Photovoltaics. *ACS Appl. Mater. Interfaces* **2014,** *6*, 1515-1524.
90. Pandey, R.; Gunawan, A. A.; Mkhoyan, K. A.; Holmes, R. J., Efficient Organic Photovoltaic Cells Based on Nanocrystalline Mixtures of Boron Subphthalocyanine Chloride and C60. *Adv. Funct. Mater.* **2012,** *22*, 617-624.
91. Pandey, R.; Zou, Y.; Holmes, R. J., Efficient, bulk heterojunction organic photovoltaic cells based on boron subphthalocyanine chloride-C70. *Appl. Phys. Lett.* **2012,** *101*, 033308.
92. Adams, I. A.; Rupar, P. A., A Poly(9-Borafluorene) Homopolymer: An Electron-Deficient Polyfluorene with "Turn-On" Fluorescence Sensing of NH3 Vapor. *Macromol. Rapid Commun.* **2015,** *36*, 1336-1340.
93. Cassidy, S. J.; Brettell-Adams, I.; McNamara, L. E.; Smith, M. F.; Bautista, M.; Cao, H.; Vasiliu, M.; Gerlach, D. L.; Qu, F.; Hammer, N. I.; Dixon, D. A.; Rupar, P. A., Boranes with Ultra-High Stokes Shift Fluorescence. *Organometallics* **2018,** *37*, 3732-3741.
94. Thanthiriwatte, K. S.; Gwaltney, S. R., Excitation Spectra of Dibenzoborole Containing π-Electron Systems: Controlling the Electronic Spectra by Changing the pπ−π* Conjugation. *J. Phys. Chem. A* **2006,** *110*, 2434-2439.
95. Urban, M.; Durka, K.; Górka, P.; Wiosna-Sałyga, G.; Nawara, K.; Jankowski, P.; Luliński, S., The effect of locking π-conjugation in organoboron moieties in the structures of luminescent tetracoordinate boron complexes. *Dalton Trans.* **2019,** *48*, 8642-8663.
96. Wakamiya, A.; Mishima, K.; Ekawa, K.; Yamaguchi, S., Kinetically stabilized dibenzoborole as an electron-accepting building unit. *Chem. Commun.* **2008**, 10.1039/B716107G, 579-581.
97. Zhang, Z.; Zhang, H.; Jiao, C.; Ye, K.; Zhang, H.; Zhang, J.; Wang, Y., 2-(2-Hydroxyphenyl)benzimidazole-Based Four-Coordinate Boron-Containing Materials with Highly Efficient Deep-Blue Photoluminescence and Electroluminescence. *Inorg. Chem.* **2015,** *54*, 2652-2659.
98. Su, X.; Bartholome, T. A.; Tidwell, J. R.; Pujol, A.; Yruegas, S.; Martinez, J. J.; Martin, C. D., 9-Borafluorenes: Synthesis, Properties, and Reactivity. *Chem. Rev.* **2021,** *121*, 4147-4192.

99. Yang, W.; Krantz, K. E.; Dickie, D. A.; Molino, A.; Wilson, D. J. D.; Gilliard Jr., R. J., Crystalline BP-Doped Phenanthryne via Photolysis of The Elusive Boraphosphaketene. *Angew. Chem. Int. Ed.* **2020,** *59*, 3971-3975.
100. Yamaguchi, S.; Shirasaka, T.; Akiyama, S.; Tamao, K., Dibenzoborole-Containing π-Electron Systems: Remarkable Fluorescence Change Based on the "On/Off" Control of the pπ−π* Conjugation. *J. Am. Chem. Soc.* **2002,** *124*, 8816-8817.
101. Iida, A.; Yamaguchi, S., Thiophene-Fused Ladder Boroles with High Antiaromaticity. *J. Am. Chem. Soc.* **2011,** *133*, 6952-6955.
102. Berger, C. J.; He, G.; Merten, C.; McDonald, R.; Ferguson, M. J.; Rivard, E., Synthesis and Luminescent Properties of Lewis Base-Appended Borafluorenes. *Inorg. Chem.* **2014,** *53*, 1475-1486.
103. Smith, M. F.; Cassidy, S. J.; Adams, I. A.; Vasiliu, M.; Gerlach, D. L.; Dixon, D. A.; Rupar, P. A., Substituent Effects on the Properties of Borafluorenes. *Organometallics* **2016,** *35*, 3182-3191.
104. Chase, P. A.; Henderson, L. D.; Piers, W. E.; Parvez, M.; Clegg, W.; Elsegood, M. R. J., Bifunctional Perfluoroaryl Boranes: Synthesis and Coordination Chemistry with Neutral Lewis Base Donors. *Organometallics* **2006,** *25*, 349-357.
105. Chase, P. A.; Piers, W. E.; Patrick, B. O., New Fluorinated 9-Borafluorene Lewis Acids. *J. Am. Chem. Soc.* **2000,** *122*, 12911-12912.
106. Chase, P. A.; Romero, P. E.; Piers, W. E.; Parvez, M.; Patrick, B. O., Fluorinated 9-borafluorenes vs. conventional perfluoroaryl boranes — Comparative Lewis acidity. *Can. J. Chem.* **2005,** *83*, 2098-2105.
107. Yang, W.; Krantz, K. E.; Freeman, L. A.; Dickie, D. A.; Molino, A.; Kaur, A.; Wilson, D. J. D.; Gilliard Jr., R. J., Stable Borepinium and Borafluorenium Heterocycles: A Reversible Thermochromic "Switch" Based on Boron–Oxygen Interactions. *Chem. Eur. J.* **2019,** *25*, 12512-12516.
108. Li, Y.; Chen, X.; Zhang, W.; Zhang, J.; Xu, L.; Qiao, Y.; Liu, K.; Wang, N.; Chen, P.; Yin, X., Substituent Modulation for Highly Bright 9-Borafluorene Derivatives with Carbazole Pendant. *Org. Lett.* **2021,** *23*, 7236-7241.
109. Farrell, J. M.; Stephan, D. W., Planar N-Heterocyclic Carbene Diarylborenium Ions: Synthesis by Cationic Borylation and Reactivity with Lewis Bases. *Angew. Chem. Int. Ed.* **2015,** *54*, 5214-5217.
110. Koelle, P.; Noeth, H., The chemistry of borinium and borenium ions. *Chem. Rev.* **1985,** *85*, 399-418.
111. Narula, C. K.; Noeth, H., Preparation and characterization of salts containing cations of tricoordinate boron. *Inorg. Chem.* **1984,** *23*, 4147-4152.
112. Narula, C. K.; Noeth, H., Contribution to the chemistry of boron. 150. Competition between adduct and cation formation in reactions between diorganylborane derivatives and pyridine or lutidines. *Inorg. Chem.* **1985,** *24*, 2532-2539.
113. Stahl, T.; Müther, K.; Ohki, Y.; Tatsumi, K.; Oestreich, M., Catalytic Generation of Borenium Ions by Cooperative B–H Bond Activation: The Elusive Direct Electrophilic Borylation of Nitrogen Heterocycles with Pinacolborane. *J. Am. Chem. Soc.* **2013,** *135*, 10978-10981.
114. Boussonnière, A.; Pan, X.; Geib, S. J.; Curran, D. P., Borenium-Catalyzed Hydroborations of Silyl-Substituted Alkenes and Alkynes with a Readily Available N-Heterocyclic Carbene–Borane. *Organometallics* **2013,** *32*, 7445-7450.
115. Devillard, M.; Brousses, R.; Miqueu, K.; Bouhadir, G.; Bourissou, D., A Stable but Highly Reactive Phosphine-Coordinated Borenium: Metal-free Dihydrogen Activation and Alkyne 1,2-Carboboration. *Angew. Chem. Int. Ed.* **2015,** *54*, 5722-5726.
116. Farrell, J. M.; Posaratnanathan, R. T.; Stephan, D. W., A family of N-heterocyclic carbene-stabilized borenium ions for metal-free imine hydrogenation catalysis. *Chem. Sci.* **2015,** *6*, 2010-2015.
117. Prokofjevs, A.; Boussonnière, A.; Li, L.; Bonin, H.; Lacôte, E.; Curran, D. P.; Vedejs, E., Borenium Ion Catalyzed Hydroboration of Alkenes with N-Heterocyclic Carbene-Boranes. *J. Am. Chem. Soc.* **2012,** *134*, 12281-12288.
118. Eisenberger, P.; Crudden, C. M., Borocation catalysis. *Dalton Trans.* **2017,** *46*, 4874-4887.
119. Adachi, Y.; Arai, F.; Jäkle, F., Extended conjugated borenium dimers via late stage functionalization of air-stable borepinium ions. *Chem. Commun.* **2020,** *56*, 5119-5122.

120. Katzman, B. D.; Maar, R. R.; Cappello, D.; Sattler, M. O.; Boyle, P. D.; Staroverov, V. N.; Gilroy, J. B., A strongly Lewis-acidic and fluorescent borenium cation supported by a tridentate formazanate ligand. *Chem. Commun.* **2021,** *57*, 9530-9533.
121. Maar, R. R.; Katzman, B. D.; Boyle, P. D.; Staroverov, V. N.; Gilroy, J. B., Cationic Boron Formazanate Dyes**. *Angew. Chem. Int. Ed.* **2021,** *60*, 5152-5156.
122. Hollister, K. K.; Molino, A.; Breiner, G.; Walley, J. E.; Wentz, K. E.; Conley, A. M.; Dickie, D. A.; Wilson, D. J. D.; Gilliard, R. J., Air-Stable Thermoluminescent Carbodicarbene-Borafluorenium Ions. *J. Am. Chem. Soc.* **2022,** *144*, 590-598.
123. Yang, W.; Krantz, K. E.; Freeman, L. A.; Dickie, D. A.; Molino, A.; Frenking, G.; Pan, S.; Wilson, D. J. D.; Gilliard Jr., R. J., Persistent Borafluorene Radicals. *Angew. Chem. Int. Ed.* **2020,** *59*, 3850-3854.
124. Ostroverkhova, O., Organic Optoelectronic Materials: Mechanisms and Applications. *Chem. Rev.* **2016,** *116*, 13279-13412.
125. Roncali, J.; Leriche, P.; Blanchard, P., Molecular Materials for Organic Photovoltaics: Small is Beautiful. *Adv. Mater.* **2014,** *26*, 3821-3838.
126. Beaujuge, P. M.; Fréchet, J. M. J., Molecular Design and Ordering Effects in π-Functional Materials for Transistor and Solar Cell Applications. *J. Am. Chem. Soc.* **2011,** *133*, 20009-20029.
127. Wang, C.; Dong, H.; Hu, W.; Liu, Y.; Zhu, D., Semiconducting π-Conjugated Systems in Field-Effect Transistors: A Material Odyssey of Organic Electronics. *Chem. Rev.* **2012,** *112*, 2208-2267.
128. Wu, W.; Liu, Y.; Zhu, D., π-Conjugated molecules with fused rings for organic field-effect transistors: design, synthesis and applications. *Chem. Soc. Rev.* **2010,** *39*, 1489-1502.
129. Anthony, J. E., Functionalized Acenes and Heteroacenes for Organic Electronics. *Chem. Rev.* **2006,** *106*, 5028-5048.
130. Wu, J.; Pisula, W.; Müllen, K., Graphenes as Potential Material for Electronics. *Chem. Rev.* **2007,** *107*, 718-747.
131. Miao, Q., Ten Years of N-Heteropentacenes as Semiconductors for Organic Thin-Film Transistors. *Adv. Mater.* **2014,** *26*, 5541-5549.
132. Bachar, N.; Liberman, L.; Muallem, F.; Feng, X.; Müllen, K.; Haick, H., Sensor Arrays Based on Polycyclic Aromatic Hydrocarbons: Chemiresistors versus Quartz-Crystal Microbalance. *ACS Appl. Mater. Interfaces* **2013,** *5*, 11641-11653.
133. McQuade, D. T.; Pullen, A. E.; Swager, T. M., Conjugated Polymer-Based Chemical Sensors. *Chem. Rev.* **2000,** *100*, 2537-2574.
134. Salunke, J. K.; Sonar, P.; Wong, F. L.; Roy, V. A. L.; Lee, C. S.; Wadgaonkar, P. P., Pyrene based conjugated materials: synthesis, characterization and electroluminescent properties. *Phys. Chem, Chem. Phys.* **2014,** *16*, 23320-23328.
135. Feng, X.; Iwanaga, F.; Hu, J.-Y.; Tomiyasu, H.; Nakano, M.; Redshaw, C.; Elsegood, M. R. J.; Yamato, T., An Efficient Approach to the Synthesis of Novel Pyrene-Fused Azaacenes. *Org. Lett.* **2013,** *15*, 3594-3597.
136. Kohl, B.; Rominger, F.; Mastalerz, M., A Pyrene-Fused N-Heteroacene with Eleven Rectilinearly Annulated Aromatic Rings. *Angew. Chem. Int. Ed.* **2015,** *54*, 6051-6056.
137. Kulisic, N.; More, S.; Mateo-Alonso, A., A tetraalkylated pyrene building block for the synthesis of pyrene-fused azaacenes with enhanced solubility. *Chem. Commun.* **2011,** *47*, 514-516.
138. Bandyopadhyay, S.; Singh, C.; Jash, P.; Hussain, M. D. W.; Paul, A.; Patra, A., Redox-active, pyrene-based pristine porous organic polymers for efficient energy storage with exceptional cyclic stability. *Chem. Commun.* **2018,** *54*, 6796-6799.
139. Bheemireddy, S. R.; Plunkett, K. N., Dicyclopenta[cd,jk]pyrene based acceptors in conjugated polymers. *Polym. Chem.* **2016,** *7*, 292-296.
140. Bhunia, S.; Bhunia, K.; Patra, B. C.; Das, S. K.; Pradhan, D.; Bhaumik, A.; Pradhan, A.; Bhattacharya, S., Efficacious Electrochemical Oxygen Evolution from a Novel Co(II) Porphyrin/Pyrene-Based Conjugated Microporous Polymer. *ACS Appl. Mater. Interfaces* **2019,** *11*, 1520-1528.
141. Figueira-Duarte, T. M.; Simon, S. C.; Wagner, M.; Druzhinin, S. I.; Zachariasse, K. A.; Müllen, K., Polypyrene Dendrimers. *Angew. Chem. Int. Ed.* **2008,** *47*, 10175-10178.

142. Shi, L.; Qi, Z.; Peng, P.; Guo, J.; Wan, G.; Cao, D.; Xiang, Z., Pyrene-Based Covalent Organic Polymers for Enhanced Photovoltaic Performance and Solar-Driven Hydrogen Production. *ACS Appl. Energy Mater.* **2018,** *1*, 7007-7013.
143. Kang, H.; Facchetti, A.; Jiang, H.; Cariati, E.; Righetto, S.; Ugo, R.; Zuccaccia, C.; Macchioni, A.; Stern, C. L.; Liu, Z.; Ho, S.-T.; Brown, E. C.; Ratner, M. A.; Marks, T. J., Ultralarge Hyperpolarizability Twisted π-Electron System Electro-Optic Chromophores: Synthesis, Solid-State and Solution-Phase Structural Characteristics, Electronic Structures, Linear and Nonlinear Optical Properties, and Computational Studies. *J. Am. Chem. Soc.* **2007,** *129*, 3267-3286.
144. Lou, A. J. T.; Marks, T. J., A Twist on Nonlinear Optics: Understanding the Unique Response of π-Twisted Chromophores. *Acc. Chem. Res.* **2019,** *52*, 1428-1438.
145. Zhong, Y.; Trinh, M. T.; Chen, R.; Purdum, G. E.; Khlyabich, P. P.; Sezen, M.; Oh, S.; Zhu, H.; Fowler, B.; Zhang, B.; Wang, W.; Nam, C.-Y.; Sfeir, M. Y.; Black, C. T.; Steigerwald, M. L.; Loo, Y.-L.; Ng, F.; Zhu, X. Y.; Nuckolls, C., Molecular helices as electron acceptors in high-performance bulk heterojunction solar cells. *Nat. Commun.* **2015,** *6*, 8242.
146. Xiao, J.; Divayana, Y.; Zhang, Q.; Doung, H. M.; Zhang, H.; Boey, F.; Sun, X. W.; Wudl, F., Synthesis, structure, and optoelectronic properties of a new twistacene 1,2,3,4,6,13-hexaphenyl-7 : 8,11 : 12-bisbenzo-pentacene. *J. Mater. Chem.* **2010,** *20*, 8167-8170.
147. Xiao, S.; Kang, S. J.; Zhong, Y.; Zhang, S.; Scott, A. M.; Moscatelli, A.; Turro, N. J.; Steigerwald, M. L.; Li, H.; Nuckolls, C., Controlled Doping in Thin-Film Transistors of Large Contorted Aromatic Compounds. *Angew. Chem. Int. Ed.* **2013,** *52*, 4558-4562.
148. Rickhaus, M.; Mayor, M.; Juríček, M., Strain-induced helical chirality in polyaromatic systems. *Chem. Soc. Rev.* **2016,** *45*, 1542-1556.
149. Shen, Y.; Chen, C.-F., Helicenes: Synthesis and Applications. *Chem. Rev.* **2012,** *112*, 1463-1535.
150. Mateo-Alonso, A., Synthetic Approaches to Pyrene-Fused Twistacenes. *Eur. J. Org. Chem.* **2017,** *2017*, 7006-7011.
151. Lu, J.; Ho, D. M.; Vogelaar, N. J.; Kraml, C. M.; Bernhard, S.; Byrne, N.; Kim, L. R.; Pascal, R. A., Synthesis, Structure, and Resolution of Exceptionally Twisted Pentacenes. *J. Am. Chem. Soc.* **2006,** *128*, 17043-17050.
152. Lu, J.; Ho, D. M.; Vogelaar, N. J.; Kraml, C. M.; Pascal, R. A., A Pentacene with a 144° Twist. *J. Am. Chem. Soc.* **2004,** *126*, 11168-11169.
153. Pascal, R. A., Twisted Acenes. *Chem. Rev.* **2006,** *106*, 4809-4819.
154. Pascal, R. A.; McMillan, W. D.; Van Engen, D.; Eason, R. G., Synthesis and structure of longitudinally twisted polycyclic aromatic hydrocarbons. *J. Am. Chem. Soc.* **1987,** *109*, 4660-4665.
155. Walters, R. S.; Kraml, C. M.; Byrne, N.; Ho, D. M.; Qin, Q.; Coughlin, F. J.; Bernhard, S.; Pascal, R. A., Configurationally Stable Longitudinally Twisted Polycyclic Aromatic Compounds. *J. Am. Chem. Soc.* **2008,** *130*, 16435-16441.
156. Bedi, A.; Shimon, L. J. W.; Gidron, O., Helically Locked Tethered Twistacenes. *J. Am. Chem. Soc.* **2018,** *140*, 8086-8090.
157. Ghasemabadi, P. G.; Yao, T.; Bodwell, G. J., Cyclophanes containing large polycyclic aromatic hydrocarbons. *Chem. Soc. Rev.* **2015,** *44*, 6494-6518.
158. More, S.; Choudhary, S.; Higelin, A.; Krossing, I.; Melle-Franco, M.; Mateo-Alonso, A., Twisted pyrene-fused azaacenes. *Chem. Commun.* **2014,** *50*, 1976-1979.
159. Valdés, H.; Poyatos, M.; Peris, E., A Nanosized Janus Bis-N-heterocyclic Carbene Ligand Based on a Quinoxalinophenanthrophenazine Core, and Its Coordination to Iridium. *Organometallics* **2015,** *34*, 1725-1729.
160. Bodwell, G. J.; Bridson, J. N.; Houghton, T. J.; Kennedy, J. W. J.; Mannion, M. R., 1,8-Dioxa[8](2,7)pyrenophane, a Severely Distorted Polycyclic Aromatic Hydrocarbon. *Angew. Chem. Int. Ed. Engl.* **1996,** *35*, 1320-1321.
161. Pham, H. D.; Hu, H.; Wong, F.-L.; Lee, C.-S.; Chen, W.-C.; Feron, K.; Manzhos, S.; Wang, H.; Motta, N.; Lam, Y. M.; Sonar, P., Acene-based organic semiconductors for organic light-emitting diodes and perovskite solar cells. *J. Mater, Chem. C* **2018,** *6*, 9017-9029.

162. Fan, W.; Winands, T.; Doltsinis, N. L.; Li, Y.; Wang, Z., A Decatwistacene with an Overall 170° Torsion. *Angew. Chem. Int. Ed.* **2017,** *56*, 15373-15377.
163. Yao, S.; Zhang, X.; Xiong, Y.; Schwarz, H.; Driess, M., Isomerization of an N-Heterocyclic Germylene to an Azagermabenzen-1-ylidene and Its Coupling to a Unique Bis(germylene). *Organometallics* **2010,** *29*, 5353-5357.
164. Neumann, W. P., Germylenes and stannylenes. *Chem. Rev.* **1991,** *91*, 311-334.
165. Wu, Y.; Liu, L.; Su, J.; Yan, K.; Wang, T.; Zhu, J.; Gao, X.; Gao, Y.; Zhao, Y., Reactivity of Germylene toward Phosphorus-Containing Compounds: Nucleophilic Addition and Tautomerism. *Inorg. Chem.* **2015,** *54*, 4423-4430.
166. Gonell, S.; Poyatos, M.; Peris, E., Pyrene-Based Bisazolium Salts: From Luminescence Properties to Janus-Type Bis-N-Heterocyclic Carbenes. *Chem. Eur. J.* **2014,** *20*, 9716-9724.
167. Mateo-Alonso, A., Pyrene-fused pyrazaacenes: from small molecules to nanoribbons. *Chem. Soc. Rev.* **2014,** *43*, 6311-6324.
168. Duong, H. M.; Bendikov, M.; Steiger, D.; Zhang, Q.; Sonmez, G.; Yamada, J.; Wudl, F., Efficient Synthesis of a Novel, Twisted and Stable, Electroluminescent "Twistacene". *Org. Lett.* **2003,** *5*, 4433-4436.
169. Yue, W.; Gao, J.; Li, Y.; Jiang, W.; Di Motta, S.; Negri, F.; Wang, Z., One-Pot Synthesis of Stable NIR Tetracene Diimides via Double Cross-Coupling. *J. Am. Chem. Soc.* **2011,** *133*, 18054-18057.
170. Kuhn, N.; Kratz, T., Synthesis of Imidazol-2-ylidenes by Reduction of Imidazole-2(3H)-thiones. *Synthesis* **1993,** *1993*, 561-562.
171. Bodwell, G. J.; Bridson, J. N.; Houghton, T. J.; Kennedy, J. W. J.; Mannion, M. R., 1,7-Dioxa[7](2,7)pyrenophane: The Pyrene Moiety Is More Bent than That of C70. *Chem. Eur. J.* **1999,** *5*, 1823-1827.
172. Al-Rafia, S. M. I.; Momeni, M. R.; Ferguson, M. J.; McDonald, R.; Brown, A.; Rivard, E., Stable Complexes of Parent Digermene: An Inorganic Analogue of Ethylene. *Organometallics* **2013,** *32*, 6658-6665.
173. Yao, S.; Xiong, Y.; Driess, M., From NHC→germylenes to stable NHC→germanone complexes. *Chem. Commun.* **2009**, 10.1039/B914060C, 6466-6468.
174. Hlina, J.; Baumgartner, J.; Marschner, C.; Albers, L.; Müller, T., Cyclic Disilylated and Digermylated Germylenes. *Organometallics* **2013,** *32*, 3404-3410.
175. Segawa, Y.; Yamashita, M.; Nozaki, K., Boryllithium: Isolation, Characterization, and Reactivity as a Boryl Anion. *Science* **2006,** *314*, 113-115.
176. Yamashita, M.; Nozaki, K., Boryl Anions. In *Synthesis and Application of Organoboron Compounds*, Fernández, E.; Whiting, A., Eds. Springer International Publishing: Cham, 2015, 10.1007/978-3-319-13054-5_1pp 1-37.
177. Romeo, L. J.; Kaur, A.; Wilson, D. J. D.; Martin, C. D.; Dutton, J. L., Evaluation of the σ-Donating and π-Accepting Properties of N-Heterocyclic Boryl Anions. *Inorg. Chem.* **2019,** *58*, 16500-16509.
178. Asami, S.-s.; Ishida, S.; Iwamoto, T.; Suzuki, K.; Yamashita, M., Isolation and Characterization of Radical Anions Derived from a Boryl-Substituted Diphosphene. *Angew. Chem. Int. Ed.* **2017,** *56*, 1658-1662.
179. Asami, S.-s.; Okamoto, M.; Suzuki, K.; Yamashita, M., A Boryl-Substituted Diphosphene: Synthesis, Structure, and Reaction with n-Butyllithium To Form a Stabilized Adduct by pπ-pπ Interaction. *Angew. Chem. Int. Ed.* **2016,** *55*, 12827-12831.
180. Dange, D.; Davey, A.; Abdalla, J. A. B.; Aldridge, S.; Jones, C., Utilisation of a lithium boryl as a reducing agent in low oxidation state group 15 chemistry: synthesis and characterisation of an amido-distibene and a boryl-dibismuthene. *Chem. Commun.* **2015,** *51*, 7128-7131.
181. Dettenrieder, N.; Dietrich, H. M.; Schädle, C.; Maichle-Mössmer, C.; Törnroos, K. W.; Anwander, R., Organoaluminum Boryl Complexes. *Angew. Chem. Int. Ed.* **2012,** *51*, 4461-4465.
182. Protchenko, A. V.; Bates, J. I.; Saleh, L. M. A.; Blake, M. P.; Schwarz, A. D.; Kolychev, E. L.; Thompson, A. L.; Jones, C.; Mountford, P.; Aldridge, S., Enabling and Probing Oxidative Addition and Reductive Elimination at a Group 14 Metal Center: Cleavage and Functionalization of E–H Bonds by a Bis(boryl)stannylene. *J. Am. Chem. Soc.* **2016,** *138*, 4555-4564.

183. Protchenko, A. V.; Birjkumar, K. H.; Dange, D.; Schwarz, A. D.; Vidovic, D.; Jones, C.; Kaltsoyannis, N.; Mountford, P.; Aldridge, S., A Stable Two-Coordinate Acyclic Silylene. *J. Am. Chem. Soc.* **2012,** *134*, 6500-6503.
184. Rit, A.; Campos, J.; Niu, H.; Aldridge, S., A stable heavier group 14 analogue of vinylidene. *Nature Chemistry* **2016,** *8*, 1022-1026.
185. Yamashita, M.; Suzuki, Y.; Segawa, Y.; Nozaki, K., Synthesis, Structure of Borylmagnesium, and Its Reaction with Benzaldehyde to Form Benzoylborane. *J. Am. Chem. Soc.* **2007,** *129*, 9570-9571.
186. Kajiwara, T.; Terabayashi, T.; Yamashita, M.; Nozaki, K., Syntheses, Structures, and Reactivities of Borylcopper and -zinc Compounds: 1,4-Silaboration of an α,β-Unsaturated Ketone to Form a γ-Siloxyallylborane. *Angew. Chem. Int. Ed.* **2008,** *47*, 6606-6610.
187. Li, S.; Cheng, J.; Chen, Y.; Nishiura, M.; Hou, Z., Rare Earth Metal Boryl Complexes: Synthesis, Structure, and Insertion of a Carbodiimide and Carbon Monoxide. *Angew. Chem. Int. Ed.* **2011,** *50*, 6360-6363.
188. Lin, T.-P.; Peters, J. C., Boryl–Metal Bonds Facilitate Cobalt/Nickel-Catalyzed Olefin Hydrogenation. *J. Am. Chem. Soc.* **2014,** *136*, 13672-13683.
189. Segawa, Y.; Yamashita, M.; Nozaki, K., Boryl Anion Attacks Transition-Metal Chlorides To Form Boryl Complexes: Syntheses, Spectroscopic, and Structural Studies on Group 11 Borylmetal Complexes. *Angew. Chem. Int. Ed.* **2007,** *46*, 6710-6713.
190. Yamashita, M.; Nozaki, K., Boryllithium: A novel boron nucleophile and its application in the synthesis of borylmetal complexes. In *Pure and Applied Chemistry*, 2008; Vol. 80, p 1187.
191. Kahveci, Z.; Sekizkardes, A. K.; Arvapally, R. K.; Wilder, L.; El-Kaderi, H. M., Highly porous photoluminescent diazaborole-linked polymers: synthesis, characterization, and application to selective gas adsorption. *Polym. Chem.* **2017,** *8*, 2509-2515.
192. Yamaguchi, I.; Tominaga, T.; Sato, M., Pd-complex-catalyzed synthesis of oligomers having a recurring benzodiazaborole unit in the main chain. *Polym. Int.* **2009,** *58*, 17-21.
193. Tian, D.; Jiang, J.; Hu, H.; Zhang, J.; Cui, C., One-Step Access to Luminescent Pentaaryldiazaboroles via C–C Double Bond Formation from Imidoylstannanes. *J. Am. Chem. Soc.* **2012,** *134*, 14666-14669.
194. Weber, L.; Böhling, L., The role of 2,3-dihydro-1-H-1,3,2-diazaboroles in luminescent molecules. *Coord. Chem. Rev.* **2015,** *284*, 236-275.
195. Weber, L.; Halama, J.; Hanke, K.; Böhling, L.; Brockhinke, A.; Stammler, H.-G.; Neumann, B.; Fox, M. A., On the ambiguity of 1,3,2-benzodiazaboroles as donor/acceptor functionalities in luminescent molecules. *Dalton Trans.* **2014,** *43*, 3347-3363.
196. Schön, F.; Greb, L.; Kaifer, E.; Himmel, H.-J., Desymmetrisation of Dicationic Diboranes by Isomerization Catalysed by a Nucleophile. *Angew. Chem. Int. Ed. n/a*.
197. Vasudevan, K. V.; Findlater, M.; Vargas-Baca, I.; Cowley, A. H., Tetrakis(imino)pyracene Complexes Exhibiting Multielectron Redox Processes. *J. Am. Chem. Soc.* **2012,** *134*, 176-178.
198. Vasudevan, K. V.; Findlater, M.; Cowley, A. H., Synthesis and reactivity of tetrakis(imino)pyracene (TIP) ligands; bifunctional analogues of the BIAN ligand class. *Chem. Commun.* **2008**, 10.1039/B719251G, 1918-1919.
199. Su, Y.; Li, Y.; Ganguly, R.; Kinjo, R., Crystalline boron-linked tetraaminoethylene radical cations. *Chem. Sci.* **2017,** *8*, 7419-7423.
200. Weber, L.; Eickhoff, D.; Chrostowska, A.; Dargelos, A.; Darrigan, C.; Stammler, H.-G.; Neumann, B., Syntheses and structures of benzo-bis(1,3,2-diazaboroles) and acenaphtho-1,3,2-diazaboroles. *Dalton Trans.* **2019,** *48*, 16911-16921.
201. Kojima, T.; Kumaki, D.; Nishida, J.-i.; Tokito, S.; Yamashita, Y., Organic field-effect transistors based on novel organic semiconductors containing diazaboroles. *J. Mater. Chem.* **2011,** *21*, 6607-6613.
202. Nishida, J.-i.; Fujita, T.; Fujisaki, Y.; Tokito, S.; Yamashita, Y., Diazaboroles with quinone units: hydrogen bonding network and n-type FETs involving a three-coordinate boron atom. *J. Mater. Chem.* **2011,** *21*, 16442-16447.

203. Yu, Y.; Dong, C.; Alahmadi, A. F.; Meng, B.; Liu, J.; Jäkle, F.; Wang, L., A p-π* conjugated triarylborane as an alcohol-processable n-type semiconductor for organic optoelectronic devices. *J. Mater, Chem. C* **2019,** *7*, 7427-7432.
204. Meng, B.; Ren, Y.; Liu, J.; Jäkle, F.; Wang, L., p–π Conjugated Polymers Based on Stable Triarylborane with n-Type Behavior in Optoelectronic Devices. *Angew. Chem. Int. Ed.* **2018,** *57*, 2183-2187.
205. Alahmadi, A. F.; Lalancette, R. A.; Jäkle, F., Highly Luminescent Ladderized Fluorene Copolymers Based on B–N Lewis Pair Functionalization. *Macromol. Rapid Commun.* **2018,** *39*, 1800456.
206. Wade, C. R.; Broomsgrove, A. E. J.; Aldridge, S.; Gabbaï, F. P., Fluoride Ion Complexation and Sensing Using Organoboron Compounds. *Chem. Rev.* **2010,** *110*, 3958-3984.
207. Loudet, A.; Burgess, K., BODIPY Dyes and Their Derivatives: Syntheses and Spectroscopic Properties. *Chem. Rev.* **2007,** *107*, 4891-4932.
208. Ulrich, G.; Goeb, S.; De Nicola, A.; Retailleau, P.; Ziessel, R., Chemistry at Boron: Synthesis and Properties of Red to Near-IR Fluorescent Dyes Based on Boron-Substituted Diisoindolomethene Frameworks. *J. Org. Chem.* **2011,** *76*, 4489-4505.
209. Yao, X.; Zhang, K.; Müllen, K.; Wang, X.-Y., Direct C−H Borylation at the 2- and 2,7-Positions of Pyrene Leading to Brightly Blue- and Green-Emitting Chromophores. *Asian J. Org. Chem.* **2018,** *7*, 2233-2238.
210. Wakchaure, V. C.; Ranjeesh, K. C.; Goudappagouda; Das, T.; Vanka, K.; Gonnade, R.; Babu, S. S., Mechano-responsive room temperature luminescence variations of boron conjugated pyrene in air. *Chem. Commun.* **2018,** *54*, 6028-6031.
211. Ji, L.; Edkins, R. M.; Lorbach, A.; Krummenacher, I.; Brückner, C.; Eichhorn, A.; Braunschweig, H.; Engels, B.; Low, P. J.; Marder, T. B., Electron Delocalization in Reduced Forms of 2-(BMes2)pyrene and 2,7-Bis(BMes2)pyrene. *J. Am. Chem. Soc.* **2015,** *137*, 6750-6753.
212. Mellerup, S. K.; Wang, S., Isomerization and rearrangement of boriranes: from chemical rarities to functional materials. *Sci. China Mater.* **2018,** *61*, 1249-1256.
213. Rao, Y.-L.; Amarne, H.; Wang, S., Photochromic four-coordinate N,C-chelate boron compounds. *Coord. Chem. Rev.* **2012,** *256*, 759-770.
214. Ren, Y.; Jäkle, F., Merging thiophene with boron: new building blocks for conjugated materials. *Dalton Trans.* **2016,** *45*, 13996-14007.
215. Su, B.; Kinjo, R., Construction of Boron-Containing Aromatic Heterocycles. *Synthesis* **2017,** *49*, 2985-3034.
216. Chen, P.; Jäkle, F., Highly Luminescent, Electron-Deficient Bora-cyclophanes. *J. Am. Chem. Soc.* **2011,** *133*, 20142-20145.
217. Chen, P.; Lalancette, R. A.; Jäkle, F., π-Expanded Borazine: An Ambipolar Conjugated B–π–N Macrocycle. *Angew. Chem. Int. Ed.* **2012,** *51*, 7994-7998.
218. Hudson, Z. M.; Wang, S., Impact of Donor−Acceptor Geometry and Metal Chelation on Photophysical Properties and Applications of Triarylboranes. *Acc. Chem. Res.* **2009,** *42*, 1584-1596.
219. Li, S.-Y.; Sun, Z.-B.; Zhao, C.-H., Charge-Transfer Emitting Triarylborane π-Electron Systems. *Inorg. Chem.* **2017,** *56*, 8705-8717.
220. Crawford, A. G.; Dwyer, A. D.; Liu, Z.; Steffen, A.; Beeby, A.; Pålsson, L.-O.; Tozer, D. J.; Marder, T. B., Experimental and Theoretical Studies of the Photophysical Properties of 2- and 2,7-Functionalized Pyrene Derivatives. *J. Am. Chem. Soc.* **2011,** *133*, 13349-13362.
221. von Grotthuss, E.; John, A.; Kaese, T.; Wagner, M., Doping Polycyclic Aromatics with Boron for Superior Performance in Materials Science and Catalysis. *Asian J. Org. Chem.* **2018,** *7*, 37-53.
222. Jäkle, F.; Baser-Kirazli, N.; Lalancette, R. A., Enhancing the Acceptor Character of Conjugated Organoborane Macrocycles: A Highly Electron-Deficient Hexaboracyclophane. *Angew. Chem. Int. Ed. n/a*.
223. Zöphel, L.; Enkelmann, V.; Müllen, K., Tuning the HOMO–LUMO Gap of Pyrene Effectively via Donor–Acceptor Substitution: Positions 4,5 Versus 9,10. *Org. Lett.* **2013,** *15*, 804-807.

224. Ji, L.; Krummenacher, I.; Friedrich, A.; Lorbach, A.; Haehnel, M.; Edkins, K.; Braunschweig, H.; Marder, T. B., Synthesis, Photophysical, and Electrochemical Properties of Pyrenes Substituted with Donors or Acceptors at the 4- or 4,9-Positions. *J. Org. Chem.* **2018,** *83*, 3599-3606.
225. Vanga, M.; Lalancette, R. A.; Jäkle, F., Controlling the Optoelectronic Properties of Pyrene by Regioselective Lewis Base-Directed Electrophilic Aromatic Borylation. *Chem. Eur. J.* **2019,** *25*, 10133-10140.
226. Yuan, K.; Kahan, R. J.; Si, C.; Williams, A.; Kirschner, S.; Uzelac, M.; Zysman-Colman, E.; Ingleson, M. J., The synthesis of brominated-boron-doped PAHs by alkyne 1,1-bromoboration: mechanistic and functionalisation studies. *Chem. Sci.* **2020**, 10.1039/C9SC05404A.
227. Casas-Solvas, J. M.; Howgego, J. D.; Davis, A. P., Synthesis of substituted pyrenes by indirect methods. *Organic & Biomolecular Chemistry* **2014,** *12*, 212-232.
228. Merz, J.; Fink, J.; Friedrich, A.; Krummenacher, I.; Al Mamari, H. H.; Lorenzen, S.; Haehnel, M.; Eichhorn, A.; Moos, M.; Holzapfel, M.; Braunschweig, H.; Lambert, C.; Steffen, A.; Ji, L.; Marder, T. B., Pyrene Molecular Orbital Shuffle—Controlling Excited State and Redox Properties by Changing the Nature of the Frontier Orbitals. *Chem. Eur. J.* **2017,** *23*, 13164-13180.
229. Krantz, K. E.; Weisflog, S. L.; Yang, W.; Dickie, D. A.; Frey, N. C.; Webster, C. E.; Gilliard, R. J., Extremely twisted and bent pyrene-fused N-heterocyclic germylenes. *Chem. Commun.* **2019,** *55*, 14954-14957.
230. Siri, O.; Braunstein, P.; Rohmer, M.-M.; Bénard, M.; Welter, R., Novel "Potentially Antiaromatic", Acidichromic Quinonediimines with Tunable Delocalization of Their 6π-Electron Subunits. *J. Am. Chem. Soc.* **2003,** *125*, 13793-13803.
231. Khramov, D. M.; Boydston, A. J.; Bielawski, C. W., Highly Efficient Synthesis and Solid-State Characterization of 1,2,4,5-Tetrakis(alkyl- and arylamino)benzenes and Cyclization to Their Respective Benzobis(imidazolium) Salts. *Org. Lett.* **2006,** *8*, 1831-1834.
232. Ohno, K.; Fujihara, T.; Nagasawa, A., Formation of boron, nickel(II) and iridium(III) complexes with an azophenine derivative: Isomerization, delocalization and extension of the π-conjugated system on coordination. *Polyhedron* **2014,** *81*, 715-722.
233. Lei, H.; Aly, S. M.; Karsenti, P.-L.; Fortin, D.; Harvey, P. D., Platinum Complexes of N,N′,N″,N‴-Diboronazophenines. *Inorg. Chem.* **2017,** *56*, 13140-13151.
234. Vitske, V.; Herrmann, H.; Enders, M.; Kaifer, E.; Himmel, H.-J., Wrapping an Organic Reducing Reagent in a Cationic Boron Complex and Its Use in the Synthesis of Polyhalide Monoanionic Networks. *Chem. Eur. J.* **2012,** *18*, 14108-14116.
235. Guo, Z.; Park, S.; Yoon, J.; Shin, I., Recent progress in the development of near-infrared fluorescent probes for bioimaging applications. *Chem. Soc. Rev.* **2014,** *43*, 16-29.
236. Yang, Y.; Hughes, R. P.; Aprahamian, I., Near-Infrared Light Activated Azo-BF2 Switches. *J. Am. Chem. Soc.* **2014,** *136*, 13190-13193.
237. Katsikini, M., Wide Band Gap Materials. In *X-Ray Absorption Spectroscopy of Semiconductors*, Schnohr, C. S.; Ridgway, M. C., Eds. Springer Berlin Heidelberg: Berlin, Heidelberg, 2015, 10.1007/978-3-662-44362-0_3pp 49-76.
238. Shinde, S. L.; Senapati, S.; Nanda, K. K., Luminescence from wide band gap materials and their applications. *Adv. Nat. Sci.: Nanosci. Nanotechnol.* **2014,** *6*, 015002.
239. Song, X.; Zhang, D.; Lu, Y.; Yin, C.; Duan, L., Understanding and Manipulating the Interplay of Wide-Energy-Gap Host and TADF Sensitizer in High-Performance Fluorescence OLEDs. *Adv. Mater.* **2019,** *31*, 1901923.
240. Yen, W. M., Efficiency considerations and emerging applications of novel wide band gap luminescent materials. *Phys. Status Solidi* **2005,** *202*, 177-184.
241. Yoshikawa, A.; Matsunami, H.; Nanishi, Y., Development and Applications of Wide Bandgap Semiconductors. In *Wide Bandgap Semiconductors: Fundamental Properties and Modern Photonic and Electronic Devices*, Takahashi, K.; Yoshikawa, A.; Sandhu, A., Eds. Springer Berlin Heidelberg: Berlin, Heidelberg, 2007, 10.1007/978-3-540-47235-3_1pp 1-24.

242. Chen, Z.; Chaitanya, W., S.; Corminboef, C.; Puchta, R.; von Rague Schleyer, P., Nucleus-Independent Chemical Shifts (NICS) as an Aromaticity Criterion. *Chem. Rev.* **2005,** *105*, 3842-3888.
243. Clar, E., *Aromatic sextet*. Wiley: London, 1972.
244. Segawa, Y.; Suzuki, Y.; Yamashita, M.; Nozaki, K., Chemistry of Boryllithium: Synthesis, Structure, and Reactivity. *J. Am. Chem. Soc.* **2008,** *130*, 16069-16079.
245. Weber, L., 1,3,2-Diazaborolyl Anions – From Laboratory Curiosities to Versatile Reagents in Synthesis. *Eur. J. Inorg. Chem.* **2017,** *2017*, 3461-3488.
246. Budy, H.; Gilmer, J.; Trageser, T.; Wagner, M., Anionic Organoboranes: Delicate Flowers Worth Caring for. *Eur. J. Inorg. Chem.* **2020,** *2020*, 4148-4162.
247. Protchenko, A.; Vasko, P.; Fuentes, M. A.; Hicks, J.; Vidovic, D.; Aldridge, S., Approaching a 'naked' boryl anion: amide metathesis as a route to calcium, strontium and potassium boryl complexes. *Angew. Chem. Int. Ed. 10.1002/anie.202011839*.
248. Makoto, Y.; Kyoko, N., Recent Developments of Boryl Anions: Boron Analogues of Carbanion. *Bull. Chem. Soc. Jpn.* **2008,** *81*, 1377-1392.
249. von Grotthuss, E.; Prey, S. E.; Bolte, M.; Lerner, H.-W.; Wagner, M., Selective CO2 Splitting by Doubly Reduced Aryl Boranes to Give CO and [CO3]2−. *Angew. Chem. Int. Ed.* **2018,** *57*, 16491-16495.
250. von Grotthuss, E.; Diefenbach, M.; Bolte, M.; Lerner, H.-W.; Holthausen, M. C.; Wagner, M., Reversible Dihydrogen Activation by Reduced Aryl Boranes as Main-Group Ambiphiles. *Angew. Chem. Int. Ed.* **2016,** *55*, 14067-14071.
251. Lorbach, A.; Bolte, M.; Lerner, H.-W.; Wagner, M., Dilithio 9,10-Diborataanthracene: Molecular Structure and 1,4-Addition Reactions. *Organometallics* **2010,** *29*, 5762-5765.
252. Su, Y.; Kinjo, R., Small molecule activation by boron-containing heterocycles. *Chem. Soc. Rev.* **2019,** *48*, 3613-3659.
253. von Grotthuss, E.; Nawa, F.; Bolte, M.; Lerner, H.-W.; Wagner, M., Chalcogen–chalcogen-bond activation by an ambiphilic, doubly reduced organoborane. *Tetrahedron* **2019,** *75*, 26-30.
254. Monot, J.; Solovyev, A.; Bonin-Dubarle, H.; Derat, É.; Curran, D. P.; Robert, M.; Fensterbank, L.; Malacria, M.; Lacôte, E., Generation and Reactions of an Unsubstituted N-Heterocyclic Carbene Boryl Anion. *Angew. Chem. Int. Ed.* **2010,** *49*, 9166-9169.
255. Bertermann, R.; Braunschweig, H.; Dewhurst, R. D.; Hörl, C.; Kramer, T.; Krummenacher, I., Evidence for Extensive Single-Electron-Transfer Chemistry in Boryl Anions: Isolation and Reactivity of a Neutral Borole Radical. *Angew. Chem. Int. Ed.* **2014,** *53*, 5453-5457.
256. Braunschweig, H.; Chiu, C.-W.; Radacki, K.; Kupfer, T., Synthesis and Structure of a Carbene-Stabilized π-Boryl Anion. *Angew. Chem. Int. Ed.* **2010,** *49*, 2041-2044.
257. Köster, R.; Benedikt, G., 9-Borafluorenes. *Angew. Chem. Int. Ed. Engl.* **1963,** *2*, 323-324.
258. Narula, C. K.; Nöth, H., Contributions to the chemistry of boron: CLVI. A convenient route to 9-borafluorenes. *J. Organomet. Chem.* **1985,** *281*, 131-134.
259. He, J.; Rauch, F.; Finze, M.; Marder, T. B., (Hetero)arene-fused boroles: a broad spectrum of applications. *Chem. Sci.* **2021**, 10.1039/D0SC05676F.
260. Adams, I. A.; Rupar, P. A., A Poly(9-Borafluorene) Homopolymer: An Electron-Deficient Polyfluorene with "Turn-On" Fluorescence Sensing of NH3 Vapor. *Macromol. Rapid Commun.* **2015,** *36*, 1336-1340.
261. Bonifácio, V. D. B.; Morgado, J.; Scherf, U., Polyfluorenes with on-chain dibenzoborole units—Synthesis and anion-induced photoluminescence quenching. *J. Polym. Sci. Pol. Chem.* **2008,** *46*, 2878-2883.
262. Hübner, A.; Qu, Z.-W.; Englert, U.; Bolte, M.; Lerner, H.-W.; Holthausen, M. C.; Wagner, M., Main-Chain Boron-Containing Oligophenylenes via Ring-Opening Polymerization of 9-H-9-Borafluorene. *J. Am. Chem. Soc.* **2011,** *133*, 4596-4609.
263. Matsumoto, T.; Ito, S.; Tanaka, K.; Chujo, Y., Synthesis, properties and structure of borafluorene-based conjugated polymers with kinetically and thermodynamically stabilized tetracoordinated boron atoms. *Polym. J.* **2018,** *50*, 197-202.

264. Gilmer, J.; Budy, H.; Kaese, T.; Bolte, M.; Lerner, H.-W.; Wagner, M., The 9H-9-Borafluorene Dianion: A Surrogate for Elusive Diarylboryl Anion Nucleophiles. *Angew. Chem. Int. Ed.* **2020,** *59*, 5621-5625.
265. Hu, X.; Soleilhavoup, M.; Melaimi, M.; Chu, J.; Bertrand, G., Air-Stable (CAAC)CuCl and (CAAC)CuBH4 Complexes as Catalysts for the Hydrolytic Dehydrogenation of BH3NH3. *Angew. Chem. Int. Ed.* **2015,** *54*, 6008-6011.
266. Jazzar, R.; Dewhurst, R. D.; Bourg, J.-B.; Donnadieu, B.; Canac, Y.; Bertrand, G., Intramolecular "Hydroiminiumation" of Alkenes: Application to the Synthesis of Conjugate Acids of Cyclic Alkyl Amino Carbenes (CAACs). *Angew. Chem. Int. Ed.* **2007,** *46*, 2899-2902.
267. Groom, C. R.; Bruno, I. J.; Lightfoot, M. P.; Ward, S. C., The Cambridge Structural Database. *Acta Crystallographica Section B* **2016,** *72*, 171-179.
268. Cordero, B.; Gómez, V.; Platero-Prats, A. E.; Revés, M.; Echeverría, J.; Cremades, E.; Barragán, F.; Alvarez, S., Covalent radii revisited. *Dalton Trans.* **2008**, 10.1039/B801115J, 2832-2838.
269. Longobardi, L. E.; Zatsepin, P.; Korol, R.; Liu, L.; Grimme, S.; Stephan, D. W., Reactions of Boron-Derived Radicals with Nucleophiles. *J. Am. Chem. Soc.* **2017,** *139*, 426-435.
270. Kasha, M., Characterization of electronic transitions in complex molecules. *Discuss. Faraday Soc.* **1950,** *9*, 14-19.
271. W. Alder, R.; E. Blake, M.; Bortolotti, C.; Bufali, S.; P. Butts, C.; Linehan, E.; M. Oliva, J.; Guy Orpen, A.; J. Quayle, M., Complexation of stable carbenes with alkali metals. *Chem. Commun.* **1999**, 10.1039/A808951E, 241-242.
272. Hatano, M.; Ishihara, K., Lewis Acids. In *Boron Reagents in Synthesis*, American Chemical Society: 2016; Vol. 1236, pp 27-66.
273. Hopkinson, M. N.; Richter, C.; Schedler, M.; Glorius, F., An overview of N-heterocyclic carbenes. *Nature* **2014,** *510*, 485.
274. Huynh, H. V., Electronic Properties of N-Heterocyclic Carbenes and Their Experimental Determination. *Chem. Rev.* **2018**, 10.1021/acs.chemrev.8b00067.
275. Budy, H.; Kaese, T.; Bolte, M.; Lerner, H.-W.; Wagner, M., A Chemiluminescent Tetraaryl Diborane(4) Tetraanion. *Angew. Chem. Int. Ed.* **2021,** *60*, 19397-19405.
276. Bigoli, F.; Demartin, F.; Deplano, P.; Devillanova, F. A.; Isaia, F.; Lippolis, V.; Mercuri, M. L.; Pellinghelli, M. A.; Trogu, E. F., Synthesis, Characterization, and Crystal Structures of New Dications Bearing the −Se−Se− Bridge. *Inorg. Chem.* **1996,** *35*, 3194-3201.
277. Choi, J.; Ko, J. H.; Jung, I. G.; Yang, H. Y.; Ko, K. C.; Lee, J. Y.; Lee, S. M.; Kim, H. J.; Nam, J. H.; Ahn, J. R.; Son, S. U., Reaction of Imidazoline-2-Selone with Acids and Its Use for Selective Coordination of Platinum Ions on Silica Surface. *Chem. Mater.* **2009,** *21*, 2571-2573.
278. Roy, G.; Jayaram, P. N.; Mugesh, G., Inhibition of Lactoperoxidase-Catalyzed Oxidation by Imidazole-Based Thiones and Selones: A Mechanistic Study. *Chem. Asian J.* **2013,** *8*, 1910-1921.
279. Srinivas, K.; Babu, C. N.; Prabusankar, G., Thermal, optical and structural properties of disulfide and diselenide salts with weakly associated anions. *J. Mol. Struct.* **2015,** *1086*, 201-206.
280. Dutton, J. L.; Battista, T. L.; Sgro, M. J.; Ragogna, P. J., Diazabutadiene complexes of selenium as Se2+ transfer reagents. *Chem. Commun.* **2010,** *46*, 1041-1043.
281. Baker, R. J.; Jones, C.; Kloth, M., Oxidation reactions of an anionic gallium(i) N-heterocyclic carbene analogue with group 16 compounds. *Dalton Trans.* **2005**, 10.1039/B505085E, 2106-2110.
282. Anker, M. D.; Coles, M. P., Isoelectronic Aluminium Analogues of Carbonyl and Dioxirane Moieties. *Angew. Chem. Int. Ed.* **2019,** *58*, 13452-13455.
283. Singh, F. V.; Wirth, T., Selenium Compounds as Ligands and Catalysts. In *Organoselenium Chemistry*, https://doi.org/10.1002/9783527641949.ch8pp 321-360.
284. Santi, C.; Santoro, S., Electrophilic Selenium. In *Organoselenium Chemistry*, https://doi.org/10.1002/9783527641949.ch1pp 1-51.
285. Iwaoka, M., Nucleophilic Selenium. In *Organoselenium Chemistry*, https://doi.org/10.1002/9783527641949.ch2pp 53-109.

286. Freudendahl, D. M.; Santoro, S.; Shahzad, S. A.; Santi, C.; Wirth, T., Green Chemistry with Selenium Reagents: Development of Efficient Catalytic Reactions. *Angew. Chem. Int. Ed.* **2009,** *48*, 8409-8411.
287. Bowman, W. R., Selenium Compounds in Radical Reactions. In *Organoselenium Chemistry*, https://doi.org/10.1002/9783527641949.ch3pp 111-146.
288. Reich, H. J.; Wollowitz, S.; Trend, J. E.; Chow, F.; Wendelborn, D. F., Syn elimination of alkyl selenoxides. Side reactions involving selenenic acids. Structural and solvent effects of rates. *J. Org. Chem.* **1978,** *43*, 1697-1705.
289. Riley, H. L.; Morley, J. F.; Friend, N. A. C., 255. Selenium dioxide, a new oxidising agent. Part I. Its reaction with aldehydes and ketones. *J. Am. Chem. Soc.* **1932**, 10.1039/JR9320001875, 1875-1883.
290. Ivanova, A.; Arsenyan, P., Rise of diselenides: Recent advances in the synthesis of heteroarylselenides. *Coord. Chem. Rev.* **2018,** *370*, 55-68.
291. Guan, Y.; Townsend, S. D., Metal-Free Synthesis of Unsymmetrical Organoselenides and Selenoglycosides. *Org. Lett.* **2017,** *19*, 5252-5255.
292. Comasseto, J. V.; Ling, L. W.; Petragnani, N.; Stefani, H. A., Vinylic Selenides and Tellurides - Preparation, Reactivity and Synthetic Applications. *Synthesis* **1997,** *1997*, 373-403.
293. Braunschweig, H.; Constantinidis, P.; Dellermann, T.; Ewing, W. C.; Fischer, I.; Hess, M.; Knight, F. R.; Rempel, A.; Schneider, C.; Ullrich, S.; Vargas, A.; Woollins, J. D., Highly Strained Heterocycles Constructed from Boron–Boron Multiple Bonds and Heavy Chalcogens. *Angew. Chem. Int. Ed.* **2016,** *55*, 5606-5609.
294. Braunschweig, H.; Dellermann, T.; Ewing, W. C.; Kramer, T.; Schneider, C.; Ullrich, S., Reductive Insertion of Elemental Chalcogens into Boron–Boron Multiple Bonds. *Angew. Chem. Int. Ed.* **2015,** *54*, 10271-10275.
295. Liu, S.; Légaré, M.-A.; Auerhammer, D.; Hofmann, A.; Braunschweig, H., The First Boron–Tellurium Double Bond: Direct Insertion of Heavy Chalcogens into a Mn=B Double Bond. *Angew. Chem. Int. Ed.* **2017,** *56*, 15760-15763.
296. Liu, S.; Légaré, M.-A.; Hofmann, A.; Braunschweig, H., A Boradiselenirane and a Boraditellurirane: Isolable Heavy Analogs of Dioxiranes and Dithiiranes. *J. Am. Chem. Soc.* **2018,** *140*, 11223-11226.
297. Goh, G. K. H.; Li, Y.; Kinjo, R., Oxidative addition of elemental selenium to 1,4,2,5-diazadiborinine. *Dalton Trans.* **2019,** *48*, 7514-7518.
298. Wentz, K. E.; Molino, A.; Weisflog, S. L.; Kaur, A.; Dickie, D. A.; Wilson, D. J. D.; Gilliard Jr., R. J., Stabilization of the Elusive 9-Carbene-9-Borafluorene Monoanion. *Angew. Chem. Int. Ed.* **2021,** *60*, 13065-13072.
299. Lim, S. F.; Harris, B. L.; Khairallah, G. N.; Bieske, E. J.; Maître, P.; da Silva, G.; Adamson, B. D.; Scholz, M. S.; Coughlan, N. J. A.; O'Hair, R. A. J.; Rathjen, M.; Stares, D.; White, J. M., Seleniranium Ions Undergo π-Ligand Exchange via an Associative Mechanism in the Gas Phase. *J. Org. Chem.* **2017,** *82*, 6289-6297.
300. Stoy, A.; Arrowsmith, M.; Eyßelein, M.; Dellermann, T.; Mies, J.; Radacki, K.; Kupfer, T.; Braunschweig, H., NHC-Stabilized 1,2-Dihalodiborenes: Synthesis, Characterization, and Reactivity Toward Elemental Chalcogens. *Inorg. Chem.* **2021,** *60*, 12625-12633.
301. Chen, E. Y.-X.; Marks, T. J., Cocatalysts for Metal-Catalyzed Olefin Polymerization: Activators, Activation Processes, and Structure−Activity Relationships. *Chem. Rev.* **2000,** *100*, 1391-1434.
302. Chen, Y.-X.; Stern, C. L.; Yang, S.; Marks, T. J., Organo-Lewis Acids As Cocatalysts in Cationic Metallocene Polymerization Catalysis. Unusual Characteristics of Sterically Encumbered Tris(perfluorobiphenyl)borane. *J. Am. Chem. Soc.* **1996,** *118*, 12451-12452.
303. Yang, X.; Stern, C. L.; Marks, T. J., Cation-like homogeneous olefin polymerization catalysts based upon zirconocene alkyls and tris(pentafluorophenyl)borane. *J. Am. Chem. Soc.* **1991,** *113*, 3623-3625.
304. Yang, X.; Stern, C. L.; Marks, T. J., Cationic Zirconocene Olefin Polymerization Catalysts Based on the Organo-Lewis Acid Tris(pentafluorophenyl)borane. A Synthetic,Structural, Solution Dynamic, and Polymerization Catalytic Study. *J. Am. Chem. Soc.* **1994,** *116*, 10015-10031.

305. Ishihara, K.; Hananki, N.; Yamamoto, H., Tris(pentafluorophenyl) boron as a New Efficient, Air Stable, and Water Tolerant Catalyst in the Aldol-Type and Michael Reactions. *Synlett* **1993,** *1993*, 577-579.
306. Parks, D. J.; Piers, W. E., Tris(pentafluorophenyl)boron-Catalyzed Hydrosilation of Aromatic Aldehydes, Ketones, and Esters. *J. Am. Chem. Soc.* **1996,** *118*, 9440-9441.
307. Sowa, F. J.; Hennion, G. F.; Nieuwland, J. A., Organic Reactions with Boron Fluoride. IX. The Alkylation of Phenol with Alcohols1. *J. Am. Chem. Soc.* **1935,** *57*, 709-711.
308. Ma, Y.; Lou, S.-J.; Hou, Z., Electron-deficient boron-based catalysts for C–H bond functionalisation. *Chem. Soc. Rev.* **2021,** *50*, 1945-1967.
309. Kinjo, R.; Donnadieu, B.; Celik, M. A.; Frenking, G.; Bertrand, G., Synthesis and Characterization of a Neutral Tricoordinate Organoboron Isoelectronic with Amines. *Science* **2011,** *333*, 610-613.
310. Protchenko, A. V.; Dange, D.; Blake, M. P.; Schwarz, A. D.; Jones, C.; Mountford, P.; Aldridge, S., Oxidative Bond Formation and Reductive Bond Cleavage at Main Group Metal Centers: Reactivity of Five-Valence-Electron MX2 Radicals. *J. Am. Chem. Soc.* **2014,** *136*, 10902-10905.
311. Wentz, K. E.; Molino, A.; Freeman, L. A.; Dickie, D. A.; Wilson, D. J. D.; Gilliard, R. J., Reactions of 9-Carbene-9-Borafluorene Monoanion and Selenium: Synthesis of Boryl-Substituted Selenides and Diselenides. *Inorg. Chem.* **2021,** *60*, 13941-13949.
312. Wang, B.; Luo, G.; Nishiura, M.; Luo, Y.; Hou, Z., Cooperative Trimerization of Carbon Monoxide by Lithium and Samarium Boryls. *J. Am. Chem. Soc.* **2017,** *139*, 16967-16973.
313. Lu, W.; Hu, H.; Li, Y.; Ganguly, R.; Kinjo, R., Isolation of 1,2,4,3-Triazaborol-3-yl-metal (Li, Mg, Al, Au, Zn, Sb, Bi) Derivatives and Reactivity toward CO and Isonitriles. *J. Am. Chem. Soc.* **2016,** *138*, 6650-6661.
314. Robinson, S.; McMaster, J.; Lewis, W.; Blake, A. J.; Liddle, S. T., Alkali-metal mediated reactivity of a diaminobromoborane: mono- and bis-borylation of naphthalene versus boryl lithium or hydroborane formation. *Chem. Commun.* **2012,** *48*, 5769-5771.
315. Protchenko, A. V.; Vasko, P.; Fuentes, M. Á.; Hicks, J.; Vidovic, D.; Aldridge, S., Approaching a "Naked" Boryl Anion: Amide Metathesis as a Route to Calcium, Strontium, and Potassium Boryl Complexes. *Angew. Chem. Int. Ed.* **2021,** *60*, 2064-2068.
316. Grigsby, W. J.; Power, P. P., Isolation and Reduction of Sterically Encumbered Arylboron Dihalides: Novel Boranediyl Insertion into C−C σ-Bonds. *J. Am. Chem. Soc.* **1996,** *118*, 7981-7988.
317. Ohsato, T.; Okuno, Y.; Ishida, S.; Iwamoto, T.; Lee, K.-H.; Lin, Z.; Yamashita, M.; Nozaki, K., A Potassium Diboryllithate: Synthesis, Bonding Properties, and the Deprotonation of Benzene. *Angew. Chem. Int. Ed.* **2016,** *55*, 11426-11430.
318. Hicks, J.; Vasko, P.; Goicoechea, J. M.; Aldridge, S., Synthesis, structure and reaction chemistry of a nucleophilic aluminyl anion. *Nature* **2018,** *557*, 92-95.
319. Hicks, J.; Vasko, P.; Goicoechea, J. M.; Aldridge, S., The Aluminyl Anion: A New Generation of Aluminium Nucleophile. *Angew. Chem. Int. Ed.* **2021,** *60*, 1702-1713.
320. Koshino, K.; Kinjo, R., Construction of σ-Aromatic AlB2 Ring via Borane Coupling with a Dicoordinate Cyclic (Alkyl)(Amino)Aluminyl Anion. *J. Am. Chem. Soc.* **2020,** *142*, 9057-9062.
321. Longobardi, L. E.; Liu, L.; Grimme, S.; Stephan, D. W., Stable Borocyclic Radicals via Frustrated Lewis Pair Hydrogenations. *J. Am. Chem. Soc.* **2016,** *138*, 2500-2503.
322. Lavallo, V.; Canac, Y.; Präsang, C.; Donnadieu, B.; Bertrand, G., Stable Cyclic (Alkyl)(Amino)Carbenes as Rigid or Flexible, Bulky, Electron-Rich Ligands for Transition-Metal Catalysts: A Quaternary Carbon Atom Makes the Difference. *Angew. Chem. Int. Ed.* **2005,** *44*, 5705-5709.
323. Accorsi, G.; Listorti, A.; Yoosaf, K.; Armaroli, N., 1,10-Phenanthrolines: versatile building blocks for luminescent molecules, materials and metal complexes. *Chem. Soc. Rev.* **2009,** *38*, 1690-1700.
324. Bencini, A.; Lippolis, V., 1,10-Phenanthroline: A versatile building block for the construction of ligands for various purposes. *Coord. Chem. Rev.* **2010,** *254*, 2096-2180.
325. Rothfuss, H.; Knöfel, N. D.; Tzvetkova, P.; Michenfelder, N. C.; Baraban, S.; Unterreiner, A.-N.; Roesky, P. W.; Barner-Kowollik, C., Phenanthroline—A Versatile Ligand for Advanced Functional Polymeric Materials. *Chem. Eur. J.* **2018,** *24*, 17475-17486.

326. Antkowiak, W. Z.; Sobczak, A., Solvent effect on the reactivity of 1,10-phenanthroline-5,6-dione towards diazomethane. *Tetrahedron* **2001,** *57*, 2799-2805.
327. Bockman, T. M.; Perrier, S.; Kochi, J. K., Dehydrosilylation versus α-coupling in the electron-transfer of enol silyl ethers to quinones. Strong solvent effect on photogenerated ion pairs. *J. Chem. Soc. Perkin Trans. 2* **1993**, 10.1039/P29930000595, 595-597.
328. Itoh, S.; Maruta, J.; Fukuzumi, S., Addition–cyclization reaction of nitroalkane anions with o-quinone derivatives via electron transfer in the charge-transfer complexes. *J. Chem. Soc. Perkin Trans. 2* **1996**, 10.1039/P29960001429, 1429-1433.
329. Itoh, S.; Nii, K.; Mure, M.; Ohshiro, Y., Novel addition of nitroalkanes to o-quinones. *Tetrahedron Lett.* **1987,** *28*, 3975-3978.
330. Wege, D., Abnormal addition of vinylmagnesium bromide to 9,10-phenanthraquinone. *Aust. J. Chem.* **1971,** *24*, 1531-1535.
331. Lamb, W. F.; Wiedmann, T.; Pongratz, J.; Andrew, R.; Crippa, M.; Olivier, J. G. J.; Wiedenhofer, D.; Mattioli, G.; Khourdajie, A. A.; House, J.; Pachauri, S.; Figueroa, M.; Saheb, Y.; Slade, R.; Hubacek, K.; Sun, L.; Ribeiro, S. K.; Khennas, S.; de la Rue du Can, S.; Chapungu, L.; Davis, S. J.; Bashmakov, I.; Dai, H.; Dhakal, S.; Tan, X.; Geng, Y.; Gu, B.; Minx, J., A review of trends and drivers of greenhouse gas emissions by sector from 1990 to 2018. *Environ. Res. Lett.* **2021,** *16*, 073005.
332. Ye, R.-P.; Ding, J.; Gong, W.; Argyle, M. D.; Zhong, Q.; Wang, Y.; Russell, C. K.; Xu, Z.; Russell, A. G.; Li, Q.; Fan, M.; Yao, Y.-G., CO2 hydrogenation to high-value products via heterogeneous catalysis. *Nature Commun.* **2019,** *10*, 5698.
333. Liu, Q.; Wu, L.; Jackstell, R.; Beller, M., Using carbon dioxide as a building block in organic synthesis. *Nature Commun.* **2015,** *6*, 5933.
334. Huang, K.; Sun, C.-L.; Shi, Z.-J., Transition-metal-catalyzed C–C bond formation through the fixation of carbon dioxide. *Chem. Soc. Rev.* **2011,** *40*, 2435-2452.
335. Schneider, J.; Jia, H.; Muckerman, J. T.; Fujita, E., Thermodynamics and kinetics of CO2, CO, and H+ binding to the metal centre of CO2reductioncatalysts. *Chem. Soc. Rev.* **2012,** *41*, 2036-2051.
336. Severin, K., Synthetic chemistry with nitrous oxide. *Chem. Soc. Rev.* **2015,** *44*, 6375-6386.
337. Kong, L.; Lu, W.; Yongxin, L.; Ganguly, R.; Kinjo, R., Formation of Boron–Main-Group Element Bonds by Reactions with a Tricoordinate Organoboron L2PhB: (L = Oxazol-2-ylidene). *Inorg. Chem.* **2017,** *56*, 5586-5593.
338. Wang, B.; Li, Y.; Ganguly, R.; Hirao, H.; Kinjo, R., Ambiphilic boron in 1,4,2,5-diazadiborinine. *Nature Commun.* **2016,** *7*, 11871.
339. Wu, D.; Kong, L.; Li, Y.; Ganguly, R.; Kinjo, R., 1,3,2,5-Diazadiborinine featuring nucleophilic and electrophilic boron centres. *Nature Commun.* **2015,** *6*, 7340.
340. Mömming, C. M.; Otten, E.; Kehr, G.; Fröhlich, R.; Grimme, S.; Stephan, D. W.; Erker, G., Reversible Metal-Free Carbon Dioxide Binding by Frustrated Lewis Pairs. *Angew. Chem. Int. Ed.* **2009,** *48*, 6643-6646.
341. Stephan, D. W.; Erker, G., Frustrated Lewis Pairs: Metal-free Hydrogen Activation and More. *Angew. Chem. Int. Ed.* **2010,** *49*, 46-76.
342. Stoy, A.; Härterich, M.; Dewhurst, R. D.; Jiménez-Halla, J. O. C.; Endres, P.; Eyßelein, M.; Kupfer, T.; Deissenberger, A.; Thiess, T.; Braunschweig, H., Evidence for Borylene Carbonyl (LHB═C═O) and Base-Stabilized (LHB═O) and Base-Free Oxoborane (RB≡O) Intermediates in the Reactions of Diborenes with CO2. *J. Am. Chem. Soc.* **2022,** *144*, 3376-3380.
343. Stoy, A.; Böhnke, J.; Jiménez-Halla, J. O. C.; Dewhurst, R. D.; Thiess, T.; Braunschweig, H., CO2 Binding and Splitting by Boron–Boron Multiple Bonds. *Angew. Chem. Int. Ed.* **2018,** *57*, 5947-5951.
344. Taylor, J. W.; McSkimming, A.; Guzman, C. F.; Harman, W. H., N-Heterocyclic Carbene-Stabilized Boranthrene as a Metal-Free Platform for the Activation of Small Molecules. *J. Am. Chem. Soc.* **2017,** *139*, 11032-11035.
345. Cheng, J.; Hu, J., Recent Advances on Carbon Monoxide Releasing Molecules for Antibacterial Applications. *ChemMedChem* **2021,** *16*, 3628-3634.

346. McMahon, S.; Rochford, J.; Halpin, Y.; Manton, J. C.; Harvey, E. C.; Greetham, G. M.; Clark, I. P.; Rooney, A. D.; Long, C.; Pryce, M. T., Controlled CO release using photochemical, thermal and electrochemical approaches from the amino carbene complex [(CO)5CrC(NC4H8)CH3]. *Phys. Chem, Chem. Phys.* **2014,** *16*, 21230-21233.
347. Faizan, M.; Muhammad, N.; Niazi, K. U. K.; Hu, Y.; Wang, Y.; Wu, Y.; Sun, H.; Liu, R.; Dong, W.; Zhang, W.; Gao, Z., CO-Releasing Materials: An Emphasis on Therapeutic Implications, as Release and Subsequent Cytotoxicity Are the Part of Therapy. *Materials* **2019,** *12*, 1643.
348. Ling, K.; Men, F.; Wang, W.-C.; Zhou, Y.-Q.; Zhang, H.-W.; Ye, D.-W., Carbon Monoxide and Its Controlled Release: Therapeutic Application, Detection, and Development of Carbon Monoxide Releasing Molecules (CORMs). *J. Med. Chem.* **2018,** *61*, 2611-2635.
349. Mann, B. E., CO-Releasing Molecules: A Personal View. *Organometallics* **2012,** *31*, 5728-5735.
350. Aho, J. E.; Pihko, P. M.; Rissa, T. K., Nonanomeric Spiroketals in Natural Products: Structures, Sources, and Synthetic Strategies. *Chem. Rev.* **2005,** *105*, 4406-4440.
351. Fominova, K.; Diachuk, T.; Granat, D.; Savchuk, T.; Vilchynskyi, V.; Svitlychnyi, O.; Meliantsev, V.; Kovalchuk, I.; Litskan, E.; Levterov, Vadym V.; Badlo, V. R.; Vaskevych, R. I.; Vaskevych, A. I.; Bolbut, A. V.; Semeno, V. V.; Iminov, R.; Shvydenko, K.; Kuznetsova, A. S.; Dmytriv, Y. V.; Vysochyn, D.; Ripenko, V.; Tolmachev, A. A.; Pavlova, O.; Kuznietsova, H.; Pishel, I.; Borysko, P.; Mykhailiuk, P. K., Oxa-spirocycles: synthesis, properties and applications. *Chem. Sci.* **2021,** *12*, 11294-11305.
352. Gober, C. M.; Carroll, P. J.; Joullié, M. M., Triazaspirocycles: Occurrence, Synthesis, and Applications. *Mini Rev Org Chem* **2016,** *13*, 126-142.
353. McLeod, M. C.; Brimble, M. A.; Rathwell, D. C.; Wilson, Z. E.; Yuen, T.-Y., Synthetic approaches to [5, 6]-benzannulated spiroketal natural products. *Pure and Applied Chemistry* **2011,** *84*, 1379-1390.
354. Perron, F.; Albizati, K. F., Chemistry of spiroketals. *Chem. Rev.* **1989,** *89*, 1617-1661.
355. Liu, L. L.; Cao, L. L.; Zhou, J.; Stephan, D. W., Facile Cleavage of the P=P Double Bond in Vinyl-Substituted Diphosphenes. *Angew. Chem. Int. Ed.* **2019,** *58*, 273-277.
356. Peltier, J. L.; Tomás-Mendivil, E.; Tolentino, D. R.; Hansmann, M. M.; Jazzar, R.; Bertrand, G., Realizing Metal-Free Carbene-Catalyzed Carbonylation Reactions with CO. *J. Am. Chem. Soc.* **2020,** *142*, 18336-18340.
357. Pranckevicius, C.; Weber, M.; Krummenacher, I.; Phukan, A. K.; Braunschweig, H., Phosphinoborylenes as stable sources of fleeting borylenes. *Chem. Sci.* **2020,** *11*, 11055-11059.
358. Walley, J. E.; Obi, A. D.; Breiner, G.; Wang, G.; Dickie, D. A.; Molino, A.; Dutton, J. L.; Wilson, D. J. D.; Gilliard, R. J., Cyclic(alkyl)(amino) Carbene-Promoted Ring Expansion of a Carbodicarbene Beryllacycle. *Inorg. Chem.* **2019,** *58*, 11118-11126.
359. Lieske, L. E.; Freeman, L. A.; Wang, G.; Dickie, D. A.; Gilliard Jr., R. J.; Machan, C. W., Metal-Free Electrochemical Reduction of Carbon Dioxide Mediated by Cyclic(Alkyl)(Amino) Carbenes. *Chem. Eur. J.* **2019,** *25*, 6098-6101.
360. Krantz, K. E.; Weisflog, S. L.; Frey, N. C.; Yang, W.; Dickie, D. A.; Webster, C. E.; Gilliard Jr., R. J., Planar, Stair-Stepped, and Twisted: Modulating Structure and Photophysics in Pyrene- and Benzene-Fused N-Heterocyclic Boranes. *Chem. Eur. J.* **2020,** *26*, 10072-10082.
361. Schleyer, P. v. R.; Maerker, C.; Dransfeld, A.; Jiao, H.; van Eikema Hommes, N. J. R., Nucleus-Independent Chemical Shifts: A Simple and Efficient Aromaticity Probe. *J. Am. Chem. Soc.* **1996,** *118*, 6317-6318.
362. Cheeseman, J. R.; Trucks, G. W.; Keith, T. A.; Frisch, M. J., A comparison of models for calculating nuclear magnetic resonance shielding tensors. *J. Chem. Phys.* **1996,** *104*, 5497-5509.
363. Becke, A. D., Density-functional thermochemistry. III. The role of exact exchange. *J. Chem. Phys.* **1993,** *98*, 5648-5652.
364. Lee, C.; Yang, W.; Parr, R. G., Development of the Colle-Salvetti correlation-energy formula into a functional of the electron density. *Phys. Rev. B* **1988,** *37*, 785-789.
365. Marques, M. A. L.; Gross, E. K. U., TIME-DEPENDENT DENSITY FUNCTIONAL THEORY. *Annu. Rev. Phys. Chem.* **2004,** *55*, 427-455.

366. Becke, A. D., Density-functional exchange-energy approximation with correct asymptotic behavior. *Phys. Rev. A* **1988,** *38*, 3098-3100.
367. Grimme, S.; Antony, J.; Ehrlich, S.; Krieg, H., A consistent and accurate ab initio parametrization of density functional dispersion correction (DFT-D) for the 94 elements H-Pu. *J. Chem. Phys.* **2010,** *132*, 154104.
368. Grimme, S.; Ehrlich, S.; Goerigk, L., Effect of the damping function in dispersion corrected density functional theory. *J. Comput. Chem.* **2011,** *32*, 1456-1465.
369. Stanger, A., Nucleus-Independent Chemical Shifts (NICS): Distance Dependence and Revised Criteria for Aromaticity and Antiaromaticity. *J. Org. Chem.* **2006,** *71*, 883-893.